NASA Conference Publication 3345

Flight Mechanics Symposium 1997

Proceedings of a conference held at
Goddard Space Flight Center
Greenbelt, Maryland
May 19 -21, 1997

NASA Conference Publication 3345

Flight Mechanics Symposium 1997

Donna M. Walls, Editor
Goddard Space Flight Center
Greenbelt, Maryland

Proceedings of a conference sponsored by
NASA Goddard Space Flight Center at
Goddard Space Flight Center
Greenbelt, Maryland
May 19 - 21, 1997

National Aeronautics and
Space Administration

Goddard Space Flight Center
Greenbelt, Maryland

1997

This publication is available from the NASA Center for AeroSpace Information,
800 Elkridge Landing Road, Linthicum Heights, MD 21090-2934, (301) 621-0390.

FOREWORD

The papers included here have been presented in summary form at the Flight Mechanics Symposium held May 19-21, 1997, at the Goddard Space Flight Center. For completeness, abstracts have been included for those papers which were presented but unavailable at the time of printing. The papers in this document are presented as received from the authors, with little or no editing.

Page intentionally left blank

CONTENTS

Page

Session 1

Session 2

Session 3

Session 4

Session 5

Session 6

SIMULATION ACCURACY OF AN APPARATUS TO TEST THE STABILITY OF SPINNING SPACECRAFT UNDER THRUST

Dominic M. Halsmer*

Amy R. Fetter**

Maduka C. Chidebelu-Eze**

An experimental laboratory apparatus is being developed to simulate the dynamics and control of spinning, thrusting spacecraft with internal mass motion. This is accomplished by floating a spacecraft model on a spherical air bearing which is accelerated along a circular path. The resultant of centrifugal and gravity forces is kept collinear with the thrust axis, hence serving as the (scaled) thrust force. Sensors provide instantaneous and continuous attitude tracking to determine the circular path characteristics for accurate modeling, and also provide cone angle growth/attenuation rates to determine stability.

A spacecraft in space with rotational kinetic energy will spin about its instantaneous mass center. In general, the mass center will be moving relative to a spacecraft fixed frame due to the presence of internal mass motion and propellant usage. This effect is difficult to simulate in a ground based laboratory using an air bearing since the spacecraft model is constrained to spin about the center of curvature of the bearing surface. Simulation fidelity is optimized by collocating the center of curvature of the bearing and the nominal system mass center of the model.

The dynamical equations of motion of a rigid, symmetric, thrusting, spinning body containing a radial mass-spring-damper are compared to those of a similar ground-based system supported by an air bearing being accelerated along a circular path. Conditions on path radius and velocity for near dynamic equivalence are obtained. Coning stability criteria for the two cases are compared. Stability regions plotted in a parameter space are found to be nearly identical for small damper masses. For a prolate spacecraft, the stability region for the laboratory simulation is a subset of the stability region for the space case. Thus, a laboratory simulation exhibiting coning stability for a prolate configuration implies stability for the actual spin-stabilized thrust maneuver. A quantitative comparison is made between an actual vehicle and a laboratory model.

INTRODUCTION

Establishing the coning stability characteristics of non-rigid, spinning spacecraft in the presence of thrust presents a formidable challenge. The importance of this problem is underscored by instabilities observed during upper-stage firings of certain solid propellant

* Associate Professor, Oral Roberts University, Engineering and Physics Department, Tulsa, OK 74171, (918) 495-6935
** undergraduate engineering student, Oral Roberts University, Engineering and Physics Department

rocket motors[1]. Analytical studies, including computer simulations, have had limited success in characterizing coning stability in these situations[2,3,4,5]. Recent measurements from hot fire tests of spinning scale model motors provide an example of an innovative experimental approach to ground-based investigation of this problem[6], however this method is limited in length of experiment and range of spacecraft characteristics. A non-combustive experimental approach is suggested to allow extensive testing over a wide range of spacecraft parameters. Such an apparatus will allow validation of previous work in this area and provide an additional perspective which is expected to yield further insight into the dynamics and control of such maneuvers. The apparatus is described and analyzed in what follows.

A ground-based, spherical air-bearing can provide near frictionless support for a spacecraft model which is free to spin, precess, and nutate as it would in the zero-g environment of space. An accurate laboratory simulation of this type requires that the model center of mass closely coincide with the center of rotation of the bearing. The vertical, gravitational support force from the stationary bearing can be scaled to model thrust magnitude but its direction is inaccurate for nonzero cone angles.

An experimental apparatus has been described which would provide a laboratory simulation of a spin-stabilized spacecraft in the presence of thrust using a non-stationary bearing.[7] This is accomplished by accelerating the bearing such that the resultant of the gravitational support force and inertial forces (on the spacecraft model) remains aligned at all times with the simulated thrust direction. The magnitude and direction of the bearing acceleration are determined from model attitude information which is continuously monitored and fed back to a closed loop control system.

The research and educational benefits of such a complex apparatus, illustrated in Figure 1, have been discussed[8], however its development and utilization also present considerable challenges. Of primary concern is the degradation in simulation fidelity which arises from the incorporation of oscillatory, internal mass motion. This causes the mass center of the spacecraft model to oscillate about the center of rotation of the accelerated bearing. What follows is an attempt to quantify this effect by comparing the equations of motion (and ensuing stability analyses) of the laboratory model with those of the actual maneuvering spacecraft.

DESCRIPTION OF DYNAMIC MODELS

The models used in this investigation are illustrated in Figure 2. The case of the stationary bearing (fixed base case) was found to be incapable of closely simulating the actual dynamics (space case) for reasons mentioned above, however it did serve as a convenient intermediate step in deriving the equations for the accelerated base case, and provided additional insight into its dynamics. Of primary interest is the comparison of the accelerated base case with the space case.

Model of the Space Case

The model of the space case consists of a symmetric rigid body of mass M, containing a particle of mass m, which is constrained to move in a slot which is perpendicular to the symmetry axis of the body. The symmetry axis is also the nominal spin axis and the thrust axis

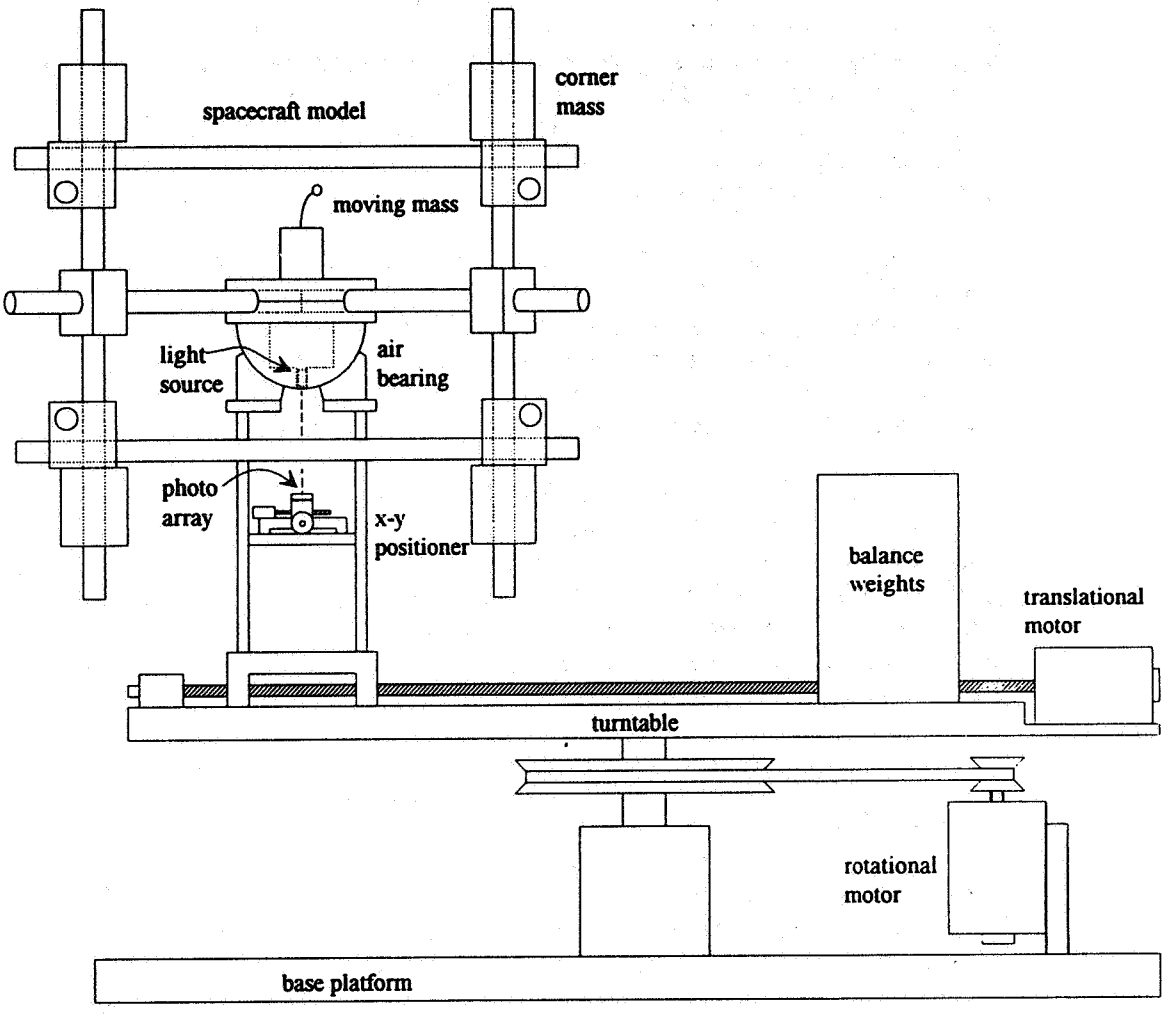

Figure 1. Apparatus Designed to Simulate a Follower Force on a Spacecraft

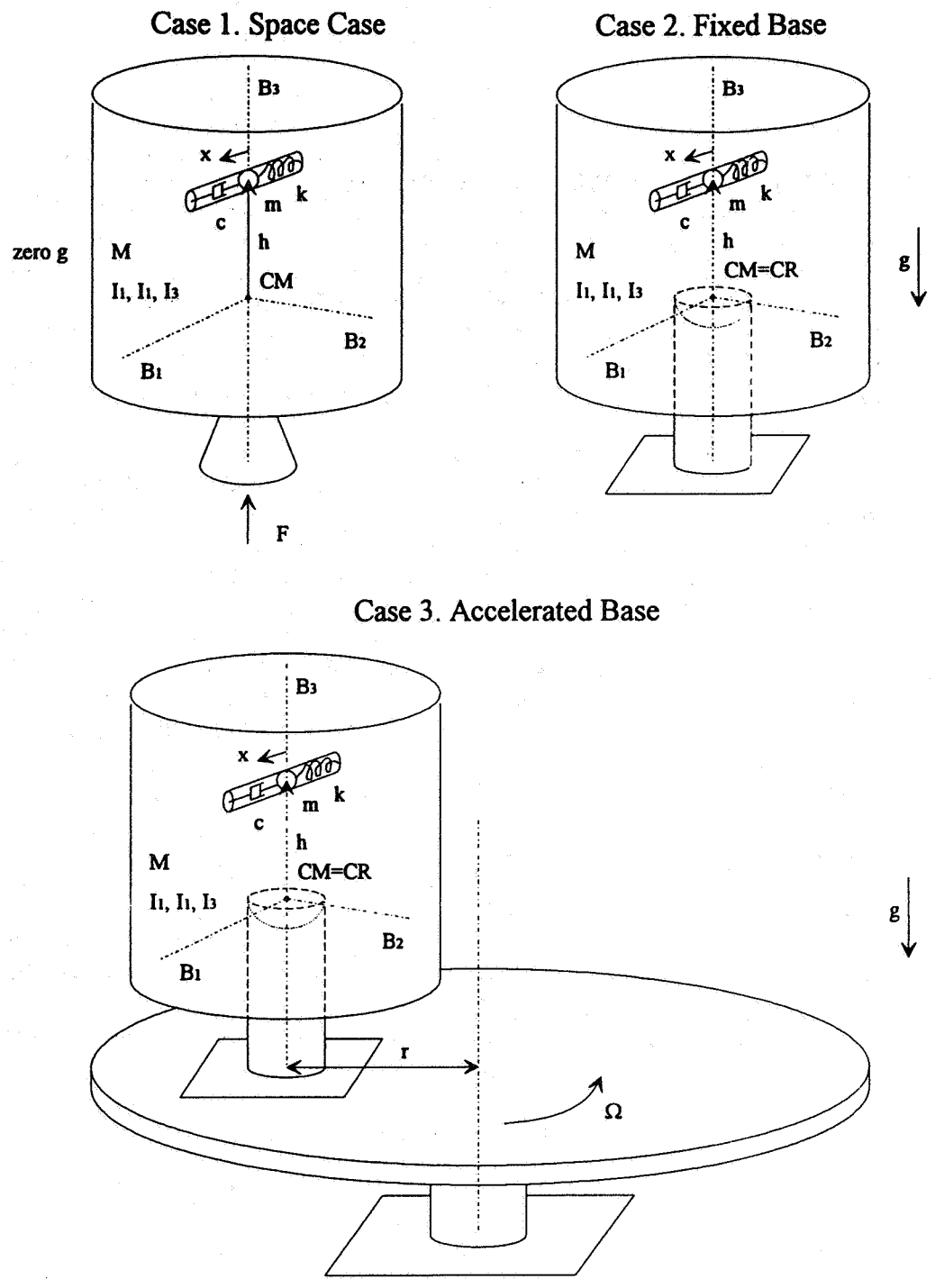

Figure 2. Cases for which Vehicle Attitude Dynamics are Compared

of the vehicle. The moments of inertia of the rigid body I_1, I_1, and I_3 are about axes B_1, B_2, and B_3 respectively. Deviation of the particle position from the symmetry axis is denoted by x which is measured in the direction of the B_1 axis. The transverse axes B_1 and B_2, and the symmetry axis B_3 are fixed in the rigid body and pass through the point CM, coinciding with the system mass center when x is zero. Movement of the particle away from the B_3 axis causes the system mass center to move off the B_3 axis, and produces a linear, elastic restoring force with spring constant k. When the particle is on the B_3 axis, it is a distance h away from the system mass center and the restoring force is zero. The distance h can be positive or negative depending on whether the particle is located fore or aft of the system mass center, respectively. When the particle velocity relative to the rigid body is nonzero, a viscous damping force with coefficient c acts on the particle in a direction opposite to its velocity in the rigid body. The thrust vector F acting along B_3 is a nonconservative force known as a follower force since it remains aligned with B_3 throughout the motion. Finally, the system is taken to be in space where acceleration due to gravity is negligible.

Model of the Accelerated Base Case

The model of the accelerated base case is identical to the model of the space case in all respects except for what follows. Instead of a zero-g environment, the system inhabits a one-g environment. The direction of the gravity force is aligned with the symmetry axis of the body when the cone angle is zero (i.e. pure spin about a vertical axis). Instead of a follower force acting along the symmetry axis, the rigid body is supported such that its nominal (when x is zero) system mass center coincides with the center of rotation of a frictionless, spherical bearing. The bearing is positioned on a horizontal turntable at a radius r. The turntable spins about a vertical axis at a speed Ω. Contrary to what is commonly expected in this environment, a vacuum is assumed, so that air drag on the spinning vehicle is not considered.

NONLINEAR EQUATIONS OF MOTION

Nonlinear Equations for the Space Case

The three governing, nonlinear, rotational equations of motion for the space case are obtained by equating the time derivative of the system angular momentum vector with the sum of the external torques acting on the system. A fourth nonlinear equation governing the motion of the particle is obtained by applying Newton's Second Law to the perturbed particle. Let ω_1, ω_2, and ω_3 be the components of the rigid body angular velocity for axes B_1, B_2, and B_3, respectively. Also let $\mu=m/(M+m)$, and $I_t=I_1+mh^2$. Then the four nonlinear equations of motion can be written as:

$$I_t\dot{\omega}_1 + (I_3 - I_t)\omega_2\omega_3 = mh\left[2\omega_3\dot{x} + (\omega_1\omega_2 + \dot{\omega}_3)x\right] \tag{1}$$

$$I_t\dot{\omega}_2 - (I_3 - I_t)\omega_1\omega_3 = \mu Fx - mh\left[\ddot{x} + (\omega_1^2 - \omega_3^2)x\right] - \mu M\left[2\omega_2 x\dot{x} + (\dot{\omega}_2 - \omega_1\omega_3)x^2\right] \tag{2}$$

$$I_3\dot{\omega}_3 = mh(\dot{\omega}_1 - \omega_2\omega_3)x - \mu M\left[2\omega_3 x\dot{x} + (\dot{\omega}_3 + \omega_1\omega_2)x^2\right] \tag{3}$$

$$\ddot{x} + \frac{c}{m(1-\mu)}\dot{x} + \left[\frac{k}{m(1-\mu)} - (\omega_2^2 + \omega_3^2)\right]x = -\frac{h}{(1-\mu)}(\dot{\omega}_2 + \omega_1\omega_3) \tag{4}$$

Nonlinear Equations for the Accelerated Base Case

The governing nonlinear equations of motion for the accelerated base case are derived by the same method as for the space case. It is convenient in this case to define a set of 3-1-3 Euler angles (ϕ, θ, ψ) relating the orientation of the body fixed frame (B_i) to a laboratory fixed frame. This particular choice of Euler angles is advantageous because ϕ, θ, and ψ correspond to the precession, cone, and spin angles of the body, respectively. In this case three additional, kinematical nonlinear equations are needed to relate the time derivatives of the Euler angles to the components on the angular velocity. In deriving the nonlinear equations of motion for this case, it quickly became clear that the turntable speed needed to match the precession rate (i.e. $\Omega=d\phi/dt$) for any hope of dynamic similarity between this case and the space case. Thus, a constraint on the table speed is already built in to the following equations. In the following equations, $S_\phi=\sin\phi$ and $C_\phi=\cos\phi$, etc. Making use of previously defined notation, the seven nonlinear equations of motion can be written as:

$$I_t\dot{\omega}_1+(I_3-I_t)\omega_2\omega_3=mh\left[2\omega_3\dot{x}+(\omega_1\omega_2+\dot{\omega}_3)x\right] \tag{5}$$

$$I_t\dot{\omega}_2-(I_3-I_t)\omega_1\omega_3=m\left(r\Omega^2S_\theta+gC_\theta\right)x-mh\left[\ddot{x}+\left(\omega_1^2-\omega_3^2\right)x\right]-m\left[2\omega_2x\dot{x}+(\dot{\omega}_2-\omega_1\omega_3)x^2\right] \tag{6}$$

$$I_3\dot{\omega}_3=mh(\dot{\omega}_1-\omega_2\omega_3)x-m\left[2\omega_3x\dot{x}+(\dot{\omega}_3+\omega_1\omega_2)x^2\right]+m\left(r\Omega^2C_\theta-gS_\theta\right)C_\psi x \tag{7}$$

$$\ddot{x}+\frac{c}{m}\dot{x}+\left[\frac{k}{m}-\left(\omega_2^2+\omega_3^2\right)\right]x=-h\left(\dot{\omega}_2+\omega_1\omega_3\right)+\left(r\Omega^2C_\theta-gS_\theta\right)S_\psi \tag{8}$$

$$\dot{\theta}=C_\psi\omega_1-S_\psi\omega_2 \tag{9}$$

$$\dot{\psi}=\omega_3-\left(S_\psi\omega_1+C_\psi\omega_2\right)\cot\theta \tag{10}$$

$$\Omega=\dot{\phi}=\left(S_\psi\omega_1+C_\psi\omega_2\right)\csc\theta \tag{11}$$

Comparison of Nonlinear Equations of Motion

In comparing the nonlinear equations, one notices that the first equation for the space case is identical to the first equation for the accelerated base case. However, a comparison of the other equations reveals apparently significant differences between the dynamics of the two cases. Comparing Eq. (2) with Eq. (6), while anticipating which terms will drop out when linearized for small cone angles, uncovers the need to scale the thrust acceleration to the acceleration of gravity (i.e. $F/(M+m)=g$). In comparing Eqs. (3) and (4) with Eqs. (7) and (8), one notes the troubling presence of terms containing ($r\Omega^2C_\theta$-gS_θ). These can be simply eliminated by requiring that $r\Omega^2C_\theta=gS_\theta$, or $r\Omega^2=g\tan\theta$. Since the table speed is already constrained to be the precession rate, this requirement places a constraint on r, the radius at which the bearing is positioned on the table at any instant in time. Because the main interest of this project is to characterize coning stability for various spacecraft characteristics, and

coning stability can be predicted by analysis of the linearized equations, the nonlinear equations will now be linearized about appropriate solutions.

DEVELOPMENT OF LINEARIZED EQUATIONS OF MOTION

Linearized Equations for the Space Case

The linear equations of motion needed to describe the transverse rotational motion of the spacecraft for small cone angles are obtained by linearizing equations (1) through (4) about the solution: $\omega_1=0$, $\omega_2=0$, ω_3=constant, and $x=0$. This results in the following equations:

$$I_t\dot{\omega}_1 + (I_3 - I_t)\omega_2\omega_3 = 2mh\omega_3\dot{x} \tag{12}$$

$$I_t\dot{\omega}_2 - (I_3 - I_t)\omega_1\omega_3 = \frac{m}{(M+m)}Fx - mh\ddot{x} + mh\omega_3^2 x \tag{13}$$

$$\dot{\omega}_3 = 0 \tag{14}$$

$$\ddot{x} + \frac{c}{m(1-\mu)}\dot{x} + \left[\frac{k}{m(1-\mu)} - \omega_3^2\right]x = -\frac{h}{(1-\mu)}(\dot{\omega}_2 + \omega_1\omega_3) \tag{15}$$

Linearized Equations for the Accelerated Base Case

The linear equations of motion needed to describe the transverse rotational motion of the bearing supported spacecraft model for small cone angles are obtained by linearizing equations (5) through (11) about the solution: $\omega_1=0$, $\omega_2=0$, ω_3=constant, $x=0$, $\theta=0$, $\Omega=0$. Previously derived constraints on table speed and bearing position have been applied. This results in the following equations:

$$I_t\dot{\omega}_1 + (I_3 - I_t)\omega_2\omega_3 = 2mh\omega_3\dot{x} \tag{16}$$

$$I_t\dot{\omega}_2 - (I_3 - I_t)\omega_1\omega_3 = mgx - mh\ddot{x} + mh\omega_3^2 x \tag{17}$$

$$\dot{\omega}_3 = 0 \tag{18}$$

$$\ddot{x} + \frac{c}{m}\dot{x} + \left(\frac{k}{m} - \omega_3^2\right)x = -h(\dot{\omega}_2 + \omega_1\omega_3) \tag{19}$$

Comparison of Linearized Equations of Motion

It is interesting to note that the kinematical equations present in the nonlinear equations for the accelerated base case are no longer needed in the linearized equations since none of the Euler angles appear in the four governing linearized equations. It is also interesting that the first three linearized equations for each case are identical, assuming that the thrust acceleration is scaled to the acceleration of gravity. The last linearized equation for each case, Eqs. (15) and (19), still exhibit a minor difference which will now be explored.

The term (1-μ) appears three times in Eq. (15), but not at all in Eq. (19). Setting μ=0 in Eq. (15) makes it identical to Eq. (19). Recalling that μ represents the ratio of the particle mass to the total system mass, it becomes evident that the stability characteristics of the accelerated base case approach those of the space case as the particle mass approaches zero. In order to understand the extent of the difference between these two cases for finite particle mass, a stability analysis has been conducted for both cases. However, before those results can be presented, it is helpful to further parameterize the equations of motion.

PARAMETERIZATION OF THE LINEARIZED EQUATIONS

The stability analyses of these cases is facilitated by simplifying the linearized equations as much as possible. To this end, let

$$\lambda = (I_3 - I_t)/I_t \tag{20}$$

$$R = \frac{h}{|h|} = \pm 1 \tag{21}$$

$$\tau = \omega_3 t \tag{22}$$

Parameterization of the Space Case

Specific to the space case equations, let:

$$T = \frac{F}{(M+m)h\omega_3^2} \tag{23}$$

$$\xi = \frac{c}{m(1-\mu)\omega_3} \tag{24}$$

$$\gamma^2 = \frac{k}{m(1-\mu)\omega_3^2} \tag{25}$$

$$\delta = \frac{mh^2}{(1-\mu)I_t} \tag{26}$$

$$y = (1-\mu)x/|h| \tag{27}$$

If prime denotes differentiation with respect to τ, equations for the space case simplify to:

$$\omega_1' + \lambda\omega_2 = 2R\delta y' \tag{28}$$

$$\omega_2' - \lambda\omega_1 = -R\delta y'' + R\delta(T+1)y \tag{29}$$

$$y'' + \xi y' + (\gamma^2 - 1)y = -R(\omega_2' + \omega_1) \tag{30}$$

Parameterization of the Accelerated Base Case

Specific to the accelerated base case equations, let:

$$G = \frac{g}{h\omega_3^2} \tag{31}$$

$$\xi_a = \frac{c}{m\omega_3} \tag{32}$$

$$\gamma_a^2 = \frac{k}{m\omega_3^2} \tag{33}$$

$$\delta_a = \frac{mh^2}{I_t} \tag{34}$$

$$z = x/|h| \tag{35}$$

If prime denotes differentiation with respect to τ, equations for this case simplify to:

$$\omega_1' + \lambda\omega_2 = 2R\delta_a z' \tag{36}$$

$$\omega_2' - \lambda\omega_1 = -R\delta_a z'' + R\delta_a(G+1)z \tag{37}$$

$$z'' + \xi_a z' + (\gamma_a^2 - 1)z = -R(\omega_2' + \omega_1) \tag{38}$$

The form of Eqs. (28) to (30) is identical to the form of Eqs. (36) to (38). Therefore, the same procedure for stability analysis applies to both cases.

STABILITY ANALYSIS

The characteristic equation for each case can be found by taking the Laplace transform of the parameterized equations, putting them in matrix form, and forming the determinant of the system matrix. The Routh-Hurwitz criteria was applied to the characteristic equations for both the space case and the accelerated base case, as was documented previously for the space case[9]. The necessary and sufficient conditions for asymptotic stability of coning are:

$$\xi > 0 \tag{39}$$

$$1 - \delta > 0 \tag{40}$$

$$\lambda\left[(\lambda+1)^2 + T\right] > 0 \tag{41}$$

$$\lambda\left[(\gamma^2 - 1)\lambda - (T+1)\delta\right] > 0 \tag{42}$$

for the space case, and:

$$\xi_a > 0 \tag{43}$$

$$1-\delta_a > 0 \tag{44}$$

$$\lambda\left[(\lambda+1)^2+G\right] > 0 \tag{45}$$

$$\lambda\left[\left(\gamma_a{}^2-1\right)\lambda-(G+1)\delta_a\right] > 0 \tag{46}$$

for the accelerated base case. The first condition for each case is always satisfied if the viscous damping coefficient is positive. The second condition for the space case is satisfied if $MI_f > m^2h^2$. This is true unless the particle mass approaches the mass of the spacecraft which is not physically reasonable. Likewise, the second condition for the accelerated base case is always satisfied for all physically reasonable parameter values.

The last two conditions for each case represent the interesting constraints on the parameters which must be met for stability. The resulting stability/instability regions are plotted in the λ versus T (or G in the case of the accelerated base) parameter space in Figure 3. The third condition is the same for both cases, assuming appropriate scaling of the spacecraft acceleration. The stability boundary corresponding to third condition appears as a parabolic curve in the parameter space. The stability boundaries corresponding to conditions (42) and (46) appear as straight lines in the parameter space. Both lines intersect the λ=0 axis at the same point, but have slightly different slopes. By substituting the original variables into the expressions for the slopes, it is discovered that the slope of the space case stability boundary always exceeds (by the amount $\mu m\omega_3{}^2$) that of the accelerated base case. Thus the extent of deviation between the stability regions for these cases depends on the particle to body mass ratio and the spin speed.

DISCUSSION AND FUTURE WORK

The development of the dynamical equations describing the motion of a spacecraft model riding on an accelerated bearing has proven to be fruitful in several ways. In comparing these equations with those of the actual spacecraft, previously suggested[7] constraints on parameters governing the bearing acceleration were independently and rigorously confirmed. Specifically, the turntable spin speed must be controlled to match the model precession rate throughout the simulation. Furthermore, the radius of the bearing position on the turntable must be controlled such that $r=g\tan\theta/\Omega^2$ throughout the simulation. Both of these constraints require immediate feedback of model attitude to highly responsive control mechanisms. The presence of a small time delay associated with the practical implementation of this feedback loop is not expected to significantly effect the fidelity of the simulation. However, this issue may require further investigation.

Comparison of Stability Regions

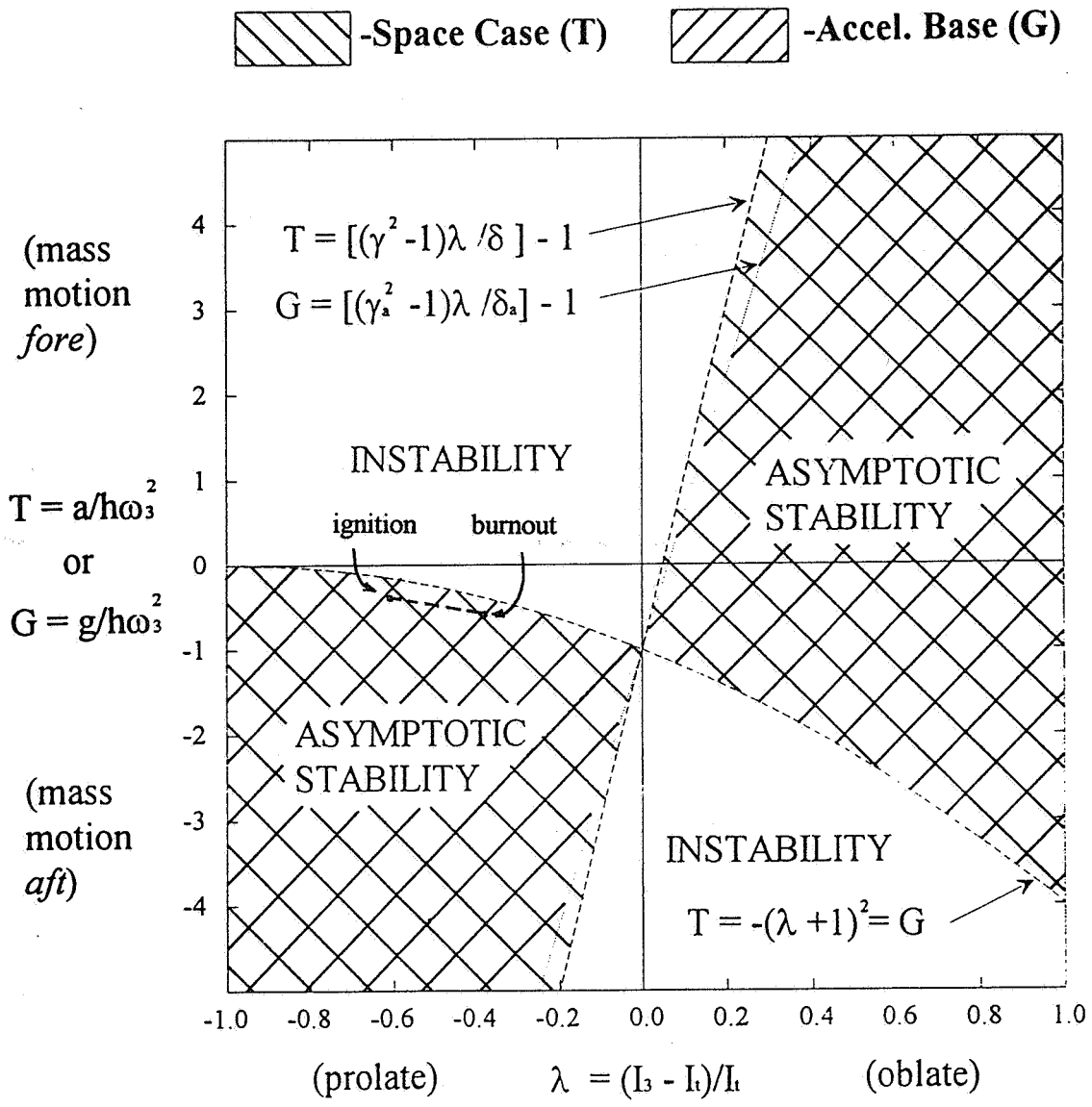

Figure 3. Comparison of Stability Regions for Space Case and Accelerated Base

An additional requirement that was confirmed is the need to scale the spacecraft acceleration due to thrust to that of the acceleration of gravity at the location of the laboratory. Strictly speaking, this severely limits the thrust levels that can be modeled, but not the range of spacecraft characteristics (including thrust level) that can be tested for stability. Recall that the stability regions were plotted in the λ vs. T (or G) parameter space. T is the acceleration divided by the particle axial position and the square of the spin speed. Stability results for a single value of T correspond to a wide range of accelerations if particle axial position and spin speed are allowed to vary. The modeling limitations will become more clearly defined as specific examples are treated. An initial example is investigated in the next section. It is also planned to investigate the effects of air drag on the model during laboratory testing since the laboratory is not anticipated to be in a vacuum. In addition, the analytical results may also be extended to include other types of mass motion such as two-dimensional motion of a particle.

The minor difference in the final stability condition for the two cases is attributed to the oscillation of the system mass center about the bearing center of rotation. This effect is unavoidable in the current plan for the apparatus. However, the quantification of this effect has shown that in many cases, it may be negligible. The stability regions (in particular, the slope of the straight line stability boundary) should be compared for each specific example that is analyzed. Some comfort was obtained by recognizing that certain overarching statements can be made for special spacecraft configurations. Spin stabilized thrust maneuvers are usually conducted by spacecraft that are prolate spinners. (A prolate shape is tall and skinny, with respect to the symmetry axis, while an oblate shape is short and fat.) Since the slope of the stability boundary for the space case always exceeds that of the accelerated base case, the stability region of the space case always contains that of the accelerated base case for all prolate configurations. This indicates that stable behavior in the laboratory simulation of a prolate vehicle implies stability of the spacecraft during the actual spin stabilized thrust maneuver.

Recent work has demonstrated that active moving mass controllers can be effective alternatives to standard coning control strategies[10,11]. It is the opinion of the author that there is potential for effective implementation of both passive and active moving mass controllers, and that the benefits of this technology for thrusting applications is yet to be realized. The development of the kind of apparatus described in this paper is currently being pursued. The objectives are to better understand the dynamics of the situation through experimental testing, and to provide a vehicle for the further investigation of moving mass control schemes for thrusting applications. Figure 4 illustrates a possible configuration for the spacecraft model of such an apparatus. This model contains an additional feature to allow variation in model inertia properties during a test.

EXAMPLE

Estimates of the time constant for nutation growth of the Mars Pathfinder vehicle (during third stage burn) have been prepared based on fuel slosh modeling.[12] The worst case

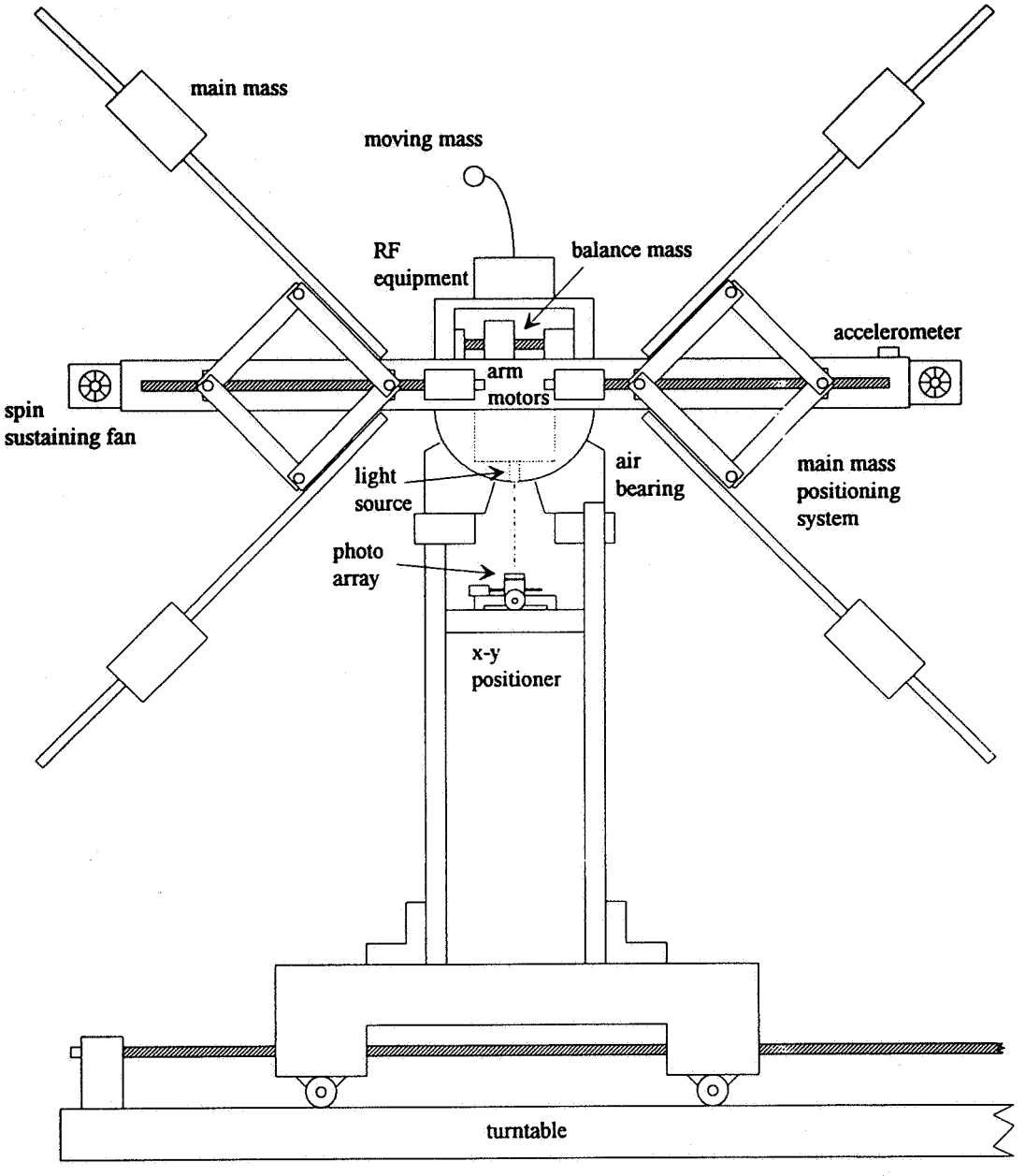

Figure 4. Accelerated Bearing w/ Variable Inertias and Redundant Attitude Sensing (Main mass positioning arms into and out of the page are ommitted for clarity.)

occurs at the maximum spin speed (80 rpm), with time constants of 300 seconds at (just after) ignition, and 100 seconds at (just before) burnout. A mass-spring-damper device was designed to counteract this instability using a linearized rigid body and particle model (space case).[9] The particle in this model is constrained to oscillate in one-dimensional motion with respect to the body. The roots of the characteristic equation for the space case were computed for various compinations of damper parameters. It was found that a damper mass corresponding to 1% of the total vehicle mass at burnout (11 kg) is capable of providing a time constant of 226 seconds at ignition and 96 seconds at burnout. The model producing these time constants does not include the dedamping mechanism, however the smaller damping time constants implies that the total vehicle (with damper and dedamper) should be stable. The damper is 0.7 m aft of the system mass center at ignition and ends up at 1.5 m aft of the mass center at burnout. This is due to the fact that the mass center moves forward 0.8 m during the burn. The damper need not be located along the vehicle centerline. A damping coefficient of c=10 kg/s and a spring constant of k=1000 kg/s^2 provided the necessary performance. A thrust force of 64437 N was used at burnout, along with spin and transverse inertias of 589.5 kg-m^2 and 920.8 kg-m^2 respectively. The path that the model follows on the stability chart is shown in Figure 3.

The proposed laboratory apparatus provides a means to validate the stabilizing mass-spring-damper control approach. The inertia ratio and the Froude number will be matched for the spacecraft and model. The thrust parameter, T on the vertical axis of the stability plot (Figure 3) in the inverse of the Froude number. The ratio of spacecraft acceleration to the acceleration of gravity is 5.93. If this same factor is used to describe the length ratio between the spacecraft and model, then the spin speed of the model will be the same as that of the spacecraft. The mass ratio can be chosen for convenience, say a factor of ten. The roots of the characteristic equation were computed from the linearized equations for the accelerated base case utilizing the aforementioned scaling factors. A time constant of 86 seconds was obtained at burnout. This value is about 10% lower than that of the space case. It is thought that this discrepancy is due to small oscillations of the model mass center about the bearing center of rotation. Obviously, this effect is not present in the space case. This example serves to quantify the accuracy of a laboratory model of this type.

CONCLUSION

A method of laboratory testing to determine the coning stability characteristics of a spin stabilized thrust maneuver has been presented. The nonlinear and linearized equations of the laboratory simulation model were compared to those of the spacecraft in space. Constraints on the operation of the experimental apparatus resulted from the comparison. Necessary and sufficient conditions for coning stability of the model and spacecraft were derived and compared. Stability regions in a parameter space were also compared. Stability regions for model and spacecraft are virtually identical if onboard moving masses are small. For prolate vehicles, the spacecraft stability region completely contains the model stability region. This suggests the value of such an apparatus in validating coning control schemes and predicting actual spacecraft behavior. Results indicate that the modeling fidelity is sufficient

to encourage the further development of such an apparatus for the purpose of providing additional insight into the dynamics and control of spinning spacecraft under thrust.

REFERENCES

1. G. A. Flandro, M. Leloudis, and R. Roach, "Flow Induced Nutation Instability in Spinning Solid Propellant Rockets, Final Report," AL-TR-89-084, 1990.
2. D. L. Mingori and Y. Yam, "Nutational Stability of a Spinning Spacecraft with Internal Mass Motion and Axial Thrust," *Proceedings of the AIAA Astrodynamics Conference*, AIAA, New York, 1986, pp.367-375.
3. A. C. Or, "Rotor-Pendulum Model for the Perigee Assist Module Nutation Anomaly," *J. of Guidance*, Vol. 15, No. 2, March-April, 1992, pp. 297-303.
4. D. M. Halsmer and D. L. Mingori, "Nutational Stability and Passive Control of Spinning Rockets with Internal Mass Motion," *J. of Guidance*, Vol. 18, No. 5, Sept.-Oct., 1995, pp. 1197-1203.
5. Y. Yam, D. L. Mingori, and D. M. Halsmer, "Stability of a Spinning Rocket with Dissipative Internal Mass Motion," to appear in *J. of Guidance*, Vol. 20, No. 2, March-April, 1997, pp. 306-312.
6. J. M. Char, J. H. Yeh, C. L. Chiu, and W. J. Lio, "The Study of Nutation Instability on Spinning Solid Propellant Rockets," AIAA 97-0699, presented at the 35th Aerospace Sciences Meeting, Reno, NV, Jan. 6-10, 1997.
7. R. X. Meyer, "Stability Tests of Spin-Stabilized Spacecraft in the Presence of Thrust," *J. of Guidance*, Vol. 14, No. 1, Jan.-Feb., 1991, pp. 206-208.
8. D. M. Halsmer, W. E. Bair, and P. Ng, "The Spinning Rocket Simulator: An Experimental Design Project for Teaching and Research," *ASEE Annual Conference Proceedings*, Washington, D.C., June 24-26, 1996.
9. D. M. Halsmer, "Nutational Stability and Passive Control of Symmetric Spinning Bodies with Axial Forcing and Internal Mass Motion," Ph.D. Dissertation, University of California at Los Angeles, CA, 1992.
10. J. E. White and R. D. Robinett III, "Principal Axis Misalignment Control for Deconing of Spinning Spacecraft," *J. of Guidance*, Vol. 17, No. 4, July-Aug., 1994, pp. 823-830.
11. R. D. Robinette III, B. R. Sturgis, and S. A. Kerr, "Moving Mass Trim Control for Aerospace Vehicles," *J. of Guidance*, Vol. 19, No. 5, Sept.-Oct., 1996, pp. 1064-1070.
12. D. Woerner, "Mars Pathfinder Launch Vehicle Nutation Analysis," Jet Propulsion Laboratory Interoffice Memorandum, July 19, 1996.

Page intentionally left blank

POLAR SPIN AXIS ANOMALY

Patrick L. Crouse ,Thomas W. Flatley, and Wendy M. Morgenstern
Goddard Space Flight Center (GSFC)
Greenbelt, Maryland

Abstract

The Global Geospace Science (GGS) Polar Plasma Laboratory (POLAR) spacecraft was launched on February 24, 1996, by a Delta II. The spacecraft, a major axis spinner, appeared to function nominally throughout the early mission phase, which included several deployments, and orbit and attitude maneuvers. Of particular interest is the fact that the spacecraft was launched with a deliberate dynamic imbalance. During a segment of early orbit operations, a pair of Lanyard Deployed Booms (LDB) were extended. These booms were not identical; the intent was that the spacecraft would be nearly dynamically balanced after they were deployed. The spacecraft contained two dynamic balance mechanisms intended to fine tune the balance on orbit. However, subsequent images taken by the science instruments on the Despun Platform during the dynamic balancing segment indicated an offset of the principal spin axis from the geometric axis. This offset produced a sinusoidal blurring of the science images sufficiently large to degrade science data below mission requirement specifications. In the end, the imbalance encountered in flight was significantly outside the correction capability of the balances. The purpose of this paper is to examine the flight data during the various deployment and maneuver stages of the early orbit operations coupled with analytical simulations to discuss some of the potential causes of the resultant imbalance.

INTRODUCTION

The Polar Plasma Laboratory (POLAR) spacecraft was launched on February 24, 1996, by a Delta II. The spacecraft, a major axis spinner, appeared to function nominally throughout the early mission phase, which included several deployments, and orbit and attitude maneuvers. The spacecraft was launched with a deliberate dynamic unbalance, i.e., with intentional products of inertia. During early orbit operations, a pair of Lanyard Deployed Booms (LDB) were extended. These booms were not identical; the intent was that the spacecraft would be nearly dynamically balanced after they were deployed. The spacecraft contained two dynamic balance mechanisms intended to fine tune the balance on orbit. However, subsequent images taken by the science instruments on the Despun Platform during the dynamic balancing segment indicated an offset of the principal spin axis from the geometric axis. This offset produced a sinusoidal blurring of the science images sufficiently large to degrade science data below mission requirement specifications. In the end, the imbalance encountered in flight was significantly outside the correction capability of the balances. The purpose of this paper is to examine the flight data during the various deployment and maneuver stages of the early orbit operations coupled with analytical simulations to discuss some of the potential causes of the resultant imbalance. These findings are compared and contrasted with those of the spacecraft manufacturer.

MISSION OVERVIEW AND SPACECRAFT DESCRIPTION

The GGS program is part of the overall International Solar Terrestrial Physics (ISTP) program designed to use multiple spacecraft in complementary orbits to assess processes in the Sun-Earth interaction chain. The GGS program uses POLAR and its sister spacecraft, the Interplanetary Physics Laboratory (WIND)

launched in November 1994, to specifically investigate the solar wind-magnetosphere coupling and the global magnetosphere energy transport. These phenomena include solar wind source and 3-D features, global plasma storage flow and transformation, deposition of energy into the atmosphere, and basic plasma states and characteristics. Both spacecraft were constructed by Lockheed Martin Corporation (formerly the Astrospace Division of General Electric) to be spin stabilized cylindrical spacecraft about 2.44 meters in diameter and 1.85 meters tall. The mission orbit for POLAR is 1.8 X 9.0 Earth Radii (Re) at an inclination of 86°, with the apogee over the North Pole to maximize auroral imaging.

The POLAR spacecraft, shown in Figure 1, has eight science instruments mounted on the spinning main body, and four imaging instruments on the despun platform on the +Z end of the spacecraft. Appendages include four 65-m radial wire antennas, two 6-m long spin axis antenna booms, a search coil, loop antenna, and two 6-m long lanyard deployed booms (LDB). The LDBs are truss-like structures canted downward from the spin plane by 3.5°, and deployed in the +/-X directions with the Magnetic Field Experiment (MFE) instrument on the +X and the Plasma Wave Investigation (PWI) instrument on the -X sides. The four radial wire antennas, referred to as +/-U and +/-V wires, and the six propellant tanks (not shown) are located in the center of gravity (CG) plane to minimize effects of any uncertainties in wire length and fuel distribution on spacecraft balance[1]. In the normal mission mode, POLAR orients the spin axis within 1° of the positive or negative orbit normal vector, and maintains a spin rate of 10 rpm. The selection of $\pm$ orbit normal is based on a Sun angle constraint of 90° to 160° from the +Z-axis due to power and thermal needs.

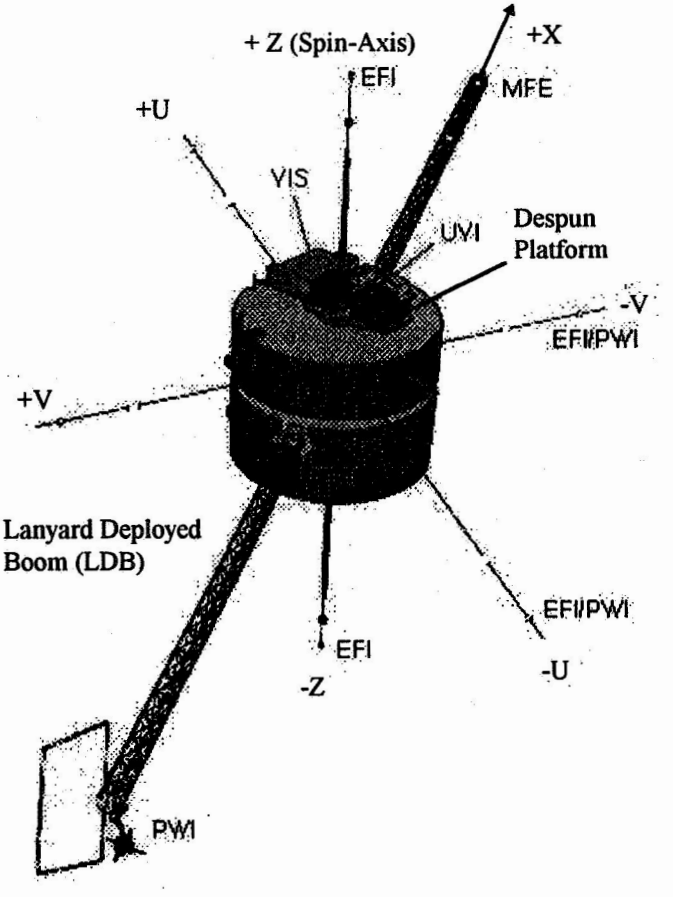

Figure 1: POLAR Spacecraft

OVERVIEW OF ANOMALY

The attitude sensors on the POLAR spacecraft are positioned so that they do not provide observation of a spin-axis offset from the principal axis. The data gathered from a series of propulsive maneuvers, and appendage deployments over the launch and early orbit (L&EO) portion of the mission indicated that the mission was proceeding nominally. During despun platform activation sequence, it was pointed to a selected star which would appear as essentially a single pixel in the instrument field of view. By taking multiple images over time, a spin axis offset would manifest itself as a sinusoidal blurring of the pixel image. The images taken during this dynamic balancing segment indicated an offset of the principal spin axis from the geometric axis of 0.26°, an order of magnitude greater than the 0.02° mission requirement. The pre-launch analysis performed by the spacecraft manufacturer indicated a worst case offset of 0.095° in the XZ plane, and 0.18° in the YZ plane[1]. The dynamic balancer masses were sized accordingly, and constrained as part of a trade study of mass versus propellant reserves. Further study of the on-flight dynamic balancing data revealed that the offset was at a phase angle of 195° which meant it was near the plane of the LDBs, which is the XZ plane. In terms of the products of inertia, the observed offset was approximately three times larger than the worst case analysis, and twice as large as the compensation capability of the balancer[1]. Additionally, movement of the balancers did not produce the predicted change in spin axis offset. Next, the dynamics of the spinning spacecraft at various stages of deployment is examined.

ANALYSIS

The Euler equations of motion are applied to the spacecraft rigid core. The effects of the hydrazine fuel and the wires are included as external torques acting on the core. We will consider only the steady state conditions. Figure 2 illustrates how the torque due to a typical flexible element is computed. Each of the six hydrazine fuel tanks, and the four wires can be characterized as a point mass, m, at a distance ℓ from an attach point, which is at a distance a from the spin axis. All the attach points and the system center of mass are in a plane normal to the nominal spin axis.

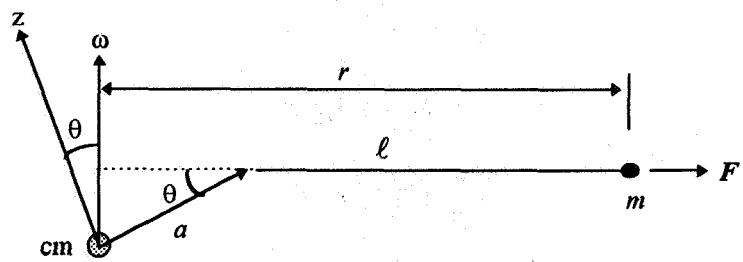

Figure 2: Torque Due to a Flexible Element

The magnitude of the torque due to the forces acting on the elemental mass is

$$T = Fa\sin\theta = ma(a\cos\theta + \ell)\omega^2 \sin\theta$$

The direction of the torque is given by

$$\hat{t} = \frac{\vec{\omega} \times \vec{a}}{a\omega\cos\theta}$$

So the torque vector, $\vec{T}$, is exactly

$$\vec{T} = T\hat{t} = \frac{m\sin\theta(a\cos\theta + \ell)\omega}{\cos\theta}\vec{\omega} \times \vec{a}$$

Assuming that θ is small, then

$$\vec{T} \approx m\sin\theta(a+\ell)\omega\vec{\omega}\times\vec{a} = \frac{m(a+\ell)\vec{\omega}\cdot\vec{a}\vec{\omega}\times\vec{a}}{a}$$

The Six Hydrazine Tanks

The values of m, a and ℓ are the same for each tank. Let $\vec{a}_i$ be a vector from the system center of mass to the center of a typical tank and let $\vec{\omega}$ be the spacecraft angular velocity vector. Let $\vec{a}_0$ be located at an arbitrary azimuth angle (ϕ) away from the +x-axis. The torque generated by each tank is

$$\vec{T}_i = m\,\frac{(a+\ell)}{a}\,\vec{\omega}\cdot\vec{a}_i\vec{\omega}\times\vec{a}_i$$

Table 1: Location of Center of Each Tank

Tank Number	Azimuth Angle	Tank Center Coordinates		
		a_x	a_y	a_z
0	ϕ	$a\cos(\phi)$	$a\sin(\phi)$	0
1	$\phi + \pi/3$	$a\cos(\phi+\pi/3)$	$a\sin(\phi+\pi/3)$	0
2	$\phi + 2\pi/3$	$-a\sin(\phi+\pi/6)$	$a\cos(\phi+\pi/6)$	0
3	$\phi + \pi$	$-a\cos(\phi)$	$-a\sin(\phi)$	0
4	$\phi + 4\pi/3$	$a\sin(\phi-\pi/6)$	$-a\cos(\phi-\pi/6)$	0
5	$\phi + 5\pi/3$	$a\sin(\phi+\pi/6)$	$-a\cos(\phi+\pi/6)$	0

Using the information provided in Table 1, the components of the torque found due to all the tanks is:

$$T_x = -3ma(a+\ell)\,\omega_z\,\omega_y$$
$$T_y = 3ma(a+\ell)\,\omega_z\,\omega_x$$
$$T_z = 0$$

Note that this result is independent of the initial phase angle (ϕ). In general, for any number of symmetrically placed tanks n greater than 2, the component torque is

$$T_x = -\frac{n}{2}ma(a+\ell)\,\omega_z\,\omega_y$$
$$T_y = \frac{n}{2}ma(a+\ell)\,\omega_z\,\omega_x$$
$$T_z = 0$$

The POLAR fuel tank radius is 11.00 in., and the distance from the spin axis to the center of the tanks is 25.10 in. The propellant density is 0.0364 lb/in^3. The remaining fuel in the propellant system is estimated to be 90.16 kg usable and 5.7 kg non-usable for a total of 95.86 kg. Assume that each tank contains 15 kg of hydrazine which contributes to the attenuation of the dynamic imbalance. The location of the center of mass of the hydrazine fuel in a tank is illustrated in Figure 3. To solve for ℓ, we have to compute the location of the center of mass of the remaining fuel. The incremental mass, dm, and the incremental mass moment are found as

$$dm = \rho\pi(r^2 - x^2)dx$$
$$dM = xdm$$

and

$$\ell = \frac{M}{m}$$

Now,

$$m = \rho\pi \int_{x_0}^{r} (r^2 - x^2)dx = \rho\pi \left[r^2 x - \frac{x^3}{3} \right]_{x_0}^{r} = 15\text{kg}$$

MACSYMA was used to obtain $x_0 = 5.37655$ in. Then the mass moment is

$$M = \rho\pi \int_{x_0}^{r} x(r^2 - x^2)dx = \rho\pi \left[\frac{r^2 x^2}{2} - \frac{x^4}{4} \right]_{x_0}^{r} = 242.461$$

Then, $\ell = 7.35$ inches (or 0.19 m), and thus, $ma(a+\ell) = 8\text{kg}\cdot\text{m}^2$.

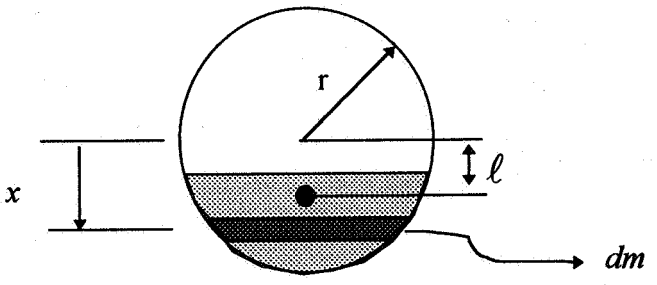

Figure 3: Location of Center of Mass of Hydrazine in Tank

The torques contributing to the dynamic imbalance attenuation are:

$$T_x = -24\omega_z\omega_y$$
$$T_y = 24\omega_z\omega_x$$
$$T_z = 0$$

Prior to the deployment of the LDBs or the wires the spacecraft moment of inertia tensor was, by design,

$$I = \begin{bmatrix} 816.80 & 10.02 & -0.69 \\ 10.02 & 685.40 & 0.31 \\ -0.69 & 0.31 & 830.50 \end{bmatrix}$$

The steady state spin axis associated with the above tensor may be found approximately by considering the first two equations arising from the condition $\vec{\omega} \times \vec{H} = 0$, where $\vec{H} = I\vec{\omega}$ is the spacecraft angular momentum vector. This relationship may be expressed by:

$$\begin{bmatrix} 0 & -\omega_z & \omega_y \\ \omega_z & 0 & -\omega_x \\ -\omega_y & \omega_x & 0 \end{bmatrix} \begin{bmatrix} 816.80 & 10.02 & -0.69 \\ 10.02 & 685.40 & 0.31 \\ -0.69 & 0.31 & 830.50 \end{bmatrix} \begin{bmatrix} \omega_x \\ \omega_y \\ \omega_z \end{bmatrix}$$

Linearized in ω_x and ω_y, the first two equations are given by:

$$10.02\ \omega_x - 145.1\ \omega_y = -0.31\ \omega_z$$
$$13.7\ \omega_x - 10.02\ \omega_y = -0.69\ \omega_z$$

Solving these equations for ω_x/ω_z and ω_y/ω_z yields

$$\omega_x/\omega_z = -0.0514$$
$$\omega_y/\omega_z = -0.00141$$

This represents a tilt of about 3°, almost completely in the -x direction.

If we include the influence of the fuel, the equation of interest becomes:

$$\begin{bmatrix} 0 & -\omega_z & \omega_y \\ \omega_z & 0 & -\omega_x \\ -\omega_y & \omega_x & 0 \end{bmatrix} \begin{bmatrix} 816.80 & 10.02 & -0.69 \\ 10.02 & 685.40 & 0.31 \\ -0.69 & 0.31 & 830.50 \end{bmatrix} \begin{bmatrix} \omega_x \\ \omega_y \\ \omega_z \end{bmatrix} = \begin{bmatrix} -24\omega_y\omega_z \\ 24\omega_x\omega_z \\ 0 \end{bmatrix}$$

Again linearizing in ω_x and ω_y, the first two equations become

$$10.02\ \omega_x - 169.1\ \omega_y = -0.31\ \omega_z$$
$$37.7\ \omega_x - 10.02\ \omega_y = -0.69\ \omega_z$$

The solution to these equations is

$$\omega_x/\omega_z = -0.0181$$
$$\omega_y/\omega_z = 0.0008$$

This represents a 1° degree tilt in the -x direction, so the fuel has attenuated the dynamic imbalance by a factor of three.

The Wires

Recall that the torques due to the wires are given by

$$\vec{T} = \frac{m(a+\ell)}{a}\vec{\omega}\cdot\vec{a}\vec{\omega}\times\vec{a}$$

where the $\vec{a}$ vectors locate the roots of the deployed wires. There are two U-wires, deployed to the same length, nominally extending radially outward from the spin axis in the first and third quadrants of the XY plane. Likewise, a pair of V-wires are deployed in the second and fourth quadrants. The component torques due to the U-wires are given by

$$T_{x_u} = -m_u a(a+\ell_u)(\omega_x+\omega_y)\omega_z$$
$$T_{y_u} = m_u a(a+\ell_u)(\omega_x+\omega_y)\omega_z$$

where m_u is the mass and ℓ_u is the length of the deployed portion of the U-wires. The torques due to the V-wires are

$$T_{x_v} = m_v a(a+\ell_v)(\omega_x-\omega_y)\omega_z$$
$$T_{y_v} = m_v a(a+\ell_v)(\omega_x-\omega_y)\omega_z$$

For all wires, a = 1.19 meters. The first deployment was that of the U-wires, which were simultaneously deployed to a length of 20 meters. The mass of wire deployed was 0.395 kg and the wire center of mass was 14.96 meters from the root.

This produced the torques:

$$T_x = -7.59(\omega_x + \omega_y)\omega_z$$
$$T_y = 7.59(\omega_x + \omega_y)\omega_z$$

The rigid core mass properties changed slightly, and the equilibrium equations become:

$$\begin{bmatrix} 0 & -\omega_z & \omega_y \\ \omega_z & 0 & -\omega_x \\ -\omega_y & \omega_x & 0 \end{bmatrix} \begin{bmatrix} 816.20 & 10.60 & -0.69 \\ 10.60 & 684.80 & 0.31 \\ -0.69 & 0.31 & 829.30 \end{bmatrix} \begin{bmatrix} \omega_x \\ \omega_y \\ \omega_z \end{bmatrix} = \begin{bmatrix} -24\omega_y\omega_z - 7.59(\omega_x + \omega_y)\omega_z \\ 24\omega_x\omega_z + 7.59(\omega_x + \omega_y)\omega_z \\ 0 + \text{second order terms} \end{bmatrix}$$

The solution of these equations is

$$\omega_x/\omega_z = -0.01534$$
$$\omega_y/\omega_z = 0.00150$$

Spin Axis Determination in Symbolic Form

Now consider the spin axis determination. The rigid core moment of inertia tensor is given by

$$I = \begin{bmatrix} I_{xx} & -I_{xy} & -I_{xz} \\ -I_{xy} & I_{yy} & -I_{yz} \\ -I_{xz} & -I_{yz} & I_{zz} \end{bmatrix}$$

Let the rigid core angular velocity vector be given by

$$\vec{\omega} = \begin{bmatrix} \omega_x \\ \omega_y \\ \omega_z \end{bmatrix}$$

The Euler Equations of Motion for the rigid core are

$$I\frac{d\vec{\omega}}{dt} + \vec{\omega} \times I\vec{\omega} = \vec{T}$$

where $\vec{T}$ is the external torque vector. At equilibrium, or steady state rotation, $\vec{\omega}$ is a constant, therefore

$$\begin{bmatrix} 0 & -\omega_z & \omega_y \\ \omega_z & 0 & -\omega_x \\ -\omega_y & \omega_x & 0 \end{bmatrix} \begin{bmatrix} I_{xx}\omega_x - I_{xy}\omega_y - I_{xz}\omega_z \\ -I_{xy}\omega_x + I_{yy}\omega_y - I_{yz}\omega_z \\ -I_{xz}\omega_x - I_{yz}\omega_y + I_{zz}\omega_z \end{bmatrix} = \begin{bmatrix} T_x \\ T_y \\ T_z \end{bmatrix}$$

Expanding further, with ω_x and ω_y considered small, the first two linearized equations become

$$-\omega_z(-I_{xy}\omega_x + I_{yy}\omega_y - I_{yz}\omega_z) + \omega_y(I_{zz}\omega_z) = T_x$$
$$\omega_z(I_{xx}\omega_x - I_{xy}\omega_y - I_{xz}\omega_z) - \omega_x(I_{zz}\omega_z) = T_y$$

or

$$I_{xy}\omega_x + (I_{zz} - I_{yy})\omega_y = T_x - I_{yz}\omega_z$$
$$(I_{xx} - I_{zz})\omega_x - I_{xy}\omega_y = T_y + I_{xz}\omega_z$$

or, if we decompose the external torque into fuel and wire components,

$$I_{xy}\omega_x + (I_{zz} - I_{yy})\omega_y = T_{x_f} + T_{x_u} + T_{x_v} - I_{yz}\omega_z$$
$$(I_{xx} - I_{zz})\omega_x - I_{xy}\omega_y = T_{y_f} + T_{y_u} + T_{y_v} + I_{xz}\omega_z$$

Let $k_f = 3ma(a+\ell)$, then the torque due to the fuel is

$$T_{x_f} = -k_f\omega_z\omega_y$$
$$T_{y_f} = k_f\omega_z\omega_x$$

The equations then become

$$I_{xy}\omega_x + (I_{zz} - I_{yy} + k_f\omega_z)\omega_y = T_{x_u} + T_{x_v} - I_{yz}\omega_z$$
$$(I_{xx} - I_{zz} - k_f\omega_z)\omega_x - I_{xy}\omega_y = T_{y_u} + T_{y_v} + I_{xz}\omega_z$$

If we let $k_u = m_u a(a+\ell_u)$ and $k_v = m_v a(a+\ell_v)$, and substitute for the torques, then

$$\left[I_{xy} + (k_u - k_v)\right]\frac{\omega_x}{\omega_z} + \left[(I_{zz} - I_{yy}) + (k_f + k_u + k_v)\right]\frac{\omega_y}{\omega_z} = -I_{yz}$$
$$\left[(I_{xx} - I_{zz}) - (k_f + k_u + k_v)\right]\frac{\omega_x}{\omega_z} - \left[I_{xy} + (k_u - k_v)\right]\frac{\omega_y}{\omega_z} = I_{xz}$$

These are simultaneous equations with ω_x/ω_z and ω_y/ω_z as unknowns which may be solved to find the body rates ratios.

Sun Angle Change

The Sun aspect angle at the time of the first deployment was approximately 95.3° and it changed by +0.12° during the deployment. This is the angle between the geometric z-axis and the Sun vector, measured once per spin by a slit Sun sensor 65° away from the +x-axis in the direction of the +y-axis. Let θ be the measured angle. The Sun vector in body coordinates at the time the angle is measured is given by

$$S_x = \sin(\theta)\cos(65)$$
$$S_y = \sin(\theta)\sin(65)$$
$$S_z = \cos(\theta)$$

Flight data shows that the fuel and the deployed wires constitute an extremely effective nutation damper. The spacecraft also contains a fluid-filled loop passive damper. The consequence of this damping is that

the angular velocity vector (in addition to the angular momentum vector) remains inertially fixed during the deployment. Since the Sun vector is also nearly inertially fixed, we can calculate a predicted Sun angle change during the deployment by assuming that $\vec{\omega}\cdot\vec{S}$ is constant.

From results given above, before deployment we have ω_x/ω_z = - 0.0181 and ω_y/ω_z = 0.0008, and a Sun angle of 95.3°. After deployment, we have ω_x/ω_z = - 0.01534 and ω_y/ω_z = 0.0015 and we let the Sun angle be 95.3 + q degrees.

$$\left.\frac{\vec{\omega}\cdot\vec{S}}{\omega_z}\right|_{\text{Pre-deploy}} = -0.0181\sin(95.3)\cos(65) + 0.008\sin(95.3)\sin(65) + \cos(95.3)$$

$$\left.\frac{\vec{\omega}\cdot\vec{S}}{\omega_z}\right|_{\text{Post-deploy}} = -0.01534\sin(95.3+q)\cos(65) + 0.0015\sin(95.3+q)\sin(65) + \cos(95.3+q)$$

Equating these two dot products and solving for q, we find q = 0.10° compared to a measured change of 0.12° or 17% lower.

Sun Angle Change in Symbolic Form

As previously noted, when the Sun passes through the Sun sensor field of view, the Sun unit vector has the components

$$S_x = \sin(\theta)\cos(65)$$
$$S_y = \sin(\theta)\sin(65)$$
$$S_z = \cos(\theta)$$

After a configuration change, assume that the new Sun vector is given by

$$S_x' = \sin(\theta)\cos(65)$$
$$S_y' = \sin(\theta)\sin(65)$$
$$S_z' = \cos(\theta)$$

Assume that the Sun angle change is q, i.e. let $\theta = \theta + q$. Then, using the trigonometric identity,

$$\sin(\theta) = \sin(\theta)\cos(q) + \cos(\theta)\sin(q)$$
$$\cos(\theta) = \cos(\theta)\cos(q) - \sin(\theta)\sin(q)$$

For q<<1, we have the approximations

$$\sin(\theta) = \sin(\theta) + q\cos(\theta)$$
$$\cos(\theta) = \cos(\theta) - q\sin(\theta)$$

and

$$S_x' = \left[\sin(\theta) + q\cos(\theta)\right]\cos(65)$$
$$S_y' = \left[\sin(\theta) + q\cos(\theta)\right]\sin(65)$$
$$S_z' = \cos(\theta) - q\sin(\theta)$$

Now, let the initial angular velocity vector be given by [ω_x,ω_y,1] and the new angular velocity vector by [ω_x',ω_y',1]. For $\vec{\omega}\cdot\vec{S}$ constant, we have

$$\frac{\omega_x}{\omega_z}S_x+\frac{\omega_y}{\omega_z}S_y+S_z=\frac{\omega_x'}{\omega_z}S_x'+\frac{\omega_y'}{\omega_z}S_y'+S_z'$$

or

$$\frac{\omega_x}{\omega_z}\sin\theta\cos65+\frac{\omega_y}{\omega_z}\sin\theta\sin65+\cos\theta=\frac{\omega_x'}{\omega_z}(\sin\theta+q\cos\theta)\cos65+\frac{\omega_y'}{\omega_z}(\sin\theta+q\cos\theta)\sin65-q\sin\theta$$

This equation may be solved for q, the Sun angle change

$$q=\frac{\sin\theta\left[\cos65\left(\frac{\omega_x}{\omega_z}-\frac{\omega_x'}{\omega_z}\right)+\sin65\left(\frac{\omega_y}{\omega_z}-\frac{\omega_y'}{\omega_z}\right)\right]}{\cos\theta\left(\frac{\omega_x'}{\omega_z}\cos65+\frac{\omega_y'}{\omega_z}\sin65\right)-\sin\theta}$$

Substituting in the numbers presented above and solving i.e., $\omega x/\omega z = -0.0181$, $\omega y/\omega z = 0.0008$, $\omega x'/\omega z = -0.01534$ and $\omega y'/\omega z = 0.0015$ and $\theta = 95.3$ degrees, we find that $q = 0.0018$ radians or 0.10°.

Products of Inertia Determined by Sun Angle Changes

Suppose that the critical products of inertia I_{xz} and I_{yz} are treated as unknowns, while all the other moment of inertia tensor elements are known. All wire deployments are symmetrical and do not change these products. Consider now a wire deployment event for which a Sun angle change is measured, such as the one just described above. There are five equations involved, and all parameters are known except for the two products of inertia:

$$\Rightarrow \quad \left[I_{xy}+(k_u-k_v)\right]\frac{\omega_x}{\omega_z}+\left[(I_{zz}-I_{yy})+(k_f+k_u+k_v)\right]\frac{\omega_y}{\omega_z}=-I_{yz}$$

$$\Rightarrow \quad \left[(I_{xx}-I_{zz})-(k_f+k_u+k_v)\right]\frac{\omega_x}{\omega_z}-\left[I_{xy}+(k_u-k_v)\right]\frac{\omega_y}{\omega_z}=I_{xz}$$

$$\Rightarrow \quad \left[I_{xy}'+(k_u'-k_v')\right]\frac{\omega_x'}{\omega_z'}+\left[(I_{zz}'-I_{yy}')+(k_f'+k_u'+k_v')\right]\frac{\omega_y'}{\omega_z'}=-I_{yz}$$

$$\Rightarrow \quad \left[(I_{xx}'-I_{zz}')-(k_f'+k_u'+k_v')\right]\frac{\omega_x'}{\omega_z'}-\left[I_{xy}'+(k_u'-k_v')\right]\frac{\omega_y'}{\omega_z'}=I_{xz}$$

$$\Rightarrow \quad q=\frac{\sin\theta\left[\cos65\left(\frac{\omega_x}{\omega_z}-\frac{\omega_x'}{\omega_z}\right)+\sin65\left(\frac{\omega_y}{\omega_z}-\frac{\omega_y'}{\omega_z}\right)\right]}{\cos\theta\left(\frac{\omega_x'}{\omega_z}\cos65+\frac{\omega_y'}{\omega_z}\sin65\right)-\sin\theta}$$

Combining these equations yields a constraint on the products I_{xz} and I_{yz}. An equation of the form

$$AI_{xz}+BI_{yz}=C$$

where A, B and C are known constants. There are two movable masses on the spacecraft, intended to fine tune the rigid core products of inertia, I_{xz} and I_{yz}, ideally to zero. Dynamic Balancer No. 1 (DB_1) is located at x = - 0.33 m and y =1.01 m. DB_2 is located at x = -1.01 m and y = - 0.33 m. The range of motion is +/- 0.51 m (20 in.). The DB_1 mass weighs 2.56 kg, so its adjustment capability is $I_{xz} = 0.43\text{kg}\cdot\text{m}^2$ and $I_{yz} = 1.32\text{kg}\cdot\text{m}^2$. The mass of DB_2 is 2.74 kg, and the capability to affect the products of inertia is $I_{xz} = 1.41\text{kg}\cdot\text{m}^2$ and $I_{yz} = 0.46\text{kg}\cdot\text{m}^2$.

Tables 2-4 illustrate the 17 major deployment events, in addition to spin, spin axis attitude, and orbit maneuvers, that occurred during the first 34 days. Table 2 contains the spacecraft dry core inertias, while Table 3 shows the values for k_f, k_u, and k_v at each stage. Table 4 shows the measured Sun angle at each stage, as well as both the observed and predicted change in Sun angle as a result of the event. The predicted change is calculated following the analysis outlined above. The search coil deploy (event 5), the lanyard deployed boom (8), the despun platform activation (14), and the movement of dynamic balancer number 2 (15) are of particular interest. The difference between the observed Sun angle change, and the predicted change for these events are about 3 to 5 times greater than the other events. The next step then was to examine the flight data more closely in search of infomation that went unnoticed during this operations period.

LAUNCH AND EARLY ORBIT REVIEW

The following sections are based on observed data during mission operations, and are described in greater detail in both Reference 1 and 2. The initial on-orbit assessment of the spacecraft shortly after launch indicated that a nominal injection had occurred. The measured spin rate was 48.1 rpm and the Sun angle was 60.7°, and the expected values were 48.2 rpm and 60.3°, respectively. Immediately, a maneuver planned to move the spacecraft to a thermal- and power-safe attitude was initiated, but one thruster failed. A backup maneuver plan was prepared, and the maneuver was completed. The Sun angle measured was 96.3°, when the target had been 95.0°. The differences in what was achieved versus what was expected was not an issue at the time, due to the large degree of uncertainty in injection attitude, and thruster performance, and the large operating range that was deemed acceptable.

Table 2: Dry Core Moments of Inertias for Deployment Phases

	Configuration	Corresponding Dry Core Inertias (kg-m^2)					
		I_{xx}	I_{yy}	I_{zz}	I_{xy}	I_{xz}	I_{yz}
1	**Pre-Deployment**	816.800	685.400	830.500	-10.020	0.690	-0.310
2	**U-Wires to 20 m**	816.200	684.800	829.300	-10.600	0.690	-0.310
3	**V-Wires to 20 m**	815.600	684.200	828.200	-10.020	0.690	-0.310
4	**Loop Antenna Deploy**	815.500	685.100	828.900	-10.050	0.870	-0.220
5	**Search Coil Deploy**	815.100	685.500	829.700	-9.990	0.670	-0.280
6	**Hat Jettison**	815.100	685.500	829.700	-9.990	0.670	-0.280
7	**U-Wires to 35 m**	814.900	685.300	829.300	-10.160	0.670	-0.280
8	**LDB Deployment**	822.500	1338.300	1474.900	-11.990	0.150	-0.150
9	**V-Wires to 35 m**	822.300	1338.100	1474.600	-11.820	0.150	-0.150
10	**U-Wires to 50 m**	822.100	1338.000	1474.300	-11.990	0.150	-0.150
11	**V-Wires to 50 m**	821.900	1337.800	1473.900	-11.820	0.150	-0.150
12	**U-Wires to 65 m**	821.800	1337.600	1473.600	-11.990	0.150	-0.150
13	**Z Boom Deployment**	865.600	1381.400	1473.600	-11.990	0.150	-0.150
14	**DSP Activation**	861.400	1385.600	1445.900	-12.100	0.040	0.030
15	**DB2 +17.5 inches**	861.941	1386.140	1445.900	-12.100	-1.187	-0.372
16	**DB2 +2.5 inches**	862.106	1386.310	1445.900	-12.100	-1.362	-0.429
17	**DB1 +8.6 inches**	862.229	1386.430	1445.900	-12.100	-1.547	0.134

Table 3: Values of k_f, k_u, and k_v for Various Deployment Phases

	Configuration	Fuel in each tank (kg)	Wire Lengths		k_f	k_u	k_v
			U-wire lengths (m)	V-wire lengths (m)			
1	Pre-Deployment	15.0	0.0	0.0	26.4	0.0	0.0
2	U-Wires to 20 m	15.0	20.0	0.0	26.4	7.6	0.0
3	V-Wires to 20 m	15.0	20.0	20.0	26.4	7.6	7.6
4	Loop Antenna Deploy	15.0	20.0	20.0	26.4	7.6	7.6
5	Search Coil Deploy	15.0	20.0	20.0	26.4	7.6	7.6
6	Hat Jettison	15.0	20.0	20.0	26.3	5.9	5.9
7	U-Wires to 35 m	15.0	35.0	20.0	26.3	13.0	5.9
8	LDB Deployment	15.0	35.0	20.0	26.3	13.0	5.9
9	V-Wires to 35 m	15.0	35.0	35.0	25.8	13.0	13.0
10	U-Wires to 50 m	15.0	50.0	35.0	25.8	22.4	13.0
11	V-Wires to 50 m	15.0	50.0	50.0	25.6	22.4	22.4
12	U-Wires to 65 m	15.0	65.0	50.0	25.6	34.1	22.4
13	Z Boom Deployment	15.0	65.0	50.0	25.6	34.1	22.4
14	DSP Activation	15.0	65.0	50.0	25.5	34.1	22.4
15	DB2 +17.5 inches	15.0	65.0	50.0	25.5	34.1	22.4
16	DB2 +2.5 inches	15.0	65.0	50.0	25.5	34.1	22.4
17	DB1 +8.6 inches	15.0	65.0	50.0	25.5	34.1	22.4

Table 4: Calculation of Spin Axis Offset and ΔSun Angle versus ΔObserved Sun Angle

	Configuration	Spin Axis Tilt By Calculation		Approximate Sun Angle (deg)	ΔObserved Sun Angle (deg)	ΔCalculated Sun Angle (deg)
		Amplitude (deg)	Phase (deg)			
1	Pre-Deployment	0.975348	177.258749	0.0000	0.0000	0.0000
2	U-Wires to 20 m	0.83842	174.15018	95.3000	0.1200	0.095175
3	V-Wires to 20 m	0.721361	175.477407	95.5100	0.0300	0.023154
4	Loop Antenna Deploy	0.903309	178.792525	96.4000	-0.1200	-0.110832
5	Search Coil Deploy	0.676216	175.751944	96.2800	0.1600	0.123519
6	Hat Jettison	0.721346	176.139059	97.6000	-0.0300	-0.022636
7	U-Wires to 35 m	0.645191	173.380901	97.7700	0.0700	0.058443
8	LDB Deployment	0.048471	104.321606	98.4000	0.3000	0.243308
9	V-Wires to 35 m	0.046379	104.296719	127.8500	-0.0100	-0.001606
10	U-Wires to 50 m	0.044977	105.33082	127.7600	0.0100	-0.001605
11	V-Wires to 50 m	0.042498	105.318298	125.2900	-0.0150	-0.001886
12	U-Wires to 65 m	0.041092	106.540249	125.2100	0.0100	-0.001646
13	Z Boom Deployment	0.050834	104.162574	123.5000	0.005	0.008656
14	DSP Activation	0.012568	-105.907236	121.7000	-0.0900	-0.051855
15	DB2 +17.5 inches	0.181985	55.835873	110.0000	0.2500	0.199719
16	DB2 +2.5 inches	0.209727	55.994845	109.0000	0.0400	0.027476
17	DB1 +8.6 inches	0.143644	-22.06278	108.0000	-0.2200	-0.199709

Search Coil and Lanyard Deployed Boom Deployments

The deployment of the PWI Search Coil was not a big event from a flight dynamics perspective, considering that the primary concern at the time was spacecraft spin rate maintenance, and this event was to produce a negligible change in spin rate. The loop antenna failed to latch properly initially, and bounced against its stops. It did latch up during a subsequent spin up maneuver, and is behaving nominally. The observed change in the Sun angle did match well with simulations performed by the spacecraft manufacturer[1]. In addition, the spacecraft was nutating at the time of the deploy, which makes the observed data less reliable.

The lanyard deployed boom (LDB) sequence appears to be more interesting. At the time, the LDB deploy seemed nominal, mainly because it produced the expected final spacecraft spin rate, and the critical criteria for operations was for the booms to deploy at the same rate. Looking closer, there is an unexpected simultaneous change in both the Sun angle, and the accelerometer measurement about two minutes into the deployment. Plots of both the Sun angle, and the accelerometer data are presented in Figures 4 and 5. Review of WIND data, which also had LDB deployments, showed no such signature. However, steady-state values of the Sun angle following the maneuver indicate a nominal change in spin axis location as a result of this deploy.

Two other data transients are seen in both the Sun and accelerometer data at 12 and 30 hours following the deployment. The 18 hour difference constitutes a single orbit. These times are coincident with orbit perigee crossing, and it was believed it was due to gravity gradient effects. But in a deployed state, the effects should theoretically only produce about 0.01° change with no hysteresis[3]. This compares well with the observed values of 0.02°. However, between the transients, there is a constant migration of the spin axis that amounts to about 0.1-0.23°. The Magnetic Field Experiment (MFE) also measured a change in the angle between the magnetic x-axis and the spacecraft spin axis of about 0.35°. Subsequent analysis indicated that if the LDB failed, the MFE would always measure a larger angle than that calculated for the spacecraft body. The information suggests that the LDB suffered a permanent deformation, which has caused a significant change in spacecraft mass properties[1].

Despun Platform Activation and Dynamic Balancing

The despun platform was activated following pyro firing. Review of this activation suggests that the firing would have caused a large mechanical disturbance to both booms, and may have caused a shift in either non-rigid boom1. However, the disturbance should not have caused the LDB to fail, and does not explain the events mentioned above. The platform was stepped up to 10 rpm to despin it from the spacecraft main body, transmitting momentum to the spacecraft and spinning it up slightly as expected. The FDD calculated the platform pointing (not spin axis) to be about 0.2° from that done onboard the satellite, but the discrepancy was attributed to imbalances, and decreased significantly following the first round of dynamic balancing. During dynamic balancing, the spin axis did not move as expected for the commanded balance mass movement. This is further indication of a change in spacecraft mass properties from what was expected.

CONCLUSIONS

A change in mass properties from those expected have caused the POLAR spin axis offset. The reason for the mass properties change is less clear. The spacecraft manufacturer, as detailed in Reference 1, performed a complete analysis of the failure scenarios, and identified some possibilities. Pre-launch analysis was reviewed, and no errors were discovered, although final spacecraft close out activities did introduce some uncertainties. Masses at the ends of the LDB had the right magnitude to cause the imbalance. Review of the procedures showed the proper weight installed, but photos do not definitively

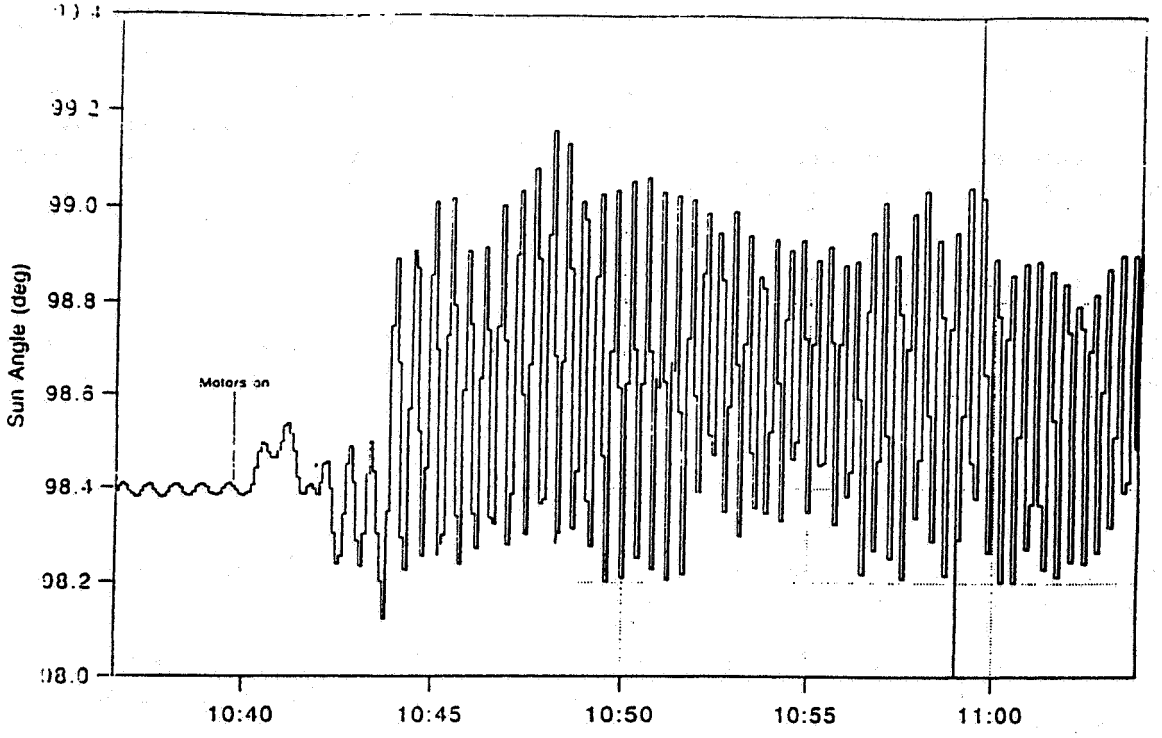

Figure 4: Lanyard Boom Deployment Sun Angle Data

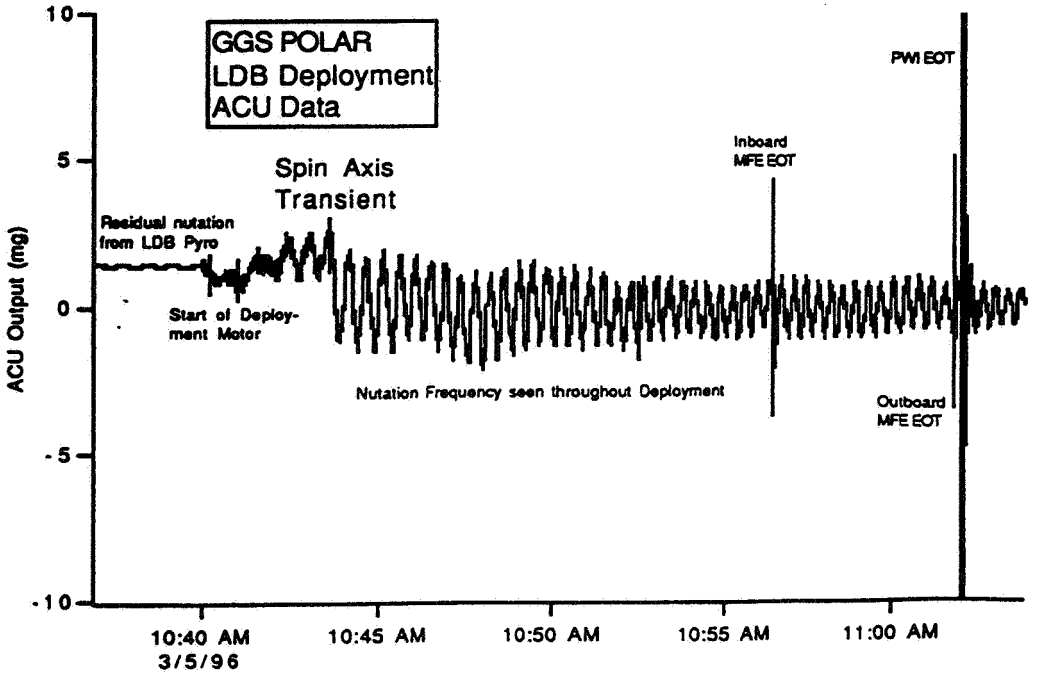

Figure 5: Lanyard Boom Deployment Accelerometer Data

show the masses as present since they would have been beneath a thermal blanket. Since the spin axis offset is in the plane of the LDB, and there is evidence of anomalous behavior during and after the deployment, the LDBs are the most likely cause of the imbalance. The properties are such that a 0.5° misalignment of one boom, or 0.25° of both booms, would cause the observed offset. While we may never know for sure, the authors share this conclusion with the spacecraft manufacturer. One positive note to make about this anomaly is that since the blurring of the science data is such a well defined pattern, post-processing software is able to recover the measurements for scientific analysis.

ACKNOWLEDGMENTS

The authors would like to thank Keith Baranoff from Lockheed Martin for his help in this investigation of the anomaly and his review of the paper. Keith has detailed knowledge of the dynamics of the spacecraft, and his assistance and knowledge have been greatly appreciated.

REFERENCES

1. Lockheed Martin Missiles and Space, "POLAR Spin Axis Anomaly Summary Report", CDRL 226, Contract No. NAS5-30503, August 19, 1996.

2. Goddard Space Flight Center, Flight Dynamics Division, 553-FDD-96/006R0UD0, *Interplanetary Physics Laboratory (WIND) and Polar Plasma Laboratory (POLAR) Postlaunch Report*, J.Dibble, July 1996.

3. Tom Flatley, GSFC, Notes, Summer 1996.

Page intentionally left blank

Thermally-Induced Structural Disturbances of Rigid Panel Solar Arrays

John D. Johnston and Earl A. Thornton

Department of Mechanical, Aerospace, and Nuclear Engineering
University of Virginia
Charlottesville, VA 22903

Abstract

The performance of a significant number of spacecraft has been impacted negatively by attitude disturbances resulting from thermally-induced motions of flexible structures. Recent examples of spacecraft affected by these disturbances include the Hubble Space Telescope (HST) and the Upper Atmosphere Research Satellite (UARS). Thermally-induced structural disturbances occur as the result of rapid changes in thermal loading typically initiated as a satellite exits or enters the Earth's shadow. Temperature differences in flexible appendages give rise to structural deformations, which in turn result in disturbance torques reacting back on the spacecraft. Structures which have proven susceptible to these disturbances include deployable booms and solar arrays. This paper investigates disturbances resulting from thermally-induced deformations of rigid panel solar arrays. An analytical model for the thermal-structural response of the solar array and the corresponding disturbance torque are presented. The effect of these disturbances on the attitude dynamics of a simple spacecraft is then investigated using a coupled system of governing equations which includes the effects of thermally-induced deformations. Numerical results demonstrate the effect of varying solar array geometry on the dynamic response of the system.

Introduction

Thermally-induced structural disturbances are typically initiated during orbital eclipse transitions during which a spacecraft exits from or enters into the Earth's shadow resulting in rapid changes in thermal loading. These sudden changes in heating may lead to the development of significant temperature differences in structures. Temperature differences through the cross-section of appendages lead to differential thermal expansion, i.e. the hot side of the appendage expands more than the cold side, which can result in significant structural deformations. Slowly developing temperature differences lead to quasi-static deformations, while rapidly changing temperature differences may excite dynamic structural motions. Thermally-induced structural disturbances may be defined as disturbance torques resulting from thermally-induced motions of flexible appendages. These disturbances may be classified as: thermal bending, thermal shock, thermally-induced vibrations, or thermal flutter.[1,2] Thermal bending disturbances are quasi-static deformations resulting from slowly varying temperature differences. Thermal shock, thermally-induced vibrations, and thermal flutter all involve dynamic structural motions initiated by rapidly developing temperature differences. Motions of flexible appendages result in rigid body rotations of the entire spacecraft, since the total angular momentum of the system must be conserved. These potentially large attitude disturbances may violate mission pointing accuracy and jitter requirements. The types of flexible appendages which are known to experience these disturbances fall into two basic categories: (1) booms (gravity gradient, antennae, and scientific instrument) and (2) solar arrays (flexible blanket and rigid panel). This paper investigates thermally-induced structural disturbances of rigid panel solar arrays.

Deployable solar arrays are typically wing-type structures which are stowed in compact form during launch and deployed once orbit has been achieved. The two most common designs are rigid panel and flexible blanket arrays.[3] Rigid panel solar array designs incorporate one or more hinged solar panels each consisting of a rigid substrate onto which solar cells are mounted. The rigid substrate is made of a lightweight honeycomb core (typically aluminum) onto which are bonded thin facesheets (typically aluminum or graphite epoxy composite).

Thermally-induced structural disturbances of rigid panel solar arrays occur as the result of temperature differences acting through the thickness of the solar panels. The corresponding structural response depends on the time scale of the thermal response as well as the physical characteristics of the solar array (coefficient of thermal expansion, natural frequency). Previous studies[4-7] have identified a number of spacecraft which experienced thermally-induced structural disturbances of rigid panel solar arrays, these include; LANDSAT 4 and 5, UARS, and TOPEX. Mathematical modeling of thermally-induced structural disturbances of rigid panel solar arrays has been previously explored by a number of authors. Bainum, et al.[8] studied thermal bending of free-free beams and plates modeled as continuous systems, subsequent to sudden changes in thermal loading to predict the effect of thermal shock on spacecraft attitude dynamics and control. Jasper and Neste[5] studied the effect of rapid thermal bending on the dynamics of the LANDSAT and UARS satellites. They utilized a lumped mass approach for formulating the disturbance torque resulting from the solar array thermal bending. Zimbelman[7] investigated the effect of solar array thermal shock on the dynamics and control of the TOPEX satellite. He presented a general formulation for determining solar panel temperatures, deformations, and the resulting disturbance torque.

The objective of this paper is to investigate the effects of thermally-induced structural disturbances of rigid panel solar arrays on the attitude dynamics of a simple spacecraft. A thermal-structural model of a rigid panel solar array is formulated based on techniques developed by Thornton[1] for studying thermally-induced vibrations of beams. The thermal-structural model of the solar array is then incorporated into an attitude dynamics formulation developed by Johnston and Thornton[9] to assess the effects of solar array deformations on the attitude dynamics of a simple spacecraft. A numerical simulation is performed to study the effect of varying solar array geometry on the dynamic response of the system. Additionally, comparison is made between results from the analytical model and finite element analyses to assess the validity of the thermal-structural model.

Mathematical Model

The problem considered is the planar motions of a simple spacecraft, Fig. 1, consisting of a rigid hub and a cantilevered flexible solar array. The rigid hub has a mass moment of inertia, I_{hub}, and a radius, R_{sc}. Two coordinate systems used in the analysis are shown in Fig. 1. The I1-I2 axes are located in an inertial reference frame fixed with respect to motions of the spacecraft. The B1-B2 axes are located in a body fixed reference frame attached to the hub with the B1 axis coinciding with the neutral surface of the undeformed solar array. The origins of both sets of axes coincide with the center of the hub. The attitude angle, θ, measures rigid body rotations of the hub about its fixed center, and $v(x,t)$ is the deformation of the solar array relative to its neutral surface. Only planar motions of the system consisting of small rotations of the hub about its center and bending vibrations of the solar array in the I1-I2 plane are considered, and there are no external forces or moments acting on the system. The solar array, Fig. 2, is modeled as a continuous panel of length L, and width W. The coordinates x, y, and z in the body fixed frame are defined as shown in Fig. 2. Figure 3 presents a cross-section of the solar array which consists of a honeycomb core of thickness, t_{hc}, onto which are bonded an upper and a lower facesheet, both of thickness t_{fc}. The distance between the centroids of the upper and lower facesheets is h. The honeycomb core has a cell size s, and a nominal foil gage t_{foil}. The honeycomb core is modeled as a uniform solid using effective properties based on the cell size and foil gage. The effects of solar cells, coverglass, and adhesives are neglected in the present analyses.

The solar array thermal model is presented in Figure 4. The problem assumes one-dimensional conduction through the thickness of the solar array subject to radiation boundary conditions on the upper and lower surfaces. The boundary conditions consist of a uniform heat flux, S, in the I1-I2 plane directed normal to the top surface of the solar array and thermal radiation from the upper and lower surfaces to a far-field temperature of 0 K. The heat flux is applied as a step function of time, such that $S = 0$ for $t < 0$ and $S = S_o$ for $t \geq 0$. The thermal loading is assumed to remain constant for small rotations of the hub and small solar array deformations, i.e. the thermal response of the solar array is assumed to be independent of the dynamic response of the system. The temperature of the solar array, $T(y,t)$, is assumed to be uniform in the x and z directions and to vary only through the thickness of the array in the y direction. The temperature is assumed constant through the thickness of the facesheets, where $T_{upper}(t)$ and $T_{lower}(t)$ are the temperatures of the upper and lower facesheets, respectively. Thus,

the temperature varies only through the honeycomb core, and the temperature difference through the thickness of the solar array is given by $\Delta T(t) = T_{upper}(t) - T_{lower}(t)$.

Analysis

The objective of the analysis is to predict the coupled dynamic response of the system as characterized by the attitude angle of the rigid hub, $\theta(t)$, and the displacements of the flexible solar array, $v(x,t)$. The analysis begins with the governing equations for the transient thermal response of the solar array, from which an approximate solution for the transient temperature difference through the thickness of the solar array can be obtained. Next, a solution for the quasi-static structural response of the solar array is determined. Finally, the equations of motion for the dynamic response of the system consisting of the rigid hub and the flexible solar array are formulated using a generalized form of Lagrange's equations for hybrid coordinate dynamical systems.

Thermal response

The governing equation for heat transfer through the thickness of the solar array is given by

$$\rho c \frac{\partial T}{\partial t} = k \frac{\partial^2 T}{\partial y^2} \tag{1}$$

where $T(y,t)$ is the solar array temperature, ρ is the mass density, c is the specific heat, and k is the thermal conductivity. The boundary condition on the upper surface ($y = + d/2$) is

$$-k \frac{\partial T}{\partial y} = \sigma \varepsilon_{upper} T^4 - \alpha_{upper} S \tag{2}$$

where σ is the Stefan-Boltzmann constant, ε is the surface emissivity, and α is the surface absorptivity. The boundary condition on the lower surface ($y = -d/2$) is

$$k \frac{\partial T}{\partial y} = \sigma \varepsilon_{lower} T^4 \tag{3}$$

The initial condition specifies that at $t = 0$ the solar array has a uniform temperature

$$T(y,0) = T_o \tag{4}$$

The transient thermal response of the solar array can be found numerically from Eqs. (1)-(4) using either finite difference methods or finite element analysis. Previous research[7] has shown that the temperature difference through the thickness of the solar array has the following approximate form

$$\Delta T(t) = \Delta T_{ss} (1 - e^{-t/\tau}) \tag{5}$$

where ΔT_{ss} is the steady state temperature difference, and τ is the thermal time constant associated with the thickness heat transfer. The form of Eq. (5) is the same as that obtained in the analysis of other types of radiantly heated spacecraft structures, such as the approximate analytical solution[1] for the temperature difference through the cross-section of a thin-walled tube. The steady state temperature difference can be obtained by writing the heat balance equations for the solar array at thermal equilibrium.[10] At steady state, the heat absorbed by the solar array is balanced by the heat re-radiated from the upper and lower surfaces by thermal radiation.

$$\alpha_{upper} S = \sigma \varepsilon_{upper} T_{upper}^4 + \sigma \varepsilon_{lower} T_{lower}^4 \tag{6a}$$

Additionally, at steady state the heat flux through the thickness of the solar panel is balanced by the thermal radiation flux from the lower surface.

$$k_{hc}\frac{(T_{upper}-T_{lower})}{t_{hc}}=\sigma\varepsilon_{lower}T_{lower}^{4} \tag{6b}$$

Equations (6a)-(6b) can be solved using an iterative solution technique to obtain the upper and lower surface temperatures, and the corresponding steady state temperature difference. The thermal time constant can be estimated from the thermal diffusivity of the honeycomb core, $\kappa = k/\rho c$, and the characteristic dimension over which the temperature varies, in this case, the thickness of the honeycomb core.

$$\tau=\frac{t_{hc}^{2}}{\kappa_{hc}} \tag{7}$$

Thus, an approximate solution for the temperature difference through the thickness of the solar array can be determined using Eqs. (5)-(7). Comparison with finite element analyses shows that this function models the actual temperature difference accurately for the case of a step function heat flux. For a ramp type heat flux loading, it is recommended that the value for the thermal time constant be determined using numerical methods.

Quasi-static structural response

The quasi-static structural response consists of a succession of equilibrium displacements each corresponding to the temperature difference at a given instant in time. There are two mathematical models suitable for analyzing the structural response of the solar array: beam and plate. The choice of model is based on the geometry of the solar array. A beam model is appropriate for a high aspect ratio (L/W) geometry, and a plate model will yield more accurate results for a low aspect ratio geometry. Criteria useful in evaluating the choice of mathematical model include quasi-static displacements and natural frequencies. In the present analyses, a Bernoulli-Euler beam model is assumed. The validity of the model will be evaluated later by comparison with finite element plate bending analyses. The quasi-static displacements, $v_{qs}(x,t)$, are obtained by neglecting terms corresponding to inertia forces in the governing equation and boundary conditions, which are as follows for a cantilevered beam,

$$EIv_{qs}^{IV}=0 \tag{8a}$$

$$\begin{aligned} &v_{qs}(0,t)=0\\ &v_{qs}'(0,t)=0\\ &v_{qs}''(L,t)=\frac{-M_T(t)}{EI}\\ &v_{qs}'''(L,t)=0 \end{aligned} \tag{8b}$$

where E is the modulus of elasticity of the facesheets, and I is the moment of inertia of the panel cross-section about the neutral axis

$$I=\left(t_{fc}h^{2}W\right)/2 \tag{9}$$

The time-dependent thermal moment, $M_T(t)$, arises due to the transient temperature difference through the thickness of the solar array and is given by

$$M_T(t) = \int_A \left[E\alpha_{cte} \left(T(y,t) - T_{ref} \right) y \right] dA \tag{10}$$

where α_{cte} is the coefficient of thermal expansion of the facesheets, and T_{ref} is a reference temperature. Eq. (10) is evaluated by assuming that only the facesheets contribute to the bending stiffness of the solar array, and that the temperatures are constant through the thickness of the facesheets. This results in the following expression for the thermal moment

$$M_T(t) = \frac{EI\alpha_{cte}}{h} \Delta T(t) \tag{11}$$

Finally, solving Eq. (8a) subject to the boundary conditions (8b) yields the solution for the quasi-static displacements of the solar array,

$$v_{qs}(x,t) = \frac{-M_T(t)}{2EI} x^2 \tag{12}$$

Dynamic response

The governing equations for the dynamic response of a simple spacecraft consisting of a rigid hub and a flexible solar array can be obtained using a generalized form of Lagrange's equations for hybrid coordinate dynamical systems.[11] The formulation used here is based on a previous study by Johnston and Thornton[9] in which a coupled system of governing equations was developed for a simple spacecraft which incorporated the effects of flexible appendage undergoing thermally-induced vibrations. The resulting governing equation for the rigid body rotations of the hub is given by

$$I_{sc}\ddot{\theta} + \int_0^L \rho A (R_{sc} + x) \ddot{v}(x,t)\, dx = 0 \tag{13}$$

where I_{sc} is the composite mass moment of inertia for the spacecraft

$$I_{sc} = I_{hub} + \rho A \int_0^L (R_{sc} + x)^2 dx \tag{14}$$

and ρA is the equivalent density per unit length of the solar array given by

$$\rho A = (2\rho_{fc} t_{fc} + \rho_{hc} t_{hc}) W \tag{15}$$

where ρ_{fc} is the density of the facesheets, and ρ_{hc} is the effective density of the honeycomb core. An expression for the thermally-induced disturbance torque, $T_{TID}(t)$, can be obtained from Eq. (13) by moving the terms corresponding to motions of the flexible solar array to the right hand side of the equation,

$$T_{TID}(t) = -\rho A \int_0^L (R_{sc} + x) \ddot{v}(x,t) dx \tag{16}$$

The governing equation for the boom deformations in the body fixed reference frame is given by

$$\rho A (R_{sc} + x)\ddot{\theta} + \rho A \ddot{v} + c_{damp} \dot{v} + EIv^{IV} = 0 \tag{17}$$

where $c_{damp} = 2\zeta\omega_n \rho A$ is the viscous damping constant, ω_n are the natural frequencies of the solar array, and ζ is the damping factor which typically has values ranging between 0.01 and 0.0001 for lightly damped structures. At $x = 0$, the solar array is cantilevered, and geometric boundary conditions are enforced

$$v(0,t) = 0 \tag{18a}$$
$$v'(0,t) = 0 \tag{18b}$$

At x = L, the solar array is free and the natural boundary conditions for the shear force and bending moment are enforced

$$EIv'''(L,t) = 0 \tag{18c}$$
$$EIv''(L,t) + M_T(t) = 0 \tag{18d}$$

An approximate form of the equations of motion stated in Eqs. (13) and (17) is obtained using modal expansion. The assumed form of the solution is

$$v(x,t) = v_{qs}(x,t) + \sum_{n=1}^{N} q_n(t)\phi_n(x) \tag{19}$$

where $v_{qs}(x,t)$ is the quasi-static response, $q_n(t)$ are the nth generalized modal coordinates, $\phi_n(x)$ are the nth shape functions, and N is the number of modes. The shape functions are chosen to be the eigenfunctions from the free vibration response of a fixed-base cantilevered beam. After the assumed form of the boom displacements is substituted into the governing equations, the result is a system of N+1 coupled linear ordinary differential equations for the discrete coordinate, $\theta(t)$, and the generalized modal coordinates, $q_n(t)$. These equations can be written in matrix form as

$$[M]\{\ddot{x}\} + [C]\{\dot{x}\} + [K]\{x\} = \{F(t)\} \tag{20}$$

where $\{x\}^T = \{\theta \; q_1 \; q_2 \; \ldots \; q_N\}$ are the generalized coordinates for the system, and [M], [C], and [K] are N+1 by N+1 constant coefficient matrices. Numerical integration of the governing equations leads to solutions for the thermally-induced dynamics of the spacecraft.

It is possible to gain some insight into the character of the thermal-structural response of a flexible appendage prior to undertaking a detailed numcrical study. A key parameter for assessing the potential of a thermally-induced dynamic response is given by Boley and Weiner.[12] The Boley parameter, B, is formed by taking the square root of the ratio of the characteristic thermal and structural response times of the system,

$$B = \sqrt{t_T / t_s} \tag{21}$$

where the characteristic thermal response time for a rigid panel solar array, $t_s = \tau$, is given by Eq. (7) and the characteristic structural response time, t_s, is the period of the fundamental mode of vibration. Boley also developed a relation for the dynamic amplification factor which gives the ratio of the maximum dynamic displacement to the maximum quasi-static displacement.

$$v_{dynamic} / v_{static} = 1 + 1 / \left(\sqrt{1 + B^2}\right) \tag{22}$$

It can be seen from Eq. (22) that for large values of B the dynamic amplification factor is on the order of one. Under these circumstances quasi-static thermal-structural analysis is justified. This is the case for a vast majority of terrestrial structures. However, for small values of B the dynamic amplification factor is greater than one and inertial terms should be included in the thermal-structural analysis. Structures with a value of B on the order of one are typically susceptible to thermally-induced vibrations when subjected to rapid changes in thermal loading.

Numerical Simulation

A numerical simulation was performed to investigate the effects of thermally-induced motions of rigid panel solar arrays on the attitude dynamics of a simple spacecraft. The results were obtained by performing numerical integration of the equations of motion using the central difference method. All of the simulations utilized N = 5 flexible modes, with a timestep based on the highest mode included. The simple spacecraft used in the study has a rigid hub with a mass moment of inertia of 2500 kg-m^2 and a radius of 1.0 m. Three different cases were considered to study the effect of varying solar array geometry on the dynamic response of the system. Table 1 presents the general solar array parameters used in the study. Each case considered a solar array with a different aspect ratio (L/W), but the same cross-sectional geometry and materials. The aspect ratios are varied between 1.0 to 5.0 which is representative of current solar array designs. The facesheets are 2.032E-04 m (0.008 in.) thick aluminum (2024 alloy). The honeycomb core is aluminum (5056 alloy) with a cell size of 6.35E-03 m (0.25 in.) and a nominal foil gage of 2.54E-05 m (0.001 in.). Table 2 presents the material properties for the facesheets and honeycomb core. Effective properties for the honeycomb core were obtained based on formulas given in reference 13. Table 3 summarizes the simulation results for all three cases.

Thermal response

The steady state thermal response of the solar array was obtained using finite element analysis. A one-dimensional finite element model of the solar array was analyzed using the commercially available program ABACUS.[14] The finite element model consisted of a one-dimensional representation of the solar array cross-section (including the facesheets) using 90 nodes through the thickness of the panel. The incident solar heating was applied as a step function at t = 0. Results show that the steady state upper and lower surface temperatures are 327.1 K and 324.3 K, respectively. This corresponds to a steady state temperature difference through the thickness of the solar panel of 2.8 K. Additionally, the finite element analysis showed that temperatures remain constant through the thickness of the facesheets which justifies earlier assumptions.

The transient temperature difference through the thickness of the solar panel was obtained using the approximate analytical solution given in Eqs. (5)-(7). The steady state upper and lower surface temperatures obtained from iteratively solving Eqs. (6a)-(6b) are 327.2 K and 324.4 K, respectively. This corresponds to a steady state temperature difference through the thickness of the solar panel of 2.8 K. These results show excellent agreement with the finite element results. Figure 5 presents the transient temperature difference through the thickness of the solar array from Eq. (5). The temperature difference reaches a steady state value of 2.8 K in approximately 10 s. It is this rapid rise in the temperature difference due to a sudden change in thermal loading which is responsible for exciting thermally-induced dynamic motions of flexible appendages.

Dynamic response

The dynamic response of the simple spacecraft consisting of the rigid hub and the flexible solar array is given in terms of the displacement of the solar array along its centerline at the free end, v(L,t), the disturbance torque resulting from the solar array motions, $T_{TID}(t)$, and the attitude angle of the hub, $\theta(t)$. Three cases were analyzed, each characterized by a different length solar array. The effect of increasing the length is to lower the fundamental frequency of the solar array, which leads to an increase in the magnitude of the thermally-induced dynamic response.

Case 1 (L/W = 1)

The results for Case 1 are presented in Figs. 6-8. The solar array has a fundamental frequency of 11.6 Hz and a Boley parameter of 4.8. Figure 6 presents a plot of the solar array end displacement in the body fixed reference frame. The motions consist of a quasi-static displacement with negligible superimposed oscillations. The quasi-static displacement has a steady state value of -3.4E-03 m. The oscillations (too small to be seen in Fig. 6), which decay rapidly, have a maximum peak to peak magnitude of 2.4E-05 m and occur at a frequency of 11.6 Hz. The motion of the solar array results in an internal disturbance torque which acts to change to orientation of

the rigid hub. The thermally-induced disturbance torque, $T_{TID}(t)$, from Eq. (16), is presented in Figure 7. The disturbance torque has a peak value of 0.15 N-m. The attitude response of the rigid hub is presented in Figure 8. The attitude response of the hub consists of a slowly developing pointing error. The pointing error has a steady state value of 7.0E-05 deg. and the rapidly decaying oscillations have a maximum peak to peak magnitude of 5.9E-07 deg. The results of Case 1 can be classified as a quasi-static response.

Case 2 (L/W = 2)

The results for Case 2 are presented in Figs. 9-11. The solar array has a fundamental frequency of 2.9 Hz and a Boley parameter of 2.4. Figure 9 presents a plot of the solar array end displacement in the body fixed reference frame, which consists of a quasi-static displacement and superimposed oscillations. The quasi-static displacement has a steady state value of -1.35E-02 m. The oscillations have a maximum peak to peak magnitude of 5.6E-04 m and occur at a frequency of 2.9 Hz. The resulting thermally-induced disturbance torque is presented in Fig. 10 and has a peak value of 0.4 N-m. The attitude angle response, Fig. 11, consists of a slowly developing pointing error superimposed with a decaying oscillation (jitter). The pointing error has a steady state value of 8.0E-04 deg., and the decaying oscillations have a maximum peak to peak magnitude of 3.8E-05 deg. The rigid body oscillations occur at the same frequency as the solar array vibrations. The oscillations are damped-out after approximately 100 s. The results seen in Case 2 can be classified as a mild thermally-induced vibrations response.

Case 3 (L/W = 5)

The results for Case 3 are presented in Figs. 12-14. The solar array has a fundamental frequency of 0.5 Hz and a Boley parameter of approximately 1.0 which suggests the likelihood of a severe thermally-induced vibrations response. Figure 12 presents a plot of the solar array end displacement in the body fixed reference frame, which consists of a quasi-static displacement and large superimposed oscillations. The quasi-static displacement has a steady state value of -8.42E-02 m, and the oscillations have a maximum peak to peak magnitude of 2.44E-02 m at a frequency of 0.5 Hz. The resulting thermally-induced disturbance torque is presented in Fig. 13 and has a peak value of 1.9 N-m. The attitude angle response, Fig. 14, consists of a slowly developing pointing error with large superimposed oscillations (jitter). The pointing error has a steady state value of 2.3E-02 deg., and the decaying oscillations have a maximum peak to peak magnitude of 7.56E-03 deg. Again, the rigid body oscillations occur at the same frequency as the solar array vibrations. The oscillations decay rather slowly and are damped-out after approximately 500 s. The results seen in Case 3 can be classified as a severe thermally-induced vibrations response.

Structural Modeling of Solar Array

In the current formulation, the solar array is modeled as a cantilever beam, yet in reality the structure behaves more like a cantilever plate. The beam model allows only bending about the z axis (see Fig. 2), but an actual solar array will undergo bending deformations about both the x and z axes. To assess the validity of the beam model used in the current formulation, finite element plate bending analyses were completed to compare the beam solution with a finite element plate model of a solar array. In terms of the quasi-static displacements, the beam model predicted the free end centerline displacements (x = L, y = 0) to within 3.0 % of the finite element analysis for an aspect ratio of 1.0 and to within 0.3 % for an aspect ratio of 5.0. However, the beam model cannot predict the curling of the solar array about the x axis. The additional displacement of the solar array sides (y = +/- W/2) relative to the centerline (y = 0) displacement is greatest for the lowest aspect ratio solar arrays. Additionally, the frequencies and mode shapes for a cantilever plate differ from those of a cantilever beam. Results show good agreement for the high aspect ratio solar array (L/W = 5) where finite element plate bending analysis predicts a fundamental frequency of 0.48 Hz compared to 0.47 Hz from the beam model. For the low aspect ratio solar array (L/W = 1) finite element plate bending analysis predicts a fundamental frequency of 12.2 Hz compared to 11.6 Hz from the beam model. Thus, the beam model is valid for high aspect ratio solar arrays, but it becomes less accurate as the aspect ratio decreases. Deeper understanding of the beam model limitations will require further numerical and experimental study.

Closing Remarks

This paper has presented an investigation of thermally-induced structural disturbances of rigid panel solar arrays. An analytical model for the thermal-structural response of the solar array based on a cantilever beam formulation was presented and shown to be valid for high aspect ratio solar arrays. The effect of these disturbances on the attitude dynamics of a simple satellite was then investigated using a coupled system of governing equations which include the effects of thermally-induced deformations. Results from a numerical simulation demonstrate that: (1) the dynamic response of the solar array consists of a quasi-static displacement and superimposed oscillations whose magnitude is related to the Boley parameter, $B = \sqrt{t_T / t_s}$ where t_T is the thermal time constant and t_s is the period of the fundamental mode of vibration, (2) due to conservation of angular momentum the hub undergoes rigid body rotations in the direction opposite to the solar array bending, (3) the dynamic response of the system is at a frequency near that of the fundamental mode of the solar array, and (4) systems for which $B >> 1.0$ will undergo a quasi-static response and those for which $B \approx 1.0$ will experience a thermally-induced dynamic response.

Acknowledgment

This research is funded by the NASA Graduate Student Researchers Program. The authors appreciate the support of our technical advisors Drs. Marvin Rhodes and Brantley Hanks of NASA Langley Research Center. The authors would also like to thank Rob Marino for his assistance in formulating the finite element models.

References

1. Thornton, E.A., *Thermal Structures for Aerospace Applications*, AIAA Education Series, American Institute of Aeronautics and Astronautics, Inc., Washington, D.C., 1996.
2. Johnston, J.D. and Thornton, E.A., "An Evaluation of Thermally-Induced Disturbances of Spacecraft Solar Array Structures," *Proceedings of the 31st IECEC*, Washington, D.C., August 11-16, 1996.
3. Rauschenbach, H.S., *Solar Cell Array Design Handbook*, New York, Van Nostrand Reinhold Company, 1980.
4. Richmond, W., "LANDSAT Thermal Snap at Sunrise/Sunset," General Electric Space Division, PIR-U-1W00-UARS-030, January 8, 1985.
5. Jasper, P.E. and Neste, S., "UARS Solar Array Snap," PIR No. U-1K21-UARS-481, General Electric Space Division, Philadelphia, PA, July 9, 1986.
6. Lambertson, M., Rohrbaugh, D., and Garrick, J., "Solar Array Thermal Snap and the Characteristics of Its Effects on UARS," Flight Mechanics/Estimation Theory Symposium, NASA Goddard Spaceflight Center, Greenbelt, MD, 1990.
7. Zimbelman, D.F., "Thermal Shock and its Effect on Spacecraft Attitude Control," Ph.D. Dissertation, University of Colorado, Boulder, CO, 1990.
8. Bainum, P.M., Hamsath, N., and Krishna, R., "The Dynamics and Control of Large Space Structures After the Onset of Thermal Shock," *Acta Astronautica*, Vol. 19, No. 1, pp.1-8, 1980.
9. Johnston, J.D. and Thornton, E.A., "Thermally-Induced Attitude Dynamics of a Spacecraft with a Flexible Boom," *AAS/AIAA Spaceflight Mechanics Symposium*, Huntsville, AL, Feb. 10-12, 1997, AIAA paper 97-178.
10. Krishna, R. and Bainum, P.M., "Dynamics and Control of Orbiting Flexible Structures Exposed to Solar Radiation," Journal of Guidance, Control, and Dynamics, Vol. 8, No. 5, Sept.-Oct., 1985, pp. 591-596.
11. Junkins, J.L. and Kim, Y., *Introduction to Dynamics and Control of Flexible Structures*, AIAA Education Series, American Institute of Aeronautics and Astronautics, Inc., Washington, D.C., 1993.
12. Boley, B.A. and Weiner, J.H., *Theory of Thermal Stresses*, John Wiley and Sons Inc., New York, 1960.
13. Gibson, L.J., *Cellular Solids*, Pergamon Press, New York, 1988.
14. ABAQUS User's Manual, Version 5.2, Hibbett, Karlsson, & Sorenson, Inc., 1992.

Table 1
SOLAR ARRAY PARAMETERS

Property	Case 1	Case 2	Case 3
L (m)	1.0	2.0	5.0
W (m)	1.0	1.0	1.0
Aspect ratio (L/W)	1.0	2.0	5.0
h (m)	9.728E-03	9.728E-03	9.728E-03
t_{fc} (m)	2.032E-04	2.032E-04	2.032E-04
t_{hc} (m)	9.525E-03	9.525E-03	9.525E-03
I (m^4)	9.615E-09	9.615E-09	9.615E-09
Msa (kg)	1.56	3.12	7.8
Damping factor, ζ	0.001	0.001	0.001
Fundamental natural frequency (Hz)	11.62	2.91	0.47
Structural time constant (s), t_s	.086	.034	2.15
Thermal time constant (s), t_T	1.96	1.96	1.96
Boley parameter, B	4.77	2.39	0.95
Dynamic magnification factor (predicted)	1.21	1.39	1.72

Table 2
MATERIAL PROPERTIES

Parameter	Facesheet	Honeycomb core
Material	AL 2024	AL 5056
Young's Modulus (N/m^2)	70E+09	-
Poisson's ratio	0.33	-
Density (kg/m^3)	2800	44.3
Thermal conductivity (W/m-K)	120	1.89
Specific heat (J/kg-K)	921	921
Thermal expansion coefficient (/K)	23.4E-06	-
Solar absorptivity (sun side)	0.79	-
Emissivity (sun side)	0.81	-
Emissivity (anti-sun side)	0.86	-

Table 3
SIMULATION RESULTS

Parameter	Case 1	Case 2	Case 3
Steady state temperature difference (K)	2.8	2.8	2.8
Quasi-static tip displacement (m)	-0.0034	-0.0135	-0.0842
Tip jitter (m)	2.37E-05	5.59E-04	0.0244
Quasi-static attitude angle (deg.)	7.0E-05	8.0E-04	0.023
Attitude angle jitter (deg.)	5.87E-07	3.83E-05	7.56E-03
Period of oscillations (s)	0.086	0.344	2.11
Frequency of oscillations (Hz)	11.63	2.91	0.47
Dynamic amplification factor	1.001	1.02	1.14

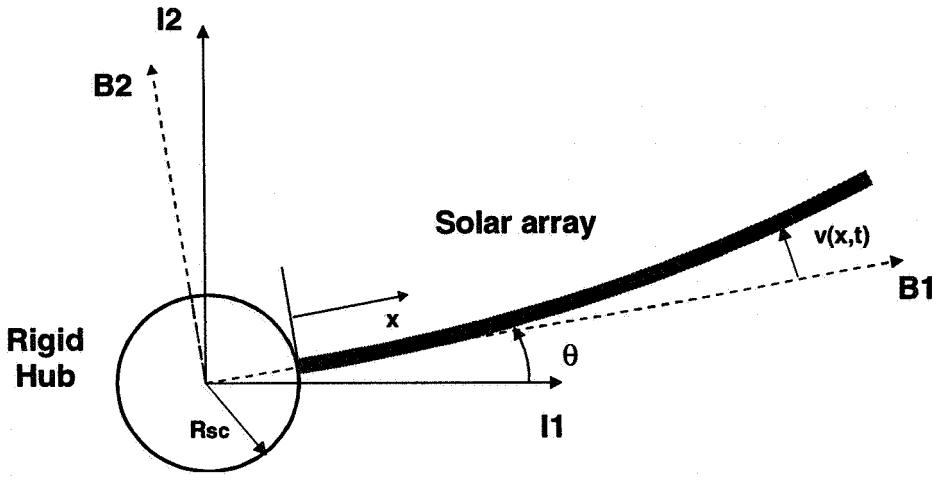

Figure 1: Spacecraft model and coordinate systems

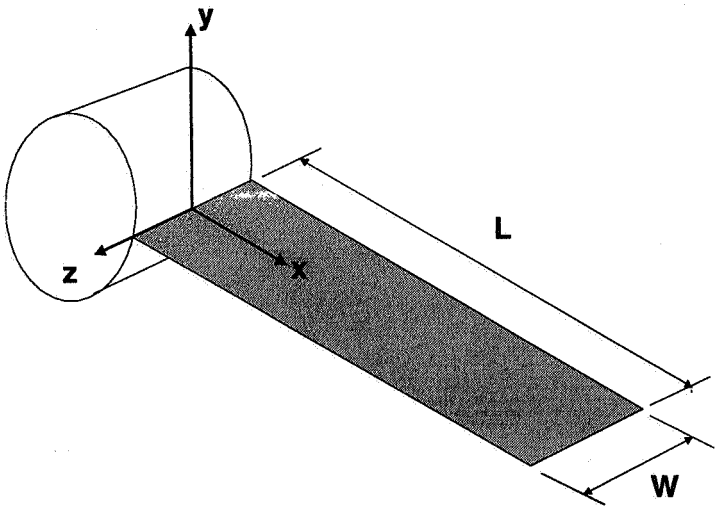

Figure 2: Solar array geometry and coordinate systems

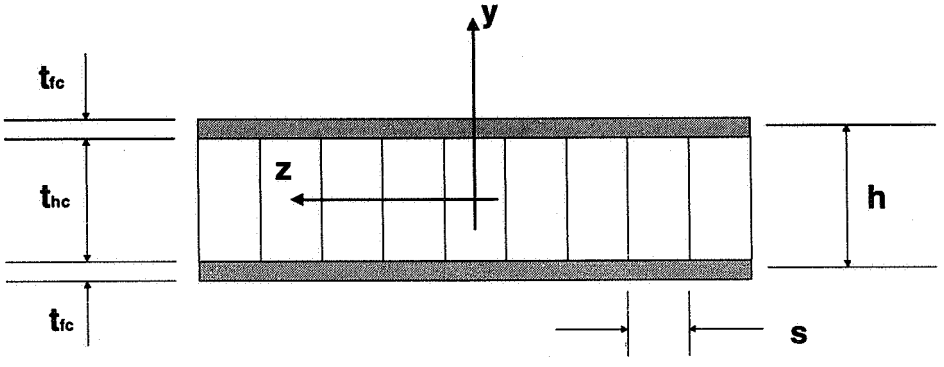

Figure 3: Solar array geometry: cross-sectional view

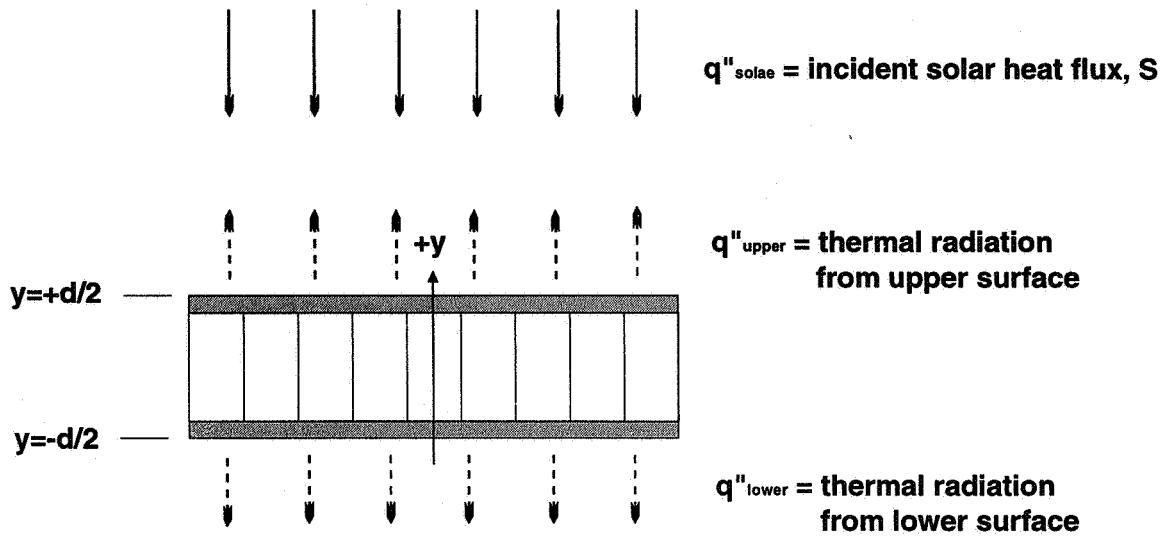

Figure 4: Solar array thermal model

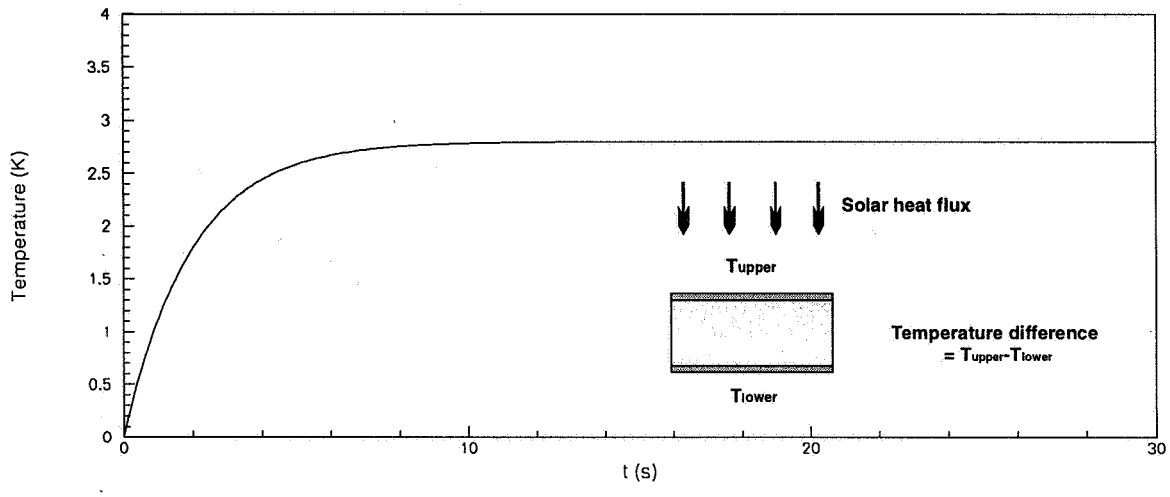

Figure 5: Temperature difference vs. time from approximate analysis

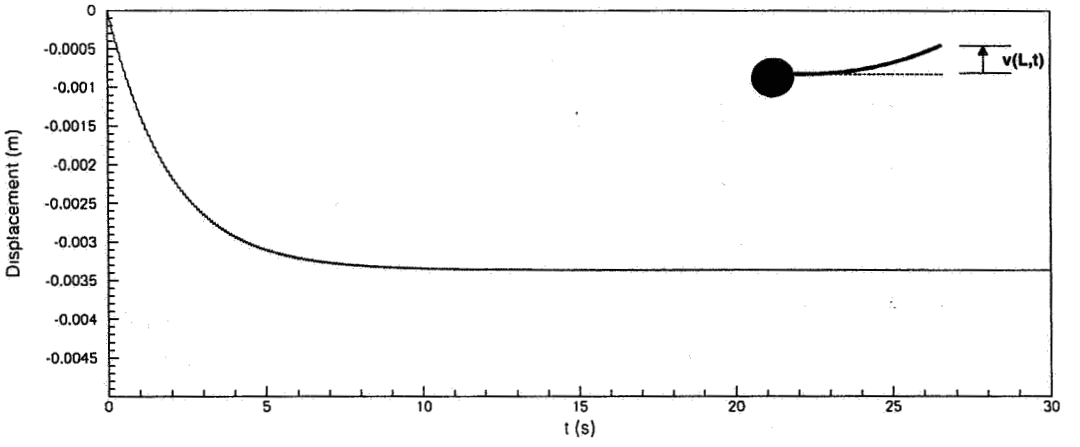

Figure 6: End displacement vs. time for Case 1 (L/W = 1)

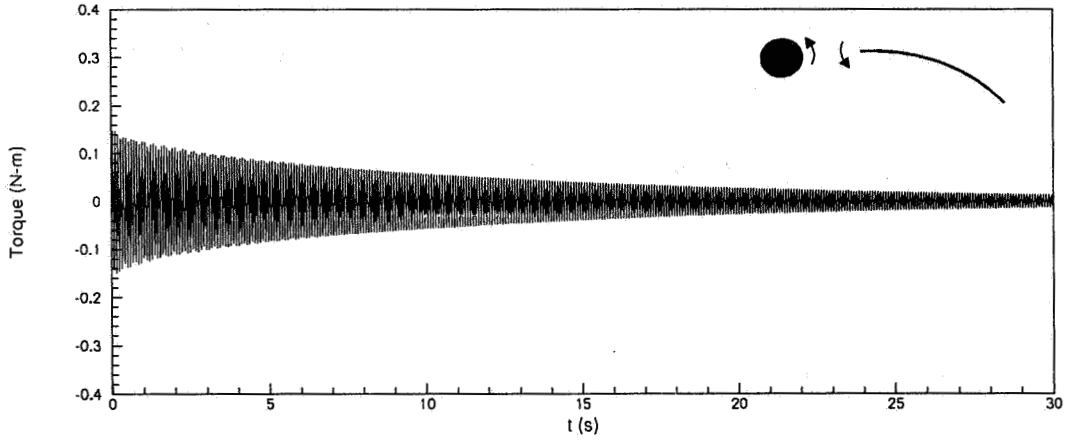

Figure 7: Disturbance torque vs. time for Case 1 (L/W = 1)

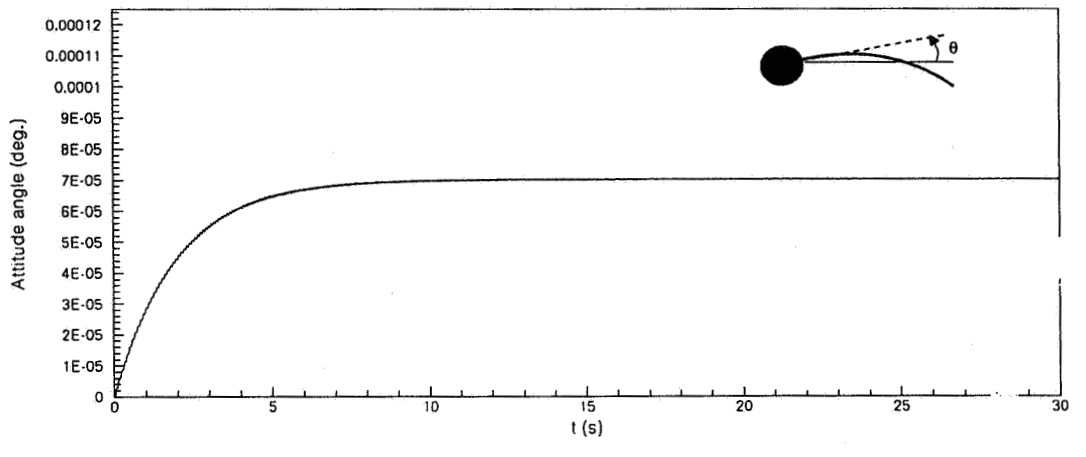

Figure 8: Attitude angle vs. time for Case 1 (L/W = 1)

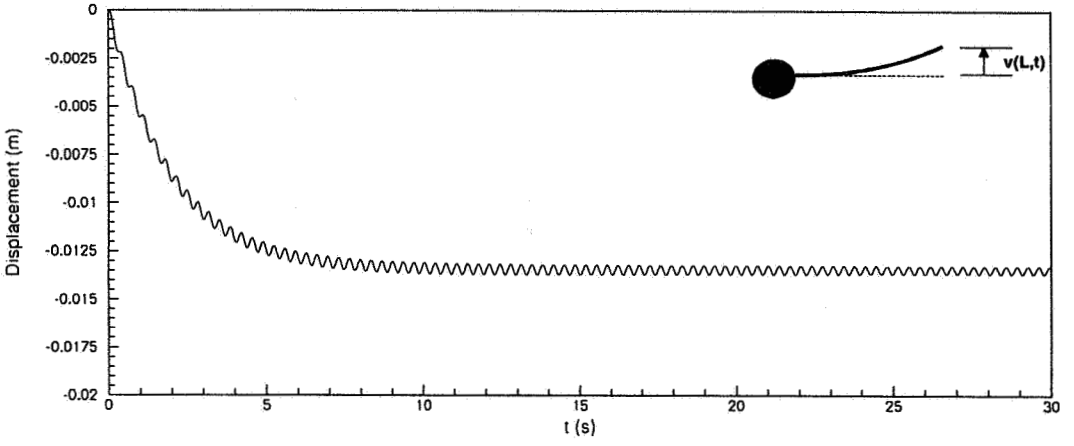

Figure 9: End displacement vs. time for Case 2 (L/W = 2)

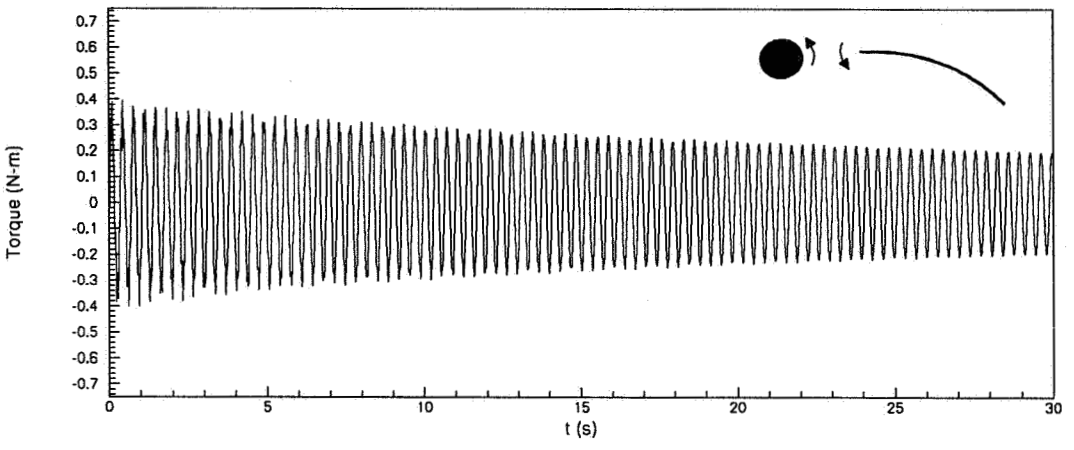

Figure 10: Disturbance torque vs. time for Case 2 (L/W = 2)

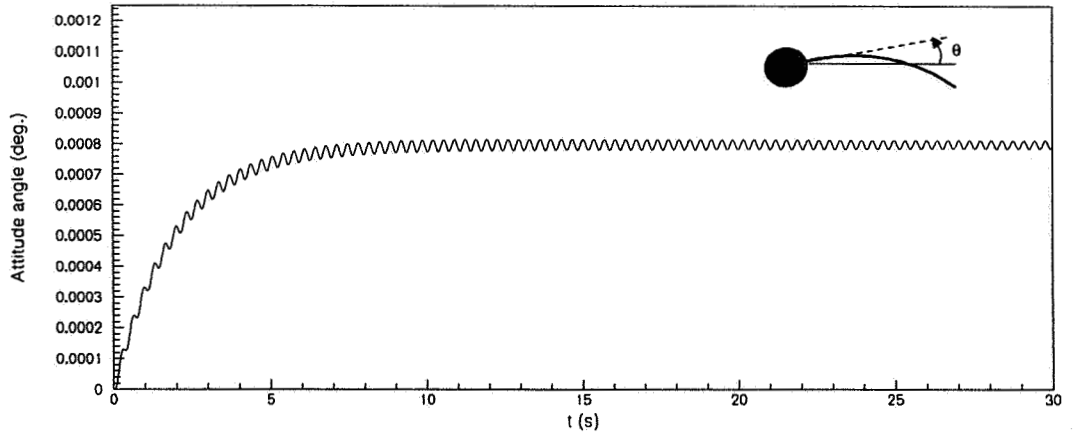

Figure 11: Attitude angle vs. time for Case 2 (L/W = 2)

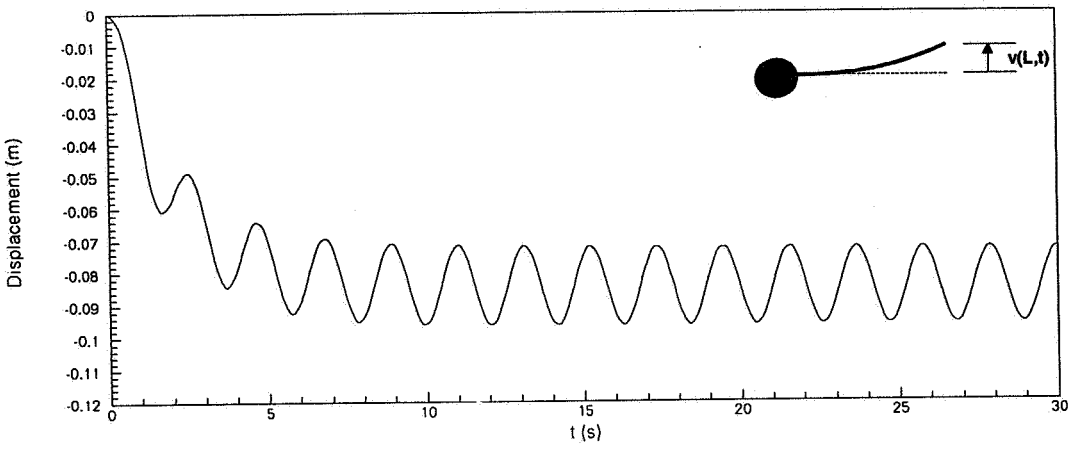

Figure 12: End displacement vs. time for Case 3 (L/W = 5)

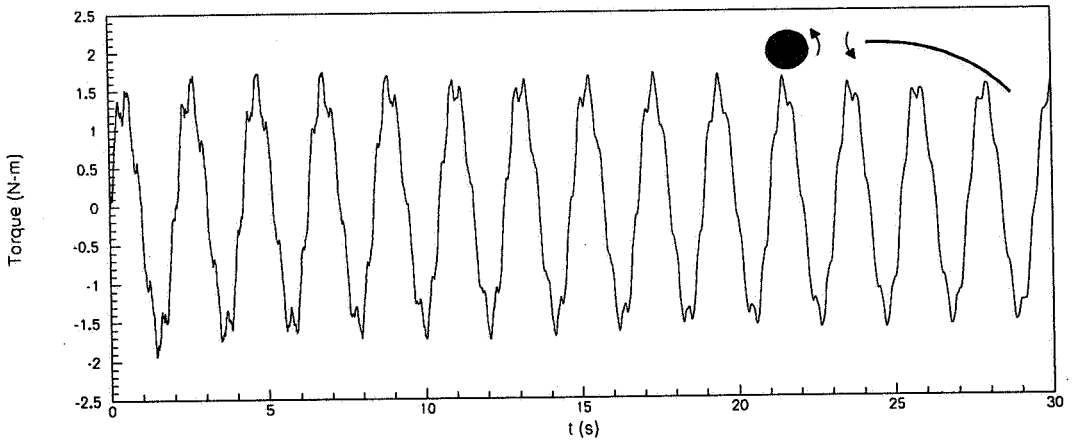

Figure 13: Disturbance torque vs. time for Case 3 (L/W = 5)

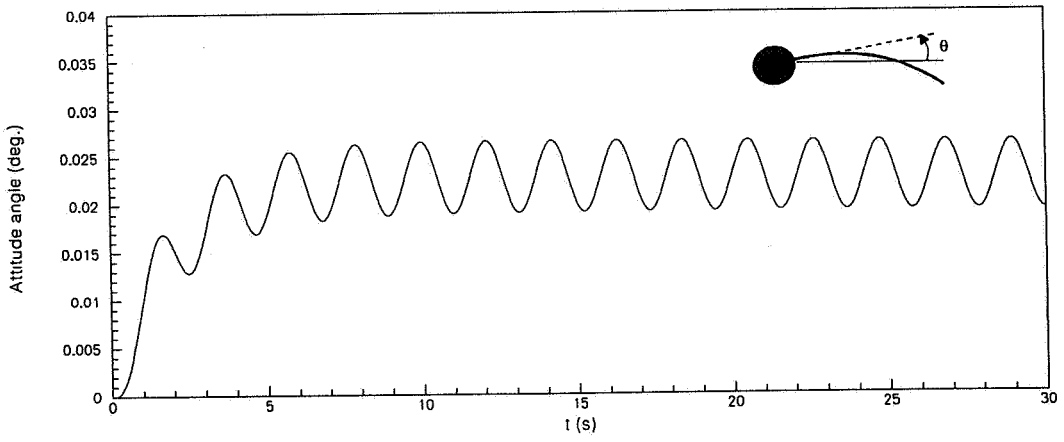

Figure 14: Attitude angle vs. time for Case 3 (L/W = 5)

Page intentionally left blank

GOES-8 Imager IMC Dynamic Range Study

Nickalaus Pinkine
National Environmental Satellite, Data and Information Service
National Oceanic and Atmospheric Administration
Washington, D.C. 20233

ABSTRACT

The Geostationary Operational Environmental Satellite (GOES) Image Motion Compensation (IMC) system provides real-time instrument pointing corrections to compensate for predictable, diurnal orbit and attitude disturbances to the spacecraft. By applying the proper pointing correction to the imager scan mirror, while the imager is scanning the earth, GOES images of the earth will appear stationary relative to a set of "fixed" geographic grid points. This capability allows users of GOES data to more accurately model and predict various weather phenomena.

Pointing corrections are achieved by simultaneously transmitting two signals to the instrument scan mirror motor electronics. One signal adjusts the mirror's North-South directional motion, while the other adjusts the mirror's East-West directional motion. In addition, the IMC system has two operational ranges, low and high, which limit the maximum available compensation to the imager scan mirror. The maximum available North-South compensation in low range is 2000 μradians compared to 8000 μradians for high range. On GOES-8, high range was the recommended mode of IMC operation prior to an IMC system anomaly which occurred in the spring of 1996. An anomaly resolution team concluded that when IMC was operated in high range, only a partial North-South compensation signal was being transmitted to the imager scan mirror. No degradation to the East-West compensation signal was detected during testing. In order to maintain Image Navigation and Registration (INR) requirements, the total IMC signal must be transmitted to the mirror electronics. After further testing failed to demonstrate that high range was fully functional, low range was selected as the operational IMC mode.

Operating GOES-8 in low range throughout the mission introduces potential INR errors, particularly when the spacecraft orbital inclination is greater than 0.35 degrees. The primary purpose of this study was to determine the magnitude and timing of these INR errors, and their impact on GOES-8 imager products for the 1996 winter solstice season. This paper presents a detailed analysis of the GOES-8 imager IMC system, utilizing quantitative results obtained through IMC simulation. Data from the 1995 winter solstice season was used by the IMC simulator to predict IMC performance for the 1996 winter solstice season.

Keywords: image navigation and registration, image motion compensation

1. INTRODUCTION

The primary purpose of this study is to characterize potential INR errors attributed to operating GOES-8 IMC in low range throughout the 1996 winter solstice season. Specifically, it is necessary to determine the magnitude of the North-South compensation signal being transmitted to the imager scan mirror as a function of time and instrument scan angle. No analysis is necessary for the East-West signal since it is functioning properly. If during an image, the magnitude of the North-South compensation signal exceeds 2000 μradians (a violation of the IMC low dynamic range threshold), possible image navigation errors and image distortion will result. The goal of this study is to determine the specific images that are potentially affected and the portions of those images which may be distorted. It is also desirable to determine over what time frame, (i.e., how many days or weeks), that these effects may last.

2.0 TYPES OF COMPENSATION

Four independent sources need to be considered when characterizing the total amount of North-South compensation applied to the imager scan mirror during imaging. The four sources of interest are Image Motion Compensation (IMC), Spacecraft Motion Compensation (SMC), Mirror Motion Compensation (MMC) and Single Chord Compensation (SCC).

2.1 Image Motion Compensation

IMC is the primary source of compensation being applied to the imager scan mirror. IMC corrects GOES images for errors caused by spacecraft orbital perturbations and thermally driven optical axis disturbances. Figure 2.1-1 is a geometrical representation of the IMC correction needed to maintain instrument pointing due to differences in the actual spacecraft orbit from the ideal geosynchronous orbit.

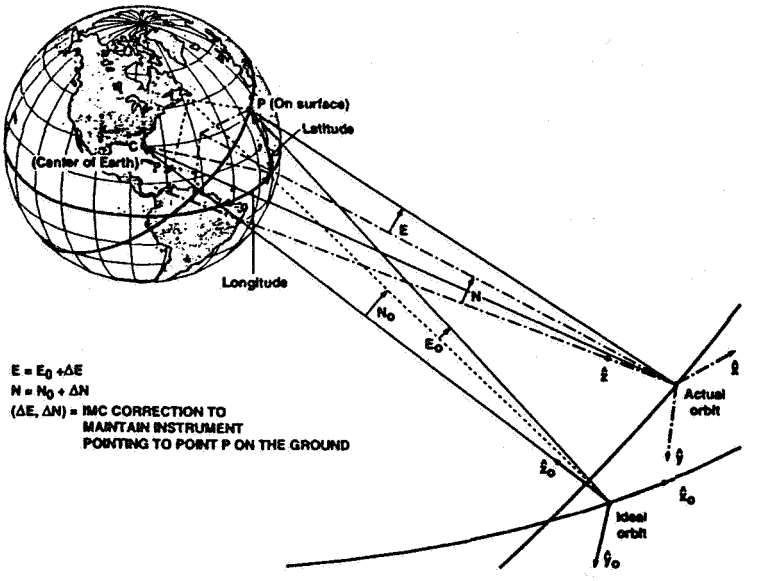

Figure 2.1-1 IMC Orbit Correction

In addition to the orbit corrections, the IMC equations also contain terms which correct for the attitude errors caused by thermal distortions to the imager. A rigorous derivation of these equations are contained in reference 1. For the purpose of IMC simulation only the first-order North/South compensation term needs to be considered. With this in mind, the following equation describes the first-order IMC correction to the North/South scan angle:

$$N_1 = -\left[r\frac{S_{N_e}}{C_{E_e}}\right]\Delta R_1 + \left[\frac{S_{E_e}S_{N_e}}{C_{E_e}}\right]\Delta\lambda - \left[r\frac{C_{N_e}}{C_{E_e}} - 1\right]L_s + \left[\frac{S_{E_e}C_{N_e}}{C_{E_e}}\right](\psi - \psi_s) - \phi - \left[\frac{S_{E_e}S_{N_e}}{C_{E_e}}\right]\theta \quad (1)$$

The residual contributions to the North/South IMC correction due to the misalignment of the optical axis of the instruments have also been derived in reference 1:

$$\Delta N_{ma} = \phi_{ma}(1 - \frac{\cos N_0}{\cos E_0}) + \theta_{ma}\sin N_0(\frac{1}{\cos E_0} + \tan E_0) \quad (2)$$

These contributions are added to the first-order North/South compensation term to get a total IMC correction:

$$\Delta N = N_1 + \Delta N_{ma} \quad (3)$$

Equation (3) describes the total North/South IMC correction being applied to the scan mirror as a function of time and mirror position. For a more detailed description of the GOES IMC system and a rigorous description of these equations see reference 1. Equation (3), which utilizes the daily IMC orbital and attitude coefficients is programmed into my IMC simulator.

2.2 Spacecraft Motion Compensation

In addition to correcting instrument pointing for predetermined orbit and attitude errors, the IMC system has been utilized to correct for spacecraft motion caused by the earth sensor "batwing" effect and the magnetometer "boom shadow" effect. The "batwing" effect is the spacecraft control system response to stray light entering the earth sensor around summer and winter solstices, resulting in significant roll and pitch attitude errors. The "boom shadow" effect is a spacecraft disturbance due to the projection of the magnetometer boom shadow on the solar sail, resulting only in a spacecraft roll error. Both the "batwing" and "boom shadow" effects have been numerically characterized for GOES-8. The maximum roll error due to "batwing" has been shown not to exceed 650 μradians during summer solstice and not to exceed 400 μradians during winter solstice. The maximum roll error due to the "boom shadow" effect has been shown not to exceed 200 μradians. Figures 2.2-1 and 2.2-2 depict the GOES-8 roll attitude behavior for the "batwing" and "boom shadow" effects respectively.

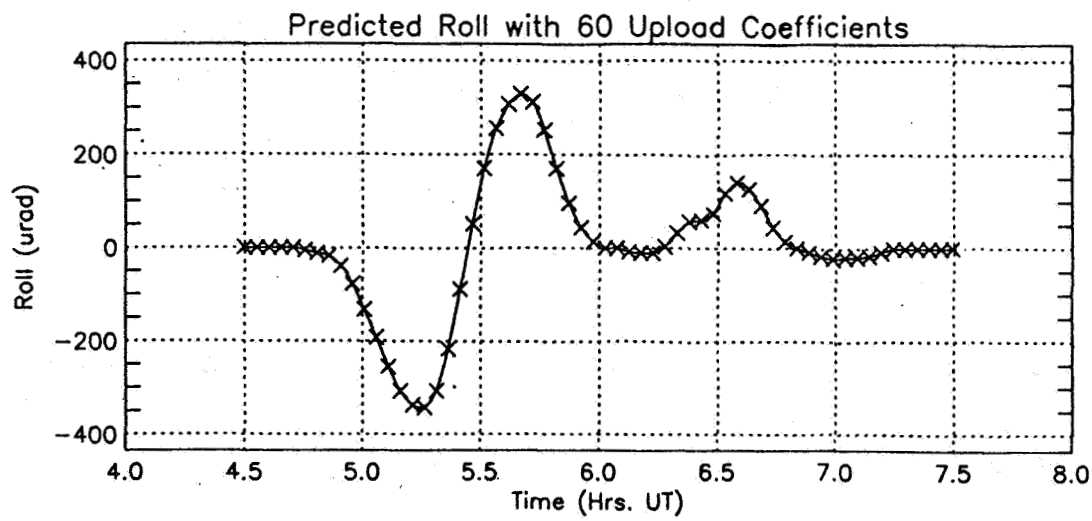

Figure 2.2-1 GOES-8 Roll Error due to "batwing"

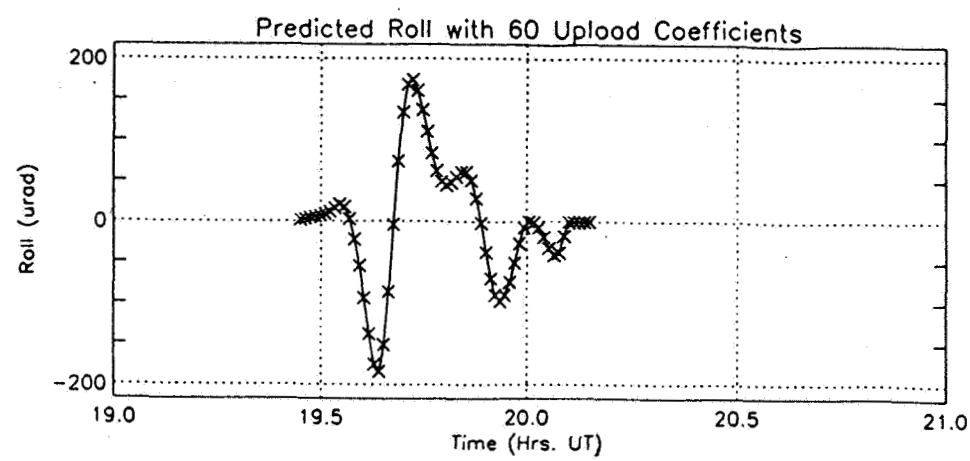

Figure 2.2-2 GOES-8 Roll Error due to "boom shadow"

For GOES-8 the "batwing" effect approximately spans November 21 thru January 23 during winter solstice and May 8 thru August 4 during summer solstice, between 04:30z and 06:30z each day. The "boom shadow" effect is longer and spans September 24 thru April 1, between 19:30z and 20:00z each day. Both of these effects are corrected on board through the IMC system. Daily SMC coefficients are loaded to the spacecraft, and added to the IMC correction signal. As a result, GOES images will not exhibit any INR errors due to spacecraft motion caused by the "batwing" and "boom shadow" effects. The daily SMC coefficients are used in my simulations to estimate the North/South compensation due to "batwing". I ignored the contribution from "boom shadow" because of its short duration (200 μradians for about 15 minutes). The bottom line is that only one image per day is affected by the "boom shadow" effect and I didn't deem it necessary to program it into the simulator for just one image.

2.3 Mirror Motion Compensation

The GOES-8 spacecraft contains two instruments, an imager and a sounder which scan independently of one another. This scan and slew motion produce spacecraft attitude variations of about 150 μradians in roll. For INR purposes, this effect requires compensation which is provided by the Mirror Motion Compensation (MMC) system. Since the contribution of MMC to the overall North/South compensation signal does not exceed 150 μradians and is very short in duration, I chose not to include MMC as part of my simulation. Instead, I decreased the IMC low dynamic range threshold used for analysis from 2000 μradians to 1850 μradians.

2.4 Single Chord Compensation

GOES-8 utilizes a "dual-chord" scanning Earth sensor which provides spacecraft roll and pitch information to the on board attitude control system. As a result of the relative satellite and lunar orbital geometries, the moon will drift into one of the Earth sensor chords several times a month. If the moon drifts into a chord of the Earth sensor, while the Earth sensor is scanning, large unpredictable attitude errors will result. In order to prevent such errors, the chord containing the intrusion will be inhibited and the Earth sensor is operated in "single-chord" mode. Single-chord mode typically lasts three hours to account for the intrusion duration and spacecraft configuration commanding.

It has been shown that the transition from dual-chord to single-chord operations can result in a time varying roll error, up to 600 μradians near spacecraft local midnight. To correct for this phenomenon, a Single Chord Compensation (SCC) algorithm was programmed into the GOES-8 flight software. The time varying single-chord correction signal is added to the IMC and MMC correction signals. Typically, SMC and SCC are not present concurrently. Figure 2.4-1 depicts the single-chord roll error correction by SCC.

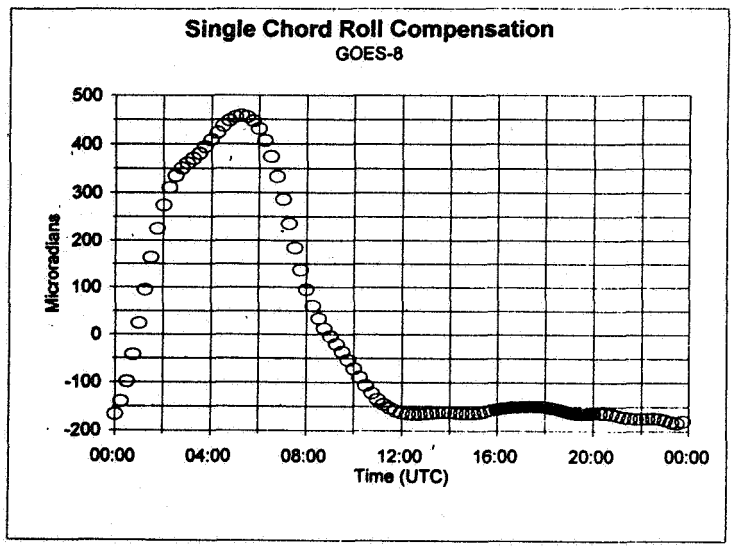

Figure 2.4-1 Single-Chord Roll Error Compensation

Due to time constraints I was unable to include the SCC corrections into my simulation. It is possible that certain single-chord images during the winter solstice could experience INR errors due to low dynamic range threshold violations.

3.0 IMC ANOMALY

3.1 IMC Anomaly Detection

The Orbit and Attitude Tracking System (OATS) provides daily orbit and instrument attitude solutions for the GOES-8 spacecraft. Satellite range and instrument star and landmark measurements are the observations needed to obtain daily solutions. INR performance of the daily solutions is maintained by the OATS and OATS personnel through observational residual monitoring. An observational residual is the difference between the OATS predicted value of a measurement and the OATS observed measurement value. It is through observation monitoring that INR performance is measured and corrected. Figure 3.1-1 shows a typical 12 hour plot of GOES-8 North/South landmark residuals from the visible channel. Notice how the residual signature oscillates evenly about zero and remains between the INR specification limits of +/- 112 μradians.

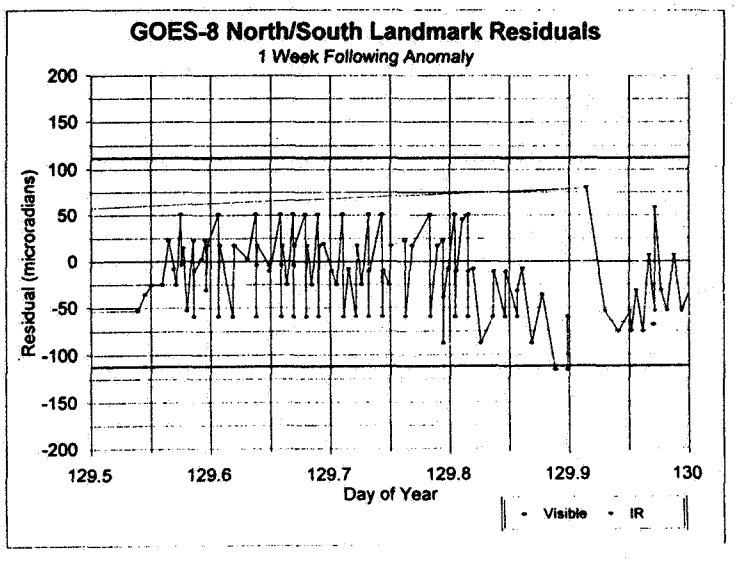

Figure 3.1-1 Normal GOES-8 Landmark Navigation

Figure 3.1-2, below, is a plot of the GOES-8 visible North/South landmark residuals taken one week earlier. Notice the sharp slope in the residual signature towards the beginning of the plot. Also, the individual landmark measurements appear to have more noise and more violations of the INR specification. It was this observation in the GOES navigation which prompted the IMC anomaly investigation.

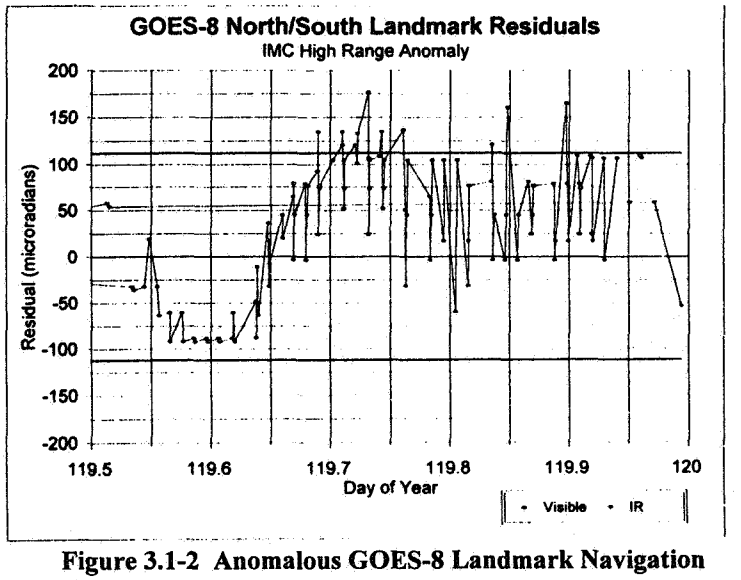

Figure 3.1-2 Anomalous GOES-8 Landmark Navigation

3.2 IMC Anomaly Investigation

The IMC anomaly was investigated by Space System Loral engineers and the cause of signal degradation was determined to be either a Teledyne relay or a Vishay resistor in the IMC electronics. If the resistor was the point of failure the only action available would require switching to the side 2 instrument electronics, which would possibly involve some recalibration of the instrument. If the relay was the problem, it was recommended that the relay be toggled to "unstick" electronic contacts. This action, if required regularly, would cause periodic disruptions to the imaging schedule. Since both of the available actions were undesirable, a study was proposed to determine if IMC high range was required to maintain INR specifications. In subsequent sections, I will show through simulation that INR impacts are minimal in low range, and that it is not necessary to use IMC high range to meet INR requirements.

4.0 IMC SIMULATION

In section 2.0, I discussed the various forms of image compensation required to maintain GOES-8 INR system specifications. When this study was proposed, a minimum amount of time was available for developing the IMC simulator and performing the analysis. With this in mind I chose to only include the contributions from IMC and SMC "batwing" when evaluating the overall North/South compensation. Although the MMC, SCC, and SMC "boom shadow" contributions aren't included in the analysis, I felt they were worthy to mention to the reader since they have an impact on the overall compensation signal. Since I didn't include the contribution from these sources, I lowered the limit of the low dynamic range threshold by an entire **20%** from 2000 μradians to 1600 μradians. This allows for 400 μradians of margin which is large enough to account for the combined effect of MMC and SMC "boom shadow" contributions or the sole effect of SCC contributions.

Utilizing the GOES-8 routine operational imaging schedule, I have a predetermined knowledge of the commanded imager start and stop scan angle coordinates as a function of time of day, as well as individual scan frame durations for each image. Knowing the scan frequency of the instrument, I can accurately predict the commanded scan angle of the GOES-8 imager to within several hundredths of a degree over an entire day. With a detailed knowledge and time history of the imager scan angle, I can then predict the required amount of North/South compensation for every GOES-8 image. Subsequently, for each image I can then report if the North/South compensation exceeds the threshold of 1600 μradians. Section 4.2 will address the specific images potentially affected by threshold violations.

4.1 Simulator Operation

The IMC simulator requires the following user inputs:

- satellite id (8 or 9)
- year/day of year (start time of simulation)
- IMC set id (IMC orbital & attitude coefficients data file identifier)
- IMC data file (file which contains the current IMC orbit & attitude coefficients)
- EVENTS data file (file which contains the daily change in solar rate)
- frame type (Full Disk, Northern Hemisphere, CONUS, Southern Hemisphere)
- SMC flag (use SMC/ignore SMC)
- SMC data file (contains the SMC compensation over time due to "batwing")

Utilizing these inputs, the IMC simulator will generate 3-dimensional plots of the North/South compensation signal and East/West compensation signal as a function of scan angle and time of day for each image of a user specified daily GOES-8 operational schedule. Figures 4.1-1 and 4.1-2 depict 3-D plots of typical GOES-8 compensation signatures for a Full Disk image.

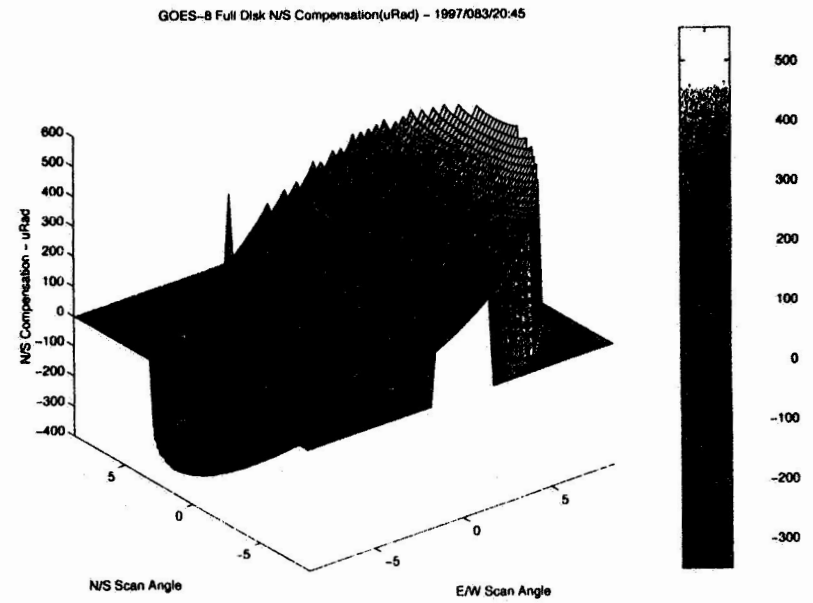

Figure 4.1-1 Typical GOES-8 North/South Compensation Signature

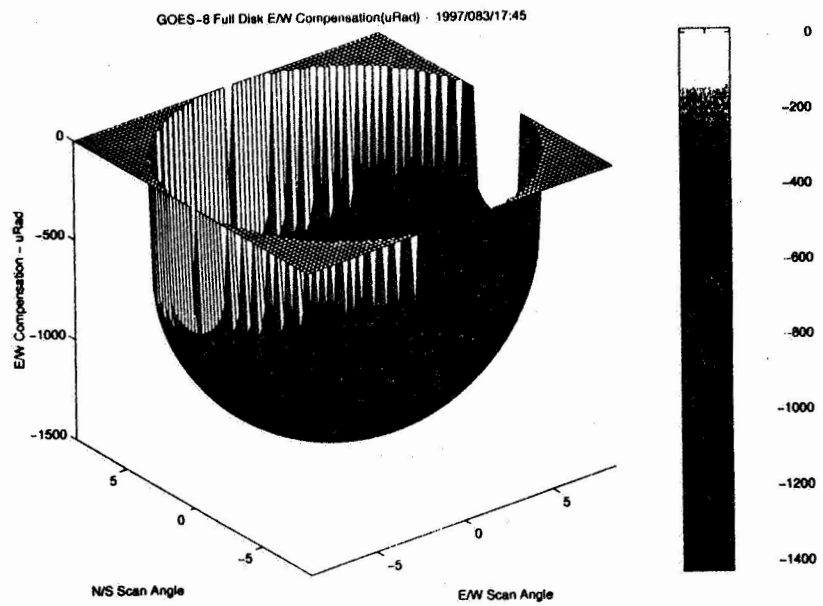

Figure 4.1-2 Typical GOES-8 East/West Compensation Signature

Notice how widely the compensation varies over the entire image for both of the above figures. These plots demonstrate the inherent complexity of the IMC equations and how difficult it can be to "visualize" IMC correction signatures. I have personally used the pet names "potato chip" to describe the North/South compensation signature and "army helmet" to describe the East/West compensation signature. Although the shapes of the compensation plots are unique and lend themselves to interesting names, the shapes are not important for the analysis at hand. I am only concerned with the absolute magnitude of the North/South compensation signal and whether it exceeds the low dynamic range threshold of 1600 μradians.

In Figure 4.1-1 it is evident from the vertical gray scale to the right of the plot that the maximum North/South compensation does not exceed 600 μradians for this particular image, which is well below the 1600 μradian threshold. This particular plot was generated from IMC data taken on day 1997/083 when the GOES-8 orbital inclination was only 0.16 degrees. In section 4.2 I will show that the magnitude of the North/South compensation signal increases with orbital inclination.

4.2 Simulation Results

In order to predict low range IMC performance for the 1996 winter solstice season, I utilized data that was collected from the 1995 winter solstice season. Data files which contain the daily IMC orbit and attitude coefficients from the winter of 1995 are archived and readily available. Since the North/South compensation increases with orbital inclination I started my investigation using a series of data files spanning from day 1995/314 thru 1996/012, during which time the minimum inclination was 0.30 degrees. Figure 4.2-1 depicts the GOES-8 orbital inclination over a 75 day period during the 1995 winter solstice season.

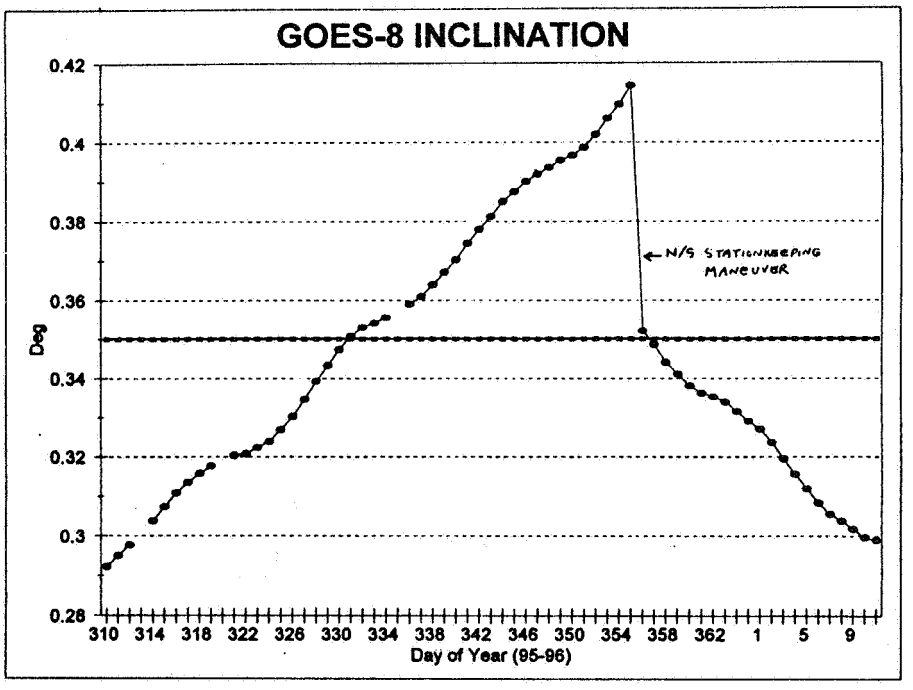

Figure 4.2-1 GOES-8 Orbital Inclination (1995 Winter Solstice Season)

For an entire operational schedule, the IMC simulator will generate a report that lists the individual scan frames where the required IMC exceeds the 1600 μradian threshold . In addition, this report lists the specific instrument scan angles and times that the IMC violations occur. Using this information I was able to estimate that possible IMC violations would occur when the spacecraft inclination was greater than or equal to 0.35 degrees. No IMC violations were detected using IMC sets where the inclination was less than 0.35 degrees. For GOES-8 this would approximately span 1996/330 - 1997/011, a period of 45 days. With this knowledge I concentrated the analysis on IMC sets where the spacecraft inclination was greater than 0.35 degrees. Figure 4.2-2 is a series of GOES-8 full disk North/South compensation plots taken from 1995/353, when the spacecraft inclination was at a maximum of 0.41 degrees.

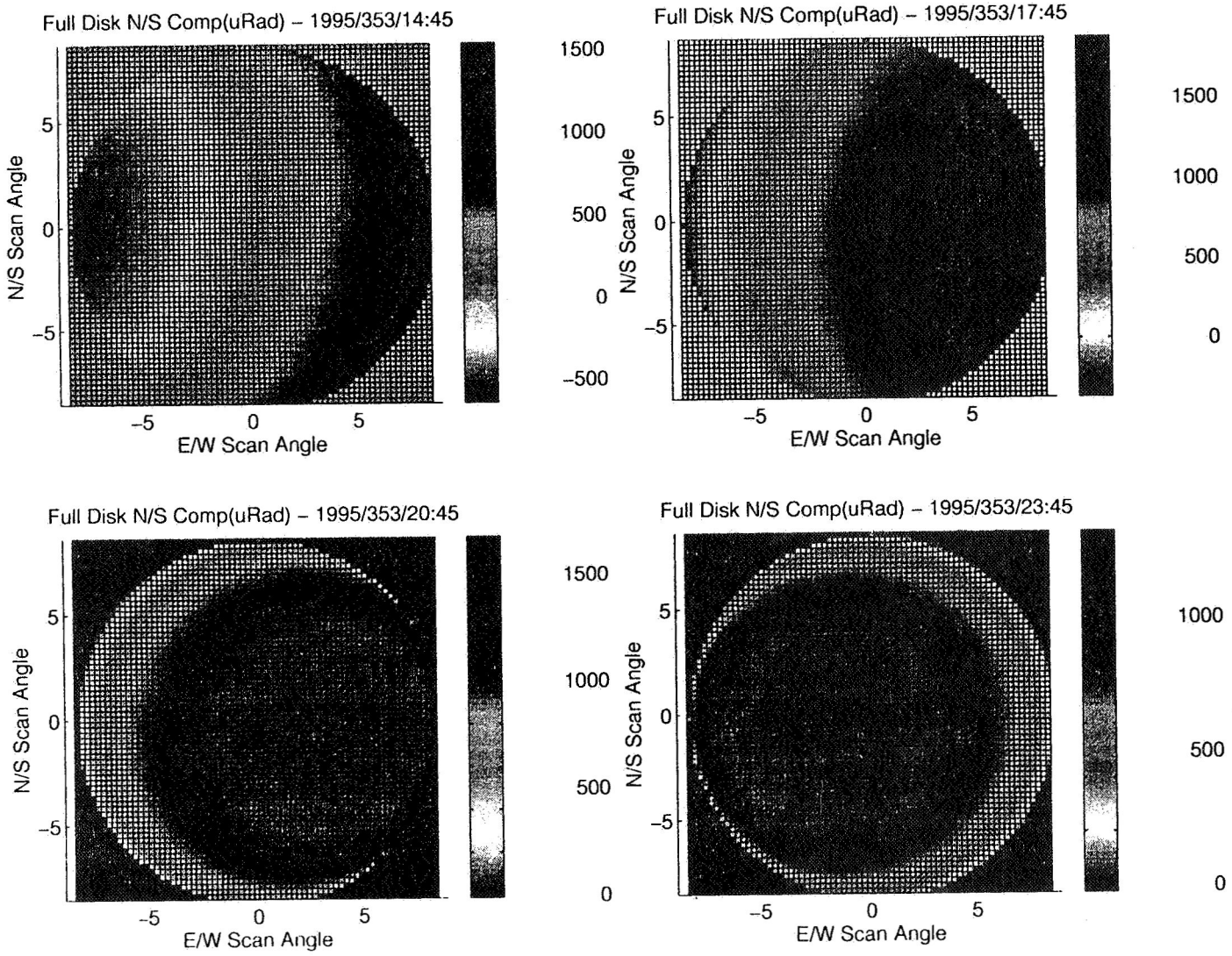

Figure 4.2-2 Variation of GOES-8 North/South Compensation for full disk images (Orbital Descending Node)

The plots in Figure 4.2-2 depict a top view perspective of the North/South compensation signature for four consecutive GOES-8 full disk images. Since these plots were originally generated in color it is difficult to see the variation of the compensation in this black and white format. The vertical scale at the right of each plot is a color bar representing the magnitude of the North/South compensation signature. For the 14:45, 17:45 and 20:45 full disk images it is evident that the 1600 μradian threshold is exceeded , but only over the eastern portion of the images and by no more than 200 μradians. One of the bigger surprises found during the analysis was the fact that no IMC violations occurred for images taken during the "batwing" period, between 04:30z - 06:30z. Recall that up to 600 μradians of North/South compensation is applied to the scan mirror during the "batwing" period. Fortunately, the IMC orbital compensation is in a direction opposite to the SMC "batwing" compensation at this time of day, which is coincident with the ascending node of the orbit. Effectively, the IMC and SMC contributions are cancelling each other. If the "batwing" effect occurred during the descending node of the orbit, the IMC and SMC contributions would have been additive and exceedingly large IMC violations would have been experienced during images between 15:45z - 17:45z. Figure 4.2-3 below, depicts a series of GOES-8 full disk images taken on the same day between 02:45z - 11:45z.

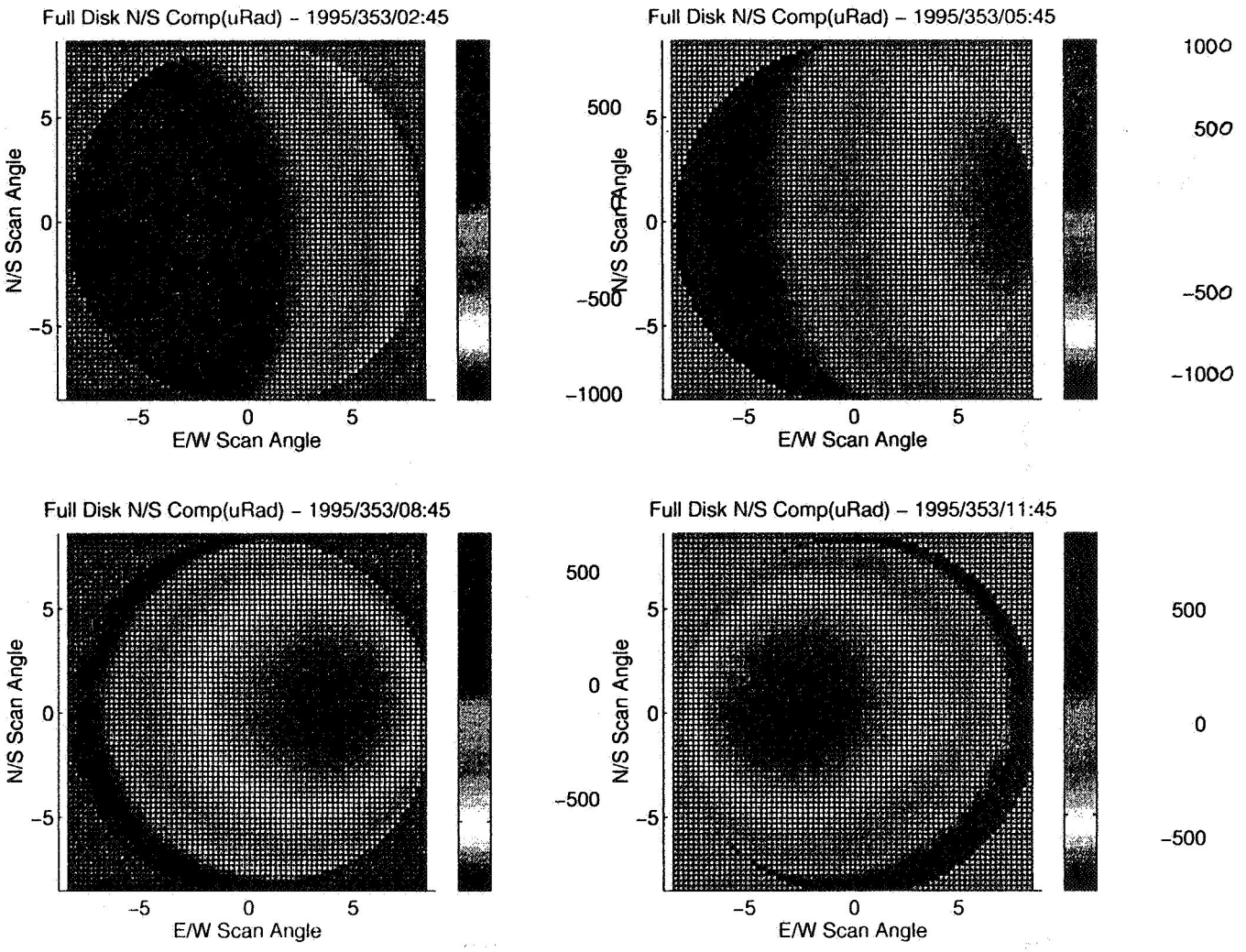

Figure 4.2-3 Variation of GOES-8 North/South Compensation for full disk images (Orbital Ascending Node)

Notice how none of the images in Figure 4.2-3 exhibit any North/South compensation values greater than 1000 μradians, well below the low dynamic range threshold. Table 1 below lists the images which may experience INR errors due to IMC low range limitations. The specific image times, as well as those portions of the images which may be affected is also listed.

Table 1. Images Affected by IMC low range operation

Image Frame	Image Times	Image Portions
Full Disk	17:45z, 20:45z	Eastern, SouthEastern Portion
Northern Hemisphere	16:15z - 22:45z (every 1/2 hour)	Eastern, SouthEastern Portion
Southern Hemisphere	16:39z - 23:09z (every 1/2 hour)	NorthEastern Portion
Continental U.S. (CONUS)	Unaffected	Unaffected

The following plots depict a time sequence of image areas potentially corrupted due to IMC low range violations. Instead of showing the variation in compensation over each image, I customized my MATLAB plots to darken those areas of an image where the threshold of 1600 μradians was exceeded. These plots are a good illustration of how the affected image areas change over time for a series of GOES-8 Northern Hemisphere images.

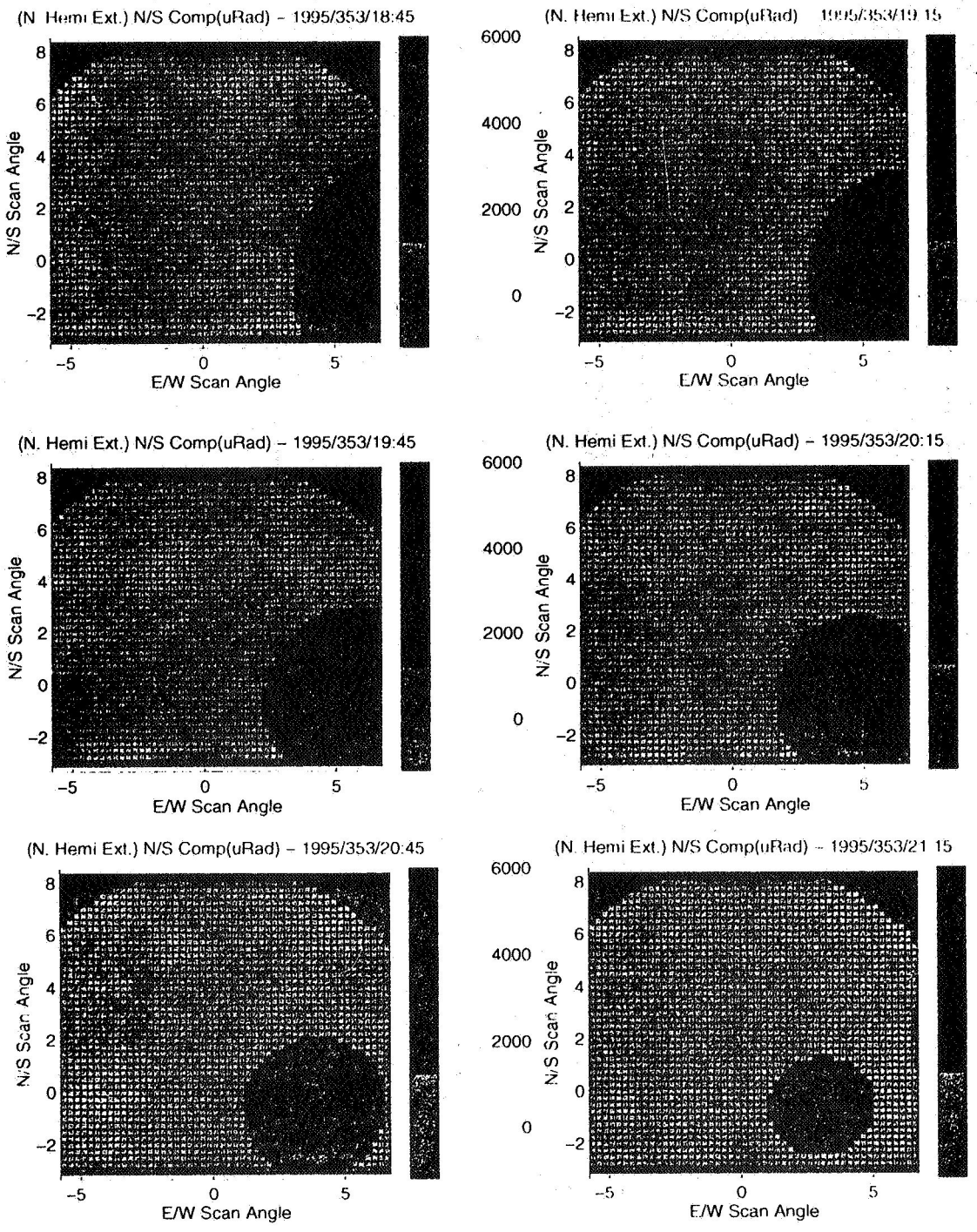

Figure 4.2-4 Time Sequence of IMC Low Range Errors (Northern Hemisphere Images, 353/18:45z - 353/22:15z)

5.0 CONCLUSIONS

The primary goal of this study was to predict specific GOES-8 image frames which may be corrupted due to IMC low dynamic range violations during the 1996 winter solstice season. This was achieved by utilizing IMC data from the 1995 winter solstice season, feeding the data into an IMC simulator and graphically analyzing the results. Instead of using a 2000 μradian dynamic range threshold, I chose to use a 1600 μradian threshold to account for unmodelled IMC contributions (MMC, SCC). Operationally, during the recent 1996 winter solstice season, there were only a handful of IMC low dynamic range violations reported in the spacecraft telemetry verification process. Investigation of these telemetry violations revealed that the violations occurred when the instrument scan angle was pointing off of the Earth disk and therefore had no impact on the images. It appears that the 20% margin of error (1600 μradians) was very conservative for estimating possible IMC violations.

In conclusion, both this study and operational navigation results have shown that IMC low range operation is acceptable for meeting GOES-8 INR system requirements for spacecraft inclinations below 0.4 degrees. If the GOES-8 inclination exceeds 0.4 degrees, there is a stronger probability that IMC violations will occur. If this is ever the case, the results of this study can be utilized to confidently predict the time of day and the locations within an image that IMC errors may occur for spacecraft inclinations greater than 0.4 degrees.

6.0 REFERENCES

The following publications are references for the preceding paper and should be consulted for more information.

1. Space Systems/Loral, Image Navigation and Registration, DRL 300-06, March 4, 1994.

2. Kelly, Kathleen A., J. Hudson, N. Pinkine, "GOES 8/9 Image Navigation and Registration Operations", Proceedings of the SPIE International Symposium of Optical Science, Engineering and Instrumentation; Conference on GOES-8 and Beyond, Denver, CO., August 4-9, 1996.

Spacecraft Slews Avoiding Celestial Objects and Maintaining Communication with Ground Station

Hari B. Hablani[†]
Boeing North American, Downey, CA

Abstract

This paper is concerned with devising a slew strategy for spacecraft such that, while slewing, the spacecraft maintains simultaneously (a) a minimum angular distance of its telescope from Sun, Moon, and Earth, and (b) communication link of its antenna with ground station. The slew technique is based on the formulation of an ideal slew plane formed by initial and final directions of the telescope and determination of azimuth and elevation coordinates of the centers of bright objects' discs relative to the ideal slew plane. If a disc intersects the ideal slew path, a minimum deviation angle is first determined for the telescope to pass the disc's center by a specified angular distance. These minimum angles for the disc centers are connected piecewise with quadratic or cubic elevation angle profiles depending on the location of the discs relative to the slew plane. Such profiles, however, may steer the telescope into a forbidden disc if the discs are large and/or nearby and possibly overlapping. The situations which cause this are determined and the equations of the disc's perimeter in terms of azimuth and elevation angles are developed so that the transgressing portion of the quadratic or cubic elevation angle profile is replaced with the corresponding segment of the disc boundary. Incremental roll angles are determined to maintain communication during slew of antennas mounted on the pitch and yaw axes of the spacecraft. Numerical illustrations show that the strategies perform as desired.

I. Introduction

Spacecraft, whether earth pointing, inertially-stabilized or interplanetary, carrying infrared sensitive payloads are sometimes required to slew from one direction in space to another in such a way that, en route, the sensitive payloads not see bright objects such as Sun, Moon and Earth, and, simultaneously, antennas not lose communication with ground station. This paper is concerned with devising strategies for these purposes. To be sure, the subject of spacecraft attitude maneuvers avoiding certain directions in space has been considered in the past. Following robotics science,[1] McInnes[2-4] utilized a composite function consisting of a harmonic potential and constraint potentials, the former having a global minimum at the desired final attitude and the latter generating vortex velocity fields centered at forbidden directions. Perhaps novel and ingenious, this procedure nonetheless is not well-founded from the standpoint of spacecraft attitude kinematics. Indeed, the examples in Refs. 1-4 reveal that a vehicle, while being slewed, moves towards, instead of away from, the avoidance cone and when near it, the payload slides aimlessly around it until pulled over incidentally by the global potential function. Thus, although the telescope boresight avoids forbidden directions, it meanders away substantially from its nominal path. Sorensen,[5] on the other hand, uses a more natural approach that requires analysis of spacecraft orbit geometry, relative motion of Sun around Earth, and varying Earth disc diameter for an elliptic orbit, and formulates the pointing constraints that minimize heat input from Sun to cryogenically cooled telescope. Furthermore, he applies differential geometry to determine possible attitudes paths. It is this vectorial kinematic and geometric approach that is utilized in this paper. A similar approach appears to have been used in Ref. 6 for interplanetary spacecraft Cassini, though details are not available yet. Also, Rivera[7] conceived of a fixed axis of rotation located somewhere in the plane that bisects the angle between the initial and the final line-of-sight directions, the exact location decided by the requirement that the boresight's path (circular arc) avoid the bright discs which intersect its original ideal path. Though well-thought-of, a shortcoming of this approach is that it results in maximum deviation of the boresight from its original minimum-angle path at half-slew angle even if the bright discs are located elsewhere far away. This is caused by the stipulation that the axis of rotation be positioned in the bisecting plane mentioned above. In contrast, the approach devised in this paper has many general features, including the one that the axis of rotation is now swerved away from its ideal orientation minimally as a function of slew angle, in accordance with the locations and sizes of the bright discs relative to the ideal minimum angle slew plane.

[†]Principal Engineering Specialist, Avionics Engineering, Flight Control Systems, Space Systems Division, Associate Fellow AIAA

The contents of this paper, then, are as follows. Section II formulates the ideal slew plane formed by the initial and the final directions of the telescope. Azimuth (in-plane) and elevation (out-of-plane) coordinates of the centers of bright celestial objects are determined relative to this plane and if their discs are found to intersect the ideal slew plane, a minimum deviation (elevation) strategy is developed so as to enable the telescope to avoid these objects. For overlapping discs, since this strategy is inadequate, a non-minimum deviation strategy is also developed. To generate a profile of elevation angle for complete range of slew (azimuth) angle the elevation angle across the ideal slew plane for one object is connected quadratically or cubicly with the elevation angle for the next object in or near the slew plane. If the elevation profile so formed steps into a disc, the transgressing segment is replaced with the disc boundary. The parametric equation of the disc boundary is also formulated in this section. Section III formulates the auxiliary roll motion for maintaining communication link of a ground station with antennas on the vehicle. The roll angle is determined such that the instantaneous signal strengths for pitch and yaw antennas normal to the roll axis are equal. This roll motion is superimposed on the boresight slew motion avoiding the celestial objects. The two algorithms are illustrated in Sec. IV in the context of a space vehicle and their performance is discussed. Section V concludes the paper.

II. Exclusion Algorithm for Boresight Slew

Figure 1 portrays the unit vector $\underline{\ell}_0$ along the initial direction of the boresight, and $\underline{\ell}_f$ along its final desired direction. It further depicts a celestial object s_i to be avoided by the telescope. A strategy for avoidance is now developed. First we formulate the ideal slew of the boresight from $\underline{\ell}_0$ to $\underline{\ell}_f$, ideal in that the celestial objects are ignored. Clearly, the most natural axis of rotation is the one normal to the plane containing the noncolinear unit vectors $\underline{\ell}_0$ and $\underline{\ell}_f$. Denote the unit vector along this axis of rotation as $\underline{b}$ (Fig. 1) and the angle between $\underline{\ell}_0$ and $\underline{\ell}_f$ as ϕ, where, by definition, $0 < \phi < \pi$. Then

$$\sin\phi = |\underline{\ell}_0 \times \underline{\ell}_f| \qquad 0 < \phi < \pi \tag{1a}$$

$$\underline{b} = (\underline{\ell}_0 \times \underline{\ell}_f)/\sin\phi \tag{1b}$$

To complete the right-handed triad associated with the unit vectors $\underline{\ell}_0$ and $\underline{b}$, define a unit vector $\underline{a}$ in the plane $\underline{\ell}_0$ - $\underline{\ell}_f$ such that

$$\underline{a} = \underline{b} \times \underline{\ell}_0 \tag{2}$$

The coordinate frame associated with the triad $\underline{\ell}_0\ \underline{a}\ \underline{b}$ (in this sequence) is denoted $x'_{b0}\ y'_{b0}\ z'_{b0}$ where the subscript b denotes the spacecraft body, 0 denotes initial orientation of the spacecraft, and prime distinguishes this frame from the spacecraft frame $x_{b0}\ y_{b0}\ z_{b0}$ where $x_{b0} = x'_{b0}$ and the axes y_{b0}, z_{b0} are related to y'_{b0}, z'_{b0} through a roll angle. Since the final desired direction $\underline{\ell}_f$ is arbitrary, the axis of rotation $\underline{b}$ or z'_{b0} is also arbitrary and generally different from the initial body axis z_{b0}.

Minimum Exclusion Maneuvers

The location of the center of a celestial object s_i can be specified through the azimuth angle α_i^* in the plane $\underline{\ell}_0$ - $\underline{\ell}_f$ (or x'_{b0} y'_{b0}) about the axis $\underline{b}$ (or z'_{b0}) and the elevation angle ε_i^* about the once-displaced axis y'_{b0} (the unit vector $\underline{c}_i$ in Fig. 1). These angles are determined as follows. If the boresight is slewed along a curvilinear path avoiding celestial objects, its orientation in the celestial sphere can be specified in terms of an azimuth angle α and an elevation angle ε. Let $x_d\ y_d\ z_d$ be the orientation of the spacecraft-attached frame that coincides with $x'_{b0}\ y'_{b0}\ z'_{b0}$ for $\alpha = 0 = \varepsilon$. These two frames are related as follows:

$$\begin{bmatrix} x_d \\ y_d \\ z_d \end{bmatrix} = \begin{bmatrix} c\varepsilon\, c\alpha & c\varepsilon\, s\alpha & -s\varepsilon \\ -s\alpha & c\alpha & 0 \\ s\varepsilon\, c\alpha & s\varepsilon\, s\alpha & c\varepsilon \end{bmatrix} \begin{bmatrix} x'_{b0} \\ y'_{b0} \\ z'_{b0} \end{bmatrix} \tag{3}$$

where s (·) = sin (·) and c (·) = cos (·). The unit vector $\underline{s}_i$ pointing to the center of the celestial object s_i can be expressed in the frame $\underline{\ell}_0\ \underline{a}\ \underline{b}$ thus

$$\underline{s}_i = \underline{s}_i \cdot \underline{\ell}_0\ \underline{\ell}_0 + \underline{s}_i \cdot \underline{a}\ \underline{a} + \underline{s}_i \cdot \underline{b}\ \underline{b} \tag{4}$$

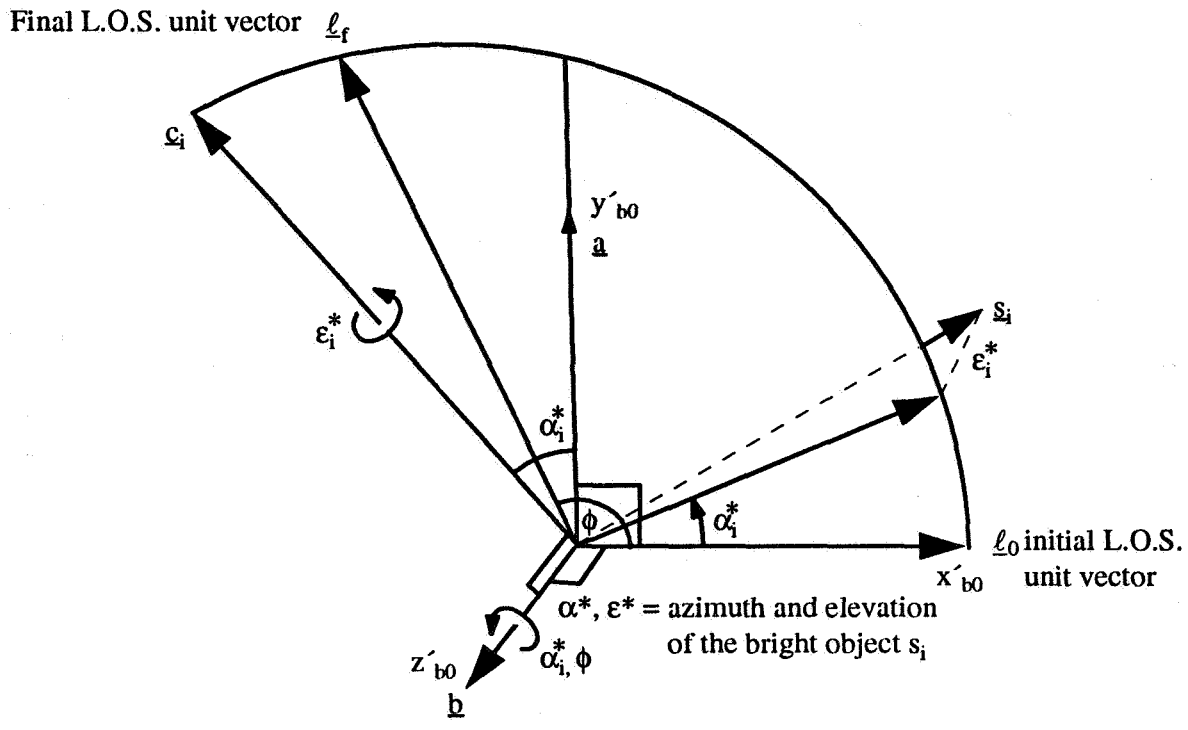

Fig. 1. Location of a celestial object relative to the ideal slew plane of the boresight

These three components of $\underline{s}_i$ are known because the unit vectors $\underline{s}_i$, $\underline{\ell}_0$, $\underline{\ell}_f$ and therefore $\underline{a}$ and $\underline{b}$ are known in some inertial frame. Furthermore, if the instantaneous boresight x_d were to point along $\underline{s}_i$, then $\underline{s}_i$ will be expressed in the frame $\underline{\ell}_0\ \underline{a}\ \underline{b}$ as, using Eq. (3),

$$\underline{s}_i = c\varepsilon_i^*\, c\alpha_i^*\ \underline{\ell}_0 + c\varepsilon_i^*\, s\alpha_i^*\ \underline{a} - s\varepsilon_i^*\ \underline{b} \tag{5}$$

Comparing the three components of $\underline{s}_i$ in Eqs. (4) and (5) we derive the following three equations.

$$\underline{\ell}_0 \text{ component: } c\varepsilon_i^*\, c\alpha_i^* = \underline{s}_i \cdot \underline{\ell}_0 \tag{6a}$$

$$\underline{a} \text{ component: } c\varepsilon_i^*\, s\alpha_i^* = \underline{s}_i \cdot \underline{a} \tag{6b}$$

$$\underline{b} \text{ component: } s\varepsilon_i^* = -\underline{s}_i \cdot \underline{b} \tag{6c}$$

Eqs. (6a) and (6b) yield

$$\alpha_i^* = \tan^{-1}\left[(\underline{s}_i \cdot \underline{a}), (\underline{s}_i \cdot \underline{\ell}_0) \right], \qquad -\pi \le \alpha_i^* \le \pi \tag{7a}$$

provided $-\pi/2 < \varepsilon_i^* < \pi/2$ so that $c\varepsilon_i^* > 0$. On the other hand, the equality of the $\underline{b}$ components, Eq. (6c), yields

$$\varepsilon_i^* = -\sin^{-1}(\underline{s}_i \cdot \underline{b}) \qquad -\pi/2 < \varepsilon_i^* < \pi/2 \tag{7b}$$

The location of a celestial object with respect to the slew plane $\underline{\ell}_0 - \underline{\ell}_f$ is thus determined via Eqs. (7). A celestial object needs to be considered for avoidance when, loosely speaking, $0 \le \alpha_i^* \le \phi$. This condition is not exact because, usually, an infrared or a hot celestial object is to be avoided by a minimum specified angle denoted ε_{spec}. That is, there is a disc of radius ε_{spec} around a celestial object s_i centered at $(\alpha_i^*, \varepsilon_i^*)$ that the boresight must not enter. For $\varepsilon_i^* = 0$, the extreme azimuth angles of the disc boundary will be $\alpha_i^* \pm \varepsilon_{spec}$ and for the s_i disc to be considered for avoidance the azimuth angle α_i^* must satisfy the condition: $-\varepsilon_{spec} \le \alpha_i^* \le \phi + \varepsilon_{spec}$. In any event, for celestial objects with $0 \le \alpha_i^* \le \phi$, the minimum deviation angle ε_i required for avoiding an object at $(\alpha_i^*, \varepsilon_i^*)$ is determined very simply as follows. Fig. 2 illustrates two celestial objects, one with $\varepsilon_i^* > 0$

and the other with $\varepsilon_i^* < 0$. Discs of radius ε_{spec} are drawn around each center $(\alpha_i^*, \varepsilon_i^*)$. One concludes from Fig. 2 that the natural rotation path of the boresight (the azimuth, α, axis) about the axis $\underline{b}$ will intersect the ε_{spec} disc if $|\varepsilon_i^*| < \varepsilon_{spec}$ and then, for boresight to avoid entering the disc, the minimum deviation angle ε_i at $\alpha = \alpha_i$ must be

$$\varepsilon_i = \begin{cases} -\varepsilon_{spec} + \varepsilon_i^* & \text{if } 0 < \varepsilon_i^* < \varepsilon_{spec} \quad (8a) \\ \varepsilon_{spec} - |\varepsilon_i^*| & \text{if } -\varepsilon_{spec} < \varepsilon_i^* < 0 \quad (8b) \\ 0 & \text{if } |\varepsilon_i^*| > \varepsilon_{spec} \quad (8c) \end{cases}$$

There are occasions, however, when the minimum deviation angles prescribed by Eqs. (8) will be unable to prevent the boresight from entering the disc around a celestial object. This will be discussed and remedied later but first we discuss the usefulness of these minimum angles. In order to slew the telescope from $\underline{\ell}_0$ to $\underline{\ell}_f$ the variation of the angle ε with α, $0 \le \alpha \le \phi$, is required. One such continuous profile, profile I, is shown in Fig. 3 for avoiding three celestial objects, each requiring a deviation of ε_i at α_i^* (i = 1, 2, 3) from α-axis. The ε-profile from $\alpha = 0$ to $\alpha = \alpha_1^*$ can be taken as quadratic satisfying the conditions

$$\varepsilon = 0 \qquad @\ \alpha = 0 \quad (9a)$$

$$\left.\begin{aligned} \varepsilon &= \varepsilon_1 \quad (9b) \\ \frac{d\varepsilon}{d\alpha} &= 0 \quad (9c) \end{aligned}\right\} \qquad @\ \alpha = \alpha_1^*$$

where the zero slope condition is added so that the profile is tangential to the ε_{spec} disc at $(\alpha_1^*, \varepsilon_1^*)$. Tangency to the disc is also the reason why ε is not varied linearly with α because otherwise the profile will surely enter the disc. The quadratic profile satisfyng the condition (9) is

$$\left.\begin{aligned} \varepsilon &= -\frac{\varepsilon_1}{\alpha_1^2}(\alpha^2 - 2\alpha\alpha_1) \quad (10a) \\ \frac{d\varepsilon}{d\alpha} &= \frac{2\varepsilon_1}{\alpha_1}\left(1 - \frac{\alpha}{\alpha_1}\right) \quad (10b) \end{aligned}\right\} \qquad 0 \le \alpha \le \alpha_1$$

where, for notational simplicity, here and in the rest of the paper occasionally, the superscript * in α_i^* is dropped. The profile from the last celestial object, s_3, to the end of the slew, $\alpha = \phi$, is constructed similarly, satisfying the conditions

$$\left.\begin{aligned} \varepsilon &= \varepsilon_3 \quad (11a) \\ \frac{d\varepsilon}{d\alpha} &= 0 \quad (11b) \end{aligned}\right\} \qquad @\ \alpha = \alpha_3$$

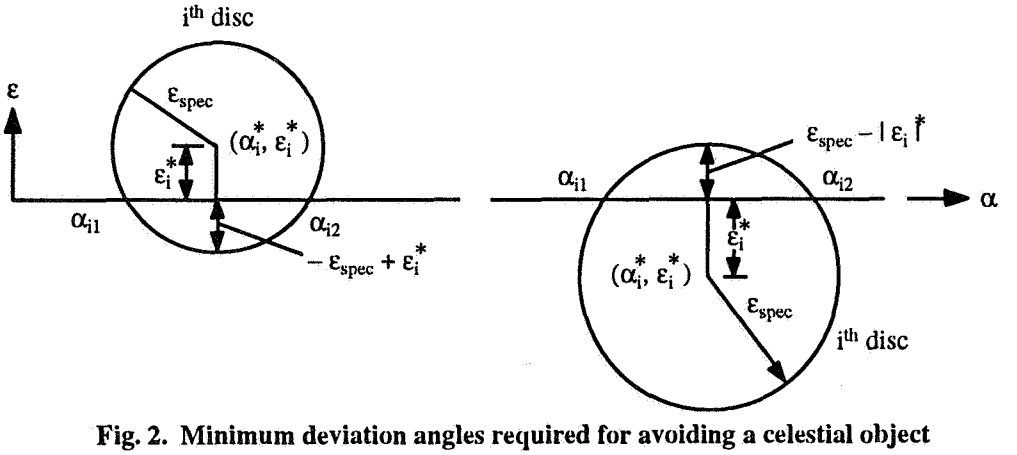

Fig. 2. Minimum deviation angles required for avoiding a celestial object

$$\varepsilon = 0 \qquad @\ \alpha = \phi \tag{11c}$$

With s_3 as the last object, the profile I is

$$\left.\begin{aligned} \varepsilon &= \frac{\varepsilon_3}{(\phi - \alpha_3)^2}\left[(\phi - \alpha_3)^2 - (\alpha - \alpha_3)^2\right] \qquad (12a)\\ \frac{d\varepsilon}{d\alpha} &= \frac{-2\varepsilon_3}{(\phi - \alpha_3)^2}(\alpha - \alpha_3) \qquad (12b) \end{aligned}\right\} \quad \alpha_3 \le \alpha \le \phi$$

Regarding the profile from the object i to i + 1, the question arises whether the profile should have zero slope at α_i , at α_{i+1}, or at both places. The zero slope profile at both ends (α_1 and α_2 in Fig. 3, profile I) is unsuitable if ε_i and ε_{i+1} both have the same sign because the dip in the profile is then prone to place the boresight in at least one of the forbidden discs. On the other hand, if $|\varepsilon_{i+1}| > |\varepsilon_i|$ and they both have the same sign, the zero slope only at i+1 is appropriate because the profile then will leave the disc i from outside and arrive at the disc i+1 tangentially at $(\alpha_{i+1},\ \varepsilon_{i+1})$. This is illustrated in Fig. 3 by the piecewise continuous profile II between α_1 and α_2 although the discs are not drawn in the figure. One such quadratic profile satisfying the conditions

$$@\ \alpha = \alpha_i \qquad \varepsilon = \varepsilon_i \tag{13a}$$

$$@\ \alpha = \alpha_{i+1} \begin{cases} \varepsilon = \varepsilon_{i+1} & (13b)\\ \dfrac{d\varepsilon}{d\alpha} = 0 & (13c) \end{cases}$$

is

$$\varepsilon = \varepsilon_{i+1} + (\varepsilon_i - \varepsilon_{i+1})\ \frac{(\alpha_{i+1} - \alpha)^2}{(\alpha_{i+1} - \alpha_i)^2} \tag{14a}$$

$$\frac{d\varepsilon}{d\alpha} = 2\,(\varepsilon_{i+1} - \varepsilon_i)\ \frac{(\alpha_{i+1} - \alpha)}{(\alpha_{i+1} - \alpha_i)^2} \tag{14b}$$

Analogously, when $|\varepsilon_i| > |\varepsilon_{i+1}|$ and they are both of the same sign, the zero slope at i will be appropriate because it will then depart from the disc i tangentially and land at the disc i+1 at $(\alpha_{i+1},\ \varepsilon_{i+1})$ from outside. This quadratic profile satisfying the conditions

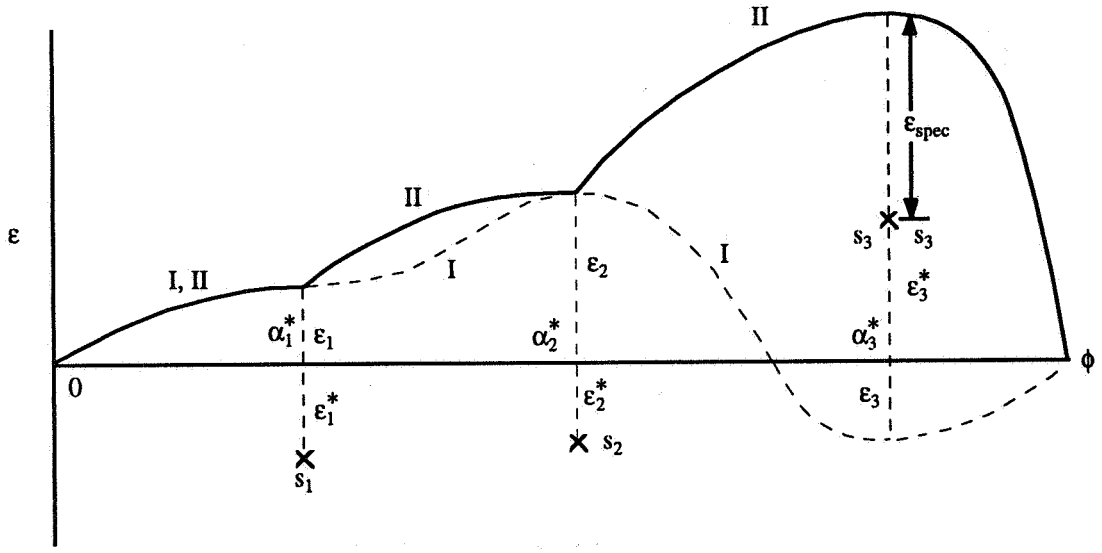

Fig. 3. Alternate non-minimum ε-profiles for excluding celestial objects

$$@\ \alpha = \alpha_i \qquad \begin{cases} \varepsilon = \varepsilon_i & (15a) \\ \dfrac{d\varepsilon}{d\alpha} = 0 & (15b) \end{cases}$$

$$@\ \alpha = \alpha_{i+1} \qquad \varepsilon = \varepsilon_{i+1} \tag{15c}$$

is

$$\varepsilon = \varepsilon_i + (\varepsilon_{i+1} - \varepsilon_i)\ \frac{(\alpha - \alpha_i)^2}{(\alpha_{i+1} - \alpha_i)^2} \tag{16a}$$

$$\frac{d\varepsilon}{d\alpha} = 2\,(\varepsilon_{i+1} - \varepsilon_i)\ \frac{(\alpha - \alpha_i)}{(\alpha_{i+1} - \alpha_i)^2} \tag{16b}$$

Finally, when ε_i and ε_{i+1} have opposite signs, as ε_2 and ε_3 in Fig. 3, and the discs are sufficiently far apart, a cubic ε profile satisfying the conditions

$$\left.\begin{aligned} \varepsilon &= \varepsilon_i \\ \frac{d\varepsilon}{d\alpha} &= 0 \end{aligned}\right\} @\ \alpha = \alpha_i \qquad \left.\begin{aligned} \varepsilon &= \varepsilon_{i+1} \\ \frac{d\varepsilon}{d\alpha} &= 0 \end{aligned}\right\} @\ \alpha = \alpha_{i+1} \tag{17}$$

between α_i and α_{i+1} (profile I, Fig. 3) is

$$\varepsilon\,(\alpha_{i+1} - \alpha_i)^3 = (\varepsilon_i - \varepsilon_{i+1})\,[2\,\alpha^3 - 3\,(\alpha_i + \alpha_{i+1})\,\alpha^2 + 6\,\alpha_i\,\alpha_{i+1}\,\alpha] \tag{18a}$$

$$- \varepsilon_i\,\alpha_{i+1}^2\,(3\,\alpha_i - \alpha_{i+1}) + \varepsilon_{i+1}\,\alpha_i^2\,(3\,\alpha_{i+1} - \alpha_i)$$

$$\frac{d\varepsilon}{d\alpha}\,(\alpha_{i+1} - \alpha_i)^3 = 6\,(\varepsilon_i - \varepsilon_{i+1})\,(\alpha - \alpha_i)\,(\alpha - \alpha_{i+1}) \tag{18b}$$

The profile I in Fig. 3 between α_2 and α_3 is one such profile.

Non-Minimum Exclusion Maneuvers

When ε_{spec} discs around two adjacent celestial objects are not far apart, the minimum angle ε-profiles are likely to enter the discs. Indeed, if the discs are large, they may overlap. A disc may be close to $\alpha = 0$ or $\alpha = \phi$ points on the α-axis, or a disc may contain $\alpha = 0$ point. Under these circumstances, the minimum deviation angles must be modified. The situation in which a disc encompasses $\alpha = \phi$ point is not considered because the desired line-of-sight direction $\underline{\ell}_f$ is then unreachable by definition. When ε_i and ε_{i+1} are of opposite signs and the cubic profile, Eqs. (18), is found to enter the disc i and/or i+1 through simulation, the minimum deviation angle ε_{i+1} at α_{i+1} must be replaced such that the boresight now passes the object i+1 tangentially at the diametrically opposite side of the disc. This is illustrated in Fig. 3, replacing $\varepsilon_3 < 0$ by $\varepsilon_3 = \varepsilon_3^* + \varepsilon_{spec} > 0$ which is of the same sign as ε_2 for the disc 2. This replacement leads to the ε-profile II between α_2 and α_3.

Fig. 4 illustrates two instances of overlapping discs. Consider Fig. 4a first which illustrates the case where $|\varepsilon_{i+1}^*| > \varepsilon_{spec}$ and therefore the natural boresight path does not intersect the disc i+1 and $\varepsilon_{i+1} = 0$. Meanwhile, the disc i is located such that the boresight path does intersect it and $\varepsilon_i > 0$. The minimum deviation ε-profile, then, is the profile-I shown in Fig. 4a. But this profile is clearly unsuitable because a part of the profile is within the disc i. A simple alternative in this instance will be to set $\varepsilon_{i+1} = \varepsilon_i$, leading to the profile II which is acceptable. Fig. 4b illustrates a situation in which ε_i and ε_{i+1} are of opposite signs, α_i^* and α_{i+1}^* of the two discs are nearby, and the discs radii are so large that the two discs overlap considerably, making the minimum deviation profile useless. To arrive at an acceptable ε-profile, then, the minimum deviation $\varepsilon_{i+1} < 0$ is replaced by $\varepsilon_{i+1} = \varepsilon_{i+1}^* + \varepsilon_{spec}$, leading to the profiles II or III.

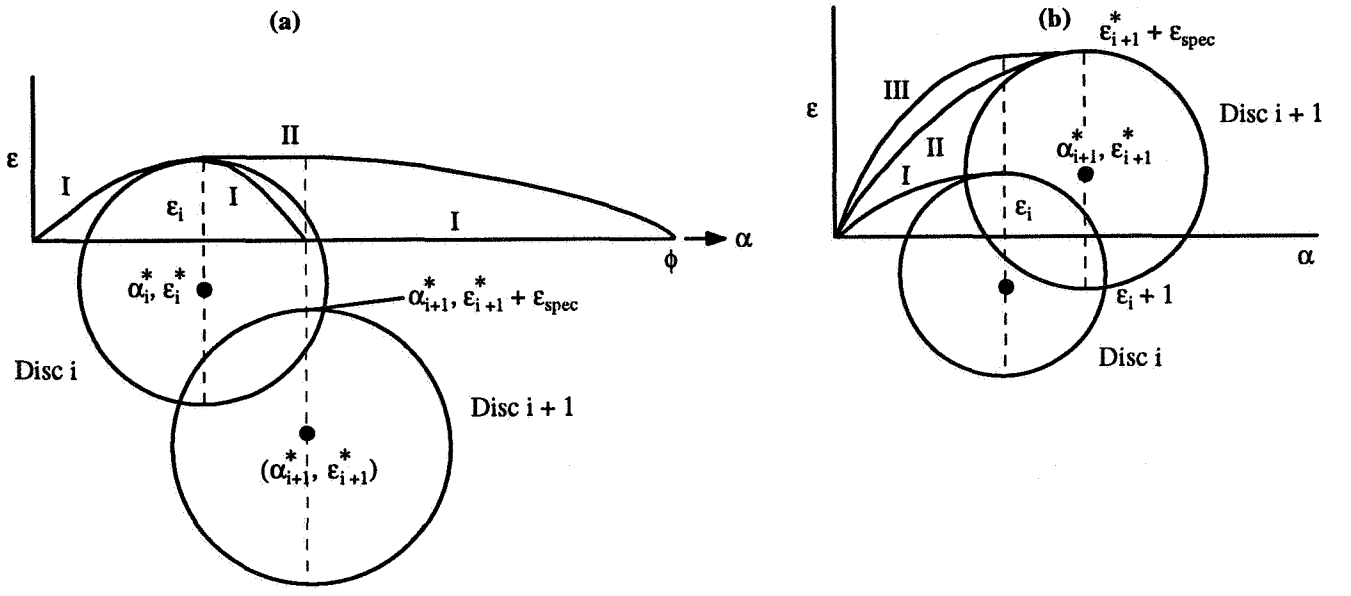

Fig. 4. Alternate non-minimum ε-profiles for overlapping discs around celestial objects

Generally speaking, such modifications in minimum deviation angles prevent the boresight from entering the discs. Occasionally, however, these modifications are inadequate. To identify and avert such situations, the (α, ε) equation of the disc is required so that if the entrance of the boresight to the disc is imminent, it may instead be commanded to slide along the disc.

Disc Equation

Fig. 5 portrays the geometry of a disc of radius $\varepsilon_{spec} > \varepsilon^*$ around a celestial object s centered at $(\alpha^*, \varepsilon^*)$. The disc intersects the boresight path at azimuths α_1 and α_2. Utilizing the transformation equation (3), the boresight axis towards the center of the disc is denoted $\underline{x}_d^*$ and the unit vector along this axis is denoted $\underline{s}$. In order to exclude the disc from the boresight slew path, the boresight at best can slide around the disc and this requires the knowledge of the disc boundary as a function of the slew angle or azimuth angle α. This is derived now.

The boresight unit vector towards any point on the disc's circumference is denoted $\underline{s}_e$ (the subscript e for exclusion). Then, clearly, the disc's circumference is governed by

$$\underline{s} \cdot \underline{s}_e = \cos \varepsilon_{spec} \tag{19}$$

Also, just as the orientation of the unit vector $\underline{s}$ is defined by $(\alpha^*, \varepsilon^*)$ coordinates, the unit vector $\underline{s}_e$ along the boresight axis x_d can be defined by the coordinates (α, ε) using Eq. (3). Hence one finds

$$\underline{s} = c\varepsilon^* \, c\alpha^* \, \underline{\ell}_0 + c\varepsilon^* \, s\alpha^* \, \underline{a} - s\varepsilon^* \, \underline{b} \tag{20a}$$

$$\underline{s}_e = c\varepsilon \, c\alpha \, \underline{\ell}_0 + c\varepsilon \, s\alpha \, \underline{a} - s\varepsilon \, \underline{b} \tag{20b}$$

Therefore, recalling Eq. (19), the dot product $\underline{s} \cdot \underline{s}_e$ yields

$$c\varepsilon \, c\varepsilon^* \, c(\alpha - \alpha^*) + s\varepsilon \, s\varepsilon^* = c\varepsilon_{spec} \tag{21}$$

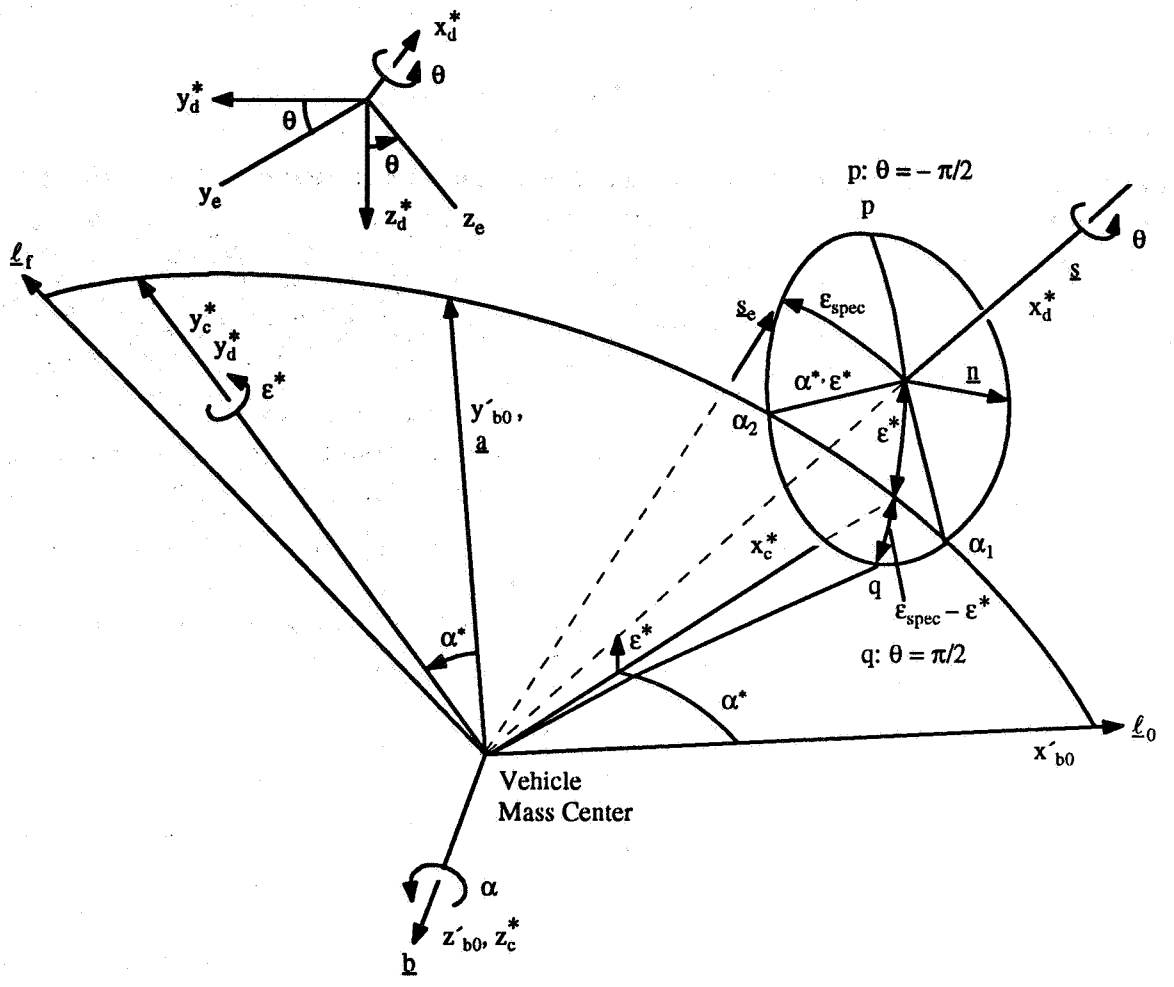

Fig. 5. Geometry of the exclusion disc relative to the slew plane

The disc is in the plane y_d^* z_d^* normal to the axis x_d^*. The frame x_d^* y_d^* z_d^* is related to the frame x'_{b0} y'_{b0} z'_{b0} through the transformation equation (3) where $\alpha = \alpha^*$ and $\varepsilon = \varepsilon^*$. Then, the unit vector $\underline{s}_e$, the components of which are given in the frame x'_{b0} y'_{b0} z'_{b0} by Eq. (20b), can be re-expressed in the frame $\mathcal{F}_d^*$: x_d^* y_d^* z_d^* through the transformation Eq. (3), yielding

$$\underline{s}_e = \begin{bmatrix} c\,\varepsilon_{spec} \\ c\varepsilon\, s\,(\alpha - \alpha^*) \\ s\varepsilon^*\, c\varepsilon\, c\,(\alpha - \alpha^*) - c\varepsilon^*\, s\varepsilon \end{bmatrix}_{\mathcal{F}_d^*} \tag{22}$$

where Eq. (21) has been employed to replace the x_d^* component of $\underline{s}_e$. Since the x_d^* component is equal to $c\varepsilon_{spec}$, the magnitude of the y_d^* and z_d^* components together must be $s\varepsilon_{spec}$, for $\underline{s}_e$ is a unit vector. On the other hand, any point on the circumference of the disc can be located by an angle θ about the axis x_d^* measured from y_d^*, as shown in Fig. 5 inset. Consequently, the y_d^* and z_d^* components of $\underline{s}_e$ are equal to $s\varepsilon_{spec}\, c\theta$ and $s\varepsilon_{spec}\, s\theta$, respectively. One thus obtains the following three equations defining the disc boundary, including Eq. (21)

$$x_d^*: \quad c\varepsilon^*\, c\varepsilon\, c\,(\alpha - \alpha^*) + s\varepsilon^*\, s\varepsilon = c\varepsilon_{spec} \tag{23a}$$

$$y_d^*: \quad c\varepsilon\, s\,(\alpha - \alpha^*) = s\varepsilon_{spec}\, c\theta \tag{23b}$$

$$z_d^*: \quad s\varepsilon^* c\varepsilon\, c(\alpha - \alpha^*) - c\varepsilon^* s\varepsilon = s\varepsilon_{spec}\, s\theta \tag{23c}$$

While y_d^* and z_d^* components define the disc boundary with θ as a parameter ($0 \le \theta \le 2\pi$), the x_d^* component ensures that the disc is of angular radius ε_{spec}.

Our objective in deriving Eqs. (23) was to determine ε as a function of the slew angle α so that, knowing α, the boresight can be slid along the disc boundary if necessary. From Eqs. (23), though the angle ε can be expressed as a function of α, difficulties arise when the disc is so large (Earth disc, for example) that $|\varepsilon^*| + \varepsilon_{spec} > \pi/2$ because then the original definition of the elevation angle ε, Eq. (7c), which imposes the requirement that $-\pi/2 < \varepsilon < \pi/2$, breaks down. Also, note that while azimuth angles α^* and α are about the same axis z'_{b0}, the elevation angles ε^* and ε are not—the angle ε^* is about α^*-displaced axis y'_{b0} (called y_c^* in Fig. 5) and ε about α-displaced axis y'_{b0} axis. As a result: a) we do not encounter the angle $(\varepsilon - \varepsilon^*)$ in Eqs. (23) although the angle $(\alpha - \alpha^*)$ does emerge; b) for large $|\varepsilon^*| + \varepsilon_{spec}$, Eqs. (23) lead to greatly distorted discs, though symmetric about $\alpha - \alpha^*$; and c) although $|\varepsilon^*| + \varepsilon_{spec}$ may be greater than $\pi/2$, Eqs. (23) still predict $|\varepsilon^*| + \varepsilon_{spec} < \pi/2$. Consequently, Eqs. (23) are given up in favor of an alternate approach yielding different and more easily usable equations, as shown below.

To maintain inherent symmetry of the disc around $(\alpha^*, \varepsilon^*)$, define $\Delta\alpha$ about z_d^*-axis and angle $\Delta\varepsilon$ about $\Delta\alpha$-displaced y_d^*-axis (both rotations are analogous, respectively, to α^* about z'_{b0} and ε^* about α^*-displaced y'_{b0}-axis). The angles $\Delta\alpha$ and $\Delta\varepsilon$ bring the axis x_d^* in alignment with the unit vector $\underline{s}_e$; that is, the boresight then rests on the circumference. Consequently, using angles $\Delta\alpha$ and $\Delta\varepsilon$ the unit vector $\underline{s}_e$ can be expressed in the frame $\mathcal{F}_d^*: x_d^*\ y_d^*\ z_d^*$ as

$$\underline{s}_e = \begin{bmatrix} c\Delta\varepsilon\, c\Delta\alpha \\ c\Delta\varepsilon\, s\Delta\alpha \\ -s\Delta\varepsilon \end{bmatrix}_{\mathcal{F}_d^*} \tag{24}$$

With the aid of the right sides of Eqs. (23), Eq. (24) yields

$$c\Delta\varepsilon\, c\Delta\alpha = c\varepsilon_{spec} \tag{25a}$$

$$c\Delta\varepsilon\, s\Delta\alpha = s\varepsilon_{spec}\, c\theta \tag{25b}$$

$$s\Delta\varepsilon = -s\varepsilon_{spec}\, s\theta \tag{25c}$$

which are much simpler equations to solve than Eqs. (23) even for large ε_{spec}; $\varepsilon_{spec} \le \pi/2$, and therefore $|\Delta\alpha| \le \pi/2$, $|\Delta\varepsilon| \le \pi/2$. Dividing Eq. (25b) with Eq. (25a), we obtain

$$\tan\Delta\alpha = c\theta \tan\varepsilon_{spec} \tag{26}$$

Eqs. (26) and (25c) furnish $\Delta\alpha$ and $\Delta\varepsilon$, both within $-\pi/2$ to $\pi/2$, as a function of the parameter θ, $-\pi \le \theta \le \pi$. For special values of θ, these equations yield

θ	$\Delta\alpha$	$\Delta\varepsilon$
0	ε_{spec}	0
$\pi/2$	0	$-\varepsilon_{spec}$
π	$-\varepsilon_{spec}$	0
$-\pi/2$	0	ε_{spec}

as anticipated. The two points $\theta = \pm\pi/2$, labeled p and q, are shown on the disc in Fig. 5.

When $\varepsilon_{spec} > |\varepsilon^*|$, the azimuth angles corresponding to the intersection of the disc with the ideal slew path are determined by expressing the unit vector $\underline{s}_e$, Eq. (24), in the frame $\underline{\ell}_0\, \underline{a}\, \underline{b}$, using transpose of Eq. (3) where α is replaced with α^* and ε with ε^*. The projection of $\underline{s}_e$ along $\underline{b}$ and its comparison with the $\underline{b}$ component in Eq. (20b) then yields

$$s\varepsilon = s\varepsilon^*\, c\Delta\varepsilon\, c\Delta\alpha + c\varepsilon^*\, s\Delta\varepsilon \tag{27}$$

Since the intersection of the disc with the ideal slew path occurs when $\varepsilon = 0$, the corresponding angle θ is found to be, in view of Eqs. (25a), (25c), and (27)

$$s\theta = \tan \varepsilon^* / \tan \varepsilon_{spec} \qquad -\pi \leq \theta \leq \pi \tag{28}$$

which leads to two values of θ, θ_1 and θ_2, corresponding $\Delta\alpha_1$ and $\Delta\alpha_2$ from Eq. (26) and $\Delta\varepsilon_1$ and $\Delta\varepsilon_2$ from Eq. (25c). And finally, the intersection azimuth angles α_1 and α_2 are determined from the $\underline{\ell}_0$ and $\underline{a}$ components of $\underline{s}_e$

$$\underline{\ell}_0 \text{component: } c\varepsilon\, c\alpha = (c\varepsilon^*\, c\alpha^*\, c\Delta\alpha - s\alpha^*\, s\Delta\alpha)\, c\Delta\varepsilon - s\varepsilon^*\, c\alpha^*\, s\Delta\varepsilon \tag{29a}$$

$$\underline{a} \text{ component: } c\varepsilon\, s\alpha = (c\varepsilon^*\, s\alpha^*\, c\Delta\alpha + c\alpha^*\, s\Delta\alpha)\, c\Delta\varepsilon - s\varepsilon^*\, s\alpha^*\, s\Delta\varepsilon \tag{29b}$$

where ε will be zero now. Eq. (29b) is divided by Eq. (29a) yielding $\tan \alpha$ ($\varepsilon = 0$ for $\theta = \theta_1$ or θ_2) which then furnishes α_1 and α_2 corresponding to $(\Delta\alpha_1, \Delta\varepsilon_1)$ and $(\Delta\alpha_2, \Delta\varepsilon_2)$.

To determine (α, ε) corresponding to a general θ and thus the disc profile for $-\pi \leq \theta \leq \pi$, we first determine $\Delta\alpha$ and $\Delta\varepsilon$ with the aid of Eqs. (25c) and (26). The angle ε can in principle be evaluated using (27), and α from Eqs. (29). The obstacle however again arises when $|\Delta\varepsilon| > \pi/2$. Although approximate, it seems considerably simpler to assume that

$$\alpha = \alpha^* + \Delta\alpha \tag{30a}$$

$$\varepsilon = \varepsilon^* + \Delta\varepsilon \tag{30b}$$

The disc circumference can be then defined with ease. Eqs. (30) are approximate because the angles α^* and $\Delta\alpha$ are about different axes, and ε^* and $\Delta\varepsilon$ are likewise about different axes.

Disc Entrance

The piecewise continuous ε-profiles were determined earlier, consisting of quadratic or cubic ε-curves as a function of the azimuth angle α. For a given α, whether this profile (that is, the boresight) will land inside a disc or not, can be determined by Eq. (23a). Specifically, if a point (α, ε) corresponding to the boresight x_d is inside a disc, the angle between x_d and the corresponding central axis x_d^* will be less than ε_{spec} and therefore the following equivalence holds

$$\text{boresight entered the disc} \Leftrightarrow c\varepsilon^*\, c\varepsilon\, c\,(\alpha - \alpha^*) + s\varepsilon^*\, s\varepsilon > c\varepsilon_{spec} \tag{31}$$

If this condition is not satisfied, the boresight is safely outside the disc. For example, if the boresight were pointing at the celestial object $(\alpha^*, \varepsilon^*)$ and hence the boresight is within the forbidden disc, the inequality (31) reduces to $1 > c\varepsilon_{spec}$ (for $\alpha = \alpha^*$ and $\varepsilon = \varepsilon^*$) which is true because $0 < c\varepsilon_{spec} < 1$ by definition. Thus, when the commanded orientation (α, ε) of the boresight in the next sample satisfies the above inequality, the boresight will enter the disc unless the next sample ε is replaced by an ε according to Eq. (30b). To do so, we first determine $\Delta\alpha$ from $\Delta\alpha = \alpha - \alpha^*$, Eq. (30a), for the disc about to be entered. Eq. (26) then yields

$$c\theta = \tan \Delta\alpha / \tan \varepsilon_{spec} \tag{32}$$

which determines two possible values of θ

$$s\theta = \pm \sqrt{1 - c^2\, \theta} \tag{33}$$

Eq. (25c) then leads to two values of $\Delta\varepsilon$, $\Delta\varepsilon > 0$ and $\Delta\varepsilon < 0$

$$s\Delta\varepsilon = \pm s\varepsilon_{spec} \left[1 - \frac{\tan^2 \Delta\alpha}{\tan^2 \varepsilon_{spec}} \right]^{1/2} \tag{34}$$

Between the two $\Delta\varepsilon$'s, that value is selected whose sign matches with the sign of the original $\Delta\varepsilon$ that would have brought the boresight inside the disc. The new ε is then calculated from Eq. (30b). With new ε, the boresight will be commanded to slide along the disc until the ε angle commanded by earlier profiles does not bring the boresight inside the disc anymore. When the telescope is slid along the disc, the slope $d\varepsilon/d\alpha$ is determined by differentiating Eq. (25a) and, in view of eqs. (30), we obtain

$$d\varepsilon/d\alpha = -\tan \Delta\alpha / \tan \Delta\varepsilon \tag{35}$$

III. Communication Maintenance

Fig. 6 illustrates communication cones of –y (pitch) and ±z (yaw) antennas considered here. If the vector from an antenna to the ground station resides in the antenna's cone, the communication link is maintained, otherwise not. The ±z antennas have in addition small null cones through which comm. is not possible. Since the cone axes of the antennas are along pitch and yaw axes, if the communication link is broken for any antenna, it is restored by a roll rotation of the vehicle about the x-axis. The magnitude of this rotation, of course, must be such that while the comm. link is regained for one antenna, it is not lost for the other since the two are mounted on orthogonal axes and signal strength for one antenna is made stronger at the expense of the signal strength for the other. It therefore seems logical to incrementally roll the vehicle about x-axis so as to maintain equal signal strengths for z or –z and –y antennas while the boresight (x-axis) is slewed from one orientation to the other.

Coordinate Transformations

Fig. 7 portrays various coordinate frames required to model the boresight slew considered in the previous section and the roll rotation for antenna comm. link. The boresight slew modeling begins from the frame $x'_{b0}\ y'_{b0}\ z'_{b0}$ ($\underline{\ell}_0\ \underline{a}\ \underline{b}$) depicted earlier in Fig. 1. The initial vehicle frame $x_{b0}\ y_{b0}\ z_{b0}$, in communication link with the ground station, has a roll angle offset equal to ($\beta_0 - \beta'_0$) from the frame $x'_{b0}\ y'_{b0}\ z'_{b0}$ about x'_{b0} axis. The roll angles β_0 and β'_0 have the following definitions. The vehicle flies in a trajectory, so a trajectory frame $x_t\ y_t\ z_t$ is defined at the instantaneous location of the vehicle's mass center. This trajectory frame may be a tangent-normal-binormal frame, a radial local-verticle-local-horizontal frame or an up-east-north frame. A nominal body frame $x''_{b0}\ y''_{b0}\ z''_{b0}$ is defined for now relative to the trajectory frame $x_t\ y_t\ z_t$ such that the boresight x''_{b0} is along the initial boresight direction $x'_{b0} = \underline{\ell}_0$ and the frame $x'_{b0}\ y'_{b0}\ z'_{b0}$ is obtained by a rotation of the frame $x''_{b0}\ y''_{b0}\ z''_{b0}$ by an angle β'_0 about the boresight axis $x''_{b0} = x'_{b0} = x_{b0}$. The initial vehicle frame $x_{b0}\ y_{b0}\ z_{b0}$, on the other hand, is obtained by a roll rotation of β_0 about x''_{b0}, the angle decided by equal signal strength communication links of pitch and yaw antennas with the ground station. The slew of the boresight x'_{b0} takes place according to the exclusion algorithm in the previous section, rotating the boresight by azimuth angle α and elevation angle ε, arriving at the frame $x_d\ y_d\ z_d$ according to Eq. (3). In the process, the initial vehicle frame $x_{b0}\ y_{b0}\ z_{b0}$ is carried to the orientation $\mathcal{F}^b$: $\bar{x}_b\ \bar{y}_b\ \bar{z}_b$ where $\bar{x}_b = x_d$. But the frame $\mathcal{F}^b$ may or may not be in communication link with the ground station anymore. If the communication link is lost, an additional β roll rotation is determined so that the

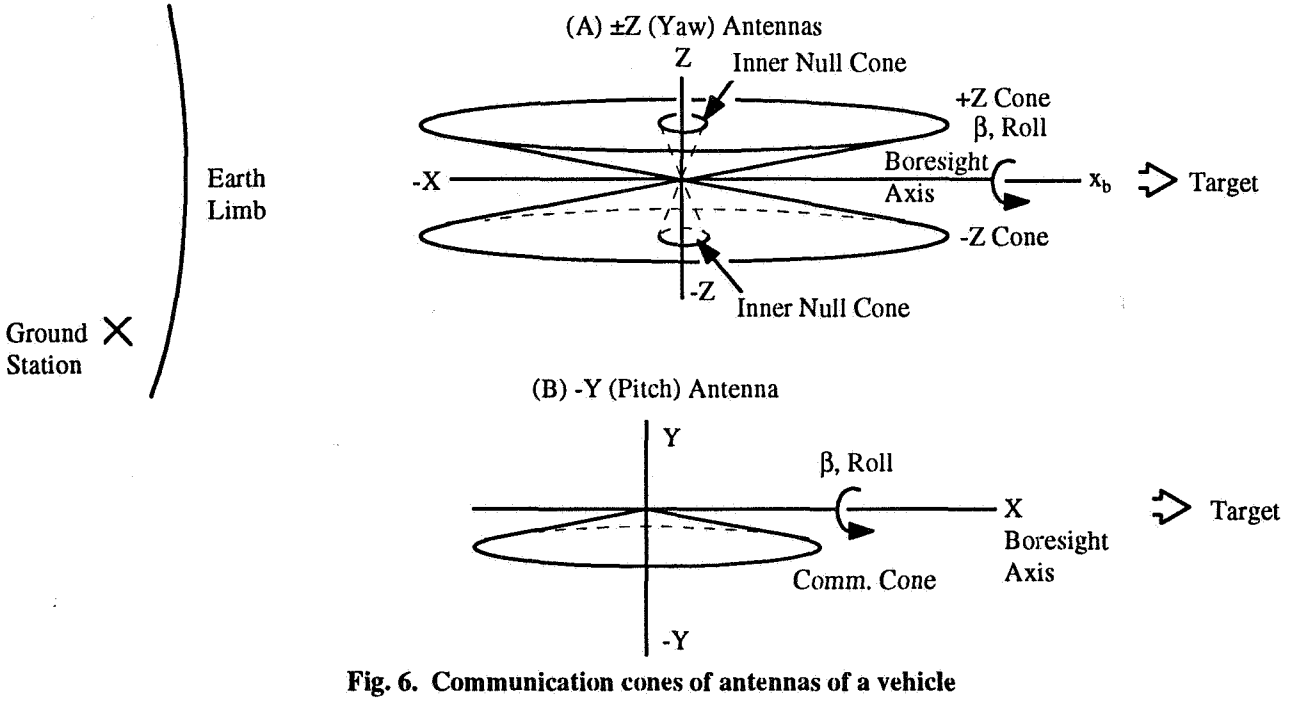

Fig. 6. Communication cones of antennas of a vehicle

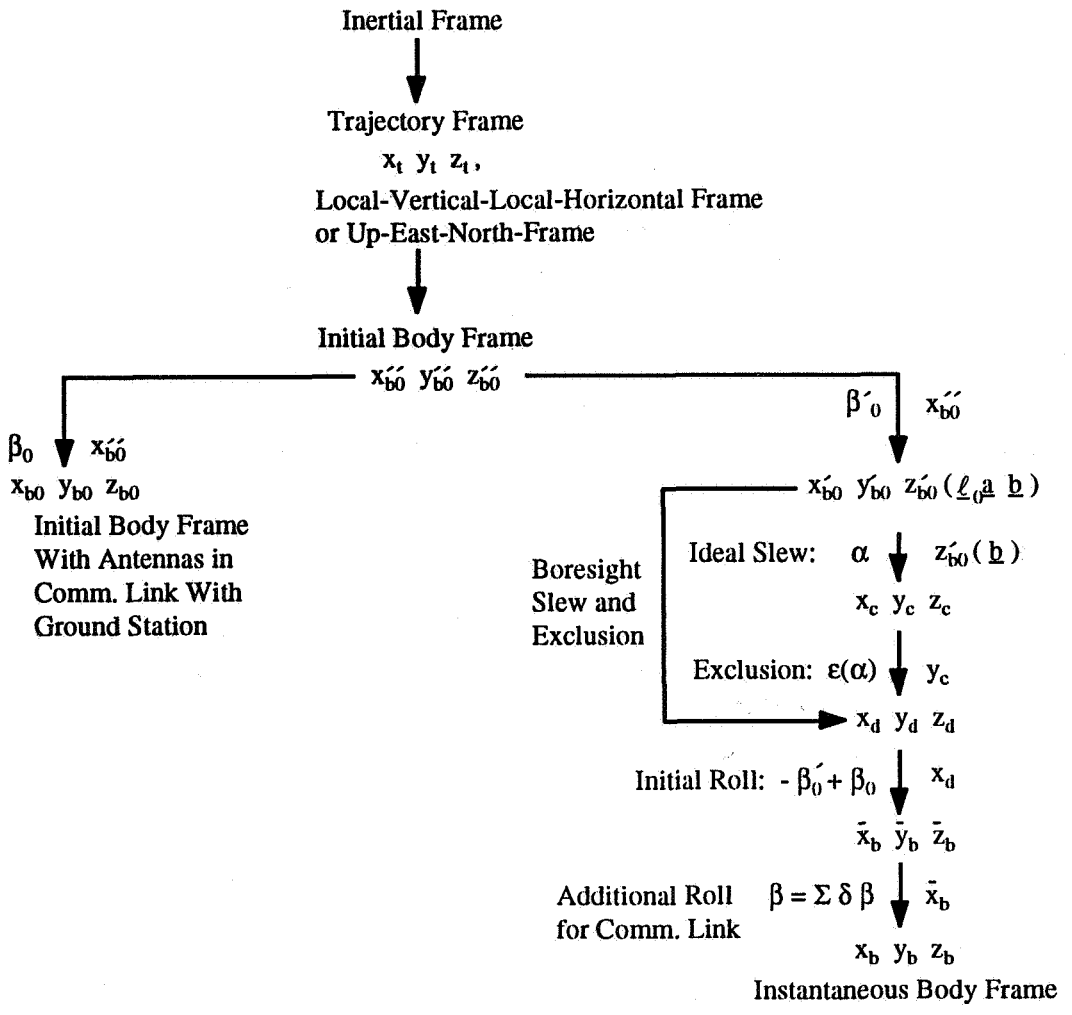

Fig. 7. Various coordinate frames required for boresight slew and communication maintenance

signal strengths of –y and either +z or –z antenna are equal again. In reality, this finite roll angle β consists of incremental roll angles $\delta\beta$'s which maintain comm. link of the antennas continuously as the azimuth and elevation angles α, ε evolve.

The frame $x'_{b0}\ y'_{b0}\ z'_{b0}$ was defined earlier with the aid of Fig. 1. Typically, the initial and the final line-of-sight unit vectors $\underline{\ell}_0$ and $\underline{\ell}_f$ are known in the initial body frame $\mathcal{F}^{b0}$: $x_{b0}\ y_{b0}\ z_{b0}$ and therefore the unit vectors $\underline{b}$ and $\underline{a}$ are also known in this frame, using Eqs. (1b) and (2). Since $\underline{a}$ and $\underline{b}$ are orthogonal to the boresight $x_{b0} = x'_{b0} = x''_{b0}$, let

$$\underline{a}^{\mathcal{F}^{b0}} = [0 \quad a_{y0} \quad a_{z0}]^T \tag{36a}$$

$$\underline{b}^{\mathcal{F}^{b0}} = [0 \quad b_{y0} \quad b_{z0}]^T \tag{36b}$$

where the superscript $\mathcal{F}^{b0}$ denotes this frame and the components are known. The angle $(\beta'_0 - \beta_0)$, to arrive at the frame $x'_{b0}\ y'_{b0}\ z'_{b0}$ from $x_{b0}\ y_{b0}\ z_{b0}$, is then given by

$$(\beta'_0 - \beta_0) = \tan^{-1}\frac{a_{z0}}{a_{y0}} = \tan^{-1}\frac{-b_{y0}}{b_{z0}} \tag{37}$$

This angle enables the transformation from the frame $\mathcal{F}^d$: $x_d\ y_d\ z_d$ to the frame $\mathcal{F}^{\bar{b}}$: $\bar{x}_b\ \bar{y}_b\ \bar{z}_b$ in Fig. 7. That the transformation from $x'_{b0}\ y'_{b0}\ z'_{b0}$ to $x_{b0}\ y_{b0}\ z_{b0}$ and from $x_d\ y_d\ z_d$ to $\bar{x}_b\ \bar{y}_b\ \bar{z}_b$ are identical may be self-evident; this can be proved analytically or numerically, but we will not attempt that here. The roll angles β_0 and β ensure communication and these are determined next.

Roll for Equalization of Pitch and Yaw Antenna Signal Strengths

Let the vehicle body frame be $\bar{x}_b\ \bar{y}_b\ \bar{z}_b$ in which the antennas may not have comm. link with the ground station. The objective is to determine the angle β so that not only the link is established for both antennas, but the signal strength is also the same for the two. Let $\underline{\rho}$ be the unit vector from the vehicle to the ground station, with the components in the frame $\mathcal{F}^{\bar{b}}$: $\bar{x}_b\ \bar{y}_b\ \bar{z}_b$ as

$$\underline{\rho}\ ^{\mathcal{F}^{\bar{b}}} = \left[\bar{\rho}_{xb}\ \bar{\rho}_{yb}\ \bar{\rho}_{zb}\right]^T \tag{38}$$

where the superscript T means transpose. When the vehicle is rolled by an angle β about the axis $\bar{x}_b$, arriving at the frame $\mathcal{F}^b$: $x_b\ y_b\ z_b$ and achieving the above objective, the components of $\underline{\rho}$ in the frame $\mathcal{F}^b$ become $[\rho_{xb}\ \rho_{yb}\ \rho_{zb}]^T$, related to the components in (38) as follows:

$$\rho_{xb} = \bar{\rho}_{xb} \tag{39a}$$

$$\rho_{yb} = \bar{\rho}_{yb}\cos\beta + \bar{\rho}_{zb}\sin\beta \tag{39b}$$

$$\rho_{zb} = -\bar{\rho}_{yb}\sin\beta + \bar{\rho}_{zb}\cos\beta \tag{39c}$$

Let $\phi_{\pm z}$ be the angle between $\pm z$ (yaw) antenna cone axis and the unit vector $\underline{\rho}$ from the vehicle to the ground station. Then

$$+z \text{ axis: } \cos\phi_{+z} = \rho_{zb} = -\bar{\rho}_{yb}\sin\beta + \bar{\rho}_{zb}\cos\beta \tag{40a}$$

$$-z \text{ axis: } \cos\phi_{-z} = -\rho_{zb} = \bar{\rho}_{yb}\sin\beta - \bar{\rho}_{zb}\cos\beta \tag{40b}$$

where the subscript + and − correspond, respectively, to the antenna along +z and −z axis. On the other hand, let ϕ_{-y} be the angle between the −y cone axis and the unit vector $\underline{\rho}$. Then

$$-y \text{ axis: } \cos\phi_{-y} = -\rho_{yb} = -\bar{\rho}_{yb}\cos\beta - \bar{\rho}_{zb}\sin\beta \tag{41}$$

Suppose we intend to achieve comm. link of +z and −y antennas with the ground station, the two desired angles being ϕ_{+z} and ϕ_{-y} not necessarily the same, though both angles are positive and within the respective comm. cones. Eqs. (40a) and (41) then yield the required roll rotation β in terms of the components of $\underline{\rho}$ prior to rotation:

$$+z \text{ antenna: } \tan\beta = \frac{\bar{\rho}_{yb}c\phi_{+z} + \bar{\rho}_{zb}c\phi_{-y}}{\bar{\rho}_{yb}c\phi_{-y} - \bar{\rho}_{zb}c\phi_{+z}} \tag{42}$$

The antenna angles ϕ_{+z} and ϕ_{-y} cannot be specified arbitrarily, though, because Eqs. (40) and (41) impose the following constraint

$$c^2\phi_{-y} + c^2\phi_z = \bar{\rho}_{yb}^2 + \bar{\rho}_{zb}^2 = 1 - \bar{\rho}_{xb}^2 \tag{43}$$

embodying the unit magnitude of the vector $\underline{\rho}$ and the fact that a roll rotation will not change the x-component $\bar{\rho}_{xb}$ of $\underline{\rho}$. If the angles ϕ_{-y} and ϕ_z are to be rendered equal for equal signal strength, Eq. (43) leads to

$$\phi_{-y} = \phi_z = \cos^{-1}\frac{1}{\sqrt{2}}\,(1 - \bar{\rho}_{xb}^2)^{1/2} \tag{44}$$

A simpler equation governing the requisite roll rotation β is then obtained from Eq. (42) by substituting $\phi_{+z} = \phi_{-y}$

$$+z \text{ antenna: } \tan\beta = \frac{\bar{\rho}_{yb} + \bar{\rho}_{zb}}{\bar{\rho}_{yb} - \bar{\rho}_{zb}} \tag{45}$$

Also, when $\phi_{+z} = \phi_{-y}$ Eqs. (40a) and (41) dictate that $\rho_{zb} = -\rho_{yb}$. Since maintaining equal signal strength for $\pm z$ and $-y$ antenna seems to be optimal, in general, one infers from Eq. (44) that for a given $\underline{\rho}$ vector the angle ϕ_{-y} ($=\phi_{\pm z}$) achievable through the rotation β specified by Eq. (45) is already fixed whether within comm. cones of the two antennas or not. If, due to some considerations, one of the two angles ϕ_{uhf} and ϕ_{ldr} ought to have a certain special value, the other angle will be specified by Eq. (43), whether within the comm. cone or not, and the corresponding roll rotation will be determined by Eq. (42).

Consider now the restoration of comm. link of ground station with the antenna along $-y$ axis and the antenna along $-z$ axis. For specified angles ϕ_{-y} and ϕ_{-z} satisfying the constraint (43), the required roll angle β is derived from Eqs. (40b) and (41). There follows

$$-z \text{ antenna: } \tan\beta = \frac{-\bar{\rho}_{yb} c\phi_{-z} + \bar{\rho}_{zb} c\phi_{-y}}{\bar{\rho}_{yb} c\phi_{-y} + \bar{\rho}_{zb} c\phi_{-z}} \tag{46}$$

analogous to Eq. (42). If ϕ_{-y} and ϕ_{-z} are stipulated to be the same, as specified by Eq. (44), Eq. (46) reduces to

$$-z \text{ antenna: } \tan\beta = \frac{-\bar{\rho}_{yb} + \bar{\rho}_{zb}}{\bar{\rho}_{yb} + \bar{\rho}_{zb}} \tag{47}$$

the counterpart of Eq. (45). Eqs. (40b) and (41) then yield $\rho_{yb} = \rho_{zb}$ after the rotation β.

In actual operation of this algorithm, the angle β will not be calculated for each sample relative to the frame $\bar{x}_b\ \bar{y}_b\ \bar{z}_b$ as shown in Fig. 7. Instead, one may calculate $\delta\beta$ rotation with respect to the frame $x_b\ y_b\ z_b$ of the previous sample and then increment the roll angle β as the azimuth and elevation angles α and ε evolve. This will maintain the same yaw antenna (either $+z$ or $-z$ antenna) in link with the ground station throughout the slew, starting from the one that resulted from the roll rotation β_0 implemented for comm. link prior to slew (Fig. 7). The angle β_0 is smaller of the two angles calculated from Eq. (45) and Eq. (47) assuming that the initial frame $x''_{b0}\ y''_{b0}\ z''_{b0}$ is the same as $\bar{x}_b\ \bar{y}_b\ \bar{z}_b$. Finally, knowing β_0, the angle β'_0 shown in Fig. 7 is determined from Eq. (37).

IV. Numerical Results and Discussion

We will now illustrate the algorithms developed above under a hypothetical circumstance. Fig. 8 illustrates three celestial objects (representing Earth, Sun and Moon) with their location with respect to the slew plane and their disc radii as shown in Table 1. In a real scenario, the location angles α^* and ε^* of celestial objects are calculated using Eqs. (7), and then α^* angles are arranged in ascending order. The disc radius of a celestial object depends on its radiation spectrum and electro-optical properties of the telescope, and could be different for different objects. The values of α^*, ε^*, and ε_{spec} shown in Table 1 are reasonable but otherwise arbitrary. According to the algorithm, an object will be ignored if $\alpha^* < -\varepsilon_{spec}$ or $\alpha^* > \phi + \varepsilon_{spec}$ but here α^* are chosen to be within $0 < \alpha^* < \phi$ where ϕ, the slew angle, in this example, is 153.1 deg. The Sun, Moon and Earth discs, centered around the corresponding (α^*, ε^*) with corresponding radius, are shown in Fig. 8a. Since for each object $\varepsilon_{spec} > |\varepsilon^*|$, these discs intersect the ideal slew path ($\varepsilon = 0$) of the boresight and Eqs. (8a) and (8b) yield minimum ε deviation angles: 10, -5, -9 deg, respectively, as shown in Table 1.

Table 1. Example of Exclusion Maneuver

Celestial Object		Center of Celestial Object α^* (deg)	Center of Celestial Object ε^* (deg)	Disc Radius ε_{spec} (deg)	Minimum Deviation Maneuvers ε_{min} (deg)	Modified Nonminimum Deviation ε (deg)
Sun	I	25	−10	20	10	−30
Moon	II	40	5	10	−5	−30
Earth	III	60	66	75	−9	−9

The parameters of Earth and Moon discs are such that Moon is completely occulted by Earth disc, and the minimum ε tip of Sun disc ($\alpha_1^* = 25$ deg, $\varepsilon_1 = 10$ deg) is also behind Earth disc (sunrise or sunset situation). Because of this last stance, the diametrically opposite tip of Sun disc I is chosen for exclusion: $\varepsilon_1 = -30$ deg. Since Moon disc II is completely eclipsed by Earth disc and since the Earth disc intersects the ideal slew path, the minimum deviation angle $\varepsilon_2 = -5$ deg is replaced with ε_1, that is, $\varepsilon_2 = \varepsilon_1 = -30$ deg. A novel feature of the exclusion maneuver in Fig. 8 is that the first quadratic profile from (0, 0) to $\alpha_1^* = 25$ deg, $\varepsilon_1 = -30$ deg steps into the Sun disc, and to avert that, the transgressing portion of the quadratic profile is replaced by the Sun disc arc. The remaining piecemeal profile does not enter any disc and therefore it is accepted as such. While executing this (α, ε) profile the angles of the boresight axis with Sun, Moon and Earth disc centers vary as shown in Fig. 8b. The angle corresponding to Sun (curve I) is minimum, 20 deg, as long as the (α, ε) profile slides along the Sun disc. The angle corresponding to the Earth center is minimum, $\varepsilon_{spec,\,3}$, equal to 75 deg when $\alpha = \alpha_3^* = 60$ deg. The angle with the Moon center, curve II, is always greater than the minimum allowed ($\varepsilon_{spec,\,2} = 10$ deg) value.

Fig. 9a compares linearly increasing ideal slew angle α with the commanded equivalent single-axis slew angle α' obtained from the instantaneous transformation matrix involving α and ε, Eq. (3), following Ref. 8. In the beginning and at the end of the slew ε equals 0, and therefore α' and α are equal, as seen in Fig. 9a. Between the two extremities, the angle α' is greater than α, the difference being proportional to the ratio of the instantaneous ε and the slew angle α; this ratio is large in the beginning in this example, and gradually diminishes to zero when α reaches ϕ. Corresponding to the angles α and α' there are two axes of rotation in space. For ideal slew, $\varepsilon = 0$ throughout $0 \leq \alpha \leq \phi$ and the ideal axis of rotation z'_{b0} (Fig. 1) in the ideal slew frame x'_{b0} y'_{b0} z'_{b0} is $[0\ 0\ 1]^T$. When $\varepsilon \neq 0$, these three components vary. Fig. 9b shows these two axes of rotation, without exclusion and with exclusion, in the initial body frame x_{b0} y_{b0} z_{b0}. As expected, the ideal axis of rotation has no component along x_{b0}-axis and the components along y_{b0} and z_{b0} are constant and nonzero. The actual axis of rotation also has zero x_{b0}-component at $\alpha = 0$, $\varepsilon = 0$. But its y_{b0} and z_{b0} components are different from their ideal counterparts so as to generate the ε profile shown in Fig. 8a. As ε varies, the three components vary as well, and as α approaches ϕ and ε approaches zero, the three components reach their ideal values.

Generally, the axis of rotation remains the same whether expressed in the initial body frame or instantaneous body frame. But in the situation at hand, the spacecraft rotates not only by α and ε angles, but also by an additional roll angle for maintaining communication of pitch and yaw antennas. The angles of these antennas (ϕ_{-y}, ϕ_z, ϕ_{-z}) with the ground station and the required roll rotation for comm. link are shown in Figs. 10a and 10b, respectively. At $t = 0$, the spacecraft is rotated by a roll angle $\beta - \beta'_0 \approx 70$ deg to bring $-y$ and $-z$ antennas in link with a ground station. Subsequently, as the spacecraft is slewed by α and ε angles, this link is maintained by incrementally rolling the vehicle about the instantanteous x_b-axis (Fig. 10b). The roll angle is determined such that the two angles ϕ_{-y} and ϕ_{-z} remain equal, as shown in Fig. 10a. The geometry of the spacecraft slew and the location of the ground station relative to the spacecraft allow the equal angles ϕ_{-y} and ϕ_{-z} to be within the communication cone limits (Fig. 10a). The x-component of the spacecraft-to-ground-station unit vector, $\underline{\rho}$, varies with slew (Fig. 10c) and it constrains what value the equal angles ϕ_{-y} and ϕ_{-z} can have for a given slew angle. Because of the equality of ϕ_{-y} and ϕ_{-z} the y and z components of $\underline{\rho}$ are equal as shown in Fig. 10c. The roll angle changes as the slew proceeds in order to maintain the comm. links with the ground station.

Concluding Remarks

The preceding numerical results and also the results not included here prove convincingly that (1) the exclusion algorithm developed in the paper slews the boresight avoiding the bright objects by specified angular distances and (2) communication links of the ground station with pitch and yaw antennas are maintained, if permitted at all by the spacecraft and ground station geometry, by rolling the vehicle about x-axis.

Acknowledgements

Technical discussions with D. Pearson and M. Rivera, lending considerable insight into the exclusion problem investigated here, are gratefully acknowledged.

References

1. Guldner, J., and Utkin, V. I., " Sliding Mode Control for Gradient Tracking and Robot Navigation Using Artificial Potential Fields," *IEEE Trans. on Robotics and Automation*, Vol. 11, No. 2, April 1995, pp. 247-254.

2. McInnes, C. R., " Large Angle Slew Maneuvers with Autonomous Sun Vector Avoidance," *Journal of Guidance, Control, and Dynamics*, Vol. 17, No. 4, 1994, p. 875-877.

3. McInnes, C. R., " Potential Function Methods for Autonomous Spacecraft Guidance and Control," *Advances in the Astronautical Sciences*, Vol. 90, Paper No. AAS 95-447, pp. 2093-2109.

4. McInnes, C. R., " Nonlinear Control for Large angle Attitude Slew Maneuvers," *Third ESA Symposium on Spacecraft Guidance, Navigation, and Control*, ESTEC, Noordwijk, the Netherlands, November 1996.

5. Sorensen, A. M., "ISO Attitude Maneuver Strategies," Paper No. AAS 93-317, pp. 975-987.

6. Singh, G., Macala, G., Wong, E., and R. Rasmussen, "A Constraint Monitor Algorithm for the Cassini Spacecraft," *AIAA Guidance, Navigation, and Control Conference*, August 1997, New Orleans, LA.

7. Rivera, M., *Fixed Rotation Axis Slew Maneuvers With Attitude Avoidance*, Inernal Technical Memo, Boeing North American, Downey, CA, August 1996.

8. Hughes, P. C., *Spacecraft Attitude Dynamics*, John Wiley & Sons, 1986, pp. 13-14.

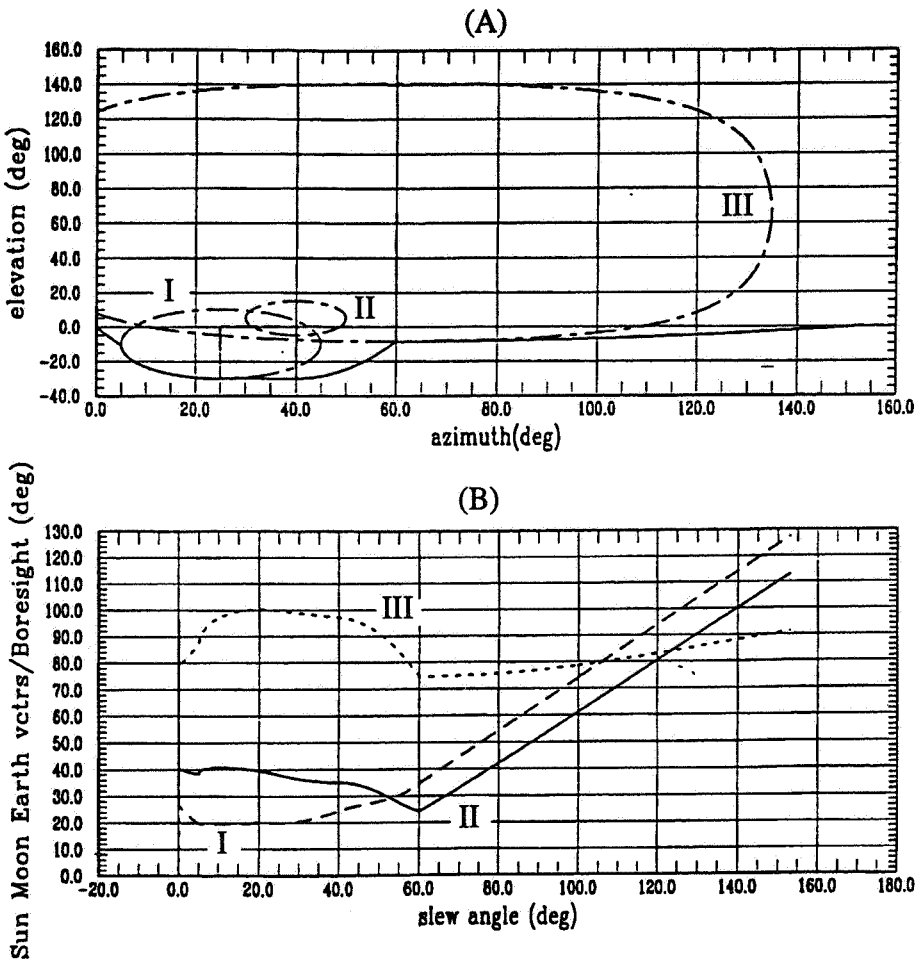

Fig. 8. Exclusion of overlapping and occulted celestial objects: (a) boresight trajectory, and (b) angle of boresight with the center of each object

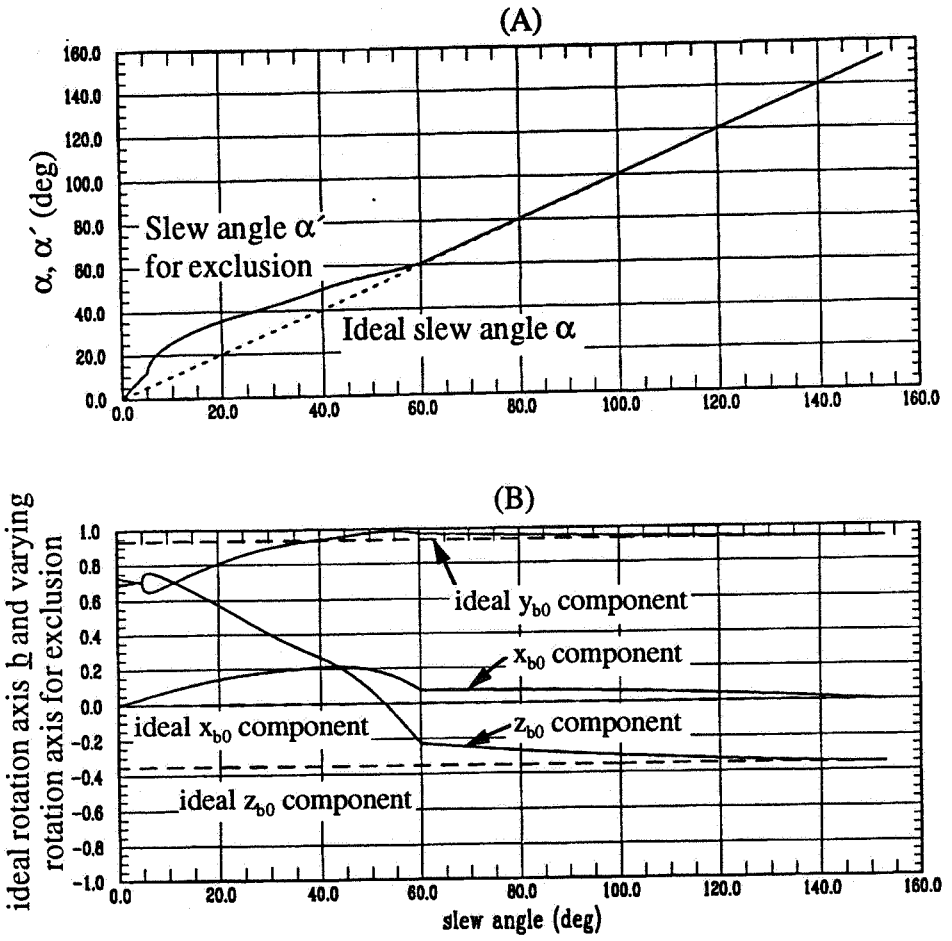

Fig. 9. Comparison of ideal slew with the slew effecting exclusion: (a) slew angles (b) components of ideal rotation axis b and components of the rotation axis effecting exclusion

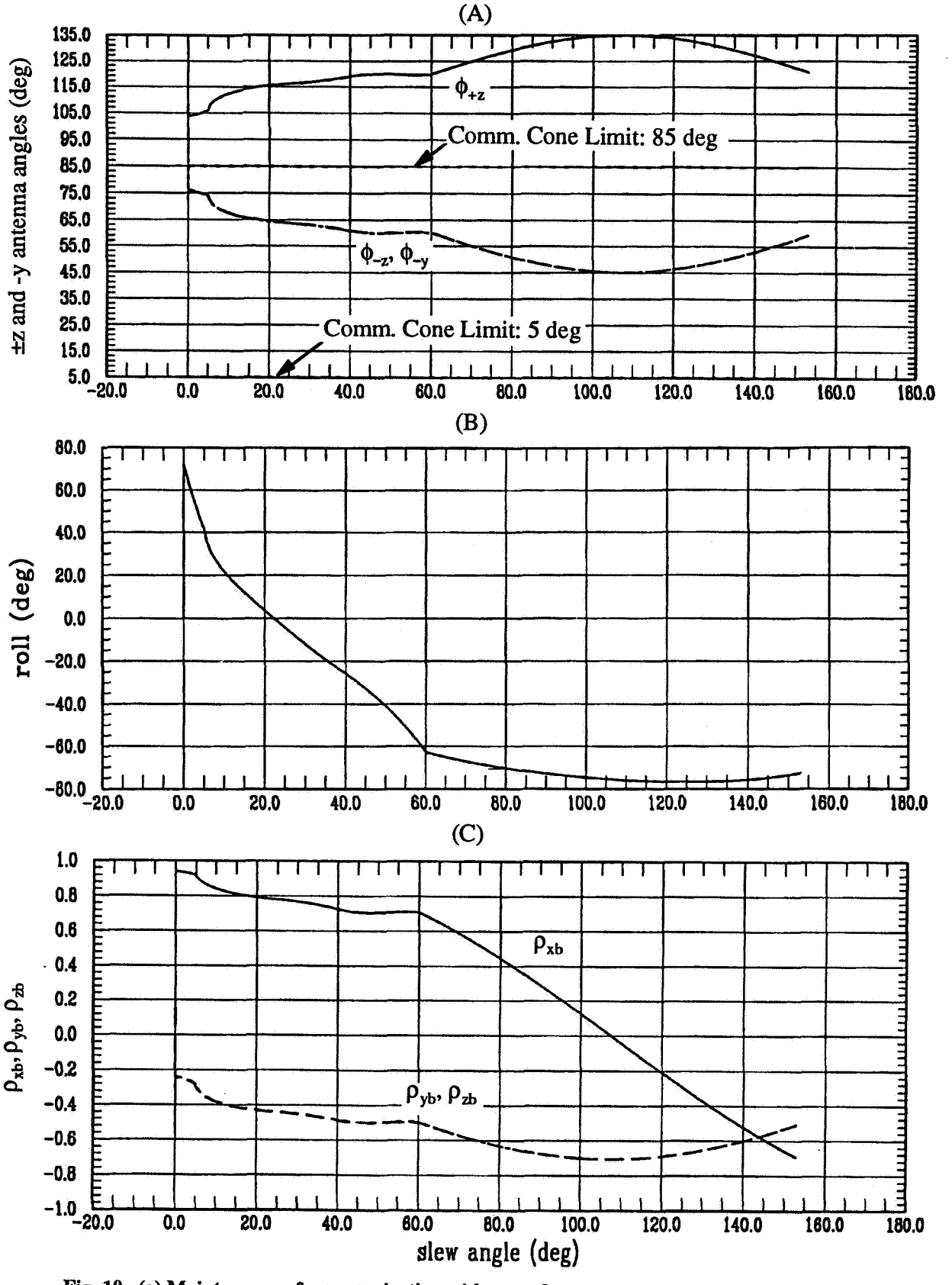

Fig. 10. (a) Maintenance of communication with –y and –z antennas; (b) required roll angle and (c) components of antenna-to-ground-station unit vector in the body frame

A B-Dot Acquisition Controller for the RADARSAT Spacecraft

Thomas W. Flatley, Wendy Morgenstern, Alan Reth, Frank Bauer
Code 712/Guidance, Navigation and Control Branch
Goddard Space Flight Center
Greenbelt, Maryland, 20904, USA

Abstract:
B-Dot is an extremely simple control law sometimes used for despinning satellites. It relies on magnetic coils or torque rods as control actuators. The control law is based on the measurement of the rate of change of body-fixed magnetometer signals. Using only a magnetometer and a magnetic moment generator, the B-Dot controller despins the spacecraft relative to the Earth's magnetic field vector. When the spacecraft carries a constant speed momentum wheel, B-Dot control will precess the wheel spin axis to the orbit normal.

The Canadian Space Agency's RADARSAT spacecraft is an Earth pointing, momentum bias system in a sun synchronous, dawn/dusk orbit. Its uses a passive Safehold Mode, relying on the momentum bias to maintain the spacecraft in a power positive state. This spacecraft presents an ideal opportunity for using B-Dot as an Sun Acquisition controller. It is an active controller, but it requires only magnetometers, magnetic torquers, and a momentum wheel, and the control law is very simple. This paper consists of two sections. The first presents a brief primer concerning a variety of magnetic controllers. The second section documents analysis and simulation results for the performance of the RADARSAT system using a B-Dot sun acquisition controller.

Introduction

We will be discussing an attitude control concept which has been frequently applied to low Earth orbit spacecraft, usually for despinning or unloading unwanted spacecraft angular momentum. A key ingredient in the B-Dot controller is the rate of change of magnetic field vector components as measured by on-board, body-fixed sensors called magnetometers. "B" is commonly used to denote the Earth's magnetic field, and the associated rate of change $^{dB}/_{dt}$, is often written $\dot{B}$. Thus, the term "B-Dot."

The actuators used in such systems are magnetic coils or torque rods. Both types of actuators produce magnetic moments which interact with the Earth's magnetic field to generate external torques on the spacecraft. The effect is calculated by the expression $\vec{T} = \vec{M} \times \vec{B}$. In SI units, the torque, $\vec{T}$, in N-m equals the cross product of the magnetic moment, $\vec{M}$, in amp-m^2 with the magnetic field, $\vec{B}$, in tesla.

With air core magnetic coils, the magnetic moment is simply the current through the coil, measured in amperes, times the area of the coil in m^2 times the number of loops in the coil. Torque rods, on the other hand, are usually long and slender, with many turns of wire wound on a cylindrical rod made of highly permeable material. The magnetic properties of the solid core dramatically amplify the magnetic moment produced by the current loops at the expense of additional weight.

Section 1: A Brief Survey of Magnetic Controllers.

1.1 B-Dot Control

In general, B-Dot control laws command, on a per-axis basis, a magnetic moment whose sign is opposite to that of the rate of change of the magnetic field along that axis.

1.1 .1 B-Dot Proportional Control

For a typical spacecraft axis, we set $M_X = -k \dot{B}_X$ for a magnetometer and a torquer aligned with the X-axis of the spacecraft, where k is a positive constant, M_X is the commanded dipole for the X-axis torquer, and B_X is the component of the Earth's magnetic field along the X-axis.

Let us apply this proportional control to the simple example depicted in Figure 1: Consider a body spinning about its Z-axis, with a moment of inertia, I_z, and a spin rate, ω_z. Let the Earth's magnetic field vector be in the X-Y plane, with a magnitude B_o. A single-axis magnetometer is aligned with X, and measures the B_x component of $\vec{B}$. Our example also includes a magnetic torquer, along the X-axis.

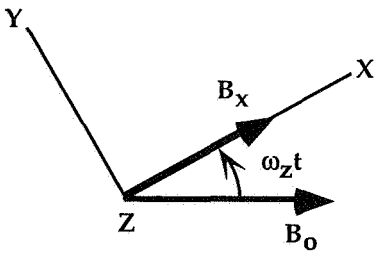

Figure 1: Geometry for Example

From this geometry, note that $B_x = B_o \cos\omega_z t$, so that $\dot{B}_x = -B_o\omega_z \sin\omega_z t$. Initial phase angle is take as zero, without loss of generality. Using the proportional control law suggested above we have a commanded dipole of

$$M_x = -k\dot{B}_x = k B_o\omega_z \sin\omega_z t$$

for the X-axis torquer. Because of the convenient geometry of this example, $\vec{M}\times\vec{B}$ will be a vector in the Z direction, with $T_z = M_x B_y$.

The geometry shows that $B_y = -B_o \sin\omega_z t$. We thus have

$$T_z = (kB_o\omega_z \sin\omega_z t)(-B_o \sin\omega_z t)$$

$$T_z = -kB_o^2\omega_z \sin^2\omega_z t$$

Over one revolution, the average value of $\sin^2\omega_z t$ will be 0.5, so the average torque generated by the proportional controller using one torquer will be: $T_{z,ave} = \frac{-kB_o^2\omega_z}{2}$.

Basic physics tells us that the rate of change of angular momentum equals the torque applied. In this example, a body spinning about its Z-axis, the angular momentum, H_z, is given by $I_z\omega_z$. Its derivative is then:

$$I_z\dot{\omega}_z = \dot{H}_z = T_{z,ave} = \frac{-kB_o^2\omega_z}{2}$$

This equation may be rewritten:

$$\dot{\omega}_z + \frac{kB_o^2}{2I_z}\omega_z = 0$$

and is of the form, $\dot{\omega}_z + \frac{\omega_z}{\tau} = 0$ where τ is a decay time constant. The solution of this equation is $\omega_z = \omega_{z_o} e^{-t/\tau}$ with $\tau = \frac{2I_z}{kB_o^2}$ and ω_{z_o} the initial spin rate. From this solution, we see that the controller causes the spin rate to decay exponentially.

If a second magnetic torque is applied along the Y-axis, we would then have the additional term $\dot{B}_y = -B_o\omega_z \cos\omega_z t$ resulting in a commanded Y-axis dipole of $M_y = -k\dot{B}_y = kB_o\omega_z \cos\omega_z t$. With this additional control authority, the resultant torque becomes:

$$T_z = M_x B_y - M_y B_x$$

$$T_z = (kB_o\omega_z \sin\omega_z t)(-B_o \sin\omega_z t) - (kB_o\omega_z \cos\omega_z t)(B_o \cos\omega_z t)$$

$$T_z = -kB_o^2\omega_z$$

$$T_z = -kB_o^2\omega_z = \dot{H}_z = I_z\dot{\omega}_z$$

which leads to the equation:

$$\dot{\omega}_z + \frac{kB_o^2\omega_z}{I_z} = 0.$$

This yields the same form of solution, $\omega_z = \omega_{z_o} e^{-t/\tau}$, but with a different time constant, $\tau = \frac{I_z}{kB_o^2}$. Comparing this to the time constant for control with the single, X-axis torquer, we see that adding the Y-axis control cuts the time constant for the spin decay in half.

Now consider the maximum allowable value for k consistent with proportional control and a finite torquer capacity. This is tantamount to setting $kB_o\omega_z = M_o$, where M_o is the maximum torquer dipole. At this maximal k value, the T_z using two torquers, becomes

$$T_{z,max} = -M_oB_o$$

This maximal estimate provides a useful benchmark for comparison to the effects of the B-Dot bang-bang controller described in the next section.

1.1.2 B-Dot Bang-Bang Control:

As an alternative to the proportional B-Dot controller, consider a bang-bang system where, instead of using proportional control to calculate the dipole command, the maximum torquer strength is always used. Let

$$M_x = -M_o\,\mathrm{sgn}\left(\dot{B}_x\right) = \begin{cases} -M_o \text{ if } \dot{B}_x > 0 \\ M_o \text{ if } \dot{B}_x < 0 \end{cases} \quad \text{and similarly,} \quad M_y = -M_o\,\mathrm{sgn}\left(\dot{B}_y\right) = \begin{cases} -M_o \text{ if } \dot{B}_y > 0 \\ M_o \text{ if } \dot{B}_y < 0 \end{cases}$$

where "sgn" stands for "sign of" and M_o is the maximum torquer dipole. Then,

$$T_z = M_xB_y - M_yB_x = \left(-M_o\,\mathrm{sgn}\,\dot{B}_x\right)\left(-B_o\sin\omega_z t\right) - \left(-M_o\,\mathrm{sgn}\,\dot{B}_y\right)\left(B_o\cos\omega_z t\right)$$

$$T_z = M_oB_o\left[\mathrm{sgn}\left(-B_o\omega_z\sin\omega_z t\right)\sin\omega_z t + \mathrm{sgn}\left(-B_o\omega_z\cos\omega_z t\right)\cos\omega_z t\right]$$

For $B_o, \omega_z > 0$,

$$\mathrm{sgn}\left(-B_o\omega_z\sin\omega_z t\right) = -\mathrm{sgn}\left(\sin\omega_z t\right)$$

$$\mathrm{sgn}\left(-B_o\omega_z\cos\omega_z t\right) = -\mathrm{sgn}\left(\cos\omega_z t\right)$$

Thus, T_z will be given by the sum of rectified sine and cosine functions. The average value of a rectified sine or cosine wave is $2/\pi$, so the average value of the torque generated by each actuator is $-\frac{2}{\pi}M_oB_o$. With two torquers, the average torque generated is:

$$T_{z,ave} = -\tfrac{4}{\pi}M_oB_o.$$

Note that the proportional control has a $T_{z,max} = -M_oB_o$. In comparison, the bang-bang controller raises the resultant torque by a factor of $\frac{4}{\pi}$, a 27% increase.

Equating the average torque to the rate of change of angular momentum we have:

$$I_z\dot{\omega}_z = -\tfrac{4}{\pi}M_oB_o$$

From the solution of this equation, we see that we have a linear spin rate decay given by

$$\omega_z = \omega_{z_o} - \frac{4}{\pi}\frac{M_oB_o}{I_z}t$$

which is faster than the exponential decay resulting from proportional B-dot control described in the last section.

1.2 $\vec{H}\times\vec{B}$ Momentum Unloading Controller

It is of interest to contrast the B-Dot control described here to the performance of an $\vec{H}\times\vec{B}$ law which is another magnetic controller often used for spacecraft momentum unloading and despin.

1.2.1 $\vec{H}\times\vec{B}$ Control, Single Axis Example

Let $\vec{M} = k\left(\vec{H}\times\vec{B}\right)$ where $\vec{H}$ is the angular momentum vector and k is an arbitrary constant. Since $\vec{T} = \vec{M}\times\vec{B}$, we have:

$$\vec{T} = k\left(\vec{H}\times\vec{B}\right)\times\vec{B}$$

$$\vec{T} = k\left[\left(\vec{H}\cdot\vec{B}\right)\vec{B} - B^2\vec{H}\right]$$

Applying this control law to our simple example, we see $\vec{H}\cdot\vec{B} = 0$, since $\vec{H}$ is perpendicular to $\vec{B}$ and $B^2 = B_o^2$.

Since $\dot{\vec{H}} = \vec{T}$, we have: $\qquad \dot{\vec{H}} = -kB_o^2\vec{H}$

Or, rearranging: $$\dot{\vec{H}} + kB_0^2\vec{H} = 0$$

Since in our example $\vec{H}$ has only a Z-component, which is given by $I_z\omega_z$, this equation becomes:

$$\dot{\omega}_z + kB_0^2\omega_z = 0$$

giving us an exponential spin rate decay with a time constant of:

$$\tau = \frac{1}{kB_0^2}$$

Compare this to the exponential decay seen with the proportional B-Dot control, where the time constant was calculated to be $\tau = \frac{I_z}{kB_0^2}$. Both controllers produce exponential decay with time constants inversely proportional to the control gain and the square of the available magnetic field strength. This highlights the fact that, for momentum unloading, B-Dot control is qualitatively identical to $\vec{H}\times\vec{B}$ control.

1.2.2 Three-Axis $\vec{H}\times\vec{B}$ Control

To round out our primer on magnetic controllers, this section is included as a brief aside, extending $\vec{H}\times\vec{B}$ beyond our simple example, to the general three-axis case.

In the general case of $\vec{H}\times\vec{B}$ control, consider: $$\dot{\vec{H}} = k\left[\left(\vec{H}\cdot\vec{B}\right)\vec{B} - B^2\vec{H}\right]$$

Taking the dot product of both sides with $\vec{H}$: $$\vec{H}\cdot\dot{\vec{H}} = k\left[\left(\vec{H}\cdot\vec{B}\right)\left(\vec{H}\cdot\vec{B}\right) - B^2\vec{H}\cdot\vec{H}\right]$$

This can be written: $$\frac{1}{2}\frac{d}{dt}\left(\vec{H}\cdot\vec{H}\right) = k\left[\left(\vec{H}\cdot\vec{B}\right)^2 - B^2\left(\vec{H}\cdot\vec{H}\right)\right]$$

$$\frac{1}{2}\frac{d}{dt}\left(H^2\right) = k\left[(HB\cos\theta)^2 - H^2B^2\right]$$

where θ is the angle between $\vec{H}$ and $\vec{B}$ and H is the magnitude of $\vec{H}$.

Continuing on,

$$H\dot{H} = kH^2B^2\left(\cos^2\theta - 1\right)$$

$$\dot{H} = -kB^2H\sin^2\theta$$

From this, it can be seen that the magnitude of $\dot{H}$ is never greater than zero, so the angular momentum is monotonically non-increasing.

For our example, with $\vec{H}$ perpendicular to $\vec{B}$ and magnitude of $\vec{B}$ equal to B_0, this expression reduces to,

$$\dot{H} = -kB_0^2H$$

a result in agreement with that shown in the previous section on $\vec{H}\times\vec{B}$.

Section 2: Possible Application of B-Dot as a RADARSAT Sun Acquisition Mode

In the ensuing discussion, Safehold Mode refers to the passive Safehold Mode, currently in use on-board the RADARSAT spacecraft. B-Dot Sun Acquisition is the authors' proposed controller, a bang-bang B-Dot control law.

2.1 Spacecraft Description

RADARSAT is a Canadian satellite launched into an 800 km altitude circular, sun-synchronous, dusk-dawn orbit in January 1996. In this orbit, the spacecraft is in full sun for approximately ten contiguous months of the year, but there is a two month season during which eclipses occur once per orbit. For RADARSAT, the eclipse season is centered around the time of summer solstice, approximately June 20, when the sun is about 32° north of the orbit normal. At this time, the solar array illumination is at a minimum, about 85% of peak when the spacecraft is in sunlight, and the spacecraft flies through the Earth's shadow in the south polar regions, further reducing the average power available.

Figure 2 shows a sketch of the RADARSAT spacecraft in its normal operational configuration. The $+X_c$ (roll) axis is nominally aligned with the velocity vector. The solar arrays face orbit normal, and the $+Z_c$ axis (yaw) points down, toward the Earth. Here, the "c" subscript refers to the "control" axes.

The spacecraft has two pairs of Y and Z axes, "mechanical" and "control." The mechanical axes are aligned with the body cube, while the control axes are aligned with the desired science attitude. The solar arrays face in the negative Y_c direction. The Synthetic Aperture Radar (SAR) looks out in the $+Z_m$ direction. To meet the science requirements, the SAR should be "rolled" 30° away from the nadir direction. This places the $+Z_c$ and the $+Z_m$ axes 30° apart, as shown in Figure 3.

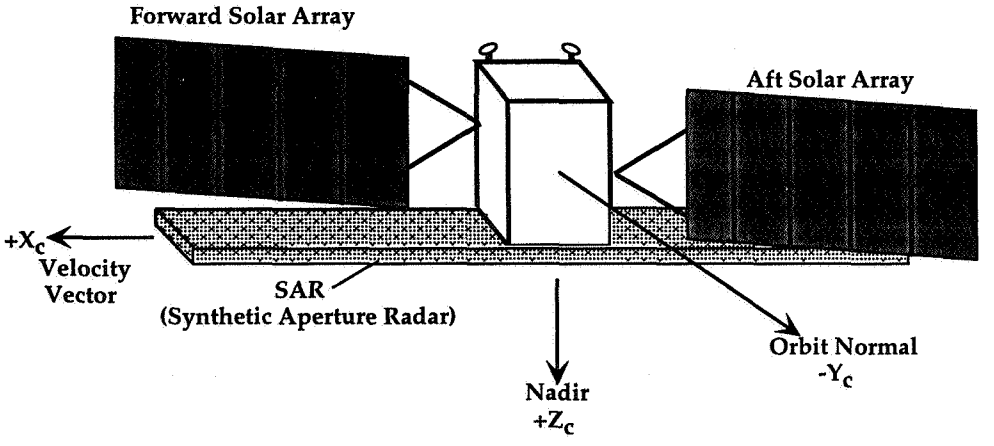

Figure 2: RADARSAT, Normal Operational Configuration

The spacecraft has a momentum wheel aligned with the Y_c axis and reaction wheels on the X_c and Z_c axes. The momentum wheel provides a momentum bias for the system along the orbit normal. Typically, such a bias is used for passive roll/yaw control on an Earth-pointed spacecraft, but the RADARSAT controller is designed so that gyroscopic coupling is thwarted, and the control closely resembles that of a three-axis, zero momentum system. This approach creates three uncoupled single-axis control channels, simplifying the controller design.

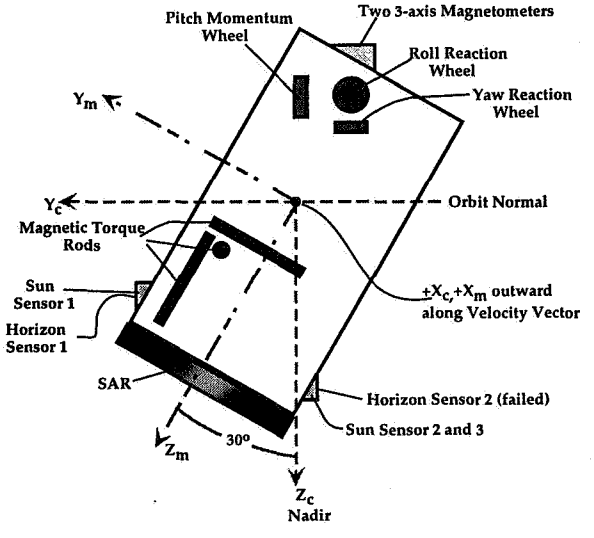

Figure 3: RADARSAT ACS Hardware

The intent of the pitch momentum bias on RADARSAT is to provide a passive Safehold Mode for the spacecraft. Its Safehold Mode, which is entered automatically in the event of a problem, simply disables all active control and sheds all non-essential loads. The momentum wheel runs down, transferring its angular momentum to the spacecraft body. The body spins up causing it to remain pointed approximately along the orbit normal, where orbit normal is approximately equal to the sunline. This places RADARSAT in a thermal and power safe condition. The solar arrays continue to receive near-nominal illumination. However, Y_c is not a principal axis, so the spin-up produces a very complex motion.

The performance of such a passive Safehold Mode is extremely sensitive to initial conditions at the time of entry. During the first eclipse season in the summer 1996, a series of spacecraft anomalies resulted in a transition to Safehold Mode under less than ideal initial conditions. The ensuing spacecraft motion led to a severe power shortage which almost resulted in a loss of mission.

2.2 Normal Equilibrium State

In its normal mode of operation, the spacecraft rotates at the orbit rate, ω_o about the $-Y_c$ axis. The momentum wheel provides a bias of 50 Nms in the same direction. Because of significant products of inertia about the controller axes, the resultant spacecraft angular momentum vector, $\vec{H}$, is not along the orbit normal in this state and potential nutation problems exist. The reaction wheels, however, can be run at bias speeds which places the system momentum vector along the $-Y_c$ axis.

Consider

$$H_x = I_{xx}\omega_x - I_{xy}\omega_y - I_{xz}\omega_z + h_{rw,x}$$
$$H_z = -I_{xz}\omega_x - I_{yz}\omega_y + I_{zz}\omega_z + h_{rw,z}$$

where: H_x, H_y, H_z are the angular momentum components
$\omega_x, \omega_y, \omega_z$ are the angular velocity components
$h_{rw,x}$, $h_{rw,y}$, $h_{rw,z}$ are the wheel momenta.

We want $H_x = H_z = 0$ when $\omega_x = \omega_z = 0$ and $\omega_y = -\omega_o$. It follows that we require:

$$I_{xy}\omega_o + h_{rw,x} = 0$$
$$I_{yz}\omega_o + h_{rw,z} = 0$$

Thus, if the roll reaction wheels runs with a momentum of $h_{rw,x} = -I_{xy}\omega_o$ and the yaw wheel runs with $h_{rw,z} = -I_{yz}\omega_o$, the spacecraft rotation about the -Y_c axis will represent an equilibrium state.

Entering the proposed B-Dot Sun Acquisition Mode from a nominal state would involve the initial conditions:

$\omega_x = 0$ $\quad h_{rw,x} = -I_{xy}\omega_o \approx$ -2 Nms
$\omega_y = -\omega_o$ $\quad h_{rw,y} = -50$
$\omega_z = 0$ $\quad h_{rw,z} = -I_{yz}\omega_o \approx$ -1 Nms

These initial conditions are assumed in all of the simulations results presented in Section 2.4.

2.3 Simulations

From the magnetic controllers discussed in section one, the authors chose a three-axis bang-bang B-Dot controller for its speed, and simplicity. It can also takes advantage of the maximum available control authority, by setting the commanded dipole to the torquer's limit, although none of our simulations depict this situation. This controller, used in conjunction with a constant speed pitch momentum wheel, will precess the wheel spin axis to orbit normal. Performance was evaluated using RADARSAT mass properties in a FORTRAN simulation of the spacecraft dynamics and kinematics.

Spacecraft dynamics were modeled by the three classical Euler equations[2]:

$$\dot{H}_x + \omega_y H_z - \omega_z H_y = T_x$$
$$\dot{H}_y + \omega_z H_x - \omega_x H_z = T_y$$
$$\dot{H}_z + \omega_x H_y - \omega_y H_x = T_z$$

T_x, T_y, T_z are components of the external torques

Classical quaternion equations were integrated to model the kinematics[2]:

$$\dot{q}_1 = \tfrac{1}{2}\left(\omega_z q_2 - \omega_y q_3 + \omega_x q_4 \right)$$
$$\dot{q}_2 = \tfrac{1}{2}\left(-\omega_z q_1 + \omega_x q_3 + \omega_y q_4 \right)$$
$$\dot{q}_3 = \tfrac{1}{2}\left(\omega_y q_1 - \omega_x q_2 + \omega_z q_4 \right)$$
$$\dot{q}_4 = \tfrac{1}{2}\left(-\omega_x q_1 - \omega_y q_2 - \omega_z q_3 \right)$$

The spacecraft attitude matrix, [A], was obtained from the quaternion elements from[2]:

$$[A] = \begin{bmatrix} q_1^2 - q_2^2 - q_3^2 + q_4^2 & 2(q_1q_2 + q_3q_4) & 2(q_1q_3 - q_2q_4) \\ 2(q_1q_2 - q_3q_4) & -q_1^2 + q_2^2 - q_3^2 + q_4^2 & 2(q_2q_3 + q_1q_4) \\ 2(q_1q_3 + q_2q_4) & 2(q_2q_3 - q_1q_4) & -q_1^2 - q_2^2 + q_3^2 + q_4^2 \end{bmatrix}$$

The nature of the RADARSAT orbit allows a very simple representation of the orbital motion. It was assumed that the orbit was inertially fixed, with the ascending node and the Earth's North Pole defining an inertial reference frame. Actually, the orbit moves at about one degree per day, keeping up with the motion of the sun, but for the short simulations described here, this effect has been ignored. Figure 4 shows the orbital representation and the spacecraft position vector components used. Axis 1 aligns with the ascending node, axis 3 corresponds to the North Pole, and axis 2 completes the right-hand coordinate frame.

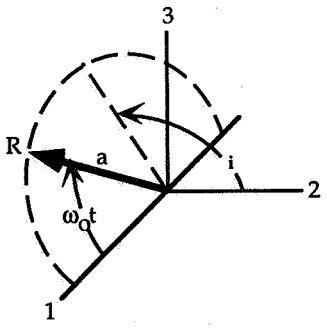

i = orbit inclination = 98.7°

a = orbit radius = $|\vec{R}|$

$\vec{R}$ is the spacecraft position vector, and $\vec{r}$ is the corresponding unit vector, $\vec{R}/a$

Let ω_o equal orbit rate. Then, we define,

$$R_1 = a\,r_1 = a(\cos\omega_o t) \qquad r_1 = \cos\omega_o t$$
$$R_2 = a\,r_2 = a(\sin\omega_o t\,\cos i) \quad \text{so} \quad r_2 = \sin\omega_o t\,\cos i$$
$$R_3 = a\,r_3 = a(\sin\omega_o t\,\sin i) \qquad r_3 = \sin\omega_o t\,\sin i$$

Figure 4: Orbital Elements

A tilted dipole model of the Earth's Magnetic field was used[2]. In the inertial frame, the field is given by:

$\vec{b} = B_o\left[\vec{m} - 3(\vec{m}\cdot\vec{r})\vec{r}\right]$ where B_o is field strength at the magnetic equator at the spacecraft altitude.

$\vec{m}$ is the unit vector along the dipole axis

$\vec{r}$ is the unit vector to the spacecraft position, with the components of $\vec{r}$, r_1, r_2, and r_3, as given above.

$\vec{m}$ is tilted 11° away from the North Pole and rotates with the Earth, so we let:

$$m_1 = \sin 11^\circ \cos\omega_E t$$
$$m_2 = \sin 11^\circ \sin\omega_E t \quad \text{where } \omega_E \text{ is Earth rate.}$$
$$m_3 = \cos 11^\circ$$

We define $\vec{B}$ as the magnetic field vector in body coordinates, so we have

$$\vec{B} = [A]\vec{b}$$

For B-Dot, we need the derivative of $\vec{B}$, which is given by

$$\dot{\vec{B}} = [A]\dot{\vec{b}} + [\dot{A}]\vec{b}$$
$$\dot{\vec{B}} = [A]\dot{\vec{b}} + [\dot{A}][A]^T\vec{B}$$

Rearranging,

$$\dot{\vec{B}} - [\dot{A}][A]^T\vec{B} = [A]\dot{\vec{b}}$$
$$\dot{\vec{B}} + [\Omega]\vec{B} = [A]\dot{\vec{b}}$$

Here, $[\Omega] = -[\dot{A}][A]^T$ is the cross product operator for the angular velocity, i.e. $\vec{\Omega} = \begin{pmatrix} 0 & -\omega_z & \omega_y \\ \omega_z & 0 & -\omega_x \\ -\omega_y & \omega_x & 0 \end{pmatrix}$.

The equation for $\dot{\vec{B}}$ can also be written

$$\dot{\vec{B}} + \vec{\omega}\times\vec{B} = [A]\dot{\vec{b}}$$
$$\dot{\vec{B}} = [A]\dot{\vec{b}} - \vec{\omega}\times\vec{B}$$

To get $\dot{\vec{b}}$, recall that $\vec{b} = B_o\left[\vec{m} - 3(\vec{m}\cdot\vec{r})\vec{r}\right]$

Then, $\dot{\vec{b}} = B_o\left[\dot{\vec{m}} - 3(\vec{m}\cdot\vec{r})\dot{\vec{r}} - 3\left(\vec{m}\cdot\dot{\vec{r}} + \dot{\vec{m}}\cdot\vec{r}\right)\vec{r}\right]$

with $\vec{m}$ and $\vec{r}$ as given above, and,

$$\dot{\vec{m}} = \begin{pmatrix} -\sin 11^\circ\omega_E \sin\omega_E t \\ \sin 11^\circ\omega_E \cos\omega_E t \\ 0 \end{pmatrix} \qquad \dot{\vec{r}} = \begin{pmatrix} -\omega_o \sin\omega_o t \\ \omega_o \cos i \cos\omega_o t \\ \omega_o \sin i \cos\omega_o t \end{pmatrix}$$

We take the external torque in the Euler equations to be that due to gravity gradient and magnetic torques. The first is given by

$$\vec{T}_{gg} = 3\omega_0^2 \hat{r} \times I\hat{r}$$
$$\hat{r} = [A]\vec{r}$$

where $\hat{r}$ is the position unit vector in body coordinates and I^1 is the spacecraft's inertia tensor:

$$I = \begin{bmatrix} I_{xx} & -I_{xy} & -I_{xz} \\ -I_{xy} & I_{yy} & -I_{yz} \\ -I_{xz} & -I_{yz} & I_{zz} \end{bmatrix} = \begin{bmatrix} 4495 & -1836 & 221 \\ -1836 & 16233 & -768 \\ 221 & -768 & 15319 \end{bmatrix} \text{kg - m}^2$$

The magnetic torques are simply $\vec{T} = \vec{M} \times \vec{B}$ where $\vec{M}$ is the magnetic moment generated by the controller and $\vec{B}$ is the magnetic field in body coordinates.

2.4 Simulation Results

The results of five simulations are described in this section. In all cases , the season was selected such that the sun was on the orbit normal; Wheels speeds were initially set to the values derived in Section 2.2; Body rates were set to zero for roll and yaw, and negative orbit rate along the pitch axis. In the first three cases, initial attitude matches the RADARSAT normal configuration described in Section 2.1, corresponding to zero attitude errors. In the last two cases, an initial attitude of 77° in pitch is assumed.

For each run, four variables are displayed in the following plots:

- The angle between the spacecraft pitch axis and the orbit normal, ideally zero.
- The spacecraft pitch angle, with the zero pitch corresponding to $+Z_c$ nadir pointing.
- The pitch wheel angular momentum.
- The spacecraft normalized power, defined as the cosine of the angle between the sunline and the solar array normal. Ideally, this is value is 100% indicated that the solar arrays perpendicular to the sunline.

The roll and yaw wheels were turned off at the start of each run, but their momentum histories are not plotted. In all of the simulations discussed here, they run down in less than 16 minutes due to coulomb and viscous friction, and remain off for all subsequent time. The first three simulations were run for a duration of 24 hours; the last two were run for approximate four and a half hours, or 16000 seconds.

2.4.1 Nominal RADARSAT Safehold Mode Entry

Run 1 begins with the spacecraft in its normal attitude with initial wheel speeds and body rates as described above. Then, the wheels were simply turned off. This represents the best case scenario for RADARSAT entering its passive Safehold Mode. The pitch wheel runs down in about 90 minutes, transferring its angular momentum to the main body. During that time, the pitch axis gradually drifts away from the orbit normal, ending up about 30° off by the time the wheel stops. The pitch angle plot shows that the spacecraft did spin up, to about four revolutions per orbit about the maximum axis of inertia. The power dropped about 15% in the equilibrium state. This state would be thermal and power-safe indefinitely. Gravity gradient torque acting on the spinning body will tend to keep the system angular momentum vector in the vicinity of the orbit normal as it moves along at 1° per day. These

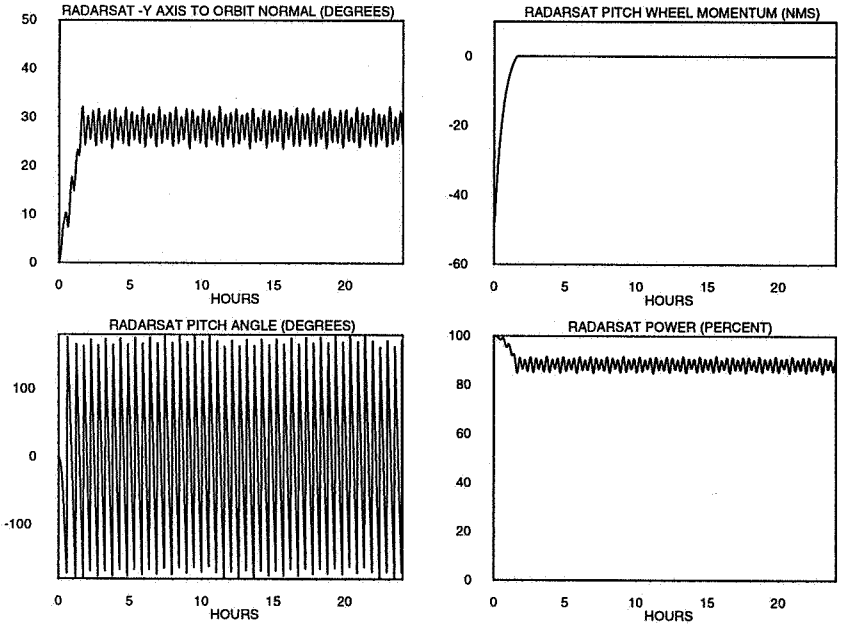

Figure 5: Nominal RADARSAT Safehold Mode Entry

torques precess the spin axis to keep up with the motion of the sun.
For nominal initial conditions, the RADARSAT Safehold Mode is acceptable. It is unforgiving, however, with respect to off-nominal initial conditions, as Section 2.4.4 demonstrates.

2.4.2 B-Dot Controller, Nominal Initial Conditions

This run shows how a bang-bang B-Dot controller using ±100 Amp-m^2 dipole levels would perform, assuming the same initial conditions as Run 1. The same variables are plotted, but note that now, the pitch wheel momentum is maintained at 50 Nms. The roll and yaw wheels still run down to zero. The pitch axis again moves away from the orbit normal, but now it wanders less than 10°. The pitch angle shows that the spacecraft initially begins to rotate with the Earth's magnetic field, about two revolutions per orbit inertially and one revolution per orbit relative to the local vertical. Near the end of the day, however, the combination of magnetic and gravity gradient torques results in gravity gradient capture indicated by the pitch angle settling to -90° , with $+X_c$ nadir pointing. Nearly full power is maintained during the entire run. This state would also be thermally and power safe indefinitely.

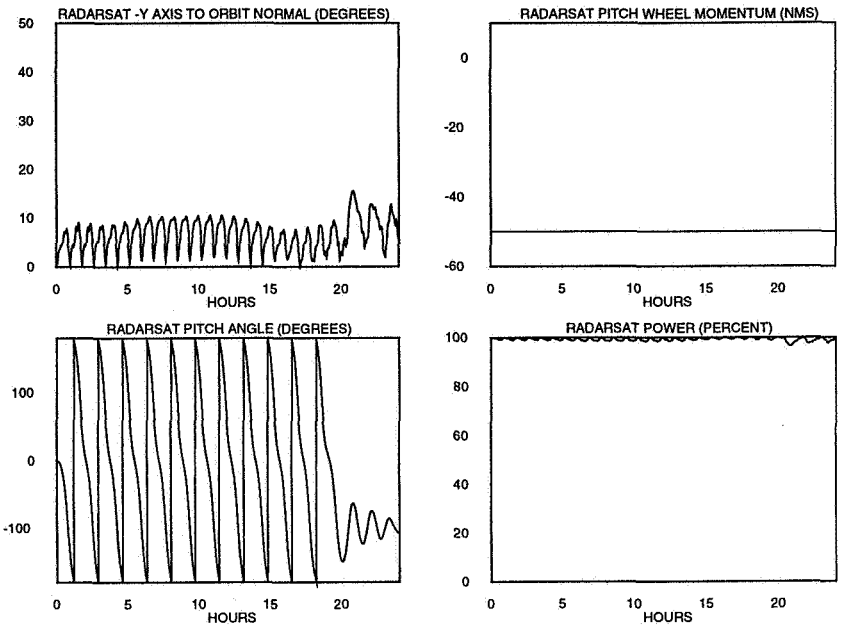

Figure 6: B-Dot Acquisition Controller, Nominal Initial Conditions

2.4.3 Nominal Safe Mode and B-Dot

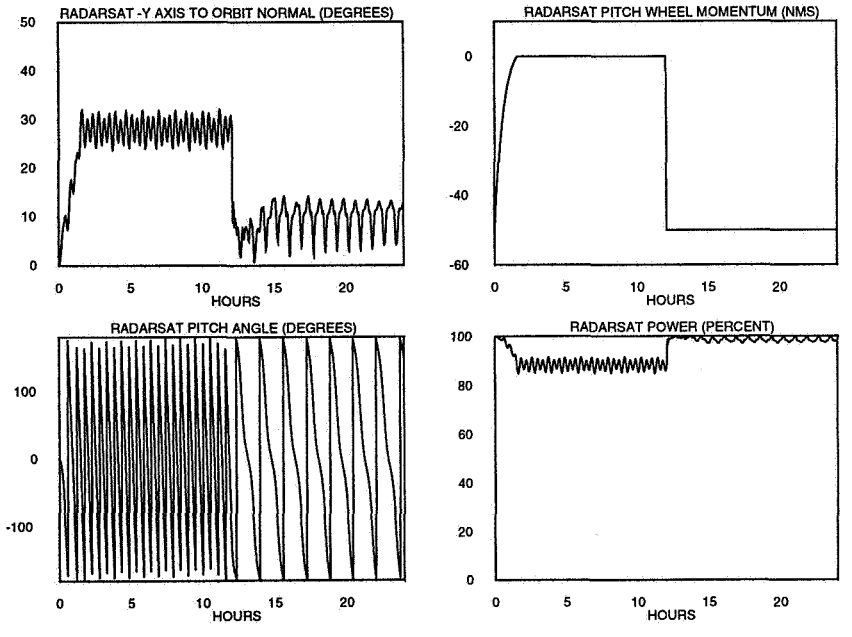

In Run 3, we repeat the first twelve hours of Run 1, the passive Safehold Mode case, then switch to the B-Dot control, as proposed for Run 2. Note the pitch wheel momentum decaying to zero, then going back up to 50 Nms at the twelve hour mark. The pitch axis quickly moves much closer to the orbit normal, the spin of the spacecraft slows down as shown by the pitch angle plot, and the power jumps to near 100% the B-Dot Sun Acquisition control scheme is initiated.

Figure 7: Nominal B-Dot Acquisition Mode

2.4.4 Passive Safehold Performance with Initial Pitch Angle of 77°

On Day 171 of 1996, the RADARSAT spacecraft entered Safehold with an initial pitch angle of 77°. Figure 8 shows the results of a Ball Aerospace simulation of the attitude motion which occurred. This data was presented at the RADARSAT ACS Evaluation Team (AET) Kickoff meeting in September, 1996. Of particular interest are the plots of the pitch and yaw angles. The first shows that the spacecraft entered a gravity gradient capture mode rather than spinning up around the pitch axis as it would have with more nominal initial conditions. As the pitch wheel spun down, gravity gradient torques on the body dumped the angular momentum that was intended to provide gyroscopic attitude stability in Passive Safehold. The yaw angle plot shows the worst effect. With no yaw stability in the gravity gradient mode, the spacecraft turned away from the sun and the solar arrays were no longer illuminated.

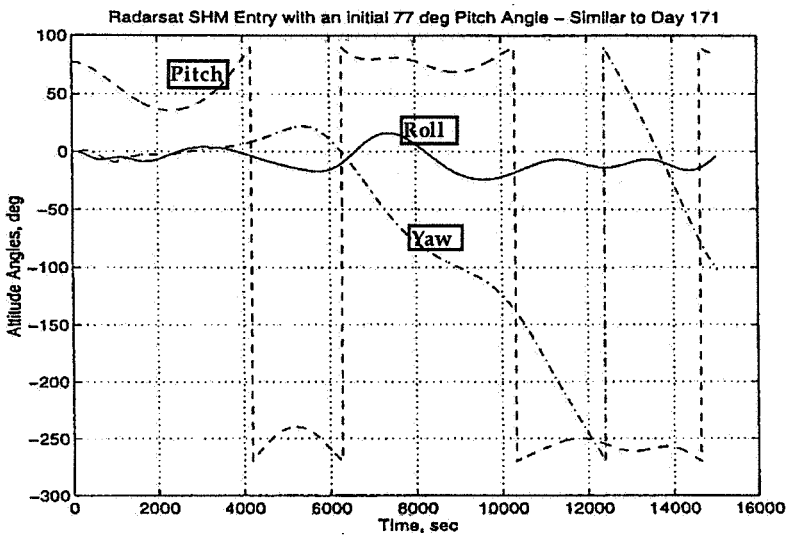

Figure 8: Ball Simulation of RADARSAT Safehold Emergency

This run, Figure 9, shows the results of the authors' simulation of this scenario. The run time of 16000 seconds was selected to facilitate easy comparison with the Ball results. The test began with nominal rates and zero roll and yaw angles. The only off-nominal initial condition was the 77° pitch angle. The pitch angle history closely matches that shown in the previous figure. Due to yaw motion, the angle between the spacecraft pitch axis and the orbit normal plot shows the 180° shift which turned the arrays backside to the sun. Also shown however is a power plot which reveals the seriousness of the situation which occurred.

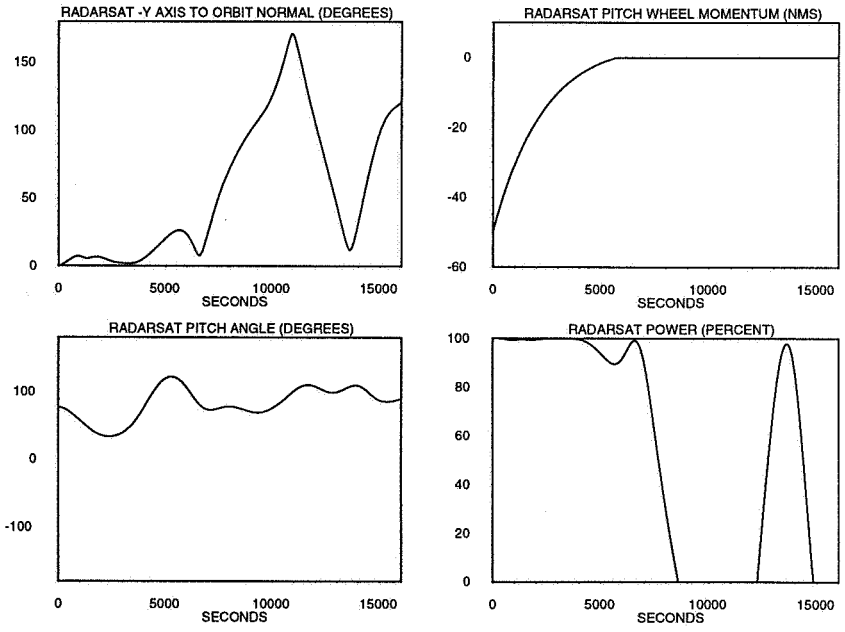

Figure 9 : Passive Safehold Performance, High Initial Pitch Angle

2.4.5 B-Dot Sun Acquisition with Initial Pitch Angle of 77°

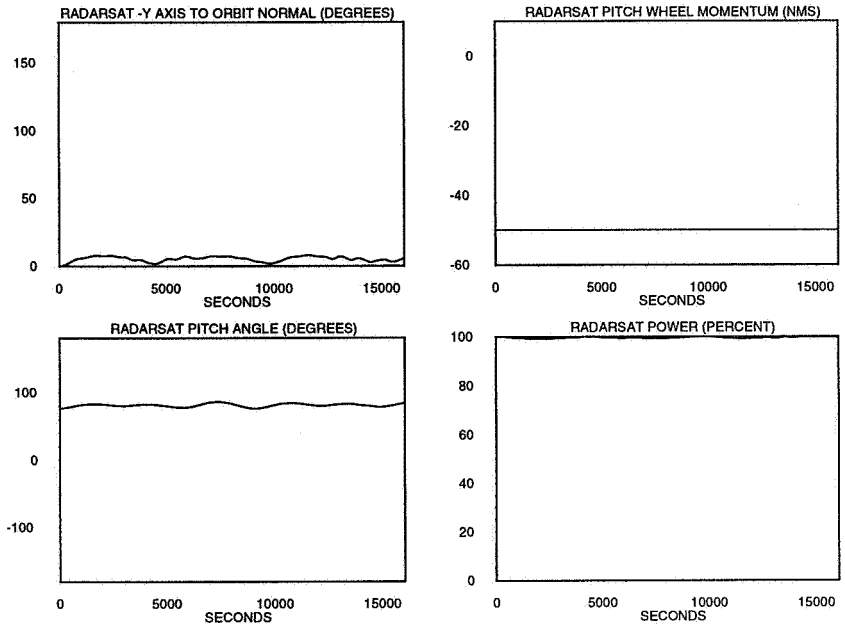

Figure 10: Proposed B-Dot Sun Acquisition , High Initial Pitch Angle

This simulation demonstrates the spacecraft attitude behavior for the proposed B-Dot Sun Acquisition controller given the same initial condition described in the last section, 2.4.4. A ± 100 A-m^2 torque level is used with the bang-bang controller. When considering the performance, note that this is not the maximum possible dipole. Control authority could be increased, by raising the commanded dipole level to the hardware limit ± 500 A-m^2.

Again, gravity gradient capture occurs, but here the -Y axis stays in the vicinity of the orbit normal, which corresponds to the sunline for the simulated season, and the solar arrays continue to produce full power. With the pitch wheel continuing to run, the system has gyroscopic roll/yaw stability which maintains the safe power and thermal conditions.

Conclusions

The passive Safemode is an acceptable strategy, given favorable initial conditions. However, it is not robust against all possible perturbations of the initial conditions, as demonstrated by the July 1996 emergency. The B-Dot Acquisition scheme examined in this paper is particularly suited to the RADARSAT system. The orbital properties are ideal for the success of B-Dot as an acquisition controller; the control law itself is extremely simple to implement; and it requires a minimal set of the available on-board sensors and actuators. Lastly, the proposed B-Dot scheme is robust against off nominal initial conditions, such as the high entry angle that resulted in the Safehold Mode emergency in July of 1996.

References:

1. RADARSAT Bus User's Manual. RSINT-ML0015-B(DRAFT). July 17, 1996.

2. Wertz, James, ed. Spacecraft Attitude Determination and Control. Kluwer Academic Publishers. Boston. 1978.

Page intentionally left blank

A Statistical Technique for Studying how a Space Vehicle's Residual Dipole Moment Degrades the Magnetic Torquer Residual Momentum Desaturation Capability***

Timothy M. Linn[1], Harold F. Zimbelman[2]

Abstract

This paper describes the effects that a space vehicle's residual dipole moment can have on residual momentum desaturation capability. Ultimately, the residual dipole moment creates undesirable disturbance torques that degrade the performance of the magnetic torquers (MT) residual momentum desaturation capability. That is, the MT are control system actuators that create torques to help desaturate any undesired system residual momentum. The MT generate a commandable magnetic dipole moment that interacts with the Earth's magnetic field to create this torque. The residual dipole moment of the space vehicle, however, also interacts with the Earth's magnetic field and creates possible undesired torques. It's these undesired torques that were studied to find a limit on the maximum allowable residual dipole moment, given certain mission constraints and magnetic torque capability. Moreover, given the time varying nature of the magnetic field during a space vehicle's orbit around the Earth, as well as the many directions that the residual momentum could be pointing, a statistical approach was taken to analyze the effects of the residual dipole moment on the MT residual momentum desaturation capability. This study will show, that under certain mission criteria, that this method is a novel approach to either finding a limit on the maximum allowable residual dipole moment, or given a residual dipole moment, what size of magnetic torquers will be necessary to have mission success.

Introduction

Magnetic torquers are control system actuators that create torques to help desaturate any undesired system residual momentum and counteract attitude drift due to environmental disturbance torques. The MT generate a commandable magnetic dipole moment that interacts with the Earth's magnetic field to create a torque. The main advantages of using MT as actuators to actively control a space vehicle is that they are relatively lightweight, require no moving parts or complex hardware and can use power generated from solar arrays, thereby eliminating usage of limited consumables. The main disadvantages of the MT are their slow response time, their near Earth use only (<35,000 km), their limited applicability due to their dependence on the direction of the magnetic field and their coarse control performance because of the magnetic field model uncertainties and long time constants.

*** Presented at: Flight Mechanics Symposium, NASA Goddard Space Flight Center (5/19/97)

1 Aerospace Engineer for the Lockheed Martin Corporation-Astronautics Division. Member of AAS

2 Professor, Dept. of Civil Engineering Technology, Metropolitan State College of Denver; Aerospace Engineering Consultant for the Lockheed Martin Corporation-Astronautics Division. Member of AAS, AIAA

The magnetic disturbance torques also result from the interaction with the geomagnetic field. This interaction is between the space vehicle's residual dipole moment and the geomagnetic field. These disturbance torques mainly occur from the space vehicle's magnetic moments, eddy currents and hysteresis. Of these primary sources, the space vehicle's magnetic moment is the dominant source of the disturbance torques. The space vehicle's magnetic moment is caused by permanent and induced magnetism and space vehicle generated current loops. The instantaneous magnetic disturbance torque, due to the space vehicle's magnetic moment M is given by:

$$N_{mag} = M \times B_v \tag{1}$$

where B_v is the geocentric magnetic flux density (wb/m^2) and M is the sum of the individual magnetic moments (A*m^2) caused by permanent and induced magnetism and space vehicle generated current loops.

The torques caused by the eddy currents and the irreversible magnetization of permeable material (hysteresis), are due to the spinning motion of the space vehicle. The torque generated from these eddy currents is given by:

$$N_{eddy} = Ke * (\omega \times B_v) \times B_v \tag{2}$$

where ω is the spacecraft's angular velocity vector and Ke is a constant coefficient which depends on the space vehicle's geometry and conductivity. Eddy currents can occur in structural material that has a permeability nearly equal to that of free space.

Finally, hysteresis occurs when a permeable material, rotating in a magnetic field H, dissipates energy in the form of heat due to the frictional motion of the magnetic domains. The energy loss over one rotational period is given by:

$$E_{hys\_loss} = V * \oint H * dB \tag{3}$$

where V is the volume of the permeable material and dB is the induced magnetic induction flux in the material. The hysteresis effects are appreciable only in very elongated "soft" magnetic material (i.e. materials for which changes in the ambient field cause large changes in the magnetic moment). The torque given by the hysteresis is given by:

$$N_{hys} = \frac{\omega * E_{hys\_loss}}{\omega^2 * dt} \tag{4}$$

where dt is the time interval over which the torque is being evaluated [ref. 1].

Analysis

In order to look at the effects of the vehicle's residual dipole moment, the torque capability of the MT was first solved. The MT need to produce a torque in the opposite direction of the undesired residual momentum ($T = -K * H_{resv}$). To look at all possible undesired residual momentums, a unit momentum sphere of all momentum directions was used to determine the MT torque capability over this entire sphere. The idea is to take a unit sphere that represents all residual momentum directions and project the torque

produced by the MT onto each vector that makes up this sphere. This torque sphere then represents the global torque capability of the MT for one instant in time, since the torque produced by the MT is a function of the time varying earth's magnetic field. Over the entire surface of the earth, then, there will be many of these torque spheres for the varying magnetic field. Before going into the statistical technique presented in this paper, a description of the geomagnetic field model and the MT control law and actuator dynamics will be described.

The geomagnetic field used for this analysis was modeled as an eighth order spherical harmonic model. The Earth's geomagnetic field, for inclined orbits, has a half-orbit period variation and for near-equatorial orbits, is essentially constant. For a given orbital radius R_o and an inclination angle i, the geomagnetic model [ref.2] was sampled 24 times, or every 15 degrees in true anomaly around each orbit with each orbit being precessed from 0 to 360 degrees in 15 degree increments of longitude of the ascending node. This procedure produces a set of geomagnetic field data with an index of 576 points, which covers the entire Earth. The geomagnetic field was then transformed from the magnetic reference coordinates to the space vehicle coordinate system. The following definitions are used for the different coordinate systems:

Coordinate System Definitions

X_I, Y_I, Z_I	Inertial Reference Coordinate System
X_m, Y_m, Z_m	Earth's Magnetic Coordinate System
L_1, L_2, L_3	Local Vertical Coordinate System
X_R, Y_R, Z_R	Space Vehicle Reference Coordinate System
X_V, Y_V, Z_V	Space Vehicle Coordinate System

β_m	Angle (deg) between the Z_I axis and the Z_m axis at t = 0.
ω_E	Earth's rotation rate (deg/sec).
ω_λ	Nodal regression rate of the orbit (deg/sec).
α	Initial position of the space vehicle in the orbit plane (deg) with respect to the ascending node.
η	Inclination angle (deg) of the orbital plane with respect to the equatorial plane.
β_e	Angle (deg) between the Z_I axis and the ascending node at t = 0.
R_o	Radius (ft) of the circular orbit from the center of the earth.
t	Time (sec) from start of orbit motion.

$B_{vcx}, B_{vcy}, B_{vcz}$	Components of the Earth's Geomagnetic Field Flux Density in the Space Vehicle coordinate system (wb/m^2).
B_{mx}, B_{my}, B_{mz}	Components of the Earth's Geomagnetic Field Flux Density in the Earth's Magnetic coordinate system (wb/m^2).

Shown in Figure 1 are the magnetic and inertial reference coordinate systems, and in Figure 2, the orbital and inertial coordinate systems. The transformation matrices, used to define the geomagnetic field vector components in the different coordinate systems, are defined by equations 5 thru 9. The geomagnetic field vector in the space vehicle coordinate system was solved using the following orbital conditions:

$\beta_e = 0, \quad \omega_\lambda = n*15, \quad \beta_m = 0, \quad \omega_E = n*15, \quad \alpha = n*15, \quad i = \text{constant}$

where n = 0,1,2,...,24.

Next, a description of the MT control law and actuator dynamics will be presented. The magnetic torquers are control system actuators that create torques by generating commandable magnetic dipole moment that interacts with the earth's magnetic field. Again, these magnetic produced torques need to be in the opposite direction of the residual momentum to desaturate the undesired momentum. Figure 3 is the block diagram that represents the general magnetic torquer control law. For this study, there were three magnetic torquers of equal capability, one placed along each axis of the space vehicle.

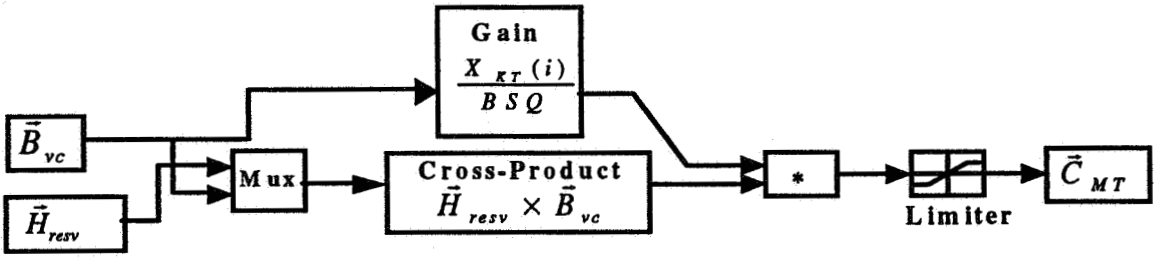

Figure 3 - Magnetic Torquer Controller Block Diagram

Where:

$\vec{B}_{vc}$ Earth's Geomagnetic Field Flux Density (wb/m^2).

$\vec{H}_{resv}$ Total Residual Angular Momentum (ft-lb-s).

$\vec{X}_{KT}$ Magnetic Torquer Control Gain.

$\vec{D}_l$ Dipole Moment Limit (wb-m; pole-cm converted to wb-m).

$\vec{C}_{MT}$ Commanded Dipole Moment (wb-m; pole-cm converted to wb-m).

Note: $1(pole-cm) = 4*\pi*10^{-10}(wb-m)$

The following equations describe the above block diagram:

$$BSQ = B_{vc}(1)^2 + B_{vc}(2)^2 + B_{vc}(3)^2 \tag{10}$$

$$\vec{v} = \vec{H}_{resv} \times \vec{B}_{vc} \tag{11}$$

$$C(i) = \frac{X_{KT}(i)}{BSQ} * v(i); \quad i = 1, 2, 3 \tag{12}$$

$$\vec{C}_{MT} = \lim(\vec{C}, \vec{D}_l) \tag{13}$$

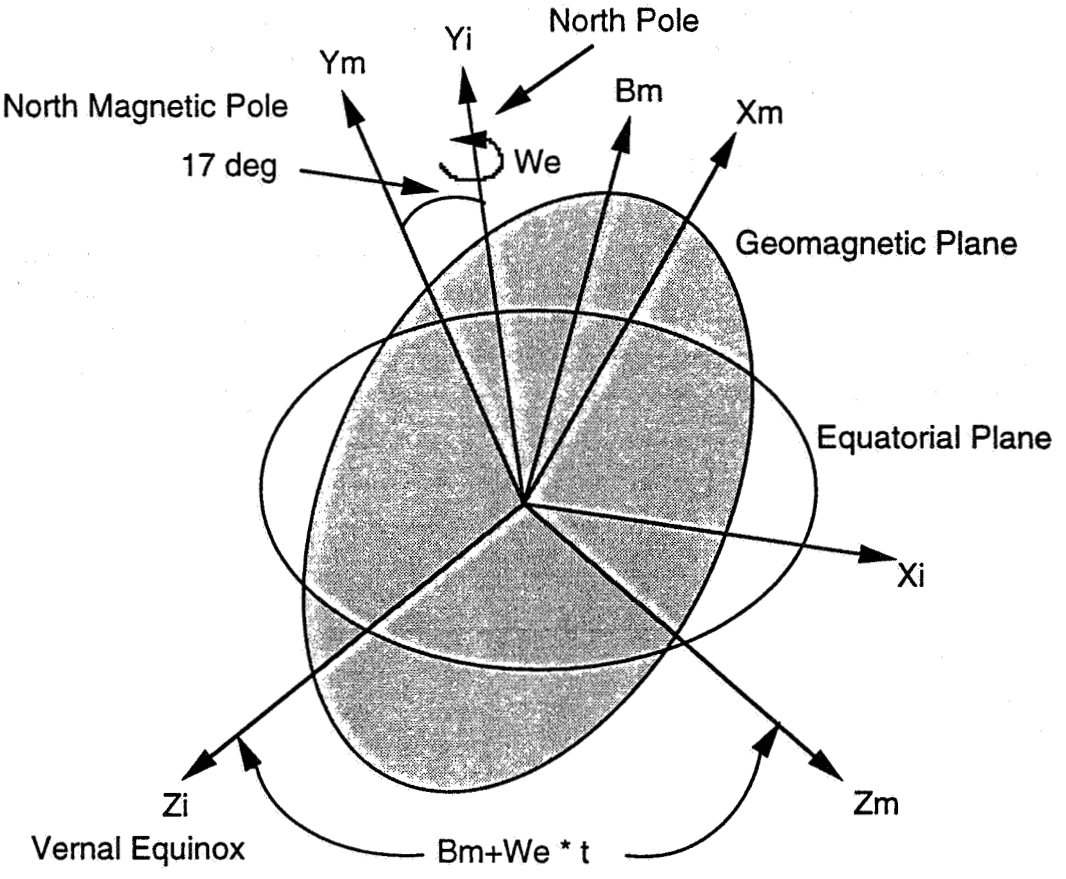

$$\begin{bmatrix} X_I \\ Y_I \\ Z_I \end{bmatrix} = T(\beta_m + \omega_E * t) * T(17^\circ) \begin{bmatrix} X_m \\ Y_m \\ Z_m \end{bmatrix} \tag{5}$$

$$\begin{bmatrix} X_I \\ Y_I \\ Z_I \end{bmatrix} = \begin{bmatrix} \cos(\beta_m + \omega_E * t) & 0 & -\sin(\beta_m + \omega_E * t) \\ 0 & 1 & 0 \\ \sin(\beta_m + \omega_E * t) & 0 & \cos(\beta_m + \omega_E * t) \end{bmatrix} \begin{bmatrix} \cos(17^\circ) & \sin(17^\circ) & 0 \\ -\sin(17^\circ) & \cos(17^\circ) & 0 \\ 0 & 0 & 1 \end{bmatrix} \begin{bmatrix} X_m \\ Y_m \\ Z_m \end{bmatrix} \tag{6}$$

Figure 1 - Magnetic and Inertial Reference Coordinate Systems

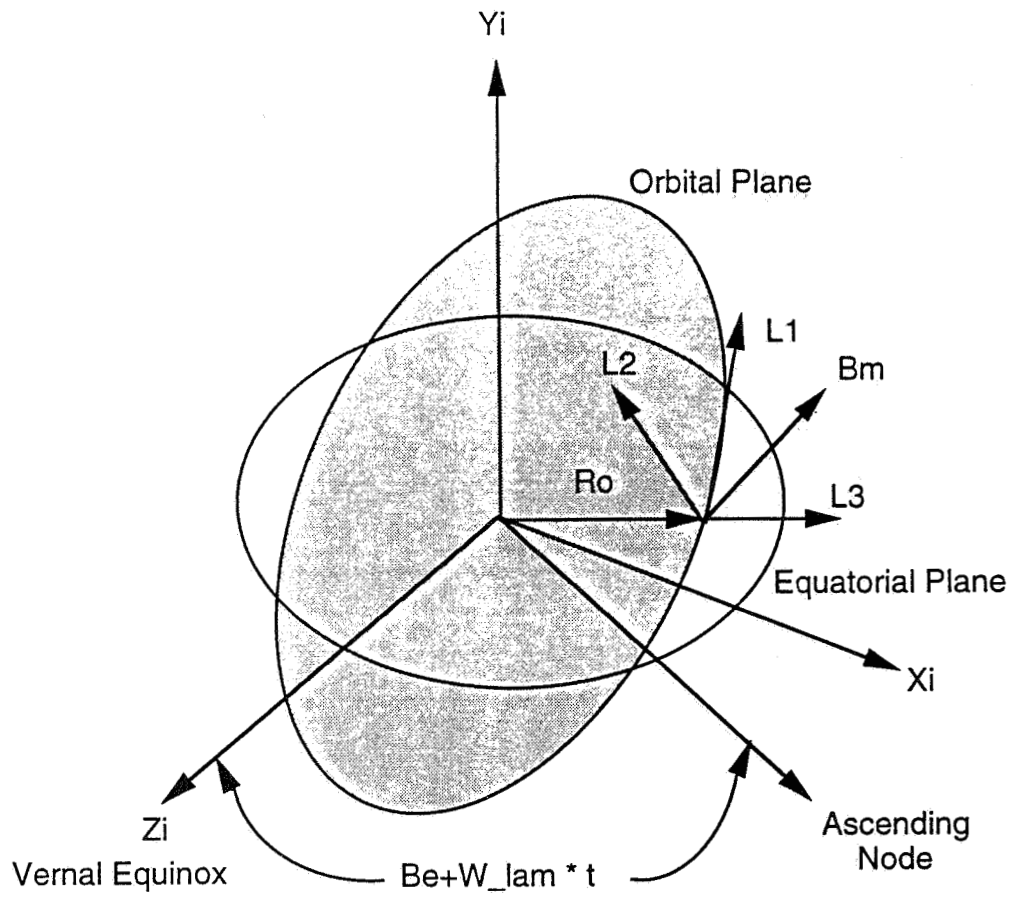

$$\begin{bmatrix} L_1 \\ L_2 \\ L_3 \end{bmatrix} = T(\alpha) * T(\eta) * T(\beta_e + \omega_\lambda * t) * \begin{bmatrix} X_I \\ Y_I \\ Z_I \end{bmatrix} \tag{7}$$

$$\begin{bmatrix} L_1 \\ L_2 \\ L_3 \end{bmatrix} = \begin{bmatrix} \cos(\alpha) & 0 & -\sin(\alpha) \\ 0 & 1 & 0 \\ \sin(\alpha) & 0 & \cos(\alpha) \end{bmatrix} \begin{bmatrix} \cos(\eta) & \sin(\eta) & 0 \\ -\sin(\eta) & \cos(\eta) & 0 \\ 0 & 0 & 1 \end{bmatrix} \begin{bmatrix} \cos(\beta_e + \omega_\lambda * t) & 0 & -\sin(\beta_e + \omega_\lambda * t) \\ 0 & 1 & 0 \\ \sin(\beta_e + \omega_\lambda * t) & 0 & \cos(\beta_e + \omega_\lambda * t) \end{bmatrix} \begin{bmatrix} X_I \\ Y_I \\ Z_I \end{bmatrix} \tag{8}$$

$$\begin{bmatrix} R_1 \\ R_2 \\ R_3 \end{bmatrix} = T_L^R \begin{bmatrix} L_1 \\ L_2 \\ L_3 \end{bmatrix} \tag{9}$$

Figure 2 - Orbital and Inertial Reference Coordinate Systems

The block diagram shown in Figure 4 represents the magnetic torquer actuator model.

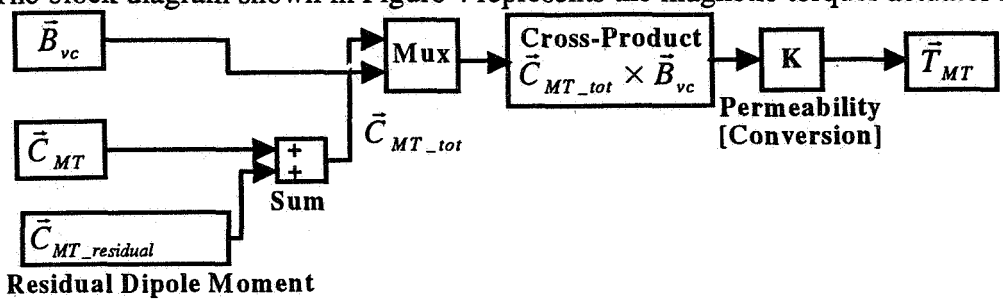

Figure 4 - Magnetic Torquer Actuator Model

Where:

$\vec{B}_{vc}$	Earth's Geomagnetic Field Flux Density (wb/m^2).
$\vec{C}_{MT}$	Commanded Dipole Moment (wb-m; pole-cm converted to wb-m).
$\vec{C}_{MT\_residual}$	Residual Dipole Moment (wb-m; pole-cm converted to wb-m).
K	Permeability Constant.

The following equations describe the magnetic torquer model:

$$K = 0.7375621 * \frac{10^7}{4\pi} \tag{14}$$

$$\vec{v}_2 = \vec{C}_{MT\_tot} \times \vec{B}_{vc} \tag{15}$$

$$\vec{T}_{MT} = K * \vec{v}_2 \tag{16}$$

It should be noted, that the magnetic torquers are the only means in desaturating undesired Z-axis vehicle residual momentum, and this Magnetic Torquer Momentum Control (MTMC) law does not always produce the best possible Z-axis vehicle torques. Therefore, in addition to this basic control law, the residual momentum command can be varied to assure that "good" magnetic torques (i.e. large magnitude in the correct direction) will be applied along the Z-axis when necessary. To assure good torques are applied along the Z-axis, the X and Y-axis residual momentums signals are set to zero. Moreover, when the basic MTMC law is altered to insure "good" Z-axis torques, the X and Y-axis torques may end up being undesirable. Since Gravity Gradient Momentum Control (GGMC) may used in conjunction with MTMC, these "bad" X and Y-axis magnetic torques can be offset by "good" gravity gradient torques while the "good" Z-axis magnetic torque continues to be applied.

With the geomagnetic field modeled, as well as the MT control law derived and MT actuator dynamics modeled, the torque produced from the MT can be solved. As shown previously, geomagnetic field data was generated and collected over the entire earth (576 indexed vectors). Next, a sphere of all possible residual momentum vectors

needed to be generated. This sphere was generated with a 32 by 32 point resolution. That is, elevation was taken in 32 equally spaced increments from +90 degrees to -90 degrees (5.625 degree steps) and for each of the 32 elevation points, azimuth was varied from 0 to 360 degrees (11.25 degree steps). The geomagnetic field data and residual momentum vectors can then processed in the above control law and magnetic torquer model and the following matrix of torque projections can be generated:

$$\begin{bmatrix} T_{MT}(1,1) & T_{MT}(1,2) & : & T_{MT}(1,32) & ::: & T_{MT}(1,1024) \\ T_{MT}(2,1) & T_{MT}(2,2) & : & T_{MT}(2,32) & ::: & T_{MT}(2,1024) \\ : & : & : & : & ::: & : \\ T_{MT}(576,1) & T_{MT}(576,2) & : & T_{MT}(576,32) & ::: & T_{MT}(576,1024) \end{bmatrix} \tag{17}$$

Each column represents the torque projections for each residual momentum vector over the entire magnetic field data set. Each row, then, is the torque projection for each magnetic field data point over the entire sphere of possible residual momentum vectors. The torque projection vectors, for each of the different magnetic fields, was then averaged along each direction in the sphere. That is, each of the above columns was averaged and a global mean torque capability sphere was produced. The following equation was used:

$$mean(T_{MT})_j = \frac{\sum_{i=1}^{576} T_{MT}(i,j)}{576}; j = 1,1024 \tag{18}$$

Figure 5 and Figure 6 are example plots of the Mean Projections of the MT. This mean torque capability sphere is for the no residual dipole moment case.

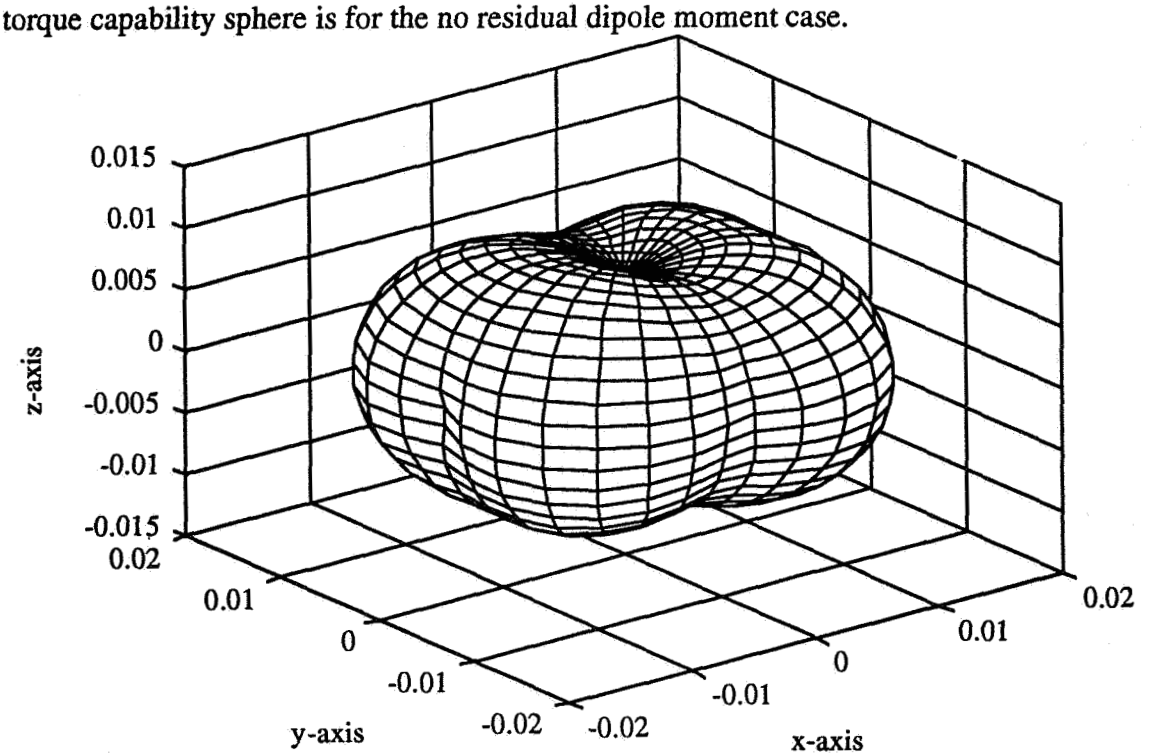

Figure 5 - Mean Projection of the MT Torque Output

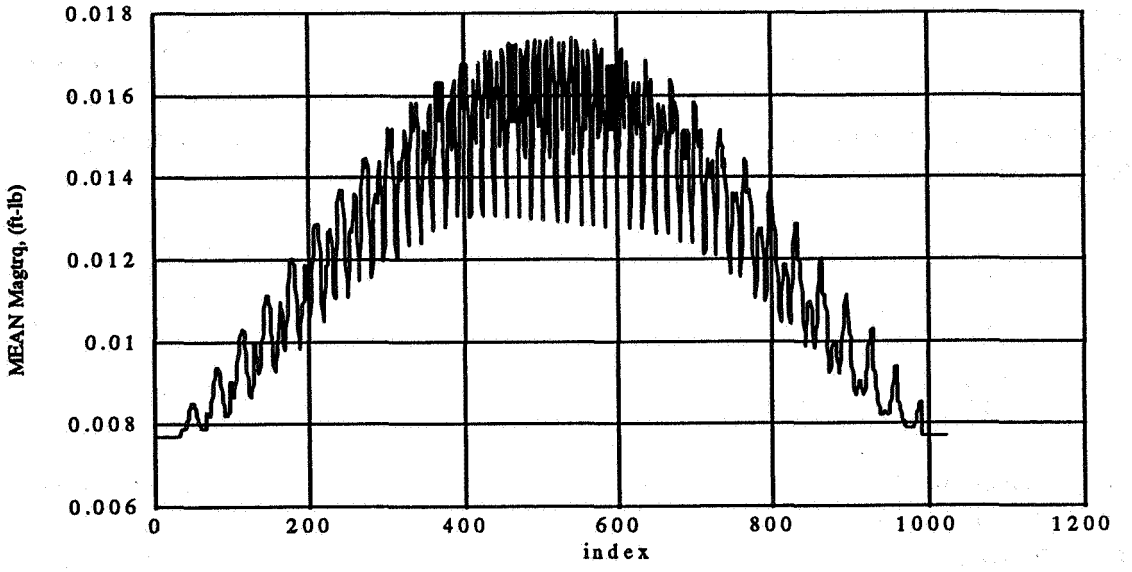

Figure 6 - Total Mean Projection of the MT Torque Output

The effects of the undesired torques produced by the residual dipole moment was determined, next, by solving for the difference (or loss) in MT torque projection due to the addition of a residual dipole moment. The total dipole moment interacting with the earth's magnetic field is then:

$$\vec{D} = \vec{C}_{MT} + \vec{C}_{MT\_residual} \tag{19}$$

The vector $\vec{D}$ is then crossed with the magnetic flux density vector, $\vec{B}_{vc}$ which produces the magnetic torque. The torque produced for a zero residual dipole moment is defined as the vector $\vec{T}$ and with the residual dipole as $\vec{T}_R$, where:

$$\vec{T} = k(\vec{C}_{MT} x \vec{B}_{vc}) \tag{20}$$

$$\vec{T}_R = k((\vec{C}_{MT} + \vec{C}_{MT\_residual}) x \vec{B}_{vc}) \tag{21}$$

where $k = 5.8693x10^5(\frac{amp-m-ft-lb}{Wb-N-m})$ is a gain constant that will define the units of the torque to be ft-lb. Then,

$$\vec{T} - \vec{T}_R = k[(\vec{C}_{MT} x \vec{B}_{vc}) - ((\vec{C}_{MT} + \vec{C}_{MT\_residual}) x \vec{B}_{vc})] = -k(\vec{C}_{MT\_residual} x \vec{B}_{vc}) \tag{22}$$

$$with: \vec{C}_R = \vec{C}_{MT\_residual}$$

$$\begin{aligned} \vec{T} - \vec{T}_R = -k[&(\vec{C}_R(2) * \vec{B}_{vc}(3) - \vec{C}_R(3) * \vec{B}_{vc}(2))i + (\vec{C}_R(3) * \vec{B}_{vc}(1) - \vec{C}_R(1) * \vec{B}_{vc}(3))j \\ &+ (\vec{C}_R(1) * \vec{B}_{vc}(2) - \vec{C}_R(2) * \vec{B}_{vc}(1))k) \end{aligned} \tag{23}$$

The change in torque capability, due to a residual dipole moment, is determined when the vector difference, $\vec{T} - \vec{T}_R$ is projected in the opposite direction of the residual momentum vector, i.e.:

$$\Delta T = -k \frac{(\vec{T} - \vec{T}_R) \bullet -\vec{H}_{resv}}{\left|\vec{H}_{resv}\right|}; (where: \bullet = dot\_product) \tag{24}$$

At each magnetic field, then, this difference in torque projection between the residual and no residual dipole moment was solved for over the unit sphere. At each new magnetic field, the solved torque projection is compared with the torque projection at the previous magnetic field and only the maximum difference (worst case for all the different magnetic fields), for each torque projection is stored. In order to solve for this difference in torque projections, a direction for the residual dipole moment had to be determined. For this study, the direction of the residual dipole moment of the vehicle was along the -Z-vehicle axis. Figure 7 and Figure 8 are plots of the maximum difference in projections of the magnetic torquers with a residual dipole moment magnitude of 20% of the capability of a magnetic torquer.

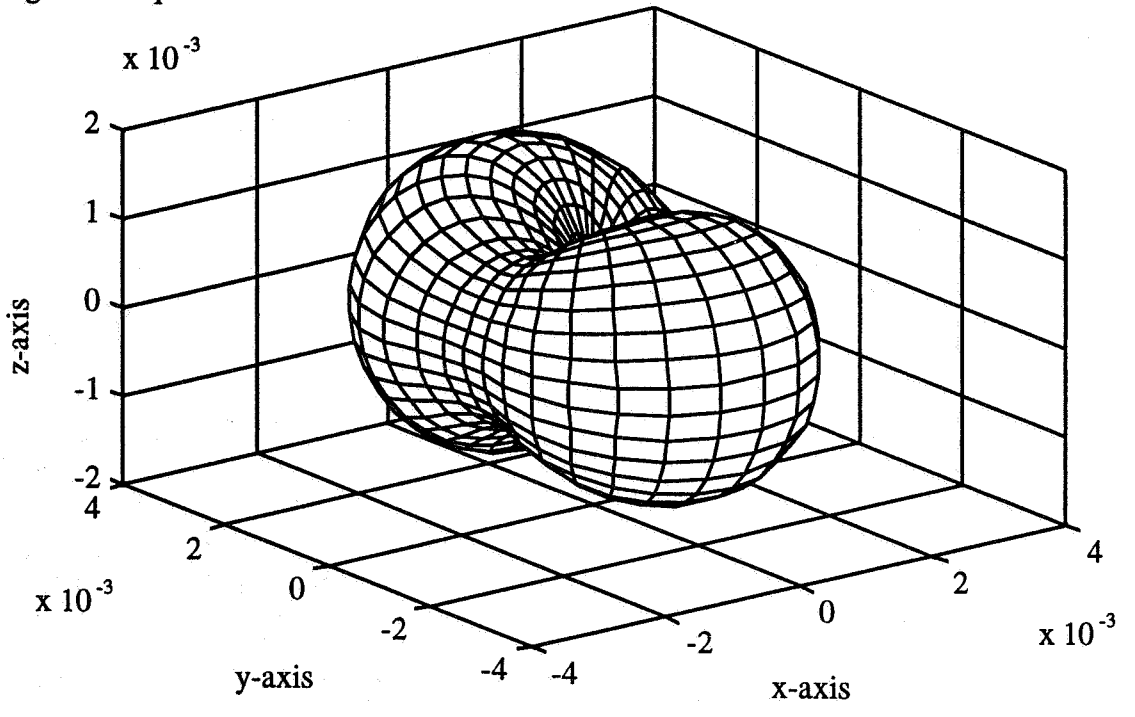

Figure 7 - Max. Difference in Projections of the MT Torque (ft-lb) with & without a Residual Dipole Moment (Residual Dipole=20% of Magnetic Torquer Capability)

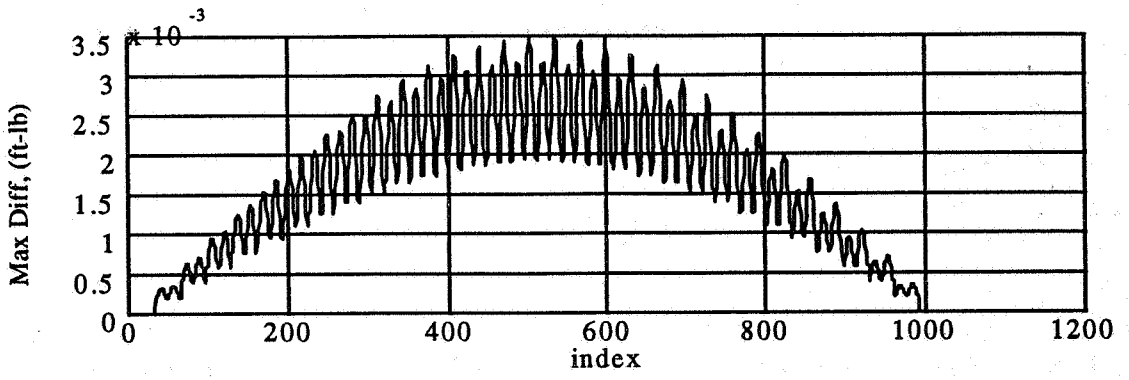

Figure 8 - Max. Difference in Projections of the MT Torque (ft-lb) with & without a Residual Dipole Moment (Residual Dipole=20% of Magnetic Torquer Capability)

From this plot of maximum losses in the projection of the MT, only the maximum value over the sphere was used (worst case over all possible residual momentum directions). Various values of the magnitude of the residual dipole moment were used to come up different maximum losses for different total residual dipole moments. A linear relation (T_{loss}) was found between maximum torque projection loss versus residual dipole moment. The following relation was found:

$$\textbf{Torque\_Loss} = T_{loss}\left(\frac{ft-lb}{pole-cm}\right) * \textbf{Residual\_Dipole\_Moment}(pole-cm) \qquad (25)$$

With the nominal, no residual dipole MT capability known, and the maximum torque losses due to a residual dipole known, data of residual momentum was generated and used for MT performance analysis. The residual momentum magnitudes used ranged from 0-18 ft-lb-s. The following criteria (requirements) were used to analyzed the MT performance with these residual momentums:

MT Performance Criteria (requirements):

1) Need Desaturation of All the Residual Momentum within t_req seconds.

The residual momentum magnitudes were plotted both as percent of cases versus residual momentum magnitude (see Figure 9) and in histogram format of the number of cases in each histogram bin (see Figure 10).

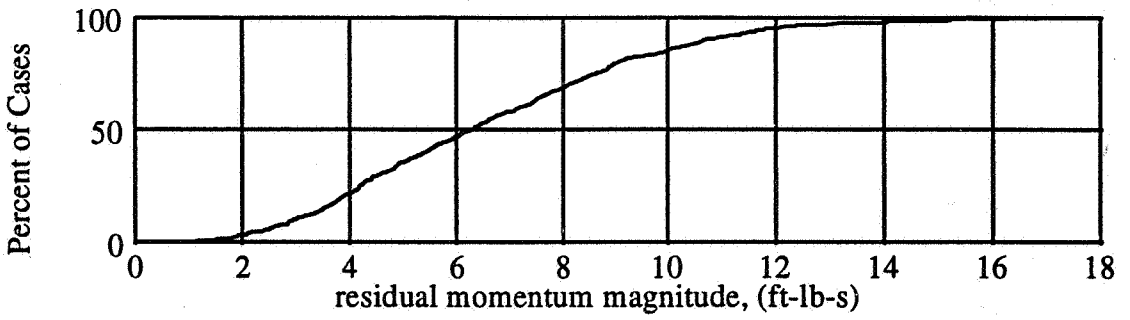

Figure 9 - Percent of Cases vs Residual Momentum Magnitude

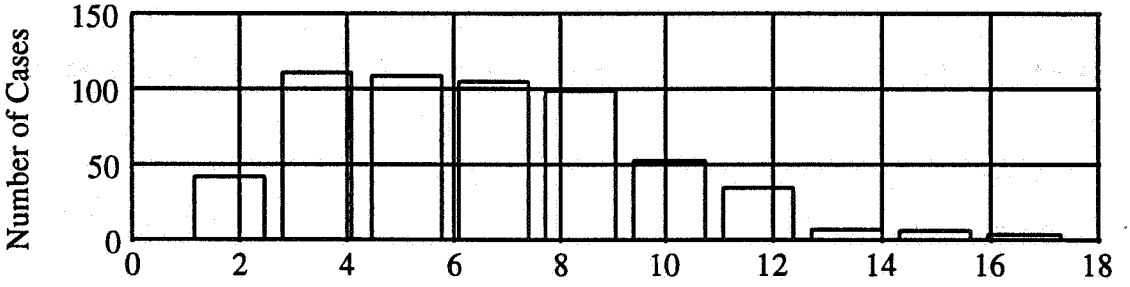

Figure 10 - Histogram of Cases

The next step was to determine the time required to run the residual momentum magnitudes down to zero based on the mean torque capability of the MT. The histogram bins were the ones that were utilized in this analysis by taking the momentum level at each bin and dividing it by the mean torque capability, of the MT, over the entire sphere. This result would be the average time it takes, for each torque capability vector in the sphere, to desaturate the residual momentum magnitude. The percentage of the torque vectors of the sphere above the t_req second limit would then be determined. This percentage is then multiplied by the total number in the bin. Each bin was processed as above, and the total sums of all the bins were added together and then divided by the total number of cases in all the bins. This was the resultant percentage of residual momentum cases that would not be able to be desaturate the residual momentum within t_req seconds. This analysis was done for total residual dipole moments between zero and 30% of the capability of a magnetic dipole moment. The percent of cases that did not desaturate the residual momentum within the t_req second requirement is shown in Figure 11.

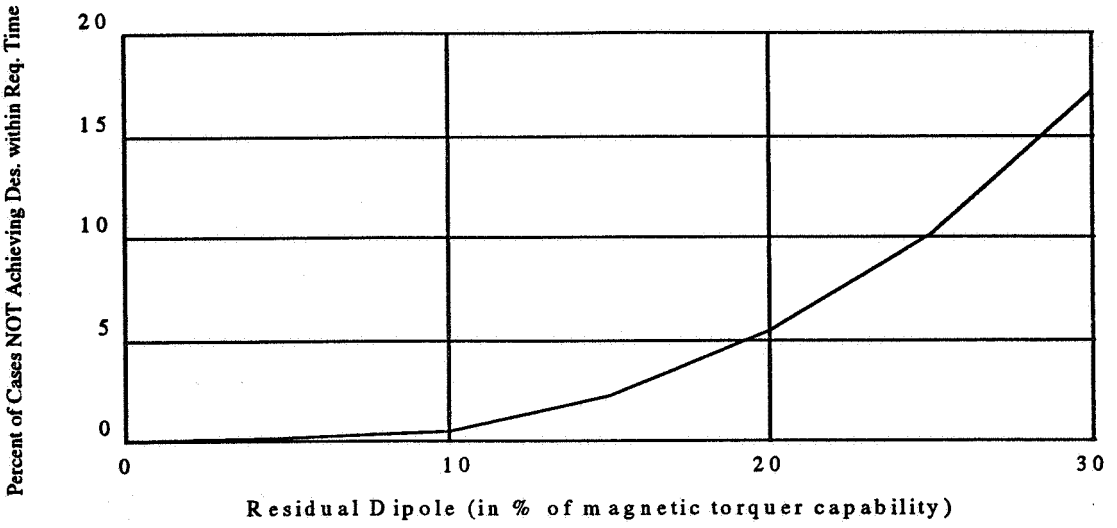

Figure 11 - Percent of Cases NOT Achieving Residual Momentum Desaturation within Time Requirement

Finally, Figure 12 illustrates the estimation of fuel use due to not achieving residual momentum desaturation all versus residual dipole moment percentage. This estimate for the additional fuel use is based on the following criteria:

Estimate of Additional Fuel Use Criteria for Not Desaturating Residual Momentum:

1) Assume **ML** year mission life =>

Events≡ ED (events/day)*365 (day/yr)***ML**(yr) (26)

2) Assume a fuel use of **FUE** (lbm) per event needing thrusters.

FUM= FUE*Events (fuel use max) (27)

FU= FUE*Events*Percent_NOT_Desaturated (28)

= FUM*Percent_NOT_Desaturated (29)

(**FU**=Fuel Use for Not Achieving Residual Momentum Desaturation)

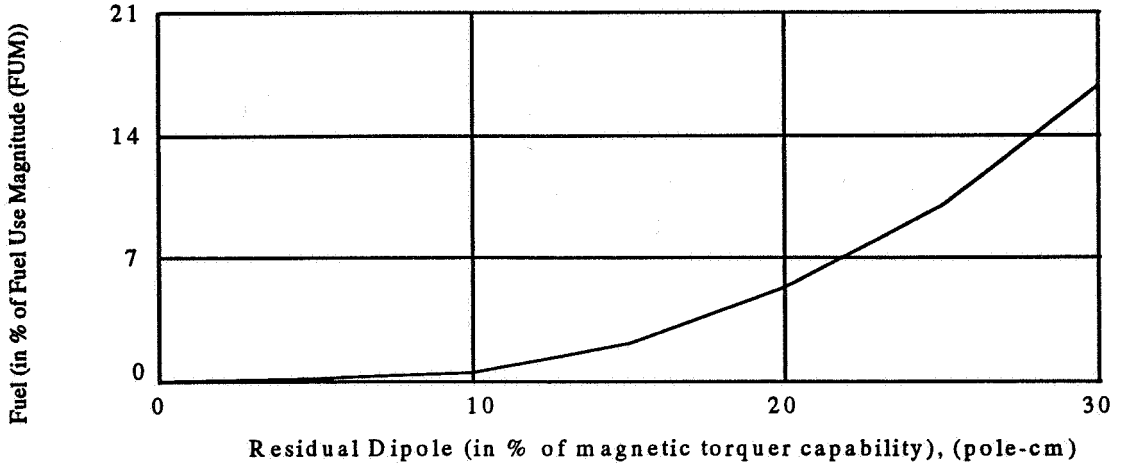

Figure 12 - Estimation of Fuel Use due to NOT Achieving Residual Momentum Desaturation

Now, based on the plot of estimated fuel use for not achieving residual momentum desaturation within t_req seconds, a maximum recommended limit on the residual dipole moment was determined. The following criteria were used in determining the maximum allowable residual dipole moment:

Maximum Allowable Residual Dipole Moment Criteria:

1) Given a **FUD** (Fuel Use per Day - for Nominal, No Residual Dipole Moment)
   => **FUT** (lbm)=**FUD**(lbm)* 365(day/yr) * **ML**(yr) (30)
   which we will assume for this study =>10% of **FUM.**
   FUT is the total projected fuel usage, for a zero residual dipole moment, over the **ML** year mission.

2) Assume a total fuel budget of **FBT**(lbm) = 20% of **FUM** over Mission Life.
   With **FUT**(lbm) projected for the nominal case, then approximately:
   => **FBT**(lbm) - **FUT**(lbm) = **FA**(lbm) (31)
   will be available for additional thruster burns due to the losses associated with a residual dipole moment .
   ∴ **FA**(lbm) = 10% of **FUM** = (20%-10%) of **FUM**: is the available fuel for additional burns due to a residual dipole.

By looking at the point on the estimated fuel use where the fuel is approximately **FA** (lbm) = 10% of **FUM**, the residual dipole can be found to be approximately 25% of the capability of a magnetic torquer. Assuming a margin of safety of 2 for the residual dipole moment, the result is that the residual dipole moment of the space vehicle can be no greater than $\frac{25\%}{2} = 12.5\%$ of the capability of the magnetic torquers. This methodology works similarly for sizing magnetic torquers when given a certain fixed space vehicle residual dipole moment.

Conclusion

This paper described the effects that a space vehicle's residual dipole moment can have on residual momentum desaturation capability. Ultimately, the residual dipole moment creates undesirable disturbance torques that degrade the performance of the magnetic torquers (MT) residual momentum desaturation capability. It's these undesired torques that were studied to find a limit on the maximum allowable residual dipole moment, given certain mission constraints and magnetic torque capability. Moreover, given the time varying nature of the magnetic field during a space vehicle's orbit around the Earth, as well as the many directions that the residual momentum could be pointing, a statistical approach was taken to analyze the effects of the residual dipole moment on the MT residual momentum desaturation capability. This study showed, that under certain mission criteria, a novel approach can be taken to find either a limit on the maximum

allowable residual dipole moment or the size of the magnetic torquers necessary to have mission success.

Acknowledgments

The authors wish to acknowledge the generous help from several individuals who gave valuable insight into this study. Jeff Coy, Doug Cornick and Jed Fletcher (Lockheed Martin-Astronautics, ACS Engineers) are gratefully acknowledged for their help and insight. Also to be acknowledged, the many engineers responsible for the continual development and design of MODSIM, which is a full non-linear simulation package that allowed for the magnetic field data to be generated. This analysis was funded by the Lockheed Martin Corporation.

References

[1] Wertz, J.R., editor of *Spacecraft Attitude Determination and Control*, D. Reidel Publishing Co., Boston, MA, 1980

[2] Plett, M., "Magnetic Field Model", *Spacecraft Attitude Determination and Control*, edited by J.R. Wertz, D. Reidel, Dordrecht, The Nederlands, 1978, pp779-786.

Page intentionally left blank

Predictive Attitude Estimation Using Global Positioning System Signals

John L. Crassidis
Department of Mechanical Engineering
The Catholic University of America
Washington, DC 20064

F. Landis Markley, E. Glenn Lightsey, Eleanor Ketchum
NASA-Goddard Space Flight Center
Greenbelt, MD 20771

Abstract

In this paper, a new algorithm is developed for attitude estimation using Global Positioning System (GPS) signals. The new algorithm is based on a predictive filtering scheme designed for spacecraft without rate measuring devices. The major advantage of this new algorithm over traditional Kalman filter approaches is that the model error is not assumed to represented by an unbiased Gaussian noise process with known covariance, but instead is determined during the estimation process. This is achieved by simultaneously solving system optimality conditions and an output error constraint. This approach is well suited for GPS attitude estimation since some error sources that contribute to attitude inaccuracy, such as signal multipath, are known to be non-Gaussian processes. Also, the predictive filter scheme can use either GPS signals or vector observations or a combination of both for attitude estimation, so that performance characteristics can be maintained during periods of GPS attitude sensor outage. The performance of the new algorithm is tested using flight data from the REX-II spacecraft. Results are shown using the predictive filter to estimate the attitude from both GPS signals and magnetometer measurements, and comparing that solution to a magnetometer-only based solution. Results using the new estimation algorithm indicate that GPS-based solutions are verified to within 2 degrees using the magnetometer cross-check for the REX-II spacecraft. GPS attitude accuracy of better than 1 degree is expected per axis, but cannot be reliably proven due to inaccuracies in the magnetic field model.

Introduction

The concept of using phase difference measurements from GPS receivers for three-axis attitude determination has been successfully proven on many systems in the past [1-3]. However, to this date only a handful of these experiments have been tested on spacecraft. One of the first space-based applications was flown on the RADCAL (RADar CALibration) spacecraft [4], which demonstrated GPS attitude determination using post-processed measurements. To obtain maximum GPS visibility, and to reduce signal interference due to multipath reflection, GPS patch antennas were placed on the top surface of the spacecraft bus. Although the antenna baselines were short for attitude determination, attitude accuracy of about 2 degrees per axis 3σ was achieved for a 0.67 meter antenna separation. Another experiment, Crista-SPAS [5], provided the first on-orbit demonstration of real-time attitude determination. The spacecraft contained an accurate gyro reference, but the coordinate frame alignment was not measured relative to the GPS attitude reference frame, which means that discrepancies between the two reference frames might account for slightly different measurements from the two systems. Over the course of the experiment the two sets of attitude

solutions agreed to within 2 degrees, which is thought to be within the alignment tolerance of the two reference frames. The first extended real-time GPS based attitude determination mission was flown on the REX-II spacecraft [6], which furthermore tested actual attitude control using GPS measurements.

The differential carrier phase error has a standard deviation of about 5 mm, which is a small fraction of the 19 cm standard wavelength [7]. However, many error sources can significantly contribute to attitude inaccuracy. These include: integer ambiguity resolution of the GPS carrier, reflections of the GPS carrier from the environment surrounding the receiver (multipath), line bias errors between receivers, receiver motion due to external distortions (e.g., thermal disturbance effects), constellation availability, tropospheric refraction, and cross-talk errors. The most significant error source and most difficult to overcome is multipath [3]. In fact, multipath effects can be a major driving source for the location of the GPS antennas on a vehicle. Many techniques have been presented to resolve the integer ambiguity problem [8]. An approach using an H_∞-type filter has been shown to improve attitude determination performance with line biases [9]. Other error sources, such as tropospheric refraction, can be modeled out for relatively short baselines (less than three meters) [3].

Three-axis attitude solutions may be found using both deterministic (point-by-point) and estimator-based (i.e., propagation of a dynamic model) techniques. The main advantage of using estimator-based techniques, such as the Kalman filter, is that the attitude can be found using a single baseline or sightline, as long as there is sufficient vehicle motion to couple errors along the unobservable baseline direction into two orthogonal axes [10]. Another advantage is that some error sources, such as line biases, can be estimated concurrently with the attitude. Fujikawa and Zimbelman [10] developed a Kalman filter using GPS signals to successfully estimate the attitude of a spacecraft and line bias using one baseline. The main advantage of deterministic methods is that an initial estimate of the attitude is not required to develop a solution. Also, deterministic methods are usually computationally more efficient as compared to estimator-based techniques. Deterministic methods can also provide an initial estimate for a filter. Choosing between deterministic and estimator-based techniques usually depends on the particular application and requirements.

In this paper a new algorithm is developed which is used to estimate the attitude of a spacecraft using GPS phase difference measurements and a dynamic model. The new algorithm is based on a predictive filtering scheme first introduced by Crassidis and Markley [11]. One of the difficulties demonstrated by Fujikawa and Zimbelman [10], using a six state Kalman filter for GPS attitude estimation, is that large attitude deviations are possible due to the effect of external torque disturbances. To overcome this difficulty the state model was appended to incorporate torque estimation. The algorithm developed in this paper, unlike the Kalman filter, does not assume that the external torque is modeled by a zero-mean Gaussian process. Instead, it is automatically determined during the estimation process, without using an appended state model. Therefore, the new algorithm provides a more practical method for attitude estimation.

The organization of this paper proceeds as follows. First, a summary of the spacecraft attitude kinematics, dynamics, and sensor models is shown. Then, a brief review of the predictive filter for nonlinear systems is shown. Next, a predictive filter is developed for the purpose of attitude estimation using GPS measurement signals and a dynamic model. This approach estimates the optimal spacecraft attitude in real-time by minimizing a quadratic cost function consisting of a measurement residual term and a model error term. Two algorithms are shown. The first uses the GPS phase difference measurements for attitude estimation, and the second uses GPS-found attitudes from deterministic approaches for attitude estimation. Finally, the predictive filter is used to estimate and verify the attitude of REX-II in order to demonstrate the usefulness of this algorithm. Case comparisons are made with respect to a magnetometer-only based solution using another predictive filter approach.

Attitude Kinematics and Dynamics

In this section, a brief review of the kinematic and dynamic equations of motion for a three-axis stabilized spacecraft is shown. The attitude is assumed to be represented by the quaternion, defined as

$$\underline{q} \equiv \begin{bmatrix} \underline{q}_{13} \\ q_4 \end{bmatrix} \tag{1}$$

with

$$\underline{q}_{13} \equiv \begin{bmatrix} q_1 \\ q_2 \\ q_3 \end{bmatrix} = \hat{\underline{n}} \sin(\theta / 2) \tag{2a}$$

$$q_4 = \cos(\theta / 2) \tag{2b}$$

where $\hat{\underline{n}}$ is a unit vector corresponding to the axis of rotation and θ is the angle of rotation. The quaternion kinematic equations of motion are derived by using the spacecraft's angular velocity ($\underline{\omega}$), given by

$$\dot{\underline{q}} = \frac{1}{2}\Omega(\underline{\omega})\underline{q} = \frac{1}{2}\Xi(\underline{q})\underline{\omega} \tag{3}$$

where $\Omega(\underline{\omega})$ and $\Xi(\underline{q})$ are defined as

$$\Omega(\underline{\omega}) \equiv \begin{bmatrix} -[\underline{\omega}\times] & \vdots & \underline{\omega} \\ \cdots\cdots & \vdots & \cdots\cdots \\ -\underline{\omega}^T & \vdots & 0 \end{bmatrix} \tag{4a}$$

$$\Xi(\underline{q}) \equiv \begin{bmatrix} q_4 I_{3\times 3} + [\underline{q}_{13}\times] \\ \cdots\cdots\cdots\cdots\cdots \\ -\underline{q}_{13}^T \end{bmatrix} \tag{4b}$$

where $I_{3\times 3}$ is a 3×3 identity matrix. The 3×3 dimensional matrices $[\underline{\omega}\times]$ and $[\underline{q}_{13}\times]$ are referred to as cross product matrices since $\underline{a}\times\underline{b} = [\underline{a}\times]\underline{b}$, with

$$[\underline{a}\times] \equiv \begin{bmatrix} 0 & -a_3 & a_2 \\ a_3 & 0 & -a_1 \\ -a_2 & a_1 & 0 \end{bmatrix} \tag{5}$$

The quaternion obeys a single constraint, given by

$$\underline{q}^T\underline{q} = \underline{q}_{13}^T\underline{q}_{13} + q_4^2 = 1 \tag{6}$$

The dynamic equations of motion, also known as Euler's equations, for a rotating spacecraft are given by [12]

$$\dot{\underline{H}} = \underline{N} - \underline{\omega}\times\underline{H} \tag{7}$$

where $\underline{H}$ is the total angular momentum, $\underline{N}$ is the total external torque (which includes, e.g., control torques, aerodynamic drag torques, solar pressure torques, etc.), and J is the inertia matrix of the spacecraft. If reaction or momentum wheels are used on the spacecraft, the total angular momentum is given by

$$\underline{H} = J\underline{\omega} + \underline{h} \tag{8}$$

where $\underline{h}$ is the total angular momentum due to the wheels. Thus, Equation (7) can be re-written as

$$\dot{\underline{H}} = \underline{N} - \left[J^{-1}(\underline{H} - \underline{h})\right] \times \underline{H} \tag{9}$$

Also, from Equations (7) and (8) the following angular velocity form of Euler's equation can be used

$$J\dot{\underline{\omega}} = \underline{N} - \dot{\underline{h}} - \underline{\omega} \times (J\underline{\omega} + \underline{h}) \tag{10}$$

which involves the derivative of the wheel angular momentum.

GPS Sensor Model

In this section, a brief background of the GPS phase difference measurement is shown. The main measurement used for attitude determination is the phase difference of the GPS signal received from two antennas separated by a baseline. The principle of the wavefront angle and wavelength, which are used to develop a phase difference, is illustrated in Figure 1.

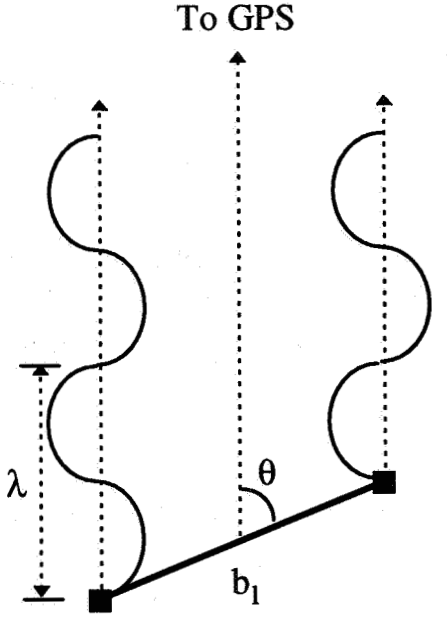

Figure 1 GPS Wavelength and Wavefront Angle

The phase difference measurement is obtained by

$$b_l \cos\theta = \lambda\left(n + \Delta\phi^0/2\pi\right) \tag{11}$$

where b_l is the baseline length, θ is the angle between the baseline and the line of sight to the GPS spacecraft, n is the number of integer wavelengths between two receivers, $\Delta\phi^0$ is the actual phase

difference measurement, and λ is the wavelength of the GPS signal. The two GPS frequency carriers are L1 at 1575.42 MHz and L2 at 1227.6 MHz. As of this writing, non-military applications generally use the L1 frequency. Then, assuming no integer offset, we define a normalized phase difference measurement $\Delta\phi$ by

$$\Delta\phi \equiv \frac{\lambda \Delta\phi^0}{2\pi b_l} = \underline{b}^T A \underline{s} \tag{12}$$

where $\underline{s} \in R^3$ is the normalized line of sight vector to the GPS spacecraft in an inertial frame, $\underline{b} \in R^3$ is the normalized baseline vector, which is the relative position vector from one receiver to another, and the attitude matrix $A \in SO(3)$, the Lie group of 3×3 orthogonal matrices with determinant 1 (i.e., $A^T A = I_{3\times3}$ and $\det A = 1$). The attitude matrix is related to the quaternion by

$$A(\underline{q}) = -\Xi^T(\underline{q})\Psi(\underline{q}) \tag{13}$$

where

$$\Psi(\underline{q}) \equiv \begin{bmatrix} -q_4 I_{3\times3} + [\underline{q}_{13}\times] \\ \cdots\cdots\cdots\cdots \\ \underline{q}_{13}^T \end{bmatrix} \tag{14}$$

and $\Xi(\underline{q})$ is given by Equation (4b).

GPS Attitude Estimation

In this section, a predictive filter for attitude estimation is developed using GPS measurements. First, a brief review of the nonlinear predictive filter is shown (see Ref. [11] for more details).

Predictive Filtering

In the nonlinear predictive filter it is assumed that the state and output estimates are given by a preliminary model and a to-be-determined model error vector, given by

$$\dot{\underline{\hat{x}}}(t) = \underline{f}(\underline{\hat{x}}(t), t) + G(t)\underline{d}(t) \tag{15a}$$

$$\underline{\hat{y}}(t) = \underline{c}(\underline{\hat{x}}(t), t) \tag{15b}$$

where $\underline{f}$ is a $p\times1$ model vector, $\underline{\hat{x}}(t)$ is a $p\times1$ state estimate vector, $\underline{d}(t)$ is a $l\times1$ model error vector, $G(t)$ is a $p\times l$ model-error distribution matrix, $\underline{c}$ is a $m\times1$ measurement model vector, and $\underline{\hat{y}}(t)$ is a $m\times1$ estimated output vector. State-observable discrete measurements are assumed for Equation (15b) in the following form

$$\underline{\tilde{y}}(t_k) = \underline{c}(\underline{x}(t_k), t_k) + \underline{v}(t_k) \tag{16}$$

where $\underline{\tilde{y}}(t_k)$ is a $m\times1$ measurement vector at time t_k, $\underline{x}(t_k)$ is the true state vector, and $\underline{v}(t_k)$ is a $m\times1$ measurement noise vector which is assumed to be a zero-mean, Gaussian white-noise distributed process with

$$E\{\underline{v}(t_k)\} = \underline{0} \tag{17a}$$

$$E\{\underline{v}(t_k)\underline{v}^T(t_{k'})\} = R\delta_{kk'} \tag{17b}$$

where R is a $m \times m$ positive-definite covariance matrix.

A loss functional consisting of the weighted sum square of the measurement-minus-estimate residuals plus the weighted sum square of the model correction term is minimized, given by

$$J = \frac{1}{2}\{\underline{\tilde{y}}(t_{k+1}) - \underline{\hat{y}}(t_{k+1})\}^T R^{-1} \{\underline{\tilde{y}}(t_{k+1}) - \underline{\hat{y}}(t_{k+1})\} + \frac{1}{2}\underline{d}^T(t_k) W \underline{d}(t_k) \tag{18}$$

where W is a $l \times l$ weighting matrix. The necessary conditions for the minimization of Equation (18) lead to the following model error solution

$$\underline{d}(t_k) = -\left\{[\Lambda(\Delta t) S(\underline{\hat{x}}_k)]^T R^{-1} \Lambda(\Delta t) S(\underline{\hat{x}}_k) + W\right\}^{-1} [\Lambda(\Delta t) S(\underline{\hat{x}}_k)]^T R^{-1} [\underline{z}(\underline{\hat{x}}_k, \Delta t) - \underline{\tilde{y}}(t_{k+1}) - \underline{\hat{y}}(t_k)] \tag{19}$$

where $\underline{\hat{x}}_k \equiv \underline{\hat{x}}(t_k)$, Δt is the measurement sampling interval, $S(\underline{\hat{x}})$ is a $m \times l$ dimensional matrix, and $\Lambda(\Delta t)$ is a $m \times m$ diagonal matrix with elements given by

$$\lambda_{ii} = \frac{\Delta t^{p_i}}{p_i!}, \quad i = 1, 2, \ldots, m \tag{20}$$

where p_i, $i = 1, 2, \ldots, m$, is the lowest order of the derivative of $c_i(\underline{\hat{x}}(t))$ in which any component of $\underline{d}(t)$ first appears due to successive differentiation and substitution for $\dot{\hat{x}}_i(t)$ on the right side. The i^{th} component of $\underline{z}(\underline{\hat{x}}, \Delta t)$ is given by

$$z_i(\underline{\hat{x}}, \Delta t) = \sum_{k=1}^{p_i} \frac{\Delta t^k}{k!} L_f^k(c_i) \tag{21}$$

where $L_f^k(c_i)$ is the k^{th} Lie derivative, defined by

$$\begin{aligned} L_f^k(c_i) &= c_i && \text{for } k = 0 \\ L_f^k(c_i) &= \frac{\partial L_f^{k-1}(c_i)}{\partial \underline{\hat{x}}} \underline{f} && \text{for } k \geq 1 \end{aligned} \tag{22}$$

The i^{th} row of $S(\underline{\hat{x}})$ is given by

$$s_i = \left\{L_{g_1}\left[L_f^{p_i-1}(c_i)\right], \ldots, L_{g_l}\left[L_f^{p_i-1}(c_i)\right]\right\}, \quad i = 1, 2, \ldots, m \tag{23}$$

where g_j is the j^{th} column of $G(t)$, and the Lie derivative is defined by

$$L_{g_j}\left[L_f^{p_i-1}(c_i)\right] \equiv \frac{\partial L_f^{p_i-1}(c_i)}{\partial \underline{\hat{x}}} g_j, \quad j=1,2,\ldots,l \tag{24}$$

Equation (24) is in essence a generalized sensitivity matrix for nonlinear systems. Therefore, given a state estimate at time t_k, then Equation (19) is used to process the measurement at time t_{k+1} to find the $\underline{d}(t_k)$ to be used in $[t_k, t_{k+1}]$ to propagate the state estimate to time t_{k+1}. The weighting matrix W serves to weight the relative importance between the propagated model and measured quantities. This weight may be found by using a measurement error covariance constraint [11].

GPS Attitude Estimation

The nonlinear predictive filter using phase difference measurements minimizes the following cost function

$$J = \frac{1}{2}\left\{\sum_{i=1}^{m}\sum_{j=1}^{n} \sigma_{ij}^{-2}\left[\Delta\tilde{\phi}_{ij}(t_{k+1}) - \underline{b}_i^T(t_{k+1}) A\left(\underline{\hat{q}}_{k+1}\right)\underline{s}_j(t_{k+1})\right]^2\right\} + \frac{1}{2}\underline{d}^T(t_k)\, W\, \underline{d}(t_k) \tag{25}$$

subject to

$$\dot{\underline{\hat{q}}} = \frac{1}{2}\Omega(\underline{\hat{\omega}})\underline{\hat{q}} = \frac{1}{2}\Xi\left(\underline{\hat{q}}\right)\underline{\hat{\omega}}, \qquad \underline{\hat{q}}(t_0) = \underline{q}_0 \tag{26a}$$

$$\dot{\underline{\hat{H}}} = \underline{N} - \left[J^{-1}\left(\underline{\hat{H}} - \underline{h}\right)\right]\times \underline{\hat{H}} + \underline{d}, \qquad \underline{\hat{H}}(t_0) = \underline{H}_0 \tag{26b}$$

$$\underline{\hat{\omega}} = J^{-1}\left(\underline{\hat{H}} - \underline{h}\right) \tag{26c}$$

where $\underline{\hat{q}}_{k+1} \equiv \underline{\hat{q}}(t_{k+1})$, m is the total number of baselines, n is the total number of available sightlines, and σ_{ij} is the standard deviation of the measurement error noise for the ijth component. The filter may be initialized using a deterministic approach to find the attitude and angular momentum [13]. Since the phase difference measurements ($\Delta\tilde{\phi}_{ij}$) are used as the required tracking trajectories, the model of a single measurement in Equation (15b) is given by

$$c(\underline{\hat{x}}) = \underline{b}_i^T A\left(\underline{\hat{q}}\right)\underline{s}_j \tag{27}$$

where

$$\underline{\hat{x}} \equiv \left[\underline{\hat{q}}^T \;\vdots\; \underline{\hat{H}}^T\right]^T \tag{28}$$

Since $\underline{c}$ depends on $\underline{\hat{q}}$ and not explicitly on $\underline{\hat{H}}$, the lowest order derivative of Equation (27) in which any component of $\underline{d}$ first appears in $\underline{\hat{q}}$ is two, so that $p_i = 2$. Therefore, the Λ and $\underline{z}$ quantities in Equations (20) and (21) are given by

$$\Lambda = \frac{\Delta t^2}{2} I_{3\times 3} \tag{29a}$$

$$z = \Delta t\, L^1_{f_{ij}} + \frac{\Delta t^2}{2} L^2_{f_{ij}} \tag{29b}$$

where the quantities $L^1_{f_{ij}}$ and $L^2_{f_{ij}}$ can be shown to be given

$$L^1_{f_{ij}} = \underline{b}_i^T \left[A(\hat{\underline{q}})\underline{s}_j \times \right] J^{-1} \left(\hat{\underline{H}} - \underline{h} \right) \tag{30}$$

$$L^2_{f_{ij}} = -\underline{b}_i^T [\hat{\underline{\omega}} \times] \left[A(\hat{\underline{q}})\underline{s}_j \times \right] \hat{\underline{\omega}} + \underline{b}_i^T \left[A(\hat{\underline{q}})\underline{s}_j \times \right] J^{-1} \left(\underline{N} - [\hat{\underline{\omega}} \times] \hat{\underline{H}} \right) \tag{31}$$

The S matrix, which is formed using Equation (23) is given by

$$S = \underline{b}_i^T \left[A(\hat{\underline{q}})\underline{s}_j \times \right] J^{-1} \tag{32}$$

The extension to multiple measurement sets is achieved by stacking these measurements, e.g.,

$$\underline{y} = \left[\Delta\phi_{11} \quad \cdots \quad \Delta\phi_{m1} \,\vdots\, \Delta\phi_{12} \quad \cdots \quad \Delta\phi_{m2} \,\vdots\, \cdots \,\vdots\, \Delta\phi_{1n} \quad \cdots \quad \Delta\phi_{mn} \right]^T \tag{33}$$

Similar stacking of the quantities z and S are used in the predictive filter. Other state variables, such the addition to line biases, can also be added easily [10]. The major advantage of the predictive filter over the traditional Kalman filter is that the torque modeling error ($\underline{d}$) is determined as part of the predictive filter's solution, whereas the state vector in the Kalman must be augmented in order to estimate for unmodeled torque disturbances and errors [10].

Another case involves using quaternion measurements given from a deterministically found attitude using GPS phase difference measurements ([1], [13], [14]). If the determined quaternions are used in the predictive filter, then the following cost function is minimized

$$J = \frac{1}{2} \left\{ \tilde{\underline{q}}(t_{k+1}) - \hat{\underline{q}}(t_{k+1}) \right\}^T R^{-1} \left\{ \tilde{\underline{q}}(t_{k+1}) - \hat{\underline{q}}(t_{k+1}) \right\} + \frac{1}{2} \underline{d}^T(t_k)\, W\, \underline{d}(t_k) \tag{34}$$

where $\tilde{\underline{q}}$ denotes the determined quaternion using the GPS phase difference measurements. For this case, the quantities Λ, $\underline{z}$, and S can be shown to be given by [15]

$$\Lambda = \frac{\Delta t^2}{2} I_{4\times 4} \tag{35a}$$

$$\underline{z} = \frac{\Delta t}{2} \Xi(\hat{\underline{q}}) \hat{\underline{\omega}} - \frac{\Delta t^2}{8} \left\{ \left(\hat{\underline{\omega}}^T \hat{\underline{\omega}} \right) \hat{\underline{q}} + 2\Xi(\hat{\underline{q}}) J^{-1} \left([\hat{\underline{\omega}} \times] \underline{H} - \underline{N} \right) \right\} \tag{35b}$$

$$S = \frac{1}{2} \Xi(\hat{\underline{q}}) J^{-1} \tag{35c}$$

The case simplifies the calculations required in the filter; however, the approach using the cost function in Equation (25) (i.e., using the phase difference measurements) can in theory determine the

attitude using one baseline, while deterministic methods fail in this case. Also, optimal determination of the quaternion from phase measurements requires a computationally expensive gradient search, and more efficient methods can be suboptimal [13]. The computation simplifies if the measurement error covariance (R) is represented as a scalar (r) times the identity matrix, due to the fact that $\Xi^T(\hat{\underline{q}})\hat{\underline{q}} = \underline{0}$ and $\Xi^T(\hat{\underline{q}})\Xi(\hat{\underline{q}}) = I_{3\times 3}$. This leads to

$$\underline{d}(t_k) = \left[J^{-2} + \frac{8r}{\Delta t^4} W\right]^{-1} J^{-1}\left\{\frac{4}{\Delta t^2}\Xi^T(\hat{\underline{q}}_k)\tilde{\underline{q}}_{k+1} + J^{-1}\left([\hat{\underline{\omega}}_k \times]\hat{\underline{H}}_k - \underline{N}_k\right) - \frac{2}{\Delta t}\hat{\underline{\omega}}_k\right\} \qquad (36)$$

Also, note that the inverse in Equation (36) has to be computed only once, which greatly simplifies the computational load. Also, if the weighting matrix W is set to zero, then Equation (36) invokes a feedback linearization of the dynamics model in Equation (26b) [15].

Attitude Estimation of REX-II

In this section, the predictive filter is used to estimate the attitude of the REX-II spacecraft. A drawing of the REX-II spacecraft is shown in Figure 2 (for a more complete description of the spacecraft see Ref. [6]). The spacecraft is passively stabilized using a 6 meter boom with gravity gradient torques and magnetic hysteresis rods for damping. REX-II is additionally actively controlled by electromagnetic coils and a pitch-axis reaction wheel, which provides a momentum bias. The vehicle attitude is expressed as a 3-2-1 yaw-pitch-roll Euler sequence [16] from the locally level orientation, as shown in Figure 3 [6]. Also, the spacecraft contains a three-axis magnetometer (TAM), from which magnetic field measurements are simultaneously available with the GPS deterministic attitude solutions.

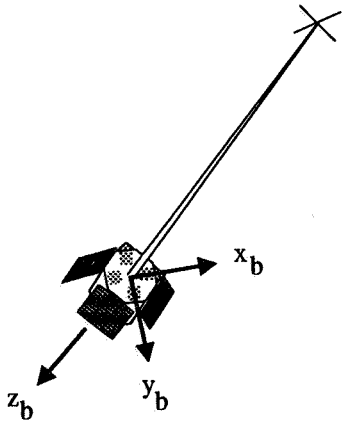

Figure 2 REX-II On-Orbit Configuration

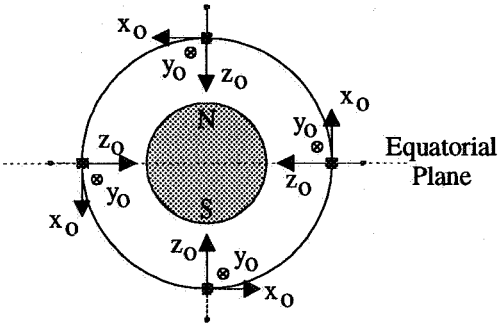

Figure 3 Locally Level Reference Attitude

The four GPS patch antennas were mounted on the top surface of the spacecraft main body in a coplanar, aligned configuration, as shown in Figure 4 [6]. All four antennas were keyed in the same direction to provide antenna phase center repeatability. The separation is 0.67 meters along the diagonal, and the gravity gradient boom extends out of the center of the main body. The M-2 and 1-3 axes were mechanically aligned to within 0.1 degrees of the spacecraft x and y body axes, respectively.

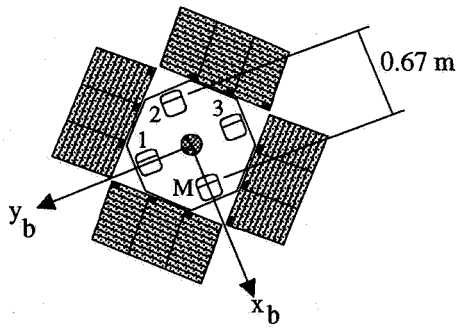

Figure 4 Antenna Placement on Spacecraft

Attitude Estimation

In this section, the predictive filter is used to estimate the attitude accuracy of the REX-II spacecraft. Since the REX-II telemetry system downloads the attitude quaternion from a deterministically found attitude, Equation (36) involving quaternion measurements is used. Also, the problem is complicated by the fact that the telemetry system is constrained to operate with low bandwidth over short ground passes (10 minutes), resulting in short time spans with full data, or very low sampling rates that cover longer times spans. Despite this complication, the GPS solution performance may still be estimated in comparison with an independent TAM-only attitude solution. Furthermore, the TAM/GPS tandem is expected to be common on future low-Earth orbit spacecraft, so it is also worthwhile to consider the potential for combining these measurements into a single, more accurate estimate of spacecraft attitude.

In order to provide an accurate (as possible) analytical model, active control laws (magnetic moment torques and the momentum bias wheel) and passive control laws (gravity gradient torques and magnetic hysteresis rods) were simulated. However, simulations showed that the fit of the data to experimental results is much better with the effect of the hysteresis rods omitted, than with this effect included [6]. This may indicate that the rods were compromised during spacecraft assembly, launch, or deployment such that the material is no longer effective.

Once a fairly accurate representation of the response of the analytical model was obtained, the next step was to design an extended Kalman filter using this model and TAM measurements only. After many attempts at tuning the filter, a reasonably estimated attitude could not be found. This may be due to the fact that data from a short time span (less than 1/3 of the orbit period) is only available at one time, and the Kalman filter may require more data to converge. Although the authors do not claim that a solution may not exist using a Kalman filter, more reasonable attitude solutions were achieved using the predictive filter approach shown in Ref. [17]. Also, the predictive filter using TAM-only measurements estimated the attitude using a dynamics model with the wheel torque only.

Since REX-II did not fly with gyros, and due to the data set limitations (either too short for filter convergence, or sampled very far apart), an accurate attitude reference that may be used as "truth" to the benchmark GPS accuracy is not possible. Other effects, such as uncertainties in the magnetic field model, and potential magnetic activity near the TAM, further complicate this issue. However, at worst, a sanity check of the GPS attitude behavior is still feasible, since attitude accuracy between 0.5 to 2 degrees is possible using a dynamics model and TAM measurements only as shown in Ref. [18].

The sampling rate is 20 seconds for the short-time span set, which lasted for 25 minutes. The long-time span data was also considered. This lasted for 24 hours, but was sampled at 6 minute intervals. A study was performed on the long span of data to test the validity of using this data for attitude estimation. This involved using a spline fit interpolation scheme to bridge the data gap. Unfortunately, a coning motion is evident along the y axis at a higher frequency than the 6 minute sample interval reveals, shown by Figure 5. The circles show 6 minute sampling, the dotted lines

show the spline fit, and the solid lines show the measurements from the short span TAM measurements. The stability of the z and x directions is apparent, since the spline fit data virtually lie on the measurement data. However, the high frequency activity is clear in the y axis, as well as the 0.004 gauss quantization.

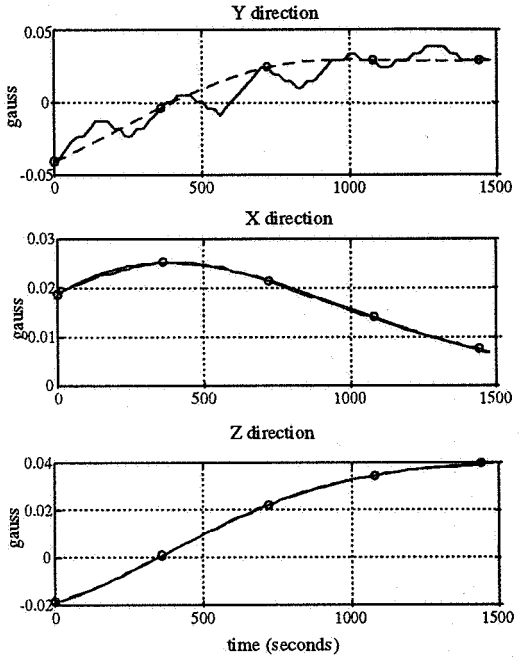

Figure 5 TAM Data for Short Span (solid), Long Span (circles), and Spline Fit (dashed)

Figure 6 shows the magnitude difference between the GPS attitude point (deterministic) solutions and the TAM-only predictive filter solutions. Although only a 25 minute (1/3 orbit) span is available, the filter was able to converge to a solution. A Kalman filter typically requires a full orbit to converge [18]. Therefore, the predictive filter provided convergence at a faster rate than an equivalent Kalman filter approach. The error in the reference geomagnetic field model, used in the TAM-only attitude computation, could be as much as 2 degrees, so that the difference in the two attitudes appears to be converging to a value within that tolerance. Further, this attitude difference seems to be smaller than for the simulated data [6]. The second plot in Figure 6 shows, for the same data span, the magnetic field measurement residual. Here, the magnetometer measurement was transformed into inertial space by both the TAM-only filtered attitude (the solid line) and GPS attitude point solutions (the dashed line). These values are then compared to the reference geomagnetic field model; where the three-axis differences are presented in Gauss. The final magnetometer residual (0.013 gauss) is equivalent to about a 1.8 degree angular residual, and the GPS point solution at that time is about 4.8 degrees. These residuals also appear to be within values predicted by the simulations [6].

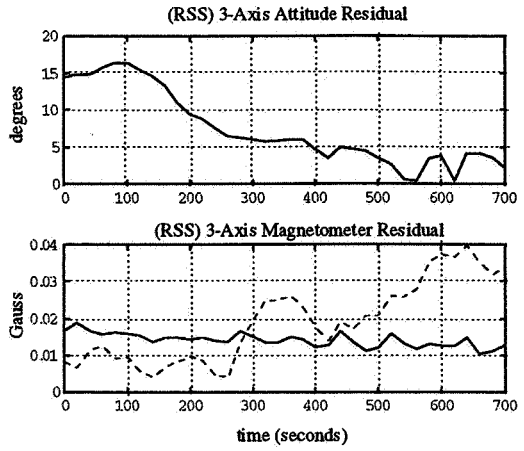

Figure 6 Attitude and TAM Error Residuals (see text for explanation)

The final case involves the blending the GPS measurements and TAM measurements using the predictive filter for a combined attitude estimate. For this case, it was determined that the measurement error sources should be nearly equally weighted to achieve the lowest residuals between the combined estimated attitude and the TAM-only estimated attitude. A plot of the magnitude residuals using this approach is shown in Figure 7. The combined predictive filter attitude seems to be converging to a residual of about 2 degrees. Although this value cannot be known accurately for this system, the methodology of the combined predictive filter approach seems to provide a reasonable method for attitude estimation.

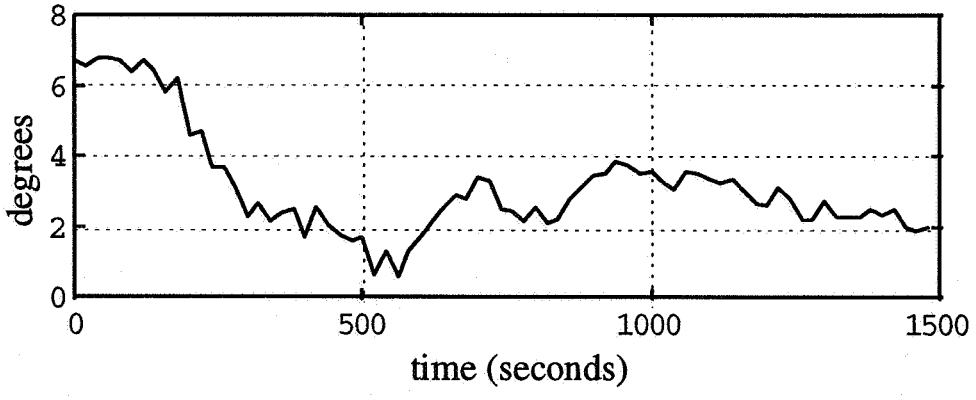

Figure 7 GPS/TAM and TAM Attitude Error Residual

Conclusions

In this paper, a predictive filter scheme was presented for attitude estimation using GPS sensor observations. This algorithm was specifically developed for spacecraft which lack angular rate sensing equipment. The new algorithm was applied to the REX-II spacecraft to investigate attitude accuracy. It was shown that the predictive filter was able to converge in less than 25 minutes (1/3 of an orbit), and was able to estimate the attitude using wheel inputs only in the dynamic model. This has clear advantages over a Kalman filter, which typically requires a compromise between convergence rate and steady-state performance, and usually requires more extensive modeling of

control and disturbance torques in the dynamics model. The magnetometer validation of the GPS attitude solutions agrees to within the measurement accuracy of the magnetic field attitude determination method (about 2 degrees). Also, GPS solutions and magnetic field measurements were combined into a single estimate for the REX-II spacecraft attitude. This combined sensor output estimator is considered to be more practical for sub-degree controller performance because it provides an acceptable attitude measurement even during periods of GPS attitude sensor outage, which has been shown to occur routinely with current GPS receiver hardware during normal spacecraft operations. GPS attitude accuracy of better than 1 degree is expected per axis, but cannot be reliably proven with this sensor complement.

References

[1] Cohen, C.E., "Attitude Determination Using GPS," Ph.D. Dissertation, Stanford University, Dec. 1992.

[2] Melvin, P.J., and Hope, A.S., "Satellite Attitude Determination with GPS," *Advances in the Astronautical Sciences*, Vol. 85, Part 1, AAS #93-556, pp. 59-78.

[3] Melvin, P.J., Ward, L.M., and Axelrad, P., "The Analysis of GPS Attitude Data from a Slowly Rotating, Symmetrical Gravity Gradient Satellite," *Advances in the Astronautical Sciences*, Vol. 89, Part 1, AAS #95-113, pp. 539-558.

[4] Lightsey, E.G., Cohen, C.E., Feess, W.A., and Parkinson, B.W., "Analysis of Spacecraft Attitude Measurements Using Onboard GPS," *Advances in the Astronautical Sciences*, Vol. 86, AAS #94-063, pp. 521-532.

[5] J.K. Brock et al, "GPS Attitude Determination and Navigation Flight Experiment," *Proceedings of the 1995 ION-GPS*, The Institute of Navigation, Palm Springs, CA, Sept. 1995.

[6] Lightsey, E.G., Ketchum, E., Flatley, T.W., Crassidis, J.L., Freesland, D., Reiss, K., and Young, D., "Flight Results of GPS-Based Attitude Control on the REX-II Spacecraft," *Proceedings of the 1996 ION-GPS*, Kansas City, MO, Sept. 1996.

[7] Garrick, J.C., "Investigation of Models and Estimation Techniques for GPS Attitude Determination," *Proceedings of the Flight Mechanics/Estimation Theory Symposium*, NASA-Goddard Space Flight Center, Greenbelt, MD, 1996, pp. 89-98.

[8] Cohen, C.E., and Parkinson, B.W., "Integer Ambiguity Resolution of the GPS Carrier for Spacecraft Attitude Determination," *Advances in the Astronautical Sciences*, Vol. 78, AAS #92-015, pp. 107-118.

[9] Smith, R.H., "An H_∞-Type Filter for GPS-Based Attitude Determination," *Advances in the Astronautical Sciences*, Vol. 89, Part 1, AAS #95-134, pp. 559-567.

[10] Fujikawa, S.J., and Zimbelman, D.F., "Spacecraft Attitude Determination by Kalman Filtering of Global Positioning System Signals," *Journal of Guidance, Control and Dynamics*, Vol. 18, No. 6, Nov.-Dec. 1995, pp. 1365-1371.

[11] Crassidis, J.L., and Markley, F.L., "Predictive Filtering for Nonlinear Systems," *Journal of Guidance, Control and Dynamics*, in print, paper #G4969.

[12] Markley, F.L., "Equations of Motion," *Spacecraft Attitude Determination and Control*, edited by J.R. Wertz, D. Reidel Publishing Co., Dordrecht, The Netherlands, 1978, pp. 521-523.

[13] Crassidis, J.L., and Markley, F.L., "A New Algorithm for Attitude Determination Using Global Positioning System Signals," *Journal of Guidance, Control and Dynamics*, accepted for publication, paper #G5138.

[14] Shuster, M.D., "The Quaternion in the Kalman Filter," *AAS/AIAA Astrodymanics Specialist Conference*, Victoria, BC, Canada, Aug. 1993, AAS Paper #93-553.

[15] Crassidis, J.L., and Markley, F.L., "Nonlinear Predictive Control of Spacecraft," *Proceedings of the 35th Aerospace Sciences Meeting and Exhibit*, Reno, NV, Jan. 1997, AIAA Paper #97-0114.

[16] Shuster, M.D., "A Survey of Attitude Representations," *The Journal of the Astronautical Sciences*, Vol. 41, No. 4, Oct.-Dec. 1993, pp. 439-517.

[17] Crassidis, J.L., and Markley, F.L., "Predictive Filtering for Attitude Estimation Without Rate Sensors," *Presented at the AAS/AIAA Space Flight Mechanics Meeting*, Austin, TX, Feb. 1996, AAS Paper #96-174.

[18] Challa, M.S., Natanson, G.A., Baker, D.E., and Deutschmann, J.K., "Advantages of Estimating Rate Corrections During Dynamic Propagation of Spacecraft Rates-Applications to Real-Time Attitude Determination of SAMPEX," *Proceedings of the Flight Mechanics/Estimation Theory Symposium*, NASA-Goddard Space Flight Center, Greenbelt, MD, 1994, pp. 481-495.

APPLICATION OF THE TWO-STEP FILTER TO PROCESS RANGING MEASUREMENTS FOR RELATIVE NAVIGATION IN AN ELLIPTICAL ORBIT

James L. Garrison* , Doctoral Candidate

Penina Axelrad, Assistant Professor

Department of Aerospace Engineering Sciences
University of Colorado, Boulder CO 80309-0429

Abstract

The two-step optimal estimator developed by Haupt, et. al. [Journal of Guidance, Control and Dynamics , Vol 19, No. 3, May-June 1996, pp 643-649] is applied to the problem of navigating one spacecraft with respect to another, both in nearby elliptical (e > 0:7) orbits. This estimator breaks a nonlinear estimation problem into a set of over determined "first step" states which are linear in the observations and "second step" states which are ultimately the states of interest. Linear estimation methods are applied to filter the observations and produce the optimal first step state estimate. The "second step" states are obtained through iterative nonlinear parameter estimation considering the first step states as observations. It has been shown that this process exactly minimizes the least squares cost function for static problems and provides a better solution than the iterated extended Kalman filter (IEKF) for dynamic problems. The two step filter is applied in this paper to process range and range rate measurements between the two spacecraft. Details of the application of the two step estimator to this problem will be given, highlighting the use of a test for ill-conditioned covariance estimates that can result from the first order covariance propagation. A comparison will be made between the performance of the two-step filter and the IEKF.

*corresponding author, presently at:
MS 328
Spacecraft and Sensors Branch
NASA Langley Research Center
Hampton VA 23681
j.l.garrison@larc.nasa.gov

Page intentionally left blank

Autonomous Navigation of the SSTI/Lewis Spacecraft Using the Global Positioning System (GPS)*

R. C. Hart
National Aeronautics and Space Administration
Goddard Space Flight Center
Greenbelt, Maryland, USA 20771

A. C. Long and T. Lee
Computer Sciences Corporation
Lanham-Seabrook, Maryland, USA 20706

Abstract

The National Aeronautics and Space Administration (NASA) Goddard Space Flight Center (GSFC) Flight Dynamics Division (FDD) is pursuing the application of Global Positioning System (GPS) technology to improve the accuracy and economy of spacecraft navigation. High-accuracy autonomous navigation algorithms are being flight qualified in conjunction with GSFC's GPS Attitude Determination Flyer (GADFLY) experiment on the Small Satellite Technology Initiative Lewis spacecraft, which is scheduled for launch in 1997. Preflight performance assessments indicate that these algorithms can provide a real-time total position accuracy of better than 10 meters (1σ) and velocity accuracy of better than 0.01 meter per second (1σ), with selective availability at typical levels. This accuracy is projected to improve to the 2-meter level if corrections to be provided by the GPS Wide Area Augmentation System (WAAS) are included.

1.0 Introduction

Autonomous navigation has the potential both to increase spacecraft navigation system performance and to reduce total mission cost. By eliminating the need for routine ground-based orbit determination and special tracking services, autonomous navigation can streamline spacecraft ground systems. Autonomous navigation products can be included in the science telemetry and forwarded directly to the scientific investigators. In addition, autonomous navigation products are available onboard to support other autonomous capabilities, such as attitude control, maneuver definition and control, and communications signal acquisition.

The Global Positioning System (GPS) is becoming a more attractive autonomous navigation option for National Aeronautics and Space Administration (NASA) spacecraft due to the recent declaration that the GPS is fully operational. Currently, roadblocks to the use of GPS on NASA spacecraft include inadequate accuracy and reliability of commercial receiver products for high-precision instrument pointing and state prediction applications, lack of standardization in the products available from commercial GPS receivers, and lack of reusable GPS navigation flight software and ground support software.

The Goddard Space Flight Center (GSFC) Flight Dynamics Division (FDD) has spent several years developing high-accuracy autonomous navigation systems for spacecraft using NASA's space and ground communications systems and is enhancing these systems to support spacecraft using GPS. A near-term goal is to flight qualify a GPS Standard Positioning System (SPS) receiver with NASA-developed navigation algorithms to provide real-time spacecraft position and velocity accuracies that adequately meet both the high-precision instrument pointing and state prediction requirements. Accuracy improvement is achieved through the implementation of a sophisticated real-time Kalman filter with high-fidelity state dynamics modeling.

The FDD has implemented these algorithms in prototype GPS navigation flight software, which executes within the resource constraints of currently available flight processors (e.g., <400 kilobytes memory and <0.5 million instructions per second). Preliminary assessments indicate that these algorithms can provide real-time onboard spacecraft navigation accuracies in the 10-meter (1σ) range using measurements from the GPS SPS. These navigation algorithms are being

* This work was supported by the National Aeronautics and Space Administration (NASA)/Goddard Space Flight Center (GSFC), Greenbelt, Maryland, under Contract NAS 5-31000.

flight qualified in conjunction with GSFC's GPS Attitude Determination Flyer (GADFLY) experiment on the Small Satellite Technology Initiative Lewis (SSTI Lewis) mission, currently scheduled for launch in May 1997. In support of the GADFLY experiment, the FDD is also assessing the quality of the measurements and solutions provided by the commercial GPS receiver on the SSTI Lewis spacecraft.

The FDD is currently evaluating algorithm enhancements to improve GPS navigation accuracy and reliability. Accuracy improvements under investigation include the use of measurement corrections that will be provided by the Federal Aviation Administration's GPS Wide Area Augmentation System (WAAS). Reliability improvements under investigation relate to self-initialization of the Kalman filter processing and autonomous fault detection and recovery.

This paper discusses the capabilities and presents a preliminary assessment of the expected on-orbit performance of the GEODE flight software algorithms.

2.0 GPS Navigational Algorithms

The basic GPS SPS commercial receiver computes the real-time three-dimensional spacecraft position and receiver time bias by solving a set of simultaneous equations constructed using pseudorange measurements to a minimum of four GPS space vehicles (SVs). These products are often referred to as the *geometric*, *point*, or *unfiltered* solutions. The major source of error in the GPS SPS measurements arises from the selective availability (SA) corruption applied to the signals and ephemerides to limit geometric solutions to approximately 100 meters (two-dimensional, 95 percent of the time) when SA is enabled. Typically, GPS receiver vendors advertise three-dimensional position accuracies on the order of 150 meters (1σ).

Because the geometric solutions are derived from measurements at a single time, they produce relatively poor velocity solutions, as compared with typical filtered orbit determination solutions. In addition, the geometric solutions can undergo significant discontinuities when the set of four GPS SVs used in the solution changes. Although the real-time position accuracy achievable using the basic geometric solution approach is adequate for some onboard applications, the position discontinuities are not acceptable for high-precision instrument pointing applications. In addition, the poor velocity accuracies are not adequate for navigation applications that require prediction of the real-time spacecraft state, such as view period prediction and maneuver planning.

The navigation algorithms discussed in this paper were developed by the GSFC FDD to meet SSTI/Lewis' real-time accuracy goal of better than 20 meters (1σ) in position and 0.03 meter/per second (1σ) in velocity using GPS SPS with SA a typical levels. These algorithms are based on mature onboard navigation systems developed for spacecraft using NASA's space and ground communications systems. The highly successful experiment on the Explorer Platform/Extreme Ultraviolet Explorer (EP/EUVE) spacecraft flight qualified high-accuracy algorithms for autonomous navigation using the Tracking and Data Relay Satellite System (TDRSS) and/or ground station carrier signals (Reference 1).

These navigation algorithms consist of the following core components:

- An extended Kalman filter (EKF) augmented with physically representative models for the gravity, atmospheric drag, and time bias and drift state process noise to provide a realistic state error covariance
- A high-fidelity state dynamics model to reduce sensitivity to measurement errors and provide high-accuracy velocity estimates, permitting accurate state prediction during signal outages or degraded coverage
- Initialization and enhanced fault detection capabilities using instantaneous geometric GPS solutions

The impact of SA clock dithering on the pseudorange measurement is typically about 25 meters (1σ), with a correlation time of approximately 5 minutes. The impact on the Doppler measurement is approximately 0.15 meter per second. The EKF algorithm samples measurements from a specific SV, nominally at a 5-minute rate, to reduce the correlation between the SA-induced measurement errors. SA clock dithering is treated as white noise without the addition of filter states or colored noise models. Real-time state prediction occurs once per second. State estimation is performed at regular intervals, e.g., every 30 seconds, using measurements to the selected GPS SV. Table 1 summarizes the set of algorithms selected to meet the GPS navigation performance goals. Detailed mathematical specifications are defined in Reference 2.

Table 1. Summary of Autonomous Navigation Algorithms

Algorithm Type	Algorithm
Primary coordinate system	• Mean equator and equinox of J2000.0 with analytic coordinate transformations
Primary time system	• Coordinated universal time (UTC)
Numerical integrator	• Runge-Kutta 4^{th}-order
Filter spacecraft acceleration model	• Joint Gravity Model-2 (JGM-2) nonspherical geopotential up to degree 30 and order 30 • Earth, solar, and lunar point masses with analytic ephemeris • Solar radiation pressure • Analytic representation of Harris-Priester atmospheric density
Spacecraft state transition matrix	• Semianalytic formulation including J_2 and Earth point mass acceleration partial derivatives
Estimator	• Extended Kalman filter with physically realistic process noise and factored covariance matrix
Estimation state	• User position and velocity vectors • Atmospheric drag coefficient correction • GPS receiver time bias and time bias drift corrections
State process noise model	• Earth gravity model errors • Random walk model for atmospheric drag correction and time reference bias and drift • Maneuver position and velocity variances uplinked prior to maneuver
Measurement model	• GPS pseudorange and Doppler with GPS receiver time and time bias and drift corrections • Geometrical editing of measurements with high ionospheric errors
Real-time spacecraft acceleration model	• Earth point mass and J_2

Processing of raw pseudorange measurements from existing GPS receivers on the EP/EUVE and TOPEX/POSEIDON (T/P) spacecraft indicates that these navigation algorithms can provide accuracies of 10 meters (1σ) in total position and 0.01 meter (1σ) per second in total velocity with SA at typical levels (Reference 3). FDD is currently evaluating algorithm enhancements to further improve GPS navigation accuracy and reliability. The real-time accuracy improvement to be gained by using a GPS SPS receiver augmented to receive SA measurement corrections broadcast by GPS WAAS was assessed and is discussed in the GPS WAAS Analysis section of this paper. This study indicates that accuracies of 2 meters (1σ) in total position and 0.002 meter per second (1σ) in total velocity are achievable using the baseline algorithms. Similar accuracies are achievable if the baseline algorithms are used with the restricted, uncorrupted GPS Precise Positioning Service (PPS). To achieve real-time onboard accuracies of better than 2 meters (1σ), the following improvements to the baseline algorithms are needed: (1) modeling of the instantaneous position of the GPS antenna phase centers with respect to the center of mass of the spacecraft, (2) improvements in the nonspherical geopotential model, and (3) modeling of the spacecraft thrust during maneuvers.

Reliability improvements under investigation relate to self-initialization of the Kalman filter processing and autonomous fault detection and recovery. The baseline navigation algorithms use the GPS receiver's geometric solution to initialize the Kalman filter processing and to support autonomous fault detection. Experience with actual GPS geometric solutions, described in the GADFLY/GEODE Performance Assessment section of this paper, has shown that filter initialization using the receiver's current geometric point solution is not always successful, primarily because of the

sensitivity of the estimation process to the initial receiver clock bias and drift values, which are not always available. In addition, geometric solutions are not available if fewer than four GPS SVs are in view.

To eliminate any dependence on the GPS receiver's point solutions, the geometric solution capability should be integrated with the baseline navigation algorithms. In this way, these algorithms can be the source for the best state solution at any time, whether it is a geometric solution or a filtered solution. FDD is currently developing and evaluating initialization algorithms, including geometric solution algorithms, smoothing\filtering of the geometric solutions, and geometric-solution-independent approaches using Doppler measurements. To increase reliability and autonomy, the baseline fault detection and data validation process should be extended and a fault recovery process should be implemented in the event that filter divergence or a fatal software error is detected.

3.0 GPS Enhanced Orbit Determination Experiment

The SSTI Lewis spacecraft, currently scheduled for launch in May 1997, will host the GPS Attitude Determination Flyer (GADFLY) experiment. The GSFC Navigation, Guidance, and Control Branch is flying the GADFLY experiment to demonstrate the ability to provide precise time and to determine spacecraft orbit and attitude using a space-qualified GPS SPS receiver (Reference 4). The GADFLY components include a space-qualified nine-channel GPS L1 frequency, coarse acquisition (C/A) code receiver interfaced with the primary spacecraft components via the Goddard Electronics Module (GEM). The GPS Attitude and Orbit Determination System (GPSAODS) receiver, developed by Space Systems/LORAL, is a redundant unit consisting of one GPS Tensor™ dual receiver, one four-channel preamplifier assembly, and four L1 receiving antennas. With SA at typical levels, the GPSAODS receiver should provide either real-time unfiltered (50 percent probability that position error $\leq$ 100 meters) or GPSAODS-filtered (mean position error $\leq$ 50 meters) state vectors and precise time (less than 1 microsecond error with respect to GPS time) via a 1-pulse-per-second discrete output to the Lewis spacecraft, when GPS data are available (References 5 and 6).

As a secondary experiment, GSFC proposed that the GADFLY GPS receiver host the GPS Enhanced Orbit Determination Experiment (GEODE) to flight qualify the NASA-developed algorithms for high-accuracy real-time navigation. The FDD designed GEODE's prototype navigation flight software to be hosted on one of the receiver's digital receiver processor units (RPUs), a RAD6000 RISC microprocessor operating at 20 megahertz, and integrated with the GPSAODS flight software components. However, the accelerated development schedule for SSTI Lewis did not provide sufficient time to integrate and validate the GEODE flight software after delivery of the GPSAODS receiver. Therefore, downlinked GPS measurements will be processed using the GEODE flight software hosted on a surrogate flight computer.

The GEODE flight software was developed to be portable and modular to facilitate reuse on other missions and incorporation in other GPS receivers or spacecraft processors. The primary development platform is a Sun Sparcstation 10 using the Solaris 2.3 operating system. GEODE has also been executed on a Pentium-based microcomputer. The current version of the GEODE flight software compiles under the GNAT Ada95 compiler and requires about 380 kilobytes of memory. Reference 3 describes the GEODE flight software architecture and design.

The FDD is currently developing an autonomous navigation (GPSNAV) application in the C++ programming language based on the prototype GEODE flight software. The GPSNAV application will be made available to any spacecraft project to support real-time autonomous navigation using GPS.

4.0 GADFLY/GEODE Performance Assessment

After launch of SSTI Lewis, the GSFC FDD will assess the on-orbit performance of the GADFLY/GEODE orbit solutions. An initial accuracy assessment will be performed by comparing the GPSAODS and GEODE solutions with moderately accurate definitive solutions obtained using S-band ground network tracking data. These S-band tracking solutions are expected to provide total position accuracies in the 25- to 50-meter (1σ) range. Subsequently, an in-depth accuracy assessment will be performed by comparing the GPSAODS and GEODE solutions with high-accuracy (i.e., submeter) solutions obtained by differential postprocessing of the GPSAODS GPS measurements together with GPS measurements obtained through the International GPS Service for Geodynamics (IGS). In addition, the noise and bias characteristics of the GPSAODS pseudorange and Doppler measurements will be analyzed.

Reference 3 discusses a preflight assessment of GEODE flight software performance by processing GPS pseudorange measurements obtained from experimental receivers flown on the EP/EUVE and T/P spacecraft. On the basis of these analyses, the expected performance of the GEODE flight software for SSTI Lewis has been projected to be 10 meters

(1σ) in total position and 0.01 meter (1σ) per second in total velocity with SA at typical levels. More recently, experiments were performed in a realistically simulated flight environment to investigate both GPSAODS and GEODE flight software performance. The results from these investigations are provided in the remainder of this section.

To support checkout of the GPSAODS receiver prior to its integration with the Lewis spacecraft, a Northern Telecom GPS simulator was used to generate GPS-like radio frequency signals that the GPSAODS receiver acquired and from which it extracted and processed ambiguous pseudorange and Doppler measurements. This simulation was performed in a flight mode in which the simulator was driven by a high-fidelity ephemeris for the SSTI Lewis spacecraft. Six-hour simulations were performed without (Case 1) and with (Case 2) SA active. The GPSAODS receiver was powered on shortly before the simulations began, and the GEODE filter was initialized after the receivers' oscillators had stabilized at about one hour into the simulations.

4.1 GPSAODS Products

The accuracy of the GPSAODS geometric solutions was evaluated by comparison with the truth ephemeris on which the simulation was based. Without SA active, the geometric solution errors were 100 meters maximum and 18 meters rms in total position and 0.1 meter per second maximum and 0.04 meter per second in total velocity. With SA active, the geometric solutions errors were 380 meters maximum and 105 meters rms in total position and 9 meters per second maximum and 0.9 meter per second rms in total velocity (a five-minute excursion to 32 meters per second was observed but has not been explained and was not included in these statistics). Figures 1 and 2 provide the total position differences for the geometric solutions for Cases 1 and 2, respectively.

In addition, the GPSAODS geometric solutions were postprocessed as measurements in a least-squares estimator using a high-fidelity dynamic model. Without SA active, the resultant *smoothed* solution errors were 14 meters maximum and 11 meters rms in total position and 0.014 meter per second maximum and 0.013 meter per second rms in total velocity. Similarly, with SA active, maximum and rms errors were 24 and 14 meters in position and 0.026 and 0.015 meters per second in velocity. The high accuracy provided by these *smoothed* solutions suggests that comparable results could also be obtained by processing the raw geometric solutions as measurements in an onboard EKF with a high-fidelity dynamic model.

In the unsmoothed GPSAODS cases, the radial and along-track components of the position differences were biased by approximately 10 meters in opposite directions. In the smoothed cases, the radial biases were removed but the along-track biases remained. When the raw GPSAODS pseudorange measurements were reprocessed using a geometric positioning algorithm with accurate measurement modeling, both the radial and along-track biases were eliminated. The noise characteristics of the GPSAODS raw pseudorange and Doppler measurements were also analyzed. Without SA active, the pseudorange noise was approximately 2.2 meters (1σ) and the Doppler noise was approximately 0.05 hertz (1σ).

4.2 GEODE Products

The GPSAODS ambiguous pseudorange and Doppler measurements were processed in the GEODE flight software. Without SA active, the GEODE flight software produced converged solutions with errors of 15 meters maximum and 4 meters rms in total position and 0.035 meter per second maximum and 0.009 meter per second rms in total velocity, in spite of data gaps of 0.5 and 1 hour in the 5-hour data processing time span. With SA active, the GEODE flight software produced converged solutions with errors of about 35 meters maximum and 9 meters rms in total position and 0.06 meter per second maximum and 0.03 meter per second rms in total velocity. Figures 3 and 4 show the total position errors for the GEODE solutions for Cases 1 and 2, respectively. Comparable results were obtained processing only pseudorange measurements and processing pseudorange and Doppler measurements. The receiver time bias and time bias drift rate estimates agreed well with those derived directly from analysis of the measurement data.

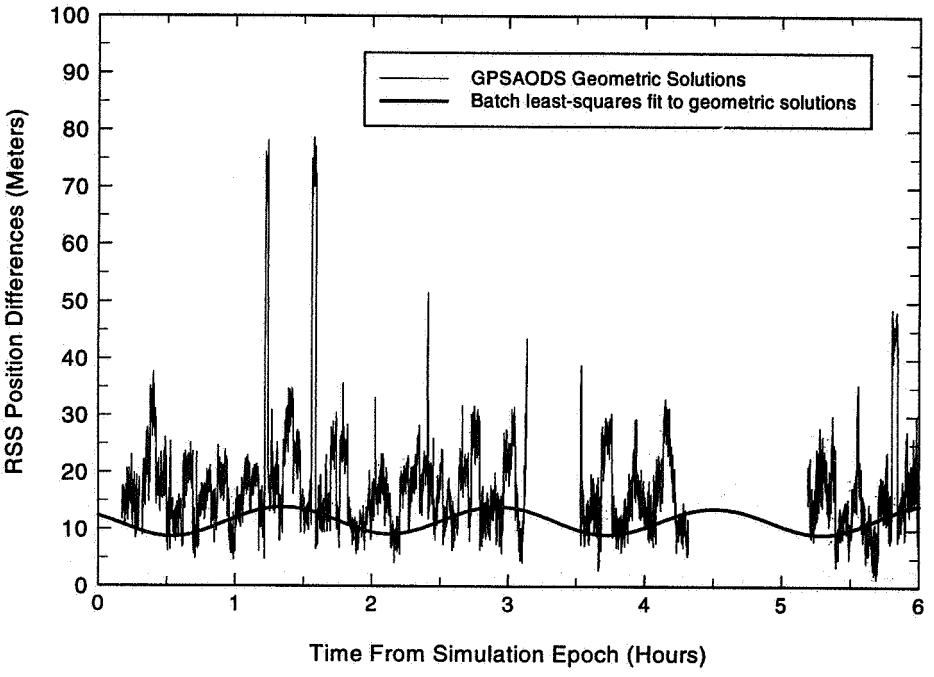

Figure 1. GPSAODS Raw Geometric Solution Versus Truth Position Differences Without SA Active

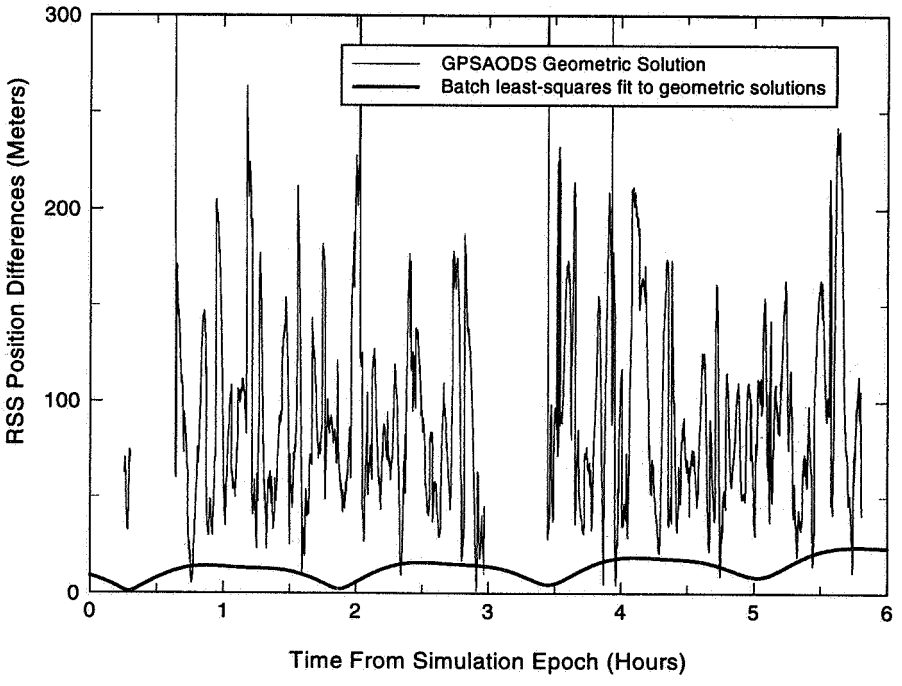

Figure 2. GPSAODS Raw Geometric Versus Truth Position Differences With SA Active

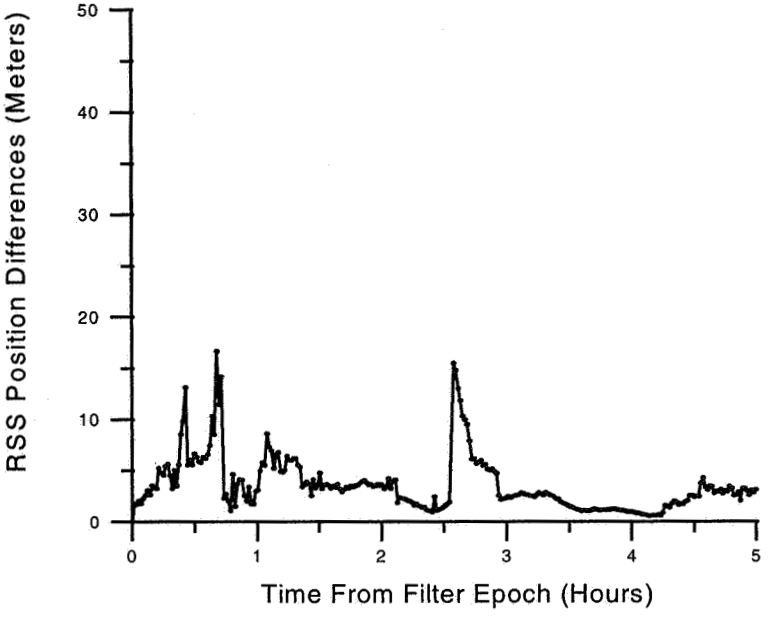

Figure 3. GEODE Solution Versus Truth Position Differences Without SA Active

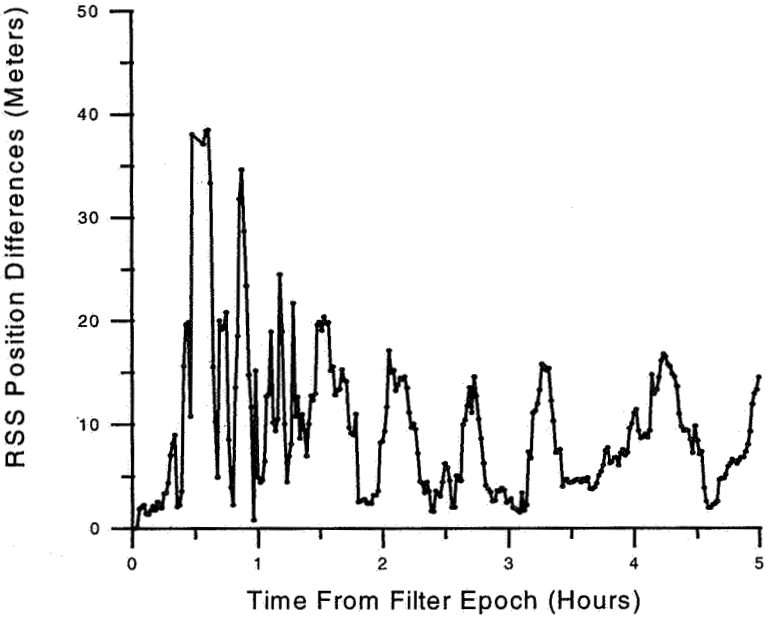

Figure 4. GEODE Solution Versus Truth Position Differences With SA Active

Figures 5 and 6 compare the total position and velocity error results for both test cases, respectively. Comparison of the raw geometric results with the GEODE filtered results clearly indicates that the GEODE's high-fidelity dynamic model significantly reduces sensitivity to SA induced measurement errors and provides high-accuracy velocity estimates.

In this evaluation, the initial GEODE flight software performance was found to be very sensitive to the accuracy of the initial receiver time bias and time bias drift and the associated initial covariances. This difficulty was due to the fact that the time bias and time bias drift values are not included in the standard GPSAODS state data packet. Therefore, accurate

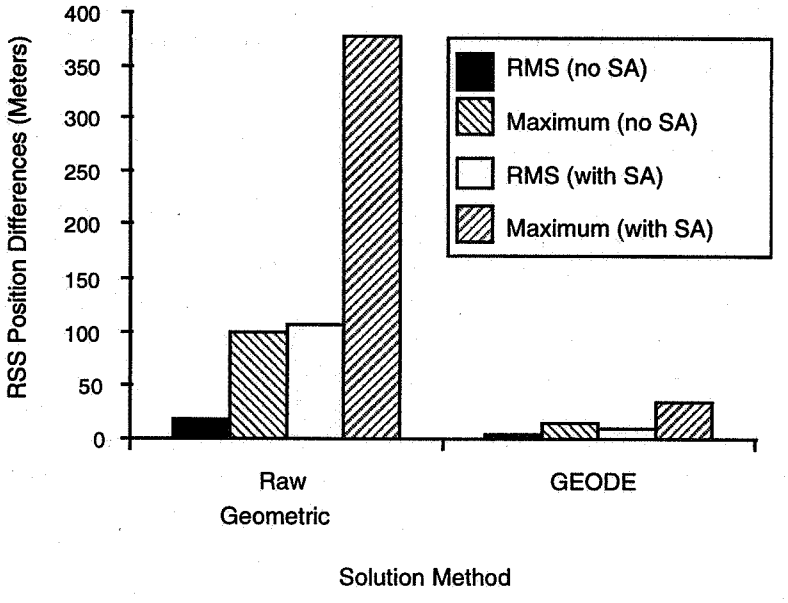

Figure 5. GPSAODS/GEODE Solution Total Position Accuracy

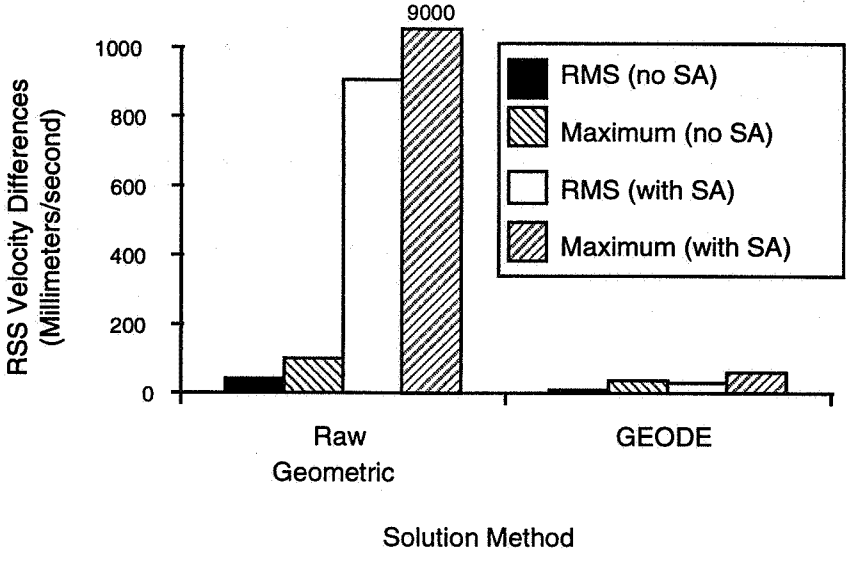

Figure 6. GPSAODS/GEODE Solution Total Velocity Accuracy

values for the GPSAODS time bias, which ranges from ±0.5 milliseconds, and the time bias rate (approximately 0.75×10^{-6} seconds per second) were not readily available for filter initialization. However, following successful initialization, the navigation algorithm was found to be highly reliable, accurately propagating through data gaps of up to 1 hour and recovering without external intervention.

5.0 GPS WAAS Accuracy Analysis

The GPS Wide-Area Augmentation System (WAAS) is being designed and developed by the United States Federal Aviation Administration (FAA) to augment GPS SPS so that it can be used as the primary navigation sensor in conjunction with a GPS single-frequency receiver modified to receive the WAAS signals. GPS WAAS will provide the following three additional services: a GPS-like ranging function to a number of geostationary communications satellites to improve availability and reliability, differential GPS corrections to improve accuracy by reducing GPS ephemeris and clock errors (both SA induced and propagation), and integrity monitoring to improve safety (Reference 7 and 8). The FAA WAAS program is expected to result in the initial operational capability in 1998.

The GPS measurement corrections provided by WAAS (initially by the United States WAAS, but eventually by a worldwide WAAS) can eliminate most of errors caused by SA. With SA errors removed or substantially reduced by using WAAS provided corrections, both geometric and filtered orbit solution accuracies are expected to improve significantly. The navigation performance improvement resulting from the use of WAAS corrections was investigated for the case of the proposed Earth Observer-1 (EO-1) mission. The objective of this analysis was to provide a conservative estimate of the real-time onboard navigation accuracy that is readily achievable assuming navigation algorithms/modeling errors realistic for the 1998 timeframe.

GPS pseudorange and Doppler measurements were simulated over a 2-day time span for the nominal EO-1 orbit (700-kilometer-altitude, 98-degree-inclination, near-circular). Table 2 summarizes the simulation error models used. Simulated measurement errors were consistent with the FAA's projected WAAS-correction accuracies (i.e., ≅2 meters in user effective range error (UERE)). In addition, GPS-like pseudorange and Doppler measurements were simulated for two WAAS geostationary (GEO) spacecraft using measurement errors of 1 meter rms. Two cases were investigated: US WAAS, for which WAAS corrections are limited to GPS SVs visible from the US, and Global WAAS, for which WAAS corrections are available globally. In the US WAAS case, the SA corruption was simulated at the 25-meter rms level for GPS SVs that were not visible from the US.

Table 2. GPS WAAS Simulation Error Models

Error Model	US WAAS	Global WAAS
WAAS-corrected pseudorange (meters rms)	2 (GPS SVs visible from US)	2 (all GPS SVs)
WAAS-corrected Doppler (hertz rms)	0.1 (GPS SVs visible from US)	0.1 (all GPS SVs)
Uncorrected pseudorange (meters rms)	25 (GPS SVs not visible from US)	Not applicable
Uncorrected Doppler (hertz rms)	1.3 (GPS SVs not visible from US)	Not applicable
WAAS GEO pseudorange (meters rms)	1	1
WAAS GEO Doppler (meters rms)	0.05	0.05
Truth Ephemeris	• 50x50 geopotential • Precise solar, lunar, and coordinate transformation data • Dynamic atmospheric density model	• 50x50 geopotential • Precise solar, lunar, and coordinate transformation data • Dynamic atmospheric density model

The GPS navigation algorithms, listed in Table 1, were used to process measurement pairs selected such that measurements from a specific GPS SV were processed no more frequently than every 300 seconds when visible. No change was made to the GEODE satellite selection algorithm; therefore, the use of corrected versus uncorrected observations is not expected to be optimal for the US WAAS case. For the US WAAS case, this produced a measurement set consisting of 33 percent WAAS corrected, 7 percent GEO, and 60 percent uncorrected measurements.

The resulting filtered solutions were compared with the truth ephemeris used in the data simulation. The total position and velocity differences between the GEODE and truth solutions were 2.2 meters and 2.1 millimeters per sec (rms) for the US WAAS case and 1.8 meters and 1.9 millimeters per sec (rms) for the Global WAAS case. These accuracy levels were found to be insensitive to the use of measurement processing rates of 1 measurement pair every 10, 30, or 70 seconds. Figures 7 and 8 show the RSS position and differences for the US WAAS and Global WAAS simulations, respectively.

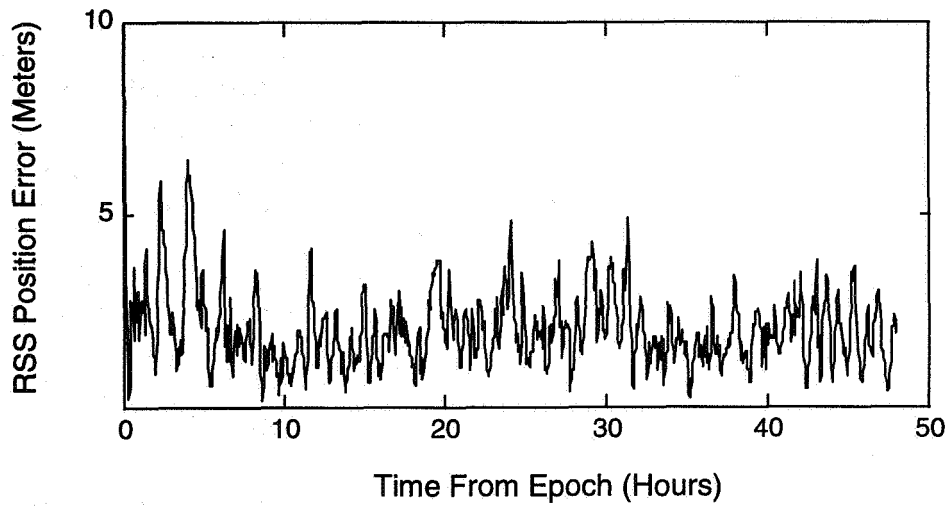

Figure 7. Position Accuracy for US WAAS Using GEODE Navigation Algorithms

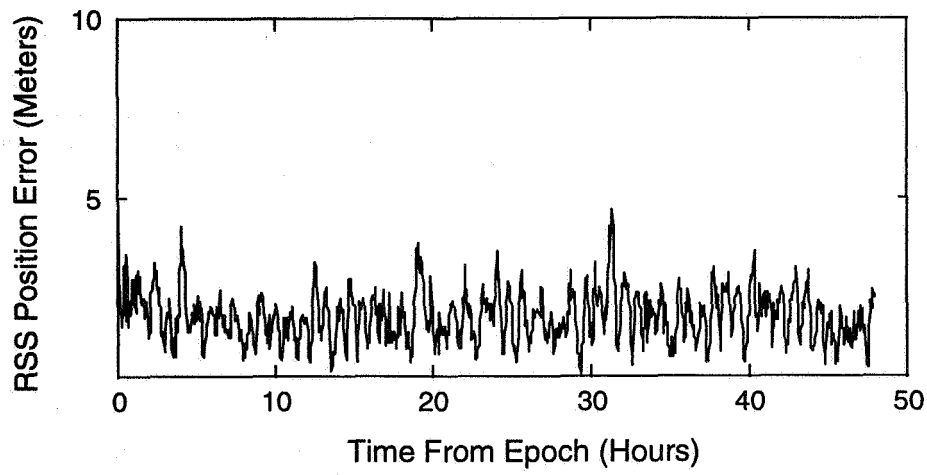

Figure 8. Position Accuracy for Global WAAS Using GEODE Navigation Algorithms

6.0 Future Directions

Future directions for GSFC FDD's GPS autonomous navigation initiatives are (1) to investigate algorithm enhancements to improve onboard accuracy and reliability using GPS, (2) to participate in a cooperative effort to build a NASA miniaturized GPS receiver, and (3) to extend the autonomous navigation applications to other flight applications such as high-eccentricity orbits and relative navigation using GPS.

Acknowledgment

The authors gratefully acknowledge the multi-organizational team that is supporting FDD's GPS initiatives. In particular, we wish to acknowledge Frank Bauer, head of the GSFC Navigation, Guidance, and Control Branch for his leadership in the GADFLY/GEODE efforts. In addition, we wish to acknowledge the significant contributions of the other members of our GEODE team—Kate Hartman and Stephen Leake of GSFC and John Crockett of Computer Sciences Corporation (CSC).

References

1. C. J. Gramling et al., "TDRSS Onboard Navigation System (TONS) Flight Qualification Experiment," *Proceedings of the Flight Mechanics/Estimation Theory Symposium 1994*, NASA Conference Publication 3265, May 17–19, 1994, p. 253–267

2. Goddard Space Flight Center, Flight Dynamics Division, 553-FDD-95/013R1UD0, *Global Positioning System (GPS) Enhanced Orbit Determination Experiment (GEODE) Mathematical Specifications Revision 1*, T. Lee and A. C. Long, prepared by Computer Sciences Corporation, March 1997

3. Roger C. Hart et al., "Global Positioning System (GPS) Enhanced Orbit Determination Experiment (GEODE) on the Small Satellite Technology Initiative (SSTI) Lewis Spacecraft," *Proceedings of the ION GPS-96*, Kansas City, Missouri, September 17–20, 1996

4. Frank H. Bauer et al., "The GPS Attitude Determination Flyer (GADFLY): A Space-Qualified GPS Attitude Receiver on the SSTI Lewis Spacecraft," *ION GPS-95 Proceedings*, ION GPS-95 Conference, Palm Springs, California, September 1995

5. Space Systems/LORAL, Specification No. E101050, *GPS Attitude and Orbit Determination System and GPS Orbit Determination System (GPSAODS and GPSODS) Performance Specification*, June 5, 1996

6. Kurt Brock et al., "GPS Attitude and Orbit Determination for Space," *ION GPS-94 Proceedings*, ION GPS-94 Conference, Salt Lake City, Utah, September 20–23, 1994

7. R. Loh, V. Wullschleger, B. Elrod, M. Lage, and F. Haas, "The U.S. Wide Area Augmentation System (WAAS)", *Navigation*, Vol. 42, No. 3 (Fall 1995), pp. 435-465

8. Per K. Enge and A. J. Van Dierendonck, "Wide Area Augmentation System," *Global Positioning System: Theory and Applications*, Vol. 2, edited by B. Parkinson and J. Spilker, American Institute of Aeronautics and Astronautics, Inc.: Washington, DC, 1996

Page intentionally left blank

Error Analysis System for Spacecraft Navigation Using the Global Positioning System (GPS)*

S. H. Truong, R. C. Hart, and K. R. Hartman
National Aeronautics and Space Administration
Goddard Space Flight Center (GSFC)
Greenbelt, Maryland, USA 20771

T. L. Tomcsik, J. E. Searl, and A. Bernstein
ECG, Inc.
Vienna, Virginia, USA 22182

Abstract

The Flight Dynamics Division (FDD) at the National Aeronautics and Space Administration (NASA) Goddard Space Flight Center (GSFC) is currently developing improved space-navigation filtering algorithms to use the Global Positioning System (GPS) for autonomous real-time onboard orbit determination. In connection with a GPS technology demonstration on the SSTI/Lewis spacecraft, FDD analysts and programmers have teamed with the GSFC Guidance, Navigation, and Control Branch to develop the GPS Enhanced Orbit Determination Experiment (GEODE) system. The GEODE system consists of a Kalman filter operating as a navigation tool for estimating the position, velocity, and additional states required to accurately navigate the orbiting Lewis spacecraft by using astrodynamic modeling and GPS measurements from the receiver.

A parallel effort at the FDD is the development of a GPS Error Analysis System (GEAS) that will be used to analyze and improve navigation filtering algorithms during development phases and during in-flight calibration. For GEAS, the Kalman filter theory is extended to estimate the errors in position, velocity, and other error states of interest. The estimation of errors in physical variables at regular intervals will allow the time, cause, and effect of navigation system weaknesses to be identified. In addition, by modeling a sufficient set of navigation system errors, a system failure that causes an observed error anomaly can be traced and accounted for. The GEAS software is formulated using Object Oriented Design (OOD) techniques implemented in the C++ programming language on a Sun SPARC workstation. The Phase 1 of this effort is the development of a basic system to be used to evaluate navigation algorithms implemented in the GEODE system.

This paper presents the GEAS mathematical methodology, systems and operations concepts, and software design and implementation. Results from the use of the basic system to evaluate navigation algorithms implemented on GEODE are also discussed. In addition, recommendations for generalization of GEAS functions and for new techniques to optimize the accuracy and control of the GPS autonomous onboard navigation are presented.

---

* This work was supported by the National Aeronautics and Space Administration (NASA)/Goddard Space Flight Center (GSFC), Greenbelt, Maryland, under Contract NAS 5-32956.

Page intentionally left blank

Autonomous Navigation With Ground-to-Space Doppler Measurements Referenced to a Temperature-Compensated Crystal Oscillator*

M. S. Radomski
Computer Sciences Corporation
Lanham-Seabrook, Maryland, USA 20706

C. J. Gramling
National Aeronautics and Space Administration
Goddard Space Flight Center
Greenbelt, Maryland, USA 20771

Abstract

The National Aeronautics and Space Administration (NASA) Goddard Space Flight Center (GSFC) has spent several years developing operational Onboard Navigation Systems (ONSs) to provide real-time autonomous, high-accuracy navigation products for spacecraft using NASA's space and ground communication systems. The highly successful Tracking and Data Relay Satellite System (TDRSS) ONS (TONS) experiment on the Explorer Platform/Extreme Ultraviolet Explorer (EP/EUVE) spacecraft, launched June 7, 1992, flight-demonstrated the ONS for high-accuracy navigation using TDRSS forward-link communications services. In late 1994, the ground station ONS (GONS) experiment, using the same EP/EUVE flight hardware, flight-demonstrated the feasibility of high-accuracy autonomous navigation using ground station forward-link communication services, with an ultrastable oscillator (USO) as the frequency reference (1 part in 10^{10} over 24 hours). This paper provides a follow-on analysis of GONS performance to assess the navigation accuracy achievable if GONS uses the significantly less stable (5 parts in 10^8 over 24 hours, compared with a specification of 1 part in 10^6) temperature-compensated crystal oscillator (TCXO), which is integral to the transponder, as a frequency reference rather than an external USO.

The GONS TCXO experiment results from a 20-day period are used to project the expected performance of an operational system. The GONS processes Doppler data derived from nominally scheduled ground station forward-link communication services using a sequential estimation algorithm enhanced by a sophisticated process noise model to provide onboard orbit and frequency determination. To evaluate the navigation accuracies achievable if a TCXO were used, actual experiment data (which used the USO as the frequency reference) were corrupted with errors from real TDRSS one-way return tracking measurements taken from EP/EUVE's TCXO. Analysis of the GONS TCXO experiment performance indicates that real-time onboard position accuracies of better than 300 meters (1σ) are achievable with as few as two tracking contacts per day for the EP/EUVE 525-kilometer altitude, 28.5-degree inclination orbit, provided the TCXO is as stable as that in EP/EUVE's TDRSS transponder. GONS using a TCXO frequency reference provides a viable option for many upcoming spacecraft missions with moderate position accuracy requirements and an interest in reducing their operational costs with autonomous navigation.

1.0 Introduction

Increases in planned use of ground stations as the sole communication medium for low Earth orbiting spacecraft prompted an experiment performed on the Explorer Platform/Extreme Ultraviolet Explorer (EP/EUVE) to investigate the potential of onboard navigation using Doppler observations of the S-band communication signals from ground sites. EP/EUVE housed hardware capable of accurately measuring the Doppler shift of a one-way forward signal from a ground station (GS) to a user spacecraft. The objectives of the Ground Station Onboard Navigation System (GONS) experiment were to demonstrate the second-generation TDRSS transponder's capability to (1) extract accurate Doppler measurements of the GS carrier signal when referenced to an ultrastable

* This work was supported by the National Aeronautics and Space Administration (NASA)/Goddard Space Flight Center (GSFC), Greenbelt, Maryland, under Contracts NAS 5-31500 and NAS 5-31000.

oscillator (USO), (2) determine achievable navigation accuracy from the data, and (3) analyze the potential of a single-station onboard orbit determination solution.

A paper presented at the 1996 Flight Mechanics/Estimation Theory Symposium (Reference 1) described the results of the GONS experiment, which are summarized below:

- Root-mean-square (RMS) measurement accuracy was better than 0.03 Hertz (Hz).
- The navigation accuracy of the GONS solution was better than 250 meters (m) (1σ) with tracking data gaps of up to 3 days. When the tracking frequency is greater than two contacts per day, ONS navigation accuracy of 125 m (1σ) was achieved, and would be bettered by an operational system.
- Single-station support provides comparable accuracy but increases the filter convergence time.

The GONS experiment was performed using, as the Doppler frequency reference, a USO external to the transponder, which may be viewed as a drawback from the standpoint of cost and complexity for a mission that may not require the accuracy of navigation thus achieved. This paper deals with studies intended to show the navigation accuracy achievable with a less stable oscillator such as the temperature-compensated crystal oscillator (TCXO) integral to the transponder.

On-orbit performance of the EP/EUVE TCXO in Transponder A is routinely monitored using TDRSS one-way return Doppler (TD1S) measurements. (Transponder B has lost its transmission capability.) The configuration of the GONS experiment and of TDRSS-based TCXO monitoring is shown in Figure 1. Measurements of the TCXO error (during a selected time span) were impressed on GONS experiment measurements over a different selected time span. The emulated onboard navigation performance with these measurements was analyzed. The results show onboard TCXO/GONS navigation to be an attractive option for a mission with as few as two ground contacts per day and 3σ accuracy requirements as low as 0.8 kilometers (km), provided the oscillator is as accurate as EP/EUVE's TCXO.

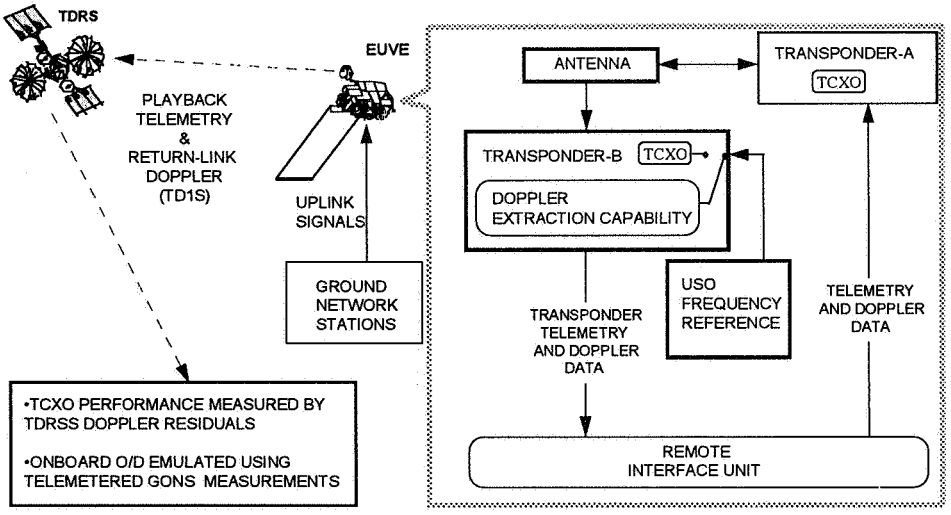

Figure 1. GONS / TCXO Experiment Configuration

Section 2 describes the measurements of EP/EUVE TCXO error. Section 3 describes their application to the GONS experiment tracking data. Section 4 describes the procedures and results of TDRSS batch Doppler orbit determination with TCXO error. Section 5 describes the procedures and results of orbit determination using the GONS measurements with impressed TCXO error. Section 6 presents the conclusions.

2.0 Observations of EP/EUVE TCXO Error

The on-orbit performance of local oscillators (LOs) aboard operational spacecraft is monitored (e.g., Reference 2), for signal acquisition and spacecraft timekeeping purposes, by comparing forward-link Doppler observations with the expectations based on a reference orbit and a perfect oscillator. In the case of EP/EUVE, the reference orbit is determined from TDRSS range and two-way Doppler observations. The uncertainty of the reference orbit and of observation modeling has a negligible effect on the one-way Doppler comparison.

The detailed results of this monitoring are electronically accessible in the form of Goddard Trajectory Determination System (GTDS) Statistical Output Reports (SORs), thanks to the efforts of the Tracking Support Group (TSG) of Allied-Signal Technical Services Corporation, on behalf of the Flight Dynamics Division (FDD) of Goddard Space Flight Center (GSFC). For EP/EUVE during the months of October and November 1995, this monitoring usually amounted to two passes per day consisting of 15 or 20 minutes (min) of continuous 10-second (sec) one-way return Doppler observations. The individual observed-minus-computed (O-C) residuals for October and November are plotted in Figure 2 and Figure 3, respectively. These figures show both systematic and random long-term (*inter*pass) variation of the TCXO error over a range of 130 Hz. Shorter term (*intra*pass) variation is as much as 40 Hz. The reference frequency of TD1S observations of EP/EUVE is 2287.5 MegaHertz (MHz). Figure 3 suggests the possibility (unconfirmed) that significant operating variations affected the spacecraft oscillator after the first week in November 1995. Therefore, the data from that month were not considered for application to GONS observations.

The GTDS O-C results underlying Reference 2 for October 1995 contained 54 SOR batches of valid TD1S tracking. All observations flagged as valid had spacing equal to their Doppler-count interval of 10 seconds, except for a single 90-second Doppler observation. Only four unflagged observations were discarded as inaccurate because of a 5-Hz discrepancy in their residuals relative to the remainder of the pass.

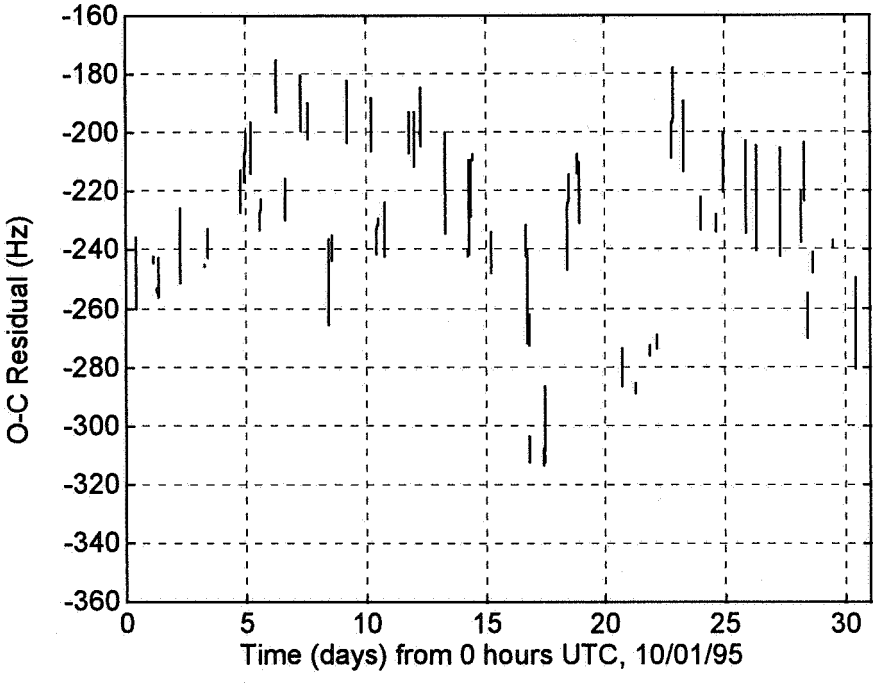

Figure 2. TD1S Residuals for EP/EUVE During October 1995

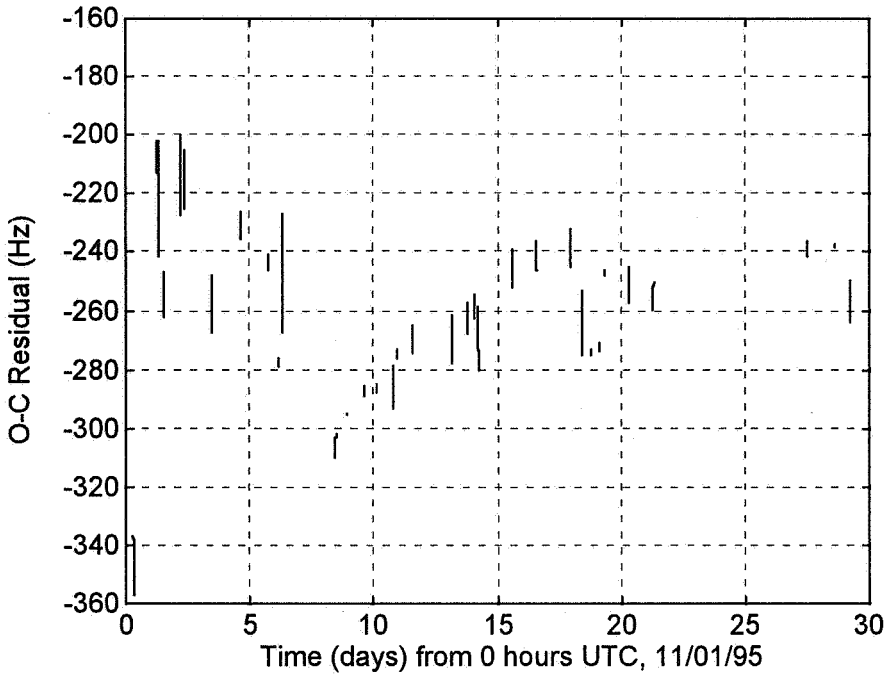

Figure 3. TD1S Residuals for EP/EUVE During November 1995

The tuning of the filter used for orbit determination with the GONS data (see below) made the long-term variation of the oscillator relatively less important than the shorter term. Single-pass residual plots were examined and found to show a variety of shapes and amplitudes for EP/EUVE, but some common patterns occurred repeatedly. Of 54 passes in October 1995, 30 passes were linear (standard deviation from a straight-line fit less than 0.35 Hz) over their first 7.5 min, and 18 of these passes had slopes between +0.016 and +0.029 Hz/sec. This is the relevant period of time for GONS data, because more than 70 percent of the GONS passes examined were less than 8 min long. Behavior after more than 7 min of tracking was usually more complex. Fourteen passes, most of them initially rather linear, suffered sharp jumps initiating reversal of slope at times ranging from 5 to 18 min from carrier lock. The behavior of the TCXO is clearly significantly affected by phenomena associated with the initiation of communication, very possibly the thermal transient associated with dissipation of transmitter power.

Four passes from the Compton Gamma Ray Observatory (CGRO) spacecraft TCXOs (both of two transponders) on November 14, 1995, were also examined. These residuals ranged from –300 to +200 Hz, with up to 270 Hz intrapass variation. Three of the passes were rather linear over the first 10 min. The remaining pass showed a double-humped shape unlike anything displayed by EP/EUVE. The GRO oscillators appear to be several times less stable than those on EP/EUVE.

3.0 GONS Measurements With Impressed TCXO Error

Although TD1S measurements could not be made during the actual GONS experiment, the TCXO performance measured at other times should be qualitatively similar to what it would have been had the GONS experiment been done using, as frequency reference, not the USO reference for Transponder B but the TCXO in Transponder A (now the sole oscillator capable of generating TD1S observations).

Even with the availability of a large amount of monitoring data on the TCXO, it would have been time consuming and uncertain to study, understand, and model, even statistically, the performance of the TCXO. The alternate approach used in this study is simply to impress actual values of TCXO error, inferred directly from EP/EUVE TD1S measurements of representative passes at other times, onto the GONS measurements.

Because of the evident correlation of TCXO error with the beginning of communication, the biases derived from TD1S residuals were applied to GONS data as a function of time from pass origin. The intrapass timing of applied

TCXO transients was, therefore, not just realistic but real. It was not possible similarly to match the interpass timing, because the TD1S passes from October 1995 were not at intervals similar to those of the GONS passes from a year earlier. In the attempt to produce an overall time history of GONS TCXO bias similar to that observed in October 1995, TD1S passes were assigned to a subset of the GONS passes on a one-to-one, monotonic basis in a variety of ways.

A 22-pass subset of the GONS observations (passes 13 through 34) was selected for analysis, extending from September 29, 1994, at 18:51:31.6705, to October 8 at 14:19:05.5535 (all times are Coordinated Universal Time (UTC)). This span was chosen to allow up to 3 days for filter settling prior to the longer of the two spans (Reference 1) with two or more passes per day.

Appendix A describes the choice of six of the nearly 10^{15} monotonic assignments of 22 of 54 TD1S passes to the GONS passes. Various loss functions were minimized over a subset of this population. All the loss functions were based on the GONS and TD1S pass start times and TD1S pass mean biases. The loss functions were intended to quantify, in various ways, the resemblance of the graph of selected mean-pass-bias versus pass start time to that of a real-time selection from the TD1S data. As demonstrated in Appendix A, no selection of TD1S passes yielded an especially close resemblance with regard to both timing and shape (values and slopes) of the graph. The six chosen selections were given reference numbers from 1 to 7 (omitting reference number 3).

The TD1S measurements are 10-sec averages. Average Doppler biases over 5.12 sec were needed for the GONS data. The TD1S residuals were interpolated to 5.12 sec on a pass-by-pass basis, as follows. The phase residuals over each coherent pass were obtained by serially summing the product of Doppler residual by Doppler-count interval. The phase residuals at 10-sec intervals (except for the single 90-sec interval) were interpolated to uniform 5.12-sec intervals. The 5.12-sec phase residuals were differenced and divided by 5.12 sec to obtain the 5.12-sec average Doppler residuals. Interpolation was by cubic splines with the "not-a-knot" end condition as implemented in MATLAB®. The maximum error in interpolation is no more than a few tenths Hz, based on graphical analysis. Exceptions to this maximum error occur at a few times when the TD1S residuals undergo step functions of order 5 Hz. Here, the interpolation fills in the step conservatively, which will be incorrect if the rise time of the step is less than 10 sec. Errors there may be as large as 5 Hz, but very few observations are affected (1 to 3 per step).

For each TD1S pass selection, a dataset of biased GONS measurements was constructed beginning with the unbiased 22-pass subset. Thus each of the numbered pass selections corresponds to a different biasing scenario, referred to as B01 through B07, for the GONS data. Each GONS pass had added to its measurements, beginning with the first valid observation, the interpolated residuals from the TD1S pass to which it was mapped. The unbiased, original GONS data constitutes biasing scenario B00. For diagnostic purposes, additional biasing scenarios Z01 through Z07 were created by adding a different constant to each biased GONS pass in B01 through B07, such that the total impressed bias would be zero at the initiation of valid tracking for each pass.

A factor of (–221/240), applied to the TD1S residuals before impressing them on the GONS measurements, would have accounted for the difference between return Doppler at 2287.5 MHz and forward Doppler at 2106.406250 MHz. That omission affects the results in Section 5 but the sign difference and 10-percent potential magnitude difference are of little significance to the conclusions.

4.0 Orbit Determination With TCXO TD1S Measurements

As a quick estimate of the effects of TCXO error on orbit knowledge, GTDS batch least-squares differential corrections (DCs) were performed using a subset of the TD1S observations. The conditions for these solutions are set forth in Table 1. (The addition of solar radiation force would have affected no solution ephemeris by more than 20 m.)

Four solutions were generated, differing only as to the data arcs covered, with lengths from 34 to 144 hours (hr), as detailed in Table 2. A fifth solution with the same 34-hr arc as the fourth was generated with LO drift (b-dot) constrained to zero instead of solved for. The main results are shown in Table 2. The tracking arc for each solution is illustrated in Figure 4. Definitive ephemeris error (Row 8 of Table 2) is taken by comparison to ephemerides generated from the FDD operational solutions, which use two-way TDRSS measurements. The FDD solution states for epochs October 4, 6, and 9 (all 0 hr, UTC) were propagated over their definitive arcs and compared to our definitive solution ephemerides. The maximum root-sum-square (RSS) position difference is recorded in Table 2.

Inaccuracy in reconstruction of operational definitive ephemerides is between 0.1 and 0.4 km (due mostly to inability to recover the originally predicted Jacchia solar activity data), worse than the accuracy of the operational solutions themselves. The figures for solution ephemeris error thus have an uncertainty of plus or minus about 0.3 km, which is relatively insignificant.

Table 1. GTDS Input Parameters

Orbit Determination Parameter or Option	EP/EUVE Value
Estimated parameters	Position and velocity at epoch, drag scaling adjustment (ρ_1), LO frequency bias and drift
Geopotential model	JGM-2 (30 x 30 or 70 x 70 [see Table 2])
Atmospheric density model	Jacchia-Roberts with definitive solar flux data and geomagnetic indices
Solar radiation force model	Not included
Coordinate system	Mean of J2000
Tracking data	TD1S (TCXO) from TDRS-4 and -5, October 4 through October 9, 1995
Data rate	All available measurements (1 per 10 sec)
Editing criterion	3σ
Measurement sigma (σ)	200 Hz
Coefficient of Drag (C_D)	2.0
Satellite area	16.3 meters^2
Satellite mass	3243.05 kilograms

Table 2. TD1S Batch Solutions and Results

Solution	5-Day	6-Day	5-Day	34-Hour	34-Hour 0-drift
Maximum geopotential order and degree	70	70	30	30	30
Drift (b-dot) (Hz/day)	2.51	4.57	2.48	–17.83	0
Bias translated to noon, October 6 (Hz)	–217.55	–218.79	–217.56	–196.12	–203.44
Drag-scaling adjustment solve-for (ρ_1)	–0.0168	0.2257	–0.0661	1.3291	–12.7728
O-C std. dev. (Hz)	6.13	9.25	6.15	1.66	1.83
Maximum RSS definitive ephemeris error (km)	6.6	7.6	6.6	12.6	9.9
Maximum RSS definitive ephemeris difference vs. 5-day 70 x 70 solution (km)	0	6.3	0.06	6.3	5.4

Figure 4 illustrates the ability of the first-order polynomial LO error model (bias plus constant drift) to fit the TCXO errors from Reference 2 (Section 2) on the various arcs. In this figure, the results of the two 5-day solutions are not shown separately, because they are graphically indistinguishable. Although the fits are reasonably good, given the rigidities of the model, much of the TCXO error still appears as orbit error of 6 to 10 km in the ephemerides. Definitive cross-track error, in the form of an orbit-plane offset, was almost as large as along-track error. The TD1S solutions have mutual inconsistency similar to their inaccuracy. The high level of error seen in these results is accounted for by the relative lack of dynamic information density in TDRSS tracking and the inflexibility of the batch LO model.

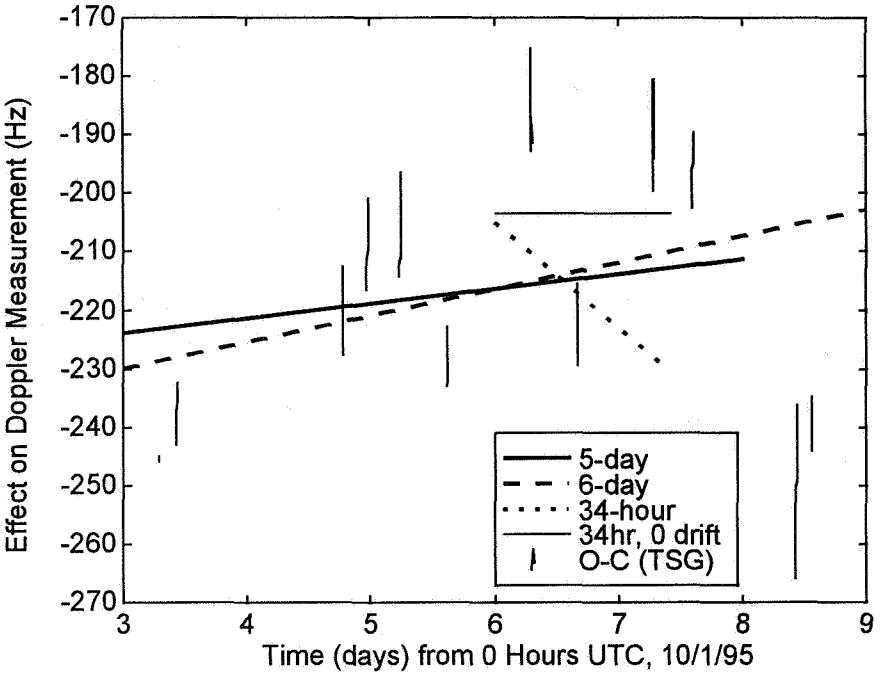

Figure 4. Fitted LO Error on Various Arcs Compared With TD1S Residuals from TSG

5.0 Orbit Determination With Impressed-TCXO GONS Measurements

Onboard orbit determination was emulated with the Prototype Filter Smoother (PFS) on the FDD mainframe computers. The PFS is an analysis tool for orbit determination that includes an extended Kalman filter with "physically connected" gravitational process noise (Reference 3). Methods, PFS settings, and procedures were similar to those used in Reference 1, but with significant adaptations to characteristics of the TCXO-impressed measurements. The input parameters for the solutions are shown in Table 3, with changes from Reference 1 printed in bold face type.

The measurement sigma (σ) was increased from 0.06 to 1.00 Hz to account for the increased measurement error associated with the TCXO. The LO frequency bias (B) sigma was increased from the value 5.0×10^{-9} (sec/sec) used for USO GONS analysis to account for the increased instability of the TCXO. In combination with the unchanged LO frequency bias half-life of 100 days—much longer than any observation spacing—the process model for TCXO error is essentially equivalent to a random walk with white noise amplitude of 5.59×10^{-8}(s/s)/day$^{1/2}$. These filter-tuning adjustments to the TCXO environment were made without the benefit of any experience with that environment and worked so well (see below) that they were not re-tuned. The addition of solar radiation force would have had no more than a 28-meter effect on solution ephemerides.

PFS filter runs, with the above tuning, were performed for all six biasing scenarios (pass selections), the unbiased B00 and two zero-initial-bias scenarios, Z00 and Z05. Ephemerides on a 600-second grid were compared with the high-quality TDRSS filter solution of Reference 1 in the role of truth model. Errors in this ephemeris are small compared to its differences from TCXO GONS solutions. The filter was initialized 91.6705 seconds before the first measurement, at the nearest even 10-minute grid point. Table 4 summarizes the measurement residuals and results of definitive ephemeris comparison.

Three-sigma errors of settled trajectories (triple the fifth row of numbers in Table 4) were better than 1 km, in all but B02. Figure 5 shows the time-dependence of RSS ephemeris position comparison for a typical solution (B05). Cross-track error is generally about half the in-track error in the settled filter ephemerides. The RSS position uncertainty estimated from the filter covariance (root variance) is shown in Figure 6 for B05, but this is essentially independent of bias scenario. The filter is partially settled after three passes in less than 1 day. Further decrease in ephemeris error and variance through about 5 or 6 days may be due mostly to increasing tracking density rather than slow filter convergence, but this was not confirmed. The filter is fully converged during the last 4 days.

Table 3. PFS Input Parameters

Orbit Determination Parameter or Option	EP/EUVE Value
Estimated parameters	Position and velocity, coefficient of drag (C_D), fractional LO frequency bias
Geopotential model	JGM-2 (30 x 30)
Atmospheric density model	Jacchia-Roberts with predictive solar flux and geomagnetic data
Solar radiation force model	Not included
Coordinate system	Mean of J2000
Tracking data	GONS (USO **+ impressed TCXO error)** from DS16, DS17, DS46, and DS66 ground stations
Data rate	Every measurement (1 per 5.12 sec)
Editing criterion	3σ
Measurement sigma (σ)	**1.0 hertz**
Filter epoch	1994 September 29 + 18:50:00 UTC
Gravity auto-correlation integrals	0.9033 minutes (radial) 0.0002 minutes (in-track) 1.8014 minutes (cross-track)
Geopotential model errors	Errors of commission (EOC) from n=2 to n=30 Errors of omission (EOO) from n=31 to n=100
Gauss–Markov parameters: C_D half-life C_D sigma LO frequency bias (*B*) half–life LO frequency bias (*B*) sigma	 14400 minutes 1.000 144000 minutes **4.75×10^{-7} (sec/sec)**
A priori C_D	2.0
A priori LO frequency bias (*B*)	**1.2×10^{-7} (sec/sec)**
A priori LO frequency bias (*B*) root variance	**4.7×10^{-8} (sec/sec)**
Constant LO frequency drift (b-dot)	**0 (sec/sec)/day**
A priori orbital state error Radial (R) position offset In-track (I) position offset Cross-track (C) position offset	 **+0.01 km** **+0.5 km** **+0.5 km**
A priori orbital state covariance (root variance) Radial (R) and cross-track (C) position In-track (I) position R, I, and C velocity components (R-dot, I-dot, C-dot) Correlations	 **0.6 km** **1.8 km** **0.9 km/s** -0.9, I-dot vs. R, and R-dot vs. I; others 0
Satellite area	16.3 meters^2
Satellite mass	3243.05 kilograms

Table 4. Summary of PFS Filter Results

Bias Scenario	B01	B02	B04	B05	B06	B07	B00	Z01	Z05
Position Error Versus TDRSS-Based Truth for Full Time Span (km)									
Maximum RSS	1.113	3.899	4.564	2.723	3.593	3.593	0.974	1.109	3.037
RMS RSS	0.315	0.671	0.694	0.478	0.602	0.624	0.284	0.310	0.496
Mean RSS	0.272	0.499	0.416	0.363	0.426	0.462	0.239	0.262	0.365
Position Error Versus TDRSS-Based Truth for Final Four Days Only (km)									
Maximum RSS	0.555	0.938	0.589	0.669	0.831	0.715	0.640	0.612	0.713
RMS RSS	0.246	0.400	0.258	0.267	0.264	0.320	0.238	0.238	0.271
Mean RSS	0.219	0.353	0.226	0.233	0.212	0.274	0.188	0.206	0.234
RMS Radial	0.035	0.060	0.058	0.033	0.042	0.036	0.027	0.049	0.036
RMS In-track	0.216	0.366	0.232	0.253	0.228	0.297	0.234	0.216	0.253
RMS Cross-track	0.113	0.149	0.106	0.080	0.127	0.113	0.038	0.084	0.091
Post-Fit O-C Measurement Residuals (Hz)									
RMS	0.095	0.123	0.095	0.114	0.110	0.109	0.053	0.091	0.113

These results are a great improvement over those obtained for batch TD1S orbit determination in Section 4. While substantial improvement had been expected, the early results, already of this quality, were treated skeptically. The run inputs and outputs were reexamined and many diagnostic tests were done. In the process, some understanding of the reasons for this success was gained, as well as insight into further improvements and how these results might extrapolate to other oscillators.

Preliminary PFS runs had been made with a priori position and velocity error set to zero (relative to the TDRSS PFS solution) and with a priori covariance 1/9th of that implied by Table 3 (one-third of the standard deviation). The substantial position and velocity offsets and initial covariance adjustments described in Table 3 were introduced to ensure that our final solutions' successes were independent of orbit information introduced with the a priori state. Past the settling period, the final runs did not compare significantly worse with the TDRSS ephemeris than did these early runs with zero a priori error. Table 5 gives the results of ephemeris comparison (RSS position difference) for biasing scenarios B01 and B05 when the filter initial conditions are varied relative to those described in Table 3—by either (1) reducing the a priori position and velocity error to zero ("0 AP" column headings) or (2) strengthening the weighting of that a priori by a factor of 9 ("σ/3" column headings). Comparisons with the TDRSS ephemeris (truth) are displayed in the left-hand columns of Table 5, and comparisons with the standard solutions (those initialized according to Table 3) are displayed in the right-hand columns. In the settled region, the solutions differing only by initial conditions differ much less from each other than from truth. In the settling region, they differ from each other and from the truth comparably. These results argue both that the filter is converging and that the results in the settled region owe little to a priori information.

Table 5. RSS Position Comparisons (km) for Varying Initial Conditions

	Compare versus Truth						Compare versus Standard			
	B01			B05			B01		B05	
	Standard	0 AP [a]	σ/3 [b]	Standard	0 AP [a]	σ/3 [b]	0 AP [a]	σ/3 [b]	0 AP [a]	σ/3 [b]
Full Time Span										
Max	1.113	1.101	1.051	2.723	2.187	1.808	1.109	1.003	1.108	1.019
RMS	0.315	0.323	0.403	0.478	0.380	0.504	0.208	0.254	0.208	0.274
Mean	0.272	0.265	0.337	0.363	0.303	0.410	0.125	0.191	0.125	0.186
Final Four Days Only										
Max	0.555	0.560	0.492	0.669	0.662	0.567	0.033	0.131	0.033	0.110
RMS	0.246	0.245	0.225	0.267	0.262	0.251	0.011	0.073	0.011	0.050
Mean	0.219	0.219	0.189	0.233	0.228	0.220	0.009	0.067	0.009	0.044

[a] Test solution initialized with zero state error in position and velocity.
[b] Test solution initialized with position and velocity covariance reduced by a factor 9 from Table 4.

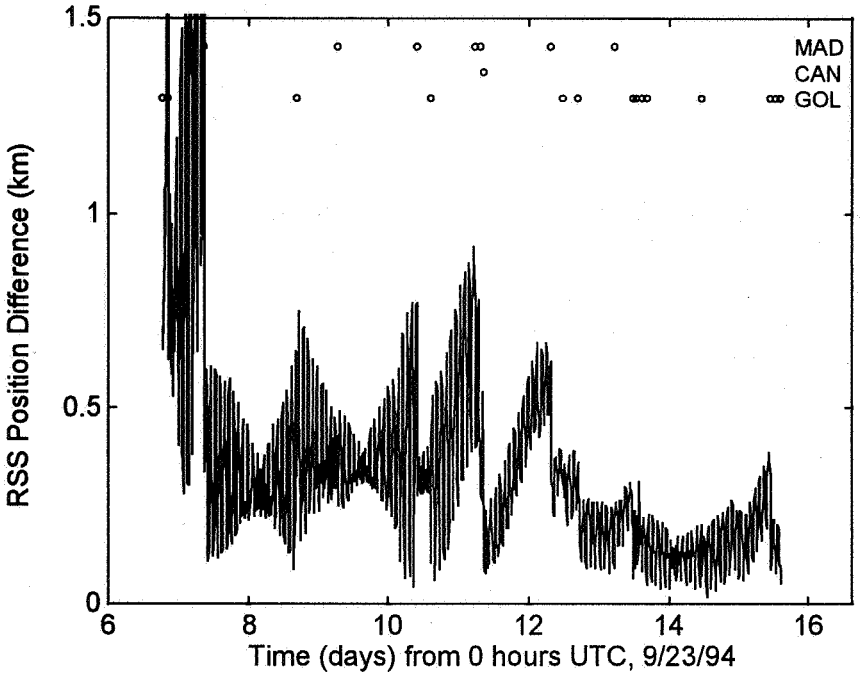

Figure 5. RSS Position Difference for B05 Versus TDRSS

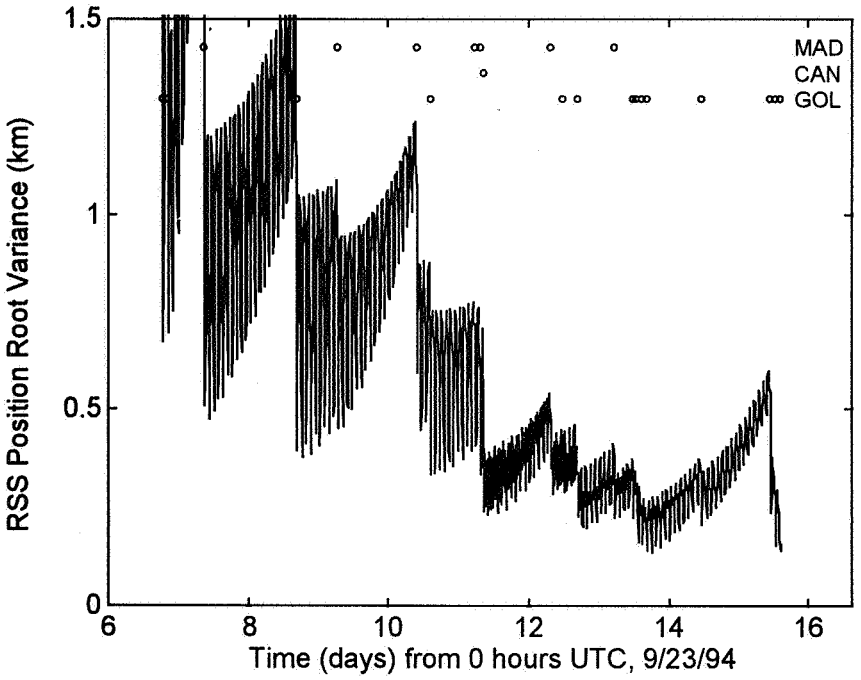

Figure 6. RSS Position Root Variance for B05

A 10-m a priori offset in radial position may seem too small when compared with the other a priori offsets. On the contrary, this offset produces a 20-m offset in semimajor axis and 3 km/day of secular in-track displacement due to the change in orbital period. The settled PFS solutions achieved semimajor-axis accuracy, as well as estimated standard deviations, that were both on the order of 2 m or less. The 10-m radial offset is, therefore, actually conservative by an order of magnitude.

The column labeled B00 in Table 4 corresponds to a solution performed with no impressed bias on the 22 passes of GONS observations. It differs from the GONS solutions of Reference 1 only by its initial conditions and the tuning adaptations made in anticipation of biased data. Its ephemeris error is only slightly less than that displayed by the various biasing scenarios (238 m settled RMS). Reference 1 summarizes the accuracy of its unbiased GONS solutions as 125 m (RMS) during periods of multiple contacts per day. As intended, re-tuning the filter degraded performance for USO-quality GONS data but quite successfully limited the damage caused by TCXO biases.

The success of the PFS solution requires explanation. Computed Doppler differences of the order of $\Delta\nu = 100$ Hz between Newtonian trajectories in the same force model cannot be associated with trajectory variation of less than or of the order of 13 km of orbit position variation ($(\Delta\nu/F_R)(cT/2\pi)$), where F_R is the reference frequency, c is the velocity of light, and T is the orbital period. Figure 7 illustrates the effectiveness of the Gauss-Markov LO bias solve-for in removing Doppler error for B05. Here, the actual Doppler bias, the post-fit estimated Doppler bias, and the time are plotted versus observation number, thus permitting the depiction of both intrapass and interpass variation for 22 passes on a single plot. The actual Doppler bias is the sum of the effect of the USO bias and the impressed (TCXO) bias; the USO effect was calculated from the linear fit of Reference 1. The filter solution for Doppler bias follows the interpass bias variation rather effectively when the passes are spaced a good fraction of a day apart but less effectively when the spacing is closer. The filter solution extracts the intrapass bias variation well because of the high dynamic rate of the ground-based Doppler effect. Total Doppler bias is removed to better than 20 Hz in the fully settled region. This is the key to the success of the GONS filter solutions.

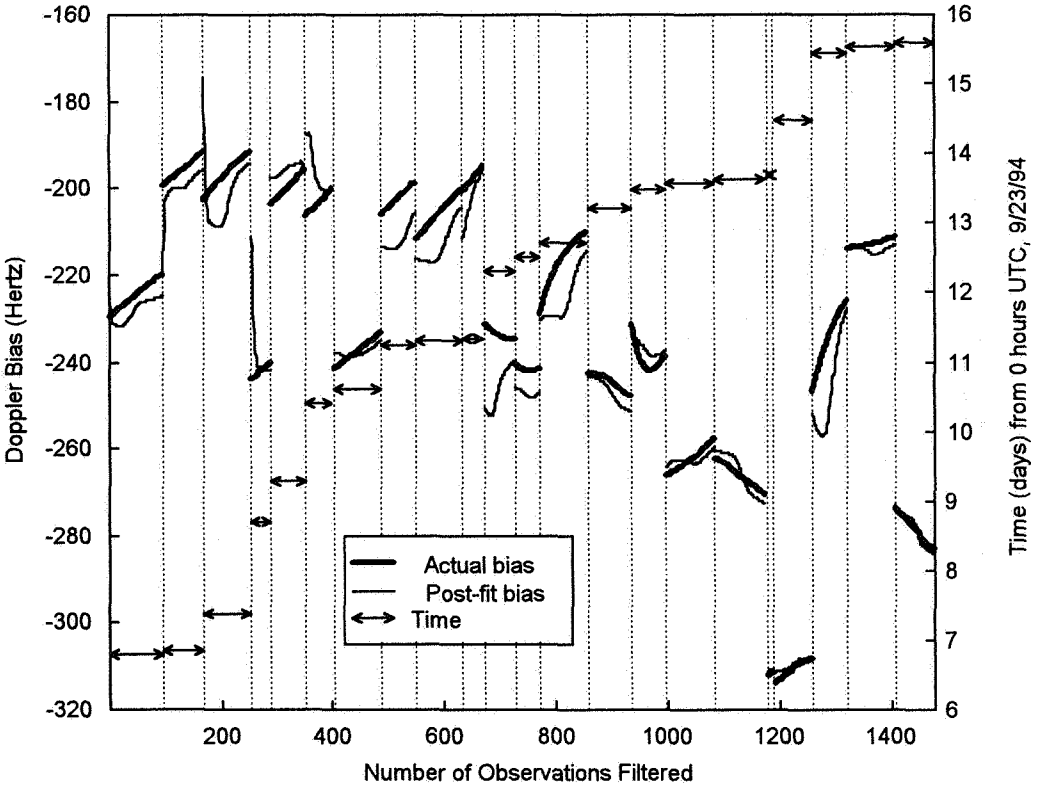

Figure 7. PFS Post-Fit Bias Compared With Actual (USO + Impressed TCXO) Bias

The results of processing the Z01 and Z05 biasing scenarios, as already shown in Table 4, confirm a hypothesis that filter solutions are less sensitive to interpass than intrapass bias variation. These biasing scenarios have minimal interpass bias variation, yet produce ephemeris error and post-fit measurement residuals not better than the full biasing scenarios. The comparison of these Z-solutions and the corresponding B-solutions is less than, or of the order of, one-third the error in the B-solutions. This observation explains the unexpectedly low level of contrast among the results of the six different biasing scenarios. Because of the high frequency of TD1S passes in which biases increased linearly (from a random initial value) with similar positive slopes, as noted in Section 2, the biasing scenarios tend to have similar intrapass bias variation for many of their passes.

Figure 6 shows a major decrease in position root-variance at 11.35 days at the time of the lone Southern-Hemisphere (Canberra (CAN or DS46)) pass. Figure 5 also displays some sign of this, although the full effect does not occur until the following pass. Except for that pass at about 260 degrees of orbit past ascending node, all the GONS observations in this study are at 90 ± 45 deg past ascending node. The CAN pass affects many ephemeris comparisons strongly, often for the better but occasionally, as in comparing Z01 versus B01, for the worse.

Much of the filter ephemeris error may be attributable to drag prediction error in the gaps between widely spaced passes. A large geomagnetic storm ($K_P = 7$), at 10.6 days from September 23, is unmodeled in our atmospheric density model based on "predicted" (i.e., constant and nominal) solar/geomagnetic activity. Using actual measured activities reduced the maximum ephemeris error for B05 in the last 4 days to 0.37 km (cf. 0.67 km).

6.0 Conclusions

Maximum ephemeris errors after full filter settling were less than 850 m in all simulated bias scenarios, with RMS errors typically in the neighborhood of 250 m, only about a factor of 2 worse than with USO GONS data in the original GONS PFS experiments of Reference 1. These results show GONS navigation with moderate-accuracy LOs to be an attractive option for a mission with as few as two ground contacts per day and 3σ accuracy requirements as low as 0.8 km, provided the oscillator is as accurate as EP/EUVE's TCXO.

Much of the error for both TCXO and USO GONS emulated onboard orbit determination may come from drag prediction error in the gaps between widely spaced passes. Short-term atmospheric density prediction, particularly in the onboard computing environment, may well be the ultimate limiting factor for onboard orbit determination schemes with infrequent tracking.

The 22 passes in the period studied were overwhelmingly concentrated near the northernmost point in the orbit. The results of this study, particularly in the last 4 days, would have been noticeably poorer without the single southern pass, and noticeably better with more southern coverage. Coverage by a single station need not be concentrated at one angle of the orbit, except where, as in the EUVE GONS experiment, the station's latitude is not less than the orbital inclination. If single-station coverage is anticipated, the station location should be chosen with orbital coverage in mind, and passes should be scheduled both northward- and southward-going to avoid a significant penalty in overall orbit-determination accuracy. This aspect of the problem requires further study to quantify the benefits of improved geometrical coverage.

The ability of the filter to isolate the effects of variable TCXO bias successfully is quite dependent on the ability of the bias process noise to open up the bias variance during the gap between passes. When sufficient time elapses for this to occur, so that the first observations in the new pass primarily update the bias rather than the orbit, the isolation of bias is remarkably successful. When passes with significant interpass LO bias variation occur too close together, bias isolation is less successful. Further investigation would be desirable to clarify the effect on the PFS filter of increasing the bias process noise and/or decreasing its Gauss-Markov lifetime. The ideal LO bias process for this application might not be Gauss-Markov because it is desirable for the variance to saturate rapidly (compared to interpass but not intrapass observation intervals) but not for the state to decay toward preconceived values in the absence of measurements. These orbit determination experiments were performed with an untuned filter. It is possible that, with further study, still more encouraging results may be obtained on the current measurements. This is an important consideration when contemplating application to a spacecraft with a less accurate reference oscillator than EP/EUVE's TCXO.

The EP/EUVE A-side TCXO is stable to about half a part in 10^7, long-term, and about two parts in 10^8, medium-term. Other TCXOs (e.g., that aboard CGRO) need not be so good; the transponder specification (Reference 4)

only requires about one part in 10^6 over 24 hours. The extrapolation of our EP/EUVE TCXO results to future missions is dependent on the quality of their oscillators. The crucial feature of such oscillators, for GONS, appears to be their medium-term (10 min, rather than 24 hours) instability, in which thermal response to transponder power dissipation may be important.

Acknowledgment

The authors wish to acknowledge Anne Long of Computer Sciences Corporation (CSC) for her technical guidance and Greg Horstkamp, then of CSC, now of the Applied Physics Laboratory (APL), for technical assistance, particularly the tuning of the PFS filter. The ongoing efforts in operations and software support of the GSFC and contractor personnel working in the FDD is always essential to any such work as this, but the contribution of the Tracking Support Group (TSG) of Allied-Signal Technical Services Corporation, who provided the TD1S residuals for EUVE TCXO performance analysis, deserves special acknowledgment here.

References

1. G. M. Horstkamp, D. J. Niklewski, and C. J. Gramling, "Autonomous Navigation with Ground Station One-Way Forward-Link Doppler Data," *Proceedings of the Flight Mechanics/Estimation Theory Symposium 1996*, NASA Conference Publication 3333, May 14–16, 1996, p. 361
2. Allied-Signal Technical Services Corporation, Tracking Support Group, "Evaluation Results for TDRSS One-way Data, October 1995", TSG 95-164, November 10, 1995
3. J. Wright, "Sequential Orbit Determination With Auto-Correlated Gravity Modeling Errors," *Journal of Guidance and Control*, vol. 4, 1981, p. 304
4. Goddard Space Flight Center, STDN No. 203.8, *Performance and Design Requirements and Specification for the Second Generation TDRSS User Transponder*, September, 1987

Appendix A

With 54 TD1S passes from October 1995, there are $54!/(22!32!) = 7.8 \times 10^{14}$ monotonic assignments of TD1S passes to GONS passes. This number precludes global optimization, so the selection was limited to those 369,150 obtainable by removing four passes from a continuous sequence of 26. Various loss functions were minimized over this population, using exhaustive search in MATLAB® on a UNIX workstation. All the loss functions were based on the GONS and TD1S pass start times and mean biases (averaged over the entirety, usually 20 minutes, of each TD1S pass). The loss functions were intended to quantify, in various ways, the resemblance of the graph of selected mean-pass-bias versus pass start time to that of a real-time selection from the TD1S data.

The first loss function considered, $J1$, is simply the standard deviation of $(T\text{-}T')$, where T is the sequence of 22 GONS pass start times and T' is the sequence of 22 selected TD1S pass start times. This loss function favors a selection of TD1S passes offset in time by a constant (of order 13 months) from the GONS passes upon which their residuals are to be impressed. The selections minimizing this loss function turn out to be consecutive (because the TD1S pass density is already less than the GONS pass density); two such were found with $J1$ less than 1 day. These TD1S passes span overall intervals of 11.1 and 10.4 days, not too much longer than the 8.8 days of the GONS data. The inter-pass average drift rates are $\Delta B/\Delta T$, where B is the sequence of 22 mean TD1S biases and Δ signifies sequential differencing. Both $J1$-optimal selections have spikes in $\Delta B/\Delta T$ above the level set by $\Delta B/\Delta T'$, the observed TD1S interpass average drift rate. The first has a peak $\Delta B/\Delta T$ approaching 0.02 Hz/s, with $\Delta B/\Delta T'$ generally about an order of magnitude less. The second selection has $\Delta B/\Delta T'$ approaching that level between a single pair of passes, while $\Delta B/\Delta T$ has two such peaks. These pass-selections produce some situations in which a large bias jump is assigned to a small interpass interval, but not to a degree unseen in the actual TD1S data.

These interpass drift rates were thought to be significant for orbit determination, so some loss functions involving them were tried in the hope of improving their realism. The loss function $J2$ is the sum of the difference $|\Delta B\text{-}\Delta T\ (\Delta B/\Delta T')|$, which compares the assigned change in mean bias between consecutive GONS passes with that which would be expected given the average drift rate between the corresponding two TD1S passes. The restricted optimum selection of TD1S passes for this loss function extends over a 14.0-day interval, significantly longer than

8.8 days. It also has, as might have been expected (given the overall factor of ΔB in the loss function terms), significantly too low contrast in the pass-mean bias (standard deviation 20 Hz compared with 32 Hz for the TD1S data overall).

To remove the bias in *J2* toward low interpass contrast, *J3* was constructed as the weighted mean average of $|\Delta T'-\Delta T|$, with weighting factor $|\Delta B/\Delta T'|$. This is a quotient, total discrepancy divided by total weight, the numerator of which is *J2*. *J4* and *J5* are similar to *J3*, with weighting functions of $|\Delta B|$ and 1, respectively. All three of these loss functions try to make the selected TD1S interpass intervals similar to the GONS intervals, but with different weighting. Significant features of the selections representing restricted (four-skip) minima of these loss functions are summarized in Table A-1.

Table A-1. Properties of TD1S Pass-Selections (GONS Biasing Scenarios)

Selection Serial #	Description	First Pass	Skipped Passes	Span (days)	*J1* (days)	std(*B*) (Hz)	max($\Delta B/\Delta T$) (milliHz/s)
1	*J1* minimum	2	None	11.1	0.95	22.9	16.0
2	*J1* local minimum	15	None	10.4	0.97	37.5	13.7
3	Unused number						
4	*J2* 4-skip minimum	1	5,11,15,16	14.0	1.86	20.2	6.0
5	*J3* 4-skip minimum	12	15,20,33,34	14.0	1.54	36.1	11.3
6	*J4* 4-skip minimum	7	9,11,14,20	12.6	1.64	33.9	14.7
7	*J5* 4-skip minimum	7	10,22	12.0	1.53	24.1	17.2
	Truth	1	None	8.8	0	31.7	11.3

A Comparative Study of the Flight Dynamics and Control Laboratory's Orbit Analysis System With the Goddard Trajectory Determination System (GTDS)

Charles McConnell* and David Schmidt**

Flight Dynamics and Control Laboratory (FDCL)
Department of Aerospace Engineering
University of Maryland
College Park, MD 20742-3200

ABSTRACT

A comparison of the Flight Dynamics and Control Laboratory's (FDCL) orbit analysis software system and the Goddard Trajectory Determination System (GTDS) has been performed. The orbit analysis system is a component in the Spacecraft Mission Analysis System (SMAS) being developed by the FDCL in cooperation with NASA's Goddard Space Flight Center. Specifically investigated were the levels of agreement between the two systems in the areas of preprocessing raw tracking data, performing orbit determination, and performing orbit prediction. In preprocessing raw tracking data, results from the SMAS was generally found to agree with those from GTDS to within the published accuracy of Unified S-band (USB) range-rate measurements. The differences were on the order of expected corrections for ionospheric and tropospheric refraction. In performing orbit estimation, results from the SMAS were found to agree well with those from GTDS. The final estimation errors from the SMAS were comparable to those from GTDS and were well within the published measurement accuracy. In performing orbit prediction, results from the SMAS were found to agree with those from GTDS to within 2 kilometers in position over 28 days. Sensitivity analysis was also performed for both orbit estimation and orbit prediction, revealing the effects of bias in tracking data and of selected modeling and input parameters.

NOMENCLATURE AND ACRONYMS

Ephemeris	Time history of a spacecraft's position and velocity
GSFC	Goddard Space Flight Center
GTDS	Goddard Trajectory Determination System
O-C	Observed minus computed
OD	Orbit determination
PODS	Precision Orbit Determination System
RMS	Root mean square
Sigma / σ	Standard deviation, especially of the white noise inherent in tracking data measurements
SMAS	FDCL's Spacecraft Mission Analysis System
STDN	Spacecraft Tracking and Data Network
STK	Satellite Tool Kit
UTDF	Universal Tracking Data Format

* Graduate Research Assistant
** Director and Professor

INTRODUCTION

The Flight Dynamics and Control Laboratory (FDCL) at the University of Maryland is developing a system for flight dynamics analysis and real-time mission support of Earth-orbiting spacecraft, the Spacecraft Mission Analysis System (SMAS). This system consists of FDCL-developed custom software modules and commercial off-the-shelf (COTS) and modified Goddard off-the-shelf (GOTS) software modules.

The focus of the activity reported herein was to assess the accuracy of the tracking data preprocessor and the orbit determination (OD) and orbit prediction software of the SMAS, using an established orbit analysis system as a benchmark. For the benchmark, the Goddard Trajectory Determination System (GTDS) was used [1]. In this evaluation, there were three particular areas of interest: 1) accuracy in preprocessing raw tracking data; 2) accuracy in OD; and 3) accuracy in orbit prediction. The SAMPEX spacecraft was used as a test case, using tracking data for this vehicle.

SOFTWARE DESCRIPTION

The SMAS is an integrated, workstation-based software system for performing trajectory and navigation analysis, as well as attitude analysis [2]. A diagram of the SMAS is shown in Figure 1. The trajectory and navigation analysis component of the SMAS, which is shown as the top half of Figure 1, includes software for orbit determination, orbit prediction, and orbit event scheduling. This software, as configured for orbit analysis, will be referred to as the orbit analysis component.

The orbit analysis component of the SMAS currently accepts raw tracking data from NASA ground stations, preprocesses the raw tracking data, performs orbit determination, and performs orbit prediction. Several orbit event scheduling and other orbit analysis capabilities, e.g. spacecraft lighting time predictions and sun vector / geomagnetic field vector co-alignment predictions, have also been implemented.

The CONVERT utility performs format and data conversion on raw tracking data from the Spacecraft Tracking and Data Network (STDN) [3]. This preprocessing of data is done before orbit determination is performed. The utility reads a Universal Tracking Data Format (UTDF) file, time sorts the data, checks for repeated data, and performs calculations and format conversions on the data.

One main module of the SMAS is the Satellite Tool Kit (STK) with the Precision Orbit Determination System (PODS) utility [4,5]. The OD process in the SMAS utilizes some data provided with PODS, plus several enhanced data sets integrated with PODS by the FDCL. The OD software uses a Bayesian batch weighted least-squares algorithm in its differential correction process. The orbit propagator uses a 12th-order Cowell numerical integration scheme to integrate the equations of motion [5,6]. Back-propagation is supported as well as forward-propagation, allowing the user to predict a spacecraft's previous trajectory without performing OD.

The remainder of this section will focus on the enhanced data sets, e.g. environmental models and astrodynamic constants, used in the orbit analysis component of the SMAS. The environmental models used by SMAS were an area of significant customization in the STK/PODS packages. The files included with STK and PODS include a geopotential model (a 36th-order Goddard Earth Model, the GEM-T1 model); a JPL planetary ephemeris; a Jacchia 1971 atmospheric density model; and a file containing data for solar/magnetic flux, Earth polar motion, and time correction. The FDCL added a 50th-order JGM2 geopotential model to be used in place of the GEM-T1 geopotential model. Other input parameters are listed in Table 1, which have been selected to yield the best comparative results.

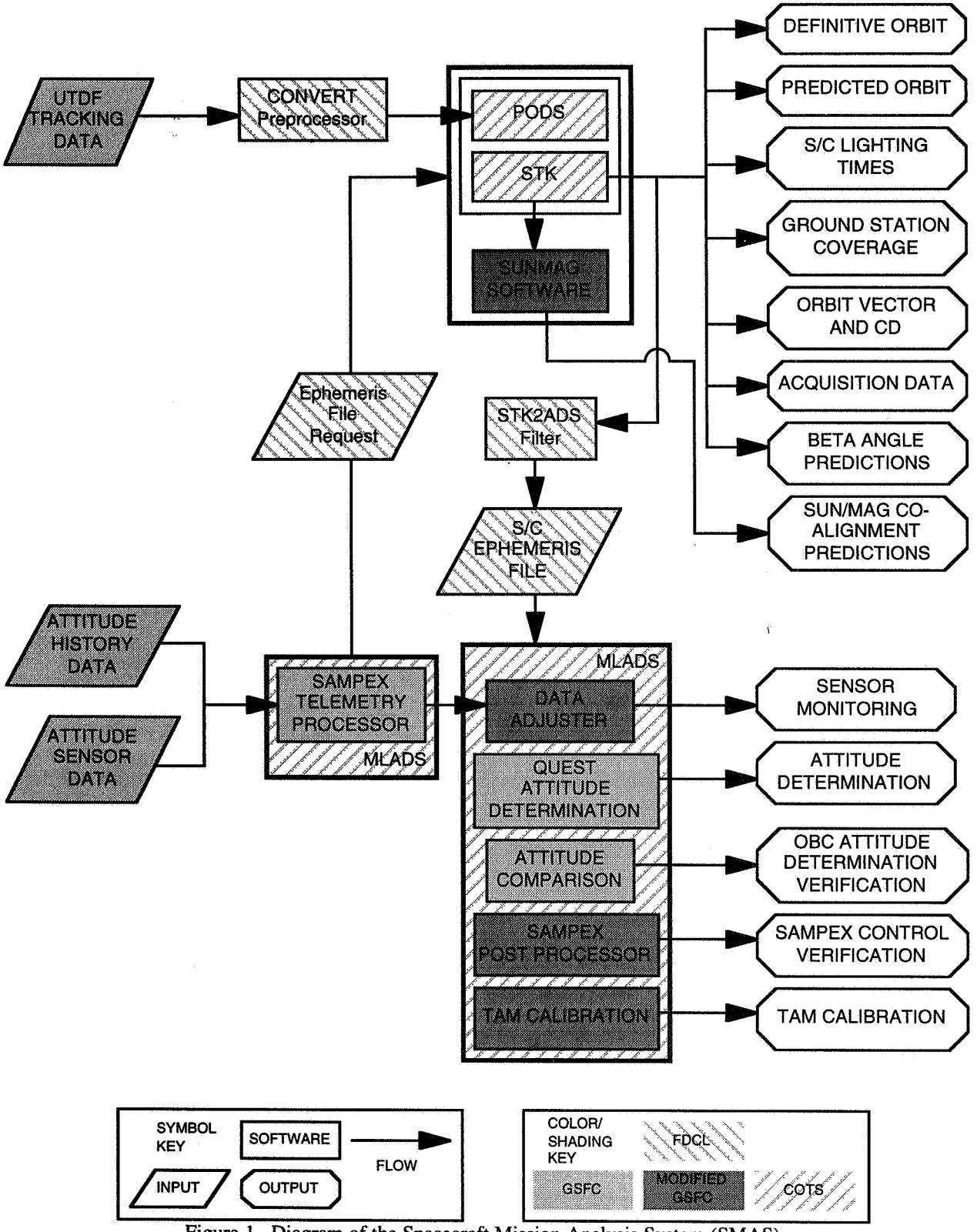

Figure 1. Diagram of the Spacecraft Mission Analysis System (SMAS).

Table 1. List of input parameters for the SMAS.

Global Parameter	Value
Geopotential model	JGM2
Order	50x50
Atmospheric density model	Jacchia 1971
Gravitational constant, GM (km^3/sec^2)	398600.64
Equatorial radius (km)	6378.1363
Inverse Flattening coefficient	298.257
Third-body perturbations	Sun and Moon
SAMPEX-Specific Parameters	
Spacecraft mass (kg)	156.76
Cross-sectional area (m^2)	1.39
A priori atmospheric drag coefficient	2.2
Solar radiation Pressure coefficient	1.2
Poker Flats, AK (WT1S) range rate bias (m/s)	2.4497104

METHOD OF APPROACH

This comparative study, as stated previously, investigated tracking data preprocessing, orbit determination, and orbit prediction. The approach to investigating each of these aspects will be summarized here. The ephemeris comparison, essential to investigating both OD and orbit prediction, will also be summarized here.

Tracking Data Preprocessing

The accuracy of the SMAS preprocessor was evaluated by comparing its range rate calculations to those from GTDS. The difference in calculated range rate was computed according to the relation

$$\Delta\dot{r} = \dot{r}_{GTDS} - \dot{r}_{SMAS} .$$

Statistical analysis (mean, median, and standard deviation calculations) was performed on the differences in calculated range rate measurements. Comparisons of range calculations and angle conversions have also been made between SMAS and GTDS, but will not be reported here.

Ephemeris Comparison

An ephemeris comparison utility was written to compare ephemerides from SMAS and GTDS. This utility reads time, position, and velocity for a SMAS ephemeris point then reads the corresponding position and velocity from the GTDS ephemeris for the same time from epoch. The root-mean-square (RMS) difference in position and velocity between the two ephemerides is computed according to the following relations for position and velocity as in [7],

$$|\Delta r| = \sqrt{(x_{GTDS}-x_{SMAS})^2 + (y_{GTDS}-y_{SMAS})^2 + (z_{GTDS}-z_{SMAS})^2}$$

$$|\Delta v| = \sqrt{(\dot{x}_{GTDS}-\dot{x}_{SMAS})^2 + (\dot{y}_{GTDS}-\dot{y}_{SMAS})^2 + (\dot{z}_{GTDS}-\dot{z}_{SMAS})^2} .$$

Orbit Determination

Accuracy in OD was evaluated in two ways. First, the final estimation errors between the tracking data and the solved-for orbit were compared. This quantity, the observed minus corrected (O-C) errors, are a measure of the

accuracy of the OD solution but is significantly affected by the accuracy of the tracking data preprocessor. Second, the definitive ephemerides, or best estimates of the spacecraft's position over the time span covered by the tracking data, were compared. This is also strongly coupled to the tracking data preprocessor, as well as to the environmental models used.

Orbit Prediction

For comparing the accuracy in orbit prediction, two approaches were taken. First, and perhaps of more practical interest, is to generate a predicted orbit after OD. This predicted orbit is then strongly coupled to the OD solution, but the accuracy of a predicted orbit is expected to be highly dependent upon the accuracy of the OD solution. So a second approach was taken as well. In this approach, the orbit propagator was uncoupled from the OD solution by starting with identical *a priori* state vectors and propagating the orbit. This isolated the orbit prediction from OD and focused on environmental modeling differences.

Sensitivity Analysis

After finding the optimal configuration for the SMAS, an investigation of the significance of the environmental models and input parameters on the accuracy of OD and orbit prediction was performed. The two major perturbations from the optimal configuration reported above are the "out-of-the-box" accuracy of STK/PODS and OD using biased tracking data. The out-of-the-box configuration of STK/PODS represents the software as delivered, using all the default input parameters and data sets. The OD using biased tracking data considers the effects of not correcting for bias in range rate measurements.

RESULTS

This section will present and interpret the results of this comparative study. The results for tracking data preprocessing, orbit determination, orbit prediction, and sensitivity analysis will be presented in order.

Tracking Data Preprocessing

The results from the comparison of range rate data from the SMAS preprocessor, CONVERT, and from GTDS are given in Table 2. The comparisons are grouped by blocks of tracking data, that is, by each pass of a ground station. The ground station's acronym is listed along with the mean, median, and standard deviation of the differences between the GTDS and SMAS range rate values.

Table 2. Statistical data for computed range rate (two-day tracking data arc).

Ground Station(s)	Mean (cm/s)	Median (cm/s)	Std. Dev. (cm/s)
WP2S/WPS8	-7.30	-1.98	16.76
WP2S/WPS8	-2.48	-0.85	8.93
DS17	-1.89	-0.88	5.87
WT1S	-2.78	-0.49	15.69
DS46	-2.82	-0.77	10.24
WT1S	-7.68	-2.48	19.70
WT1S	-13.01	-4.46	20.98
WT1S	-3.56	-0.71	15.30
DS46	-1.50	0.23	9.02
WPSA	5.01	2.61	8.61

As seen in Table 2, the average and median differences are near the published accuracy of range rate measurements for these ground stations (10 cm/sec), while some of the standard deviations are larger. It should be noted that the range rate from SMAS has not been corrected for ionospheric or tropospheric refraction, as has the GTDS range rate. Note also that during the sixth and seventh blocks (for WT1S), the spacecraft was at low elevation angles throughout the pass, where refraction effects are most significant. These passes also exhibit the largest differences in range rate between SMAS and GTDS, which suggests that those effects were the dominant contributor to the differences observed.

Orbit Determination

The final O-C errors from SMAS and operational GTDS were also compared. Statistical data on the absolute values of the final O-C errors are shown in Table 3 below. As seen in Table 3, the final O–C errors from SMAS are all smaller than the published 10 cm/sec accuracy (one-sigma) of the range rate measurements from these ground stations. The average final O-C error reported by the OD software was 2.7 cm/second, which is well within the accuracy (one-sigma) of the range rate measurements.

Table 3. Statistical data for final O-C errors.

Ground	GTDS Residuals			FDCL Residuals		
Station(s)	Mean	Median	Std. Dev.	Mean	Median	Std. Dev.
WP2S/WPS8	1.44	1.41	1.05	1.92	2.10	0.67
WP2S/WPS8	0.95	0.80	0.58	2.58	1.62	2.20
DS17	4.01	4.14	1.45	3.44	3.61	1.52
WT1S	0.44	0.43	0.31	2.56	2.24	1.73
DS46	1.55	1.49	1.01	0.58	0.30	0.65
WT1S	0.58	0.44	0.43	1.82	1.92	1.09
WT1S	2.78	3.09	1.45	4.79	4.88	2.37
WT1S	1.60	1.97	1.07	0.95	0.89	0.51
DS46	1.52	1.34	0.97	1.75	1.41	1.15
WPSA	2.23	1.72	1.76	1.76	1.36	1.36

Figure 2 shows the differences in position and velocity over the two-day definitive orbit. As seen from these results, the SMAS definitive orbit is within 100 meters of the GTDS definitive orbit over the two-day tracking data arc. This accuracy meets the requirements of many current and future missions.

Orbit Prediction

After an OD solution was obtained, the orbit was predicted over a 28-day period. The plots in Figure 3 show the position and velocity differences between the SMAS and GTDS ephemerides over 28 days. The position difference reaches a maximum of nearly 2 kilometers. Note that the accuracy requirements for SAMPEX are to be within 5 kilometers after *one* day.

Figure 4 shows the position and velocity differences for the propagate-only 28-day ephemeris. This ephemeris was generated by propagating the GTDS solve-for orbit vector. As seen from this data, these position and velocity differences are of the same magnitude as for the OD-based 28-day ephemeris. Again, this accuracy is well within the requirements for the SAMPEX mission.

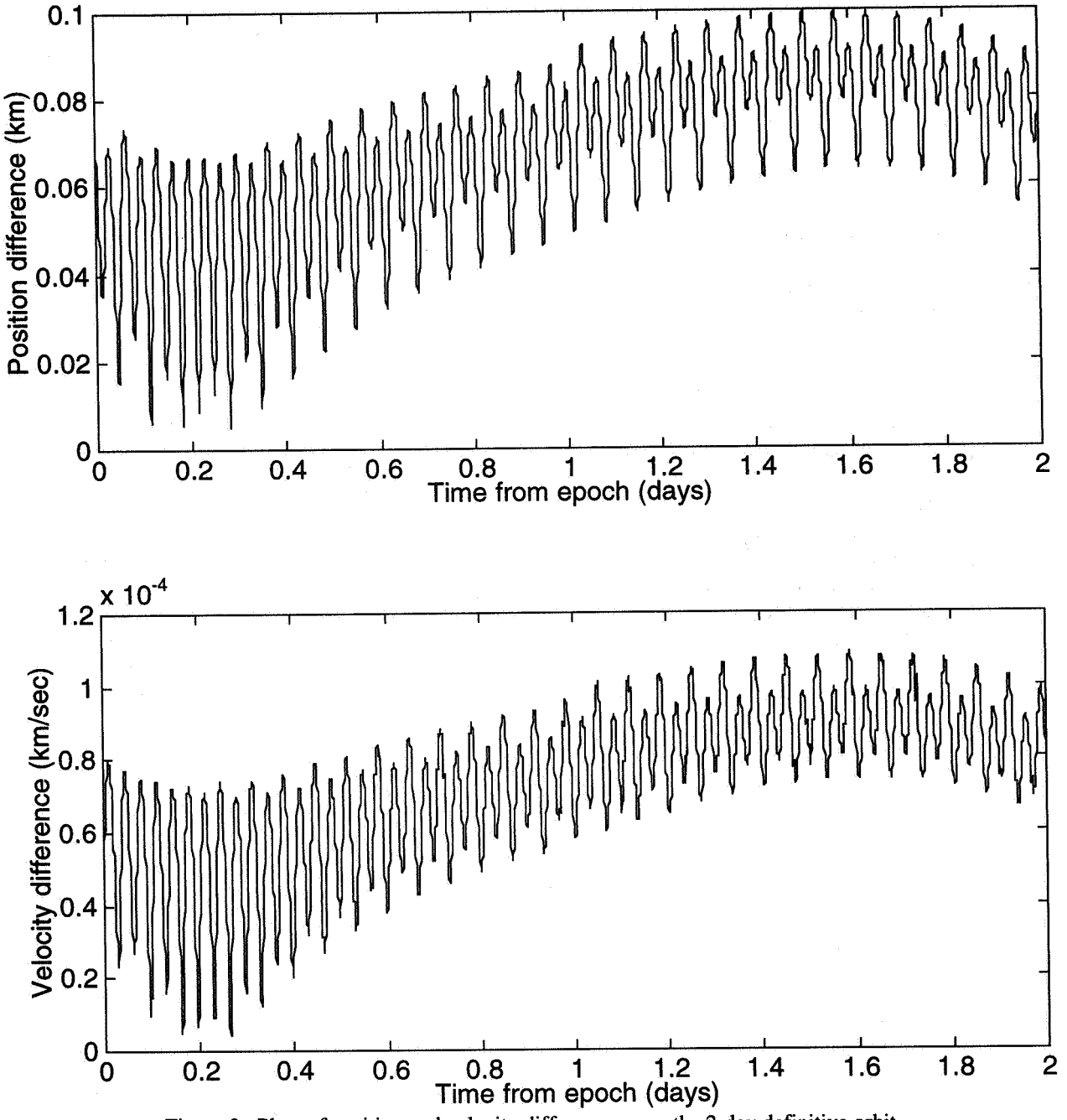

Figure 2. Plots of position and velocity differences over the 2-day definitive orbit.

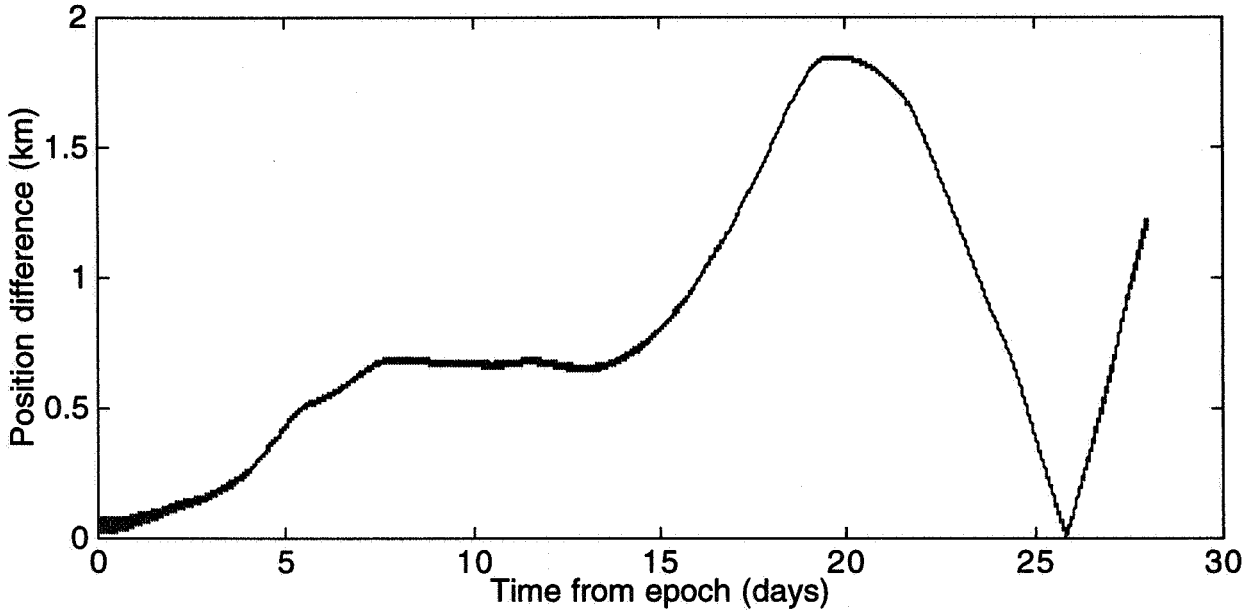

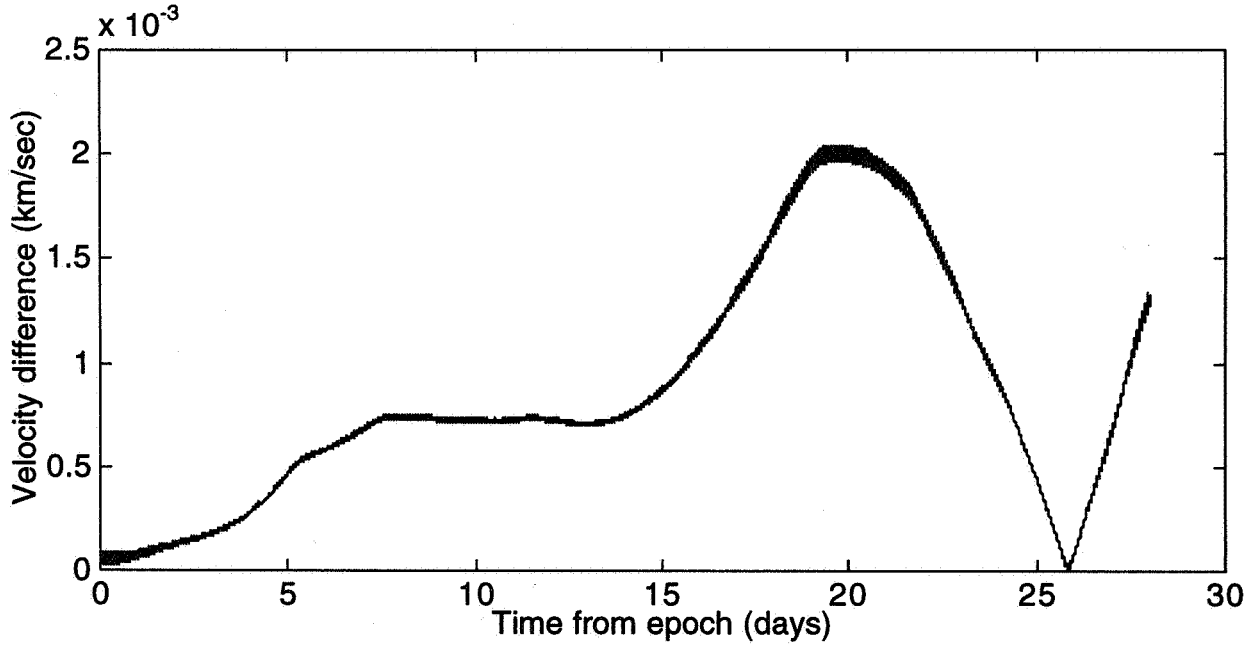

Figure 3. Plots of position and velocity difference throughout the OD-based 28-day predicted orbit.

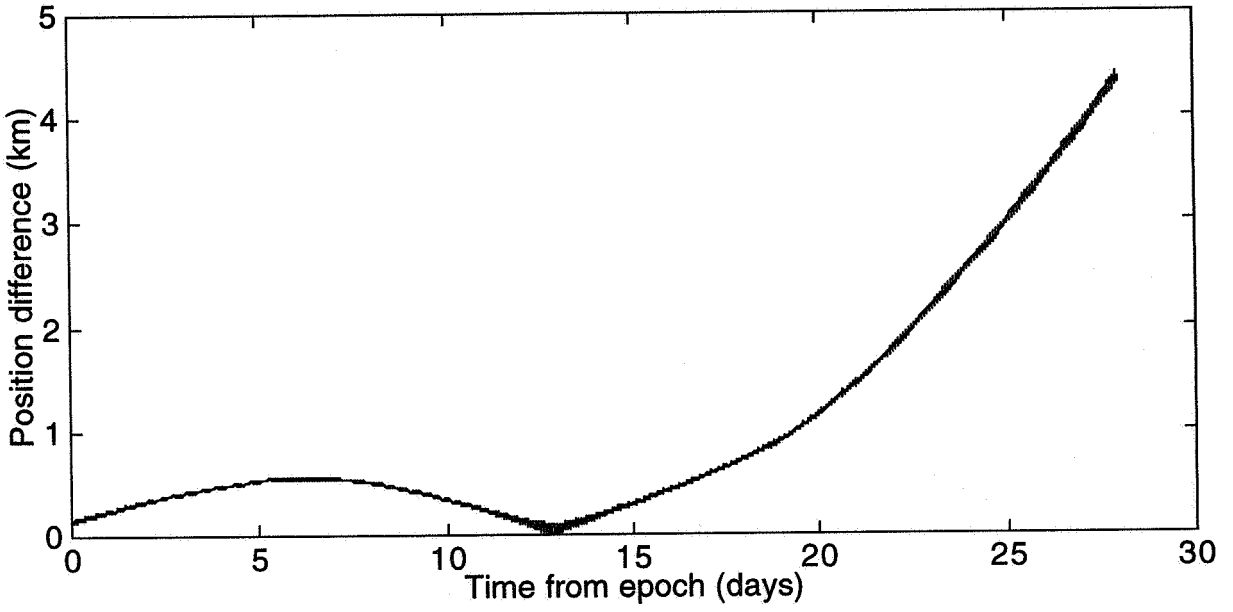

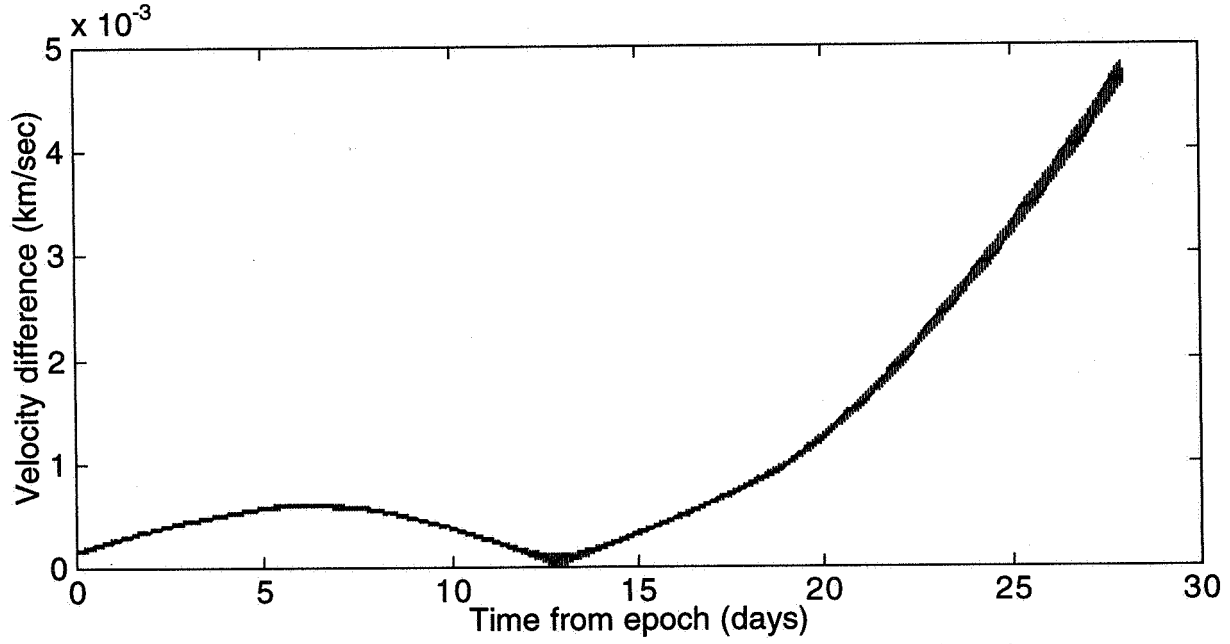

Figure 4. Plots of position and velocity differences over 28 days, propagation only.

Sensitivity Analysis

One non-optimal configuration of interest is the "out-of-the-box" configuration for the STK/PODS package. Without the customization done by the FDCL, the STK/PODS package does not agree with GTDS to nearly the degree of accuracy shown above. For orbit determination, final O-C errors were on the order of 90 cm/s, which is much greater than the accuracy (one-sigma) of the range rate measurements, and the position difference reaches 2 km for a 2-day definitive orbit. For orbit prediction, the largest position differences exceed 160 km for a 28-day OD-based ephemeris (see Figure 5) and 140 km for a 28-day propagate-only ephemeris.

Another non-optimal configuration of interest is when biases in tracking data have not been corrected. One of the ground stations that tracks SAMPEX has a 2.4 m/s bias in range rate. If this bias is not removed, the final O-C errors are on the order of 40 cm/s, compared to those shown in Table 2.

SUMMARY AND CONCLUSIONS

This study has shown that the orbit analysis generated with the SMAS agrees very well with that from the GTDS. In particular, the tracking data preprocessing and range-rate data agree to within the published accuracy of the tracking systems. The orbit-determination results, including the position and velocity differences between definitive orbit, agree to within 100 m and 0.12 m/sec, respectively, over a two-day solution. And the predicted orbits agree to within 2 km and 2.5 m/sec, respectively, over a 28-day prediction.. This accuracy is well within the mission requirements for SAMPEX, and many other missions. Hence, this software package would appear to be a viable option for orbit analysis for future missions.

REFERENCES

1. Goddard Trajectory Determination System (GTDS) Mathematical Theory, NASA's Operational GTDS Mathematical Specification, Revision 1, Edited by Computer Sciences Corporation and NASA Goddard Space Flight Center, Contract NAS 5-31500, Task 213, July 1989.
2. Reedy, S., McConnell, C., and Schmidt, D., "An Integrated Spacecraft Mission Analysis System for Flight Dynamics Analysis and Mission Support," Presented at the Flight Mechanics Symposium, NASA Goddard Space Flight Center, Greenbelt, MD, May 19-21, 1997.
3. McConnell, C., Cummings, S., and Schmidt, D., "Comprehensive Report on the CONVERT Tracking Data Preprocessor," Flight Dynamics and Control Lab, University of Maryland, 1997.
4. Satellite Tool Kit User's Manual, Analytical Graphics, Inc., July 1996.
5. Precision Orbit Determination System User's Manual, Analytical Graphics, Inc., March 1997.
6. Knapp, Chris, Computer Sciences Corporation, Meeting on 4 September 1996.
7. Fonte, J., Neta, B., Sabol, C., Danielson, D., and Dyar, W., "Comparison of Orbit Propagators in the Research and Development Goddard Trajectory Determination System (R&D GTDS). Part I: Simulated Data," Presented at the AAS/AIAA Astrodynamics Specialist Conference, Halifax, Nova Scotia, Canada, August 14-17, 1995, paper AAS 95-431.
8. Marr, Greg, Goddard Space Flight Center, Private communication, October 1996.

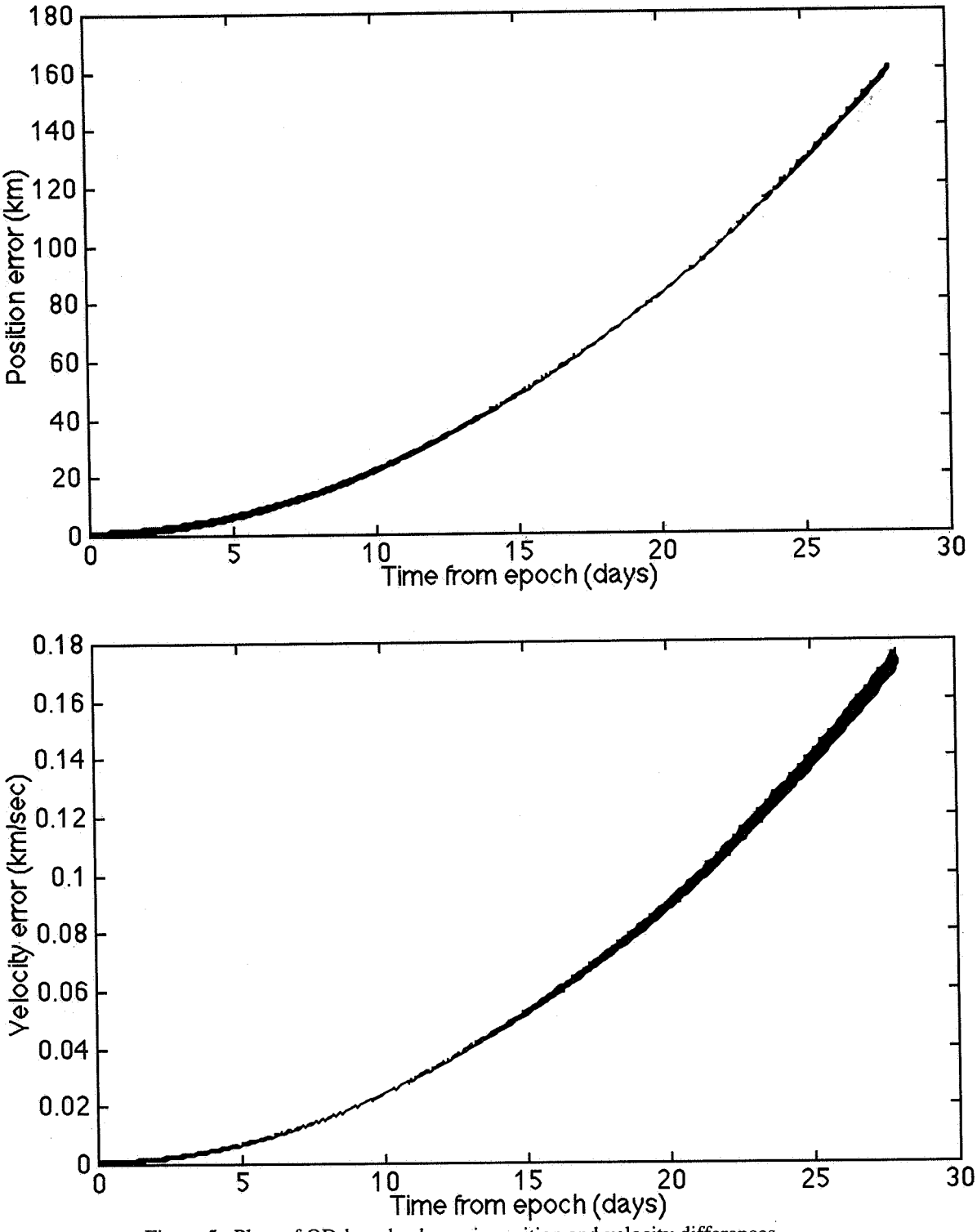

Figure 5. Plots of OD-based ephemeris position and velocity differences.

Page intentionally left blank

An Integrated Spacecraft Mission Analysis System for Flight Dynamics Analysis and Mission Support

Scott Reedy
Charles McConnell
David Schmidt

Flight Dynamics and Control Laboratory
University of Maryland
College Park, MD 20742-3200

ABSTRACT

An integrated, workstation-based software package has been developed for flight dynamics analysis and spacecraft mission support. Analysis consists of navigation and trajectory analysis, critical-event prediction, attitude analysis, plus acquiring and processing the required data. In the past this may have been performed by separate groups of analysts acting in parallel, on several types of computing platforms. In contrast, this paper discusses an integrated, workstation-based approach, the Spacecraft Mission Analysis System (SMAS). The Spacecraft Mission Analysis System is a integrated package that includes Commercial Off-the-Shelf (COTS) software modules, modified Goddard Off-the-Shelf (GOTS) software modules, and custom software developed by the Flight Dynamics and Control Laboratory (FDCL). The SMAS has analysis capabilities for orbit determination and prediction, orbit event predictions, attitude determination, on-board computer performance verification, and attitude sensor monitoring. In addition, the system currently has the capacity to access raw tracking data in the Universal Tracking Data Format (UTDF), and attitude telemetry files for the Solar, Anomalous, and Magnetospheric Particle Explorer (SAMPEX) spacecraft. Details of the capabilities of the SMAS, as well as, sample results using the SAMPEX mission will be presented.

1.0 INTRODUCTION

In an effort to reduce the life cycle costs for existing and future spacecraft missions it will be necessary to reduce the number of man-hours for ground support and analysis. This requires increased autonomy of the spacecraft, and/or reducing the man-hours required for performing ground based analysis and support. Reductions in ground-based analysis may be realized with new analysis techniques and software. And the research into the area of tools and techniques performaed by the FDCL has led to the development of Spacecraft Mission Analysis System (SMAS).

The SMAS is an integrated collection of software packages for performing spacecraft flight dynamics analysis and mission support. The SMAS several Commercial Off-the-Shelf (COTS) analysis modules, NASA Goddard Off-the-Shelf (GOTS) software modules, and custom software developed by the Flight Dynamics and Control Laboratory (FDCL), all integrated to operate interactively on a UNIX workstation. Spacecraft support using the SMAS can be performed by a single analysis team, consisting of one or two analysts, using a single workstation.

This document describes the SMAS and its capabilities. First, Section 2 gives an overview of the system, including a summary of what the SMAS does and how it works. Details of the various analysis capabilities are then described in Sections 3 through 6. Sample results using the Solar, Anomalous, and Magnetospheric Particle Explorer (SAMPEX) mission are then provided in Section 7.

2.0 SYSTEM OVERVIEW

2.1 Flight Dynamics Analysis

Flight dynamics analysis is the process of generating information related to the position and orientation of a spacecraft relative to a selected reference frame, predicting mission-critical events, and monitoring on-board systems. When analysis is performed on a "near real-time" schedule it can be referred to as mission support.

Flight dynamics analysis can be divided into four major categories: data acquisition and preprocessing, trajectory and navigation analysis, attitude analysis, and results formatting and delivery. Data acquisition and

preprocessing deals with obtaining spacecraft data and converting data to formats compatible with analysis software. Trajectory and navigation analysis is comprised of orbit determination, orbit prediction, and mission event prediction. Attitude analysis consists of attitude determination, on-board computer (OBC) performance verification, and attitude sensor monitoring. Finally, results formatting and delivery provides interested parties with analysis results in proper formats.

2.2 Flight Dynamics Analysis Process

The flight dynamics analysis process is illustrated in Figure 1. Preprocessing software is used to read data and perform necessary format conversions. Analysis of the spacecraft trajectory and attitude are then performed. The attitude analysis depends upon information generated during the trajectory analysis, as depicted by the cross-feeds between the two analyses in Figure 1. Lastly, results are formatted and delivered.

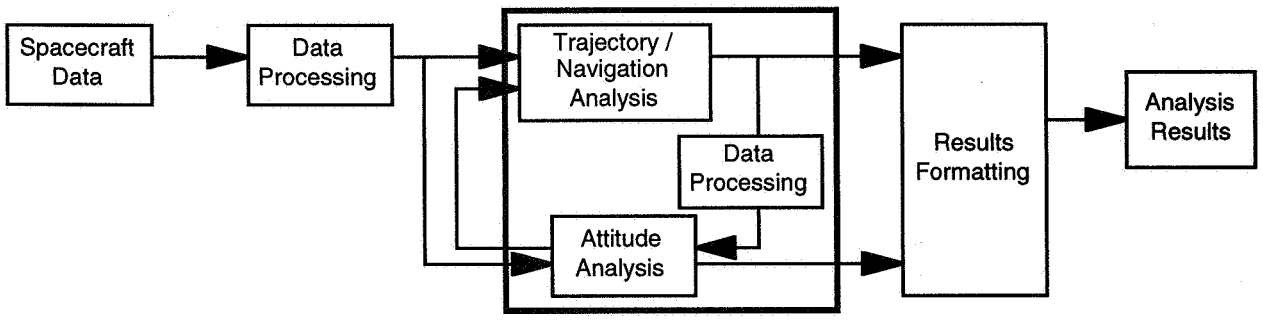

Figure 1, Flight dynamics analysis process.

2.3 SMAS Software

The SMAS is an integrated, workstation-based software system for performing trajectory and navigation analysis, as well as attitude analysis. A diagram of the SMAS is shown in Figure 2. The trajectory and navigation analysis component of the SMAS, which is shown as the top half of Figure 1, includes software for orbit determination, orbit prediction, and orbit event scheduling. This software, as configured for orbit analysis, will be referred to as the orbit analysis component.

The orbit analysis component of the SMAS currently accepts raw tracking data from NASA ground stations, preprocesses the raw tracking data, performs orbit determination, and performs orbit prediction. Several orbit event scheduling and other orbit analysis capabilities, e.g. spacecraft lighting time predictions and sun vector / geomagnetic field vector co-alignment predictions, have also been implemented.

The CONVERT utility developed by the FDCL, performs format and data conversion on raw tracking data from the Spacecraft Tracking and Data Network (STDN) [1]. This preprocessing of data is done before orbit determination is performed. The utility reads a Universal Tracking Data Format (UTDF) file, time sorts the data, checks for repeated data, and performs calculations and format conversions on the data.

One main module of the SMAS is the Satellite Tool Kit (STK) with the Precision Orbit Determination System (PODS) utility [2,3]. The OD process in the SMAS utilizes some data provided with PODS, plus several enhanced data sets integrated with PODS by the FDCL. The OD software uses a Bayesian batch weighted least-squares algorithm in its differential correction process. The orbit propagator uses a 12th-order Cowell numerical integration scheme to integrate the equations of motion [3,4]. Back-propagation is supported as well as forward-propagation, allowing the user to predict a spacecraft's previous trajectory without performing OD.

Software modules originally developed by the Goddard Space Flight Center (GSFC) include a utility for predicting sun-vector and magnetic-field vector alignment (SUNMAG), and the MATLAB Attitude Determination System (MLADS) [5,6]. Both of these packages have been modified by the FDCL for integration into the SMAS. The utility for ephemeris-file format conversion routine (STK2ADS) was also developed by the FDCL.

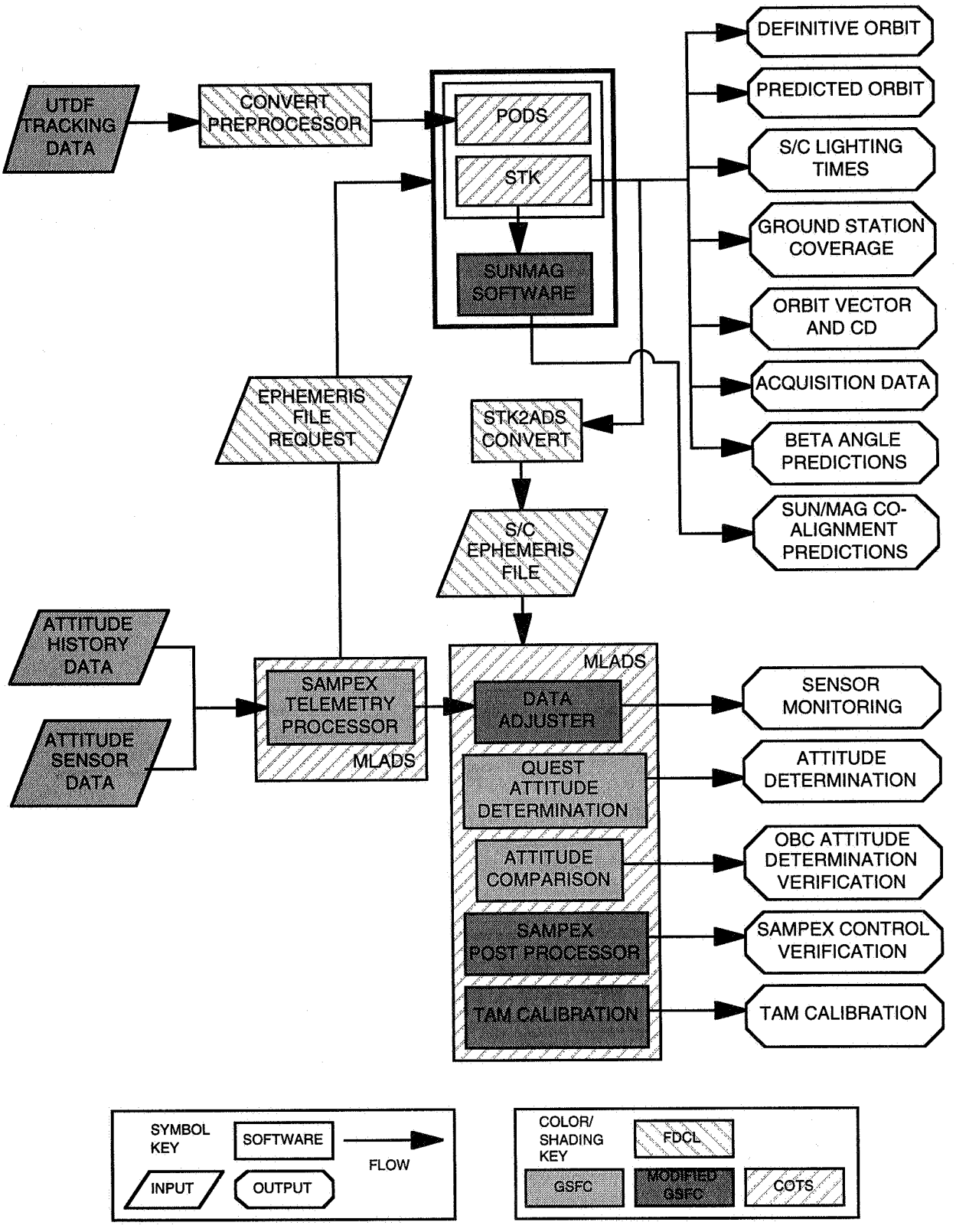

Figure 2, SMAS software diagram

3.0 DATA ACQUISITION AND PREPROCESSING

Data acquisition and preprocessing deals with obtaining and formatting data for analysis. Spacecraft data consists of tracking data and attitude-sensor telemetry. Tracking data is spacecraft position and velocity information, such as range and range-rate data, typically obtained from ground tracking stations. Attitude telemetry contains time histories of attitude quaternions, sensor output, and actuator data down-linked to ground stations.

3.1 Data Acquisition

Currently, spacecraft tracking and attitude data is acquired from GSFC via File Transfer Protocol (FTP).

3.2 Data Preprocessing

In several cases, it is necessary to preprocess data before analysis can proceed. The SMAS currently has the capability to preprocess spacecraft tracking data in Universal Tracking Data Format (UTDF) and attitude telemetry data for the SAMPEX mission. A data processing utility, STK2ADS, has also been developed for converting spacecraft ephemeris files generated in STK to a format easily readable in MATLAB.

3.2.1 Tracking data preprocessing

Spacecraft tracking data is obtained from the NASCOM network as UTDF files. This data format is not directly compatible with the STK/PODS module. Therefore, preprocessing of the UTDF data into one of the compatible formats is required. The CONVERT utility was built by FDCL staff to convert 72 or 75-byte UTDF data to the GEOS-C Data format, which is compatible with STK/PODS.

The CONVERT tracking data preprocessor reads a UTDF file, time-sorts the data, checks for duplicate data points, performs calculations and data conversions, and then writes tracking data in GEOS-C data format.

3.2.2 SAMPEX telemetry data preprocessing

Attitude analysis is performed using the MLADS. The MLADS accepts MATLAB compatible files. Therefore, telemetry processing of unique data formats, such as binary data packets, must be created. The MLADS has a telemetry processor for raw SAMPEX sensor and attitude files. This routine reads binary SAMPEX data files into MATLAB and converts units if required.

3.2.3 STK ephemeris processing

A data preprocessor is also used to interface an STK generated ephemeris file with the MLADS. The program STK2ADS reads an STK-generated ephemeris, adds a file header, and rewrites the data in the appropriate format. The header contains the file start time, stop time, data interval, spacecraft name, and the propagator used to generate the ephemeris.

4.0 TRAJECTORY AND NAVIGATION ANALYSIS

Trajectory and navigation analysis consists of orbit determiantion, orbit prediction, and orbit mission event prediction. Orbit determination is the best estimate of a spacecraft's orbit based on tracking data. Orbit prediction is the process of propagating an orbit state vector to estimate future spacecraft orbital states. Lastly, orbit event prediction involves predicting future mission events, such as spacecraft lighting times, ground station view times and acquisition data, sun angle predictions, and sun vector / geomagnetic field vector co-alignment predictions.

4.1 Orbit Determination and Prediction

For orbit determination and orbit prediction, the SMAS utilizes the STK/PODS COTS module. This package uses a batch least-squares algorithm to estimate the spacecraft's orbit based on tracking measurements [2,3] and has several orbit propagators for orbit prediction. The FDCL has customized this module with additional geopotential models, a ground station database, more-accurate astrodynamic constants, and optimal estimation control parameters. Orbit determination and prediction results from the FDCL customized STK/PODS module have been shown to agree well with similar results obtained from the Goddard Trajectory Determination System [7].

4.2 Orbit Event Prediction

Several orbit events are currently generated using the SMAS. These include spacecraft lighting times, ground station coverage, spacecraft acquisition data, Sun angle predictions, and Sun/magnetic field vector co-alignment predictions. The SMAS uses STK to generate spacecraft lighting times, ground station coverage, and spacecraft acquisition data. Lighting times are predicted times and duration's a spacecraft will be in Sunlight, partial eclipse, or total eclipse. Ground station coverage deals with the times a spacecraft can be viewed by selected ground stations. Acquisition data is used to indicate to the ground tracking stations where and when to point an antenna in order to acquire a spacecraft. Predictions of the Sun angle, defined as the angle between the vector pointing to the Sun and the orbit normal, are computed using an FDCL developed utility. Lastly, the SMAS predicts Sun/magnetic field vector with a modified GOTS utility.

5.0 ATTITUDE ANALYSIS

Flight dynamics attitude analysis includes estimation of the the orientation of the spacecraft relative to a reference frame, and verifying the performance of on-board systems such as the OBC and attitude sensors. The SMAS uses an FDCL modified version of the MLADS for these analyses.

5.1 Attitude Determination

Attitude determination is the process of estimating the relationship between vectors measured in a spacecraft fixed coordinate system, as well as in a reference coordinate system. A measurement vector is the position of a known object or quantity, such as the Sun, as seen in a spacecraft coordinate system by an on-board sensor. Reference vectors are generated in an inertial coordinate frame for each measurement vector. These reference vectors are computed using environmental models, such as a Solar-Lunar-Planetary (SLP) ephemeris for the positions of the Earth and Sun, or the Inernational Geomagnetic Reference Field (IGRF) model for the Earth's magnetic field. The SMAS currently includes algorithms for processing two Digital Sun Sensors (DSS), which measures the position of the Sun, and two Three-Axis Magnetometers (TAM), which measure the three components of the Earth's magnetic field.

Currently, two single-frame estimation techniques are availible in the SMAS, the TRIAD (deterministic) algorithm and the QUEST (optimal) algorithm [8-10]. Both methods require at least two sensors in order to determine the attitude of the vehicle. Using the MLADS graphical user interface, attitude determination results can be viewed graphically as quaternions and Euler angles.

5.2 OBC Performance Verification

OBC performance verification can include checking OBC attitude determination, control performance, and/or ephemeris calculations. The SMAS has analysis capabilities for verifying performance of OBC attitude determination and computing information related to the control of the SAMPEX spacecraft. OBC attitude verfication is performed, using the MLADS, by comparing ground computed quaternions with OBC computed quaternions. This comparison is done by rotating the single-frame quaternions to the times of the OBC quaternions and then comparing the two. Statistics about the comparison are then calcuated. SAMPEX control performance is examined by computing variances of the Euler angles, the Sun angle, the pseudozentih angle, and the ram constraint angle in a Sun frame as defined in reference [11].

5.3 Sensor Monitoring

It may be necessary to monitor attitude sensors periodically to confirm that systems are operating nominally. Using the MLADS this is easily accomplished with a graphical interface. Sensor data can be viewed after telemetry processing, and data points not consistent with data trends can be examined closely or omitted from analysis.

In addition to monitoring attitude sensors, periodic calibrations of sensors may also be required. Currently the SMAS has the ability to perform attitude dependent three-axis magnetometer calibration using a modified version of a routine provided in the MLADS. This computes the TAM bias, scale factor/misalignment matrix, magnetic torquer compensation matrix, and associated statistics.

6.0 RESULTS FORMATTING AND DELIVERY

Results from the flight dynamics analysis process are delivered to "customers" such as the spacecraft flight operations team, for use in the command and control of the vehicle. Therefore, to best interface with the operations team it may be necessary to reformat some results. Transferring results to the flight operations team can be accomplished using FTP. Another options currently being examined is to post results on a World-Wide-Web page for public comsumption.

7.0 EXAMPLE ANALYSIS

The recent case study used in the evaluation of the SMAS was the SAMPEX mission. SAMPEX is the first of the Small Explorer (SMEX) missions, and was launched on July 2, 1992 into a 550 x 750 km orbit, at 82 degrees inclination [10,12,13]. Tracking, telemetry, and command are performed via several existing ground stations.

The spacecraft is a three-axis stabilized satellite, equipped with a digital sun sensor (DSS) and three-axis magnetometer (TAM) for attitude determination, and a magnetic torquer assembly (MTA) and a reaction wheel (RW) for attitude control. On-board attitude determination and control are computed using the TRIAD algorithm, with attitude quaternions stored everytime the vehicle attitude changes by one degree. The following discussion will parallel the above description of the system. Analysis will be presented based on tracking data taken on February 5-7, 1997 and sensor and attitude data taken on February 7, 1997.

7.1 Data Acquisition and Preprocessing

SAMPEX tracking data is currently scheduled to be received every Monday, Wednesday, and Friday. Attitude telemetry is obtained daily Monday through Friday. Tracking data is recieved in 72-byte UTDF format and is converted to GEOS-C using the CONVERT utility.

Sensor and attitude data is read into the MLADS using the SAMEX telemetry processor. The data is then converted from SAMPEX counts to units consistent with the Multimission Three-Aix Stabilized Spacecraft (MTASS) Flight Dynamics Support System (FDSS). Figure 3 shows a sample of processed Sun sensor data.

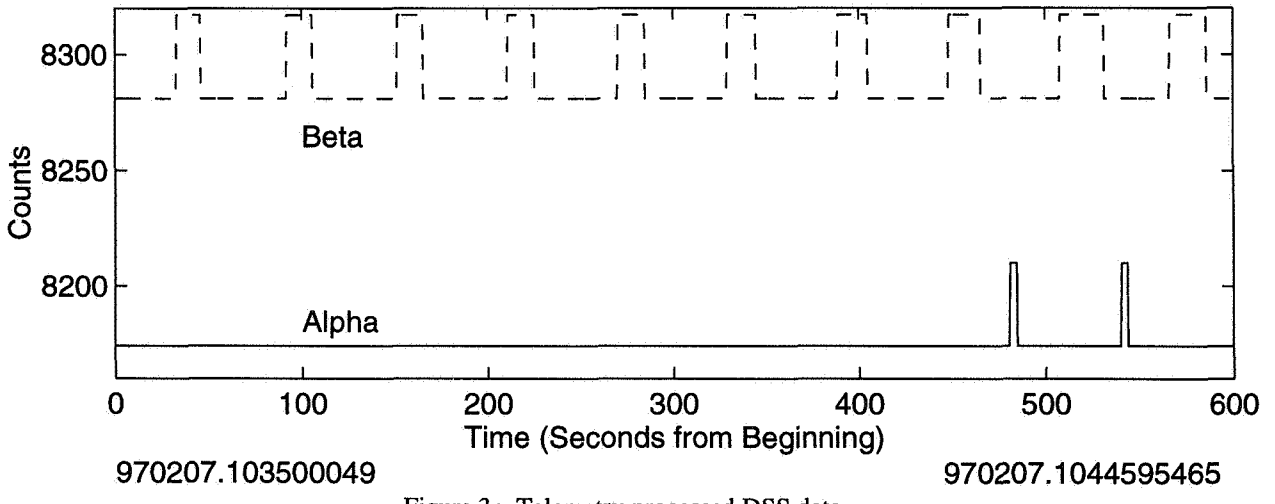

Figure 3: Telemetry processed DSS data

7.2 Trajectory and Navigation Analysis

For SAMPEX, the required trajectory and navigation analysis is divided into "daily" and "weekly" results. The "daily" results are generated every Monday, Wednesday, and Friday, and include determination of the orbit vector and drag coefficient, generation of a predicted ephemeris and generation of acquisition data. "Weekly" results also include acqisition data, as well as spacecraft ground track; Sun angle predictions; and Sun-

vector/magnetic-field-vector co-alignment angles. These are generated on Fridays for a 28-day period beginning at 0 hours GMT the following Monday [14].

7.2.1 Orbit determination and prediction

Orbit determination and prediction is performed using the modified STK/PODS software module. This module uses tracking data obtained over a 58- or 82-hour period to determine the definitive orbit, and generates the orbit vector and drag coefficient for the beginning of the day corresponding to the orbit vector determined. In addition, a 7-day ephemeris is predicted and used for attitude analysis and acquisition data. Lastly, a 28-day ephemeris is created for use in predicting "weekly" SAMPEX products.

7.2.2 Orbit event prediction

Orbit event prediction for SAMPEX is performed using several modules, including STK, SUNMAG, and a Beta angle prediction utilitiy. Using the 7-day ephemeris predicted, spacecraft acquisition data is generated, along with ground station view times, a spacecraft ground track, and predicted spacecraft lighting times for a 28-day period. Sun vector/magnetic field vector co-alignment predictions are then computed, and the Sun-angle predictions are performed using the Beta angle utility developed by the FDCL.

In addition to the above events, others of interest include, for example, the periods of crossing over the mid-latitude region, and periods of crossing the south-atlantic anomoly. Sample reports summarizing such predicted times are shown in Table 1 and Table 2, respectively.

AreaTarget-Mid_Latitude_Region-To-Vehicle-SAMPEX_19970207: Access Summary Report

Access	Start Time (UTCG)	Stop Time (UTCG)	Duration (sec)
1	10 Feb 1997 00:00:00.00	10 Feb 1997 00:23:48.67	1428.674
2	10 Feb 1997 01:25:56.18	10 Feb 1997 01:58:49.96	1973.777
3	10 Feb 1997 03:01:50.97	10 Feb 1997 03:33:48.19	1917.227
4	10 Feb 1997 04:37:53.02	10 Feb 1997 05:09:19.74	1886.722
5	10 Feb 1997 06:13:01.00	10 Feb 1997 06:44:57.10	1916.095
	o		
	o		
	o		
413	9 Mar 1997 15:00:41.17	9 Mar 1997 15:35:17.71	2076.545
414	9 Mar 1997 16:37:37.56	9 Mar 1997 17:13:09.81	2132.248
415	9 Mar 1997 18:14:33.59	9 Mar 1997 18:50:30.64	2157.045
416	9 Mar 1997 19:51:16.62	9 Mar 1997 20:26:19.19	2102.579
417	9 Mar 1997 21:27:38.71	9 Mar 1997 22:01:13.90	2015.196
418	9 Mar 1997 23:03:24.68	9 Mar 1997 23:36:13.77	1969.093

Global Statistics

Min Duration	1	10 Feb 1997 00:00:00.00	10 Feb 1997 00:23:48.67	1428.674
Max Duration	400	8 Mar 1997 18:05:45.85	8 Mar 1997 18:41:45.73	2159.888
Mean Duration				2022.149
Total Duration				845258.480

Table 1, Periods of Crossing the Mid-latitude Region

7.3 Attitude Analysis

7.3.1 Attitude determination

Attitude analysis begins by generating measurement and reference vectors. This is done using the MLADS data adjuster, which was modified by the FDCL. Measured Sun vectors are generated from DSS measurements, and corresponding reference vectors are read from an SLP file. The vector output of the TAM is corrected for bias and effects of torquer bar influences, then a ninth order IGRF model using 1990 coefficients is used to compute the reference magnetic field vector. In generating both reference vectors, the spacecraft position is obtained from the ephemeris file generated in STK. The output of the data adjuster can then be viewed graphically or in tabular form, as shown in Figure 4 and Table 3, for the TAM measurements and reference vectors, respectively.

AreaTarget-South_Atlantic_Anomaly-To-Vehicle-SAMPEX_19970207: Access Summary Report

Access	Start Time (UTCG)	Stop Time (UTCG)	Duration (sec)
1	10 Feb 1997 00:25:47.48	10 Feb 1997 00:47:16.13	1288.644
2	10 Feb 1997 01:00:45.37	10 Feb 1997 01:15:10.69	865.321
3	10 Feb 1997 02:08:01.73	10 Feb 1997 02:21:35.07	813.343
4	10 Feb 1997 02:32:12.88	10 Feb 1997 02:56:15.66	1442.776
5	10 Feb 1997 04:08:00.99	10 Feb 1997 04:35:32.25	1651.255
	o		
	o		
	o		
462	9 Mar 1997 18:45:39.57	9 Mar 1997 19:14:19.15	1719.577
463	9 Mar 1997 20:26:01.98	9 Mar 1997 20:49:25.84	1403.861
464	9 Mar 1997 21:05:19.20	9 Mar 1997 21:12:31.13	431.934
465	9 Mar 1997 22:08:25.26	9 Mar 1997 22:24:36.40	971.136
466	9 Mar 1997 22:35:15.06	9 Mar 1997 22:56:49.64	1294.580

Global Statistics

Min Duration	220	23 Feb 1997 00:51:36.08	23 Feb 1997 00:54:53.67	197.594
Max Duration	460	9 Mar 1997 15:28:58.15	9 Mar 1997 16:01:13.77	1935.613
Mean Duration				1447.070
Total Duration				674334.536

Table 2, Periods of Crossing the South-Atlantic Anomoly

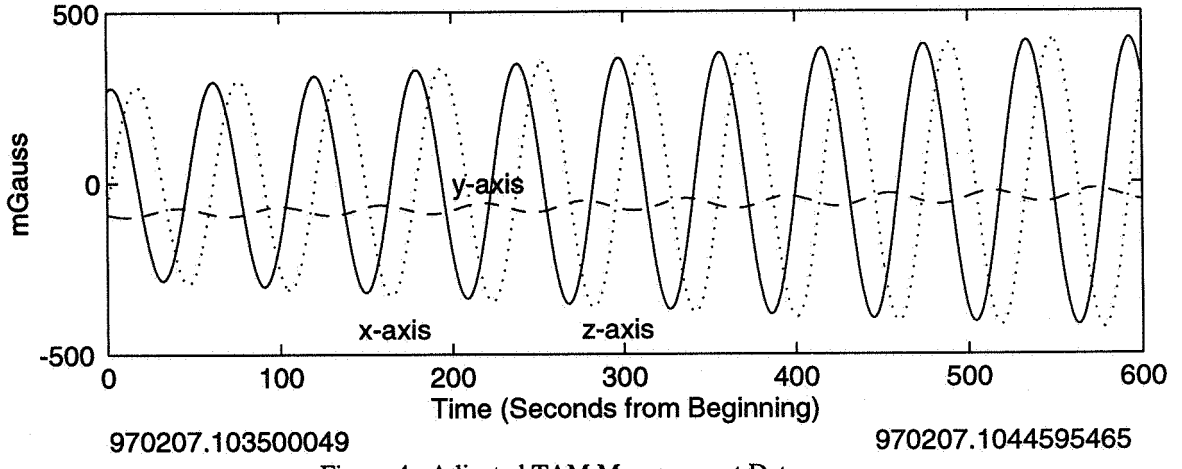

Figure 4, Adjusted TAM Measurement Data

Table 3, Sample reference TAM data in Tabular format

YYMMDD.HHMMSSmmm	X-axis (mG)	Y-axis (mG)	Z-axis (mG)
970207.1035000496	1.184311674380559e+02	2.360618212567443e+02	1.247491793654644e+02
970207.1035005488	1.185104233527069e+02	2.362011985225806e+02	1.246074006581876e+02
970207.1035010479	1.185896186899121e+02	2.363405175283418e+02	1.244655004433938e+02
970207.1035015471	1.186687533848854e+02	2.364797781885184e+02	1.243234787691050e+02
970207.1035020463	1.187478273812836e+02	2.366189804203714e+02	1.241813356807788e+02
970207.1035025492	1.188274330124566e+02	2.367591632818068e+02	1.240380081514656e+02
970207.1035030484	1.189063849685715e+02	2.368982479651160e+02	1.238956214711904e+02
970207.1035035476	1.189852868106326e+02	2.370372775078515e+02	1.237531100897450e+02
970207.1035040468	1.190641169307888e+02	2.371762447415612e+02	1.236104809092626e+02
970207.1035045497	1.191434766185580e+02	2.373161905115886e+02	1.234666638447572e+02

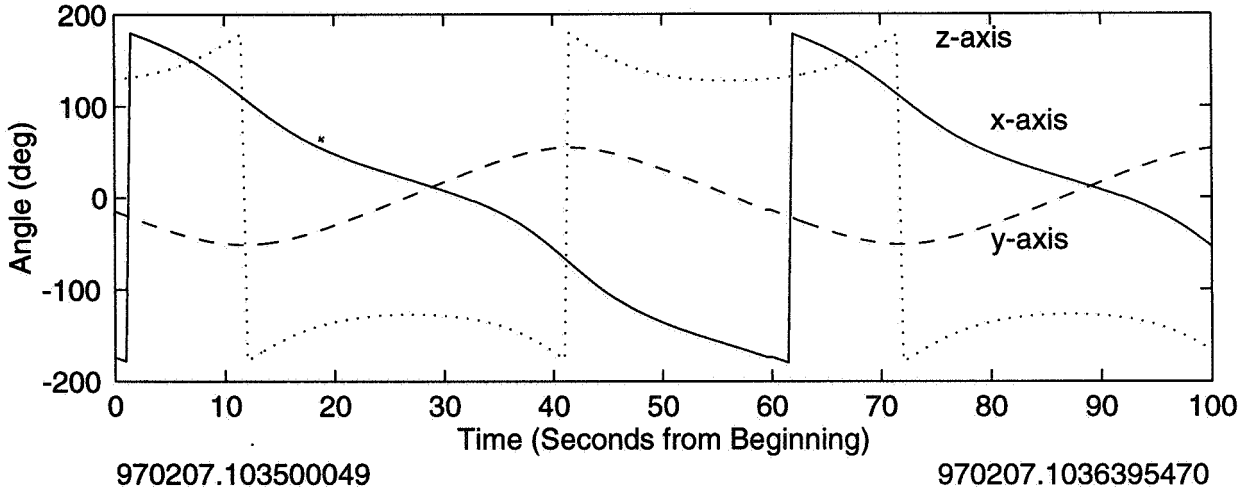

Figure 5, Euler Angle History

Attitude determination is performed using the QUEST algorithm. Results can be viewed as either quaternions or Euler angles, in graphical and tabular form. Figure 5 shows Euler angles corresponding to QUEST attitude results.

7.3.2 OBC performance verification

SAMPEX OBC attitude determination results are verified by comparing the ground-computed attitude history to those computed on-board the vehicle. The comparison is performed using a MLADS option. Statistics about the Euler angles, the mean and standard deviation, are displayed in a window when the comparison is complete. These results are printed to a report file, as shown in Table 4. SAMPEX has a two degree per axis accuracy requirement, therefore, the number and percentage of comparison points exceeding these limits are also computed.

```
SAMPEX OBC ATTITUDE DETERMINATION PERFORMANCE REPORT FILE

Stored OBC Quaternion History Start Time =  970204.114716101
Stored OBC Quaternion History Stop Time  =  970207.104510080

Ground Computed Quaternion Start Time =  970207.103500050
Ground Computed Quaternion Stop Time  =  970207.104459547

Comparison Start Time =  970207.103500000
Comparison Stop Time =  970207.104500000

Euler Angle Sequence =  2 - 1 - 3

Number of OBC and Ground Computed Attitude Quaternions Compared =  1198.000000

                Mean Error (deg)      Error STD (deg)
X-Axis        0.2944138944076143   0.3051926093108637
Y-Axis       -1.531463853061803    0.7685610499646889
Z-Axis       -0.3088042591185573   0.3286522358926362

Estimation Comparison Limit Checks

              Limit (deg)   # Points Over       Percentage Over
X-Axis         2.00000            0             0.0000000000
Y-Axis         2.00000          380            31.7195330000
Z-Axis         2.00000            0             0.0000000000
```

Table 4 Sample attitude comparison results report

SAMPEX control performance verification is done by computing the variance in Euler angles, the Sun angle, the pseudozenith angle, and the ram constraint angle in a Sun coordinate frame. The SAMPEX post-processor option in the MLADS is used for these computations. Angle variances are displayed in a window and then printed to a report when the processing is complete. Table 5 contains a sample SAMPEX OBC Control Verification report.

```
SAMPEX OBC CONTROL PERFORMANCE REPORT FILE

Ground Quaternion Start Time =  970207.103500050
Ground Quaternion Stop Time  =  970207.104459547

X-Axis Euler Angle Variance (deg) =   51.8217028438366
Y-Axis Euler Angle Variance (deg) =    1.77643839383983
Z-Axis Euler Angle Variance (deg) =    0.609665538960451

Sun Angle Variance (deg) =    1.8781172222304

Pseudozenith Angle Variance (deg) =  104.32808660923

Ram Constraint Angle Variance (deg) =  51.0293925046285
```

Table 5, Sample SAMPEX control verification

7.3.3 Sensor monitoring

SAMPEX attitude sensor monitoring, and calibration, is performed on an as needed basis. Monitoring is done by viewing the telemetry processing results graphically and looking for data which has spikes, or is not consistent with observed trends. Sensor calibration tasks for SAMPEX are comprised of computing the TAM bias. Results of a TAM calibration are printed to a report, a sample of which is shown in Table 6.

```
SAMPEX THREE-AXIS MAGNETOMETER CALIBRATION REPORT FILE
 Start time =  970207.103500050  Stop time =  970207.104459547

 Old bias =   700.0000000   700.0000000   700.0000000

 New bias =   703.1248388   701.2586634   701.0968185

 Old SF/Align Matrix =   1.0000000   0.0000000   0.0000000
                         0.0000000   1.0000000   0.0000000
                         0.0000000   0.0000000   1.0000000

 New SF/Align Matrix =    1.0088988   -0.0831806   -0.0081068
                          0.0158213    0.9661495    0.0116067
                         -0.0011203    0.0024631    0.9950176

 Compensation Matrix C:  tam=tam + C * mta

 Old Compensation Matrix =   0.7000000   -0.0699980   -0.0699980
                             0.2800000    1.0900000    2.1000000
                            -0.5300000    0.6300000   -1.5800000

 New Compensation Matrix =   -0.7700597   -0.0225569   -0.6193168
                              0.0524921    1.2491221    1.9546606
                             -1.1008405    0.3432101   -1.1318349

 Sum of Old Residuals (Bmeas^2 - Bref^2)   5.804144e+09

 Sum of New Residuals (Bmeas^2 - Bref^2)   1.076742e+09

 Old average RMS residual   5.526735

 New average RMS residual   1.586739

 Covariance of computed bias =   0.05333333            0            0
                                       0   0.05333333            0
                                       0            0   0.05333333

 Covariance of computed SF/Alignment =   8.173914e-07   3.601322e-07   5.555304e-09
                                         3.601322e-07   1.238009e-05   4.546305e-07
                                         5.555304e-09   4.546305e-07   8.322521e-07

 Covariance of computed Comp Matrix =   0.09259322   0.01152379    -0.0147163
                                        0.01152379   0.002012573   -0.002550774
                                       -0.0147163   -0.002550774    0.004098286
```

Table 6, Sample TAM Calibration Report

8.0 CONCLUSIONS

The Spacecraft Mission Analysis System is a completely integrated, workstation-based system for performing spacecraft flight dynamics analysis and mission support. The system integrates Commercial Off-the-Shelf, modified Goddard Off-the-Shelf, and FDCL developed software. The system can perform a variety of orbit

and attitude related analyses, including orbit determination and prediction, orbit event scheduling, attitude determination, and on-board system verifications. It is modular in form, and flexible by design, to allow for relatively easy reconfiguration, to make it applicable for different missions.

9.0 REFERENCES

1. McConnell, C., Cummings, S., and Schmidt, D., "Comprehensive Report on the CONVERT Tracking Data Preprocessor," Flight Dynamics and Control Lab, University of Maryland, 1997.

2. Satellite Tool Kit User's Manual, Analytical Graphics, Inc., July 1996.

3. Precision Orbit Determination System User's Manual, Analytical Graphics, Inc., March 1997.

4. Knapp, Chris, Computer Sciences Corporation, Meeting on 4 September 1996.

5. Harman, R., "MATLAB Attitude Determination System Users Guide," Preliminary Report, GSFC, Jan. 1997.

6. Harman, R., "MATLAB Attitude Determination System Functional Specification," Preliminary Report, GSFC, Oct. 1996.

7. McConnell, C., Schmidt, D., "A Comparison Study of the Flight Dynamics and Control Laboratory's Orbit Analysis System With the Goddard Trajectory Determination System (GTDS)," Presented at the Flight Mechanics Symposium, NASA Goddard Space Flight Center, May 1997.

8. Shuster, M., Oh, S., "Three-Axis Attitude Determination from Vector Observations," Journal of Guidance and Control, Vol.4, No. 1, Jan-Feb 1981, pp. 70-77.

9. Wertz, J. R. (ed.), *Spacecraft Attitude Determination and Control*, D. Reidel Publishing Co., Dordrecht, 1984.

10. Lambertson, M., Keat, J., Scheidker, E., "Multimission Three-Axis Stabilized Spacecraft (MTASS) Flight Dynamics Support System (FDSS) Mathematical Background," Goddard Space Flight Center, September 1993.

11. Crouse, P. "Solar, Anomalous, and Magnetospheric Particle Explorer (SAMPEX Real-Time Attitude Determination System for Personnal COmputer (SRTADS/PC) Specifications Document," Goddard Space Flight Center Flight Dynamics Division, September 1991.

12. Keating, T., et. al., "Small Explorer Mission 1 (SMEX-1) Solar, Anomalous, and Magnetospheric Particle Explorer (SAMPEX) Flight Dynamics Support System (FDSS) Requirements Specifications," NASA GSFC, July 1990.

13. Raina, P., et. al., "Small Explorer Mission 1 (SMEX-1): Solar, Anomalous

14. Crouse, P., Private Commumications, February 1997.

Distortion and Alignment Calibration of a CCD-Based Fine Sun Sensor

by
Dr. Mark Pittelkau
CTA Space and Telecommunications Systems, Inc.

Abstract

CTA Space Systems has developed a CCD-based fine sun sensor that delivers medium accuracy (0.03 degrees) at very low cost. The philosophical, theoretical, and practical considerations for calibrating this sensor are discussed in this paper. This paper shows that a physical interpretation of the calibration parameters leads to an unnecessarily complicated parameter estimation algorithm. Three physical parameters are included in the model, however. These are the center offset coordinates and a focal-length correction. The least-squares estimation technique is briefly reviewed, and a formula is derived for the covariance of both the estimated parameters and of the corrected data. A fixed-point alignment correction algorithm is also derived so that raw sensor data may be corrected. Results of a simulated calibration of the sensor are shown.

1 Introduction

CTA Space and Telecommunications Systems has developed a CCD-based fine sun sensor that delivers medium accuracy (0.03 degrees) at very low cost. The philosophical, theoretical, and practical considerations for calibrating this sensor are discussed in this paper. In particular, the approach of Schuster et al. [1, 2] is modified and extended in this paper and is applied to an actual calibration problem. The discussion is general enough to be widely applied to a variety of sensors. This paper discusses the physical interpretation of the alignment error model and shows that the estimation technique in [2] is unnecessarily complicated as a result of insisting on a physical interpretation of the calibration parameters. This paper gives a more natural view. Three new physical parameters are introduced to the model, however. These are the center offset coordinates and a focal-length correction for the sensor. The center offsets are shown to be linearly dependent on existing calibration coefficients, and are subsequently eliminated from the model. The least-squares estimation technique is briefly reviewed, and a formula is derived for the covariance of both the estimated parameters and of the corrected data. A fixed-point alignment correction algorithm is also derived so that raw sensor data may be corrected. Results of a simulated calibration of the sensor are shown.

Schuster and Lopes [1, 2] considered the problem of focal plane calibration and showed what problems can arise in the present day approach of alternatively estimating rotation and distortion parameters. This iteration occurs both incidentally and deliberately due to either a lack of understanding of the total system calibration problem or a "cultural" problem in which sensor alignment calibration and focal plane calibration are often performed by independent teams with little regard for each other's function. It is made apparent in this paper that insistence on having a physical interpretion of the calibration parameters leads to an unnecessarily constrained and possibly inferior least-squares solution. This paper addresses the calibration problem but dismisses much of the physical interpretation of the calibration parameters. It is anticipated that this paper will clarify the work in [1, 2] and that the approach is more practical. One important contribution here is an algorithm for the computation of the stimulus vector (the input vector to the sensor—the sun vector for a sun sensor, for example) given the raw measurement and the calibration coefficients.

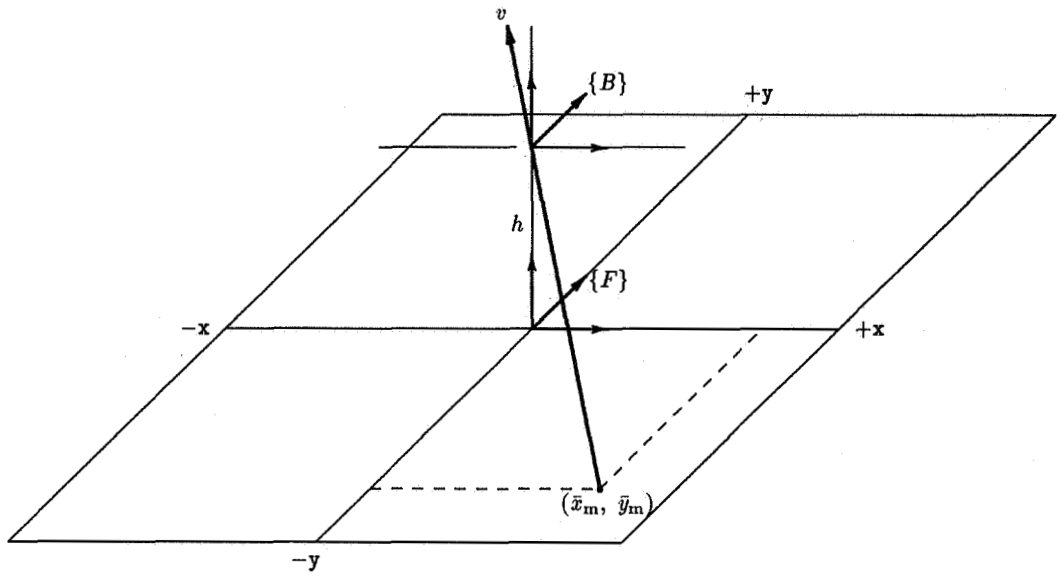

Figure 1: Fine Sun Sensor coordinate systems.

2 Focal Plane Distortion Model

The sensor coordinate systems are shown in Figure 1. The boresight coordinate system $\{B\}$ is located at the center of a pinhole, while the focal plane coordinate system $\{F\}$ is located on the focal plane. Note that $\{F\}$ is not necessarily located directly below $\{B\}$, nor is it necessarily aligned with $\{B\}$. The true focal length shown in the figure is h. The stimulus vector v in $\{B\}$ has coordinates $(x,\ y,\ 1)$. The rotation of $\{F\}$ with respect to $\{B\}$ due to misalignment, along with focal length error and distortion of the focal "plane" results in the measurement vector $(\bar{x}_m,\ \bar{y}_m,\ h)$. The Fine Sun Sensor produces a centroid sun location measurement $(\bar{x}_c,\ \bar{y}_c)$ relative to the $(-x_{max},\ -y_{max})$ corner of the CCD array. The sun vector measurement is then given by

$$\begin{bmatrix} \bar{x}_m \\ \bar{y}_m \\ h \end{bmatrix} = \begin{bmatrix} \bar{x}_c - \bar{x}_o \\ \bar{y}_c - \bar{y}_o \\ h \end{bmatrix} \tag{1}$$

where $x_o = 512$ pixels and $y_o = 512$ pixels are the nominal center offsets and where h is the nominal focal length conveniently expressed in units of pixels (1 pixel = 0.009 mm). We now scale this so that the focal length is non-dimensional and nominally equal to 1:

$$\begin{bmatrix} x_m \\ y_m \\ 1 \end{bmatrix} = \begin{bmatrix} x_c - x_o \\ y_c - y_o \\ 1 \end{bmatrix} \tag{2}$$

Let $v'' = Rv$ be the vector measured in focal plane coordinates, where $v = (x,\ y,\ 1)^T$ is a stimulus vector in boresight coordinates, R is a rotation matrix, and $v'' = (x'',\ y'',\ z'')^T$. Schuster [1] showed that the elements of $v' = v''/z''$ can be represented by a polynomial Taylor series expansion of the form

$$v' = \begin{bmatrix} x' \\ y' \\ 1 \end{bmatrix} = \begin{bmatrix} x \\ y \\ 1 \end{bmatrix} + \begin{bmatrix} \tilde{F}_1(x,y) \\ \tilde{F}_2(x,y) \\ 0 \end{bmatrix} \tag{3}$$

where

$$\begin{aligned}\tilde{F}_1(x,y) &= \sum_{i=0}^{\infty}\sum_{j=0}^{\infty} a_{ij}x^i y^j \\ &= a_{0,0} + a_{1,0}x + a_{0,1}y + a_{1,1}xy + a_{2,1}x^2 + a_{1,2}y^2 + a_{2,2}x^2y^2 + \cdots \\ \tilde{F}_2(x,y) &= \sum_{i=0}^{\infty}\sum_{j=0}^{\infty} b_{ij}x^i y^j \\ &= b_{0,0} + b_{1,0}x + b_{0,1}y + b_{1,1}xy + b_{2,1}x^2 + b_{1,2}y^2 + b_{2,2}x^2y^2 + \cdots\end{aligned} \tag{4}$$

and where the $a_{i,j}$ and $b_{i,j}$ can be computed by a recursion in terms of the elements of R.

In practice, of course, the two series need to be terminated to a relatively low order since there is necessarily a practical limit to the number of alignment parameters that can be estimated. This limit is due to the time and expense required to take measurements to obtain calibration data. In addition, real-time measurement calibration should not require a large amount of processing. A reasonable low-order model is possible only if the rotation and distortion are small. Large á priori rotations can be removed by applying these rotations to the stimulus vectors. Note that these two series do not need to be truncated to the same order, although there is usually no compelling reason to make them different. Here we define *order* to be equal to $\max(i,j)$. We also define *total order* to be equal to $\max(i+j)$.

To obtain a more complete model of the measurements than (3), nominal center offsets x_o and y_o, center offset corrections δ_x and δ_y, a non-dimensional focal length correction f, and measurement noise η_x and η_y are included in the model. The model is now

$$\begin{aligned}x_c &= x_o + x + \delta_x + fx + F_1(x,y) + \eta_x \\ y_c &= y_o + y + \delta_y + fy + F_2(x,y) + \eta_y\end{aligned} \tag{5}$$

where

$$\begin{aligned}F_1(x,y) &= \sum_{i=0}^{r}\sum_{j=0}^{r} a_{ij}x^i y^j \\ F_2(x,y) &= \sum_{i=0}^{r}\sum_{j=0}^{r} b_{ij}x^i y^j\end{aligned} \tag{6}$$

are of order r and total order $2r$.

With the inclusion of the center offsets and the focal length correction, the rotation error model becomes

$$v'' = \delta + (1+f)Rv \tag{7}$$

where $\delta = (\delta_x \ \delta_y)^T$. It is shown in [1, 2] that for small rotations $\boldsymbol{\theta} = (\theta_1, \ \theta_2, \ \theta_3)^T$, the truncated model for v'' is

$$\begin{aligned}x_c &= x_o + x + \delta_x + fx - \theta_2 + \theta_3 y + \theta_1 xy - \theta_2 x^2 + \eta_x \\ y_c &= y_o + y + \delta_y + fy + \theta_1 - \theta_3 x - \theta_2 xy + \theta_1 y^2 + \eta_y\end{aligned} \tag{8}$$

Comparing this with (5) yields the equations and parameter constraints

$$\delta_x - \theta_2 = -a_{0,0} \tag{9}$$
$$\delta_y + \theta_1 = b_{0,0} \tag{10}$$
$$f = a_{1,0} \stackrel{c}{=} b_{0,1} \tag{11}$$
$$\theta_1 = a_{1,1} \stackrel{c}{=} a_{0,2} \stackrel{c}{=} b_{0,2} \tag{12}$$
$$\theta_2 = -a_{2,0} \stackrel{c}{=} -a_{2,0} \stackrel{c}{=} -b_{1,1} \tag{13}$$
$$\theta_3 = a_{0,1} \stackrel{c}{=} -b_{1,0} \tag{14}$$
$$a_{1,2} \stackrel{c}{=} a_{2,1} \stackrel{c}{=} 0 \tag{15}$$
$$b_{1,2} \stackrel{c}{=} b_{2,1} \stackrel{c}{=} 0 \tag{16}$$

where $\stackrel{c}{=}$ means "constrained to be equal to".[1] Some of the constraints go away for $r = 1$. It would appear from this model that θ_1 and θ_2 *are* distinguishable from the center offsets since θ_1 and θ_2 not only appear linearly with δ_x and δ_y, but also are coefficients of x^2 and y^2. The converse was claimed in [1, 2].

Consider the approximation[2] $R = I - [\boldsymbol{\theta}\times]$. Subsituting this into (7) yields

$$\begin{aligned} x_c &= x_o + x + \delta_x + fx - \theta_2 + \theta_3 y + \eta_x \\ y_c &= y_o + y + \delta_y + fy + \theta_1 - \theta_3 x + \eta_y \end{aligned} \tag{17}$$

which is the same as (8) except that the total order 2 terms do not appear. The rotation angles θ_1 and θ_2 cannot be distinguished from the center offsets in this model. Indeed, when generating data for the purpose of estimating parameters, it is best to compute $R(\boldsymbol{\theta})$ exactly instead of using the approximation $R = I - [\boldsymbol{\theta}\times]$, otherwise the estimated coefficients of the xy, x^2, and y^2 terms should be expected to be zero.

The series expansion (4) can be also used to model focal plane distortion. Terms of up to order two represent a small rotation, and so all terms of total order less than one can be omitted from the distortion model. Coefficients of the remaining terms form a parameter vector $\boldsymbol{\lambda}$. Observe that terms of total order two are not eliminated from the distortion model since they by themselves do not represent rotations.

In [2] there is some discussion about the order of rotation and distortion when modeling these error processes. Consider what happens to a stimulus vector input into the boresight. We have a reference frame attached to (what we believe is) the focal plane, which may be rotated slightly with respect to the boresight frame. Thus, the first step is to transform the stimulus vector from boresight coordinates to focal plane coordinates. Next, the focal plane may have undulations in it, and other distortions such as lens or pinhole effects may contribute to error. Thus it makes sense to apply a distortion model to the rotated stimulus vector, not the other way around. Mathematically, a stimulus vector v undergoes a rotation transformation $v' = \mathcal{R}(v, \boldsymbol{\theta})$, and the result is distorted to get $v'' = \mathcal{D}(v', \boldsymbol{\lambda})$, where $\mathcal{R}$ and $\mathcal{D}$ are the rotation and distortion functions represented by their respective truncated and constrained polynomial series. Note that the composition $v'' = \mathcal{D}(\mathcal{R}(v, \boldsymbol{\theta}), \boldsymbol{\lambda})$ is just another polynomial in the form of (4).

Unfortunately this representation of the rotation and distortion models leads to a relatively complicated estimation algorithm. The partial derivatives with respect to $\boldsymbol{\theta}$ are functions of the estimated parameters [2, eq. 58], and so the least-squares estimator is non-linear and requires iteration for convergence of the estimates. This in itself can lead to problems.

[1] The constraint on the coefficients $a_{0,1}$ and $b_{1,0}$ is incorrect in [2]; the correct constraint is shown in (14).

[2] The matrix cross product operator $[\boldsymbol{\theta}\times]$ is such that $[\boldsymbol{\theta}\times]v = \boldsymbol{\theta} \times v$. It is sometimes written $\boldsymbol{\theta}^\times$.

If one does not insist on having a physical interpretation of the calibration parameters $a_{i,j}$ and $b_{i,j}$, then it is not necessary to consider rotational and distortion parameters separately[3] or to be concerned with any particular order of application of $\mathcal{R}$ and $\mathcal{D}$. In addition, the partial derivatives do not depend on the estimated parameters. Any linear dependencies among the parameters can be eliminated automatically by using either the QR decomposition with pivoting or by using the singular value decomposition. A lucid discussion of the QR decomposition with pivoting can be found in [3, 4] and is summarized in the following section.

3 Least-Squares Estimation of Calibration Parameters

Consider the set of equations $Ax = y$. For any m by n matrix A with $m > n$, there exists an orthogonal matrix Q and an upper triangular matrix R such that

$$Q^T A = \begin{bmatrix} R \\ 0 \end{bmatrix} . \tag{18}$$

If Q is partitioned such that $Q = [Q_1,\ Q_2]$, where Q_1 has n columns, then $A = Q_1 R$. Now, if A and Q_1 are partitioned such that $A = [A_1,\ A_2]$ and $Q_1 = [Q_{11},\ Q_{12}]$, where A_1 and Q_{11} have k columns, and if R is partitioned such that

$$R = \begin{bmatrix} R_{11} & R_{12} \\ 0 & R_{22} \end{bmatrix} , \tag{19}$$

where R_{11} is a $k \times k$ matrix, then

$$Q_{11}^T A_1 = R_{11} , \tag{20}$$

which allows us to solve the truncated least-squares problem with any number of columns deleted without recomputing the entire solution.

If A has rank k, there is a permutation E such that $Q^T AE = R$, R_{11} is of full rank, and $R_{22} = 0$. The QR decomposition with pivoting will place the diagonal of R in descending order of magnitude so that the rank can be determined by inspection of these elements. With the partition $AE = [A_1,\ A_2]$, A_1 has k columns and is of full rank and A_2 is linearly dependent on A_1. Then with the partition $E^T x = \begin{bmatrix} x_1 \\ x_2 \end{bmatrix}$, we can then set $x_2 = 0$ and solve the truncated least-squares problem $A_1 x_1 = y$ to obtain the minimum residual norm solution x_1. This solution is obtained by solving the upper triangular system $R_{11} x_1 = Q_{11}^T y$. The reader will be relieved to know that Matlab provides this capability.

From (5), the partial derivative of $\begin{bmatrix} x_m \\ y_m \end{bmatrix} = \begin{bmatrix} x_c - x_o \\ y_c - y_o \end{bmatrix}$ with respect to the parameter vector $p = [\delta_x\ \delta_y\ f\ a_{0,0}\ \cdots\ a_{r,r}\ b_{0,0}\ \cdots\ b_{r,r}]^T$ is given by the Jacobian matrix

$$J = \begin{bmatrix} 1 & 0 & x & 1 & x & xy & \cdots & x^r y^r & 0 & 0 & 0 & \cdots & 0 \\ 0 & 1 & y & 0 & 0 & 0 & \cdots & 0 & 1 & x & xy & \cdots & x^r y^r \end{bmatrix} . \tag{21}$$

Because f appears nonlinearly in the model (7), iteration may be required to obtain accurate estimates. Note that the estimation of the a and b coefficients could be performed separately if it were not for the estimation of f. It is obvious that linear dependencies among the columns have already been introduced in the model. Namely, the first and second columns are identical to the columns corresponding to $a_{0,0}$ and $b_{0,0}$, while the third column, which corresponds to f, is linearly dependent on columns corresponding to $a_{1,0}$ and $b_{0,1}$. These first two columns are eliminated á priori along

[3] When no distinction is made between rotation and distortion parameters, they will be referred to collectively as distortion parameters.

with the first two elements of p. (QR decomposition with pivoting will choose the linearly dependent columns somewhat arbitrarily.) The center offsets are thus possibly buried in $a_{0,0}$ and $b_{0,0}$ and the focal length is possibly buried in $a_{1,0}$ and $b_{0,1}$.

Now consider the parameter vector $p' = [\delta_x\ \delta_y\ f\ \theta_1\ \theta_2\ \theta_3]$. This vector contains only the physical parameters in (8). The Jacobian matrix J' derived by differentiating (8) with respect to p' is easier to obtain than applying the constraints to (21). This Jacobian is

$$J' = \begin{bmatrix} 1 & 0 & x & xy & -(1+x^2) & y \\ 0 & 1 & y & 1+y^2 & -xy & -x \end{bmatrix} . \tag{22}$$

Of course, higher order terms could also be added to model distortion. Again, because f appears nonlinearly in the model (7), iteration may be required to obtain accurate estimates. If the measurement vectors are divided by $1+f$ on each iteration (replacing the original vectors), then f will converge to zero. Note that δ will be scaled by the focal length.

The least-squares problem is now written

$$Ap = \begin{bmatrix} J_1 \\ J_2 \\ \vdots \\ J_m \end{bmatrix} p = \begin{bmatrix} x_{\mathrm{m}_1} - x_1 \\ y_{\mathrm{m}_1} - y_1 \\ \cdots\cdots\cdots \\ x_{\mathrm{m}_2} - x_2 \\ y_{\mathrm{m}_2} - y_2 \\ \cdots\cdots\cdots \\ \vdots \\ \cdots\cdots\cdots \\ x_{\mathrm{m}_m} - x_m \\ y_{\mathrm{m}_m} - y_m \end{bmatrix} , \tag{23}$$

where the J_i are functions of the stimulus $(x_i,\ y_i)$. The A matrix corresponding to either J (after the first two columns are eliminated) or to J' is of full column rank provided that enough measurements of appropriate spatial distribution are taken. If the distortion is of order r, then we need at least $2(r+1)^2 + 1$ measurements at different locations in the focal plane for the A matrix to be full column rank. (Assume the center offset parameters are no longer included in J so that it is full column rank.) Since this number of measurements grows rapidly with r, and since calibration data is expensive to collect via theodolite, a practical distortion model is of fairly low order. The minimum number of measurement pairs required for the model in (22) would appear to be three, but of course more are needed to make the estimate error covariance smaller. This covariance is given next.

Denote the covariance matrix of the measurement error by Σ^2. If the least-squares equation $Ap = y$ is statistically weighted so that $\Sigma^{-1}Ap = \Sigma^{-1}y$, then the error in the estimated parameters is given by $P = (A^T\Sigma^{-2}A)^{-1}$. (This presumes that the stimulus vectors used to compute A were measured with great precision.) For $\Sigma^2 = \sigma_\eta^2 I$, where $\sigma_\eta^2 = \mathrm{cov}(\eta_x) = \mathrm{cov}(\eta_y)$, the covariance is $P = (A^TA)^{-1}\sigma_\eta^2$. Of much greater interest than P is the covariance S of a corrected measurement. If the measurement $(x_\mathrm{m},\ y_\mathrm{m})$ and the stimulus $(x,\ y)$ are independent of the estimated parameters, this covariance is given by

$$S(x,\ y) = J(A^T\Sigma^{-2}A)^{-1}J^T + \Sigma^2 , \tag{24}$$

where $J = J(x,\ y)$. If the measurement is one of the same measurements used to compute the coefficients, then this equation is a slight underestimate. This is also true if $(x,\ y)$ is a function of $(x_\mathrm{m},\ y_\mathrm{m})$.

4 Alignment and Distortion Correction Algorithm

In practice it may be desirable to correct sensor measurements for distortion error. That is, we are interested in the stimulus vector $(x,\ y,\ 1)^T$ corresponding to the raw measurements $(x_\mathrm{m},\ y_\mathrm{m},\ 1)^T$.

Although parameter estimation is discussed in [1, 2], there is no algorithm provided to compute $(x,\ y,\ 1)^T$ given $(x_{\rm m},\ y_{\rm m},\ 1)^T$. Since (5) is nonlinear mapping from the input $(x,\ y)$ to the output $(x_{\rm m},\ y_{\rm m})$, there is no closed-form solution to obtain $(x,\ y)$. However, for small parameters a fixed-point iteration works well. A Newton iteration is less appealing because of the extra computation required to compute the partial derivative, though a comparison of the two algorithms would be worthwhile. Assume that δ_x, δ_y, and f are eliminated from the calibration model (the change to the following algorithm is trivial if these parameters are present). Let $w = (x,\ y)^T$, $w_{\rm m} = (x_{\rm m},\ y_{\rm m})^T$, and $F(w) = (F_1(x,\ y),\ F_2(x,\ y))^T$. The fixed-point iteration is simply

$$w_{i+1} = w_{\rm m} - F(w_i)\,, \qquad w_0 = w_{\rm m}\,. \tag{25}$$

The iteration is converged when $||w_{i+1} - w_i|| < \tau(1 + ||w_i||)$, where τ is an error tolerance.

A proof of convergence (or conditions for convergence) is not complete at this time. However, one may make use of the fact that $F_1(x,\ y)$ and $F_2(x,\ y)$ can be written as

$$F_1(x,\ y) = \boldsymbol{x}^T A \boldsymbol{y} \qquad F_2(x,\ y) = \boldsymbol{x}^T B \boldsymbol{y} \tag{26}$$

where

$$A = \begin{bmatrix} a_{0,0} & a_{0,1} & \cdots & a_{0,r} \\ a_{1,0} & a_{1,1} & \cdots & a_{1,r} \\ \vdots & \vdots & \ddots & \vdots \\ a_{r,0} & a_{r,1} & \cdots & a_{r,r} \end{bmatrix} \qquad B = \begin{bmatrix} b_{0,0} & b_{0,1} & \cdots & b_{0,r} \\ b_{1,0} & b_{1,1} & \cdots & b_{1,r} \\ \vdots & \vdots & \ddots & \vdots \\ b_{r,0} & b_{r,1} & \cdots & b_{r,r} \end{bmatrix} \tag{27}$$

and where

$$\boldsymbol{x}^T = \begin{bmatrix} 1 & x & x^2 & \cdots & x^r \end{bmatrix} \qquad \boldsymbol{y}^T = \begin{bmatrix} 1 & y & y^2 & \cdots & y^r \end{bmatrix}\,. \tag{28}$$

One may also use the fact that $|\boldsymbol{x}^T A \boldsymbol{y}| < \bar{\sigma}_A |\boldsymbol{x}^T \boldsymbol{y}|$, where $\bar{\sigma}_A$ is the largest singular value of A. So far, actual test data has shown convergence in 5 iterations for $\tau = 10^{-8}$ and $r = 1$. Convergence occurs only when the estimated parameters are small. This makes sense since $\bar{\sigma}_A$ is small for small parameters.

Whether or not one needs to actually calibrate the measurements depends on the application. It is probably most useful in photogrammetry. At first glance one may believe that the iterative correction algorithm is required in the measurement update of a Kalman filter used in on-orbit attitude determination. This is not true if the correction is small. Since the residuals are the difference between the measured and the predicted vectors, one can apply the correction F to the predicted vector rather than to the measurement. If F is large, though, the measurement sensitivity matrix computed in the Kalman filter should depend on F, or the iterative correction should be applied to the measurement. The latter seems preferable since the modification to a standard set of flight software is then minimal.

Remark: Note that (24) is not the covariance of the estimated stimulus vector $(x,\ y)$. The derivation of that covariance is difficult and may be the subject of further work.

5 Results

A grid of experimental raw data is generated by all 25 possible coordinate pairings

$$(x_i,\ y_j) : x_i,\ y_j \in \{-1.5, -0.75, 0.0, 0.75, 1.5\},\ 1 \le i,\ j \le 5\,. \tag{29}$$

The true center is at $(0,\ 0)$ and the true focal length is 0.85. A somewhat arbitrary distortion model, in non-dimensional coordinates, is given by

$$\begin{aligned} \tilde{x} &= 0.05 + (f + 0.01)x - 0.03xy + 0.01x^2 \\ \tilde{y} &= 0.05 + (f - 0.02)y + 0.05xy + 0.03y^2 \end{aligned} \tag{30}$$

where $f = -0.15$. The measurements are given by

$$\begin{aligned} x_{\mathrm{m}} &= x + \tilde{x} + \eta_x \\ y_{\mathrm{m}} &= y + \tilde{y} + \eta_y \end{aligned} \tag{31}$$

where $\sigma_{\eta_x} = \sigma_{\eta_y} = 5.236(10^{-4})$. Note that this distortion model satisfies few of the constraints in equations (9)—(16).

In what follows, the center offsets were not included in the general parameter list since they are redundant. The corresponding columns of J were eliminated á priori. Also in each case the measurement vector was not normalized to make the third component unity. Why? Because how can one know the value of z' in (3)? In practice, we can only divide by the nominal focal length.

Four graphs are shown for each test case. Each graph is a contour plot over the focal plane. The first graph is the distortion error introduced by a distortion model, which is (30) in case 1, and (7) in cases 2 and 3. The second graph is the correction to the measurement required to produce the stimulus vector. This correction is, of course, the term $F(w)$ on the right hand side of (25) after the iteration converges. The third plot is the error in this estimated stimulus vector, which is the difference between the true stimulus and the stimulus computed from (25). The fourth graph is the approximate covariance of the corrected measurement from (24).

Test Case 1

Calibration coefficients were estimated with the model order $r = 2$. The least-squares algorithm eliminated the $b_{0,1}$ parameter (effectively making it zero) to make the A matrix full rank. The estimated coefficients are and their true values (in parenthesis) are as follows:

$$\begin{aligned} f &= -0.17 \quad (-0.15) \\ a_{0,0} &= 0.0500 \quad (0.05) \\ b_{0,0} &= 0.0498 \quad (0.05) \\ a_{1,0} &= -0.0302 \quad (-0.14) \\ b_{0,1} &= 0.0 \quad (-0.17) \\ a_{1,1} &= -0.0299 \quad (-0.03) \\ b_{1,1} &= 0.0501 \quad (0.05) \\ a_{2,0} &= 0.0101 \quad (0.01) \\ b_{0,2} &= 0.0303 \quad (0.03) \end{aligned} \tag{32}$$

The focal length parameter is confused with $a_{1,0}$ and $b_{0,1}$. More precisely, either of these parameters can be considered the true focal length, while their difference represents some additional distortion. Regardless of what physical interpretation is preferred, the mean square residual error is a mere $3.9(10^{-4})$, which is less than the measurement noise. Graphical results of the calibration are shown in Figure 2. Figure 2a is a contour plot of the distortion plus measurement noise. The measurements were corrected by using the iterative algorithm, where 8 to 16 iterations were required for convergence with $\tau = 10^{-8}$. The corrected measurements shown in Figure 2b obviously closely match the distortion error. The error in the correction shown in Figure 2c is typically much less than 0.001, but peaks at about 0.0012. The covariance of the predicted measurement (from (24)) shown in Figure 2d is symmetric, as should be expected. The contours are not smooth due to the paucity of data.

Test Case 2

Results for the model in (7) were also produced. The true parameters are $\delta_x = \delta_y = 0.05$, $f = -0.15$, $\theta_1 = 0.018$, $\theta_2 = 0.009$, and $\theta_3 = 0.025$. The nonlinear model (7) was used to generate the

measurement data. The stimulus vectors are the same as before. Estimates were computed for two models. The first uses the general Jacobian matrix J (21) with order $r = 2$. The second uses the Jacobian matrix J' (22).

Calibration coefficients were estimated with the model order $r = 2$. Again, the least-squares algorithm eliminated the $b_{0,1}$ parameter. The estimated coefficients are and their true values are as follows:

$$\begin{aligned}
\delta_x - \theta_2 \sim a_{0,0} &= 0.0425 \quad (0.041) \\
\delta_y + \theta_1 \sim b_{0,0} &= 0.0652 \quad (0.068) \\
f &= -0.1504 \quad (-0.15) \\
\theta_3 \sim a_{0,1} &= 0.0211 \quad (0.025) \\
-\theta_3 \sim b_{1,0} &= -0.0212 \quad (-0.025) \\
\theta_1 \sim a_{1,1} &= 0.0001 \quad (0.018) \\
-\theta_2 \sim b_{1,1} &= 0.0001 \quad (0.009) \\
-\theta_2 \sim a_{2,0} &= 0.0001 \quad (0.009) \\
\theta_1 \sim b_{0,2} &= 0.0003 \quad (0.018)
\end{aligned} \tag{33}$$

The rotation angles θ_1 and θ_2 are confused with the center offsets. This seems a bit surprising since the columns of the Jacobian matrix are linearly independent, except for the focal length parameter. The algorithm eliminated the $b_{0,1}$ term, which corresponds to f. Nevertheless, the mean square residual is only $3.9(10^{-4})$, which again is less than the measurement noise. Graphical results of this case are shown in Figure 3. As can be seen, the calibration does very well. For this case, the correction function converged in 10 iterations.

Test Case 3

This case uses the Jacobian matrix (22) to estimate calibration coefficients for the model (8). None of the six parameters were eliminated from the model. The estimated coefficients and their true values are as follows:

$$\begin{aligned}
\delta_x &= 0.0425 \quad (0.041) \\
\delta_y &= 0.0653 \quad (0.068) \\
f &= -0.1504 \quad (-0.15) \\
\theta_1 &= 0.0001 \quad (0.018) \\
\theta_2 &= -0.0001 \quad (0.009) \\
\theta_3 &= 0.0212 \quad (0.025)
\end{aligned} \tag{34}$$

The rotation angles θ_1 and θ_2 are confused again with the center offsets. This seems a bit surprising since the columns of the Jacobian matrix are indeed linearly independent; none were eliminated during the QR decomposition and the A matrix is of full rank and well-conditioned. Despite this, the mean square residual is only $4.8(10^{-4})$, a little larger than in the general unconstrained case above but still less than the measurement noise. Graphical results of this case are shown in Figure 4. Again the calibration does very well. The correction function converged in 10 iterations, as in the previous case.

It was found that if the measured vector $(x_m,\ y_m,\ 1)^T$ is divided by $1 + f$ and the estimation repeated using this modified vector, the estimated f goes to zero and the other physical parameters nearly achieve their proper values, with the exception of the center offsets, which are too large by a factor of $1 + f$. More work will be performed to analyze this situation.

6 Summary

The distortion and alignment models originally proposed by Schuster and Lopes [1, 2] are presented. Center offsets and a focal length parameter have been introduced into the model. Practical least-squares estimation of coefficients of these models is discussed and the covariance matrix for a corrected sensor measurement is given. In addition, a new alignment and distortion correction algorithm is introduced. This algorithm produces the stimulus vector at the input of the sensor that corresponds to the measurement at the output of the sensor. Three test cases are presented. These tests show that the center offsets are often confused with rotations about the focal plane axes, even when the coefficient matrix is of full rank. However, the fact that the residual error is small shows that the model and estimated parameters are valid. Furthermore, the error in the estimated stimulus vectors is small. These results demonstrate that regardless of what physical interpretation may be attributed to the coefficients of the general alignment and distortion model, what is of utmost importance is that the measurements can be calibrated to good accuracy. In light of this, it is proposed that the polynomial series model of Schuster and Lopes be replaced by orthogonal functions such as Legendre or Chebyshev polynomials or Fourier series.

References

[1] M. Schuster, *Focal-Plane Representation of Rotations*, Journal of Astronautical Sciences.

[2] M. Schuster and R. V. F. Lopes, *Parameter Interference in Distortion and Alignment Calibration*, Paper AAS 94-186, AAS/AIAA Spaceflight Mechanics Meeting, February 14–16, 1994.

[3] J. J. Dongarra, et al., *Linpack Users' Guide*, SIAM, 1982.

[4] G. H. Golub and C. F. Van Loan, *Matrix Computations*, The Johns Hopkins University press, 1989.

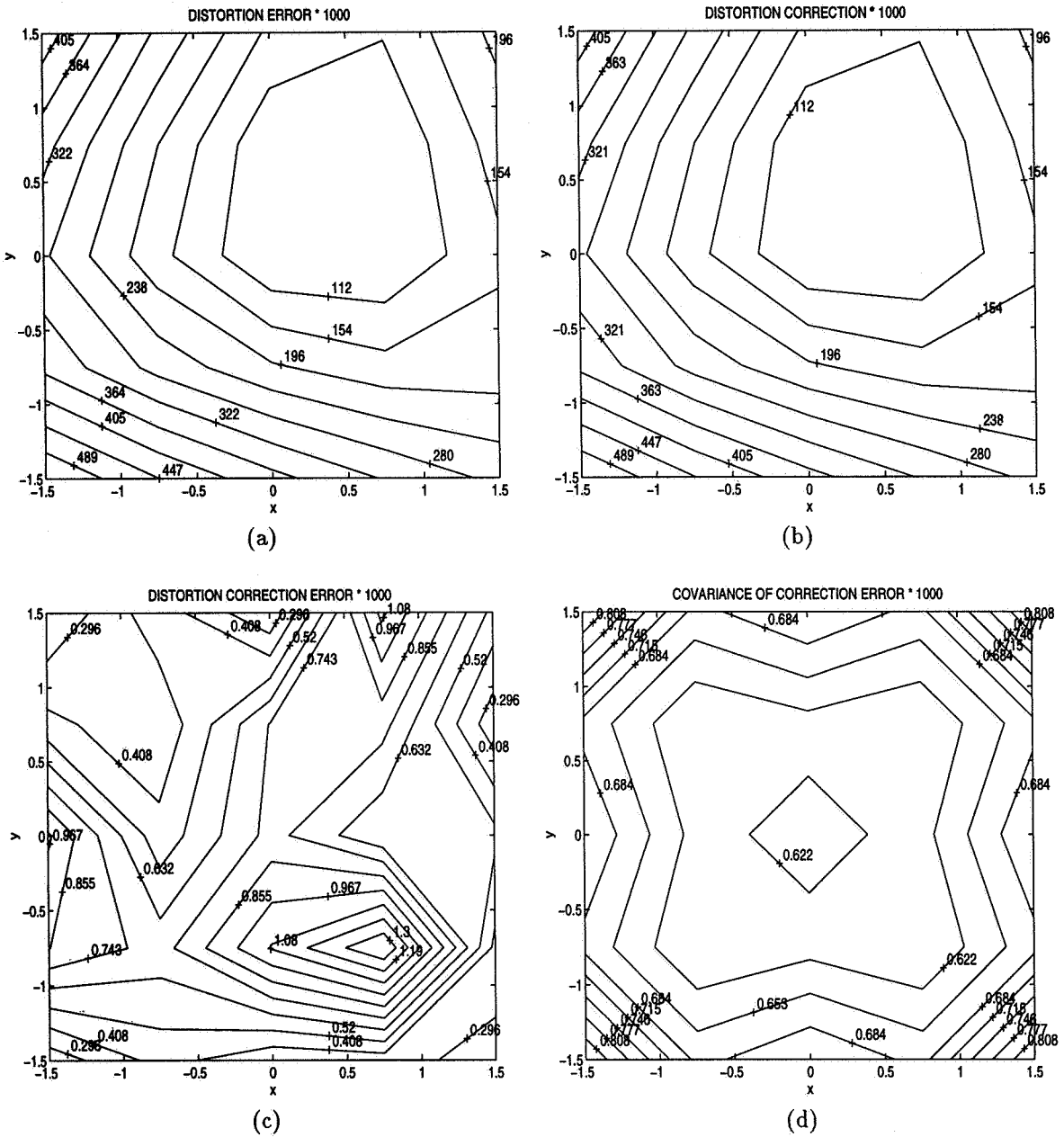

Figure 2: Results for the arbitrary distortion and general Jacobian J with $r = 2$.

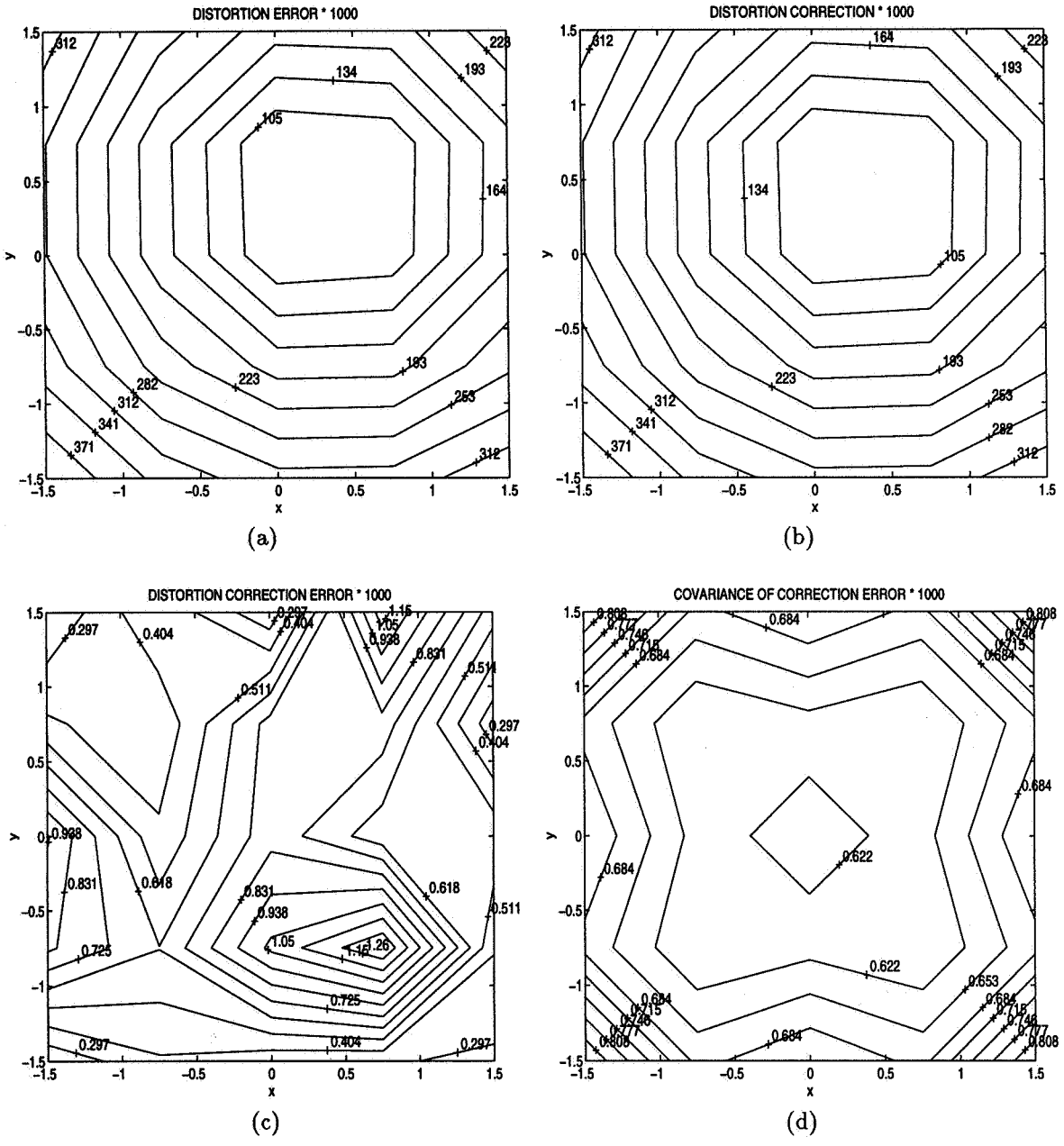

Figure 3: Results for the physical model and general Jacobian J with $r = 2$.

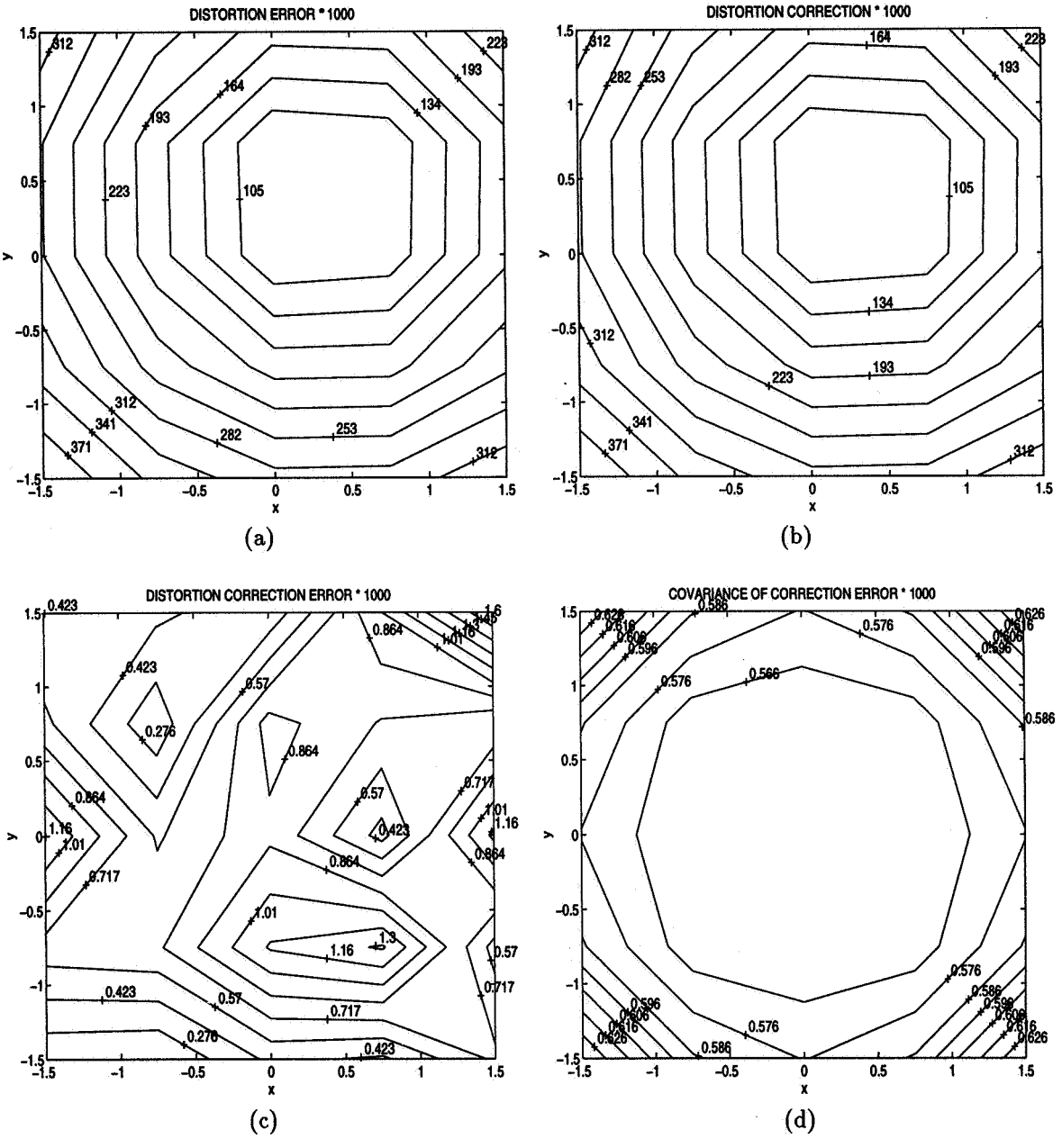

Figure 4: Results for the physical model and the Jacobian J'.

Page intentionally left blank

Measuring Angular Velocity with Accelerometers

David Sonnabend*

Abstract

Are gyros necessary? 2 scenarios are examined here in which either linear or angular accelerometers can provide an adequate substitute. The 1st has a spacecraft in a free tumble after launch, too fast for star tracker acquisition. It's shown that, with the help of a reaction wheel, an estimate of angular velocity, accurate enough to program despin thrust, is obtainable. The 2nd assumes initially accurate pointing, prior to a main engine firing. Again, with either accelerometer type, high bandwidth angular velocity information may be found, suitable for attitude control.

1 Discussion

The possibility of using accelerometers to measure angular velocity, in place of gyros, is very interesting. Here it's shown that both linear and angular accelerometers, together with a reaction wheel, and an observer based on rigid body dynamics can perform such a measurement. 1st, some accelerometer fundamentals. The instrument is rigidly mounted to a carrier vehicle, also assumed here to be rigid, for simplicity. Inside, a proof mass is more or less free to move in 1 or more axes, but is restrained by a forcing system to remain centered in the instrument. The force vector required to do this is a measure of the non-gravitational acceleration to which the instrument is subjected. Single and 3 axis versions are generally available. 3 axis accelerometers usually have aspherical proof masses, when the forcing system must also supply a torque vector, to prevent rotation. What these instruments can measure is analyzed in the next section.

2 Angular Accelerometers

Consider a carrier vehicle that is rigid, except for a set of reaction wheels. Then, if the vehicle has an inertia tensor $\mathbf{J}$, and is rotating with instantaneous angular velocity $\boldsymbol{\omega}$, then the total angular momentum is

$$\mathbf{L} = \mathbf{H} + \mathbf{J}\boldsymbol{\omega} \tag{1}$$

*President, Analytical Engineering Co., Boulder, CO, 303-530-9641

where $\mathbf{H}$ is the total inertial angular momentum stored in the wheels. This ignores details such as where to account for the inertia tensor of the wheels; but this finesse isn't significant here.

Now torque is the rate of change of angular momentum; so, on observing this derivative in moving vehicle axes,

$$\dot{\mathbf{L}} + \boldsymbol{\omega} \times \mathbf{L} = \boldsymbol{\tau}_e \tag{2}$$

where the right side is the *external* torque applied to the vehicle. On substituting (1), this relation becomes:

$$\mathbf{J}\dot{\boldsymbol{\omega}} = (\mathbf{H} + \mathbf{J}\boldsymbol{\omega}) \times \boldsymbol{\omega} + \boldsymbol{\tau}_e - \boldsymbol{\tau}_w \tag{3}$$

where $\boldsymbol{\tau}_w$ is the total torque applied to the wheels by the vehicle. These are the Euler equations of motion of a rigid body plus wheels. The disadvantage of requiring cross product terms is offset by the lack of a $\mathbf{J}$ term, as this is invariant in vehicle coordinates.

Now consider the accelerometer. The observable is the torque $\boldsymbol{\tau}_p$ applied to the proof mass by the case to hold it fixed in the instrument. If the accelerometer is forced to rotate at an angular velocity $\boldsymbol{\omega}$, then the above analysis shows that the torque required to hold the proof mass still is:

$$\boldsymbol{\tau}_p = \mathbf{I}\dot{\boldsymbol{\omega}} + \boldsymbol{\omega} \times (\mathbf{I}\boldsymbol{\omega}) \tag{4}$$

in which $\mathbf{I}$ is the proof mass inertia tensor. Thus, $\dot{\boldsymbol{\omega}}$ is directly measurable only if $\boldsymbol{\omega}$ lies along a proof mass principle axis, an unlikely event.

It's necessary to express this in components. For this, the mathematics is greatly eased if it can be assumed that the principle axes of $\mathbf{I}$ are aligned with those of $\mathbf{J}$. This assumption will be made in what follows, starting with (4):

$$\tau_{p1} = I_1\dot{\omega}_1 + (I_3 - I_2)\omega_2\omega_3 \tag{5}$$
$$\tau_{p2} = I_2\dot{\omega}_2 + (I_1 - I_3)\omega_1\omega_3 \tag{6}$$
$$\tau_{p3} = I_3\dot{\omega}_3 + (I_2 - I_1)\omega_1\omega_2 \tag{7}$$

Note that all actual proof mass designs have various symmetries, when some of the nonlinear terms may vanish. Next, define the measurements as

$$z_i = \tau_{pi}/I_i \quad ; \quad i = 1,\ 2,\ 3 \tag{8}$$

This is always possible, as $I_i > 0$ for any physical body. Then, these equations may be rewritten as

$$z_1 = \dot{\omega}_1 + Q_1\omega_2\omega_3 \ ; \ z_2 = \dot{\omega}_2 + Q_2\omega_1\omega_3 \ ; \ z_3 = \dot{\omega}_3 + Q_3\omega_1\omega_2 \tag{9}$$

where

$$Q_1 \equiv (I_3 - I_2)/I_1 \ ; \ Q_2 \equiv (I_1 - I_3)/I_2 \ ; \ Q_3 \equiv (I_2 - I_1)/I_3 \tag{10}$$

As a 1st case, suppose the vehicle is in a free tumble, with no wheels or external torque. Then (3) may be written as

$$\dot{\omega}_1 + R_1\omega_2\omega_3 = \dot{\omega}_2 + R_2\omega_1\omega_3 = \dot{\omega}_3 + R_3\omega_1\omega_2 = 0 \tag{11}$$

where the vehicle inertia ratios R_i have been defined in exactly the same way as the Q_i. On subtracting these from (9) we find

$$z_1 = (Q_1 - R_1)\omega_2\omega_3 \;\; ; \;\; z_2 = (Q_2 - R_2)\omega_1\omega_3 \;\; ; \;\; z_3 = (Q_3 - R_3)\omega_1\omega_2 \tag{12}$$

Thus we have 3 equations in the 3 unknowns ω_i. Unfortunately, there is a basic ambiguity because $-\boldsymbol{\omega}$ yields the same z_i as $\boldsymbol{\omega}$. However, a sort of solution is possible — if we form the combination

$$\frac{z_2 z_3}{z_1} = \frac{(Q_2 - R_2)(Q_3 - R_3)}{Q_1 - R_1}\omega_1^2 \tag{13}$$

and 2 similar relations. So, in principle, all the ω_i^2 can be determined from the measurements. Of course, the ratios tell us there could be numerical difficulties. For example, if the vehicle is spinning on a principle axis, then all $z_i = 0$, and about all we could infer is that the spin, if any, is about *some* principle axis.

We may also combine (9) and (11) to eliminate the quadratic terms, when we get

$$R_i z_i = (R_i - Q_i)\dot{\omega}_i \tag{14}$$

From this we see that the sign of z_i tells us whether ω_i is increasing or decreasing. Thus, if any $z_i \neq 0$, then a short observation of ω_i^2 reveals the information needed to completely determine ω_i. Moreover, the remaining components may be computed immediately from (12). It must be emphasized that the relations (11 - 14) depend on the assumed dynamics, and only apply when there is no external torque or wheel usage.

A vehicle symmetry could cause this procedure to fail. For example, if $J_2 = J_3$, then $R_1 = 0$, and $R_2 = -R_3$. (11) then tells us that $\dot{\omega}_1 = 0$, and ω_1 is constant. the remaining relations in (11) then integrate immediately to

$$\omega_2 = A\sin(R_3\omega_1 t + \phi) \qquad ; \qquad \omega_3 = A\cos(R_3\omega_1 t + \phi) \tag{15}$$

where A and ϕ depend on the unknown initial conditions. The observable is then

$$z_1 = \frac{1}{2}Q_1 A^2 \sin(2R_3\omega_1 t + 2\phi) \tag{16}$$

In this case, ω_1 falls out as soon as the frequency of this sinusoid can be determined. Further vehicle symmetry would mean that the vehicle has a spherical inertia tensor, when all $R_i = 0$, all $\dot{\omega}_i = 0$, and the z_i are all constant. Then (13) may yield some or all of the $|\omega_i|$; but there is no obvious way to get the signs.

The possibilities for vehicle symmetry would all be known in advance; but the mischance of an unknown spin on a principle axis would only be signaled if all $z_i = 0$. In either case we can sort the matter out if we are willing to use a wheel. To analyze this, we may return to (3), set $\boldsymbol{\tau}_e = \mathbf{0}$, and write it out in components. Suppose only the 1st axis wheel is used: $\mathbf{H} = [h,\ 0,\ 0]^T$. Then in place of (11) we have:

$$\dot{\omega}_1 + R_1\omega_2\omega_3 + \frac{\tau_w}{J_1} = \dot{\omega}_2 + R_2\omega_1\omega_3 + \frac{h}{J_2}\omega_3 = \dot{\omega}_3 + R_3\omega_1\omega_2 - \frac{h}{J_3}\omega_2 = 0 \tag{17}$$

Next, (9) may be used to replace the quadratic term in the 1st of these:

$$(Q_1 - R_1)\dot{\omega}_1 + R_1 z_1 + \frac{Q_1}{J_1}\tau_w = 0 \tag{18}$$

Now suppose we activate this wheel at time t_0. Then at time t we have

$$(Q_1 - R_1)(\omega_1 - \omega_{10}) + R_1 \int_{t_0}^{t} z_1(\eta)d\eta + \frac{Q_1}{J_1}h = 0 \tag{19}$$

so the change in ω_1 in this interval is readily computed. Note that this may be done accurately even if the wheel torque is uncertain or irregular.

In the remaining equations of (17), we again use (9), but this time to replace the $\dot{\omega}$ terms:

$$R_2 z_2 + \left[(R_2 - Q_2)\omega_1 + \frac{h}{J_2}\right]\omega_3 = R_3 z_3 + \left[(R_3 - Q_3)\omega_1 - \frac{h}{J_3}\right]\omega_2 = 0 \tag{20}$$

Now for $t < t_0$, the vehicle is in a free tumble, following which, ω_1 responds nearly linearly to h. On the other hand, the precession behavior doesn't begin to change until there is an appreciable h. Thus, for a short time, there should be little change in ω_2 and ω_3. Thus, if $t - t_0$ is short, we can difference both equations in (20) at these times, and eliminate $\omega_1 - \omega_{10}$ with (19). This leaves linear algebraic equations, solvable for ω_2 and ω_3, after which ω_1 can come from either relation in (20). While these values may be used immediately for despin control, they may be refined by then turning off τ_w, and using (17) as the basis for a dynamic observer, with the estimated ω_i as starting values. That the wheel may continue to spin makes no difference, as h is always known accurately. Theoretically, the initial tumble may be too fast for this to work, given the limited τ_w capability; but this tumble rate is limited in any practical application.

The other situation in which an angular accelerometer can substitute for a gyro is if a large thruster, with an unknown misalignment, is to be controlled by small side thrusters to balance the undesired torque. If the vehicle begins under star tracker control, so that $\boldsymbol{\omega}(t_0) = \mathbf{0}$, then the angular accelerometer's job is quite straightforward. With no wheel usage, and very small $\boldsymbol{\omega}$, (3) reduces to $\mathbf{J}\dot{\boldsymbol{\omega}} = \boldsymbol{\tau}_e$; while from (4) and (8) we have $\dot{\boldsymbol{\omega}} = \mathbf{z}$, and the desired control is $\boldsymbol{\tau}_e = \mathbf{J}\mathbf{z}$; and if rate stabilization is also desired,

$$\boldsymbol{\omega}(t) = \int_{t_0}^{t} \mathbf{z}(\eta)d\eta \tag{21}$$

However, as there is likely to be a residual bias $\mathbf{z}_B$ in $\mathbf{z}$, especially if this bias arises because of the thruster acceleration, some modification is needed. After including the bias we have

$$\dot{\boldsymbol{\omega}} = \mathbf{z} - \mathbf{z}_B \tag{22}$$

so the torque command is in error by an amount $\mathbf{J}\mathbf{z}_B$, and the rate estimate is in error by $\mathbf{z}_B(t - t_0)$.

The simple way to deal with this is to break the maneouvre up into pieces, with restabilization with the star tracker between firings. The number of pieces would depend on the length of the maneouver, and the error specifications. Since extra firings are bad for several reasons, it's fortunate that there is a better way.

As the star tracker is the normal input to the S/C attitude observer, an accurate estimate of $\boldsymbol{\omega}$ is available, provided $\boldsymbol{\omega}$ remains small enough that the star tracker doesn't lose lock. With bias, the numerical integration yields

$$\boldsymbol{\omega}(t) = \int_{t_0}^{t} \mathbf{z}(\eta)d\eta - \mathbf{z}_B(t - t_0) \tag{23}$$

and as both $\boldsymbol{\omega}$ and $\mathbf{z}$ are measured, this serves to give an estimate of $\mathbf{z}_B$. With this, we merely set the torque command to

$$\boldsymbol{\tau}_e = \mathbf{J}(\mathbf{z} - \mathbf{z}_B) \tag{24}$$

The performance of such a system can't be determined without a design of the joint observer; here, it's sufficient to show that everything needed for the calculation is observable.

3 Linear Accelerometers

Can a linear 3 axis accelerometer also measure $\boldsymbol{\omega}$? Depends. Suppose the S/C center of mass (CM) is at a position $\mathbf{x}$, relative to an external inertial coordinate system. Then suppose the linear accelerometer is at a position $\mathbf{r}$, relative to the CM. Then the inertial position of the instrument is

$$\mathbf{y} = \mathbf{x} + \mathbf{r} \tag{25}$$

Suppose further that the S/C is rotating about the CM at a rate $\boldsymbol{\omega}$. Then on differentiating this we find

$$\dot{\mathbf{y}}^i = \dot{\mathbf{x}}^i + \dot{\mathbf{r}}^i = \dot{\mathbf{x}}^i + \boldsymbol{\omega} \times \mathbf{r} \tag{26}$$

where the superscript i signifies that the derivative is inertial; while no superscript is used for body derivatives. Also, $\mathbf{r}$ is fixed in the S/C, so $\dot{\mathbf{r}} = 0$. On differentiating again,

$$\ddot{\mathbf{y}}^i = \ddot{\mathbf{x}}^i + \dot{\boldsymbol{\omega}} \times \mathbf{r} + \boldsymbol{\omega} \times (\boldsymbol{\omega} \times \mathbf{r}) \tag{27}$$

and no superscript is needed for $\dot{\boldsymbol{\omega}}$, as it is the same in both systems. Now only non-gravitational acceleration is measured, so the ideal instrument sees

$$\mathbf{Z} = \ddot{\mathbf{y}}^i - \mathbf{g} = \mathbf{a} + \dot{\boldsymbol{\omega}} \times \mathbf{r} + \boldsymbol{\omega} \times (\boldsymbol{\omega} \times \mathbf{r}) \tag{28}$$

where $\mathbf{a}$ is the non-gravitational part of $\ddot{\mathbf{x}}^i$. Here, the $\dot{\boldsymbol{\omega}}$ term is coriolis, and the last term is centripetal acceleration. This is the measurement model, corresponding to (4) and (8) in the last section.

Like there, we may make use of the S/C dynamics. With no wheel use, we have from (3):

$$\mathbf{J}\dot{\boldsymbol{\omega}} = (\mathbf{J}\boldsymbol{\omega}) \times \boldsymbol{\omega} + \boldsymbol{\tau}_e \tag{29}$$

and if we use this to eliminate $\dot{\boldsymbol{\omega}}$ from (28), we see that $\mathbf{Z}$ is an even function of $\boldsymbol{\omega}$, regardless of the assumptions made about $\mathbf{a}$ and $\boldsymbol{\tau}_e$, and we have again found that the system can't be solved uniquely for $\boldsymbol{\omega}$. However, the similarity to the angular accelerometer, analyzed in the last section, suggests that we should try the same trick — turn on a wheel in 1 axis, and thus introduce a term in the dynamics that is linear in $\boldsymbol{\omega}$.

As before, let's 1st consider the free tumble case; i.e., $\mathbf{a} = \boldsymbol{\tau}_e = \mathbf{0}$. On again employing only the 1st wheel, and using (3) to eliminate $\dot{\boldsymbol{\omega}}$ from (28), some algebra yields

$$Z_1 = \left[r_2\left(1 + R_3\right)\omega_2 + r_3\left(1 - R_2\right)\omega_3\right]\omega_1 - r_1\left(\omega_2^2 + \omega_3^2\right) - \left(\frac{r_2}{J_3}\omega_2 + \frac{r_3}{J_2}\omega_3\right)h \tag{30}$$

$$Z_2 = r_1\left(1-R_3\right)\omega_2\omega_1 + r_3\left(1+R_1\right)\omega_2\omega_3 - r_2\left(\omega_1^2+\omega_3^2\right) + \frac{r_1}{J_3}\omega_2 h + \frac{r_3}{J_1}\tau_w \tag{31}$$

$$Z_3 = r_1\left(1+R_2\right)\omega_3\omega_1 + r_2\left(1-R_1\right)\omega_2\omega_3 - r_3\left(\omega_1^2+\omega_2^2\right) + \frac{r_1}{J_2}\omega_3 h - \frac{r_2}{J_1}\tau_w \tag{32}$$

where everything is in body coordinates, and the dimensionless numbers R_i are again the S/C inertia ratios defined in the last section.

The behavior mentioned above may now be seen explicitly. Without the wheel terms on the extreme right of these equations, the measurements Z_i are composed of purely quadratic terms in $\boldsymbol{\omega}$; and if any $\boldsymbol{\omega}$ satisfies this system, so does $-\boldsymbol{\omega}$. However, operation of the 1st wheel adds terms linear in ω_2 and ω_3, thus offering a method of breaking the symmetry, and isolating the actual $\boldsymbol{\omega}$.

A digression on the algebraic properties of the system may be helpful. We have 3 equations to solve in the 3 unknown components of $\boldsymbol{\omega}$. The system is complete, and of algebraic degree 6; and thus possesses 6 solutions, some of which may be complex. Since the measurements are of an actual physical system, at least 2 of these solutions must be completely real. Moreover, prior to turning the wheel on, if 1 solution is complex, the symmetry demands that there be 4. Thus, there are either 2 real solutions or 6. Here I've defined a solution as complex if any ω_i is complex. My conjecture is that, without wheels, there are always 4 complex solutions; and that adding the wheel destroys the left-right symmetry, but not the 4 + 2 classification of the solutions.

Geometry offers further insight. Consider the 3 dimensional space, whose axes are the ω_i in body coordinates. I'll call this $\boldsymbol{\omega}$ space. The actual condition of the S/C, with or without wheels, is described by a single point in this space, which may move about continuously with time. There are some physical bounds that help limit the space to be searched.

1st, the reason for asking the accelerometer to determine $\boldsymbol{\omega}$ was because the star tracker couldn't lock in to a star field. Knowing this excludes a closed region in $\boldsymbol{\omega}$ space, surrounding the origin, whose shape depends on the tracker rate characteristics, and its boresight direction in body coordinates. If 2 trackers are used, there are 2 such volumes excluded. Also, in any practical situation, there are physical limits on the severity of the tumble, which implies a presumably larger closed region in which $\boldsymbol{\omega}$ is *included.*

A tighter geometrical constraint can be found from (28). Letting

$$\mathbf{q} \equiv \mathbf{r} \times \boldsymbol{\omega} \tag{33}$$

we can show that

$$\mathbf{r} \cdot \mathbf{Z} = -\mathbf{q} \cdot \mathbf{q} \tag{34}$$

from which the magnitude q is readily computed. But geometry tells us that the magnitudes are related by

$$q = rw\sin\phi \tag{35}$$

where ϕ is the angle between $\boldsymbol{\omega}$ and $\mathbf{r}$. On considering all values of ϕ, this tells us that $\boldsymbol{\omega}$ lies on an infinite tube like manifold, whose axis lies along $\mathbf{r}$, and which has a bulge centered on the origin, of diameter q/r. Since all other points on the manifold are further away, we must have

$$\omega \geq \sqrt{-\mathbf{r}\cdot\mathbf{Z}}/r \tag{36}$$

Of course, the relation (34) isn't independent of (30 - 32); and I haven't found a further use for it. Anyway, this bound may be stronger than the star tracker bound.

How do we solve this system? Let's consider the most obvious iterative method. In advance, the star tracker and severity limit bounds are computed. Then, if the star trackers fail to lock up, a measurement is taken, and this procedure follows:

1) The bound (36) is computed, and a point ω_0 is selected within the still included region.

2) Starting from ω_0, a gradient technique is applied to (30 - 32), with no wheel terms, possibly augmented with a quasi Newton technique when the gradient levels off.

Comment: If the conjecture is correct, then only the final ω and $-\omega$ will satisfy (30 - 32). Then, it's possible that asymmetrical bounds will exclude 1 solution; but this is quite unlikely. So we continue:

3) The 1st axis wheel is turned on, raised to a momentum h, and held at this speed. A measurement $\mathbf{Z}'$ is made.

Comment: Any direction for $\mathbf{H}$ could be chosen; but (30 - 32) specifically apply only to a 1st axis wheel. Also, the reason for holding at the preassigned value h is that, at constant speed, the uncertain motor torque just balances the uncertain drag torque, so that $\tau_w = 0$ during both measurements. If we now repeated the technique 2), we would likely find that the solutions have wandered a bit, and are no longer equal and opposite, but we still couldn't tell which one is correct.

One more trick is needed. If the time to reach the steady h is short compared to the free precession periods, then only ω_1 can change significantly. Thus, if we subtract the 2 sets of measurements, we would get approximately:

$$Z_1' - Z_1 = \left[r_2\left(1 + R_3\right)\omega_2 + r_3\left(1 - R_2\right)\omega_3\right]\Delta\omega_1 - \left(\frac{r_2}{J_3}\omega_2 + \frac{r_3}{J_2}\omega_3\right)h \tag{37}$$

$$Z_2' - Z_2 = r_1\left(1 - R_3\right)\omega_2\Delta\omega_1 - 2r_2\omega_1\Delta\omega_1 + \frac{r_1}{J_3}\omega_2 h \tag{38}$$

$$Z_3' - Z_3 = r_1\left(1 + R_2\right)\omega_3\Delta\omega_1 - 2r_3\omega_1\Delta\omega_1 + \frac{r_1}{J_2}\omega_3 h \tag{39}$$

This system is linear in ω, and has a unique solution for any given $\Delta\omega_1$. The latter is available from the 1st equation in (3):

$$\dot{\omega}_1 = -R_1\omega_2\omega_3 - \frac{\tau_w}{J_1} \tag{40}$$

when integration yields approximately

$$\Delta\omega_1 = -R_1\omega_2\omega_3\Delta t - \frac{h}{J_1} \tag{41}$$

Thus, our procedure continues

4) Perform a 1 dimensional search on $\Delta\omega_1$, until a solution ω of (37 - 39) satisfies (41). Despin control could be initiated based on this solution; but a better solution needs 1 more step:

5) Using $\mathbf{Z}'$, and the result of 4) with $\omega_1 \rightarrow \omega_1 + \Delta\omega_1$ to start the iteration, repeat the solution technique 2). The improved solution should be accurate enough to compute either a thruster angular momentum impulse, or a new wheel setting $\mathbf{H}$ that will reduce $\boldsymbol{\omega}$ sufficiently to permit star tracker lock up. This should work. If not, we can

6) Go back to 1), allowing for $\mathbf{H} \neq \mathbf{0}$.

Finally, let's return to the situation of a large thruster with an unknown misalignment. Just as in the angular accelerometer discussion, with no wheels, and initial star tracker control, so that $\boldsymbol{\omega}$ is initially zero and remains small, (3) reduces to $\mathbf{J}\dot{\boldsymbol{\omega}} = \boldsymbol{\tau}_e$. This time the accelerometer is linear, and (28) becomes

$$\mathbf{Z} = \mathbf{a} + \mathbf{a}_B + \dot{\boldsymbol{\omega}} \times \mathbf{r} \tag{42}$$

where I've again added the instrument bias. Once again we can numerically integrate this and obtain

$$\int_{t_0}^{t} \mathbf{Z}(\eta) d\eta = (\mathbf{a} + \mathbf{a}_B)(t - t_0) + \boldsymbol{\omega} \times \mathbf{r} \tag{43}$$

and again $\boldsymbol{\omega}$ is measured by the star tracker, so this may be solved for $\mathbf{a} + \mathbf{a}_B$, permitting us to isolate $\dot{\boldsymbol{\omega}} \times \mathbf{r}$. This isn't quite what we want, as the component of $\dot{\boldsymbol{\omega}}$ along $\mathbf{r}$ can't be solved for. However, unlike the angular accelerometer, where we put the instrument is important. Suppose we choose the 1st body axis as the nominal thrust axis. If the accelerometer is also placed on this axis, then $r_2 = r_3 = 0$, and the measurement becomes

$$\mathbf{Z} = \mathbf{a} + \mathbf{a}_B + r_1[0,\ \dot{\omega}_3,\ -\dot{\omega}_2]^T \tag{44}$$

Thus, as soon as the integration (43) has yielded a reliable value of $\mathbf{a} + \mathbf{a}_B$, the components τ_{e2} and τ_{e3} are known, and thruster commands can be issued to counter them. This doesn't deal directly with rotation about the thrust axis; but that rotation doesn't affect the manoeuvre. By and by, the star tracker will sense the rotation, and either jets or the thrust axis wheel may be commanded to counter it.

This procedure doesn't separate $\mathbf{a}$ and $\mathbf{a}_B$. However, for a fixed nominal thrust, $\mathbf{a}_B$ isn't likely to vary much from 1 firing to the next. Thus, after the 1st firing, $\mathbf{a}$ (really its integral) is available from ground tracking, when $\mathbf{a}_B$ may be determined, and used on subsequent firings.

4 Summary

It's been shown that either an angular or linear 3 axis accelerometer can substitute for a rate gyro set, in applications including an unknown free tumble, or in controlling cross axis large thruster torques, both of which require high bandwidth measurements. The angular accelerometer gives cleaner results; but linear accelerometers are much more common. Especially for the latter, further analysis and simulation will be needed to establish the accuracy and numerical stability.

HIGH ACCURACY SIGNAL PROCESSING FOR LOW-COST EARTH SENSORS

Richard H. Anderson* and Lawrence L. Ames**

Low-cost earth sensors tend to be low-accuracy sensors. There are three reasons for this: lack of symmetrical horizon sensing, not enough horizon samples and lack of error-detection signal processing. Satellite Sensor Systems has developed a line of low-cost earth sensors which addresses all of these problems. The sensors use multi-linear arrays of pyroelectric detectors. For geosynchronous and mid-altitude earth orbit (GEO and MEO) applications eight horizons are sampled and for low earth orbit (LEO) applications four horizons are sampled. At each horizon, local radiance corrections are applied and a spatial horizon location obtained. A best-fit circle (or ellipse) is applied to the multiple horizon positions with a least-squares fit incorporating an iterative error detection algorithm that weighs each horizon position according to its deviation from the circle. Applying this process, with a simulation program, to a GEO model using all of the worst case radiance-gradient and cloud conditions defined for the GOES program resulted in pointing errors of less than ±0.005 degrees. For the LEO systems maximum radiance errors should be less than 0.02 degrees. The above include automatic rejection of both sun and moon interference. In addition, models of both the detector and sensor using all of their parametric properties have been created. A development model earth sensor was constructed and tested. This sensor's test results are consistent with the processing algorithm and parametric modeling results. The above process allows the analytical prediction of the performance for most earth-sensing applications. The performance of several proposed configurations are presented.

* President, Satellite Sensor Systems, 2 Sandstone, Portola Valley, CA 94028-8033
Phone: (415) 851-4165, FAX: (415) 851-4189, E-mail: dicka@best.com.

** L. Ames Engineering Services, 1218 Willow Street, San Jose, CA 95125-4337
Phone: (408) 279-0266, E-mail: lames@aol.com

INTRODUCTION

The technology described in this paper is the result of work performed on Low-Cost Earth Sensors (LCES) by Satellite Sensor Systems. A development model earth sensor has been produced and high accuracy signal processing algorithms developed for both geosynchronous (GEO), mid level (MEO), and low (LEO) earth orbit applications. These algorithms have been analytically tested against most worst-case orbital earth radiance conditions. A performance model of the earth sensors has been created and adjusted to the performance parameters of the development hardware. This allows the accurate prediction of performance for proposed new configurations of the technology. This paper will briefly describe the technology and present the results of the above development effort. Several possible configurations will then be presented to show the adaptability of the technology. A more detailed sensor description and the results of the development model testing are presented in Ref. 1.

SENSOR DESCRIPTION

Overview

All of the LCES systems use the same basic approach, and thus a majority of the parts are common. The earth is imaged through wide-field optics and a resonant chopper to a detector array at the focal plane. The multi-detector array is configured to observe the earth at four or more horizons. The chopper operates in a sinusoidal motion, exposing the detector alternately to the chopper surface and the earth's image through the optics at the extremes of motion. This produces an AC signal which is proportional to the radiance difference between the chopper and what the detectors see through the optics. Some of the detectors will see space, some the earth, and some will be positioned at a horizon and will produce a signal somewhere between space and earth. These signals are illustrated in Figure 1.

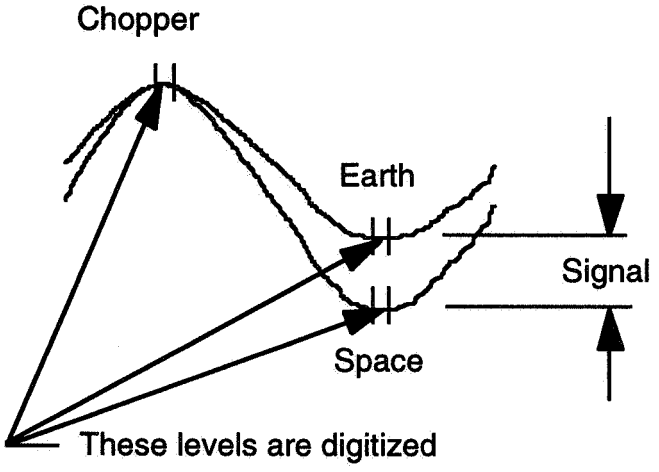

Figure 1 Detector Input Signals

The signals from the detectors are multiplexed and digitized at the "Chopper" and the "Space/Earth" positions as shown in Figure 1. The "Signal" level shown is the typical space-earth difference signal seen by the conventional earth sensor. The detector array will observe several horizons and the signal processing will determine the location of each sensed horizon corrected for local radiance conditions. A best-fit circle (ellipse) is then applied to the horizon positions with a proprietary error detection system which minimizes the effect of errors caused by the sun, moon, and local weather conditions.

GEO Configuration

For GEO applications, the earth is imaged directly on the focal plane as illustrated in Figure 2. The focal plane has been configured with four parallel linear arrays as illustrated in Figure 3. The two outer arrays, located at ±6 deg, cover 42 deg with thirteen 3 deg and two 1.5 deg detectors. The two inner arrays, located at ±3 deg, have nine 3 deg detectors. This arrangement provides eight horizon locations and can handle altitudes from 11,500 km to 90,000 km. The off-axis range is ±20 deg in pitch and ±10 deg in roll.

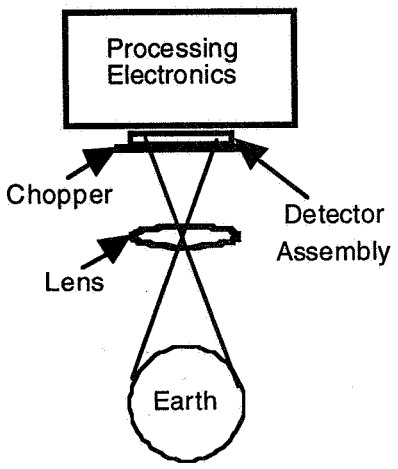

Figure 2 Basic Sensor Approach

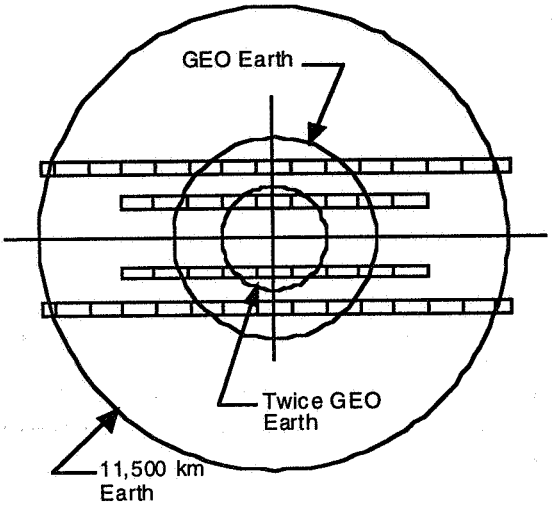

Figure 3 GEO Detector Pattern

LEO Configuration

For LEO applications, the earth is reflected from the four faces of a pyramid, through the optics, then onto the focal plane as illustrated in Figure 4. The focal plane has been configured with four linear arrays in the shape of an "X" as illustrated in Figure 5. The faces of the pyramid are adjusted to the orbital altitude and the arrays each contain eight 2 deg detectors to cover attitude/altitude variations.

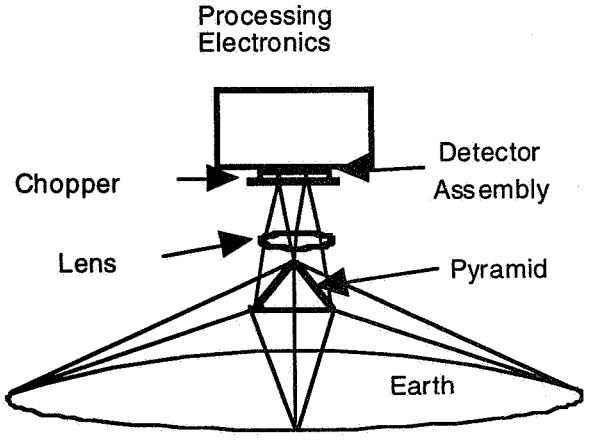

Figure 4 LEO Sensor Approach

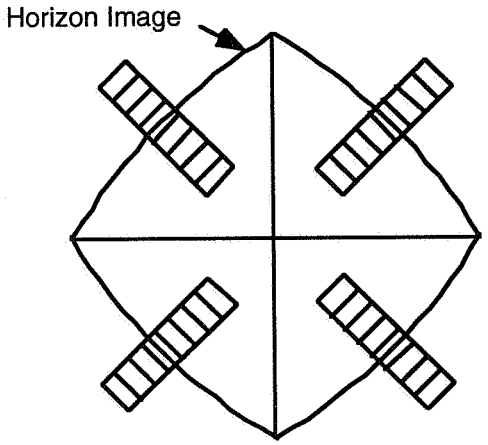

Figure 5 LEO Detector Pattern

ATTITUDE CALCULATIONS

Overview

The detector signals are digitized and then processed by the computer algorithm. The code processes the redundant data from multiple arrays of detectors to find the azimuth and elevation angles of the earth center. It can also find the apparent earth diameter when in the acquisition mode, or it can use a predetermined diameter in track mode for increased accuracy and algorithm robustness. If the earth's image is so far from its nominally centered position that the horizon falls near or beyond the end of one or more arrays, then the position accuracy is reduced, but the code still gives data sufficient for a control loop.

The code is quite insensitive to imperfect data. Shorted or dead pixels are ignored. If the sun is within the field of view, it too is ignored. The code uses a set of detector information to compensate the data for variations in pixel position, size, and response. Sensor drift and seasonal, longitudinal, and latitudinal variations are ignored by normalizing each horizon crossing. By utilizing redundant data, the impact of deviations (e. g. , a cloud system on the horizon, or the sun just behind the horizon) is greatly reduced.

The algorithm first sorts the pixel responses, discarding zeros, shorts, and maximums (the sun if it is within the field of view). Nominal "earth" and "space" values are defined to account for sensor drift, and then the horizon crossings are found as a sequence of "space-horizon-earth" or "earth-horizon-space" readings. The code accounts for a horizon crossing near a pixel boundary and uses the local value for "earth" at each crossing in order to account for local variations.

Horizon Location

The horizon location is determined in the same fashion for all applications. The signal from the one (or two) detector(s) across the horizon are normalized with respect to the signals from the full space and full earth signals adjacent to it (them). This eliminates the chopper signal, adjusts for local radiance conditions, and provides a signal proportional to the position of the horizon along the detector. With the calibrated spatial location of the detector, this is converted to a position with (x,y) coordinates.

Fitting Routine

Once a set of horizon crossing (x,y) coordinates are found, eight points for the GEO configuration and four points for the LEO configuration they can be corrected, as needed, for the earth's ellipticity. They are then fit with a weighted, iterative, least-squares algorithm. The data points are equally weighted for the first pass, but thereafter the weighting is proportional to the closeness of each point to the fit. This iterative process improves the fit by discounting those crossings that don't fit the prescribed shape because of a storm or the sun/moon near the horizon.

By writing the equations in terms of the earth's center with minor displacements from a known position, the fit can be approximated by linear functions. As there are only two or three parameters to be found (the x and y coordinates of the center, and, in the acquisition mode, the apparent radius), the fit can be performed using weighted "normal equations", which involves nothing worse than quickly inverting a 3x3 matrix. As this is an iterative approximation, a couple quick extra passes increase the accuracy. Four passes are used for the first fit, and for fits from the randomly generated data used to test the code; two passes are more than enough when the earth's slowly moving image on the focal plane is virtually unchanged from the previous frame.

SIMULATION PROGRAM

We tested the algorithm by processing simulated detector data. Depending on the choices of the user, the simulation code folded in random unknown variations in the size, position, and response of the detector pixels, projected a non-uniform earth image on the array, added in Gaussian noise and a number of randomly scattered defective pixels, and positioned the sun

somewhere in the field of view, including possibly between two pixels and/or partially obscured by the earth's horizon. The simulation gave the fitting code the radius when testing the track mode, but had the code find the apparent radius in the acquisition mode. It also produced a file which would allow the input position to be compared to the sensor attitude output.

ANALYTICAL RESULTS

The above attitude calculation software was combined with the simulation program to produce the signals expected from a uniform earth from any position to simulate attitude or place different signals into each detector to simulate radiance and interference error signals. Detector noise and position errors were also simulated. We found the fitting code to be robust and quite accurate. The following is a summary of the results from these analyses.

Noise Errors

For the 8-horizon GEO system the results gave an output noise of 0.020 deg rms when a Gausian distributed noise with a 1% rms value with respect to a full space-earth signal was input. This is the standard deviation from a run of 1000 cases and is calculated per chopper cycle. These values would then be decreased by the square root of the number of chopper cycles averaged. For the "X" detector pattern similar runs were made. The results were 0.016 deg rms.

Detector Position Errors

Similar analyses were made for detector position. These analyses assumed that the detector positions could be measured to an accuracy of 0.01 deg rms for the initial calibration. This error would nominally be accounted for with the alignment data but part of it may occur if there is a sun/moon error source present and some of the horizons are dropped from the circle fitting. The results for the GEO pattern were 0.0038 deg rms in pitch and 0.0057 deg rms in roll. For the "X" pattern the results were 0.0048 deg rms in pitch and 0.0046 deg rms in roll. These values would be less than this in orbit (since the detector position errors are constant) and are therefor probably negligible.

Errors From Incrimental Radiance Changes

Several cases were run changing the value of a single detector in a GEO (8-horizon) array to determine if there are any combinations that might cause a problem. For each case the value of the detector signal was changed from 0 to 1023, 1 step at a time. Cases were run for the space, horizon, and earth detectors. The results are shown in Figures 6, 7, and 8 respectively. The polarity of the signals is dependent upon the quadrant where the error occurs. The results below are in the upper left quadrant.

From these results it can be seen that all of the errors are less than 0.001 deg for pitch and 0.005 deg for roll. The nominal signal amplitudes in the simulation for a uniform earth at null were: space 25; horizon 580; earth 925. The outputs tended to vacillate about these nominal values as the run amplitude values went through them. Figure 6 is indicative of response to solar interference where the signal would gradually increase to saturation. In Figure 7 the part to the left of 580 represents cold clouds and that to the right represents solar interference. For Figure 8, only the portion to the left of 925, representing cold clouds, would have "real world" significance.

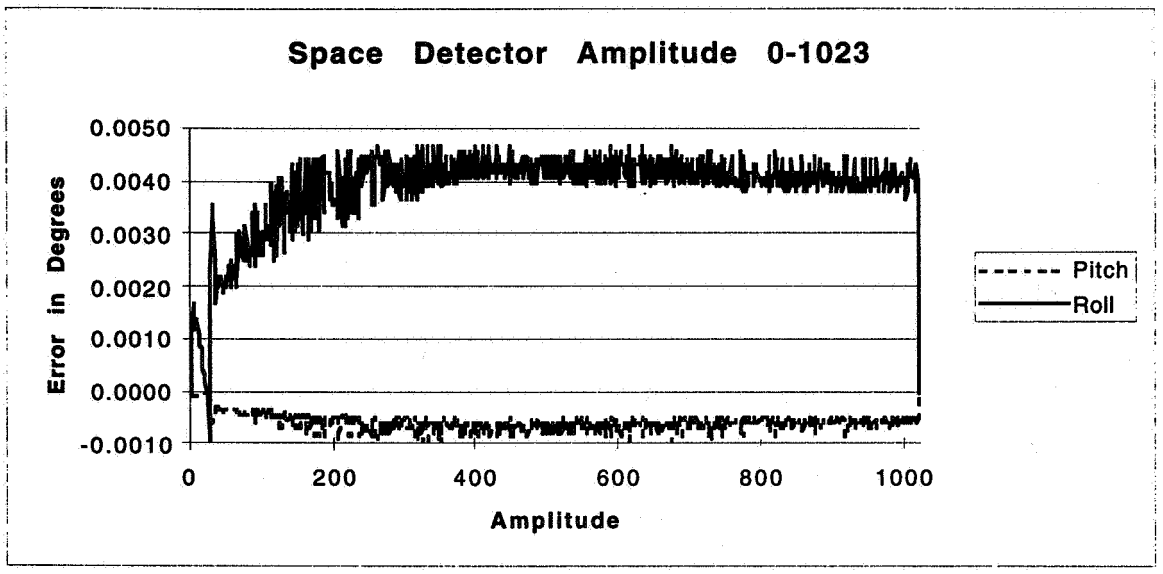

Figure 6 Space Detector Variation Errors

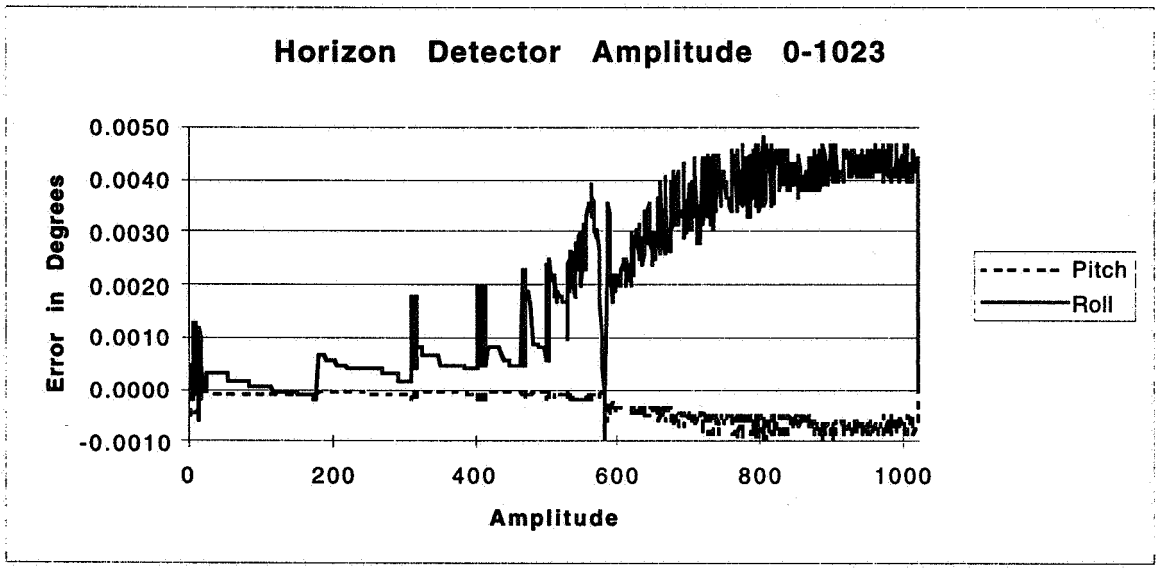

Figure 7 Horizon Detector Variation Errors

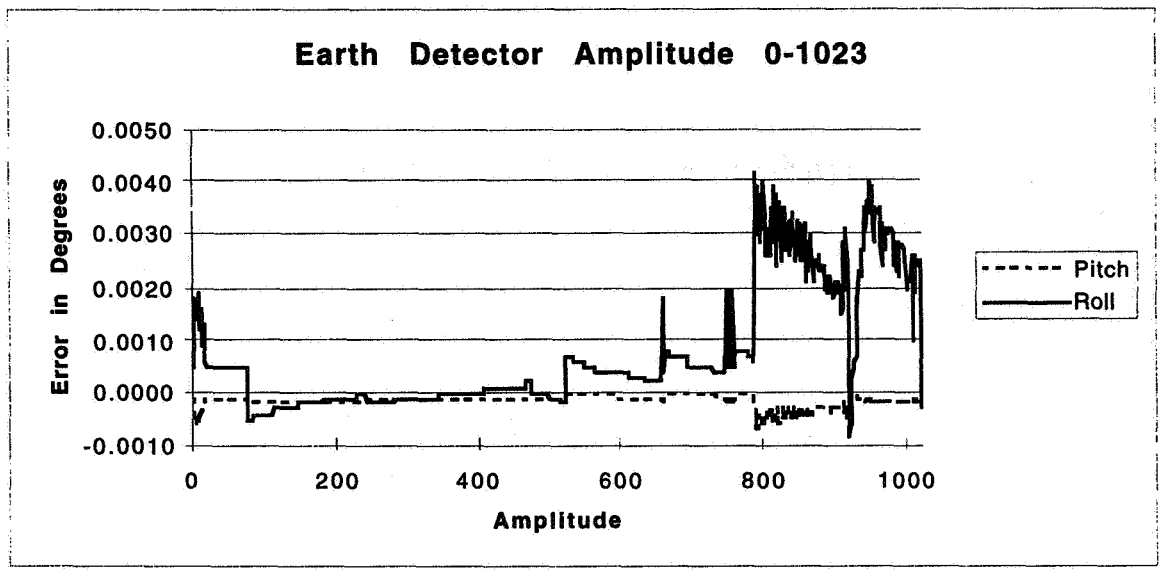

Figure 8 Earth Detector Variation Errors

Errors from Orbital Conditions

Many cases were run to simulate worst case radiance errors from the earth, sun and moon interference, and various combinations of these sources. Table 1 presents the results of these analyses for the GEO (8-horizon) sensor with the error values in deg. The "Error Source" values used are typical of what one might experience from a GEO orbit. The results show no errors greater than 0.005 deg for the given radius (track mode) conditions and 0.06 deg for the unknown radius(acquisition mode) conditions under all probable inputs. Similar cases were run for the 4-horizon sensor and the given values were all less than 0.013 deg and unknown values less than 1.1 deg. Again, polarity is dependent upon the quadrant the error source is in.

Table 1

GEO SIMULATED ORBITAL ERRORS

Run #	Error Source	Given Radius		Unknown Radius	
		Pitch	Roll	Pitch	Roll
0	Baseline	0.0000	0.0000	0.0000	0.0000
1	Full sun in space detector	-0.0005	0.0036	-0.0010	0.0017
2	Full sun in horizon detector	-0.0007	0.0044	-0.0004	0.0033
3	1% sun in space detector	-0.0003	0.0020	-0.0004	0.0041
4	1% sun in horizon detector	-0.0003	0.0020	-0.0004	0.0039
5	1% cloud in horizon detector	-0.0001	0.0029	-0.0001	0.0014
6	1% cloud in earth detector	-0.0004	0.0031	-0.0006	0.0042
7	1% cloud on 2 horizons	-0.0010	0.0043	0.0102	-0.0110
8	5% cloud on horizon	0.0000	0.0009	0.0011	-0.0005
9	10% E-W gradient (worst case)	-0.0013	0.0062	-0.0006	0.0043

10	Sun in Row A & 2% cloud in Row B	-0.0011	0.0045	0.0031	-0.0023
11	Sun in Row B & 2% cloud in Row A	-0.0002	0.0036	0.0004	0.0008
12	Sun in Row A & 2% cloud in Row D	-0.0008	0.0020	0.0069	0.0171
13	Worst seasonal N-S gradient	0.0000	-0.0022	0.0000	0.0005
14	10% E-W gradient & sun in Row D	0.0000	-0.0057	-0.0060	-0.0056
15	Worst N-S gradient & sun in Row A	0.0000	-0.0022	0.0000	0.0005
16	Sun (5%) passing between 2 rows	-0.0012	0.0047	-0.0339	0.0553
17	Full sun in 2 rows	-0.0012	0.0043	-0.7658	1.0577
18	Failed Row A array	0.0000	0.0004	0.0000	0.0044
19	Failed Row A & sun in Row B	0.0000	0.0002	0.0000	-0.0043
20	Failed Rows A & B	0.0000	0.0003	0.0000	0.0136
21	Failed Rows A & C	0.0000	0.0062	0.0000	0.0045
22	2% cloud in 4 West horizons	0.0333	0.0000	0.0333	0.0000
23	2% cloud in 4 North horizons	0.0000	0.0034	0.0000	-0.0359

Linearity

Several linearity conditions were simulated. Two hundred cases each were run for pitch and roll, to ±20 deg and ±10 deg respectively, with the other axis at zero. These results are illustrated in Figures 9 and 10. One thousand cases were run for combinations of pitch and roll between ±8 deg and ±3 deg respectively. The standard deviation from the correct position was 0.0009 deg rms in pitch and 0.0095 deg rms in roll for all of the cases.

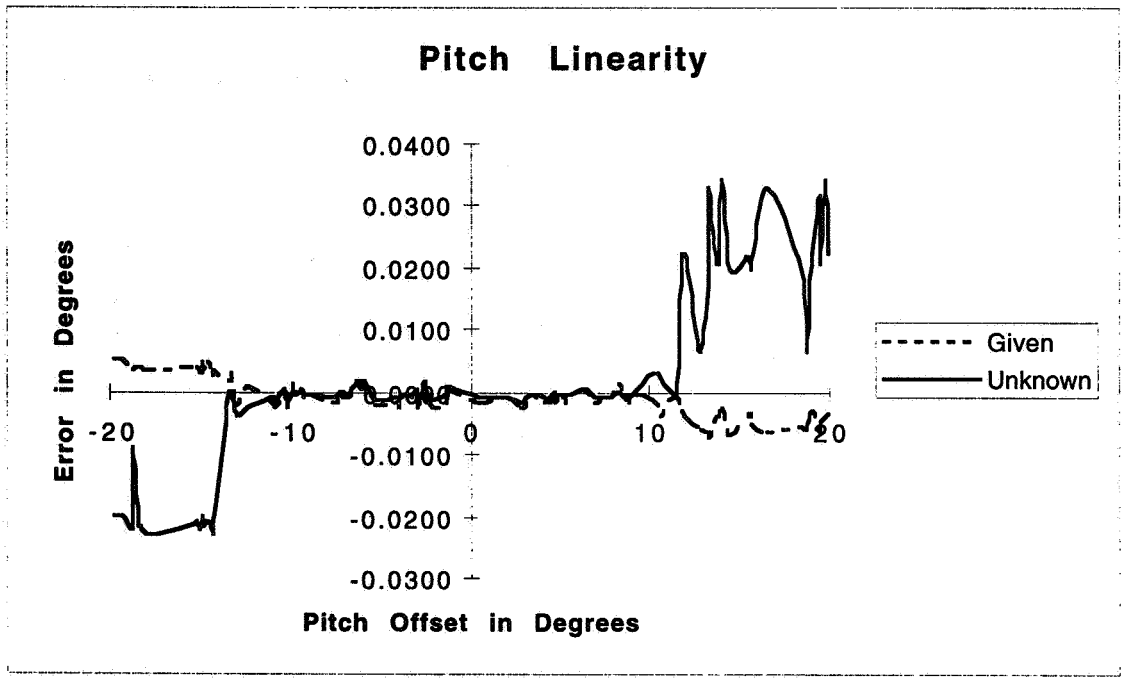

Figure 9 Pitch Linearity Analysis Results

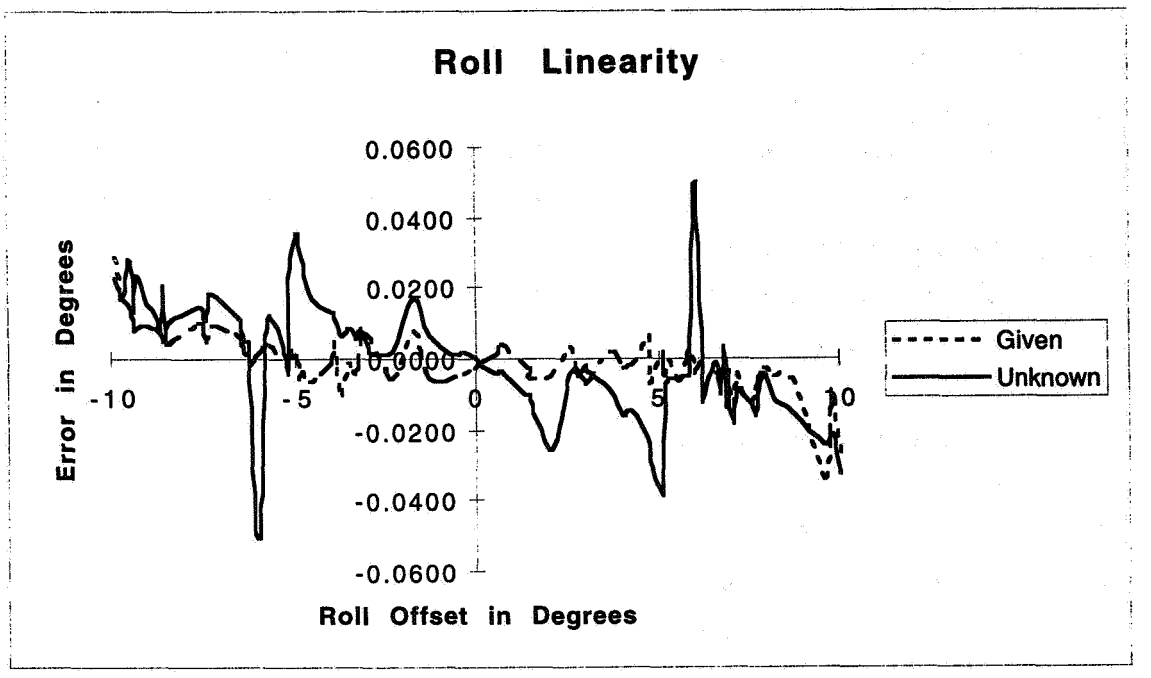

Figure 10 Roll Linearity Analysis Results

PERFORMANCE MODEL

A model of the sensor with inputs for all of the detector physical parameters, sensor optical characteristics, electronic characteristics, and input signal has been created. This model has been correlated with the development sensor results and the parameters adjusted to fit. The model uses 35 detector parameters and 29 sensor parameters (input or derived). This model allows us to adjust parameters to make performance/configuration trades for any proposed application and feel confident of the proposed results. This performance model predicts a noise-equivalent-angle for the GEO sensor of 0.008 deg rms per update, or 0.002 deg rms per sec. This is consistent with the predicted S/N of over 250 as compared to the 100 used in the simulations discussed above.

Detector Performance

Table 2 lists the parameters and their probable values for the Lithium Tantalate ($LiTaO_3$) pyroelectric detectors in the arrays planned for the GEO LCES. Some of the parameters are characteristic of the material, some are chosen as design values, and some are derived from equations which relate their performance. The frequency sensitive values are normalized to 1 Hz. These parameters match the performance of the development model sensor.

Table 2

DETECTOR PARAMETERS

Parameter	Symbol/Equation	Value	Units
Length of detector	l	1.30E-01	cm
Width of detector	b	5.00E-02	cm
Area of detector	$A_d = lb$	6.50E-03	cm^2
Thickness of detector	t	5.00E-03	cm

Dielectric constant	ε_0	4.30E+01	
Dielectric factor	KO	8.86E-14	$F \cdot cm^{-1}$
Emissivity	ε	9.00E-01	
Thermal conductivity	k	3.90E-02	$W \cdot cm^{-1} \cdot K^{-1}$
Stefan-Boltzmann constant	σ	5.67E-12	$W \cdot cm^{-2} \cdot K^{-4}$
Temperature	T	2.50E+01	°C
Absolute temperature	$T_a = T + 273$	2.98E+02	K
Specific heat	c_v	3.20E+00	$J \cdot cm^{-3} \cdot K^{-1}$
Amplifier stray capacitance	c_a	1.20E-12	F
Pyroelectric coefficient	P	2.30E-08	$C \cdot cm^{-2} \cdot K^{-1}$
FET leakage current	I_g	1.80E-14	A
Electron charge	e	1.60E-19	C
Capacitance	$c = \varepsilon_0 A_d KO/t$	4.95E-12	F
Noise bandwidth	BW	1.00+00	Hz
Boltzmann constant	κ	1.38E-23	$W \cdot s \cdot K^{-1}$
Loss tangent	tan δ	1.50E-03	
Thermal time constant-conduction	$\tau_{tc} = c_v A_d/k$	5.33E-01	s
Thermal time constant-radiation	$\tau_{tr} = c_v A_d/(4\varepsilon\sigma A T_a^3)$	2.96E+01	s
Thermal time constant	$\tau_t = 1/[(1/\tau_{tc})+(1/\tau_{tr})]$	5.24E-01	s
Frequency of operation	f	1.80E+01	Hz
Current responsivity	$\Re_{di} = (2\pi f\tau_t P)/\{c_v t[1+(2\pi f\tau_t)^2]^{1/2}\}$	1.29E-06	$A \cdot W^{-1}$
Load resistor	R_L	8.00E+10	Ω
Network impedance	$Z_i = R_L/\{1+[2\pi f R_L(c+c_a)]^2\}$	1.44E+09	Ω
Voltage responsivity	$\Re_d = \Re_{di} Z_i$	1.86E+03	$V \cdot W^{-1}$
Noise due to FET gate current	$N_F = Z_i(2eI_g BW)^{1/2}$	1.09E-07	$V \cdot Hz^{-1/2}$
Resistor thermal noise	$N_R = Z_i(4\kappa T_a BW/R_L)^{1/2}$	6.52E-07	$V \cdot Hz^{-1/2}$
Loss tangent noise	$N_L = Z_i(4\kappa T_a 2\pi f c \tan\delta)^{1/2}$	1.69E-07	$V \cdot Hz^{-1/2}$
Noise from FET at frequency	N_{ef}	3.50E-08	$V \cdot Hz^{-1/2}$
Total detector noise voltage	$V_{nd} = [N_F^2 + N_R^2 + N_L^2 + N_{ef}^2]^{1/2}$	6.83E-07	$V \cdot Hz^{-1/2}$
Noise-equivalent-power	$NEP = V_n/\Re_d$	3.67E-10	$W \cdot Hz^{-1/2}$

Sensor Signal Levels

The signal and noise levels for the GEO sensor, their conversion to the sensor output, and the amplifier gain levels are calculated in this section. The values chosen for design parameters are those expected in any final design. There may be some variation when all aspects of the design are executed. Again, the equations listed below are for the calculated parameters in Table 3. Some of the values in Table 3 are brought over from those in Table 2.

Table 3

SENSOR PERFORMANCE PARAMETERS

Parameter	Symbol/Equation	Value	Units
Radiance from earth within 15μ band	L_e	4.08E-04	$W \cdot cm^{-2} \cdot sr^{-1}$
Focal length of lens	f_L	2.54E+00	cm
Diameter of lens	D	2.54E+00	cm
F/No.	$F = f_L/D$	1.00E+00	
Area of aperture	$A = \pi D^2/4$	5.07E+00	cm^2
Area of detector	A_d	6.50E-03	cm^2
Field-of-view	$\Omega = A_d/f_L^2$	1.01E-03	sr
Transmission of lens	T_1	7.50E-01	
Transmission of filter	T_2	6.00E-01	
Total transmission of optics	$T_O = T_1 T_2$	4.50E-01	
Modulation factor	M	4.00E-01	
Power on detector	$P_d = LA\Omega T_O M$	3.75E-07	W
Detector responsivity	$\Re_d$	1.86E+03	$V \cdot W^{-1}$
Detector equivalent voltage	$V_d = P_d \Re_d$	6.97E-04	V
Detector noise voltage	V_{nd}	6.83E-07	$V \cdot Hz^{-1/2}$
Detector noise-equivalent-bandwidth	NEB_d	7.25E+00	Hz
Amplifier noise voltage	V_{na}	1.80E-08	$V \cdot Hz^{-1/2}$
Amplifier noise-equivalent -bandwidth	NEB_a	4.00E+01	Hz
Total noise voltage	$V_n = [(V_{nd} NEB_d^{1/2})^2 + (V_{na} NEB_a^{1/2})^2]^{1/2}$	1.84E-06	V rms
Detector signal-to-noise ratio	$S/N_d = V_d/V_n$	3.78E+02	
Detector angle	α	3.00E+00	deg
Detector noise-equivalent-angle	$NEA_d = 8^{1/2} \alpha S/N_d$	2.24E-02	deg rms
Sensor noise-equivalent-angle	$NEA_S = NEA_d/8^{1/2}$	7.93E-03	deg rms
Sensor noise-equivalent-angle per sec	$NEA_{S/s} = NEA_d/f^{1/2}$	1.87E-03	deg rms

PROPOSED CONFIGURATIONS

SSS has proposed several LCES configurations to meet special customer requirements. The following gives a brief summary of some of these to illustrate the wide range of applications which can be covered with this approach.

Table 4 presents the summary specifications of some of the types of sensors possible. These specifications include temperature and age variations.

Table 4

POSSIBLE SENSOR APPLICATIONS

Config.	Altitude (10^3km) Min-Max	Range (deg) Pitch/Roll	NEA/sec (deg rms)	Instrument Error (deg 3σ)	Radiance Error (deg 3σ)
GEO	11.5-90	±20/±10	0.003	0.02	0.005
GPS	17.6-23	±2	0.005	0.02	0.01
Odyssey	7.4-13.9	±5	0.005	0.02	0.01
LEO	0.8-2.0	±5	0.007	0.05	0.02
Elliptical	0.5-9.0	±5	0.01	0.05	0.03
Single Line	N/A	±20	0.01	0.05	0.05

CONCLUSIONS

An earth sensor technology has been created which allows for modeling of all design parameters and processing algorithms. The performance of these models has been correlated with development sensor hardware performance. This allows the accurate prediction of the performance for sensor configurations covering most earth-orbiting applications.

ACKNOWLEDGMENTS

The Authors would like to acknowledge the team at Spiricon, Inc. for their excellent support in the LCES design and development effort and Alan Doctor of Servo Corp. for his assistance in the development of the detector relationships.

REFERENCE

1. R. H. Anderson, "The Development of a Family of Low Cost Earth Sensors", 20th Annual AAS Guidance and Control Conference, Breckenridge, Colorado, paper AAS 97-043, February 5-9, 1997.

Ground-Support Algorithms for Simulation, Processing, and Calibration of Barnes Static Earth Sensor Measurements: Applications to Tropical Rainfall Measuring Mission Observatory*

G. A. Natanson
Computer Sciences Corporation (CSC)
Lanham-Seabrook, Maryland, USA

Abstract

New algorithms are described covering the simulation, processing, and calibration of penetration angles of the Barnes static Earth sensor assembly (SESA) as implemented in the Goddard Space Flight Center Flight Dynamics Division ground support system for the Tropical Rainfall Measuring Mission (TRMM) Observatory. The new treatment involves a detailed analysis of the measurements by individual quadrants. It is shown that, to a good approximation, individual quadrant misalignments can be treated simply as penetration angle biases. Simple formulas suitable for real-time applications are introduced for computing quadrant-dependent effects.

The simulator generates penetration angles by solving a quadratic equation with coefficients uniquely determined by the spacecraft's position and the quadrant's orientation in geocentric inertial (GCI) coordinates.

Measurement processing for attitude determination is based on linearized equations obtained by expanding the coefficients of the aforementioned quadratic equation as a Taylor series in both the Earth oblateness coefficient ($\alpha \approx 1/150$) and the angle between the pointing axis and the geodetic nadir vector. A simple formula relating a measured value of the penetration angle to the deviation of the Earth-pointed axis from the geodetic nadir vector is derived. It is shown that even near the very edge of the quadrant's field of view (FOV), attitude errors resulting from quadratic effects are a few hundredths of a degree, which is small compared to the attitude determination accuracy requirement (0.18 degree, 3σ) of TRMM.

Calibration of SESA measurements is complicated by a first-order filtering used in the TRMM onboard algorithm to compute penetration angles from raw voltages. A simple calibration scheme is introduced where these complications are avoided by treating penetration angles as the primary raw measurements, which are adjusted using biases and scale factors. In addition to three misalignment parameters, the calibration state vector contains only two average penetration angle biases (one per each pair of opposite quadrants) since, because of the very narrow sensor FOV (± 2.6 degrees), differences between biases of the penetration angles measured by opposite quadrants cannot be distinguished from roll and pitch sensor misalignments. After calibration, the estimated misalignments and average penetration angle biases are converted to the four penetration angle biases and to the yaw misalignment angle. The resultant biases and the estimated scale factors are finally used to update the coefficients necessary for onboard computations of penetration angles from measured voltages.

* This work was supported by the National Aeronautics and Space Administration /Goddard Space Flight Center, Greenbelt, Maryland, under Contract NAS 5-31000.

Page intentionally left blank

Star Identification Without Attitude Knowledge: Testing with X-Ray Timing Experiment Data

Eleanor Ketchum*
NASA GSFC Code 745
Greenbelt, MD 20771

As the budget for the scientific exploration of space shrinks, the need for more autonomous spacecraft increases. For a spacecraft with a star tracker, the ability to determinate attitude from a lost in space state autonomously requires the capability to identify the stars in the field of view of the tracker. Although there have been efforts to produce autonomous star trackers which perform this function internally, many programs cannot afford these sensors. The author previously presented a method for identifying stars without a priori attitude knowledge specifically targeted for onboard computers as it minimizes the necessary computer storage. The method has previously been tested with simulated data. This paper provides results of star identification without a priori attitude knowledge using flight data from two 8 by 8 degree charge coupled device star trackers onboard the X-Ray Timing Experiment.

* eleanor.ketchum@gsfc.nasa.gov, (301) 286-1170 (voice), (301) 286-1763 (fax)

Page intentionally left blank

Attitude Determination For GEO Satellites

Andy Wu
Hughes Aircraft Company
Mail Station EO/E1/D125
P.O. Box 902
El Segundo, California 90245
Tel. 310-616-4858

Abstract

Normal mode attitude determination algorithms for geosynchronous orbit (GEO) satellites are derived and their attitude determination performance are analyzed in this paper. The attitude determination system is comprised of a Litton's hemispheric resonator gyro inertial reference unit (HIRU), Barnes static Earth sensor assemblies (ESAs), a two-axis Adcole fine Sun sensor (FSS), and an onboard spacecraft control processor (SCP). Real-time knowledge of spacecraft attitude with respect to an inertial reference frame is maintained by propagating the HIRU data during each computation cycle. Earth/Sun sensor data are processed using extended Kalman filtering to estimate and correct the attitude determination errors, the gyro bias errors, and the Earth sensor bias errors. A fixed gain filter without computing the covariance matrix is derived to simplify the estimation algorithm. A Matlab-based time domain nonlinear simulation model is developed to evaluate the attitude determination algorithm performance. Simulation results show that precision attitude determination (less than $\pm$ 0.05 deg per axis) during normal mode operation is achieved using the selected attitude hardware and algorithms.

1.0 Introduction - Attitude Determination Algorithm Overview

For future three-axis stabilized geosynchronous communication satellites built by Hughes, the Attitude Determination and Control System (ADCS) will be designed to provide the spacecraft inertial attitude with accuracy better than $\pm$ 0.05 deg in roll, pitch, and yaw in order to meet the overall pointing requirement during the normal Earth pointing mode. The selected attitude hardware for precision attitude determination consists of (1) the Litton's HIRU mounted on a radiator panel, (2) the two axis Adcole FSS mounted on the aft structure for sun viewing near sunset, (3) Barnes static ESAs mounted at three places on the nadir structure to optimize Earth viewing angles, and (4) the Spacecraft Control Processor (SCP) which hosts the ADCS software and all sensor and actuator input/output (I/O) functions.

This paper describes the design and performance evaluation of precision attitude determination algorithms using the aforementioned attitude sensors. A functional block diagram of the attitude determination algorithms is show in Figure 1. The algorithms are partitioned into three major modules : attitude propagation, attitude estimation, and attitude correction. Listed below are the nomenclature used throughout the paper:

$\omega^{B}_{I\leftarrow B}$: a 3x1 vector representing three angular rates of a Body reference frame with respect to an Inertial reference frame, where the vector is expressed in Body reference frame.

C^{O}_{B} : a 3x3 direction cosine matrix representing the attitude of an Orbital reference frame with respect to a Body reference frame.

Q^{O}_{B} : a quaternion presented by a 4x1 vector specifying the rotation of an Orbital reference frame with respect to a Body reference frame.

1.1 Attitude Propagation.

HIRU data is periodically sampled (every 32 msec.) into the SCP, compensated for known measurement errors such as input axis misalignments, converted into body reference frame, and corrected for gyro biases. The compensated gyro data is then used to numerically integrate a set of euler parameters (or quaternion) that specify the spacecraft attitude with respect to an orbital reference frame.

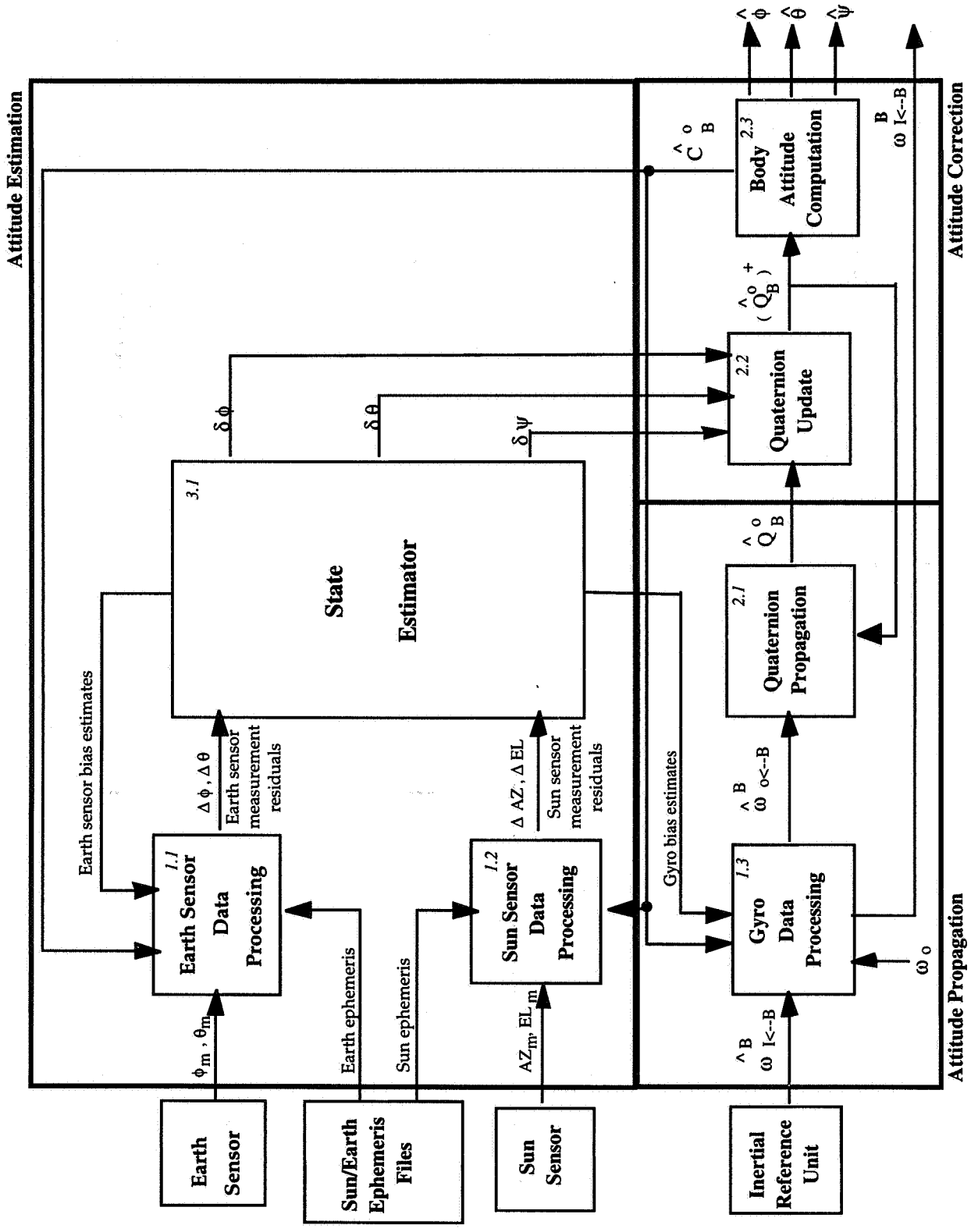

Figure 1 GEO Satellite Attitude Determination Functional Block Diagram

1.2 Attitude Estimation.

Because of the initial attitude error used in quaternion integration and the accumulated effect of both gyro measurement errors and integration truncation and round off errors, attitude determined by processing only gyro data

will contain errors that grow with time. The gyro measurement errors include gyro random walk, bias instability, resolution, and scale factor error. The function of the attitude estimator is to use Earth/Sun sensor data to estimate the spacecraft attitude determination errors. In addition, the attitude estimator estimates the gyro biases to be compensated in gyro data processing submodule, thus reducing the rate of error growth between updates or in the absence of the Sun sensor and improving spacecraft rate stability.

1.3 Attitude Correction.

At the end of each Earth/Sun sensor measurement cycle, the spacecraft attitude will be updated in accordance with equations summarized in Figure 2.2 using body attitude error estimates provided by the attitude estimator. The spacecraft roll, pitch, and yaw attitudes are then computed as shown in Figure 2.3.

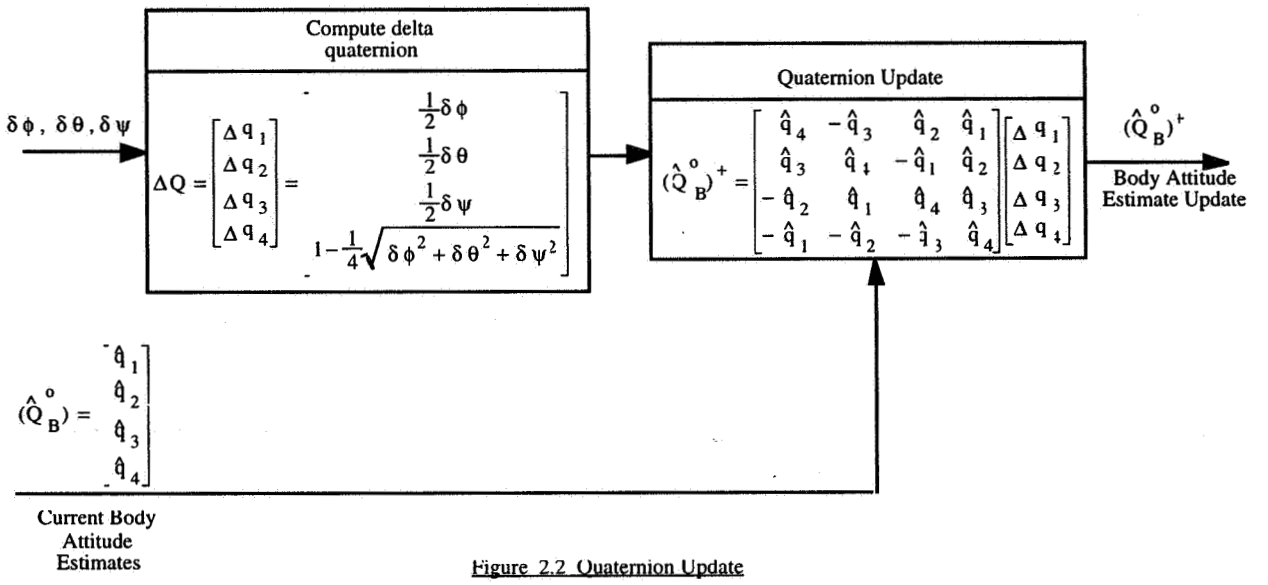

Figure 2.2 Quaternion Update

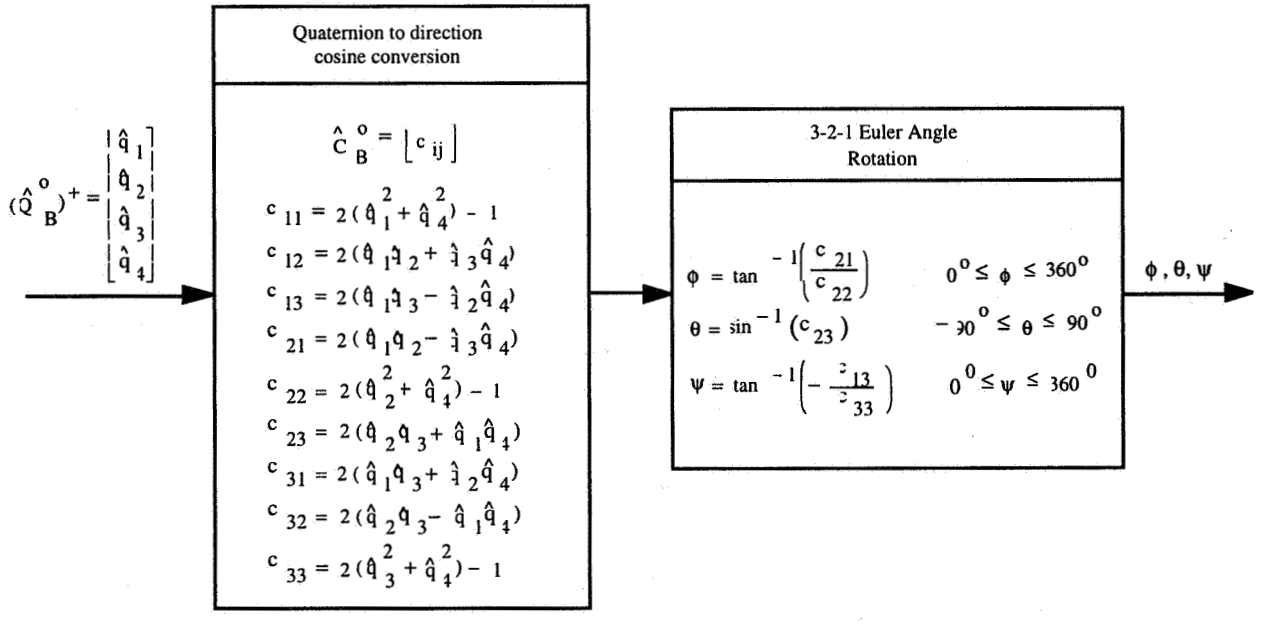

Figure 2.3 Body Attitude Computation

In the following, we will derive the attitude estimator using Kalman filtering techniques, design a fixed gain estimator to simplify filter computation, describe a time-domain simulation model using Matlab simulation language, and present the simulation results.

2.0 Derivation of Attitude Estimator

The application of Kalman filtering theory to attitude estimation requires : (1) to define the state variables to be estimated and their dynamics, (2) to express the measurements (or Earth/Sun observations) in terms of defined state variables, and (3) if necessary, to linearize the state equations and measurement equations.

2.1 State Variables and Dynamic Equations.

The dynamics of spacecraft attitude, represented by a quaternion Q_B^O, satisfies following well-known kinematics equations of motion :

$$\dot{Q}_B^O = \Omega\left(\omega_{O\leftarrow B}^B\right) * Q_B^O \qquad (1)$$

$$\Omega\left(\omega_{O\leftarrow B}^B\right) = \begin{bmatrix} \frac{1}{2}\omega_{O\leftarrow B}^B(1) \\ \frac{1}{2}\omega_{O\leftarrow B}^B(2) \\ \frac{1}{2}\omega_{O\leftarrow B}^B(3) \\ 0 \end{bmatrix} \qquad (2)$$

where "*" in Equation (1) denotes the quaternion multiplication [1,2]. The truth spacecraft attitude is obtained by integrating Equation (1) with given initial conditions and truth body rates, $\omega_{O\leftarrow B}^B$. Since the spacecraft attitude, $\hat{Q}_B^O$ is computed using a numerical integration of following differential equations :

$$\dot{\hat{Q}}_B^O = \Omega\left(\hat{\omega}_{O\leftarrow B}^B\right) * \hat{Q}_B^O \qquad (3)$$

with

$$\hat{\omega}_{O\leftarrow B}^B = -\left[\hat{C}_B^O\right]\omega_{I\leftarrow O}^O + \hat{\omega}_{I\leftarrow B}^B \qquad (4)$$

where

$$\omega_{I\leftarrow O}^O = \begin{bmatrix} 0 \\ -\omega_o \\ 0 \end{bmatrix} ; \quad \omega_o = \text{orbital rate } (\approx 15 \text{ deg/hr for a geosyncronized orbit})$$

and $\hat{\omega}_{I\leftarrow B}^B$ are the measured body inertial rates provided by the HIRU, the computed spacecraft attitude, $\hat{Q}_B^O$ will be different from the truth spacecraft attitude, Q_B^O.

Let ΔQ_B^O denote the error quaternion satisfying :

$$Q_B^O = \left(\Delta Q_B^O\right) * \hat{Q}_B^O \qquad (5)$$

with $\Delta Q_B^O = \left[\Delta q_1 \quad \Delta q_2 \quad \Delta q_3 \quad 1 - \sqrt{\Delta q_1^2 + \Delta q_2^2 + \Delta q_3^2}\right]^T$; and Q_B^O, $\hat{Q}_B^O$ satisfy Equations (1) and (3) respectively. By taking a time derivative of both sides of Equation (5), one obtains the following error quaternion dynamic equations :

$$\Delta\dot{Q}_B^O = \Omega\left(\hat{\omega}_{O\leftarrow B}^B\right) * \Delta Q_B^O - \Delta Q_B^O * \Omega\left(\hat{\omega}_{O\leftarrow B}^B\right) + \Omega(\Delta\omega) * \Delta Q_B^O \qquad (6)$$

with

$$\Delta\omega = \Delta\omega_{I\leftarrow B}^B + [\delta C]\left[\hat{C}_B^O\right]\omega_{I\leftarrow O}^O \qquad (7)$$

$$\Delta\omega^{B}_{I\leftarrow B} = \omega^{B}_{I\leftarrow B} - \hat{\omega}^{B}_{I\leftarrow B} = \begin{bmatrix} \Delta\omega_x \\ \Delta\omega_y \\ \Delta\omega_z \end{bmatrix} \tag{8}$$

and δC satisfies :

$$C^{O}_{B} = (I + \delta C)\hat{C}^{O}_{B} \tag{9}$$

The gyro error vector, $\Delta\omega^{B}_{I\leftarrow B}$ defined in Equation (8) can be expressed as :

$$\Delta\omega^{B}_{I\leftarrow B} = \begin{bmatrix} \Delta\omega_x \\ \Delta\omega_y \\ \Delta\omega_z \end{bmatrix} = \begin{bmatrix} \Delta b_x \\ \Delta b_y \\ \Delta b_z \end{bmatrix} + \begin{bmatrix} n_{rwx} \\ n_{rwy} \\ n_{rwz} \end{bmatrix} \tag{10}$$

$$\text{with} \quad \begin{bmatrix} \dot{\Delta b}_x \\ \dot{\Delta b}_y \\ \dot{\Delta b}_z \end{bmatrix} = \begin{bmatrix} n_{rrwx} \\ n_{rrwy} \\ n_{rrwz} \end{bmatrix} \tag{11}$$

where n_{rw} are gyro angle random walk noises and n_{rrw} are gyro rate random walk noises. Based on Equations (6) and (11), the three attitude errors : $2\Delta q_1$, $2\Delta q_2$, $2\Delta q_3$ and three gyro bias errors : Δb_x, Δb_y, Δb_z are selected as state variables to be estimated.

2.2. Linearization of Dynamic Equations.

By substituting Equations (7), (8) and (10) into Equation (6), one notes that Equation (6) is a nonlinear function of defined states variables. To apply the Kalman filtering techniques, one needs to linearize the dynamic equations - Equation (6).

Linearization of Equation (6) can be obtained by using small angle approximations to a direction consine matrix $\hat{C}^{O}_{B}$,

$$\hat{C}^{O}_{B} \approx \begin{bmatrix} 1 & -\hat{\psi} & \hat{\theta} \\ \hat{\psi} & 1 & -\hat{\phi} \\ -\hat{\theta} & \hat{\phi} & 1 \end{bmatrix} \tag{12}$$

and an attitude error matrix δC,

$$\delta C \approx \begin{bmatrix} 0 & -\delta\psi & \delta\theta \\ \delta\psi & 0 & -\delta\phi \\ -\delta\theta & \delta\phi & 0 \end{bmatrix} \tag{13}$$

with

$$\begin{bmatrix} \phi \\ \theta \\ \psi \end{bmatrix} = \begin{bmatrix} \hat{\phi} + \delta\phi \\ \hat{\theta} + \delta\theta \\ \hat{\psi} + \delta\psi \end{bmatrix} \equiv \begin{bmatrix} \hat{\phi} - 2\Delta q_1 \\ \hat{\theta} - 2\Delta q_2 \\ \hat{\psi} - 2\Delta q_3 \end{bmatrix} \tag{14}$$

and $\hat{\omega}^{B}_{O\leftarrow B} \equiv 0$. By substituting Equations (12) through (14) into Equation (6) and maintaining only the first-order terms, one obtains the following linear dynamic equations :

$$\begin{bmatrix} \dot{\delta\phi} \\ \dot{\delta\theta} \\ \dot{\delta\psi} \end{bmatrix} = \begin{bmatrix} 0 & 0 & \omega_0 \\ 0 & 0 & 0 \\ -\omega_0 & 0 & 0 \end{bmatrix} \begin{bmatrix} \delta\phi \\ \delta\theta \\ \delta\psi \end{bmatrix} - \begin{bmatrix} \Delta\omega_x \\ \Delta\omega_y \\ \Delta\omega_z \end{bmatrix} \qquad (15)$$

2.3 Measurement Equations.

In the following we will derive the measurement residuals (Earth sensor measurement residuals and Sun sensor measurement residuals) and expressed them as a function of the above defined state variables.

2.3.1 Earth Sensor Measurement Residuals.

In Earth pointing mode, Barnes ESAs measure the spacecraft roll and pitch angles directly. The measured spacecraft roll and pitch angles, ϕ_m and θ_m are corrected for the biases first, and then subtracted from the estimated spacecraft roll and pitch angles, $\hat{\phi}$ and $\hat{\theta}$ to form the measurement residuals :

$$\begin{bmatrix} \Delta\phi \\ \Delta\theta \end{bmatrix} = \begin{bmatrix} -\hat{\phi} + \phi_m \\ -\hat{\theta} + \theta_m \end{bmatrix} \qquad (16)$$

The Earth sensor biases, $\hat{\phi}_{mb}$, $\hat{\theta}_{mb}$ are provided by the attitude estimator, and the estimated spacecraft roll and pitch angles are computed using the current body attitude estimates, $\hat{C}_B^O$:

$$\hat{\phi} = \tan^{-1}\left(\frac{-\tilde{r}_e^B(2)}{\tilde{r}_e^B(3)} \right) \qquad (17)$$

$$\hat{\theta} = -\sin\left(\tilde{r}_e^B(1) \right) \qquad (18)$$

$$\tilde{r}_e^B = \left[\hat{C}_B^O \right] \begin{bmatrix} 0 \\ 0 \\ 1 \end{bmatrix}$$

where $\tilde{r}_e^B$ is the estimated Earth unit vector expressed in spacecraft body reference frame.

2.3.2 Sun Sensor Measurement Residuals

Figure 2 shows the Sun sensor geometry, where the Sun sensor boresight is mounted in the roll/yaw plane at an angle, θ_m (= -70 deg), negative from the roll axis. When the Sun is within the sensor field-of-view (FOV), $\pm$ 32 deg as indicated in the figure, the sensor measures two angles , AZ_m and EL_m , azimuth and elevation angles in the FSS frame. Given the Sun Ephemeris data : sum azimuth and elevation angles, AZ_s and EL_s in the orbital frame, the Sun unit vector in the orbital frame can be computed as follows :

$$\tilde{r}_s^O = \begin{bmatrix} \cos(EL_s)\cos(AZ_s) \\ \sin(EL_s) \\ -\cos(EL_s)\sin(AZ_s) \end{bmatrix} \qquad (19)$$

The Sun sensor measurement residuals are defined as the differences between the estimated Sun azimuth and elevation angles and the measured Sun azimuth and elevation angles in the FSS frame :

$$\begin{bmatrix} \Delta EL \\ \Delta AZ \end{bmatrix} = \begin{bmatrix} \tilde{EL} \\ \tilde{AZ} \end{bmatrix} - \begin{bmatrix} EL_m \\ AZ_m \end{bmatrix} \qquad (20)$$

where the estimated Sun azimuth and elevation angles in the FSS frame are given by :

$$\tilde{AZ} = \tan^{-1}\left(\frac{-\tilde{r}_s^{ss}(3)}{\tilde{r}_s^{ss}(1)}\right) \qquad (21)$$

$$\tilde{EL} = \sin^{-1}\left(\tilde{r}_s^{ss}(2)\right) \qquad (22)$$

$$\text{with} \quad \tilde{r}_s^{ss} = \left[C_{ss}^{B}\right]\left[\hat{C}_{B}^{O}\right]\tilde{r}_s^{O} \qquad (23)$$

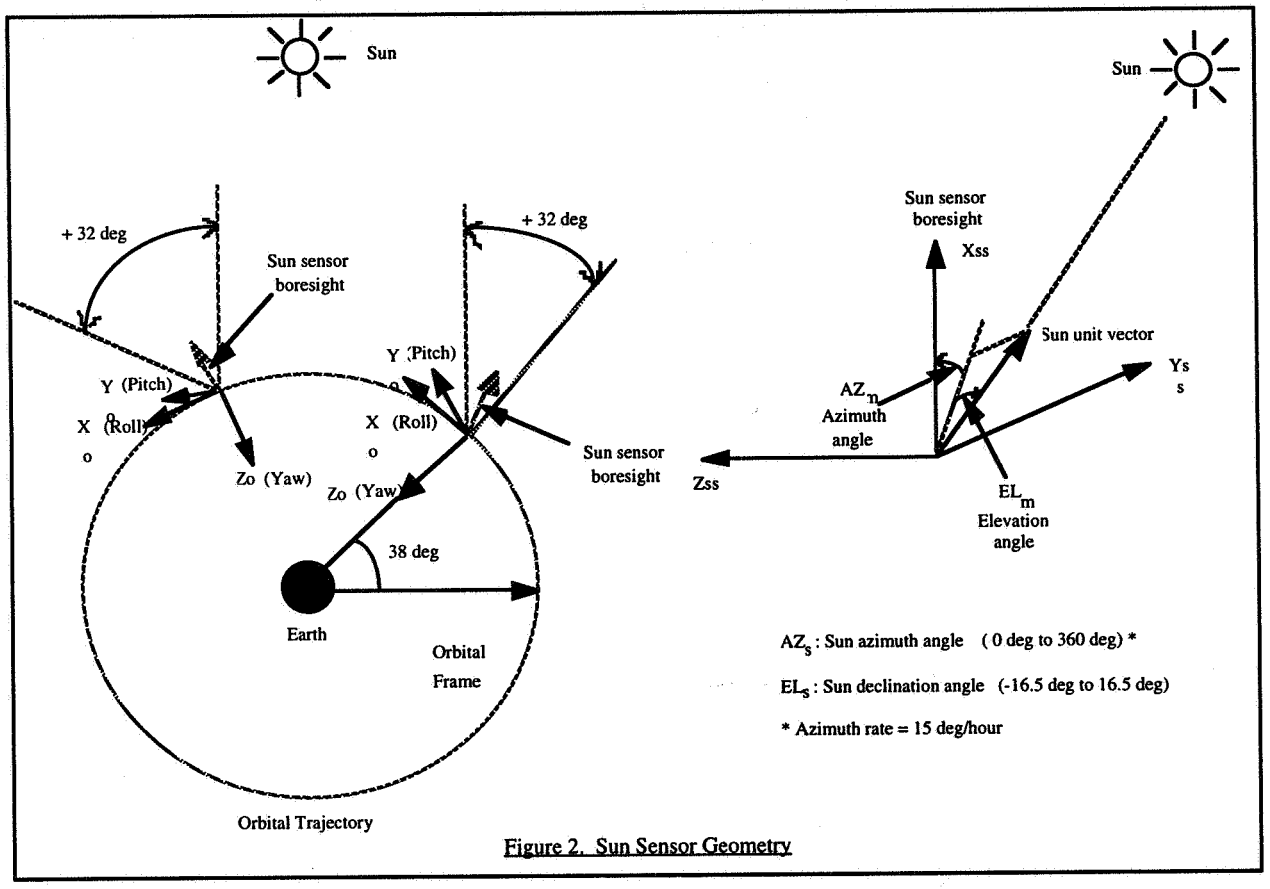

Figure 2. Sun Sensor Geometry

2.4 Linearization of Measurement Equations

2.4.1 Linearization of Earth Sensor Measurement Equations

Let $\Delta\phi_m$, $\Delta\theta_m$ denote the Earth sensor measurement errors, then the measured spacecraft roll and pitch angles, ϕ_m and θ_m are related to the truth spacecraft roll and pitch angles, ϕ and θ as follows :

$$\begin{bmatrix}\phi_m \\ \theta_m\end{bmatrix} = \begin{bmatrix}\phi - \Delta\phi_m \\ \theta - \Delta\theta_m\end{bmatrix} \qquad (24)$$

Substituting Equations (14) and (24) into Equation (16) gives :

$$\begin{bmatrix}\Delta\phi \\ \Delta\theta\end{bmatrix} = \begin{bmatrix}\delta\phi - \Delta\phi_m \\ \delta\theta - \Delta\theta_m\end{bmatrix} \qquad (25)$$

which are linear functions of state variables, $\delta\phi$ and $\delta\theta$.

2.4.2. Linearization of Sun Sensor Measurement Equations

Similarly, let ΔEL_m and ΔAZ_m denote the Sun sensor measurement errors, then the measured azimuth and elevation angles, EL_m and AZ_m are related to the truth azimuth and elevation angles, EL and AZ in the FSS frame as follows :

$$\begin{bmatrix} EL_m \\ AZ_m \end{bmatrix} = \begin{bmatrix} EL - \Delta EL_m \\ AZ - \Delta AZ_m \end{bmatrix} \tag{26}$$

where the truth azimuth and elevation angles in the FSS frame are given by :

$$AZ = \tan^{-1}\left(\frac{-r_s^{ss}(3)}{r_s^{ss}(1)}\right) \tag{27}$$

$$EL = \sin^{-1}\left(r_s^{ss}(2)\right) \tag{28}$$

$$\text{with} \quad r_s^{ss} = \left[C_{ss}^{B}\right]\left[C_{B}^{O}\right]\tilde{r}_s^{O} \tag{29}$$

By applying Taylor series expansion to Equations (27) and (28), the truth azimuth and elevation angles in the FSS frame can be expressed as :

$$\begin{bmatrix} EL \\ AZ \end{bmatrix} = \begin{bmatrix} \tilde{EL} \\ \tilde{AZ} \end{bmatrix} + [D]\,\delta r + O\left(\delta r^2\right) \tag{30}$$

$$D = \begin{bmatrix} 0 & \dfrac{1}{\cos(EL_m)} & 0 \\ -\dfrac{\sin(AZ_m)}{\cos(EL_m)} & 0 & -\dfrac{\cos(AZ_m)}{\cos(EL_m)} \end{bmatrix} \tag{31}$$

$$\delta r = r_s^{ss} - \tilde{r}_s^{ss} \tag{32}$$

where r_s^{ss}, $\tilde{r}_s^{ss}$ satisfy Equations (29) and (23) respectively. By substituting Equations (9), (13), (19), (23), (26), (29), (30), (31), and (32) into Equation (20) with

$$C_{ss}^{B} = \begin{bmatrix} \cos\theta_m & 0 & -\sin\theta_m \\ 0 & 1 & 0 \\ \sin\theta_m & 0 & \cos\theta_m \end{bmatrix}$$

and truncating the higher-order terms, one obtains the linearized Sun sensor measurement equations :

$$\begin{bmatrix} \Delta EL \\ \Delta AZ \end{bmatrix} = \begin{bmatrix} -\sin(AZ_s) & 0 & -\cos(AZ_s) \\ \tan(EL_s)\cos(AZ_s) & -1 & -\tan(EL_s)\sin(AZ_s) \end{bmatrix}\begin{bmatrix} \delta\phi \\ \delta\theta \\ \delta\psi \end{bmatrix} + \begin{bmatrix} \Delta EL_m \\ \Delta AZ_m \end{bmatrix} \tag{33}$$

In obtaining the above equations, we utilize the facts that : $EL_s \cong EL_m$ and $AZ_s \cong AZ_m + \theta_m$.

2.5 Time Varying Kalman Filter

Given the linear dynamic equations - Equations (11) and (15), and linear measurement equations - Equations (25) and (33), we can design an attitude estimator using Kalman filtering techniques.

Let x be a 8x1 state vector : $x = \left[\delta\theta \;\; \Delta b_y \;\; \Delta\theta_e \;\vdots\; \delta\phi \;\; \Delta b_x \;\; \delta\psi \;\; \Delta b_z \;\; \Delta\phi_e\right]^T$ containing 3 attitude errors ($\delta\phi$, $\delta\theta$, $\delta\psi$), 3 gyro bias errors (Δb_x, Δb_y, Δb_z), and 2 Earth sensor bias errors ($\Delta\phi_e$, $\Delta\theta_e$), and y be a 4x1 measurement vector : $y = [\Delta\theta \;\; \Delta AZ \;\; \Delta\phi \;\; \Delta EL]^T$ when The Sun is within the sensor FOV and otherwise, y be a 2x1 measurement vector : $y = [\Delta\theta \;\; \Delta\phi]^T$. In state-space representation, Equations (11), (15), (25), and (33) becomes :

$$\dot{x} = Ax + \omega \qquad (34)$$

$$y = Hx + n \qquad (35)$$

where

$$A = \begin{bmatrix} 0 & -1 & 0 & & & & & \\ 0 & 0 & 0 & & & 0_{3x5} & & \\ 0 & 0 & 0 & & & & & \\ & & & 0 & -1 & \omega_0 & 0 & 0 \\ & & & 0 & 0 & 0 & 0 & 0 \\ & 0_{5x3} & & -\omega_0 & 0 & 0 & -1 & 0 \\ & & & 0 & 0 & 0 & 0 & 0 \\ & & & 0 & 0 & 0 & 0 & 0 \end{bmatrix}$$

where The Sun is within the sensor FOV, the measurement matrix H is given by :

$$H = \begin{bmatrix} 1 & 0 & 1 & 0 & 0 & 0 & 0 & 0 \\ -1 & 0 & 0 & c_{24} & 0 & c_{26} & 0 & 0 \\ 0 & 0 & 0 & 1 & 0 & 0 & 0 & 1 \\ 0 & 0 & 0 & c_{44} & 0 & c_{46} & 0 & 0 \end{bmatrix}$$

$$c_{24} = \tan(EL_s)\cos(AZ_s)$$

$$c_{26} = -\tan(EL_s)\sin(AZ_s)$$

$$c_{44} = -\sin(AZ_s)$$

$$c_{46} = -\cos(AZ_s)$$

otherwise,

$$H = \begin{bmatrix} 1 & 0 & 1 & 0 & 0 & 0 & 0 & 0 \\ 0 & 0 & 0 & 1 & 0 & 0 & 0 & 1 \end{bmatrix}$$

$$\omega = \left[n_{rwy} \;\; n_{rrwy} \;\; n_{eb\theta} \;\; n_{rwx} \;\; n_{rrwx} \;\; n_{rwz} \;\; n_{rrwz} \;\; n_{eb\phi}\right]^T;$$

$$n = \left[n_\theta \;\; \Delta AZ_m \;\; n_\phi \;\; \Delta EL_m\right]^T.$$

It is noted that two new states : the Earth sensor bias errors, $\Delta\phi_e$, $\Delta\theta_e$ are added to the original 6 states previously defined in Section 2.1 to improve attitude determination accuracy. Based on Equations (34) and (35), the discrete attitude estimator can be implemented as follows:

(a) Propagation : Between the Sun/Earth observations, the estimator propagates the covariance matrix P and the estimated state vector, $\hat{x}$:

$$P^-(t + \Delta t) = \phi(\Delta t)\, P^+(t)\, \phi^T(\Delta t) + Q_n(t) \qquad (36)$$

$$\hat{x}^-(t + \Delta t) = \phi(\Delta t)\, \hat{x}^+(t) \qquad (37)$$

where $\phi(\Delta t) = e^{A\Delta t}$ is the state transition matrix, $Q_n(t) = E\left\{\Gamma(\Delta t)\omega(t)\omega^T(t)\Gamma^T(\Delta t)\right\}$ is the process noise covariance matrix with $\Gamma(\Delta t) = \int_0^{\Delta t} e^{A\tau} d\tau$, and the covariance matrix P is defined as :

$$P^+(t) = E\left\{\left(x(t) - \hat{x}^+(t)\right)\left(x(t) - \hat{x}^+(t)\right)^T\right\}$$

(b) Correction : Upon the Sun/Earth observations at time t+Δt, the estimator computes the measurement matrix H as defined in Equation (35) and the time varying estimator gain matrix, $K_c(t + \Delta t)$:

$$K_c(t + \Delta t) = P^-(t + \Delta t) * H * \left(H * P^-(t + \Delta t) * H^T + R\right)^{-1} \qquad (38)$$

where $R = E\left\{nn^T\right\}$ is the 4x4 measurement noise covariance matrix. It updates the covariance matrix, P and the estimated state vector, $\hat{x}$:

$$P^+(t + \Delta t) = \left(I_{8x8} - K_c(t + \Delta t) * H\right) * P^-(t + \Delta t) * \left(I_{8x8} - K_c(t + \Delta t) * H\right)^T + K_c(t + \Delta t) * R * K_c(t + \Delta t)^T \qquad (39)$$

$$\hat{x}^+(t + \Delta t) = \hat{x}^-(t + \Delta t) + K_c(t + \Delta t) * \Delta y(t + \Delta t) \qquad (40)$$

$$\Delta y(t + \Delta t) = y(t + \Delta t) - H * \hat{x}^-(t + \Delta t) \qquad (41)$$

and also updates the spacecraft attitude, gyro bias estimates, and the Earth sensor bias estimates :

$$\delta\theta = d\hat{x}(1) ; \delta\phi = d\hat{x}(4) ; \delta\psi = d\hat{x}(4) ;$$

$$\hat{b}_1 = \hat{b}_1 + d\hat{x}(5) ; \hat{b}_2 = \hat{b}_2 + d\hat{x}(2) ; \hat{b}_3 = \hat{b}_3 + d\hat{x}(7) ;$$

$$\hat{\theta}_{mb} = d\hat{x}(3) ; \hat{\phi}_{mb} = d\hat{x}(8)$$

where $d\hat{x} = K_c(t + \Delta t) * \Delta y(t + \Delta t)$.

2.6 Attitude Estimator With Fixed Gains

Implementation of the time varying attitude estimator described by Equations (36) through (41) requires intensive real time computations of Kalman filtering gain matrix and covariance matrix. To reduce the SCP computation throughput, a fixed gain filter without computing the covariance matrix is desired.

2.6.1. Earth Sensor Only Case

When The Sun is not within the sensor FOV, the only attitude measurements come from the Earth sensors. In this case, the measurement matrix H is a constant matrix. Since the pitch axis dynamics is decoupled from the roll/yaw axes dynamics, the two constant gain matrices $K_{\theta e}$ (2x1) matrix and $K_{\phi e}$ (3x1) matrix can be obtained by solving the following two discrete Riccati Equations :

Pitch axis estimator :

$$P_1 = M_1 - M_1 H_1^T \left(R_1 + H_1 M_1 H_1^T\right)^{-1} H_1 M_1$$

$$M_1 = \phi_1(\Delta t) P_1 \phi_1^T(\Delta t) + \Gamma_1(\Delta t) Q_1\{t\} \Gamma_1^T(\Delta t)$$

Roll/yaw axes estimator :

$$P_2 = M_2 - M_2 H_2^T \left(R_2 + H_2 M_2 H_2^T\right)^{-1} H_2 M_2$$

$$M_2 = \phi_2(\Delta t) P_2 \phi_2^T(\Delta t) + \Gamma_2(\Delta t) Q_2\{t\} \Gamma_2^T(\Delta t)$$

with

$$K_{\theta e} = P_1 H_1^T R_1^{-1} \qquad (42)$$

$$K_{\phi e} = P_2 H_2^T R_2^{-1} \qquad (43)$$

It is noted that the pitch Earth sensor bias error is not observable in the pitch axis estimator, and both the roll Earth sensor bias error and roll gyro bias error are not observable in the roll/yaw axes estimator. Hence those states are excluded in the above constant gains computations.

2.6.2. Sun/Earth Sensors Case

When The Sun is within the sensor FOV, the measurement matrix H becomes time varying matrix with components depending on Sun azimuth and elevation angles. In addition, the Sun elevation measurement residual, ΔEL has non-zero components, c_{24} and c_{26} when the Sun elevation angle is not equal to zero. These non-zero components will cause a coupling between the pitch axis estimator and the roll/yaw axes estimator even the pitch axis dynamics is decoupled from the roll/yaw axes dynamics.

The approach we use to obtain estimators that do not require to compute covariance matrices is to partition the filter gains into two parts : time varying gains followed by constant gains. The first part is obtained by pre-multiplying the measurement outputs, y with a time varying matrix T such that :

$$\tilde{y} = Ty = THx + Tn = \tilde{H}x + Tn \qquad (44)$$

where $\tilde{H}$ has constant components corresponding to states to be estimated. Hence with the matrix $\tilde{H}$, the constant gain matrices can be obtained by solving a set of discrete Riccati equations similar to Equations (42) and (43).

It is noted that the matrix T will have components with extreme large amplitude when the Sun azimuth angle is close to 90 degrees (or near noon time). This large amplitude will amplify the noises as indicated in Equation (44). Hence certain exclusion zones are implemented in both estimators as shown in Figure 3 (Region Ds) when using the Sun sensor data. Region C is also added to the roll/yaw estimator for estimating the roll Earth sensor bias error. The constant gains and their filter inputs are given in Figure 4.

3.0 Simulation Model Description and Simulation Results

A time domain nonlinear simulation model coded with Matlab language was developed to evaluate the attitude determination performance. The model simulates : (1) the spacecraft orbital motion, (2) the truth spacecraft attitude, (3) the gyro noises, (4) the Sun/Earth sensor errors, and (5) the attitude determination algorithms - attitude propagation, attitude estimation, and attitude correction. Both time varying Kalman filter algorithms and fixed gains filter algorithms were evaluated in the simulations for performance comparison. Table 1 lists the assumptions made in the simulations including sensor noises/errors, initial conditions and filter processing rates.

Figure 5 shows the time responses of spacecraft roll, pitch, yaw attitude errors when the Earth sensors have only bias errors. The gyro bias estimation errors and Earth sensor bias estimation errors are shown in Figures 6 and 7 respectively. In Figures 5 through 7, the solid curves represent the attitude performance with time varying gains and dashed curves represent the attitude performance with fixed gains. As shown in the figures the attitude performance with fixed gains is compatible with the attitude performance with time varying gains. However, the fixed gains filter takes longer time (after 4 orbits) to converge as compared to the time varying gains filter. The results indicate that the filter can accurately estimates the Earth sensor biases and meets the $\pm$ 0.05 deg. attitude performance accuracy requirements.

4.0 Conclusions

The normal mode attitude determination algorithms using data from continuously running gyros and Sun/Earth sensors for GEO mission has been described in this paper. A 8 state time varying filter bas been formulated and derived using Kalman filtering techniques. A fixed gain filter without the need for computing the covariance matrix is also derived to simplify the algorithms. A computer simulation model simulating the basic functions of attitude determination algorithms, attitude sensors and spacecraft motion has been developed to evaluate the filter performance. Covariance analysis and time domain analysis have been performed for both time varying gain filter and fixed gain filter. The simulation results indicate that the attitude performance of the fixed gain filter is compatible with that of the time varying gain filter and the attitude knowledge of 0.05 deg (3 sigma) requirement can be met with the selected attitude hardware and the fixed gain filter.

5.0 References

[1] : G. D. Niva, "The Use of Quaternion with an All-Attitude IMU," AAS 82-026, Annual Rocky Mountain Guidance and Control Conference, Jan. 30 - Feb. 3, 1982.

[2] : J. F. Yocum, "HS-601HP Attitude Estimation Using Quaternions," Hughes Space and Communication Company IDC Ref. TN10/0805, Sept. 21, 1995.

[3] : J. R. Wertz, "Spacecraft Attitude Determination and Control," D. Reidel Publishing Company, 1986.

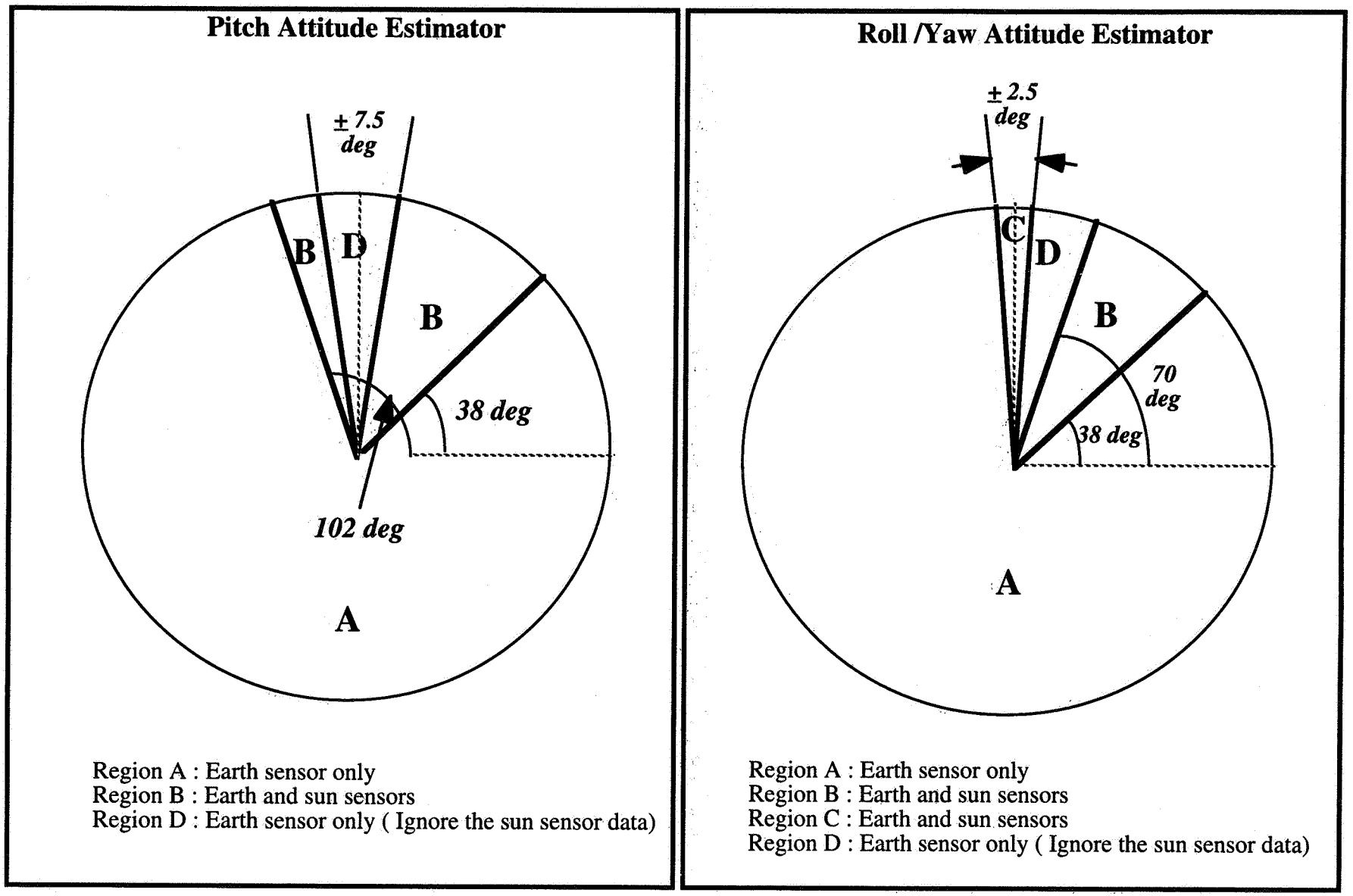

Figure 3 Fixed Gain Filter Region Definition

Estimator		Kalman Filter Inputs	Constant Gains								Eigenvalues/ Time constants (min)
			Pitch	Roll	Yaw	Gyro ptich bias	Gyro roll bias	Gyro yaw bias	Earth sensor pitch bias	Earth sensor roll bias	
Pitch Attitude	Region A/D	$y1 = \Delta\theta_e$	2.3258 e-03			-1.1891 e-06					-1.5704e-03/10.6 -7.5807e-04/22
	Region B	y1	5.6181 e-04			-3.6278 e-07			4.6640 e-03		-5.2559e-03/3.17 -1.7711e-03/9.4 -7.3274e-04/22.7
		y2	-2.5167 e-03			1.3205 e-06			1.7520 e-03		
	Region A/D	$y1 = \Delta\phi_e$		3.6883 e-03	1.1018 e-02			-1.1883 e-06			-3.4683e-03/4.8 -1.1342e-04 +1.1052e-04 j/6.61
Roll - Yaw Attitude	Region B	$y1 = \Delta\phi_e$		2.3254 e-03	-4.8010 e-06		-1.1886 e-06	-3.5405 e-08			-1.8729e-03/8.9 -1.5993e-03/10.4 -7.4291e-04 + 1.0381e-05 j/1.41
		$y2 = -\tan(AZs)\,\Delta\phi_e$ $-\{1/\cos(AZs)\}\,\Delta EL$		-6.5347 e-06	2.6264 e-03		4.1292 e-08	-1.3864 e-06			
	Region C	$y1 = \Delta\phi_e$		4.3749 e-04	4.3713 e-04					4.7413 e-03	-5.2623e-03/3.17 -1.8950e-03/8.79 -7.3249e-05/227.5
		$y2 = \Delta EL$		-2.0359 e-03	-1.8952 e-03					1.4404 e-03	

Figure 4 Constant Kalman Filter Gains

Table 1. Attitude Determination Matlab Model Simulation Parameters

Earth Sensor Noise (1 sigma)	Sun Sensor Noise (1 sigma)	Gyro Noise (1 sigma)	Initial Errors	Filter Processing Rate
o Random noise : 0.01 deg @ 2Hz o Bias : 0.03 deg o Radiance errors : 0.016 deg with 7~14 days period o Thermal errors : 0.018 deg with 24 hrs period	o Random noise : 0.03 deg	o Angle random walk : 0.001 deg/sqrt(hr) o Rate random walk : 0.002 deg/hr*sqrt(hr) o Angle white noise : 0.054 arc sec/sqrt(Hz)	o Roll error : 0.1 deg o Pitch error : -0.2 deg o Yaw error : 0.57 deg o Gyro bias error : 0.06 deg/hr	o Gyro processing rate : 2 Hz o Filter processing rate : 1 Hz

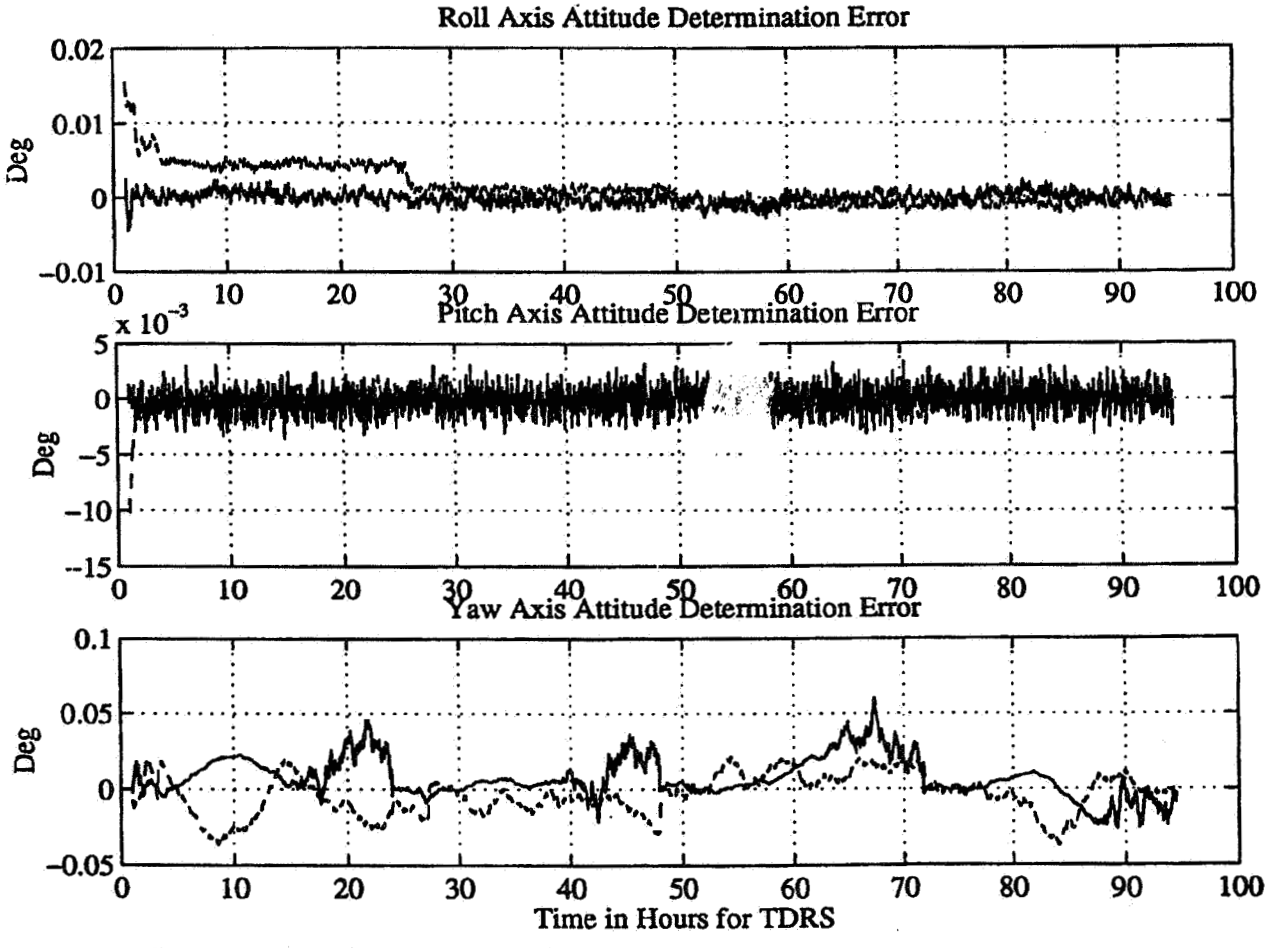

Figure 5. Attitude Determination Performance - Spacecraft Roll, Pitch, and Yaw Errors

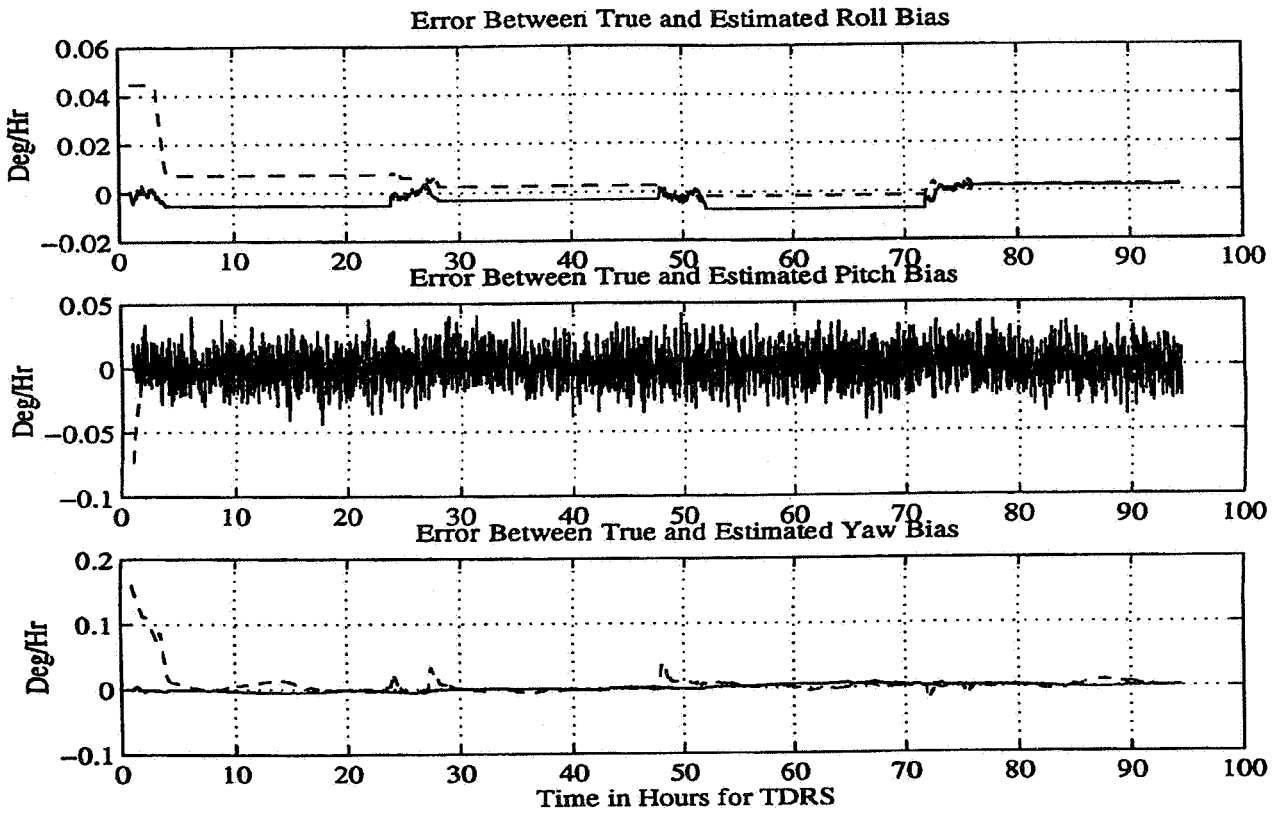

Figure 6. Attitude Determination Performance - Gyro Bias Errors

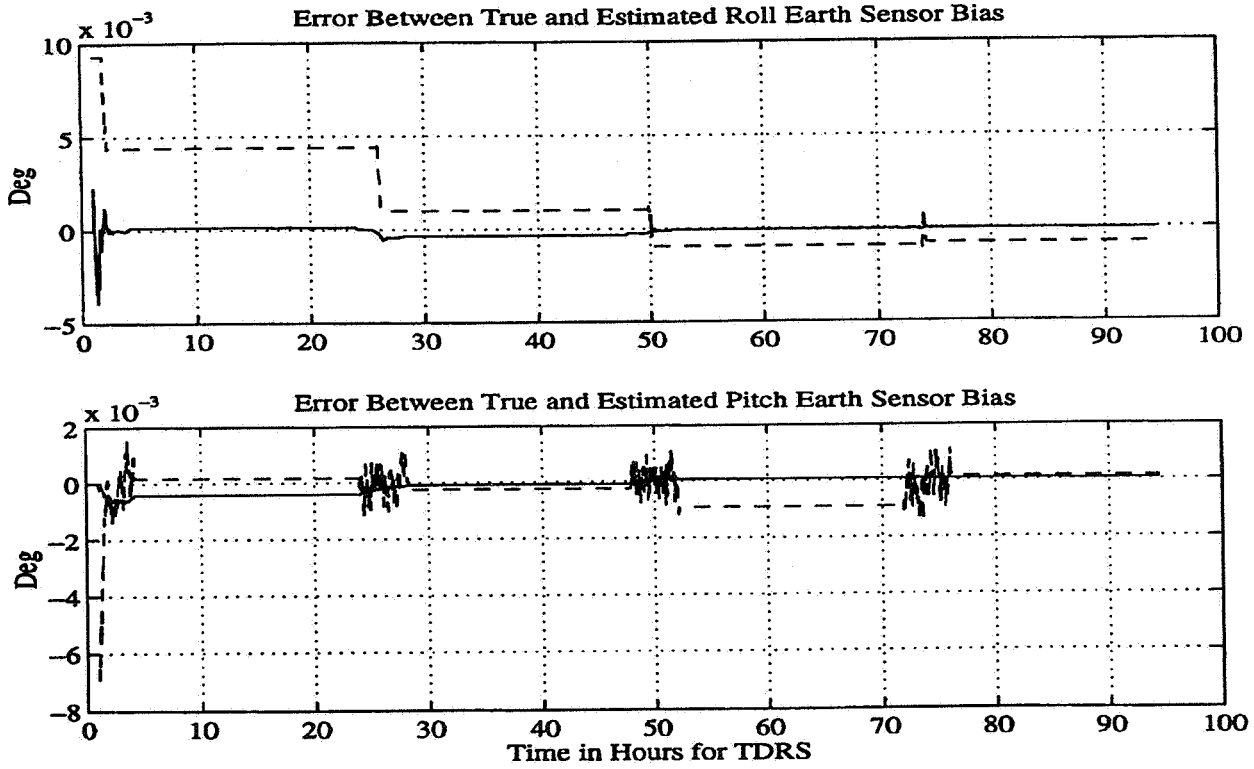

Figure 7. Attitude Determination Performance - Earth Sensor Bias Errors

Page intentionally left blank

TDRS YAW ESTIMATOR IMPROVEMENTS

Dennis J. Pugh
Lockheed Martin Corporation
White Sands, New Mexico, USA

ABSTRACT

This paper describes the changes implemented to improve the accuracy and operability of the yaw estimator during equinox and solstice. The solstice problem has always been assumed to be associated with the offline prediction of environmental disturbance torques. Changes to the environmental disturbance torque prediction process were implemented. These changes improved the performance of the yaw estimation process in general but did not solve the solstice problem. Changes to the Fine Sun Sensor (FSS) calibration process improved the performance during the solstice period. These changes to the FSS calibration process improved the performance during the equinox period as well. Overall results to date have been excellent.

BACKGROUND

The Tracking and Data Relay Satellite System (TDRSS) was designed to provide data relay and tracking services for space vehicles in low earth orbit. Each Tracking and Data Relay Satellite (TDRS) has two single access 4.9 meter antennas to provide S-Band and K-band user support. The TDRS spacecraft also contains an electronically steered multiple access system. To accurately point the TDRS antennas the spacecraft attitude must be known. The roll and pitch positions are determined from the spacecraft earth sensors. Yaw is observed using a sun sensor mounted on a solar array. This method is used while the solar array paddle is primarily in the yaw axis. When the solar array rotates primarily into the roll axis, the yaw is determined by estimation.

The yaw estimator calculates the spacecraft yaw attitude angle using telemetered readings of the fine sun sensor, the earth sensor and the reaction wheel speeds. The algorithm uses a seven state discrete Luenberger observer. This observer is reconfigured to an estimator using only earth sensor and wheel speed measurements during periods of the orbit that are unfavorable to yaw measurement. The estimator periods are 6 hours centered around local spacecraft noon and midnight. The algorithm has two offline calibrations. One of the offline processes uses historical spacecraft momentum to predict environmental disturbance torques. The other process calibrates the Fine Sun Sensor using data collected when the Solar Array is completely in the roll axis.

Environmental disturbance torques are predicted from historical spacecraft momentum. A least squares curve fit of the historical spacecraft momentum using only higher order terms is performed. The resulting equation is differentiated into a torque prediction equation. This torque prediction equation is used in the real time part of the algorithm.

The output of the FSS is calibrated daily to remove error associated with the aging of the FSS device. Calibration data is taken twice a day at spacecraft noon and midnight. At these times the solar array has completely rotated into the roll axis. A series of 50 time stamped FSS readings are taken along with roll axis position and solar array mis-alignment. A least squares curve is fitted to the 50 points and a noon/midnight point is derived. This derived point is stored in a database along with its corresponding sun incidence angle. The collection of stored data is least squares curve fitted to produce coefficients. These coefficients are used by the real time part of the algorithm to translate FSS telemetry into sun incidence

angles. The FSS assembly is composed of two devices one for summer and one for winter. Thus there are two independent sets of data and coefficients.

PROBLEMS

Yaw estimation has historically had problems around equinox and solstice. These problems have been mitigated by the TDRS Analyst's (TA's) manual control of the offline processing.

During the equinox the FSS assembly changes from one device to the other. During the transition time the readings may come from both devices over a day. The real time software is directed to use a line segment input by the TA to derive the sun incidence angle. An incorrect analysis by the TA can lead to yaw angle error in both estimation and observer modes.

At solstice, the sun is at its maximum angle relative to the spacecraft body. Since this angle is at its greatest value it has been assumed that yaw angle errors at solstice were caused by incorrect torque coefficients from the environmental disturbance torque process. However, over time the TA's found that yaw angle errors could be mitigated by controlling the FSS data.

The most obvious operational problem is the heavy TA involvement at equinox and solstice. Additionally the TA's would like to have more control of the raw data. In the first TDRS ground terminal the TA's routinely cut the environmental disturbance torque momentum file down to 24 hours of data. The EDT process was designed to use up to 144 hours (six days) of data. The TA's also desired the ability to remove FSS data points from the FSS data set.

SOLUTIONS

The yaw error during the solstice period was the greater of the two problems. Early attempts to correct the solstice yaw error concentrated on the environmental disturbance torque prediction process. The ability of the TA to control the solstice problem by controlling FSS data pointed to the FSS calibration. Since an FSS change was unlikely to be implemented before the next solstice, the environmental disturbance torque prediction process was looked at first. Implementation of the changes to the environmental disturbance torque process occurred prior to the next solstice and by the lack of impact on the solstice problem suggested that the FSS calibration was the cause of the yaw error during solstice.

ENVIRONMENTAL DISTURBANCE TORQUE IMPROVEMENTS

The early attempt to correct the estimator problem near solstice was the addition of momentum smoothing. The smoothing algorithm (called momentum modeling) is described in Software Task Requirement (STR) Attitude Control System (ACS) 3 part D. While the smoothing concept was sound the implementation had problems. Improvements to this implementation resulted in significant day to day improvement in the accuracy of the yaw estimator.

Momentum smoothing was necessary because the calculation of momentum during estimator mode was dependent upon the yaw angle. The yaw angle error during estimator mode would cause a significant error in the momentum data. This error would then feed back into the yaw estimation process to corrupt the yaw value during estimator mode. To alleviate this problem the least squares fit was performed multiple times. In-between each least squares fit the estimator period momentum points were changed. The points were replaced with points derived from the least square fit equation. The existing implementation integrated the torque equations and used the last observer momentum point as the constant of integration. This approach maintained a significant discontinuity at estimator to observer transitions.

The error in the momentum data is mostly seen in the spacecraft roll (X body) axis. The yaw simulator replaces the observed X body estimator period momentum with momentum computed from the torque coefficients from the least squares fit of the momentum data set. This least squares fit momentum is translated into the X attitude reference axis. ACS 3 part D incorrectly refers to this translation as X body momentum. For small attitude angles it is approximately X body momentum, but is really a translation to the attitude reference coordinate system. The observed inertial reference momentum is also translated into the Z attitude reference axis. The X attitude reference axis is set to use the least square fit momentum while the Z attitude reference axis will use the observed estimator momentum. This combined attitude reference momentum is translated back into inertial coordinates. The least squares fit is then redone on this new data set. This process is repeated until a TA specified number of cycles has been performed. After approximately three cycles, there is little change in the data.

The early simulation process used the integral of the torque equation to compute a least squares fit momentum. In order to compute actual momentum, the torque equation requires a constant of integration. ACS 3 part D accomplishes this by taking the difference between two successive points and adding to previous momentum. The start of this process is the last observed momentum point from observer mode data (This point becomes the constant of integration). By using the last point of observer data as a constant of integration, the estimator data is skewed. It creates a discontinuity in momentum data at the estimator to observer transition and it is not representative of the observed data. Figure 1 is an inertial plot of TDRS-D observed momentum for several days in March. Figure 2 is an inertial plot after the 6th cycle of ACS 3 part D. Note the significant skewing of the data in the inertial X-axis plot.

The ACS 3 part D integral of the torque equations is not the correct and complete integral of the torque equations. The integration is just the X body integral of torque and drops Z components from the integral. The difference between the complete integral of the torque equation and the ACS 3 part D equation becomes insignificant to the skewing caused by the estimator momentum replacement process. Figure 3 is an inertial plot after the 6th cycle using the correct torque integral. The result is the essentially same as ACS 3 part D.

To avoid skewing the data, the least squares fit momentum should have been calculated from the momentum coefficients (not torque coefficients). This data is representative of the observed momentum data. It spreads the discontinuity of the estimator to observer transition over the whole estimator period. Figure 4 is an inertial plot after the 6th cycle of such an implementation. Note there is no skewing of the data in the inertial X-axis plot. This improvement to use direct momentum was added to the operational system.

Prior to the use of direct momentum, the TA's tended to reduce the data used by the environmental torque prediction process to 24 hours of data. Following the improvement they made no changes to the data. This led to the identification of another problem. After every roll/yaw momentum unload there would be high estimator to observer yaw transitions. This occurred because the value for roll/yaw axis momentum unloading was incorrectly set in the updatable database. Once the proper values were set, the TA's involvement with the environmental torque prediction process was reduced to reading the software generated daily report. Planned changes to allow the operator more control over the data have been postponed.

FINE SUN SENSOR IMPROVEMENTS

After implementation of the environmental torque prediction process improvements a review of the FSS calibration was performed. Several observations caused changes to the calibration process that improved the overall performance of the yaw estimator and reduced operator involvement in this process.

Figure 5 is a plot of TDRS-A data for one year. This plot is a complete data set for both FSS devices. Note that the data set appears as an almost straight line with symmetric curves at each end. The ends occur

at solstice. The design of the FSS device causes the falloff toward solstice. The data going toward the solstice has a greater absolute value than the return data. This is attributable to degradation of the FSS device over time. It is expected to be between two to five percent per year. There is a slight discontinuity at the zero crossing. This is due to the change in FSS devices. Also note that the slope of the line near zero is similar for both sides of zero.

The old implementation used the following equation for basis a function to calibrate each side of the FSS data:

$$\text{estimated data} = f_0 + f_1 V_{fss} + f_2 V_{fss}**2 + f_3 V_{fss}**3$$

This equation did not provide a proper response at the solstice ends. Analysis of the data, from one solstice to the other, indicated that the data set resembled a sine wave crossing zero close to zero. The following new basis equation was selected:

$$\text{estimated data} = f_0 + f_1 V_{fss} + f_2 V_{fss}**3 + f_3 V_{fss}**5$$

This happens to be the first four terms of the series expansion for the sine function. This is also an odd function which means that the separate device curves can be replaced with one curve. This was not possible with the old equation (due to the square term). In addition the single equation would reduce the amount of TA interaction with the FSS software during equinox periods.

The data is pre-processed to account for FSS device degradation and zero crossing discontinuity. An FSS degradation percentage is applied to all of the points based on age of the data point. Thus, for older points more degradation is applied. Secondly each point is biased by a small amount to adjust the zero crossing. In the real time processing of FSS data only the bias is applied. Degradation is not an issue in the real time processing since calibration occurs once or twice a day.

Specifying the FSS device degradation amount and zero crossing bias is an additional task for the TA. However these tasks only need to be performed once per year. Overall, the TA spends less time on FSS calibration due to several other changes that improve the operability of the FSS calibration process. These changes include point selection and specifying number of points used.

Point selection allows the TA to choose a time interval of points for the calibration. The TA can specify a delete point(s) interval and a reinstate point(s) interval. For the delete point interval the FSS calibration software updates a delete field in the database for all points within a time interval. When the FSS calibration software reads in points to be considered for the calibration all points with the delete field set will be discarded. The TA can reinstate these points by specifying them with the reinstate point(s) interval. Though iterative input, the TA may edit out many intervals. Point editing is necessary to remove corrupted points (such as points taken during an attitude recovery).

Specifying the number of points used allows the TA to set a sliding scale. The TA has the ability to specify the minimum (6 to 360) and maximum (6 to 360) number of points to be used in the calibration. This feature can be useful during FSS device transition (equinox).

FUTURE CHANGE

During the Canberra ADPE Replacement Project (CARP) it was necessary to re-examine the yaw estimator process. Several changes were made to account for a two degree rolled spacecraft. A significant problem with momentum calculation was the lack of a spacecraft body to attitude reference coordinate transformation. A full TDRS body to attitude reference transformation was added. This change may be added to the normal system in the future.

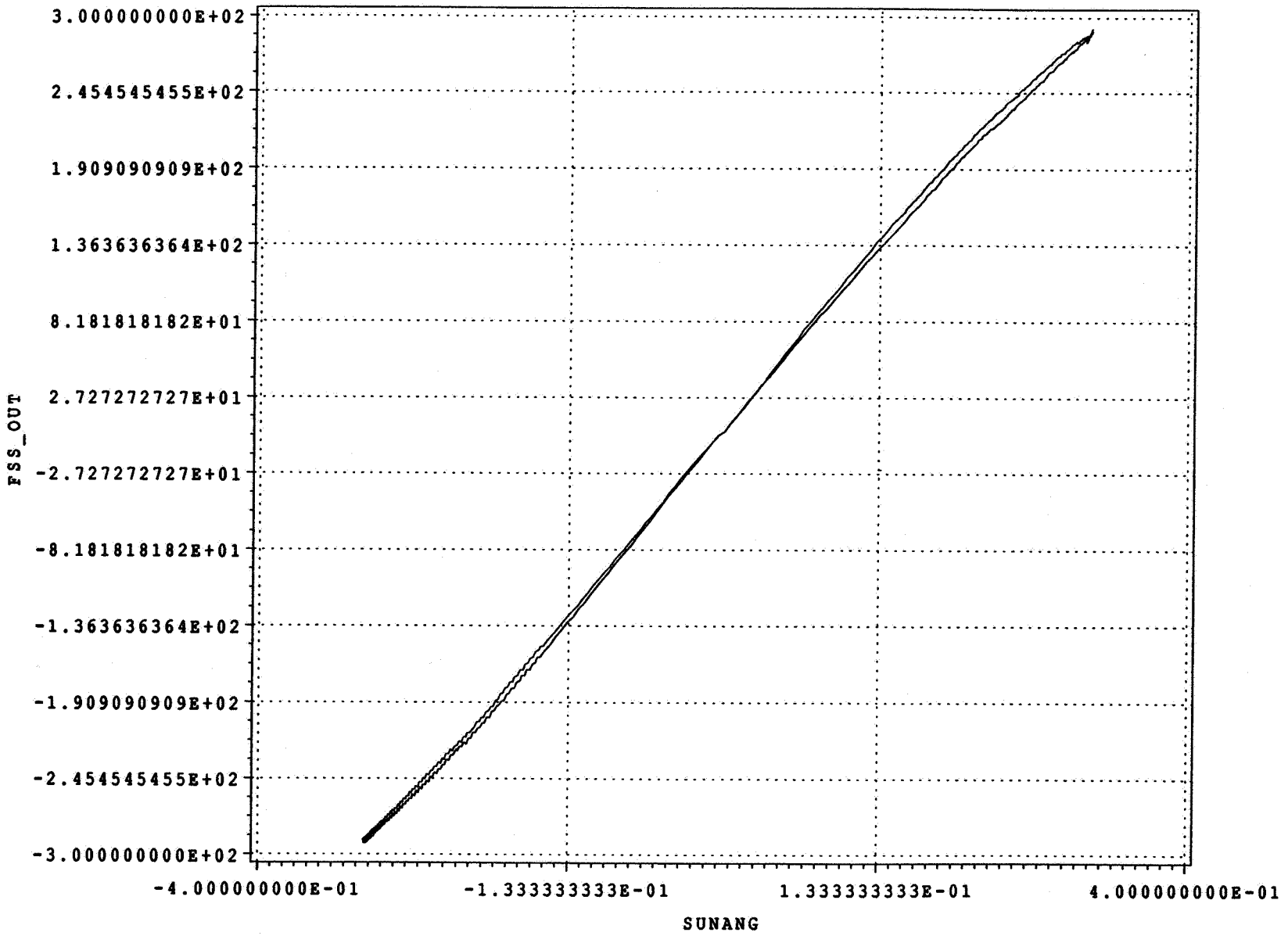

FIGURE 5: TDRS – A FSS Data

SUMMARY

Since implementation, the normal estimator to observer yaw transitions rarely exceed the 0.25 standard by which the yaw estimator performance is judged. The TA's day to day involvement in the environmental disturbance torque prediction process and the FSS calibration has been reduced to reading the daily software generated report.

ACKNOWLEDGMENTS

The author wishes to acknowledge the contributions of Jeff Franke, Aaron Goodman, Gary Nesbit and Steve Staich to the development and implementation of the yaw estimator improvements. The author would also like to thank Bob Jenkins for making it possible for Steve Staich to be involved.

REFERENCES

1. NASA, "STGT Algorithms and Constraints Interface Control Document", 1994.

3. NASA, "Software Task Requirement, Attitude Control System Number 3", 1989.

2. S. Staich, AL Cohen and EA. Berkery, "Yaw Attitude Estimation for the Tracking and Data Relay Satellite System, IAA Guidance and Control Conference, 1984

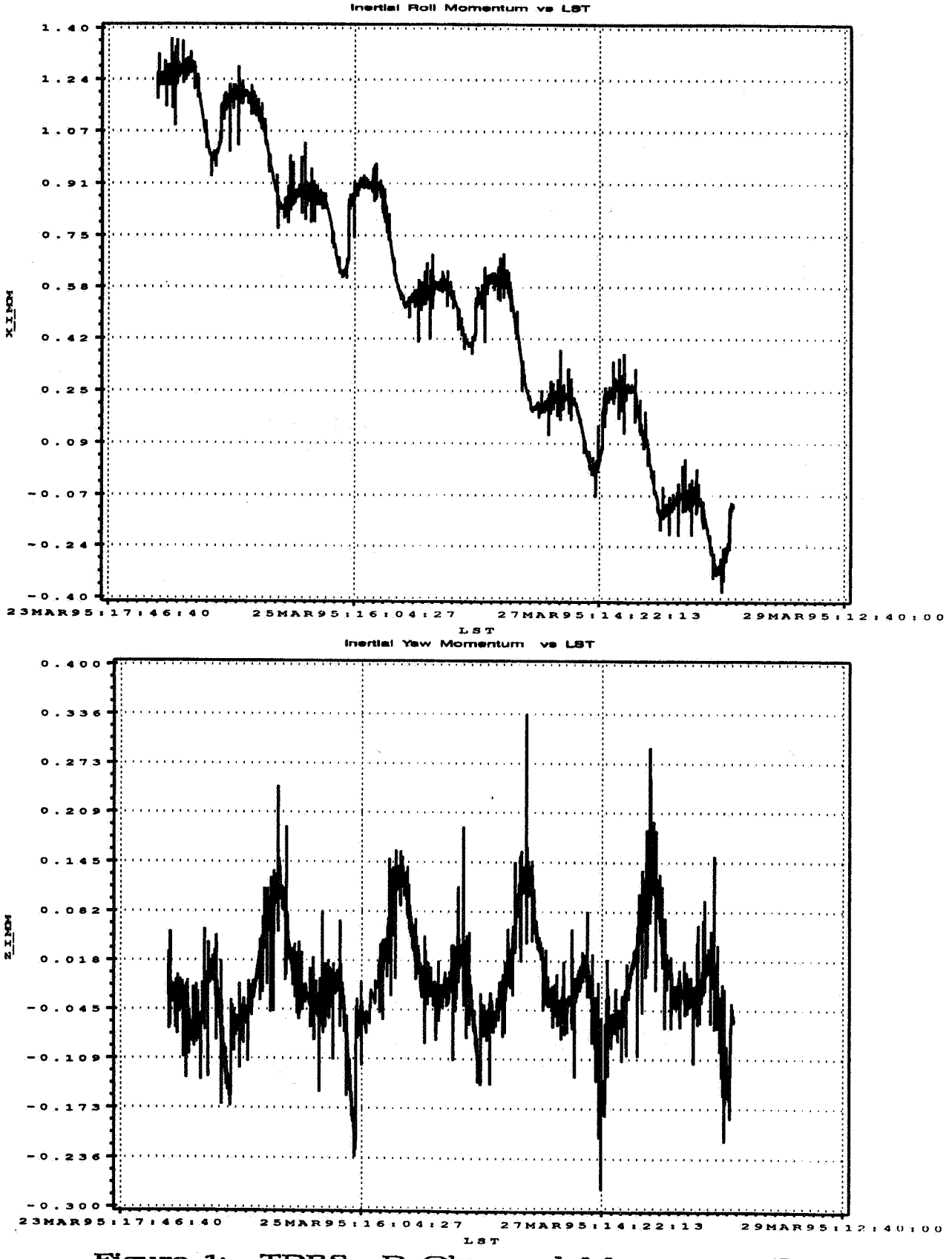

Figure 1: TDRS – D Observed Momentum Data

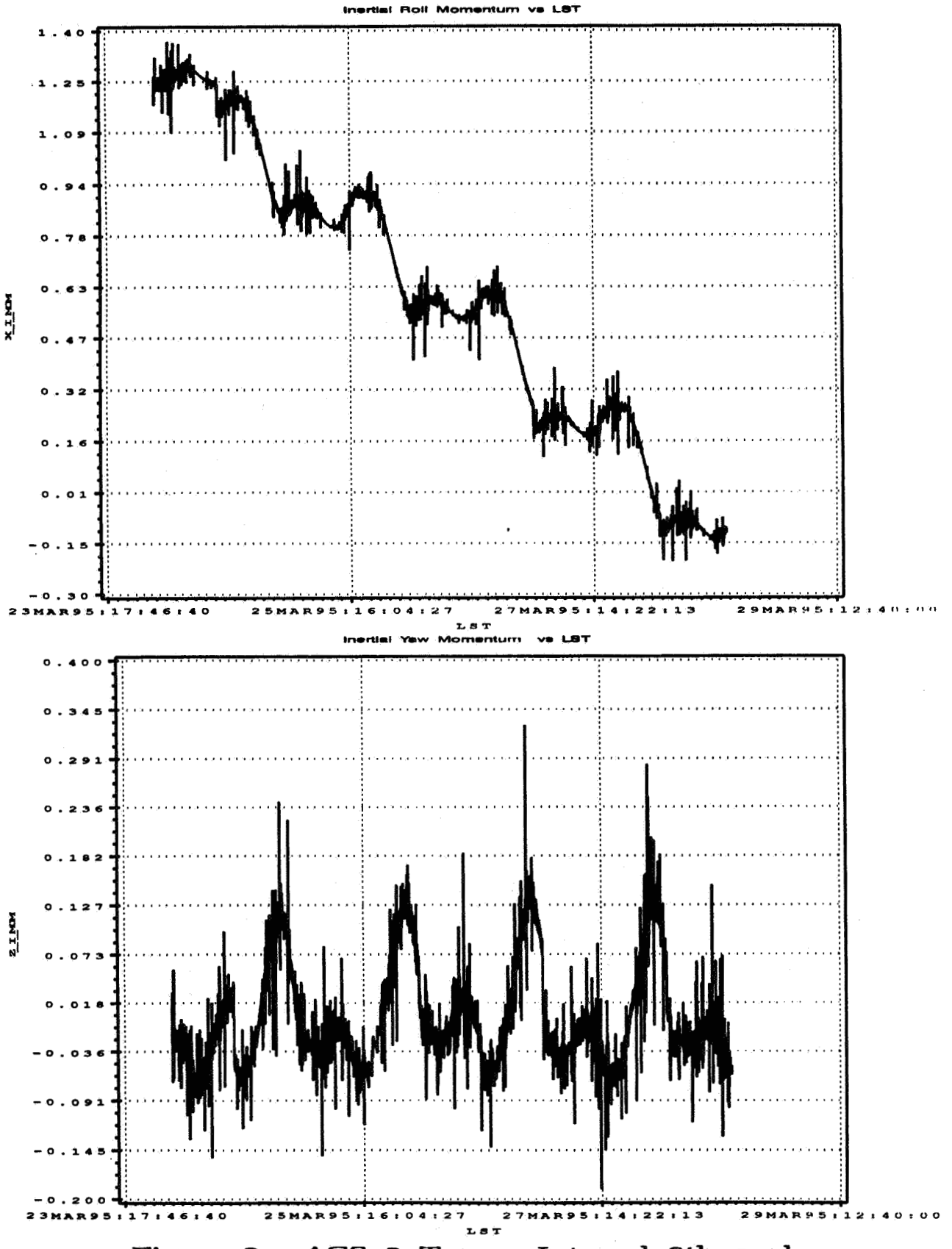

Figure 2: ACS 3 Torque Integral 6th cycle

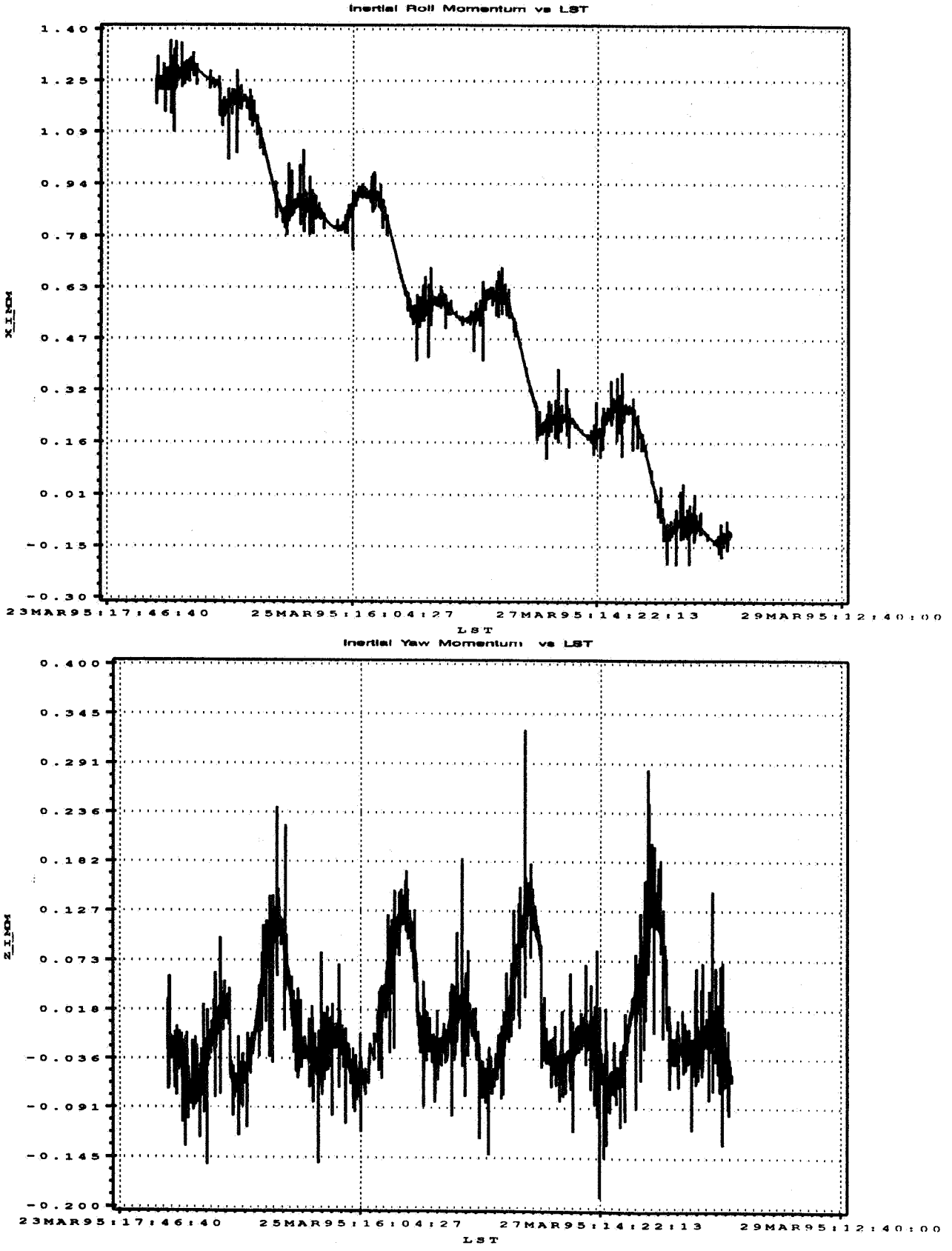

Figure 3: Correct Torque Integral 6th cycle

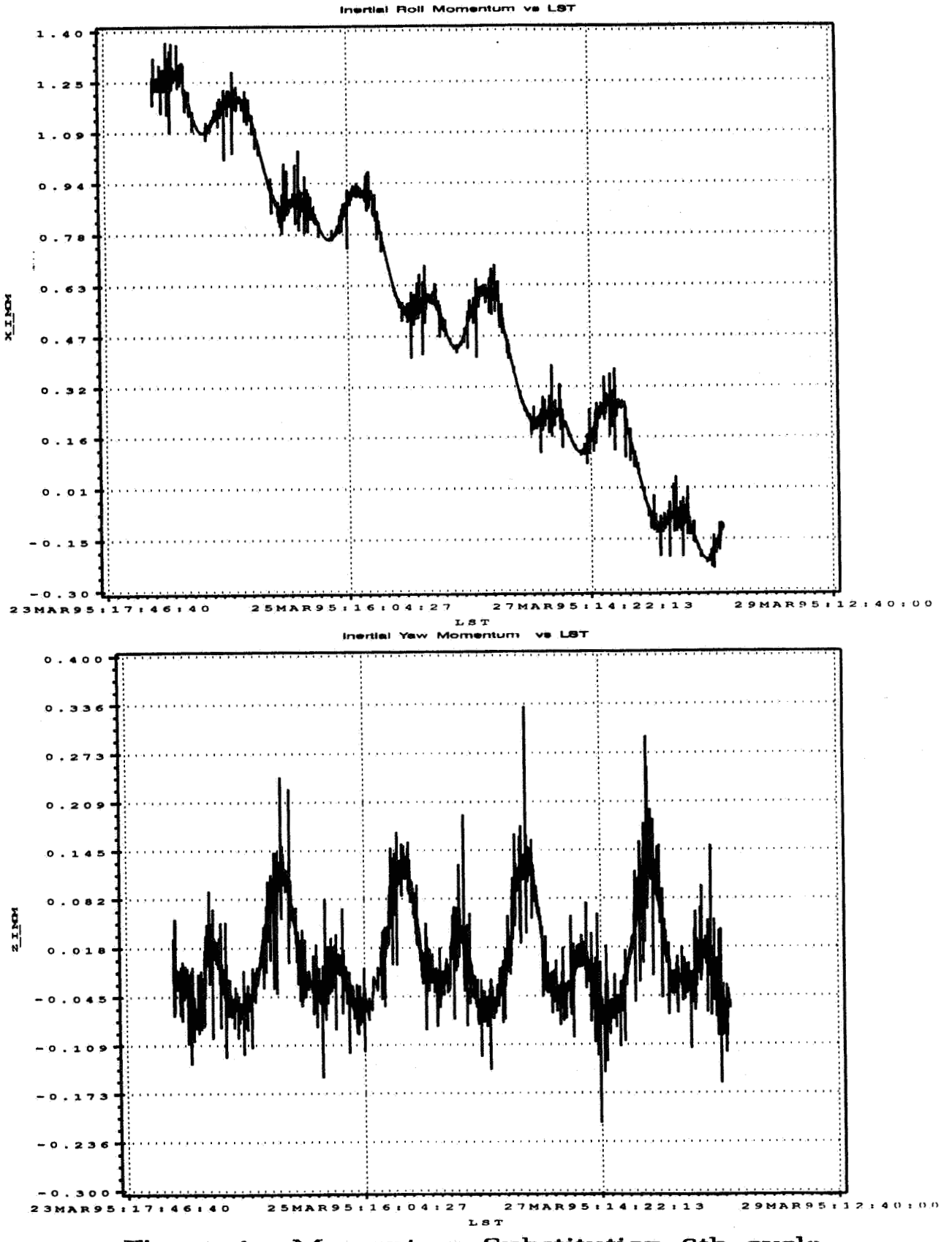

Figure 4: Momentum Substitution 6th cycle

Coping with GOES Data Gaps

Donald Chu, John Tsui and Wyatt Wallace
Lockheed-Martin Space Mission Systems
Seabrook, MD

David Herndon, Ph.D.
Tyche Corporation
Castro Valley, CA

Joseph Harris
Independent Associates
Baltimore, MD

Nickalaus Pinkine
National Environmental Satellite, Data and Information Service
National Oceanic and Atmospheric Administration
Washington, DC

Abstract

Geostationary Operational Environmental Satellites (GOES) image motion compensation (IMC) relies on the instrument attitude and orbit being close to that predicted from the previous day's observations. This enables today's attitude and orbit solutions to be used to correct tomorrow's images. Because gyro data is usually not available, observation gaps cause large errors in the Orbit and Attitude Trajectory System (OATS) attitude profiles. Although these errors fall within the gap, when the next day does not have the same gap, the predictions bear the brunt of these errors. Several alternative methods have been tried to correct this problem including the use of old observations, a priori information and simulated observations. Including old observations in the gap period controls the attitude but requires significant manual intervention. Using a priori solutions slows the response to attitude profile changes outside the gap such as those caused by transitions into and out of eclipse. Simulating observations keeps down such transient effects but has not provided as good attitude solutions inside the gap. When the next day has the same gap, none of these improves on the baseline method of just processing through the gap. While no one method is ideal, together these four provide an array of gap-handling techniques that covers all situations. The stubbornness of the gap problem points out the need for either gyro data or regularly spaced observations and, more generally, the difficulty of predicting the future.

Background

GOES provides Earth images with resolution of one kilometer (km). To take full advantage of this resolution, it is necessary to know the spacecraft attitude within an angle corresponding to a 1 km error on the ground. From the 36,000 kilometer GOES altitude, this corresponds to 28 microradians or 6 arc-seconds. Because it takes twenty-six minutes to scan the entire Earth, GOES instrument pointing must be stable to this accuracy to avoid image distortion. To accomplish this, a steerable mirror adjusts the imager pointing direction to compensate for spacecraft attitude motion and thermal distortion. Because GOES has limited onboard computing capability, the Image Motion Compensation (IMC) commands to the mirrors are determined on the ground each day using the current day's observations and areuplinked for use the next day.

The imager provides East-West and North-South "scan angle" observations to locate stars and landmarks in its field of view. In addition, range observations come from the Wallops Island tracking station. The nominal observation schedule is four stars every half hour and as many landmarks in between. Star and

landmark observations have standard deviations of about 30 microradians. Range observations come four times an hour and have standard deviation of about 1 meter (m). The OATS takes these observations and solves for instrument attitude plus orbital elements. Because the GOES Digital Inertial Reference Assembly, i.e. gyro, is normally not turned on, there is no kinematic model for the attitude motion. Attitude is "propagated" assuming that variations in each angle can be represented by a Fourier series with period of one day reflecting the belief that the attitude variations are thermally induced. OATS generates ephemerides using a sixth order geopotential model including solar radiation, lunisolar and planetary perturbations.

This system of using the predicted attitude and orbit works amazingly well. Figure 1 shows GOES-9 residuals obtained on day 96/055 using the IMC set computed from day 96/054 observations.

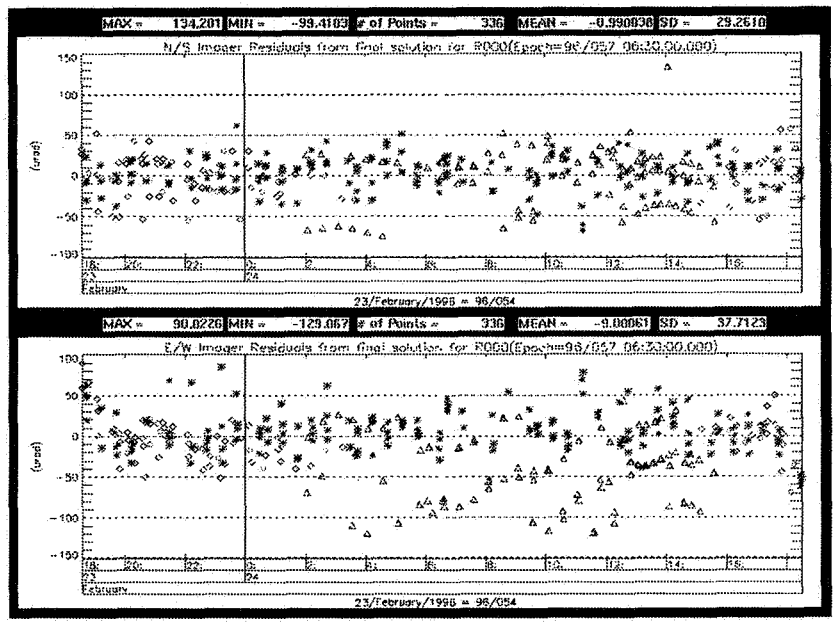

Figure 1. Typical Predicted Observation Residuals

Naturally, the predictions can be improved by using more recent observations. So, when instrument observation residuals exceed certain thresholds for an extended period of time, short span attitude adjustments (SSAAs) are made to the constant order terms of the Fourier series. With these corrections to the IMC "parent" set, observation residuals are normally kept below the 112 microradian daytime limit and the 168 microradian nighttime limit. But when something happens that changes the normal diurnal cycle, residuals may reach several hundred microradians.

The Gap Problem

Sometimes observations are lost due to Sun interference, attitude maneuvers and other causes, and several hours may pass between observations. For 45 days around the vernal and autumnal equinoxes, GOES passes behind the Earth. During eclipse, both imager and range observations are lost for up to 3 hours. In addition, the sharp transition from light to dark and back disrupts the slowly varying thermal variations captured in the Fourier series.

Because of these gaps and observation noise, the estimated Fourier series coefficients become almost unobservable. Many different profiles may fit all the observations but be unrealistic inside the gap. Some

of these attitude solutions within the gap exceed the compensation range of the instrument and so can not be commanded. Figure 2 shows two attitude profiles for day 96/054 and their difference. The first is computed using all observations and is assumed to be correct. The second is computed without observations between 08:30 and 10:30 UTC. This gap corresponds to loss of data due to eclipse on a typical day (96/067). Although the second profile fits the available observations, its attitude over the two hour gap deviates by up to 150 microradians from the true attitude.

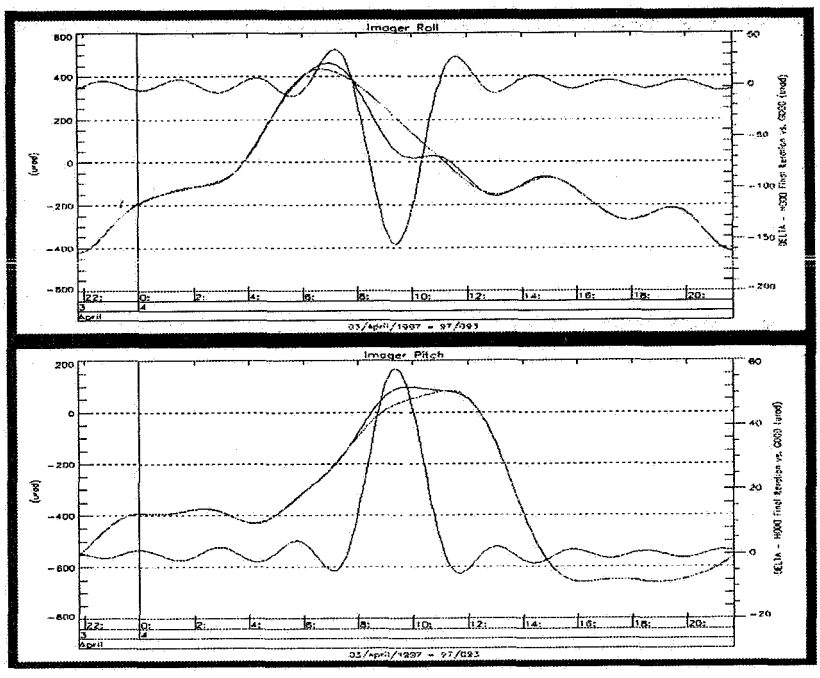

Figure 2. Gap Effect on Attitude

These attitude differences could show up directly as residuals if the next day did not have the same observation gap. Several methods have been tried to reduce the excursions in the gap:

1. Include old star observations with current observations.
2. Utilize an a priori solution from before the gap.
3. Simulate observations within the gap.

Because IMC success is measured by the smallness of the predicted residuals, this is the principal criterion used here to evaluate the different methods for handling gaps. Attitude, in and of itself, is not of interest. In particular, post-gap observation residuals are of special interest because they can cause noticeable distortion in the first new image.

Baseline

Standard practice is to use two days of observations and to process through any gaps. The idea behind using two days is the hope that an occasional gap may not occur on both days. The observations on one day then help compensate for the gap on the other day. Figure 2 shows the pitch and roll profiles used for IMC on day 96/067. Observations came from days 96/065 and 96/066 which had gaps on both days from 8:30 to 10:30 UTC. Like the attitude shown in figure 2, the portion of this profile within the gap period is probably inaccurate.

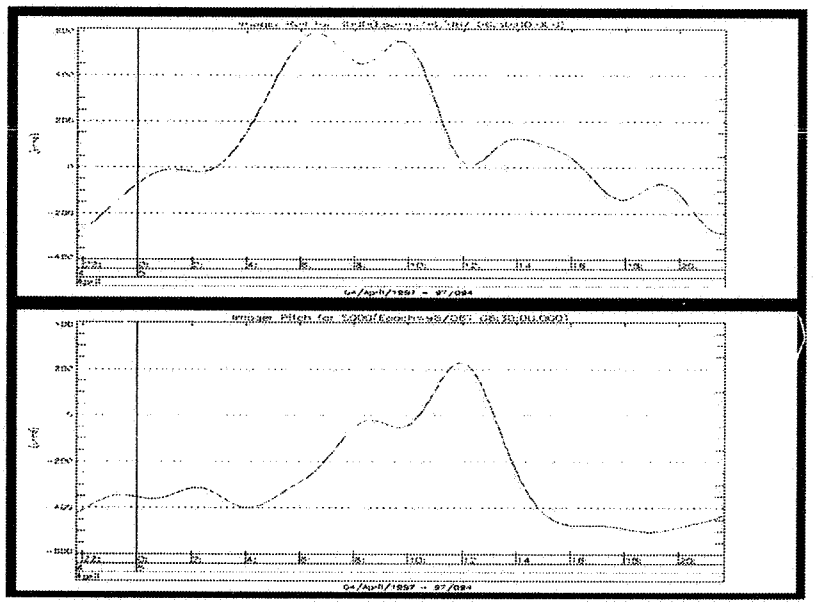

Figure 3. Roll and Pitch Profiles - Two-Day Baseline

Residuals for this baseline solution are given in figure 4. Star residuals are shown with asterisks. Visual, i.e. daytime, landmark residuals are shown with diamonds. IR landmarks are shown with triangles. Because GOES-9 is not imaging over the eclipse period, attitude errors over the gap do not show up as large residuals, and these residuals are not bad in spite of the observation gap. Because SSAAs can correct for secular trends, the residual spread is more important than its absolute value.

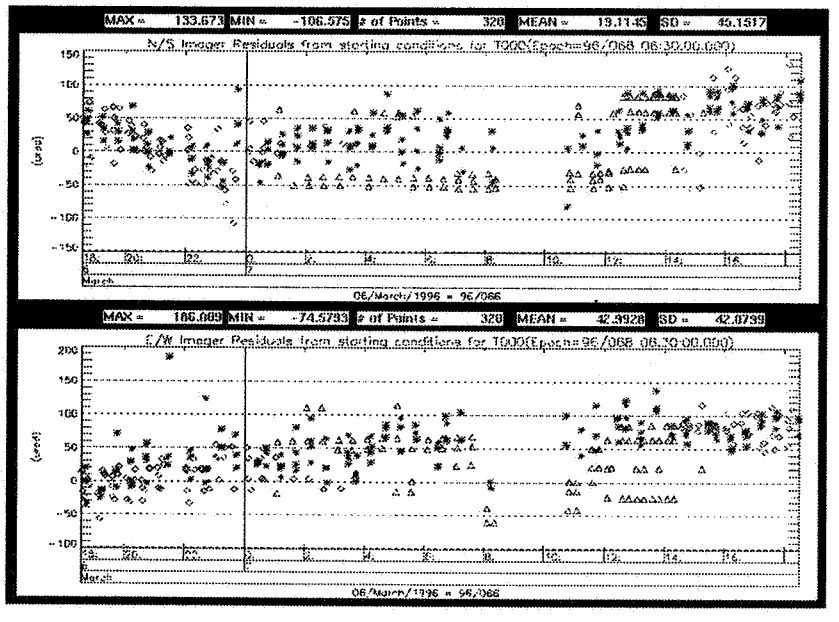

Figure 4. Residuals Obtained Using Two-Day Baseline

Including Old Observations

In the old observations approach, the data span starts with the last day without a gap and ends at the current day. Data from all the days between must be flagged as unusable. Not all observations from the gap-free day are used. Because orbit does not repeat from day to day the way attitude normally does, orbit observations are not used; they would be inconsistent with the current day's observations. Only star observations are independent of orbit and are used despite their age. Landmark gaps do not cause problems for orbit estimation because the propagation model forces the orbit to be realistic. Figure 5 shows the roll and pitch profiles computed for day 96/067 using old observations.

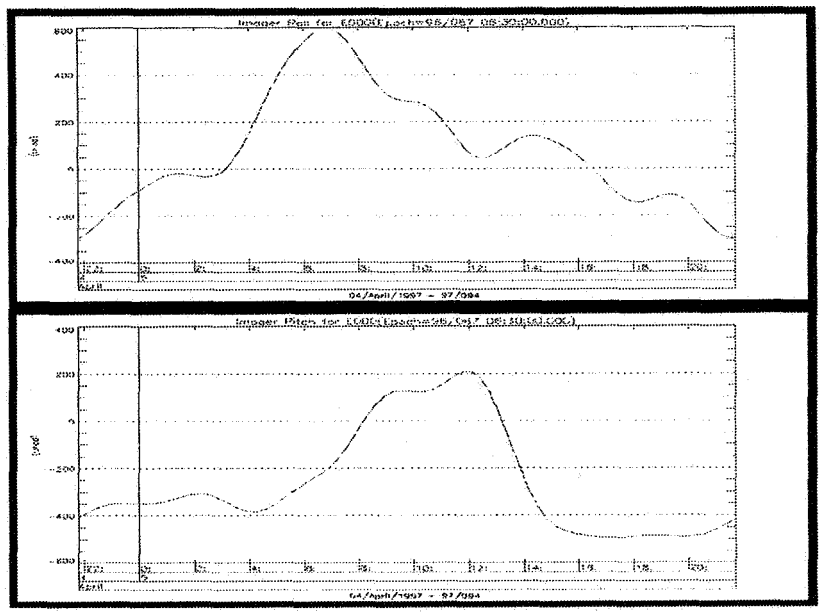

Figure 5. Roll and Pitch Profiles - Old Observations Approach

Only those stars actually within the gap are used. This minimizes inconsistency with current star observations. During eclipse, for example, normal thermal variations are disrupted by the entry into and exit from shadow. Transients occur, and old observations do not reflect these transients. Not reflecting the entry transient is acceptable because images are not scheduled during eclipse. Not reflecting the exit transient is more serious because imaging is resumed following eclipse. Figure 6 shows predicted residuals for day 96/067. The IMC was computed from day 96/066 observations supplemented over the 8:30 to 10:30 gap by old observations from day 96/056. Day 96/056 was the last day before eclipse season started.

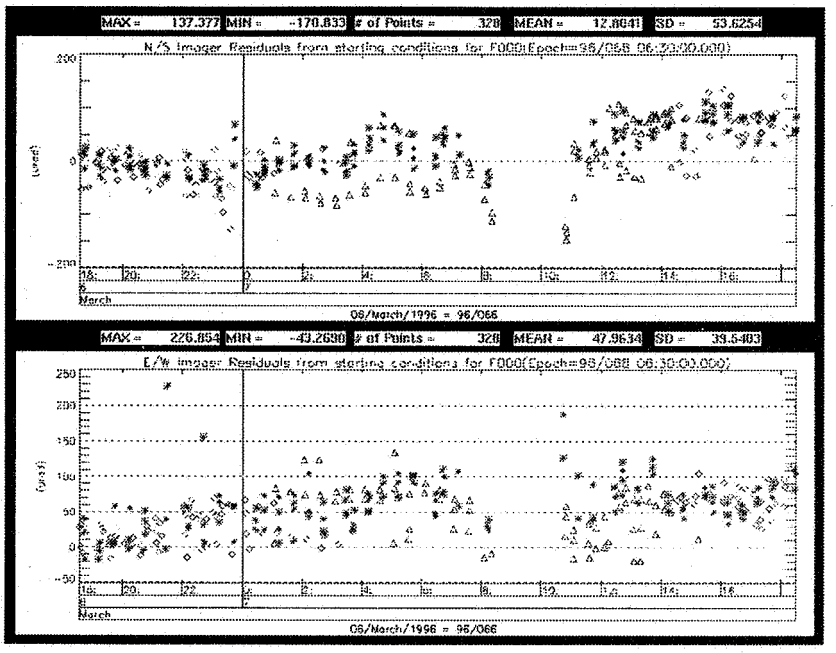

Figure 6. Residuals Obtained Using Old Observations

As shown in figure 6, the old observations approach actually increases the residuals compared to the baseline and introduces spikes following eclipse. This may be because the attitude in the gap is very different from that of the pre-gap days. Using such erroneous old observations can evidently distort the profile outside the gap. Deleting some of the old observations near the edges of the gap period might have helped reduce the spike. Operationally, the disadvantage of the old observations approach is that it requires special attention. Flagging observations manually can be time consuming and is one more thing to remember at what is often an already confusing time. Another complication is that observation files have limited capacity. If gap periods last more than twenty-six days, as in eclipse season, old observations must be recovered from the archives.

Using An A Priori Solution

Assuming Gaussian white noise on the observations, the solution and covariance from a least squares problem contain all the information from the original observations. Therefore, it was proposed to use the solution and covariance from the last gap-free day instead of the observations themselves. [1] This avoids the need to flag data and keep the old observations on the system. In the a priori approach, the old solution is used as an observation and is weighted by the inverse of its covariance. [2] For the same reason that the old observations approach uses only stars, the a priori approach uses only the attitude portion of the solution and covariance. As shown in figure 7, the a priori approach gives an attitude close to that obtained using old observations.

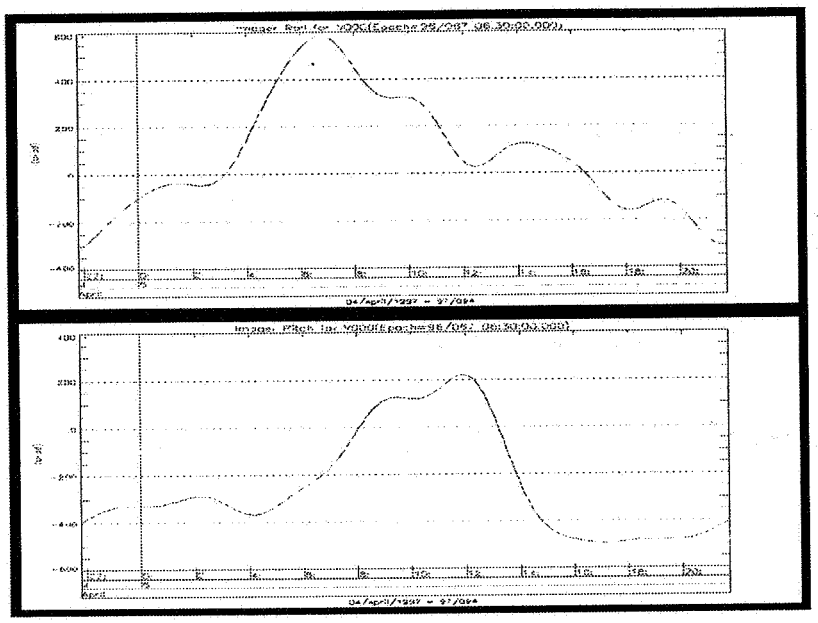

Figure 7. Roll and Pitch Profiles - A Priori Approach

The a priori approach is easy to use but has a problem in that once observations are converted into a solution and covariance, it is not possible to separate them by time. In the old observations approach, only stars from the gap period were used. In a sense, the a priori approach uses all the old star observations, even the ones following eclipse that do not reflect the exit transients. This introduces errors into the new solution. [3] Figure 8 shows the larger residuals at 10:30 UTC following eclipse.

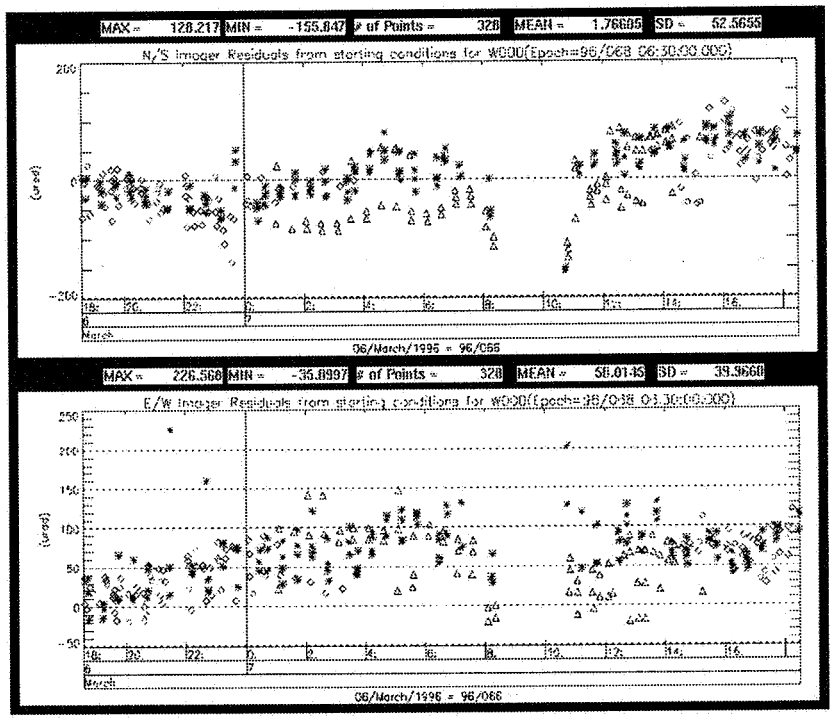

Figure 8. Residuals Obtained Using An A Priori Solution

Using an a priori solution increases the residuals over those of the baseline, and there are also post-eclipse spikes similar to those obtained using old observations. Because the a priori solution applies to the entire day, there is no way to limit information from the pre-gap days to the current gap period.

Simulating Observations

In order to get away from the a priori assumption of attitude repeatability over the entire day, observations were simulated using attitude estimated from current data. Before solving for orbit and attitude in OAD, attitude in the gap was estimated from star observations using a smoother. [4] This was accomplished by filtering forward and backward and then "averaging" the two filter solutions. The smoothed attitude was then used to simulate star observations only over the gap period. Again, only star observations were used and simulated because the orbit solution was not yet known. Figure 9 shows the roll and pitch profiles obtained by filling the gap with simulated observations. Within the gap, the attitude is not as close to that of the baseline and old observations profiles as are those of the a priori. This suggests that the gap attitude obtained by simulating observations may not be as accurate as that of the a priori approach.

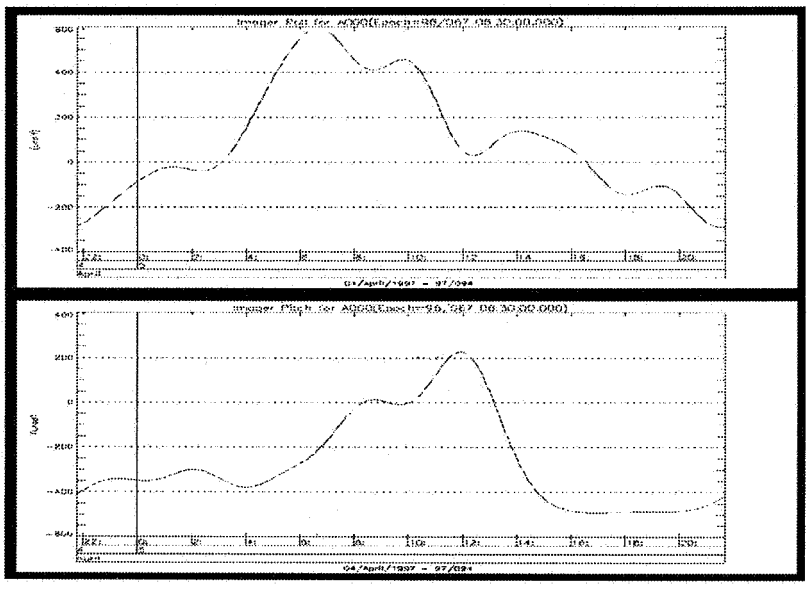

Figure 9. Roll and Pitch Profiles - Simulated Observations Approach

In filling the gap, only one star per window was simulated. Even though this is one fourth the nominal star density, it was adequate to constrain the attitude. For the sake of observability, the star was simulated in different quadrants of the field of view for each window. Figure 10 shows the residuals obtained using simulated observations in the gap.

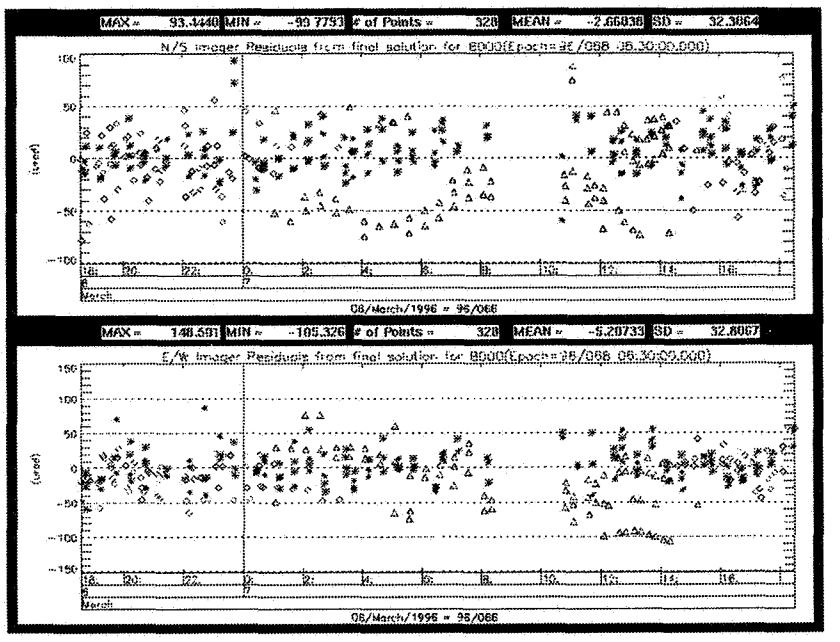

Figure 10. Residuals Obtained With Simulated Observations

Although the residuals are not as small as the baseline, this approach gives an IMC set that is within the imager dynamic range and that better follows transients without having to flag observations. There are not the large spikes seen with the old observations and a priori methods. Where the simulated observations method falls short is that its within-gap solutions are not accurate. On the last day of eclipse, the old observations approach is still necessary to avoid large residuals in the former eclipse period. Table 1 gives some statistics for the baseline method and each of the three alternative methods. First, it lists the overall root mean square value of all the residual types. Second, it lists the spread of the landmarks following eclipse. Spread is important because SSAAs can remove a bias, but spread shows up as image distortion.

	Overall RMS		Post-Gap Spread	
	NS	EW	NS	EW
Two-Day Baseline	49.0	60.2	150	150
Old Observations	55.1	62.2	200	200
A Priori	52.6	70.4	200	200
Simulated Observations	52.5	63.8	150	200

Table 1. Comparison of Gap Handling Methods

When the next day has the same gap as the current day, the baseline approach is best both overall and post-eclipse. Of course, if the next day had no gap, the residuals over this period could be disastrous. Of the alternative methods, the old observations and simulated observations approaches perform better than the a priori outside the gap. As discussed above, this is because they limit their input to the gap period. Inside the gap, the old observations and a priori approaches do better than the simulated observations approach. This is likely due to problems with the smoother used to estimate the gap attitude.

Discussion

The GOES gap problem is interesting for several reasons. First, it recalls the underlying assumption of uniformly spaced data in curve fitting problems. Gaps can result in unrealistic solutions. Second, it demonstrates the value of a propagation model. Without gyro data, the attitude in the gap wanders. The orbit, which has a good propagation model, is unaffected by gaps. Third, it points out that a priori solutions reflect all of the observations, not just the ones in the gap. Fourth, it recommends the use of wavelets rather than Fourier series to represent attitude over time as well as frequency.

Our experience with the baseline and these three alternative approaches to handling observation gaps can be summarized as follows:

1. Ignoring the gap works best when the next day has a gap.
   But when the next day has no gap, the errors can be horrendous.
2. Including old observations works well but is operationally cumbersome.
   Observations are currently archived after twenty-six days..
3. A priori solutions introduce errors when the current and a priori profiles differ.
   Post-eclipse transients cause residuals to be large.
4. Filling the gap with simulated observations is operationally convenient.
   But attitude profiles in the gap may inaccurate.

It would have been good to combine the virtues of the a priori and gap-filling approaches. The a priori provides accurate attitudes inside the gap, and gap-filling provides control over where attitude information is to be applied. By using the a priori attitude rather than sequentially estimating it, the simulated observations approach could be simplified and improved. If a smoother were really needed, it ought to be done for both attitude and orbit in order to serve as an alternative to the current batch algorithm. The resulting profiles could then be Fourier analyzed to give IMC coefficients for uplink. This would be a reasonable first step toward real-time IMC which might eliminate this and many other problems resulting from the need to predict orbit and attitude a day in advance.

Acknowledgments

Support for this paper was provided under NOAA contract number 50DGNE500016. The authors also wish to acknowledge Dr. Kwok Ong of Space Systems/Loral for designing and programming the a priori enhancement to the OATS system.

References

1. Kwok Ong (Space Systems/Loral), OATS Software Enhancement: Implementation of OAD A Priori Processing, 5 February 1996
2. Wertz, J.R., Spacecraft Attitude Determination and Control, D. Reidel Publishing Company, 1980, pp.447-459
3. John Tsui and Wyatt Wallace (Lockheed Martin SMS), OAD Eclipse Study, September 1996
4. Gelb, A., Applied Optimal Estimation, MIT Press, 1970

A Predictive Attitude Determination Algorithm

John L. Crassidis
Department of Mechanical Engineering
The Catholic University of America
Washington, DC 20064

F. Landis Markley
Guidance, Navigation, and Control Branch, Code 712
Goddard Space Flight Center
Greenbelt, MD 20771

Abstract

In this paper, a new and efficient algorithm is developed for attitude determination from vector observations. The new algorithm, called the Predictive Attitude Determination (PAD) algorithm, is derived from a general nonlinear predictive filter approach. Traditional deterministic algorithms are shown to be suboptimal for anisotropic measurement errors. The major advantage of the PAD algorithm is that it can be easily be applied to the case where anisotropic measurement errors exist. Also, an analytical expression is derived for the steady-state attitude error covariance, which is shown to be equivalent to the optimal covariance derived from maximum likelihood techniques. Simulation studies indicate that the new algorithm is able to accurately determine the attitude of a spacecraft, even for radically anisotropic measurement errors.

Introduction

Attitude determination refers to the identification of a proper orthogonal rotation matrix so that the measured observations in the body frame equal the reference frame observations mapped by that matrix into the body frame. If all the measured and reference vectors are error free, then the rotation (attitude) matrix is the same for all sets of observations. However, if measurements errors exist, such as noise, then a least-squares type method must be used. For this case, the most common method for determining the attitude matrix uses a loss function first posed by Wahba [1]. This problem involves finding an orthogonal rotation matrix which minimizes the weighted sum of the squares of the observation residuals.

Since its origination in 1965, there have been many algorithms developed which minimize Wahba's loss function. The first practical method was given by Davenport's q-method [2], which solves for the quaternion representation of the rotation matrix. However, this method requires an eigenvalue/eigenvector decomposition of a dimension 4 matrix, which may be computationally intense. A more efficient method was proposed by Shuster [3], called the QUEST algorithm, which simplifies the q-method approach by solving for the components of a Gibbs vector, and uses the fact that any meromorphic function of a dimension 3 matrix can be represented as a quadratic in that matrix. Other methods solve for the attitude matrix directly (e.g., see Refs. [4-5]). In particular, the FOAM algorithm [5] has been shown to be comparable to QUEST in computational speed, and has also been shown to be more robust in some cases. Still other methods which address Wahba's problem can be found in Ref. [6-8].

In Wahba's problem each vector residual is weighted by a scalar number to reflect the relative importance of each sensor. Shuster [9] has shown that Wahba's problem is equivalent to a maximum

likelihood estimation problem, where the scalar weight is equal to the scalar inverse variance of the measurement error process. Shuster [10] has further shown that a scalar variance is a good approximation of the actual measurement errors, except in the case where the measurement errors are radically anisotropic. An anisotropic measurement error may be produced by a single-axis failure or degradation in the sensor. This was evident for the Hubble spacecraft where single axis failures occurred on both three-axis magnetometers in 1992 (unfortunately, the failures occurred on the same axis). If these corrupt measurements are used for attitude determination, then the solution to Wahba's problem using scalar weighting is not optimal (as will be shown). Therefore, algorithms such as QUEST and FOAM can produce suboptimal attitude solutions.

In this paper, a new and efficient algorithm is derived which determines the attitude for both isotropic and anisotropic measurement errors. The algorithm is based on a predictive filtering scheme for nonlinear systems [11]. This scheme has been successfully applied to estimate the attitude of a spacecraft using a dynamic model for rate information [12]. The predictive filter developed in this paper is essentially reduced to a deterministic approach, since the corrections required to update the model are not weighted in the predictive filter loss function. Therefore, the new algorithm is known as a Predictive Attitude Determination (PAD) algorithm. Also, an analytical expression is derived for the attitude error covariance. It will be further shown that when the measurement errors are isotropic, the PAD steady-state attitude error covariance is identical to the QUEST covariance in Ref. [3].

The organization of this paper proceeds as follows. First, a summary of Wahba's problem is shown. Then, Wahba's problem is generalized for anisotropic measurement errors. Also, attitude covariance expressions are shown for the original and generalized loss functions. Next, a brief review of the predictive filter for nonlinear systems is shown. Then, the PAD algorithm and covariance expression are developed. Finally, the PAD algorithm is used to determine a simulated spacecraft's attitude using two star trackers as sensors, with a single-axis failure in one tracker.

Background

In this section, Wahba's problem is reviewed. Also, a generalized version of Wahba's problem is shown, which involves anisotropic measurement errors. A covariance expression is also derived for the generalized problem. Wahba's original problem, modified to include the covariance weighting [9], involves finding a proper orthogonal matrix A that minimizes the following loss function

$$J(A)=\frac{1}{2}\sum_{i=1}^{n}\sigma_i^{-2}\left(\underline{\tilde{b}}_i-A\underline{r}_i\right)^T\left(\underline{\tilde{b}}_i-A\underline{r}_i\right) \tag{1}$$

where $\underline{r}_i$ are the representations of the directions to some observed object, $\underline{\tilde{b}}_i$ are the measured observations in the spacecraft body frame (the tilde denotes measurement), σ_i are the standard deviations of the corresponding measurement errors, and n is the number of observations. Since the attitude matrix is assumed orthogonal, the loss function in Equation (1) can be shown to be equivalent to minimizing the following loss function

$$J(A)=-\text{trace}\left(A\,B^T\right) \tag{2}$$

where

$$B=\sum_{i=1}^{n}\sigma_i^{-2}\left(\underline{\tilde{b}}_i\,\underline{r}_i^T\right) \tag{3}$$

A convenient expression for the attitude matrix is the quaternion representation, defined as [13]

$$\underline{q} \equiv \begin{bmatrix} \underline{q}_{13} \\ q_4 \end{bmatrix} \tag{4}$$

with

$$\underline{q}_{13} \equiv \begin{bmatrix} q_1 \\ q_2 \\ q_3 \end{bmatrix} = \hat{\underline{e}} \sin(\theta/2) \tag{5a}$$

$$q_4 = \cos(\theta/2) \tag{5b}$$

where $\hat{\underline{e}}$ is a unit vector corresponding to the axis of rotation and θ is the angle of rotation. The quaternion satisfies a single constraint, given by

$$\underline{q}^T \underline{q} = \underline{q}_{13}^T \underline{q}_{13} + q_4^2 = 1 \tag{6}$$

The attitude matrix is related to the quaternion by

$$A(\underline{q}) = -\Xi^T(\underline{q})\Psi(\underline{q}) \tag{7}$$

where

$$\Xi(\underline{q}) \equiv \begin{bmatrix} q_4 I_{3\times 3} + [\underline{q}_{13}\times] \\ \cdots\cdots\cdots\cdots \\ -\underline{q}_{13}^T \end{bmatrix} \tag{8a}$$

$$\Psi(\underline{q}) \equiv \begin{bmatrix} -q_4 I_{3\times 3} + [\underline{q}_{13}\times] \\ \cdots\cdots\cdots\cdots \\ \underline{q}_{13}^T \end{bmatrix} \tag{8b}$$

where $I_{3\times 3}$ is a 3×3 identity matrix. The 3×3 matrix $[\underline{q}_{13}\times]$ is referred to as cross product matrix since $\underline{a}\times\underline{b} = [\underline{a}\times]\underline{b}$, with

$$[\underline{a}\times] \equiv \begin{bmatrix} 0 & -a_3 & a_2 \\ a_3 & 0 & -a_1 \\ -a_2 & a_1 & 0 \end{bmatrix} \tag{9}$$

From Equation (2) it is clear that the quaternion representation leads to a loss function that is quadratic in the quaternions. An efficient algorithm which minimizes this loss function is given by the QUEST algorithm [3].

As seen in Equation (1), the 3×1 measurement errors are assumed to be isotropic, (i.e., the covariance is assumed to be given by a scalar times the identity). The generalized version of Wahba's loss function for anisotropic errors can be derived using maximum likelihood. Assuming a Gaussian distribution for the error process leads to the following generalized loss function

$$J(A)=\frac{1}{2}\sum_{i=1}^{n}\left(\tilde{\underline{b}}_i-A\underline{r}_i\right)^T R_i^{-1}\left(\tilde{\underline{b}}_i-A\underline{r}_i\right) \tag{10}$$

where R_i represents the measurement error covariance matrix of the i^{th} measurement (for a detailed discussion of the measurement error model see Ref. [9]). From Equation (10), it is clear that an anisotropic covariance matrix leads to a quartic dependence if the quaternion representation is used. A general solution can be found be using a nonlinear least-squares approach, but this may be extremely computational intense. Another method involves finding a scalar value which minimizes the error between the loss functions in Equations (10) and Equation (1) [14]. Therefore, algorithms such as the q-method [2] and QUEST [3] may be used, but may produce suboptimal attitude solutions. Other methods which determine the attitude matrix, such as FOAM [5], also yield sub-optimal solutions in this case. The error introduced by using the scalar approach can be investigated by deriving its attitude covariance error, which can be shown to be given by [14]

$$P_{\text{body}}=E\left\{\delta\underline{\alpha}^T\delta\underline{\alpha}\right\}\approx\left[\sum_{i=1}^{n}a_i\left[\tilde{\underline{b}}_i\times\right]^2\right]^{-1}\sum_{i=1}^{n}a_i^2\left[\tilde{\underline{b}}_i\times\right]R_i\left[\tilde{\underline{b}}_i\times\right]^T\left[\sum_{i=1}^{n}a_i\left[\tilde{\underline{b}}_i\times\right]^2\right]^{-1} \tag{11}$$

where $\delta\underline{\alpha}$ represents a small angle error, and $E\{\ \}$ denotes expectation. In actuality, $\tilde{\underline{b}}_i$ should be replaced with $A_{\text{true}}\,\underline{r}_i$, but Equation (11) is extremely accurate for low noise. Note that if $R_i=\sigma_i^2 I$, setting $a_i=\sigma_i^{-2}$ yields

$$P_{\text{body}}\approx-\left[\sum_{i=1}^{n}\sigma_i^{-2}\left[\tilde{\underline{b}}_i\times\right]^2\right]^{-1} \tag{12}$$

Therefore, in this case the covariance in Equation (11) would be identical to the covariance given by QUEST [3].

An attitude error covariance can also be derived from the generalized loss function in Equation (10). This is accomplished by using results from maximum likelihood estimation [9]. The Fisher information matrix for a parameter vector $\underline{x}$ is given by

$$F_{xx}=E\left\{\frac{\partial}{\partial\underline{x}\,\partial\underline{x}^T}J(\underline{x})\right\}_{\underline{x}_{\text{true}}} \tag{13}$$

where $J(\underline{x})$ is the negative log likelihood function, which is the loss function in this case. If the measurements are Gaussian and linear in the parameter vector, then the error covariance is given by

$$P_{xx}=F_{xx}^{-1} \tag{14}$$

Now, the attitude matrix is approximated by

$$A=e^{-[\delta\underline{\alpha}\times]}A_{\text{true}}\approx\left(I-[\delta\underline{\alpha}\times]+\frac{1}{2}[\delta\underline{\alpha}\times]^2\right)A_{\text{true}} \tag{15}$$

Equations (15) is next substituted into Equation (10) to determine the Fisher information matrix. First-order terms vanish in the partials, and third-order terms become zero since $E\{\delta\underline{\alpha}\}=\underline{0}$. Also, assuming that the quartic terms are negligible leads to the following form for the optimal covariance

$$P_{\text{opt}} \approx \left[\sum_{i=1}^{n}\left[\underline{\tilde{b}}_i\times\right]R_i^{-1}\left[\underline{\tilde{b}}_i\times\right]^T\right]^{-1} \tag{16}$$

Note that the optimal covariance in Equation (16) reduces to the covariance in Equation (12) if the condition $R_i=\sigma_i^2 I$ is true. Also, the diagonal elements of covariance in Equation (16) are always smaller or equal to the corresponding elements in Equation (11). Therefore, methods which minimize Wahba's original loss function for anisotropic measurement errors can produce suboptimal results.

Predictive Attitude Determination

In this section, the predictive attitude determination (PAD) algorithm is derived. First, a brief review of the nonlinear predictive filter is shown (see Ref. [11] for more details). Then, the filter algorithm is reduced to a deterministic-type approach for attitude determination. Finally, a covariance expression for the attitude errors using PAD are derived.

Predictive Filtering

In the nonlinear predictive filter it is assumed that the state and output estimates are given by a preliminary model and a to-be-determined model error vector, given by

$$\dot{\underline{\hat{x}}}(t)=\underline{f}\left(\underline{\hat{x}}(t),t\right)+G(t)\,\underline{d}(t) \tag{17a}$$

$$\underline{\hat{y}}(t)=\underline{c}\left(\underline{\hat{x}}(t),t\right) \tag{17b}$$

where $\underline{f}$ is a $p\times 1$ model vector, $\underline{\hat{x}}(t)$ is a $p\times 1$ state estimate vector, $\underline{d}(t)$ is a $l\times 1$ model error vector, $G(t)$ is a $p\times l$ model-error distribution matrix, $\underline{c}$ is a $m\times 1$ measurement vector, and $\underline{\hat{y}}(t)$ is a $m\times 1$ estimated output vector. State-observable discrete measurements are assumed for Equation (17b) in the following form

$$\underline{\tilde{y}}(t_k)=\underline{c}\left(\underline{x}(t_k),t_k\right)+\underline{v}(t_k) \tag{18}$$

where $\underline{\tilde{y}}(t_k)$ is a $m\times 1$ measurement vector at time t_k, $\underline{x}(t_k)$ is the true state vector, and $\underline{v}(t_k)$ is a $m\times 1$ measurement noise vector which is assumed to be a zero-mean, Gaussian white-noise distributed process with

$$E\left\{\underline{v}(t_k)\right\}=\underline{0} \tag{19a}$$

$$E\left\{\underline{v}(t_k)\underline{v}^T(t_{k'})\right\}=R\delta_{kk'} \tag{19b}$$

where R is a $m\times m$ positive-definite covariance matrix.

A loss functional consisting of the weighted sum square of the measurement-minus-estimate residuals plus the weighted sum square of the model correction term is minimized, given by

$$J=\frac{1}{2}\left\{\underline{\tilde{y}}(t_{k+1})-\underline{\hat{y}}(t_{k+1})\right\}^T R^{-1}\left\{\underline{\tilde{y}}(t_{k+1})-\underline{\hat{y}}(t_{k+1})\right\}+\frac{1}{2}\underline{d}^T(t_k)\,W\,\underline{d}(t_k) \tag{20}$$

where W is a $l\times l$ weighting matrix. The necessary conditions for the minimization of Equation (20) lead to the following model error solution

$$\underline{d}(t_k)=-\left\{\left[\Lambda(\Delta t)S(\underline{\hat{x}}_k)\right]^T R^{-1}\Lambda(\Delta t)S(\underline{\hat{x}}_k)+W\right\}^{-1}\left[\Lambda(\Delta t)S(\underline{\hat{x}}_k)\right]^T R^{-1}\left[\underline{z}(\underline{\hat{x}}_k,\Delta t)-\underline{\tilde{y}}(t_{k+1})-\underline{\hat{y}}(t_k)\right] \tag{21}$$

where $\underline{\hat{x}}_k\equiv\underline{\hat{x}}(t_k)$, Δt is the measurement sampling interval, $S(\underline{\hat{x}})$ is a $m\times l$ dimensional matrix, and $\Lambda(\Delta t)$ is a $m\times m$ diagonal matrix with elements given by

$$\lambda_{ii}=\frac{\Delta t^{p_i}}{p_i!},\quad i=1,2,\ldots,m \tag{22}$$

where p_i, $i=1,2,\ldots,m$, is the lowest order of the derivative of $c_i(\underline{\hat{x}}(t))$ in which any component of $\underline{d}(t)$ first appears due to successive differentiation and substitution for $\dot{\hat{x}}_i(t)$ on the right side. The i^{th} component of $\underline{z}(\underline{\hat{x}},\Delta t)$ is given by

$$z_i(\underline{\hat{x}},\Delta t)=\sum_{k=1}^{p_i}\frac{\Delta t^k}{k!}L_f^k(c_i) \tag{23}$$

where $L_f^k(c_i)$ is the k^{th} Lie derivative, defined by

$$\begin{aligned} L_f^k(c_i)&=c_i && \text{for } k=0\\ L_f^k(c_i)&=\frac{\partial L_f^{k-1}(c_i)}{\partial\underline{\hat{x}}}\underline{f} && \text{for } k\geq 1\end{aligned} \tag{24}$$

The i^{th} row of $S(\underline{\hat{x}})$ is given by

$$s_i=\left\{L_{g_1}\left[L_f^{p_i-1}(c_i)\right],\ldots,L_{g_l}\left[L_f^{p_i-1}(c_i)\right]\right\},\quad i=1,2,\ldots,m \tag{25}$$

where g_j is the j^{th} column of $G(t)$, and the Lie derivative is defined by

$$L_{g_j}\left[L_f^{p_i-1}(c_i)\right]\equiv\frac{\partial L_f^{p_i-1}(c_i)}{\partial\underline{\hat{x}}}g_j,\quad j=1,2,\ldots,l \tag{26}$$

Equation (26) is in essence a generalized sensitivity matrix for nonlinear systems. Therefore, given a state estimate at time t_k, then Equation (21) is used to process the measurement at time t_{k+1} to find the $\underline{d}(t_k)$ to be used in $[t_k,t_{k+1}]$ to propagate the state estimate to time t_{k+1}. The weighting matrix W serves to weight the relative importance between the propagated model and measured quantities. If this matrix is set to zero, then no weight is placed on the model corrections.

PAD Algorithm

In the PAD algorithm it is assumed that the model is given by the quaternion kinematics model. PAD requires no dynamics model; it assumes that the attitude rate is adequately modeled by a constant model error $\underline{d}$ between measurements, so that

$$\dot{\hat{\underline{q}}} = \frac{1}{2}\Xi(\hat{\underline{q}})\underline{d} \tag{27}$$

where $\hat{q}$ denotes the determined quaternion. Since the body measurements $(\tilde{\underline{b}}_i)$ are used as the required tracking trajectories, the output vector in Equation (18) is given by (dropping the subscript i for the moment)

$$\underline{c}(\hat{\underline{x}}) = A(\hat{\underline{q}})\underline{r} \tag{28}$$

The lowest order time derivative of $\hat{\underline{q}}$ in Equation (28) in which any component of $\underline{d}$ first appears in Equation (27) is one, so that $p_i = 1$. Therefore, the Λ and $\underline{z}$ quantities formed from Equations (22) and (23) are given by

$$\Lambda = \Delta t\, I \tag{29a}$$

$$\underline{z}(\hat{\underline{x}}, \Delta t) = \underline{0} \tag{29b}$$

The derivative of Equation (28) with respect to $\hat{\underline{q}}$ can be shown to be given by

$$\frac{\partial \underline{c}}{\partial \hat{\underline{q}}} = -2\Xi^T(\hat{\underline{q}})\Gamma(\underline{r}) \tag{30}$$

where

$$\Gamma(\underline{r}) \equiv \begin{bmatrix} -[\underline{r}\times] & \vdots & -\underline{r} \\ \cdots\cdots & \vdots & \cdots\cdots \\ \underline{r}^T & \vdots & 0 \end{bmatrix} \tag{31}$$

Therefore, the S matrix in Equation (21), which is formed using Equation (25) is given by

$$S = -\Xi^T(\hat{\underline{q}})\Gamma(\underline{r})\Xi(\hat{\underline{q}}) = \left[A(\hat{\underline{q}})\underline{r}\times\right] \tag{32}$$

The 3×3 matrix $\left[A(\hat{\underline{q}})\underline{r}\times\right]$ is analogous to the sensitivity matrix used in a Kalman filter (see Ref. [15]). This matrix has rank 2, which reflects the fact that there is no information about rotations around the current measurement vector. For a deterministic attitude solution the weighting matrix W is set to zero in Equation (21). Therefore, the extension for multiple vector measurement sets, assuming that the errors between vector measurement sets are uncorrelated, is given by the following model error

$$\underline{d}(t_k) = \frac{1}{\Delta t}\left\{\sum_{i=1}^{n}\left[A(\hat{\underline{q}}_k)\underline{r}_i\times\right]R_i^{-1}\left[A(\hat{\underline{q}}_k)\underline{r}_i\times\right]\right\}^{-1}\sum_{i=1}^{n}\left[A(\hat{\underline{q}}_k)\underline{r}_i\times\right]R_i^{-1}\left(\tilde{\underline{b}}_i(t_{k+1}) - A(\hat{\underline{q}}_k)\underline{r}_i\right) \tag{33}$$

The inverse expression in Equation (33) exists only if at least two of the vector observations are not parallel, which is equivalent to all methods which solve Wahba's problem. The determined quaternion can be found by integrating Equation (27) from time t_k to t_{k+1}. Since $\underline{d}$ is constant over this interval, the discrete propagation for Equation (27) found in Ref. [16] can be used. It should be noted that Equation (33) represents an exact linearization for an interval Δt (see Ref. [17]). However, for practical applications the sampling rate should be well below Nyquist's limit [18].

In order to derive an attitude error covariance from Equation (33), a propagated expression can be derived using a similar approach found in Ref. [15]. Assuming continuous measurements and small Δt, the propagated attitude error covariance can be shown to be given by ([15], [19])

$$\dot{P} = -[\underline{d}\times]P - P[\underline{d}\times]^T + E\left\{\underline{\eta}\underline{\eta}^T\right\} - PS^T R^{-1} S\,P/\Delta t \tag{34}$$

where

$$S = \left\{\left[A(\underline{q})\underline{r}_1\times\right]^T \,\vdots\, \left[A(\hat{\underline{q}})\underline{r}_2\times\right]^T \,\vdots\, \cdots \,\vdots\, \left[A(\hat{\underline{q}})\underline{r}_n\times\right]^T\right\}^T \tag{35}$$

The measurements in PAD play two roles: 1) dynamics model replacement, similar to gyros used in [15], and 2) actual attitude update, similar to line-of-sight observations used in [15]. Thus, measurement errors contribute to both $E\left\{\underline{\eta}\underline{\eta}^T\right\}$ (similar to process noise) and to the last term in Equation (34) (similar to the usual continuous-time Kalman filter). The Δt term is due to the conversion of the discrete-time measurements to continuous time ([19], [20]) (note, in the limit $\Delta t \to 0$). The term $E\left\{\underline{\eta}\underline{\eta}^T\right\}$ is a covariance due to the continuous-time measurements, with

$$\underline{\eta} = \frac{1}{\Delta t}\left\{\sum_{i=1}^{n}\left[A(\hat{\underline{q}})\underline{r}_i\times\right]\overline{R}_i^{-1}\left[A(\hat{\underline{q}})\underline{r}_i\times\right]^T\right\}^{-1}\sum_{i=1}^{n}\left[A(\hat{\underline{q}})\underline{r}_i\times\right]\overline{R}_i^{-1}\underline{v}_i \tag{36}$$

where $\underline{v}_i$ is the continuous measurement noise with covariance $\overline{R}_i$. The expectation in Equation (34) is therefore given by

$$E\left\{\underline{\eta}\underline{\eta}^T\right\} = \frac{1}{\Delta t^2}\left\{\sum_{i=1}^{n}\left[A(\hat{\underline{q}})\underline{r}_i\times\right]\overline{R}_i^{-1}\left[A(\hat{\underline{q}})\underline{r}_i\times\right]^T\right\}^{-1} \tag{37}$$

Next, assuming that the transients in Equation (34) decay quickly leads to the following steady-state condition

$$E\left\{\underline{\eta}\underline{\eta}^T\right\} \approx PS^T R^{-1} S\,P/\Delta t \tag{38}$$

Solving for P and converting to discrete-time (i.e., using the approximation $\Delta t\,P$ [21]), yields the following discrete-time steady-state covariance

$$P_{\text{pad}} \approx \left[\sum_{i=1}^{n}\left[A(\hat{\underline{q}}_k)\underline{r}_i\times\right]R_i^{-1}\left[A(\hat{\underline{q}}_k)\underline{r}_i\times\right]^T\right]^{-1} \tag{39}$$

This expression is essentially equivalent to the optimal covariance for the generalized version of Wahba's problem, shown by Equation (16). Therefore, the PAD algorithm is in essence equivalent to solving Wahba's generalized loss function. Also note that the approximation in Equation (39) is valid only for small Δt (i.e., well below Nyquist's limit).

If the measurement errors are isotropic for each vector observation, then the model error in Equation (33) can be rewritten by setting $R_i = \sigma_i^2 I$. Noting that $[\underline{a}\times]\underline{a} = \underline{0}$ for any $\underline{a}$ leads to the following simple model error solution

$$\underline{d}(t_k) = \frac{1}{\Delta t}\left\{\sum_{i=1}^{n} \sigma_i^{-2}\left[A(\hat{\underline{q}}_k)\underline{r}_i\times\right]^2\right\}^{-1} \sum_{i=1}^{n} \sigma_i^{-2}\left[A(\hat{\underline{q}}_k)\underline{r}_i\times\right]\tilde{\underline{b}}_i(k+1) \tag{40}$$

Also, the covariance in Equation (39) reduces down to

$$P_{\text{pad}} \approx -\left[\sum_{i=1}^{n} \sigma_i^{-2}\left[A(\hat{\underline{q}}_k)\underline{r}_i\times\right]^2\right]^{-1} \tag{41}$$

which is essentially equivalent to the QUEST covariance shown in Ref. [3]. Also, since Equation (39) or (41) is used to determine the model error, the PAD algorithm determines the steady-state attitude error covariance as part of its solution.

Error Analysis

In this section, an error analysis is shown with respect to initial condition errors and sampling interval. The continuous output estimate can be shown to be given by [11]

$$\dot{\hat{\underline{y}}} = S\underline{d} \tag{42}$$

where

$$\hat{\underline{y}} = \left\{\left[A(\hat{\underline{q}})\underline{r}_1\right]^T \,\vdots\, \left[A(\hat{\underline{q}})\underline{r}_2\right]^T \,\vdots\, \cdots \,\vdots\, \left[A(\hat{\underline{q}})\underline{r}_n\right]^T\right\}^T \tag{43}$$

and S is given by Equation (35). The error dynamics model between the measured and estimated observations can easily be shown to be given by

$$\dot{\underline{e}} = -\frac{1}{\Delta t}Q\underline{e} + [I - Q]\dot{\tilde{\underline{y}}} \tag{44}$$

where $\underline{e} = \tilde{\underline{y}} - \hat{\underline{y}}$, and

$$Q = S P_{\text{pad}} S^T R^{-1} \tag{45}$$

Since at least two vector observations are required in the PAD algorithm, the matrix Q will always be positive semi-definite. Therefore, as long as the body observations are non-parallel and bounded, then the error in Equation (44) is also bounded for any initial condition error. Also, the error dynamics are a function of $1/\Delta t$, which means that the errors converge faster as the sampling interval decreases, which is intuitively correct.

Spacecraft Simulation

In this section, an example is shown using PAD to determine the attitude from simulated star tracker measurements. The star tracker measures the tangent of two angles, α and β, resulting in a body vector given by

$$\underline{b}_i = \frac{1}{\sqrt{\left(\tan^2 a_i + \tan^2 \beta_i + 1\right)}} \begin{bmatrix} \tan a_i \\ \tan \beta_i \\ 1 \end{bmatrix} \tag{46}$$

where the z-axis of the tracker is along the boresight. The star tracker measurements are obtained by adding Gaussian noise to $\tan a_i$ and $\tan \beta_i$, with a 3σ value of 18 arc-sec. Measurements are sampled at 1 second intervals. The theoretical measurement error covariance for the model in Equation (46) is not isotropic. However, Shuster [10] has shown that if the noise variances on $\tan a_i$ and $\tan \beta_i$ are relatively equal and small, then the true covariance can be effectively replaced by an isotropic matrix.

The spacecraft is assumed to be earth-pointing with a rotation rate about the spacecraft y-axis (negative orbit normal) of 0.0011 rad/sec. The spacecraft z-axis is defined to be pointed nadir, and the x-axis completes the triad. Two trackers are used in the simulation. The first one has its boresight along the spacecraft y-axis, and the second has its boresight along the spacecraft x-axis. In the first simulation it assumed that both trackers measure two stars each with about a 0.5 degree separation between them. A plot of the attitude errors and 3σ bounds using the PAD algorithm is shown in Figure 1. These errors agree with the errors produced using the QUEST algorithm.

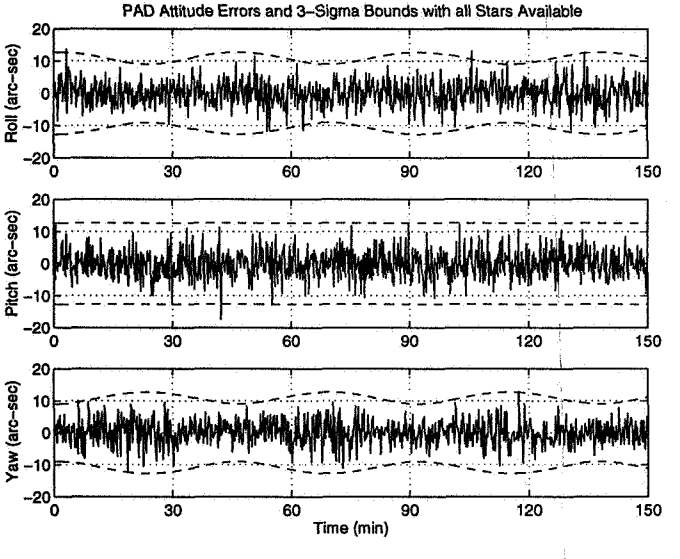

Figure 1 PAD Attitude Errors Using Both Trackers

In the next simulation, it is assumed that the second tracker has a single axis failure in $\tan \beta_i$. The disadvantage of methods which solve Wahba's original loss function is that they cannot use the single axis information from the second tracker. This is due to the fact that a scalar measurement error variance is assumed. Therefore, in order to use QUEST, only the first tracker measurements are used. A plot of the attitude errors and bounds using QUEST for this case is shown in Figure 2. Since the first tracker's boresight is along the spacecraft y-axis, the pitch axis has the largest error.

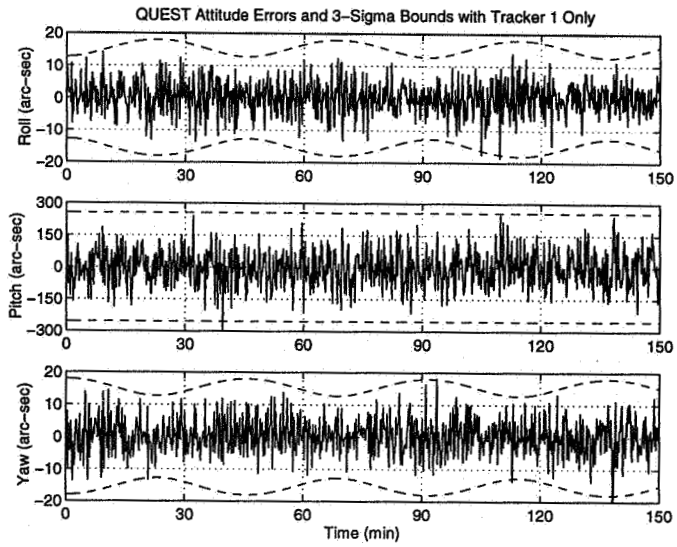

Figure 2 QUEST Attitude Errors Using Tracker 1 Only

The PAD algorithm can still use the single axis information from the second tracker. This is accomplished by using an inverse covariance matrix for that tracker given by

$$R_2^{-1} = \begin{bmatrix} \sigma^{-2} & 0 & 0 \\ 0 & 0 & 0 \\ 0 & 0 & 0 \end{bmatrix} \tag{47}$$

The (3,3) element is also set to zero since no information of the magnitude is known by the single axis failure. A plot of the PAD pitch error and bound using two stars in the first tracker and only one star with the single axis failure in the second tracker is shown in Figure 3 (the roll and yaw errors are approximately the same as the one-tracker case, due to the configuration of the trackers). Clearly, the pitch errors are reduced significantly compared with the QUEST solution in Figure 2.

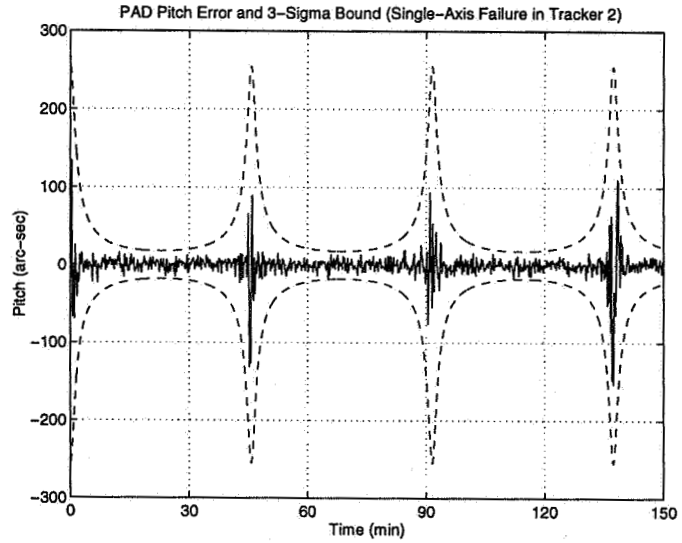

Figure 3 PAD Pitch Error with a Single Axis Failure on Tracker 2

A plot of the 3σ pitch error bounds from both the QUEST solution and PAD solution is shown in Figure 4. The peaks at 45, 90, and 135 minutes for PAD are due to attitude geometry, and to the fact that only one axis in Tracker 2 is used in the measurement. Depending on the attitude geometry, the PAD algorithm reduces the error by an order of magnitude from the QUEST solution. Although this simulation represents an extreme case, it clearly proves that the PAD algorithm provides a viable approach for attitude determination when anisotropic errors exist.

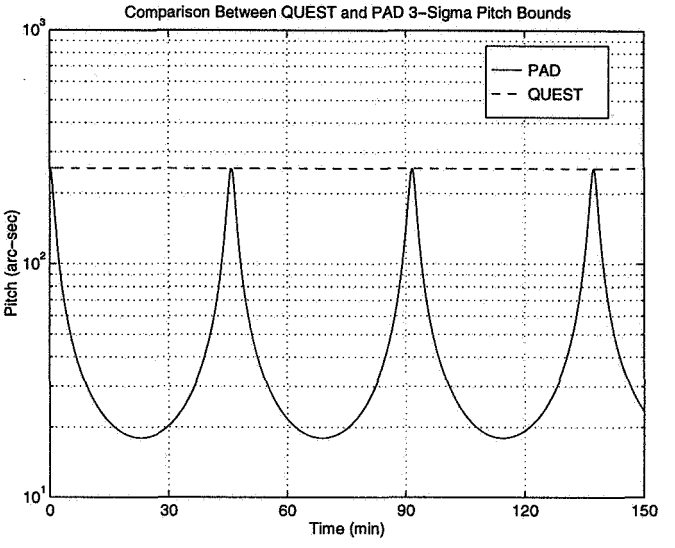

Figure 4 QUEST and PAD Pitch Error Bounds

Also, a test for initial condition errors was performed. A number of Monte Carlo runs was simulated using a normalized random vector for the initial quaternion. A plot of the convergence of the PAD algorithm for one case is shown in Figure 5. In each case, the PAD algorithm is able to converge within seven sampling intervals. The PAD algorithm may be initialized by picking two well-separated stars, and using TRIAD or two-observation (no iteration) QUEST or FOAM. However, this example shows that the attitude converges even for large initial condition errors.

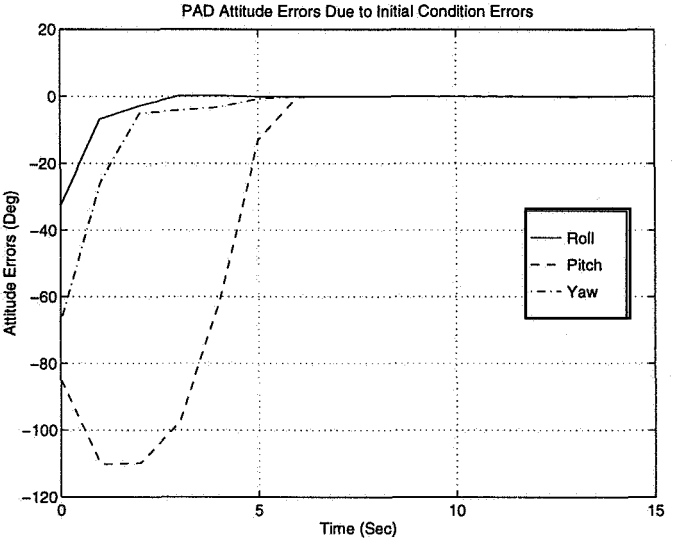

Figure 5 PAD Convergence to Initial Condition Errors

Algorithm Computational Comparisons

The PAD algorithm is compared with QUEST and FOAM for computational floating point operations (FLOPS). In these comparisons, it is assumed that all vector observations are normalized and have isotropic errors only. All simulations were performed using MATLAB, and all matrix functions (such determinant, adjoint, etc.) were written out explicitly for the QUEST and FOAM algorithms. Also, the FOAM rotation matrix was converted to a quaternion, but this only requires 9 FLOPS. Since FOAM and QUEST do not require the attitude error covariance to calculate the attitude, two sets of test comparisons were made. The first one calculates the FLOPS without the covariance calculation in FOAM and QUEST, and the second calculates the FLOPS with the covariance calculation. PAD implicitly solves for the error covariance as part of its solution, so the number of FLOPS is the same in both sets. The number of FLOPS for n vector observations without calculating the covariance in both QUEST and FOAM is given by

$$\begin{aligned} F_{\text{PAD}} &= 332 + 67(n-2) \\ F_{\text{QUEST}} &= 326 + 30(n-2) \\ F_{\text{FOAM}} &= 392 + 30(n-2) \end{aligned} \tag{48}$$

From Equation (48) it is clear that the QUEST algorithm requires the least number of FLOPS for any number of observations. Also, FOAM requires less number of FLOPS than PAD when three or more observations are present. The number of FLOPS for n vector observations with calculating the covariance in both QUEST and FOAM is given by

$$\begin{aligned} F_{\text{PAD}} &= 332 + 67(n-2) \\ F_{\text{QUEST}} &= 442 + 57(n-2) \\ F_{\text{FOAM}} &= 482 + 30(n-2) \end{aligned} \tag{49}$$

For this case, PAD requires the least number of FLOPS until $n = 7$. When seven or more observations are present, then FOAM requires the least number of FLOPS. The QUEST algorithm overcomes PAD for the least number of FLOPS when thirteen or more observations are present. Also, FOAM overcomes QUEST for the least number of FLOPS when four or more observations are present. This is consistent with the CPU comparison shown in Ref. [5]. These case comparisons show that the PAD algorithm seems to be quite efficient in comparison to other attitude determination algorithms.

An advantage of both QUEST and FOAM is that they provide a point-by-point solution, independent of the sampling interval. As mentioned previously, PAD is a function of the sampling interval. A test was performed in order to investigate the effects of sampling interval. It is assumed that the propagation of the quaternion model in Equation (27) is performed at the sampling interval. Also, both trackers with two stars each are assumed in the simulations. The quaternion propagation frequency for an earth-point spacecraft is given by half the orbit rate. Nyquist's upper bound with a safety factor of 10 is about 500 seconds. Results for the 3σ attitude errors produced for different sampling intervals in PAD are shown in Table 1. This shows that the errors start to become significant with a sampling interval of about 100 seconds, and are quite significant with a sampling interval of 500 seconds. Although this study shows that PAD can produce large errors for large sampling intervals, the sampling intervals used for typical on-board spacecraft applications (e.g., in a Kalman filter) are well within the region where PAD provides accurate results.

Table 1 PAD 3σ Attitude Errors for Various Sampling Intervals

Δt (sec)	Roll (arc-sec)	Pitch (arc-sec)	Yaw (arc-sec)
1	11	12	11
10	11	12	11
50	37	13	37
100	130	13	130
250	800	80	800
500	3000	700	3000
750	8,000	3,000	8,000
1000	30,000	600,000	30,000

Conclusions

In this paper, a new algorithm was developed for attitude determination. The major advantage of this new algorithm over traditional algorithms, such as QUEST and FOAM, is that it is easily applicable to the case where anisotropic measurement errors exist. Also, the algorithm is computationally simpler than an extended Kalman filter approach, since no dynamics model is needed. The steady-state attitude error covariance for the new algorithm was shown to be equivalent to the optimal covariance, derived by solving a generalized form of Wahba's problem. Also, the attitude error covariance was shown to reduce to the QUEST covariance when isotropic conditions exist. Simulation studies indicated that the PAD algorithm provides a viable approach for attitude determination even when radically anisotropic errors exist. Finally, the PAD algorithm seems to be computationally comparable to both the QUEST and FOAM algorithms when isotropic measurement errors exist for all observations.

References

[1] Wahba, G., "A Least Squares Estimate of Spacecraft Attitude," Problem 65-1, *SIAM Review*, Vol. 7, No. 3, July 1965, p. 409.

[2] Lerner, G.M., "Three-Axis Attitude Determination," *Spacecraft Attitude Determination and Control*, edited by J.R. Wertz, D. Reidel Publishing Co., Dordrecht, The Netherlands, 1978, pp. 426-428.

[3] Shuster, M.D., and Oh, S.D., "Attitude Determination from Vector Observations," *Journal of Guidance and Control*, Vol. 4, No. 1, Jan.-Feb. 1981, pp. 70-77.

[4] Markley, F.L., "Attitude Determination Using Vector Observations and the Singular Value Decomposition," *The Journal of the Astronautical Sciences*, Vol. 36, No. 3, July-Sept. 1988, pp. 245-258.

[5] Markley, F.L., "Attitude Determination from Vector Observations: A Fast Optimal Matrix Algorithm," *The Journal of the Astronautical Sciences*, Vol. 41, No. 2, April 1993, pp. 261-280.

[6] Bar-Itzhack, I.Y., "Polar Decomposition for Attitude Determination from Vector Observations," *Proceedings of the Flight Mechanics/Estimation Theory Symposium*, NASA-Goddard Space Flight Center, Greenbelt, MD, May 1992, pp. 243-257.

[7] Mortari, D., "Energy Approach Algorithm for Attitude Determination from Vector Observations," *Advances in the Astronautical Sciences-Space Flight Mechanics*, Vol. 89, 1995, AAS paper #95-207, pp. 773-784.

[8] Mortari, D., "Euler-q Algorithm for Attitude Determination from Vector Observations," *AAS/AIAA Space Flight Mechanics Meeting*, Austin, TX, Feb. 1996, AAS Paper #96-173.

[9] Shuster, M.D., "Maximum Likelihood Estimation of Spacecraft Attitude," *The Journal of the Astronautical Sciences*, Vol. 37, No. 1, Jan.-March 1989, pp. 79-88.

[10] Shuster, M.D., "Kalman Filtering of Spacecraft Attitude and the QUEST Model," *The Journal of the Astronautical Sciences*, Vol. 38, No. 3, July-Sept. 1990, pp. 377-393.

[11] Crassidis, J.L., and Markley, F.L., "Predictive Filtering for Nonlinear Systems," *Journal of Guidance, Control and Dynamics*, in print, paper #G4969.

[12] Crassidis, J.L., and Markley, F.L., "Predictive Filtering for Attitude Estimation Without Rate Sensors," *AAS/AIAA Space Flight Mechanics Meeting*, Austin, TX, Feb. 1996, AAS Paper #96-174.

[13] Markley, F.L., "Parameterization of the Attitude," *Spacecraft Attitude Determination and Control*, edited by J.R. Wertz, D. Reidel Publishing Co., Dordrecht, The Netherlands, 1978, pp. 414-416.

[14] Crassidis, J.L., and Markley, F.L., "Attitude Determination Using Global Positioning System Signals," *AIAA Journal of Guidance, Control, and Dynamics*, in review.

[15] Lefferts, E.J., Markley, F.L., and Shuster, M.D., "Kalman Filtering for Spacecraft Attitude Estimation," *Journal of Guidance, Control and Dynamics*, Vol. 5, No. 5, Sept.-Oct. 1982, pp. 417-429.

[16] Spence, C.B., and Markley, F.L., "Attitude Propagation," *Spacecraft Attitude Determination and Control*, edited by J.R. Wertz, D. Reidel Publishing Co., Dordrecht, The Netherlands, 1978, pp. 564-566.

[17] Hunt, L.R., Luksic, M., Su, R., "Exact Linearizations of Input-Output Systems," *International Journal of Control*, Vol. 43, No. 1, 1986, pp. 247-255.

[18] Palm, W.J., *Modeling, Analysis, and Control of Dynamic Systems*, John Wiley & Sons, NY, 1983, pp. 230-231.

[19] Crassidis, J.L., "Integrated Estimation and Identification for Robust Control of Multivariable Systems," Ph.D. Dissertation, State University of New York at Buffalo, May 1993.

[20] Gelb, A., *Applied Optimal Estimation*, MIT Press, MA, 1974.

[21] Farrenkopf, R.L., "Analytic Steady-State Accuracy Solutions for Two Common Spacecraft Attitude Estimators," *Journal of Guidance and Control*, Vol. 1, July-Aug. 1978, pp. 282-284.

Page intentionally left blank

Solar and Magnetic Attitude Determination for Small Spacecraft

Kurt Woodham (Litton Amecom/SSO)[1]
Kathie Blackman (the Hammers Company)[2]
Paul Sanneman (Welch Engineering, Ltd.)[3]

During the Phase B development of the NASA New Millennium Program (NMP) Earth Orbiter-1 (EO-1) spacecraft, detailed analyses were performed for on-board attitude determination using the Sun and the Earth's magnetic field. This work utilized the TRMM 'Contingency Mode' as a starting point but concentrated on implementation for a small spacecraft without a high performance mechanical gyro package. The analyses and simulations performed demonstrate a geographic dependence due to diurnal variations in the Earth magnetic field with respect to the Sun synchronous, nearly polar orbit. Sensitivity to uncompensated residual magnetic fields of the spacecraft and field modeling errors is shown to be the most significant obstacle for maximizing performance. Performance has been evaluated with a number of inertial reference units and various mounting orientations for the two-axis Fine Sun Sensors. Attitude determination accuracy using the six state Kalman Filter executing at 2 Hz is approximately 0.2°, 3-sigma, per axis. Although EO-1 was subsequently driven to a stellar-based attitude determination system as a result of tighter pointing requirements, solar/magnetic attitude determination is demonstrated to be applicable to a range of small spacecraft with medium precision pointing requirements.

1. EO-1 Background

Earth Orbiter-1 (EO-1) is a NASA New Millennium Program (NMP) spacecraft which will cofly with Landsat-7 in a sun-synchronous, 705 Km orbit with a 10:30 am descending node. EO-1 is scheduled to launch on a dual-manifest with SACC-C in May, 1999, and is the first earth-based science NMP mission for NASA's Mission to Planet Earth (MTPE). The spacecraft is maintained nominally in a geocentric nadir orientation by three orthogonally mounted Ithaco Type A reaction wheels in a zero momentum bias configuration. Momentum management is performed using three orthogonally mounted 60 A-m^2 magnetic torquer bars. In addition to the nominal pointing capability, the attitude determination and control subsystem has been designed to facilitate a number of instrument calibration modes, requiring both deep-space and sun-pointing inertial holds and a lunar-pointing raster scan sequence.

The Design Convergence Review (DCR) configuration of the spacecraft is shown in Figure 1.1. The basic layout of the spacecraft remains consistent with this diagram — however the current design has reduced the array size to two panels, and the graphite-epoxy composite bus structure has been replaced with an all aluminum structure.

The primary payload of the EO-1 mission is the Advanced Land Imager (ALI) instrument, under development by the Massachusetts Institute of Technology, Lincoln Laboratory (MIT/LL). This next generation imager utilizes innovative focal plane technologies to produce Landsat-like multi-spectral and pan-chromatic (MS/PAN) imaging at a fraction of the mass, power and cost of traditional imagers. Additionally, the ALI instrument will produce hyper-spectral data in SWIR and VNIR infrared regimes via a pushbroom-type wedge imaging spectrometer (WIS). The ALI Focal Plane Assembly (FPA) layout is shown in Figure 1.2. A grating imaging spectrometer (GIS), with characteristics given in Figure 1.2, is used for WIS validation, and is mounted adjacent to the ALI FPA.

In addition to the ALI, EO-1 is also host to a number of other NMP technologies which will be validated during various aspects of the mission. These include a steerable X-Band phased array antenna; a lightweight flexible solar array experiment; a fiber-optic data-bus connecting the ALI and the Wideband Advanced Recorder & Processor (WARP); and a dual-nozzle pulsed-plasma thruster (PPT) which will be used for a pitch axis attitude control experiment late in the mission timeline.

[1]Kurt Woodham
Litton Amecom/SSO
5115 Calvert Rd
MS 1-22
College Park, MD 20740
301-454-9987

[2]Kathie Blackman
the Hammers Company
7474 Greenway Center
Suite 710
Greenbelt, MD 20770
301-345-5300

[3]Paul Sanneman
Welch Engineering, Ltd.
15200 Shady Grove Rd
Suite 450
Rockville, MD 20850
301-947-5162

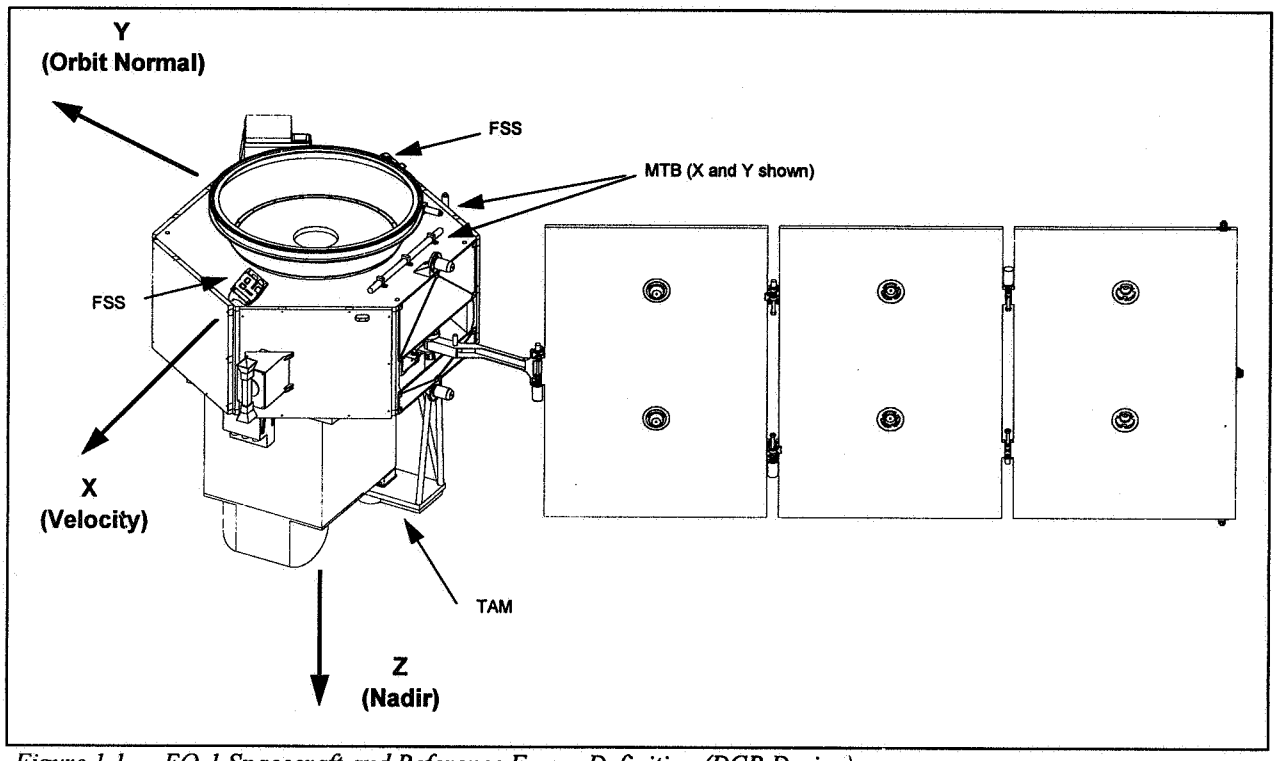

Figure 1.1 — EO-1 Spacecraft and Reference Frame Definition (DCR Design)

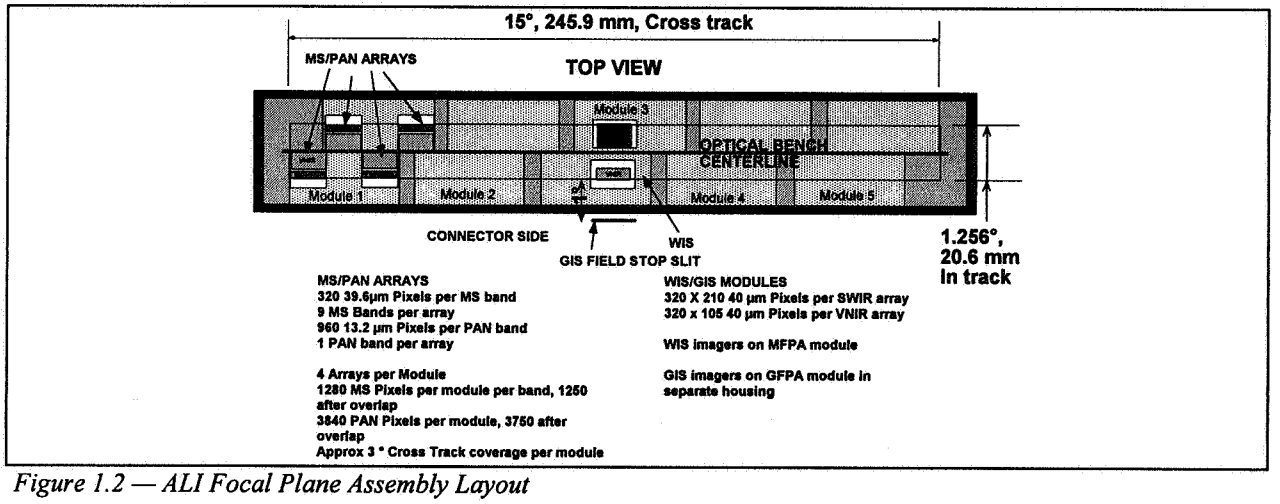

Figure 1.2 — ALI Focal Plane Assembly Layout

2. EO-1 Attitude Determination

Pointing accuracy requirements for the baseline EO-1 design were selected as 0.25°, 3σ per axis. These requirements were based on preliminary evaluation of science needs, and were conducive to the development of a relatively low-cost attitude determination system for EO-1. Given that the EO-1 flight software (FSW) architecture was to leverage as much as possible from TRMM FSW architecture, the TRMM contingency mode attitude determination method was a logical candidate for EO-1. This is substantiated in [1] which demonstrates attitude determination accuracy in the range of 0.1 degrees 1σ, using a configuration similar to that of the TRMM contingency design.

The TRMM contingency mode was developed by GSFC Code 712 for the TRMM program as a backup to the primary earth-sensor based attitude determination. Attitude knowledge requirements for the primary system is 0.18° 3σ per axis. In the event of an earth-sensor failure, the contingency mode can blend digital sun sensor (DSS), gyro and three-axis magnetometer (TAM) measurements in a six-state Kalman filter to provide degraded attitude knowledge. Although the contingency requirement called for knowledge of 0.7°, 3σ per axis, the performance of the DSS/TAM based system for TRMM exhibited simulated performance significantly better than the requirement, and was selected early in the EO-1 program as the baseline method for the Phase B conceptual spacecraft.

One of the initial tasks of the spacecraft attitude control subsystem (ACS) team was to evaluate the performance of the contingency mode attitude determination method against the top-level EO-1 pointing accuracy requirement. It was determined through various trade studies discussed in this paper, that the baseline requirement was aggressive but achievable, and would require careful TAM placement upon the spacecraft and careful control of on-board magnetic contamination.

A subsequent program-level review of the science fidelity objectives showed that baseline pointing accuracy requirements were not sufficient to meet band-to-band registration goals for the WIS. This was presented at the EO-1 Systems Requirements Review, at which the EO-1 science team presented a request for a five-fold increase in yaw-axis pointing accuracy to 0.05°, 3σ. Before abandoning the baseline method altogether, the EO-1 ACS team was requested to evaluate the best possible performance which could be expected for an EO-1 specific implementation of the TRMM contingency design. This paper also presents the results of this evaluation.

At the conclusion of the spacecraft DCR, the baseline attitude determination method was changed to an autonomous star tracker (AST) based system. A preliminary evaluation of EO-1 end-to-end pointing has been completed, and it is predicted that the performance of the AST-based attitude determination system will meet the aggressive science fidelity goals.

3. Contingency Mode Description

A detailed description of the contingency mode update filter equations is given in [2-3]. The single modification to these equations for EO-1 accounts for the introduction of the gyro angle white noise in the state noise covariance matrix Q.:

$$Q = \begin{bmatrix} \sigma_e^2 + \sigma_v^2 T + \frac{1}{3}\sigma_u^2 T^3 & -\frac{1}{2}\sigma_u^2 T^2 \\ \frac{1}{2}\sigma_u^2 T^2 & \sigma_u^2 T \end{bmatrix}$$

where σ_e^2 is defined as the angle white noise covariance, σ_v^2 is the angle random walk covariance and σ_u^2 is the rate random walk covariance. This modification was required since the angle white noise, or electronic noise, is not negligible for either the candidate HRG or RLG units evaluated for use on EO-1.

The process flow of the attitude determination sequence [4] is shown in Figure 3.1. TAM, DSS and IRU data is processed to produce measurements of the magnetic field vector, the sun vector and spacecraft angular rates, respectively, in the body frame. Note that the TAM measurement is adjusted for calibrated contamination from the MTB's, and the IRU rate measurement is adjusted by the estimate of the gyro drift rate bias from the previous update cycle. As will be discussed in Section 4, the accuracy of the TAM contamination calibration is a dominant factor in achieving optimal attitude determination performance.

Measurement matrices for all three axes are formed from on-board models of the magnetic field and the sun vector. TAM and DSS measurements are compared against these ephemeris-generated vectors, and are disregarded if the residual in any axis is greater than a predetermined threshold. The state noise covariance matrix is propagated, and the state vector initialized to a zero vector. If the TAM and/or DSS data passed the residual check, the Kalman filter is executed. The updated state vector is mapped into optimal estimates of an error quaternion and the drift rate bias error for each axis. Finally, these error estimates are applied to the propagated inertial to body quaternion estimate and the estimated gyro drift rate bias to form optimal estimates for both. Note that the diagonal elements of the state

noise covariance matrix are subjected to a sign and magnitude check after propagation and after being updated by the Kalman filter.

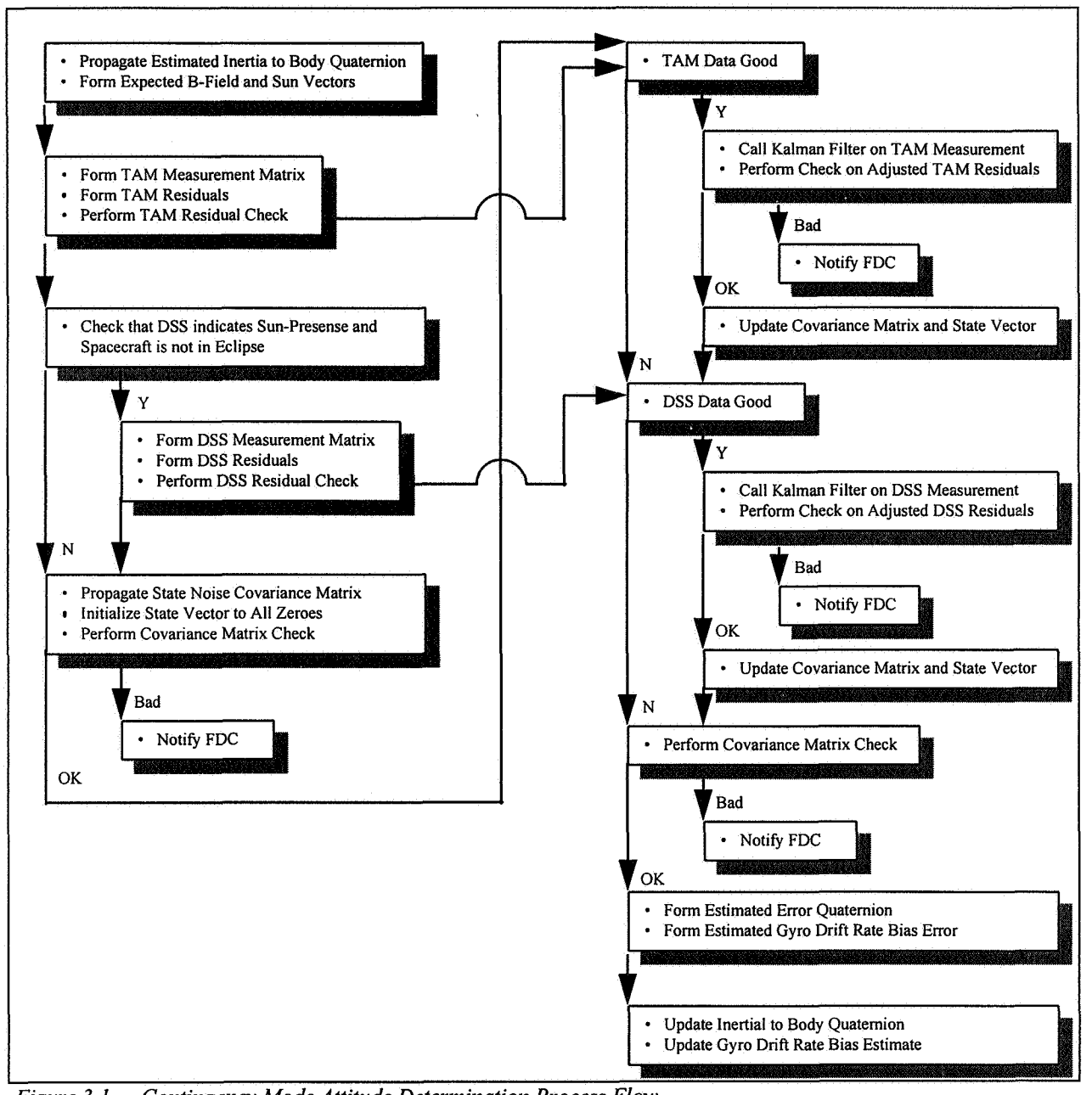

Figure 3.1 — Contingency Mode Attitude Determination Process Flow

4. Performance

The EO-1 attitude determination performance was analyzed using an EO-1 high fidelity (HiFi) simulation. This simulation is the same one used on the TRMM spacecraft project, modified for EO-1 orbit parameters and spacecraft characteristics. The gyro model includes the effects of rate random walk, rate white noise and angle white noise parameters, which are based on the gyro specifications. The magnetic field "truth" model is a 10^{th} order International Geomagnetic Reference Field (IGRF) model. In order to simulate magnetic field measurement errors, the magnetic field measurements are generated using a 6^{th} order IGRF model with a five year offset in the coefficients. The TAM sensor noise is modeled using a zero mean Gaussian white noise process with a standard

deviation of 0.06 μT. The Fine Sun Sensor (FSS) noise is modeled using a zero mean Gaussian white noise process with a standard deviation of 0.017°. Note that 'FSS' is used to delineate the higher-performance sun-sensor (0.017° accuracy, 32° half-cone angle) used on EO-1 from the TRMM DSS (0.05° accuracy, 50° half-cone angle)

4.1. Gyro Selection

Two medium performance gyros, the Litton Space Inertial Reference Unit (SIRU) hemispherical resonator gyro (HRG), and the Allied Signal LCGA-20 ring laser gyro (RLG), were considered for use on EO-1. The attitude determination performance using these gyros will be compared to the performance using the TRMM high performance Kearfott SKIRU D-II mechanical gyro and the low performance Allied Signal LCGA-14 RLG.

4.1.1. Gyro Noise Modeling

The noise characteristics derived from the gyro specifications and used to model each of the gyros are shown in Table 4.1.

Table 4.1 — Gyro Noise Parameters

Gyro	Rate Random Walk (σ_u) (asec/sec$^{3/2}$)	Angle Random Walk (σ_v) (asec/sec$^{1/2}$)	Angle White Noise (σ_e) (asec)
Kearfott SKIRU-DII	3.500E-05	0.007	-
Litton SIRU/HRG	5.103E-05	0.060	0.063
Allied Signal LCGA-20	1.021E-05	0.180	0.065
Allied Signal LCGA-14	1.021E-04	1.200	0.380

Note that the SKIRU-DII has negligible angle white noise, because it is a mechanical gyro. The rate random walk accounts for the long-term drift rate variation, and will show up in the attitude determination error if there occurs a length of time with no Kalman filter fine sun sensor or magnetometer updates, and the solution is propagated on gyros only. The angle random walk causes the short-term drift rate variations, which will drive the gyro performance effect on the nominal attitude determination performance with all Kalman filter updates enabled. The SIRU angle random walk standard deviation is an order of magnitude larger that that of the SKIRU-DII, and the LCGA-20 has a standard deviation three times larger than the SIRU. The LCGA-14 angle random walk standard deviation is significantly larger at over six times that of the LCGA-20. The effect of the angle random walk noise value on the Kalman filter performance can be seen in the simulation results.

4.1.2 Gyro Simulation Results

A three day attitude determination simulation was run for each gyro using the Kalman filter with gyro propagation, consistent magnetometer measurement updates, and fine sun sensor measurement updates when available. The only differences between each simulation run were the gyro noise inputs, and the Kalman filter variance, or knowledge of the gyro noise values. The Kalman filter knowledge of each of the three types of noise was set to 1.5 times the modeled value. The Kalman filter converges to steady state performance within a 24 hour period. The 3σ and peak attitude determination errors for days 2 and 3 of a 3 day simulations, using each of the three gyros, are summarized in Table 4.2.

Table 4.2 — Attitude Determination Dynamic Error for Second Two Days of Three Day Simulation

Gyro	3σ Error (degree)			Peak Error (degree)		
	Roll	Pitch	Yaw	Roll	Pitch	Yaw
Kearfott SKIRU D-II	0.105	0.018	0.106	0.068	0.037	0.072
Litton SIRU/HRG	0.133	0.053	0.136	0.100	0.073	0.120
Allied Signal LCGA-20	0.139	0.066	0.145	0.120	0.081	0.140
Allied Signal LCGA-14	0.234	0.394	0.268	0.280	0.530	0.240

The 3σ roll and yaw attitude determination errors are over 25% greater and the pitch errors are almost three times greater using the SIRU than when using the SKIRU D-II. The results using the LCGA-20 are even a little worse, which was expected from a knowledge of the relative angle random walk noise values. The Kalman filter performance breaks down with the low performance LCGA-14, which provides significantly poorer attitude

determination performance for all axes, especially in pitch. For precision pointing spacecraft like EO-1, the gyro selection must be limited to the high and medium performance gyros for fine sun sensor and magnetometer based attitude determination.

The ACS team was directed at the EO-1 spacecraft Design Convergence Review to eliminate the LCGA-20 from consideration to avoid powered-ascent restrictions of RLGs. It is recommended that RLG gyros that are not hermetically sealed remain powered off for 30-45 minutes after launch to prevent corona arcing. At that time, the Litton SIRU was selected as the EO-1 gyro.

4.1.2. Roll/Yaw Coupling

The simulation results show a roll/yaw coupling trend over each orbit period and a diurnal trend over each day. The roll/yaw coupling is a result of having poor observability about the spacecraft sun pointing axis. As the EO-1 spacecraft enters sunlight at orbit 6 am over the north pole, the sun is in the FSS 1 field of view and the spacecraft roll axis vector is pointed toward the sun. The fine sun sensor has high accuracy pitch and yaw measurements, but has no roll measurement about the sun line. As the spacecraft reaches the orbit noon position near the earth's equator, it has rotated 90° about the pitch axis to remain earth pointing so that the spacecraft negative yaw axis vector is pointed toward the sun. In this orientation, the FSS 2 will provide high accuracy roll and pitch measurements, but no yaw measurement about the sun line. The uncertainty in the roll/yaw attitude interchanges every 90° and provides the roll/yaw coupling sine waves with orbit period seen in the SIRU attitude determination error plot in Figure 4.1.

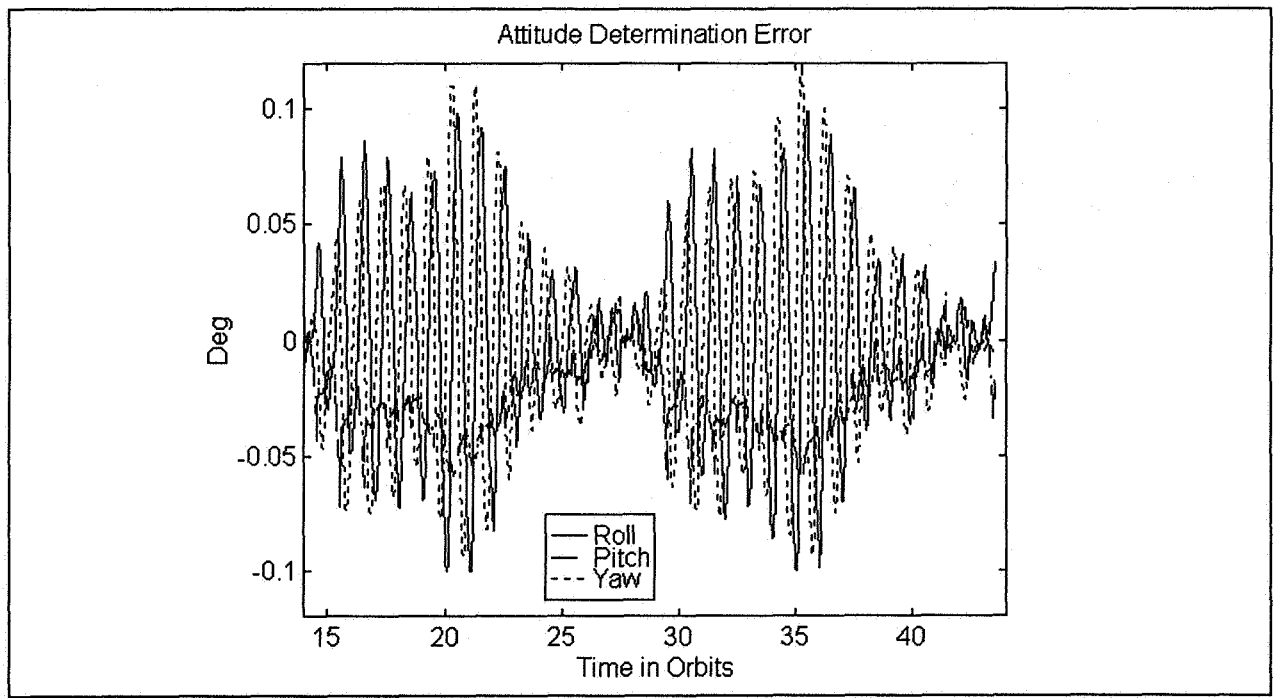

Figure 4.1 — Attitude Determination Error (Two Days)

The diurnal trend is a result of the angle between the magnetic field vector and the sun line, and will be discussed in Section 4.4. This trend results in more accurate attitude determination during some orbits than others. Table 4.3 shows the average of the "best" attitude determination orbits selected from each day of the simulation run.

Table 4.3 — Attitude Determination Dynamic Error for Best Orbit

Gyro	3σ Error (degree)			Peak Error (degree)		
	Roll	Pitch	Yaw	Roll	Pitch	Yaw
Kearfott SKIRU D-II	0.056	0.006	0.056	0.029	0.015	0 029
Litton SIRU/HRG	0.024	0.019	0.026	0.016	0.019	0.024
Allied Signal LCGA-20	0.032	0.019	0.012	0.027	0.022	0.010
Allied Signal LCGA-14	0.091	0.105	0.092	0.074	0.096	0.063

4.2. FSS Placement

In addition to performing the IRU trade study discussed in Section 4.1, an additional study was performed to evaluate the optimal orientation of the two FSS heads. On TRMM, the first DSS boresight was rotated 35° off the +X spacecraft axis toward the -Z axis and the second was rotated 35° off the -X spacecraft axis toward the -Z axis. Both DSS boresights were then rotated 30° off the X-Z plane toward the -Y axis. This placement was selected to optimize sun visibility for yaw measurements to provide yaw control in addition to the roll and pitch control based solely on earth sensor measurements in nominal mission mode. The fields of view of the two sensors are spaced evenly through the sunlight portion of the orbit. The TRMM DSS orientations were fixed before implementation of the contingency mode, and therefore were not optimized for use in the DSS/TAM based Kalman filter attitude determination.

Two FSS placement options were considered for EO-1 in addition to the TRMM configuration. The first option was designed to optimize for measurement accuracy in the northern hemisphere where the majority of the science observations were to take place. This was accomplished by placing the two FSS fields of view next to each other with the first starting at the very beginning of the sunlight portion of the orbit. The first sensor boresight is 17° off the spacecraft +X axis toward the -Z axis, and the second is 17° off the -Z axis toward the +X axis. Both boresights are again rotated 30° off the X-Z plane in the -Y direction. The second placement option was designed to minimize the drift in the attitude solution through the eclipse portion of the orbit. The FSS 1 field of view is located in the same location as in the first option, so that the measurements are available as soon as the spacecraft enters sunlight. The FSS 2 field of view is located just before the spacecraft enters the eclipse portion of the orbit. In this configuration, the second sensor boresight is located 17° off the -X spacecraft axis toward the -Z axis, and then rotated 30° off the X-Z plane in the -Y direction. The three placement options are shown in Figure 4-2.

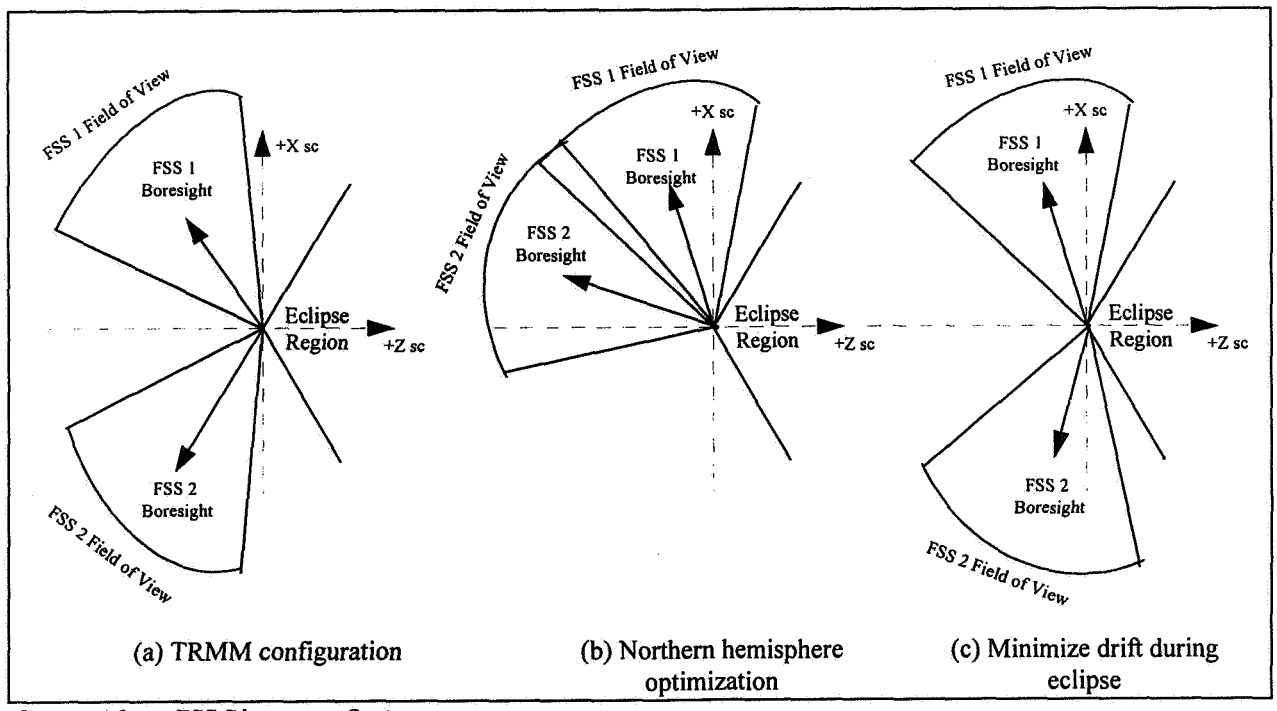

Figure 4.2 — FSS Placement Options

The same attitude determination simulation that was used for the gyro selection was run using each of the three FSS placement options. The Kalman filter performance was insensitive to the FSS placement when using the low drift characteristics of the SIRU gyro.

4.3. Attitude Estimation using Magnetic Field

The Earth's magnetic field has been used for spacecraft attitude estimation, both ground-based and via on-board processing, on numerous satellites. Due to the physics of the field generation, a spherical harmonic model has been recognized as the selection of choice to balance both computational efficiency and accuracy. The complexity of on-board models has increased significantly over the past 5-10 years due to the both memory and CPU advances in spacecraft computers. For example, the Explorer Platform/ Extreme Ultra-Violet Experiment (EP/EUVE) launched in 1992 utilizes a 3rd order model, while the X-ray Timing Explorer (XTE) launched in 1996 has a 10th order model capability in the attitude control computer. The following sections provide details on the error sources involved with using the Earth field for on-board, real-time attitude estimation.

4.3.1. Summary of the Earth Field from EO-1 Orbit

The EO-1 HiFi simulation of the Earth magnetic field uses a 10th Order spherical harmonic model representation as the truth field. To facilitate the following discussions, a set of reference plots of the magnetic field vector components in the Orbital Reference Frame (ORF) are provided in Figure 4.3. Also presented in this figure is a contour plot of the magnetic field magnitude versus latitude and longitude. As discussed in the following section, diurnal variations occur as the Earth rotates with respect to the sun-synchronous orbit plane. As an Earth remote sensing mission, the EO-1 spacecraft commanded attitude will be very near to the ORF. Note in Figure 4.3 that the pitch axis field magnitude remains the smallest, with an obvious beat pattern between the orbital period and Earth rotation period, while expected roll/yaw coupling occurs twice per orbit period.

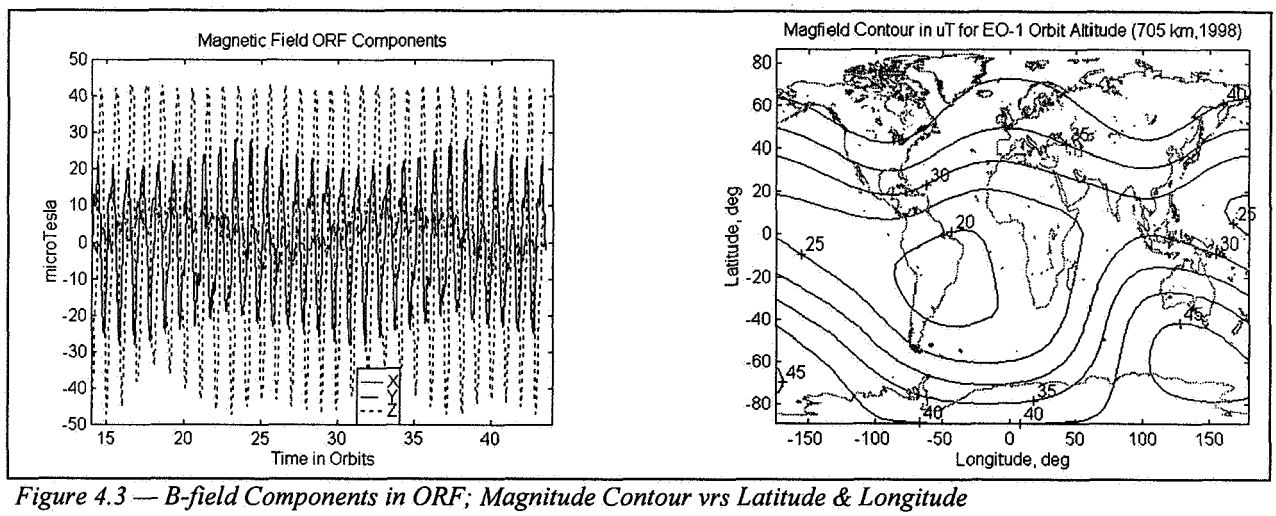

Figure 4.3 — B-field Components in ORF; Magnitude Contour vrs Latitude & Longitude

4.3.2. Magnetic Attitude Error Budget

For analyses and simulations of expected performance, conversion of the truth magnetic field to a measurement update in the Kalman Filter must be performed with more than the addition of a white noise process. Due to the variation of the magnetic field vector in inertial space, a six state Kalman filter which uses magnetic field measurements that have only white noise can have nearly idealistic performance as indicated by attitude determination error. Due to the numerous error sources involved in attitude estimation via the Earth magnetic field, an error budget was established to identify and quantify the various degradations to pointing knowledge. This error budget, shown in Figure 4.4, defines the two main branches of error - those sources associated with generating an expected magnetic vector and those sources associated with the actual measurement process. Numerical values will be discussed in terms of μT; conversion to angular error can be performed using the measured magnetic field vector, which varies in magnitude from 0.2 to 0.45 μT.

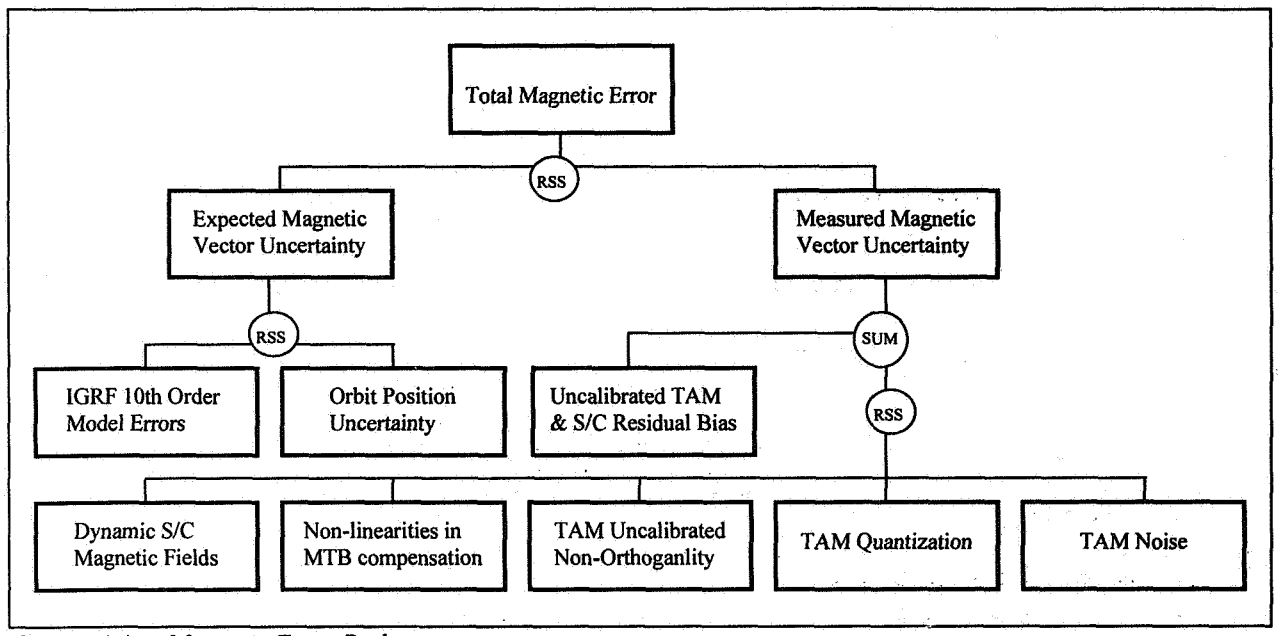

Figure 4.4 — Magnetic Error Budget

4.3.3. Magnetic Field Modeling Errors

Sources of error in modeling the magnetic field include the order of spherical harmonic representation, the accuracy and epoch of the model coefficients, anomalous conditions in the actual field vector due to magnetic storms and solar activity and accuracy of the spacecraft ephemeris knowledge, which is an input to the calculations. For our analyses, these effects were approximated using two modifications of the magnetic field model used by the Kalman Filter processing: 1) the model was reduced from 10th to 6th order; and 2) the coefficients were modified to have a five year epoch error. Figure 4.5 provides a plot of the magnetic field modeling error, both as a field magnitude and vector direction error.

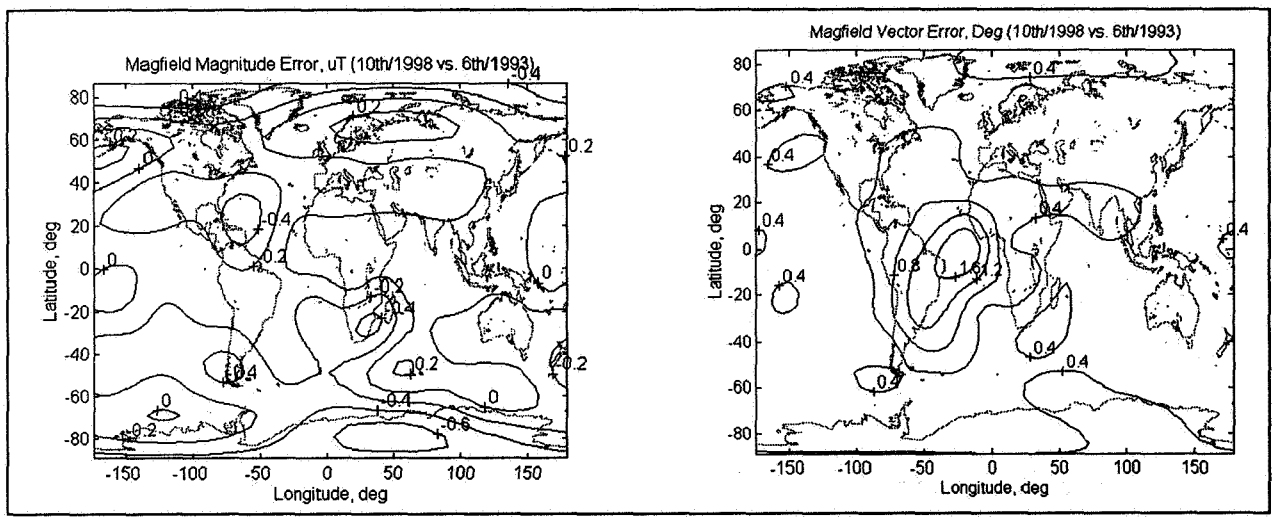

Figure 4.5 — Magnetic Field Modeling Error (Vector Magnitude and Direction)

4.3.4. Magnetic Field Measurement Errors

Sources of error involved in the measurement of the field by a three axis magnetometer include sensor noise, bias, alignment and quantization effects as well as residual static and dynamic fields created by other satellite electronics and structures, especially magnetic torquer coils used for momentum management. Typical TAM sensor noise specifications are relatively insignificant (1-10 nT). Quantization can be held below (30 nT/count) using a 12-bit

analog -to -digital converter and 60 uT (0.6 G) total range. TAM static misalignment can be largely calibrated out, but the calibration residual must still be accounted for in the error budget. The most significant of the measurement error sources are related to S/C residual and dynamic fields, which can be expected to be on the order of 0.1-5.0 uT. A complete spacecraft systems engineering commitment to 'magnetic policing' must be adhered to since magnetically noisy boxes must be far separated from the TAM and harness routing of electric currents involved in solar array and battery operations must be well planned to avoid creation of current path loops. Corruption of the TAM based on nearby magnetic torquer coils must be mitigated by frequent estimation and updating of MTB-to-TAM compensations matrices. Residual dipoles of the MTBs must be analyzed frequently and updated if necessary to ensure long-term terms are kept in check. On-orbit calibration of the magnetic residual/bias in the S/C and TAM, the alignment of the TAM and the MTB coupling is exacerbated by the fact that the TAM also serves as the one of the prime attitude sensors for ground-based attitude estimation.

4.3.5. Summary of Simulation Results

Table 4.4 provides a summary of the HiFi simulations performed to verify the expected degradation of attitude determination performance due to field modeling errors and uncompensated static residual field (i.e. bias). The first row illustrates the performance achievable if there are no deviations of the actual field with respect to the modeled field and no bias (not realistic!). The addition of the magnetic model errors as shown in Figures 4.5 results in an order of magnitude degradation in the 3-sigma values, with the roll/yaw coupling evident. Note that due to the sinusoidal nature of the error, the statistical analysis of the performance may be counter-intuitive - the peak values are less than the 3-sigma values (which were formed using 3 times the standard deviation). As shown in the last two rows of Table 4.4, the addition of residual bias to the TAM measurements causes further degradation of the roll/yaw performance by a factor of 2 for the 0.1 uT bias and by a factor of greater than 3 for the 0.5 uT bias. The 0.1 uT bias performance is at the limit of the EO-1 pointing allocation for attitude determination error (0.2 degrees) for the Phase B pointing accuracy requirement of 0.25 degrees.

Table 4.4 — Magnetic Measurement Errors, and Effect on Attitude Determination Accuracy

Model Error*	Residual Dipole Bias Error (μT)	Mean Error Pitch (degree)	3s Error (degree)			Peak Error (degree)		
			Roll	Pitch	Yaw	Roll	Pitch	Yaw
No	0.0	0.001	0.011	0.006	0.010	0.012	0.009	0.012
Yes	0.0	0.024	0.133	0.053	0.136	0.100	0.073	0.120
Yes	0.1	0.054	0.264	0.066	0.270	0.190	0.097	0.200
Yes	0.5	0.133	0.651	0.099	0.645	0.360	0.250	0.390
*6^{th} vrs 10^{th} Order IGRF Model with 5 Year Offset								

4.4. Geographical Dependence

As mentioned in the previous two sections, simulation results of the attitude determination accuracy exhibit both a roll/yaw quarter-orbit interchange of uncertainty, and a diurnal variation in peak magnitude in all three axes. The latter effect appears as a "beat" pattern in Figure 4.1, with the greatest performance in attitude determination being observed over a two to three orbit period, out of the approximately 14 orbit daily cycle. This section explores the cause of this diurnal variation in performance, and quantifies the expected performance as a function of latitude and longitude.

The FSS is a two axis sensing device which generates a horizontal and vertical reading of the sun vector within its field of view. Since it senses only one inertial reference source, it can only supply two attitude angles, with the third angle, about the line of sight (LOS) to the sun, remaining undetermined. Therefore to complete the three axis attitude determination, it is necessary to sense a second, uncorrelated inertial reference. Concurrent TAM measurement of the local magnetic field satisfies this criteria - however, since the fidelity of the TAM measurement is low compared to that of the FSS, and the solar ephemeris is known much more precisely than the precise orientation of the true magnetic field vector, the TAM/FSS combination is not a particularly well matched set. With the inclusion of a 6-state Kalman filter, a high-precision IRU, and careful attention to magnetic cleanliness and calibration, the performance achieved in attitude determination using these two inertial vectors makes it a viable option for low-cost medium pointing performance spacecraft.

Given that the two independent sensors cannot resolve attitude about either the LOS vector to the sun or the local magnetic field vector, it is obvious that the best observability for three axis attitude determination occurs when the two vectors are orthogonal. Conversely, it follows that the worst observability would be when the vectors are close to colinear. Since the earth's magnetic field is dominated by a tilted dipole, as described in [5], it follows that there are orientations of the dipole that provide optimal observability with respect to the sun vector for three axis attitude determination. Note that the orientation of the earth's dipole roughly corresponds to the inclination of EO-1's sun-synchronous orbit, and therefore the plane of the dipole would rotate into the orbit plane briefly each day.

Data used to generate Figure 4.1 was screened for the orbits of highest attitude determination performance, and the results were plotted against the latitude/longitude points of the orbit track. Figure 4.5 shows the results of this data reduction, and illustrates which land-mass regions would experience the best attitude determination performance. Note that the ascending portions of these orbits, seen in Figure 4.5 over Africa and western Europe occur in eclipse, and are therefore not viable candidates for science observations using the ALI. Conversely, the descending portions of these orbits occur over Alaska and northwestern Canada before continuing out over the Pacific Ocean. Since EO-1 is a demonstration mission, this type of "region of best performance" screening was a valid consideration for determining optimal ground targets for science validation — however these land masses did not constitute regions of high interest for project scientists.

Further investigation of the high performance orbits identified in Figure 4.5 determined that they occur when the Earth's dipole is in the EO-1 orbit plane. Although this is not intuitive, it is surmised that this configuration provides optimal observability as the spacecraft exits and enters the penumbra, and the uncertainty in the roll axis is minimized by the TAM measurement. Since the drift stability of the SIRU is high, the benefit of this high observability region is realized for the duration of the ascending or descending pass on that orbit.

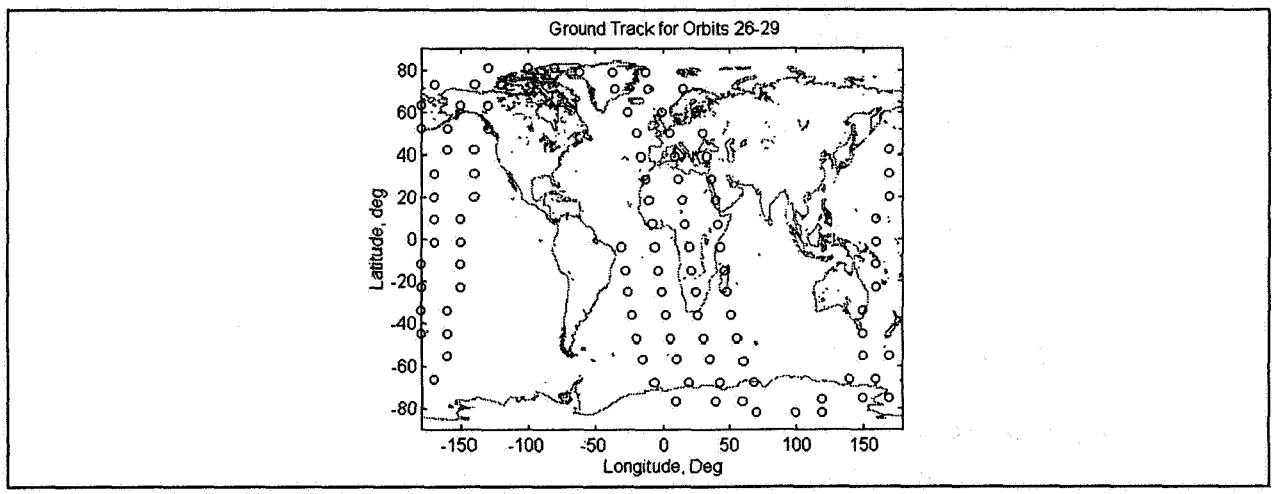

Figure 4.5 — Ground Tracks for Orbits with Highest Performance

To complete the study of geographic variations in performance, attitude determination results for each descending pass were sorted into relatively low, medium and high performance on a per-axis basis, and plotted against latitude and longitude. The results of this analysis are shown in Figure 4.6 for roll and yaw, and Figure 4.7 for pitch. These results demonstrate that, in general, uncertainty is passed between the roll and yaw axes, with yaw most accurate at high latitude regions and roll most accurate around the equator. Note that pitch is generally determined to a much higher precision than roll or yaw, since it is sensed by the FSS at both polar and equatorial crossings, and is not subjected to the roll/yaw uncertainly interchange discussed above.

Also shown in Figure 4.6 is that roll determination is relatively accurate at high latitudes for longitudes of -50° to -150°, and yaw determination is relatively accurate at equatorial latitudes for longitudes of approximately -100° to -200°. These results correlate with Figure 4.5, which again shows orbits of highest accuracy having descending nodes of -50° to -150° longitude.

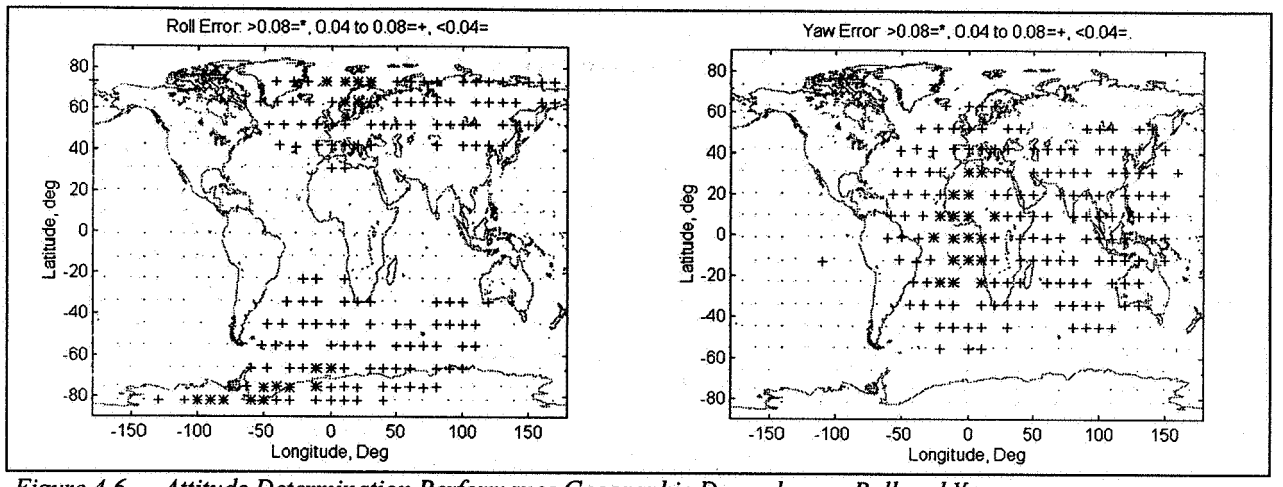

Figure 4.6 — Attitude Determination Performance Geographic Dependence - Roll and Yaw

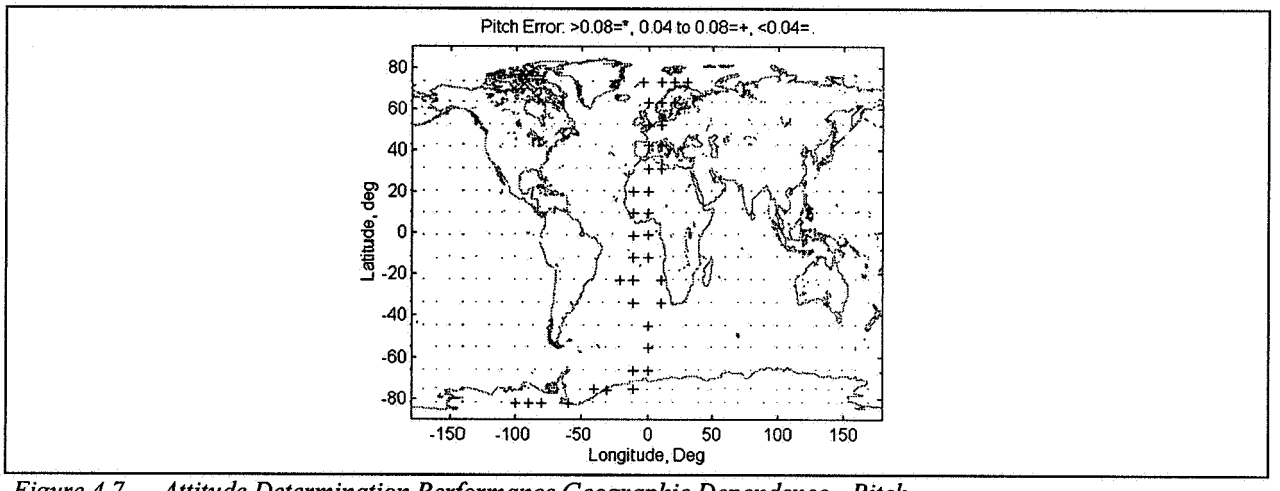

Figure 4.7 — Attitude Determination Performance Geographic Dependence - Pitch

5. Conclusions

The TRMM contingency mode was extensively evaluated for use as the baseline attitude determination method for the EO-1 spacecraft. Included in this evaluation was a trade study to select a gyro whose performance would be amenable to achieving the baseline attitude knowledge requirements. The outcome of this study indicated that a SIRU-class gyro with high drift stability was required. Additionally, a trade study to evaluate the optimal orientation of the two FSS heads was performed, which indicated that performance was relatively insensitive to reasonable variations in FSS orientation. This was linked to the low drift characteristics of the gyro. Finally, a end-to-end evaluation of TAM measurement contamination was performed to provide an initial assessment of magnetic cleanliness of the spacecraft, and required calibration accuracies. As an ancillary study, geographic variations in attitude determination performance was evaluated to the cause of this geographic dependence, and to determine which potential science imaging targets would be observed during orbits exhibiting the best attitude determination performance. It was determined the best observability occurred when the dipole was contained in the EO-1 orbit plane.

In conclusion, it has been demonstrated that 0.25° 3σ accuracies in attitude determination is an aggressive, but achievable target for on-board FSS/TAM attitude determination. This level of accuracy can be realized without the high-precision SKIRU-II gryo package, however, a gyro with SIRU class performance characteristics is required. along with the higher precision sun sensor package. Perhaps the most crucial element to consider is the accuracy of the TAM measurement of the local magnetic field. Achieving the baseline accuracy cited above would require

aggressive policing of on-board sources of magnetic contamination, careful placement of the TAM on the spacecraft, as well as extensive on-orbit calibration of spacecraft residual fields and MTB influence on TAM measurements.

6. Acknowledgments

The authors wish to express their appreciation to Dr. John Crassidis, Dr. Steven Andrews and Alan Reth of GSFC Code 712 for their assistance in performing the work documented herein. This work was supported under GSFC contract NAS5-32650.

7. References

1 *Sensor Studies Task: Spacecraft Attitude Determination Accuracy From Mission Experience* Flight Dynamics Division Code 550 , 1/94 (553-FDD-93/098R0UD0)

2 Crassidis, J.L., Andrews, S.F., and Markely, F.L.,"Contingency Designs for Attitude Determination of TRMM" *1995 GSFC FDD Flight Mechanics/Estimation Theory Symposium*, 1995

3 Lefferts, E.J., Markely, F.L., and Shuster, M.D., "Kalman Filtering for Spacecraft Attitude Estimation" *Journal of Guidance, Control and Dynamics*, Vol. 5, No. 5, Sept.-Oct. 1982, pp. 417-429

4 *TRMM ACS Algorithm Document*, GSFC Code 712 10/2/95

5 Wertz, J.R. (ed.), *Spacecraft Attitude Determination and Control*, D. Reidel Publishing Co., Dordrecht, The Netherlands, 1984

Page intentionally left blank

The Earth Radiation Budget Satellite Tumble of 1987 Revisited: Magnetometer-Only Estimates of the Attitude and Rates

M. Challa, S. Kotaru, and G. Natanson
Computer Sciences Corporation
10110 Aerospace Road
Lanham-Seabrook, MD 20706 USA

Abstract

The Earth Radiation Budget Satellite (ERBS) experienced an uncontrolled tumble on July 2, 1987, with spacecraft rates of the order of 2 deg/sec. During a substantial span of this contingency period of about 12 hours, the Sun and Earth sensor data were not useful and the gyro telemetry was saturated, so that the three-axis magnetometer (TAM) was the only reliable attitude sensor. ERBS attitude and rates for this period are estimated using TAMONLY (a recently developed system that estimates attitude and rates using a TAM and spacecraft dynamical models) after enhancing the system to include thruster torques in the spacecraft dynamics. It is shown that the spacecraft rates estimated by the Kalman filter and by the deterministic algorithm in TAMONLY agree closely, both algorithms confirming rates as high as 2 deg/sec. These rate estimates are also in close agreement with valid gyro data. Using TAM residuals, TAMONLY's attitude accuracies during the high-rate period are estimated to be 2.5 deg. The consistency of the results is demonstrated by their independence from a priori errors. The effects of models of thrusters, spacecraft mass properties, and TAM noise on the filter estimates are treated in detail. Enhancements stabilizing the deterministic solutions in high-rate situations are also described.

1. Introduction

The Earth Radiation Budget Satellite (ERBS) is an Earth-pointing, momentum-biased spacecraft (Refs. 1 and 2) that was launched in July 1984 into a near-circular orbit of about 52 degrees (deg) inclination and an altitude of about 610 kilometers (km). The attitude hardware includes two infrared Earth sensors, two two-axis Fine Sun sensors, two three-axis gyros, a three-axis magnetometer (TAM), a pitch-axis momentum wheel, four magnetic torquer bars (MTBs), and eight thrusters used for both orbit and attitude maneuvers.

On July 2, 1987, ERBS went into an uncontrolled tumble for about 200 minutes (min) as a result of a command sequence error during the monthly thruster-assisted yaw maneuver (Ref. 3). The spacecraft was despun using thrusters and magnetic torquers, and the nominal mission mode was regained after about 12 hours (hr). Significant control system events during this contingency are listed in Table 1. (As shown in Table 1, times will be denoted hereafter in seconds elapsed since 19870702.140000.) The resultant large attitude errors resulted in the loss of Earth in the horizon sensors, considerable Earth interference as well as very limited Sun presence in the Sun sensors (Ref. 3), and saturation of the gyro telemetry. Thus, the TAM was the only reliable sensor during much of the contingency. Fig 1 shows the gyro telemetry, and we see significant gyro rates (note the saturation values of ±0.13 degrees/second (deg/sec)) when the yaw maneuver is initiated at 4628 seconds (sec). Numerous polarity reversals of the gyros take place until 17,128 sec; at which point, the thruster-assisted G-Rate mode was initiated to null the rates about the spacecraft X and Z axes. Magnetic de-spin via the B-Dot mode was initiated at 29,295 sec, and the transition to nominal mission mode was accomplished at 42,652 sec. As can be seen in Fig. 2, the TAM telemetry during this period also show rapid polarity reversals indicating spacecraft rates of the order of 2 deg/sec during the tumble.

Limited attitude results were obtained in an initial study of this ERBS contingency (Ref. 3) by relying on sparse Sun sensor data, coupled with propagation of the attitude and rates. However, neither detailed rate estimates nor the accuracies of the attitude estimates were provided there. The objective of this paper is to extend the results of Ref. 3 by estimating ERBS attitude and rates during the tumble by inputting the TAM measurements and control system data to TAMONLY—a recently developed system that combines a deterministic magnetometer-only algorithm with a Kalman filter for gyroless spacecraft.

Table 1. ERBS Control System Events During Time Span of Data Studied

Epoch of Data = 870702.140000
End of Data = 870702.233000

YYMMDD.HHMMSS	Event	Sec From Epoch
870702.151708	**Thrusters enabled; begin maneuver**	4628
.151710	MCS loops open	4631
.151812	Reverse Scanwheels	4692
to .152600		to 5160
.153002	Change RCS reference direction (-XF to XF)	5402
.153422	Thrusters disabled	5662
.153448	Thrusters enabled	5688
.153452	Reverse momentum wheel	5692
to .154340		to 6220
.154348	MCS loops closed	6228
.154350	Thrusters disabled	6230
.162524	Thrusters enabled	8724
.184528	**G-Rate mode begin**	17128
.202504	Reverse Scanwheels	23104
.202510	Reverse momentum wheel	23110
.204200	Normal mission mode	24120
.204202	Thrusters disabled	24122
.204518	Gyrocompassing	24318
.204531	Thrusters enabled	24331
.205200	Thrusters disabled	24720
.213554	Thrusters enabled	27354
.213641	Thrusters disabled	27401
.215816	Thrusters enabled	28696
.220815	Thrusters disabled; **B-Dot mode begin**	29295
.220815	ACS power down (for RCS)	33330
.....	.....	.....
870703.0308	**B-Dot mode end; Normal mission mode begin**	

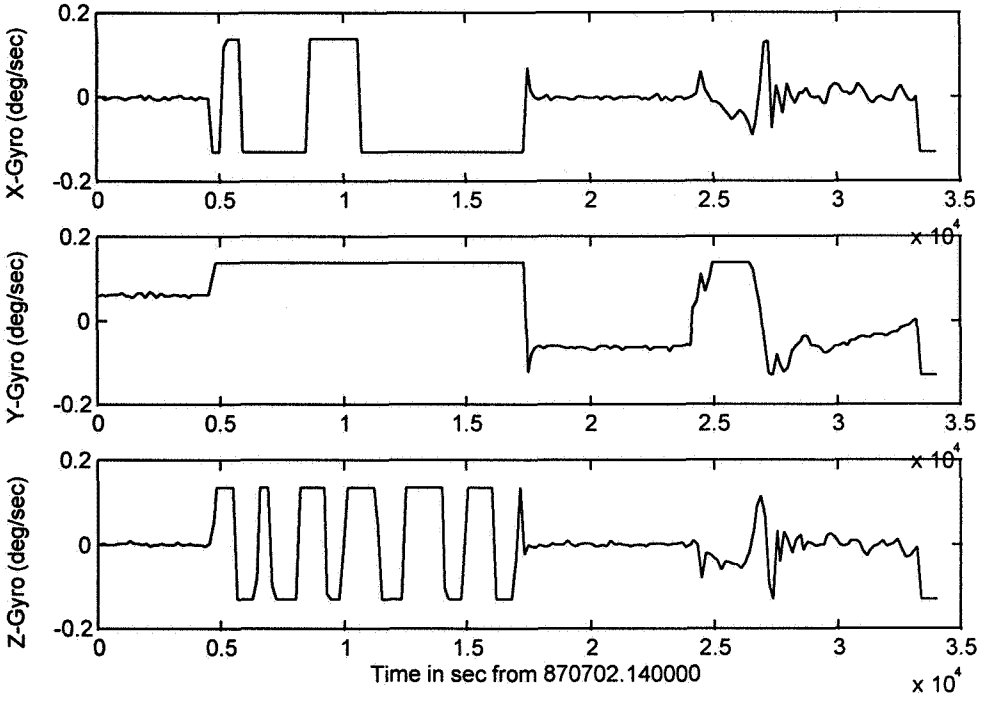

Figure 1. ERBS Gyro Data During the Tumble

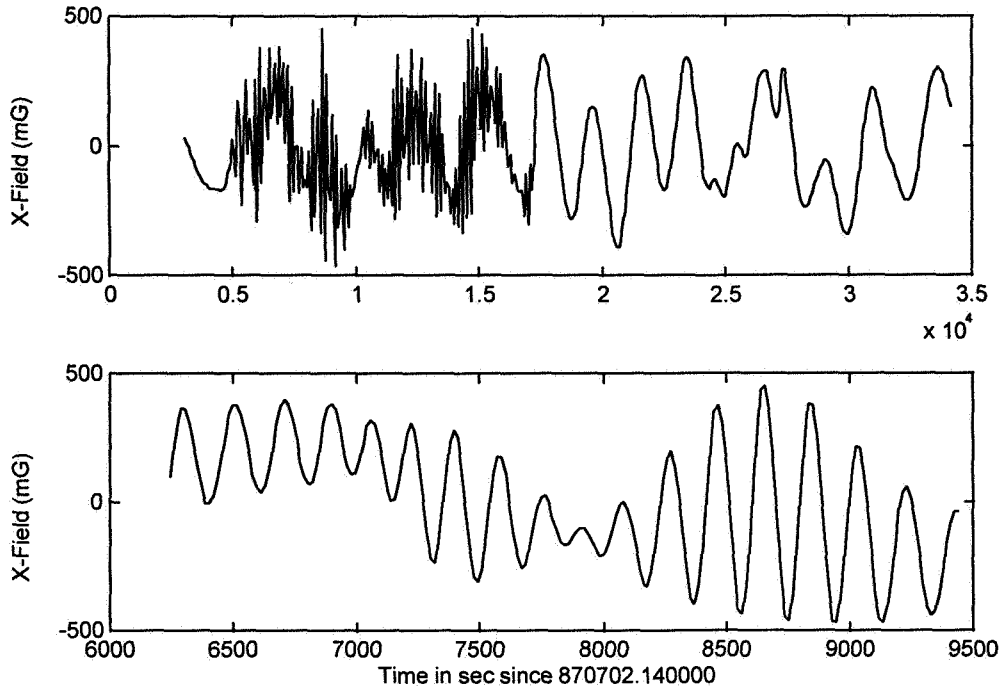

Figure 2. ERBS TAM Measurements During the Tumble

TAMONLY has been applied successfully in the past (Refs. 4 through 7) by using in-flight data to study numerous TAM-only scenarios of ERBS as well as the gyroless Solar, Anomalous, and Magnetospheric Particle Explorer (SAMPEX). Because TAMONLY can estimate ERBS nominal attitude and rates to accuracies of from 0.2 to 0.4 deg and from 0.002 to 0.005 deg/sec (Ref. 6), it is opportune to use the system to study this ERBS tumble. The current case is more difficult than the past studies, however; because on one hand, the "truth" data are limited to the few unsaturated gyro data (Fig. 1), whereas on the other hand, numerous factors ranging from Kalman filter noise parameters to dynamical quantities such as thruster torques affect the estimates.

The remainder of this paper is organized as follows: Section 2 describes the algorithms in TAMONLY, and is followed by highlights of ERBS modeling in Section 3. Section 4 describes the criteria for assessing accuracies of the attitude and rate estimates. The results are given in Section 5, which include the Kalman filter results for various choices of the model parameters, together with results from the deterministic algorithm. Finally, Section 6 summarizes the conclusions.

2. Description of TAMONLY

Conceptually, TAMONLY is successful because the magnetic field usually changes sufficiently during an orbit to allow the TAM to sense the complete attitude (i.e., all three Euler angles). Further, because the angular velocity is essentially the time derivative of the attitude, the complete spacecraft state (both attitude and rates) can conceivably be estimated by processing TAM measurements spanning, say, a third of an orbit. Relying only on the TAM measurements would be of particular advantage in the current study in view of the questionable validity of the limited Sun sensor data that were contaminated by the Earth albedo at numerous times during the entire contingency (Ref. 3).

Two novel algorithms are used in tandem in TAMONLY: Deterministic Attitude Determination from Magnetometer-Only Data (DADMOD) (Refs. 8 through 10), and Real Time Sequential Filter (RTSF) (Refs. 11 through 12). These algorithms are

briefly described below. Note that both algorithms model the evolution of the spacecraft angular velocity, $\vec{\omega}$, via Euler's equation:

$$\frac{d\vec{L}}{dt} = \vec{N}_{ext} - \vec{\omega} \times \vec{L} \tag{1}$$

where $\vec{N}_{ext}$ is the total external torque acting on the spacecraft (modeled as the sum of the gravity gradient, magnetic control, and thruster torques), and $\vec{L}$ is the angular momentum of the spacecraft. $\vec{L}$ is given by $\vec{L} = I\vec{\omega} + \vec{h}$, where I is the inertia tensor, and $\vec{h}$ is the angular momentum of the wheels. As a practical matter, note that we always resolve Eq. (1) in the body coordinate system (BCS) where the components of $\vec{\omega}$ are denoted $(\omega_x, \omega_y, \omega_z)$.

2.1 Deterministic Magnetometer-Only Attitude and Rate Determination (DADMOD)

The DADMOD uses the relationships among the time derivatives of the magnetic field in inertial and spacecraft body coordinates over a batch of data to compute the attitude and body rates. The attitude can be determined via the TRIAD algorithm (also known as the "algebraic" method in Ref. 13) if the components of two independent vectors can be obtained in the reference and body frames. The DADMOD approaches the problem by specifying these vectors to be $\vec{B}$ and its first time derivative, $\dot{\vec{B}}$. The above components of these vectors are related via

$$A\vec{B}^R = \vec{B}^A \tag{2a}$$

$$A\dot{\vec{B}}^R = \dot{\vec{B}}^A + \vec{\omega}^A \times \vec{B}^A \tag{2b}$$

where A is the attitude matrix, and the superscripts R and A imply that the vectors have been resolved in the reference and body frames, respectively. The crucial difficulty in implementing the TRIAD algorithm, of course, is that $\vec{\omega}$ is unknown.

The problem can be cast in the form of transcendental equations as follows. Taking into account that the vector lengths must be the same in the different frames, the projection, $\vec{\omega}_\perp$, of $\vec{\omega}$ onto the plane perpendicular to $\vec{B}$ can be expressed as a known function, $\vec{\omega}_\perp(\Phi)$, of an unknown angle, Φ, between the vectors $A[\vec{B}^R \times \dot{\vec{B}}^R]$ and $[\vec{B}^A \times \dot{\vec{B}}^A]$. The attitude matrix, A, then depends only on the angle Φ and the problem involves determining two unknowns: Φ and the component ω_1 of $\vec{\omega}$ in the direction of $\vec{B}$. These unknowns can be related by combining the kinematic relationship between the second derivatives, $\ddot{\vec{B}}^A$ and $\ddot{\vec{B}}^R$, with the dynamics for the $\dot{\vec{\omega}}$ given by Euler's equations. By representing the angular velocity vector in the body frame as $\omega^A = \omega_\perp(\Phi) + \omega_1 \hat{B}^A$, with $\hat{B}^A = \vec{B}^A / |\vec{B}^A|$, and taking into account the attitude matrix is the known function A(Φ) of the angle Φ, one can represent the resultant equations in the following schematic form:

$$\vec{\Lambda}_0(\Phi) + \vec{\Lambda}_1(\Phi)\omega_1 + \vec{\Lambda}_2\omega_1^2 = \vec{0} \tag{3}$$

where the vector coefficients $\vec{\Lambda}_0(\Phi)$, $\vec{\Lambda}_1(\Phi)$, and $\vec{\Lambda}_2$ parametrically depend on the reference and body components of the geomagnetic field vector, their first and second time derivatives, the spacecraft's inertia tensor the total external torque, the angular momentum of wheels, and its first time derivative. Their explicit expressions in the body frame are given in Ref. 10. (See also the note on p. 3 in Ref. 4 correcting Eqs. (25a) through (25c) in Ref. 10. In addition, Eq. (25a) of Ref. 10 should include the time derivative of the wheel momentum disregarded in the earlier works.) It is essential that the vectors $\Lambda_1(\Phi)$ and $\vec{\Lambda}_2$ are defined as the cross-products:

$$\vec{\Lambda}_1(\Phi) \equiv \hat{B}^A \times \vec{H}_1(\Phi), \quad \vec{\Lambda}_2 \equiv \vec{\Omega}_2 \times \vec{B}^A \tag{4}$$

where

$$\vec{H}_1(\Phi) \equiv \dot{\vec{B}}^A + A(\Phi)\dot{\vec{B}}^R + I^{-1}\left[\vec{B}^A \times \left(I\vec{\omega}_\perp(\Phi) + \vec{h}\right) + \vec{\omega}_\perp(\Phi) \times I\vec{B}^A\right] \tag{5}$$

and

$$\vec{\Omega}_2 \equiv I^{-1}\left[I\hat{B}^A \times \hat{B}^A\right] \tag{6}$$

It can be shown that the vector $\vec{\Lambda}_0(\Phi)$ must be perpendicular to the geomagnetic field vector $\vec{B}^A$, regardless of the particular value of the unknown angle Φ. The two equations for the unknown quantities Φ and ω_1 should be thus obtained by projecting vector Eq. (3) on two directions perpendicular to the geomagnetic field vector, $\vec{B}^A$. In general, this would lead to the two quadratic equations in ω_1, which coefficients depend on the unknown angle Φ.

In previous works (Refs. 4, 8, 9, and 10), this set of equations was solved by finding roots of one of these quadratic equations at each value of Φ and substituting them into the second equation; the resultant transcendental equation in Φ was then solved numerically. This numerical procedure proved to be sufficiently efficient for nominal rates of about 1 RPO (References 4, 8, 9, 10, and 12); however, for the high rates encountered in situations such as the SAMPEX acquisition mode (Ref. 6) or the ERBS tumble here, the discriminant of the quadratic equation for ω_1 was found to be very sensitive to errors in both computed time derivatives of magnetic field and control torques. In many cases, no solution was detected because the discriminant became negative as a result of numerical errors.

To avoid the above problem, the current work finds ω_1 from the linear equation, which was obtained by projecting Eq. (3) onto the vector

$$\vec{\Xi}_1(\Phi) \equiv \vec{\Lambda}_1(\Phi) - \hat{\Lambda}_2\left(\vec{\Lambda}_1(\Phi) \bullet \hat{\Lambda}_2\right) \tag{7a}$$

where $\hat{\Lambda}_2 = \vec{\Lambda}_2 / |\vec{\Lambda}_2|$. The second equation is then obtained by projecting vector Eq. (3) onto the perpendicular direction:

$$\vec{\Xi}_2(\Phi) \equiv \vec{B}^A \times \vec{\Xi}_1(\Phi) \tag{7b}$$

The algorithm becomes unstable if the vector $\vec{\Lambda}_1(\Phi)$ vanishes near the solution sought for. This happens if vector $\vec{H}_1$ becomes either parallel or antiparallel to the magnetic field vector. Note that vectors in Eq. (4) are also ill-defined when $|\Lambda_2|$ becomes small. However, in this case the projection of Eq. (3) onto any direction perpendicular to the magnetic field is linear in ω_1 (unless again the vector $\Lambda_1(\Phi)$ vanishes near the solution sought for). As a result, the precise definition of the direction $\vec{\Xi}_1(\Phi)$ becomes nonessential.

2.2 Real-Time Sequential Filter

The real-time sequential filter's (RTSF's) state vector, $\vec{X}$, comprises the four components of the attitude quaternion, $\vec{q}$, and the three components of the rate-corrections $\vec{b}$ to $\vec{\omega}$:

$$\vec{X} = \left[\vec{q}^T \;\; \vec{b}^T\right]^T \tag{8}$$

where the superscript T denotes transpose.

The RTSF uses sensor data to estimate $\vec{q}$ as well as $\vec{b}$, with $\vec{b}$ being estimated kinetically in the same manner as gyro biases for a gyro-based spacecraft, that is, by attributing differences between the measured and propagated attitudes to errors in $\vec{\omega}$. The $\vec{b}$ estimates are then used to correct $\vec{\omega}$, and these corrected rates are used as initial conditions to propagate Euler's equation to the next measurement time. The propagation of $\vec{b}$ is modeled via the following first-order Markov model:

$$\frac{d\vec{b}}{dt} = -\tau^{-1}\vec{b} + \vec{\eta}_b \tag{9}$$

where $\vec{\eta}_b$ is a white noise term, and τ is a finite time constant. The novel feature of the RTSF is that $\vec{b}$ represents rate errors accumulated during propagation between measurements, so that a suitable value for τ is the time between measurements: 5 sec for the SAMPEX data and 16 sec for the ERBS data used here. In contrast, the same model, when used for gyro bias estimation, requires τ of several hours.

The RTSF rate-correction estimates have been found accurate to within 0.0003 deg/sec, and this feature makes it a very robust and accurate real-time algorithm. In particular, the RTSF converges successfully in TAM-only situations using Inertial Initial

Conditions (IIC), where the a priori spacecraft state is taken as one of rest in the Geocentric Inertial Coordinates (GCI) with the BCS axes coinciding with the GCI axes.

2.3 System Overview

Input to TAMONLY consists of a dataset of processed spacecraft data, with a minimal requirement of timetags and measured and reference magnetic fields, together with control torque data such as angular momenta of the wheels and torquer dipole moments. A notable enhancement of the present study over those in Refs. 4 through 7 is that TAMONLY now includes thruster torques in its control torque model.

As described in Ref. 5, TAMONLY first uses the DADMOD solutions over a small (100-sec) batch of TAM measurements at epoch to initialize the RTSF, with the RTSF's TAM residuals and rate errors used to identify the correct DADMOD solution. These deterministic initial conditions (DIC) ensure as well as speed up convergence of the RTSF. When a suitable DADMOD epoch solution cannot be identified, TAMONLY relies on the RTSF with the IIC noted above.

3. Aspects of ERBS Modeling

3.1 Thrusters

The ERBS hydrazine propulsion system comprises two spherical tanks connected to a common manifold that feeds eight hydrazine thrusters labeled A, B, C, D, 1, 2, 3, and 4 (Refs. 1, 2, and 14). Although the thrusters are used primarily for orbit maneuvers, they are also used during attitude maneuvers. The available telemetered thruster pressure data indicate that during the tumble only the B, D, and 2 thrusters were active, and thus torques produced by only these thrusters are studied here. The thruster events are shown in Table 2, and various aspects of the thrusters in the BCS are shown in Table 3. (Note also that, from Table 2, several gaps occurred in the telemetry.)

Table 2. Thruster Events During the Tumble

YYMMDD.HHMMSS	Event	Sec from Epoch
870702.151723	Thruster D Enabled	4643
.152955 to.153215	Gap in thruster data	5395 to 5535
.153222	Thruster D Disabled	5542
.153225	Thruster B Enabled	5545
.153302	Thruster B Disabled	5582
.153318 to .153543	Gap in thruster data	5598 to 5743
.153556 to .154620	Gap in thruster data	5756 to 6380
.154943 to.160507	Gap in thruster data	6581 to 7507
.160507	Thrusters B and 2 Enabled	7507
.161111 to.162526	Gap in thruster data	7871 to 8726
.162526	All Thrusters Disabled	8726
.162856 to.201235	Gap in thruster data	8936 to 22353

Table 3. Thrust Direction and Thruster Torques (BCS)

Thruster	Center of Mass Location (m)	Mounting Angles (azimuth, elevation) (deg)	Thrust Unit Vector	Thruster Torque (N-m) (Assuming Nominal Thrust of 0.95 N)
Delta V B	(0.0, -0.051, -2.215)	(270, 78)	(0.0, -0.2079, 0.9781)	(0.3688, 0.0065, 0.0014)
Delta V D	(0.0, 0.051, -2.215)	(90, 78)	(0.0, 0.2079, 0.9781)	(0.4469,-0.0065, 0.0014)
Bow Tie 2	(0.853, 0.132, -0.625)	(110, -20.0)	(-0.3420, -0.8753, -0.3420)	(-0.2519, 0.3558,-0.6586)

The ERBS thrusters work in the blow-down mode for getting fuel into them through catalyst beds used for igniting the fuel. Thus, the pressure exerted by the inert pressurant decreases as fuel from the tank is emptied, with the thrust varying from a maximum of 2.38 N for tank pressures of 409 psia at launch to a minimum of 0.52 N for tank pressures of 60 psia toward the end of the mission.

The telemetry data for Thruster D showed a recorded average tank pressure of 140 psia at 4643 sec, which agrees with the value of 140 psia from Thruster B data at 5555 sec. However, the average tank pressure telemetered when Thrusters 2 and B

were fired simultaneously during 7507 sec through 7859 sec is 317 psia, which is assumed to be incorrect because both fuel tanks are interconnected, and the pressure must decrease with time. On the basis of personal discussions with the manufacturer, it was confirmed that the pressure recording of 140 psia is the reasonable average tank pressures during the period of the tumble. This shows clearly that at least some of the thruster data is suspect and that one must be selective in using the thruster data.

After consulting with the spacecraft manufacturer (Ref. 14), the thruster torques were generated using the following assumptions:

- The thrust forces developed by thrusters were interpolated for the recorded tank pressures from the telemetry data, and a constant thrust of 0.95 N was assigned to each thruster for the tumble period.
- The change in the location of the center of mass of the spacecraft and its inertia tensor is negligible due to fuel depletion in the tumble period.

The corresponding thruster torques in the BCS are also given in Table 3.

3.2 Spacecraft Inertia Tensor

The ERBS is assumed to be a rigid body in this study, although a considerable mass of the spacecraft is a result of the liquid propellant. In addition, during the course of the mission, considerable uncertainty exists about the amount of propellant remaining in the spacecraft. These two factors introduce corresponding uncertainties in the numerical values of the spacecraft's inertia tensor, and this range of numerical values is illustrated in Table 4 together with the mnemonic labels: *Pre-Launch, Manufacturer,* and *Calibrated.* The Pre-Launch tensor is for the fully fueled spacecraft (Ref. 2), the Manufacturer tensor reflects the values estimated by the spacecraft manufacturer for the tumble period (Ref. 14), and the Calibrated values were obtained using least-square fits in earlier ERBS dynamics studies (Ref. 15).

Table 4. ERBS Momenta of Inertia Used

Component	Pre-Launch (Ref. 2) (kg-m^2)	Manufacturer (Ref. 14) (kg-m^2)	Calibrated (Ref. 6) (kg-m^2)
I_{XX}	2814.3	2821.0	3200.0
I_{YY}	4138.3	4528.0	4591.0
I_{ZZ}	2721.2	3010.0	3150.0
I_{XY}	0.0	39.0	-38.0
I_{XZ}	0.0	-9.0	-20.0
I_{YZ}	0.0	-37.0	34.0

3.3 Choosing the RTSF Noise Parameters

The filter's noise parameters studied here are the following and are collectively referred to here by Σ.

- σ: the root-mean-square (r.m.s) value of the noise in the TAM telemetry (in units of mG)
- p : the limiting value of the error covariance of the rate corrections, $\vec{b}$, in Eq. (8). p is related to the Markov noise term $\vec{\eta}_b$ via: $p = \dfrac{\left\langle |\vec{\eta}_b|^2 \right\rangle \tau}{2}$ where $\langle \ldots \rangle$ denotes the mean. Thus, the strength of the Markov noise is denoted by p rather than by $\vec{\eta}_b$. The units of p are rad^2/sec^2.

4. Procedures and Criteria for Assessing Accuracies of Estimates

The lack of truth models for attitude and rates (with the exception of intermittently available valid gyro data) necessitates a careful examination of the numerous factors affecting the accuracy of the RTSF, and using the best numerical values for the spacecraft's dynamical parameters and the Kalman filter's noise models. Thus the following criteria/procedures were used to arrive at the best estimates:

- **Propagation-only studies.** The correctness of some important dynamical quantities that affected the accuracy of the Euler-propagated rates needed to be clarified at the outset of the study (numerical values of the spacecraft's inertia

tensor elements, validity of the telemetered thruster data for the tumble period, and validity of the thruster torque models used here). This clarification was accomplished by starting the RTSF in propagation-only mode *before the onset of the tumble* using accurate a priori attitude and rates, and then comparing these propagated rates with the unsaturated gyro data. Thus, no estimation was performed by the filter, and deviations from the gyro data arise from propagation errors.

Note that even accurate models can yield large errors at the end of a long time span because of the cumulative effects of numerous small errors in models, a priori state, numerical integration, and control data errors such as residual dipole moments and wheel misalignments. Thus, our concern here is only the relative merits of the model parameters; ultimately we rely on the robustness of the RTSF to compensate for the remaining errors in the dynamics.

- **TAM residuals and the TAM angle.** The TAM residuals are the difference between the actual and predicted TAM measurements, where the predicted measurements are the product of the RTSF attitude propagated from the previous observation time and the reference magnetic field in GCI at the current spacecraft location. The TAM angle is the angle between the actual and predicted TAM measurements and is thus a scalar parameterization of the residuals.

  The TAM residuals are the primary criterion for judging the accuracy of the RTSF attitude estimates, and past experience shows that satisfactory performance results in TAM residuals within 10 mG and TAM angles within 1 deg. Note, however, that the TAM residuals are significantly affected by the numerical values chosen for the RTSF's sensor noise parameters. Also, DADMOD is not useful here because DADMOD generates multiple solutions, each with zero residuals.

- **Rate-correction estimates.** Another important output of the RTSF is its rate-correction estimates, which may be viewed as "rate residuals." If Δt is the time between observations, then the rate corrections at a given observation time, t, are essentially the differences between (1) the rates propagated from $t - \Delta t$ to t using Euler's equation, and (2) those obtained by kinematically differencing the estimated attitudes at $t - \Delta t$ and t. Thus, because the accuracy of the RTSF attitude estimates depends on the sensor noise parameters, the rate corrections are affected by these parameters as well as the Markov noise parameter $\vec{\eta}_b$ in Eq. (9). Past experience shows that satisfactory performance results in rate errors of the order of 2 deg/hr. Although it has been our practice in the past to tune the RTSF in order to simultaneously minimize the TAM residuals as well as the rate corrections, in view of the numerous uncertainties regarding the dynamical quantities here, the rate corrections are deemed of lesser importance than the TAM residuals.

- **Consistency of results.** In general, the accuracy of the filter estimates is reflected in their independence from the a priori attitude and rates used to generate the results. This criterion has been used to validate the final results by ascertaining that essentially the same estimates are reproduced irrespective of the start time and initial RTSF parameters for the run.

- **Agreement between RTSF and DADMOD results.**

5. Results

5.1 Propagation-Only Results

As noted in Section 3, it is not a priori clear whether to include the torques due to any of the Thrusters D, B, and 2. The eight cases of thruster treated independently, together with the three choices for the inertia tensor, yield a total of 24 cases of dynamical parameters to be tested, and separate propagation-only runs were made for each case. Every run commenced at the same *pretumble* time of 3043 sec using the same accurately known attitude and rates to start the RTSF.

Figs. 3a through 3c show selected rate results from these propagation-only runs using only the Manufacturer and Calibrated tensor because the Pre-Launch tensor consistently yielded the worst results. (Note that the vertical scales vary widely in the figures.) We find that omitting the thruster torques completely (Fig. 3a) introduces large errors, but so does including all the available thruster torques (Fig. 3b). The most reasonable results arise when only the D-thruster data and the Calibrated tensor are used (Fig. 3c), although the magnitudes of the peak rates are only about 1 deg/sec. We thus see another reason to suspect the validity of the telemetry for Thrusters B and 2.

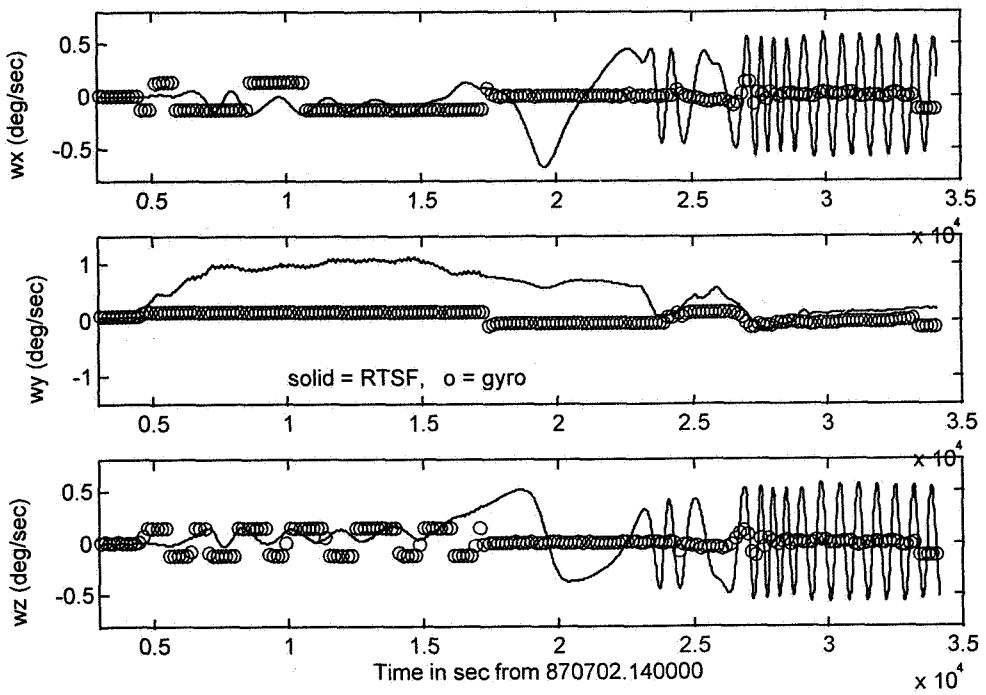

Figure 3a. Propagation-Only Results For Spacecraft Rates Using Manufacturer's Inertia Tensor and Omitting Thruster Torques

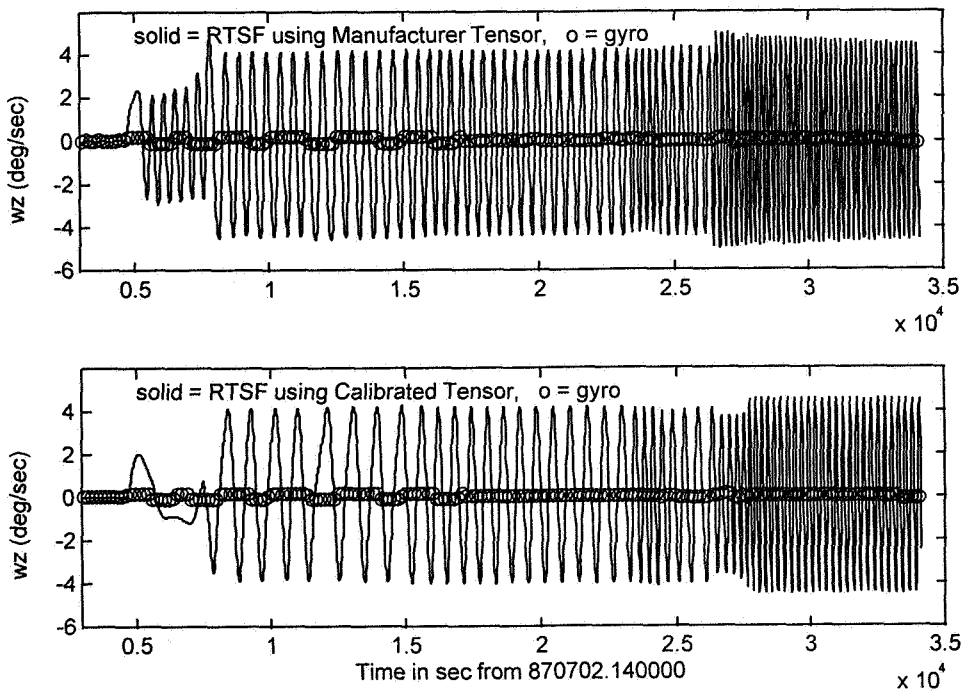

Figure 3b. Propagation-Only Results For the Z-Axis Rate Using All Thruster Torques and Different Inertia Tensors

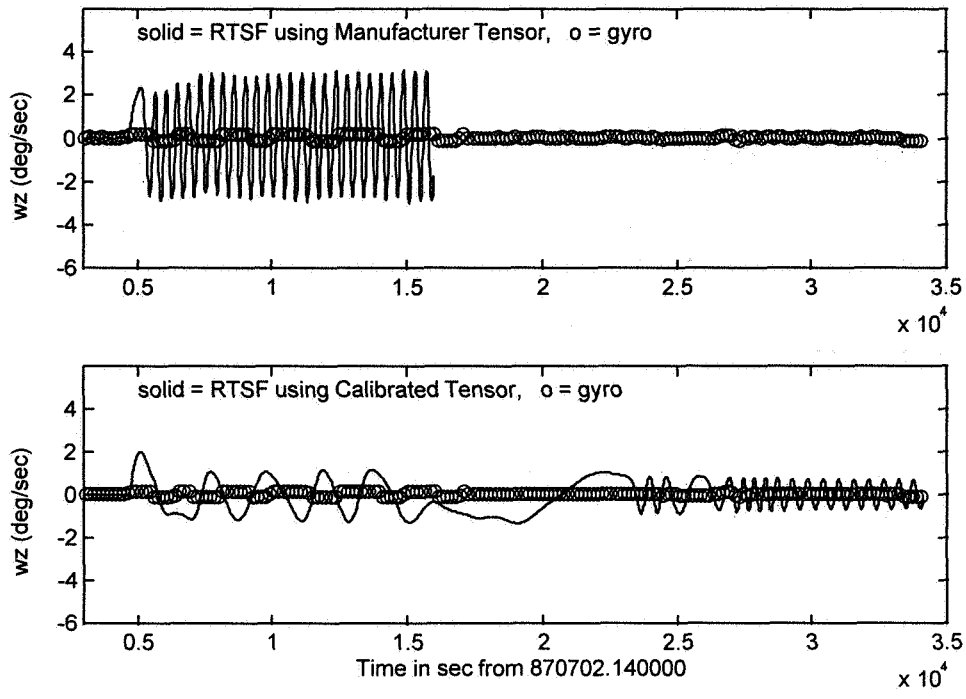

Figure 3c. Propagation-Only Results For the Z-Axis Rate Using Only D Thruster Torques and Different Inertia Tensors

5.2 RTSF Results Using TAM Data

A large number of runs was made using the Calibrated tensor of Table 4 and various values of Σ, and the results were assessed using the statistics of the filter's TAM residuals and the rate corrections during the high-rate tumble period between 4627 and 17,459 sec. Some selected results are given in Table 5, which illustrate the following points.

- For identical Σ, the Manufacturer and Pre-Launch tensors yield the smallest and largest TAM residuals, respectively. Thus, the Manufacturer tensor results are superior to those of the Calibrated one, although Fig. 3c indicates otherwise.
- As expected, for a given tensor, the TAM residuals worsen as Σ is varied to give more weight to the rate corrections.
- Using all thruster data degrades the results for the TAM residuals as well as the rate corrections, irrespective of the tensor.
- The best results are obtained when $\Sigma = \{0.4\text{ mG}, 1 \times 10^{-4}\text{ rad}^2/\text{sec}^2\}$, which is noticeably different from Ref. 6 where r.m.s. TAM residuals of 3 mG and r.m.s. rate corrections of 1 deg/hr were obtained using $\Sigma = \{6.4\text{ mG}, 3 \times 10^{-8}\text{ rad}^2/\text{sec}^2\}$. The best results are shown in Fig. 4, and it is very encouraging to note the excellent agreement among the RTSF rate estimates and the unsaturated gyro data in Fig. 4a. Fig. 4c shows selected TAM residuals and rate corrections. The r.m.s. TAM angle value of 2.47 deg in Fig. 4c is taken here as an estimate of TAMONLY's inaccuracies.

The consistency of the results was tested by running the RTSF with the above Σ values from different starting points during the tumble but using IIC (i.e., with no a priori knowledge of the attitude and rates). Results from one such run starting at 6259 sec are presented in Fig. 5, and we found that the rates converged to within 0.2 deg/sec of those in Fig. 4 by about 7000 sec; they are within 0.00015 deg/sec from 10,000 sec onwards. Note that the large a priori attitude errors are manifest as an initial TAM angle of about 25 deg in Fig. 5. Similar results were obtained by starting the RTSF with IIC at two other starting points, thus establishing that the results of Fig. 4 are not far from the truth.

Table 5. Statistics of RTSF TAM Residuals and Rate Corrections for Various Values of Σ

$\Sigma = (\sigma, p)$ (mG, rad^2/sec^2)	Tensor Mnemonic (Thruster Data Used)	TAM Residuals 1st row: mean 2nd row: r.m.s. (x, y, z) (mG)	TAM angle (deg)	Rate-Corrections 1st row: mean 2nd row: r.m.s. (x, y, z) (deg/hr)
(1.4, 10^{-4})	Manufacturer(D)	(-0.59, -1.27, 0.19) (8.57, 9.22, 9.88)	2.00 2.47	(5.36, 7.00, -21.23) (166.44, 141.13, 139.15)
(1.4, 10^{-8})	-do-	(-1.28, 0.48, -0.89) (11.28, 13.01, 12.61)	2.70 3.56	(11.80, 5.65, -32.78) (169.30, 101.35, 138.94
(6.4, 10^{-8})	-do-	(0.97, -5.17, -0.32) (84.15, 108.37, 107.10)	22.58 32.10	(51.54, 4.25, -17.96) (243.60, 150.09, 199.34)
(1.4, 10^{-4})	Calibrated (D)	(0.23, -1.41, 0.53) (12.82, 11.18, 10.70)	2.53 2.97	(10.61, 1.37, -105.15) (184.23, 137.75, 218.32)
(1.4, 10^{-8})	-do-	(-1.51, -0.25, 0.60) (17.14, 14.72, 14.08)	3.39 4.03	(17.61, 0.90, -99.68) (168.18, 123.16, 202.18)
(6.4, 10^{-8})	-do-	(6.46, -19.68, 7.83) (93.79, 152.25, 121.61)	32.08 39.26	(99.94, 4.64, -80.07) (326.88, 153.95, 290.91)
(0.4, 10^{-4})	Pre-Launch (D)	(-0.24, -1.94, 0.33) (14.63, 12.14, 11.55)	2.79 3.30	(23.57, 3.82, -121.87) (191.57, 163.37, 247.68)
(6.4, 10^{-8})	-do-	(9.56, -31.16, -9.59) (101.38, 159.48, 132.65)	33.34 40.39	(125.18, 4.760, -61.94) (338.88, 159.11, 319.25)
(0.4, 10^{-4})	Manufacturer(All)	(-0.77, -1.64, 0.10) (10.55, 10.11, 10.17)	2.23 2.83	(-5.04, 16.50, -13.84) (177.14, 154.13, 199.92)
(0.4, 10^{-4})	Calibrated (All)	(-0.02, -3.75, 0.04) (14.34, 12.48, 12.19)	2.84 3.42	(-3.37, 6.77, -89.41) (207.91, 162.05, 265.02)
(0.4, 10^{-4})	Pre-Launch (All)	(-0.25, -4.43, -0.79) (16.84, 14.82, 13.25)	3.24 3.94	(13.62, 11.58, -117.01) (230.77, 183.38, 314.11)

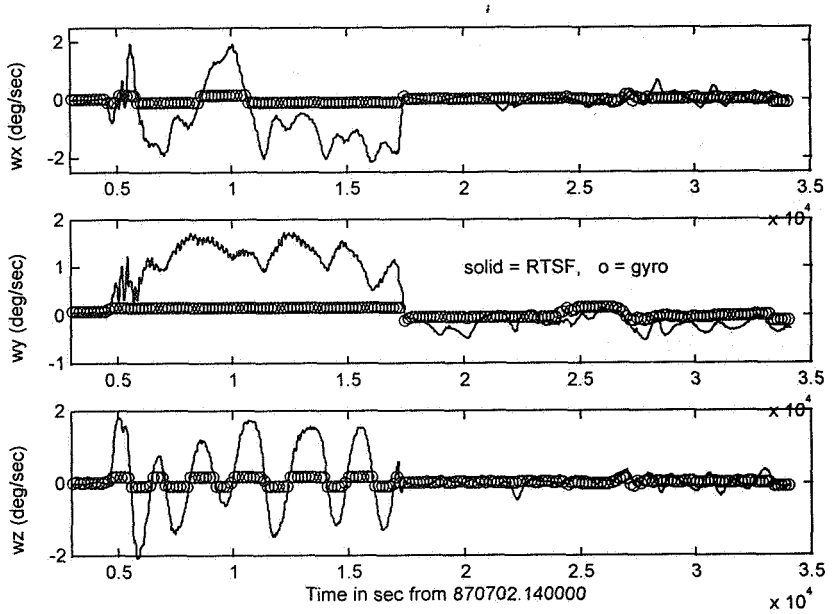

Figure 4a. "Best" TAMONLY Results for Spacecraft Rates Obtained Using Manufacturer's Inertia Tensor and Σ *= {0.4 mG,* 10^{-4} *rad^2/sec^2}*

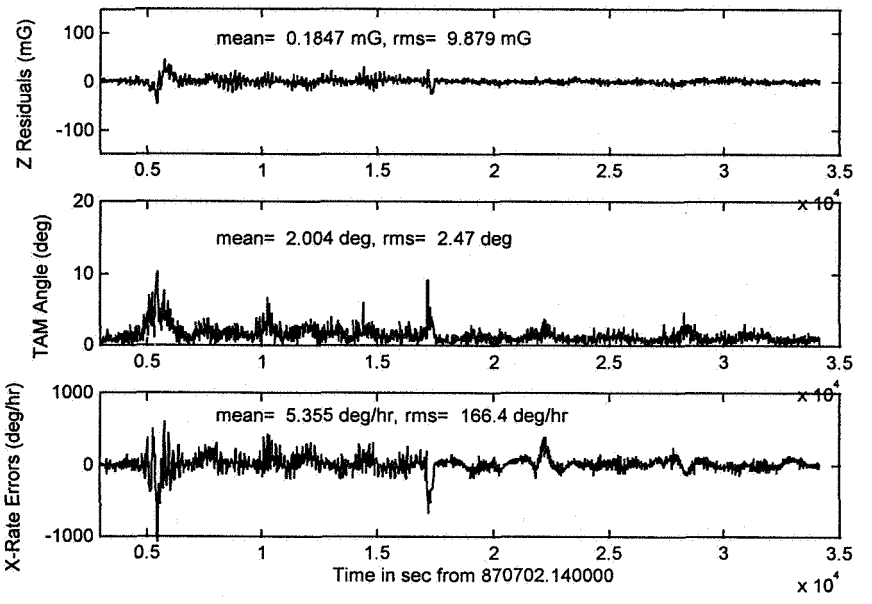

Figure 4b. Selected TAM Residual and Rate-Error Estimates from the Run of Figure 4a Showing Error Statistics for the High-Rate Period (4627 sec to 17,459 sec)

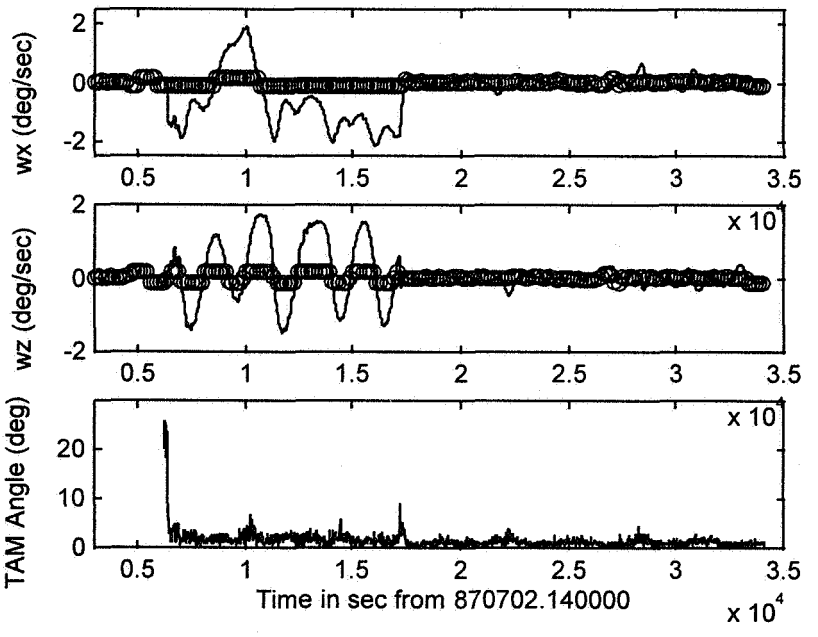

Figure 5. Results Obtained Using Same Parameters as in Figure 4a But Starting at 6259 sec

5.3 Results Using DADMOD

Two complications arise when applying the DADMOD to the high-rate period: (1) the algorithm necessarily fails when the magnetic field changes much faster in the BCS than in the GCI, and (2) because DADMOD does not compensate for errors in the dynamical model, it is more sensitive to these errors than is the RTSF. The former problem is overcome using the DADMOD enhancements of Section 2. The latter problem is partially avoided in the preliminary results reported here by omitting the thruster torques.

Fig. 6 presents preliminary results using the Manufacturer tensor (results using the Calibrated tensor are very similar). Comparing with the RTSF results of Fig. 4, we see that at each time, a DADMOD rate solution agrees very well with the RTSF estimate. (Note that an independent criterion must be used to distinguish between the correct and spurious DADMOD solutions.) It is worth pointing out that the DADMOD solutions strongly oscillate between 6600–7200 and 7500–8200 sec (barely visible in the figure), and these could be due to a variety of reasons such as some thruster activity, numerical instabilities, or inertia tensor effects.

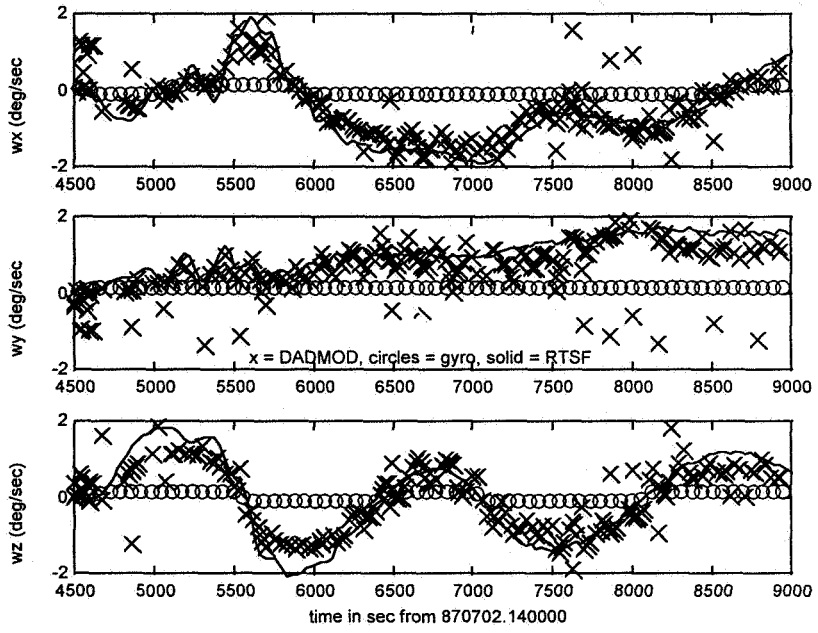

Figure 6. DADMOD Results Using the Manufacturer Inertia Tensor

6. Conclusions

The ERBS 1987 tumble has been studied extensively, using only TAM and control data as input to an enhanced version of the recently developed system, TAMONLY, which includes thruster torques computed from telemetered thruster data. The rate estimates from TAMONLY's Kalman filter confirm that the spacecraft rates were as high as 2 deg/sec and are in excellent agreement with unsaturated gyro data, as well as solutions from an enhanced version of TAMONLY's deterministic algorithm. Additional validation of the Kalman filter's rate estimates was done by showing their independence from the filter's a priori conditions. Based on the TAM residuals, the attitude results during the high-rate period are estimated to be accurate to within 2.5 deg.

The influence of dynamical model parameters was extensively studied through propagation-only runs, which indicate that some of the thruster data are questionable and also indicates that the most appropriate inertia tensor is the Calibrated tensor of Table 5. In general, the dynamical uncertainties in this study were also evidenced by the large rate corrections estimated by the Kalman filter. Thus, the filter results also indicate errors in the thruster data, but in contradiction with the propagation-only results, show that the Manufacturer tensor yields the best results.

References

1. G. Nair, K. Liu, B. Fang, M. Radomski, and S. Smith, *Earth Radiation Budget Satellite (ERBS) Attitude Ground Support System (AGSS) Functional Specifications and Requirements*, Goddard Space Flight Center, Flight Dynamics Division, CSC/SD-82/6013, prepared by Computer Sciences Corporation, September 1982

2. M. Phenneger et al., *Earth Radiation Budget Satellite (ERBS) Attitude Analysis and Support Plan*, Goddard Space Flight Center, Flight Dynamics Division, CSC/TM-84/6071, prepared by Computer Sciences Corporation, August 1984
3. J. Kronenwetter, M. Phenneger, and W. Weaver, "Attitude Analysis of the Earth Radiation Budget Satellite (ERBS) Yaw Turn Anomaly," *Proceedings of the Flight Mechanics/Estimation Theory Symposium,* NASA Conference Publication No. 3011, Goddard Space Flight Center, Greenbelt, MD, May 1988
4. G. Natanson, M. Challa, J. Deutschmann, and D. Baker, "Magnetometer-Only Attitude and Rate Determination for a Gyroless Spacecraft," *Proceedings of the Third International Symposium on Space Mission Operations and Ground Data Systems,* NASA Conference Publication 3281, Greenbelt, MD, November 1994, pp. 791–798.
5. M. Challa and G. Natanson, "A PC-Based Magnetometer-Only Attitude-and-Rate Determination System for Gyroless Spacecraft," *Proceedings of the Flight Mechanics and Estimation Theory Symposium,* NASA Conference Publication No. 3299, Goddard Space Flight Center, Greenbelt, MD, May 1995
6. M. Challa and C. Wheeler, "Accuracy Studies of a Magnetometer-Only Attitude-and-Rate Determination System," *Proceedings of the Flight Mechanics and Estimation Theory Symposium,* NASA Conference Publication No. 3333, Goddard Space Flight Center, Greenbelt, MD, May 1996
7. M. Challa, G. Natanson, and C. Wheeler, "Simultaneous Determination of Spacecraft Attitude and Rates Using Only a Magnetometer," *Proceedings of the American Institute of Aeronautics and Astronautics (AIAA)/American Astronautical Society (AAS) Astrodynamics Specialist Conference,* San Diego, CA, July 1996
8. G. Natanson, S. McLaughlin, and R. Nicklas, "A Method of Determining Attitude From Magnetometer Data Only," *Proceedings of the Flight Mechanics/Estimation Theory Symposium 1990,* NASA Conference Publication 3102, Goddard Space Flight Center, Greenbelt, MD, May 1990
9. G. Natanson, J. Keat, and S. McLaughlin, *Sensor and Advanced Attitude Studies: Deterministic Attitude Computation Using Only Magnetometer Data*, Goddard Space Flight Center, Flight Dynamics Division, 554-FDD-91/010, prepared by Computer Sciences Corporation, March 1991
10. G. Natanson, "A Deterministic Method for Estimating Attitude From Magnetometer Data Only," Paper No. IAF-92-0036, *Proceedings of the World Space Congress,* Washington, D.C., September 1992
11. M. Challa, *Solar, Anomalous, and Magnetospheric Particle Explorer (SAMPEX) Real Time Sequential Filter (RTSF): Evaluation Report*, Goddard Space Flight Center, Flight Dynamics Division, 553-FDD-93/024R0UD0, prepared by Computer Sciences Corporation, April 1993
12. M. Challa, G. Natanson, D. Baker, and J. Deutschmann, "Advantages of Estimating Rate Corrections During Dynamic Propagation of Spacecraft Rates—Applications to Real-Time Attitude Determination of SAMPEX," *Proceedings of the Flight Mechanics/Estimation Theory Symposium 1994,* NASA Conference Publication No. 3265, Goddard Space Flight Center, Greenbelt, MD, May 1994
13. J. Wertz ed., *Spacecraft Attitude Determination and Control*, D. Reidel Publishing Co., Dordrecht, Holland, 1985, pp. 424–425
14. Zubin Emsley (Ball Aerospace Corporation), private communication, July 1996
15. E. Harvie, *ERBS Supplemental Dynamic Model Analysis*, Goddard Space Flight Center, Flight Dynamics Division, prepared by Computer Sciences Corporation, May 2, 1991

Accurate Magnetometer/Gyroscope Attitudes Using a Filter With Correlated Sensor Noise*

J. Sedlak and J. Hashmall
Computer Sciences Corporation
Lanham-Seabrook, MD, USA 20706

Abstract

Magnetometers and gyroscopes have been shown to provide very accurate attitudes for a variety of spacecraft. These results have been obtained, however, using a batch-least-squares algorithm and long periods of data. For use in onboard applications, attitudes are best determined using sequential estimators such as the Kalman filter.

When a filter is used to determine attitudes using magnetometer and gyroscope data for input, the resulting accuracy is limited by both the sensor accuracies and errors inherent in the Earth magnetic field model. The Kalman filter accounts for the random component by modeling the magnetometer and gyroscope errors as white noise processes. However, even when these tuning parameters are physically realistic, the rate biases (included in the state vector) have been found to show systematic oscillations. These are attributed to the field model errors. If the gyroscope noise is sufficiently small, the tuned filter "memory" will be long compared to the orbital period. In this case, the variations in the rate bias induced by field model errors are substantially reduced. Mistuning the filter to have a short memory time leads to strongly oscillating rate biases and increased attitude errors.

To reduce the effect of the magnetic field model errors, these errors are estimated within the filter and used to correct the reference model. An exponentially-correlated noise model is used to represent the filter estimate of the systematic error. Results from several test cases using in-flight data from the Compton Gamma Ray Observatory are presented. These tests emphasize magnetometer errors, but the method is generally applicable to any sensor subject to a combination of random and systematic noise.

1. Introduction

Measurement of the geomagnetic field provides a convenient and relatively economical basis for determining the attitude of low-Earth orbiting spacecraft. When joined with a model of the spacecraft dynamics, the magnetic field can be filtered to obtain attitude and rate estimates (Reference 1). However, the filtering algorithm is much simpler and usually more accurate when the field data is combined with body rates measured by rate-integrating gyroscopes. It has been shown elsewhere (References 2 and 3) that surprisingly accurate attitude estimates are possible with well-calibrated magnetometers. Furthermore, the spacecraft need not carry more accurate sensors (*e.g.*, star trackers) to calibrate the magnetometer. The calibration process can be "bootstrapped" by using attitudes derived from uncalibrated magnetometers for an initial calibration, using this first calibration to improve the attitudes, and repeating until the solution parameters converge (Reference 3).

Even when star tracker and precise gyroscope data are available to obtain the best possible magnetometer calibration, it is found that some sensor errors remain. To the extent that these errors are non-random, it may be possible to understand them and possibly to reduce them. The purpose of this paper is to investigate the systematic errors remaining when solving for attitudes and gyroscope rate biases using

*This work was supported by the National Aeronautics and Space Administration (NASA) / Goddard Space Flight Center (GSFC), Greenbelt, Maryland, under Contract NAS 5-31000.

only magnetometer and gyroscope data. In Section 2, these systematic errors are demonstrated, and it is suggested that they come from errors in the reference model rather than the sensor itself. Section 3 presents a method to reduce the effects of these errors, making this sensor complement a more viable choice for onboard attitude control for low-to-moderate accuracy missions or for contingency conditions. Section 4 gives test results using this method.

In order to study the systematic errors of magnetometer/gyroscope attitude estimates, the true attitude must be known with sufficient accuracy. In practice, verification of attitude accuracy often would rely on an inspection of the magnetometer residuals (measured minus predicted magnetic fields), but for analysis, it is more interesting to consider a mission where a more accurate sensor complement is available to establish a reference attitude. In this paper, attitude estimates for the Compton Gamma Ray Observatory (CGRO) are studied. The attitude estimated onboard is used as the reference to which the magnetometer/gyroscope based attitudes and rate biases are compared. The onboard computer (OBC) determines the attitude using data from two NASA standard Ball fixed-head star trackers (FHSTs) and a Teledyne DRIRU II-type dry rotor inertial reference unit (IRU). The FHSTs, IRU, and the Schoenstedt three-axis magnetometer (TAM) have all been previously calibrated using attitudes derived from the FHSTs and IRU. The OBC attitudes are accurate to better than 30 arcsec per axis (1σ) (Reference 4).

2. Systematic Errors

Three software tools for state determination are used in this study. A batch estimator that can solve for IRU and TAM biases along with the attitude (Reference 5) was used in some of the early work. The second tool is a Kalman filter for attitude and IRU bias estimation roughly similar to the OBC filter. This is referred to as the Unit Vector Filter (UVF) in Reference 6. The third estimator is a modification of the UVF, discussed in the next section.

Input data for all the tests described in this paper come from a May 3, 1993 telemetry set consisting of almost 5 orbits of the CGRO spacecraft. CGRO is in a nearly circular orbit with an inclination of 28.5 deg and an altitude of 380 km. Its attitude is nearly constant for this time span. The inertial-to-body frame transformation is a 3-2-1 sequence of Euler rotation angles of (31.0, -42.7, -21.6) deg. The IRU data come every 0.256 sec and TAM data every 3.072 sec in this telemetry. Reference vectors for the TAM are generated using the International Geomagnetic Reference Model (IGRF). Current coefficients to order 10 are used.

The first series of tests were performed with a batch estimator. It is not surprising that attitude errors are found to decrease as batch size increases. The scatter of solutions from different batches of the same duration also decreases. However, it was noticed that the scatter was particularly large for durations less than one full orbit. For these batches, it was found that the estimated IRU biases depend on the location of the spacecraft in its orbit. These results motivated a more detailed study of the variability of the estimated IRU bias using a sequential estimator such as the UVF.

The UVF was used to track the bias over several orbits using TAM and IRU data. By adjusting the IRU process noise parameters, the filter can be made more or less responsive to time dependences of the IRU bias. The IRU noise model (Reference 7) is assumed to include a random walk of the accumulated angle and a random walk of the bias. With a large noise source driving the bias random walk, the filter can follow a slowly time-varying bias.

Figure 1 shows the UVF gyro bias estimates using noise parameters of 10^{-13} rad^2/sec for the accumulated angle random walk and 10^{-19} rad^2/sec^3 for the bias random walk. These are about an order of magnitude larger than the physical values expected for the DRIRU II. The sensor noise for the TAM is taken to be 3 mG. (In the UVF algorithm, this TAM noise is divided by the reference field magnitude to obtain an angular 1σ uncertainty for the observed magnetic field unit vector.) The IRU biases in Figure 1 and elsewhere in this paper are actually bias corrections after the rates have been adjusted using the best calibration parameters available. Therefore, the expected bias corrections are all zero.

The filter has been initialized with a good estimate of the true state. The biases are set equal to zero and the attitude is taken from the OBC. The state error covariance is initialized with 0.05 deg attitude error and 0.005 deg/hr bias error on each axis. These values allow the filter to converge quickly. In separate tests, initializing the biases to larger values (near 1 deg/hr) strongly affects estimates for the first few hours, but by the 5th orbit the filter settles down to agree with values shown in Figure 1.

There is a significant oscillation in the Z-axis bias at the orbital frequency and smaller oscillations in the X- and Y-biases (possibly at multiples of the orbital period). The Z-axis uncertainties are expected to be larger than the other axes since the body Z-axis is aligned closest to the Earth's magnetic pole. With the low inclination orbit, this means the variation of the magnetic field is smallest along Z. This makes the Z-bias and the Z-axis attitude rotation somewhat less observable than those of the other axes.

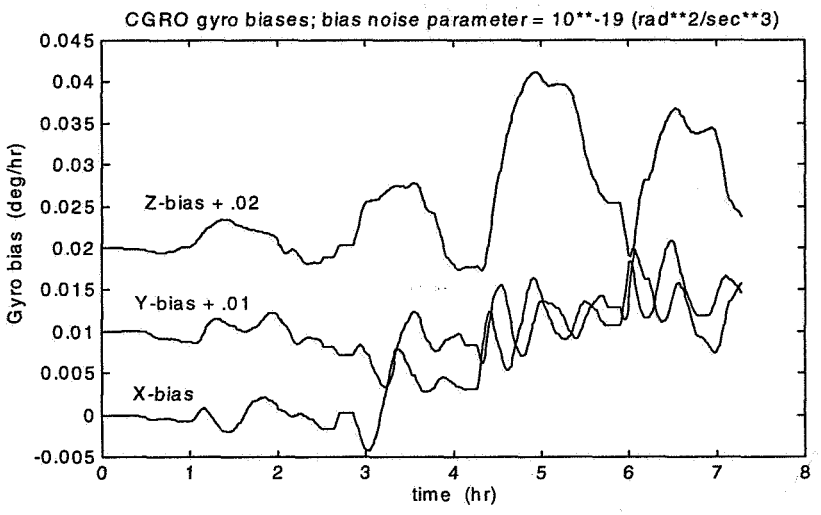

Figure 1. Gyro biases for 5-orbit time span; Y- and Z-biases are offset for clarity.

The process noise is responsible for the time increase of the state error covariance. As such, it controls the filter memory time. The effective memory time for filter errors of a given size is roughly the variance divided by the noise source. For bias errors of magnitude 0.01 deg/hr and a bias noise of 10^{-19} rad^2/sec^3, the memory time is 6.5 hr. This is close to the total length of the data set. Thus, the noise needs to be increased if the purpose is to follow the IRU biases.

Figure 2 shows the biases for a similar case, but here the bias noise is increased to 10^{-15} rad^2/sec^3. Note the scale of Figure 2 is nearly 100 times larger than that of Figure 1. The filter memory is only a few seconds for errors as small as 0.01 deg/hr; however, it again is 6.5 hrs for errors on the order of 1 deg/hr. The large oscillations indicate an error that varies systematically with the orbital period. While there may be thermal variations as the spacecraft moves in and out of Earth shadow, they would be expected to show

up as more abrupt changes, with the sunlit period roughly twice the shadow period. The sinusoidal variations seen in Figure 2 are more likely due to small errors in the geomagnetic reference field model. Other studies using CGRO data have found geographically fixed errors in the field model up to 5 mG (Reference 8).

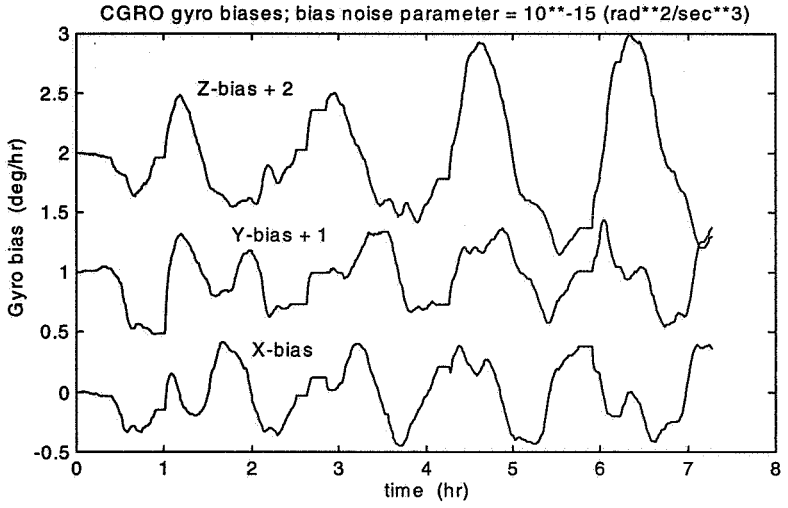

Figure 2. Gyro biases for 5-orbit time span with large bias process noise; Y- and Z-biases are offset for clarity.

Statistical results for a series of test cases are given in Table 1. Results for tests reported here and below are averages over the final orbit in the data set, allowing almost 4 orbits for filter convergence. The bias noise covers 6 orders of magnitude in this table. The entries ΔX, ΔY, and ΔZ indicate attitude differences between the UVF and the OBC estimates about the body axes. It is clear that deviations in both the attitude and the IRU biases increase dramatically as the bias noise increases. As seen in Figure 2, this is due to systematic variations rather than a random scatter of solutions.

Table 1. Filter Statistics Over One Orbit for a Range of IRU Bias Process Noise

σ^2_{bias} (rad^2/sec^3)	10^{-15}	10^{-17}	10^{-19}	10^{-21}
RMS (arcsec)				
ΔX	376	163	106	56
ΔY	365	159	112	97
ΔZ	1093	253	82	57
RSS	1213	340	175	126
Mean (deg/hr)				
IRU bias-X	-0.0080	0.0131	0.0147	0.0091
IRU bias-Y	-0.0311	-0.0017	0.0029	0.0015
IRU bias-Z	0.0351	-0.0101	0.0096	0.0066
Std. dev. (deg/hr)				
IRU bias-X	0.2684	0.0238	0.0029	0.0014
IRU bias-Y	0.2503	0.0292	0.0030	0.0011
IRU bias-Z	0.6171	0.0555	0.0052	0.0021
RSS	0.7179	0.0671	0.0067	0.0028

The next question is whether the systematic errors can be reduced by a judicious choice of noise parameters. The values in Table 1 indicate that the best solutions correspond to the smallest bias noise parameters. Simply reducing the noise is not a practical solution for an onboard filter since there is a risk

of the filter becoming too unresponsive. A single outlying IRU point can cause the state to propagate far from truth without a corresponding increase in the state error covariance, and the filter would recover only very slowly.

Rather than simply reducing the bias noise, it might be possible to vary the filter tuning parameters to match the hypothetical systematic errors in the reference field. Where the field errors are consistently the largest, the TAM noise could be increased to give less weight to measurements taken in that region of the orbit. This approach continues to treat the error as white noise, but with an artificially adjusted strength. A better solution is to account for the systematic errors explicitly. In the next section, a filter is developed which approximately solves for the systematic error and uses it to correct the observation residuals. The state vector is increased by 3 components, but there is only a small overall increase in complexity.

3. Correlated Noise Filter

Recognizing that the remaining bias and attitude errors are caused by some combination of systematic and random errors in the TAM residuals, the approach taken here is to augment the state vector with a simple correction term for the residual. It is assumed that the errors inherent to the sensor are well-represented by white noise. However, the systematic errors presumably derive from the reference field model and are modeled as exponentially-correlated random variables. Since the sources are physically distinct for the sensor and model errors, the white and correlated noise sequences are taken to have no cross-correlation. The choice of exponential-correlations keeps the model simple; only a single time constant is needed for each axis. (In practice, the same time constant has been used for all three axes.) The filter follows trends in the residuals, but a residual correction estimated at one filter update decays exponentially with time until the next update. This filter is derived in Reference 9, where alternative implementations are given. The approach described below uses the simplest of these algorithms, which also is the least stable numerically. Long-term stability tests still need to be performed.

Let x_i represent the error state components for the attitude, α, and IRU bias, Δb, at time t_i. The filter estimates the error state to avoid complications from the attitude quaternion normalization constraint in the full state. Details are given in Reference 10. The state is propagated from t_i to t_{i+1} according to

$$x_{i+1} = \Phi_i x_i + w_i \tag{1}$$

where Φ_i makes use of data from the IRU, corrected for the bias, and where w_i is a white noise sequence. In a continuous-time model, the corresponding white noise source is taken to have spectral density

$$Q(t) = \begin{bmatrix} \sigma_{att}^2 I & 0 \\ 0 & \sigma_{bias}^2 I \end{bmatrix} \tag{2}$$

where I is the 3×3 identity matrix. The matrix Φ_i and the relationship between $Q(t)$ and its discrete-time counterpart, Q_i, are given, for example, in Reference 6.

The sensor residual, y_i, is normally given as

$$y_i = H_i x_i + v_i \tag{3}$$

where H_i models the linear sensor response to the state, and where v_i is the uncorrelated noise with

$$R_{TAM} = E\left[v_i v_i^T\right] = \sigma_{TAM}^2 I \tag{4}$$

An expression for H_i is given below, along with an added correction depending on an exponentially correlated noise term, ε_i. In a continuous-time model , the evolution equation for ε would be

$$\dot{\varepsilon}(t) = -\beta\,\varepsilon(t) + u(t) \tag{5}$$

The correlation time for ε is $\tau = 1/\beta$. From Eq. (5), the discrete-time model is

$$\varepsilon_{i+1} = \Psi\varepsilon_i + u_i \tag{6}$$

with

$$\Psi_i = e^{-\beta\Delta t_i} I \tag{7}$$

$$q_i = E\left[u_i u_i^T\right] \tag{8}$$

$$E\left[u(t_1)u^T(t_2)\right] = q(t_1)\delta(t_1 - t_2) \tag{9}$$

The spectral density, $q(t)$, is assumed constant. Let p be the variance of $\varepsilon(t)$, representing a measure of the systematic error in the sensor residuals. Take p to be a constant equal to $\sigma^2_{corr} I$. With a constant variance, one must have $q = 2\beta p$. Evaluating Eq. (8) leads to

$$q_i = \sigma^2_{corr}\left(1 - e^{-2\beta\Delta t_i}\right) I \tag{10}$$

The model statistics of the sensor residuals are determined by the parameters σ_{TAM} and σ_{corr}. These, along with the IRU noise sources in Eq. (2), are the parameters available for tuning the filter.

Now, the augmented state can be written as

$$x_i^a = \begin{bmatrix} x_i \\ \varepsilon_i \end{bmatrix} \tag{11}$$

The propagation equations for the augmented state and its covariance, P^a, are

$$x_{i+1}^a = \Phi_i^a x_i^a + \begin{bmatrix} w_i \\ u_i \end{bmatrix} \tag{12}$$

$$\Phi_i^a = \begin{bmatrix} \Phi_i & 0 \\ 0 & \Psi_i \end{bmatrix} \tag{13}$$

$$P_{i+1}^a = \Phi_i^a P_i^a \Phi_i^{aT} + Q_i^a \tag{14}$$

$$Q_i^a = \begin{bmatrix} Q_i & 0 \\ 0 & q_i \end{bmatrix} \tag{15}$$

The observation model is constructed by expanding the residual to first-order in the state. Let the true inertial frame magnetic field vector be related to the reference model as

$$V_{true} = V_{ref} + \varepsilon \tag{16}$$

where the time subscript i is suppressed for convenience. The body frame measured field then is

$$\begin{aligned} B_{meas} &= B_{true} + v \\ &= e^{[\alpha\times]} A_{est} V_{true} + v \end{aligned} \tag{17}$$

where

$$[\alpha\times] = \begin{pmatrix} 0 & -\alpha_z & \alpha_y \\ \alpha_z & 0 & -\alpha_x \\ -\alpha_y & \alpha_x & 0 \end{pmatrix} \tag{18}$$

and A_{est} is the a priori estimate of the attitude matrix and α is the unknown correction to the estimated attitude needed to rotate it to the true state. The estimated measurement vector is

$$B_{est} = A_{est}\left(V_{ref} + \varepsilon_{est}\right) \tag{19}$$

Expanding the residual, one finds

$$\begin{aligned} y &= B_{meas} - B_{est} \\ &= -\left[A_{est}\left(V_{ref} + \varepsilon_{est}\right)\times\right]\alpha + A_{est}\Delta\varepsilon + v \end{aligned} \tag{20}$$

where $\Delta\varepsilon = \varepsilon - \varepsilon_{est}$ is the correlated noise component of the error state. Thus, the sensitivity matrix for the augmented state is

$$H^a = \left[-\left[A_{est}\left(V_{ref} + \varepsilon_{est}\right)\times\right] \quad 0_{3\times3} \quad A_{est} \right] \tag{21}$$

and the filter sensor noise covariance reduces to the uncorrelated part, R_{TAM}, from the term v.

4. Results

A series of tests have been run for various choices of the correlation time, τ. Based on plots of the TAM residuals from the uncorrelated UVF and after some experimentation, the noise terms were taken to be $\sigma_{TAM} = 1$ mG and $\sigma_{corr} = 2$ mG. Table 2 summarizes some of these results. The bias noise is taken to be 10^{-19} rad^2/sec^3 so these tests should be compared to the 2nd last column in Table 1.

For values of τ below 10 sec, it is found that the correlated noise filter approaches the corresponding UVF results, as required. In the limit of zero correlation time, the propagation submatrix Ψ vanishes, and Eq. (6) and Eq. (19) show that the augmented state just contributes another white noise term, u, to the sensor residual.

For larger values of τ, the very small IRU bias means and standard deviations given in Table 2 indicate that the filter has succeeded in estimating and accounting for the correlated noise, rather than forcing systematic variations in the IRU biases.

The improvement over the UVF is best for the $\tau = 100$ sec case. The root-sum-square attitude error is reduced from 175 to 100 arcsec. Figure 3 shows a plot of the attitude differences between the correlated noise filter and the OBC estimates. The error rotation about each axis is given for both the $\tau = 0.1$ sec and

Table 2. Correlated Noise Filter Statistics Over One Orbit for a Range of Correlation Times

τ (sec)	0.1	100	500	1000
RMS (arcsec)				
ΔX	124	70	115	123
ΔY	118	54	30	18
ΔZ	100	45	17	27
RSS	198	100	120	127
Mean (deg/hr)				
IRU bias-X	0.0163	0.0028	0.0010	0.0011
IRU bias-Y	0.0034	0.0002	-0.0001	-0.0001
IRU bias-Z	0.0110	-0.0003	-0.0004	-0.0004
Std. dev. (deg/hr)				
IRU bias-X	0.0037	0.0007	0.0003	0.0003
IRU bias-Y	0.0039	0.0004	0.0002	0.0002
IRU bias-Z	0.0068	0.0007	0.0004	0.0005
RSS	0.0086	0.0011	0.0005	0.0007

$\tau = 100$ sec cases. The $\tau = 0.1$ sec results are similar to the uncorrelated UVF solutions. It is evident that including correlated noise in the filter reduces both the mean error and the attitude oscillations that had accompanied the IRU bias variations shown in Figure 1.

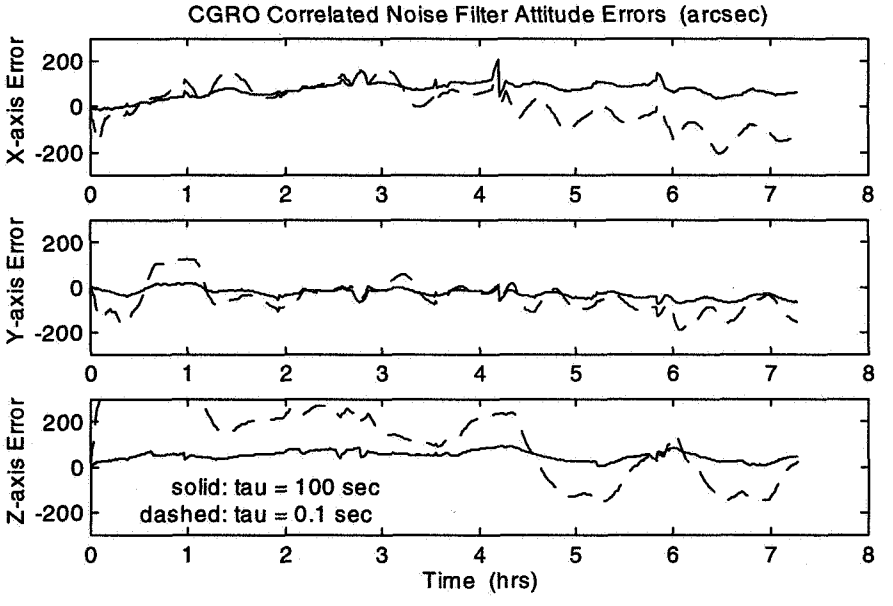

Figure 3. Correlated Noise Filter attitude errors (arcsec) for correlation times of 100 sec (solid) and 0.1 sec (dashed).

Figure 4 presents the systematic residual error estimates, ε, attributed to reference magnetic field model errors. The values of ε are corrections to be added to the magnetic field model in the inertial frame. Although the time dependence of the errors do not reduce to a simple pattern, the dominant orbital frequency and some low multiples are apparent.

Essentially the same solution for the residuals is found for larger values of the correlation time. Some of the high frequencies (jitter) are suppressed when τ is increased to 1000 sec, but all the low frequency structure remains. It is probable, though, that the high frequencies represent uncorrelated noise that needs to be present to reflect the relative contributions from σ_{TAM} and σ_{corr}.

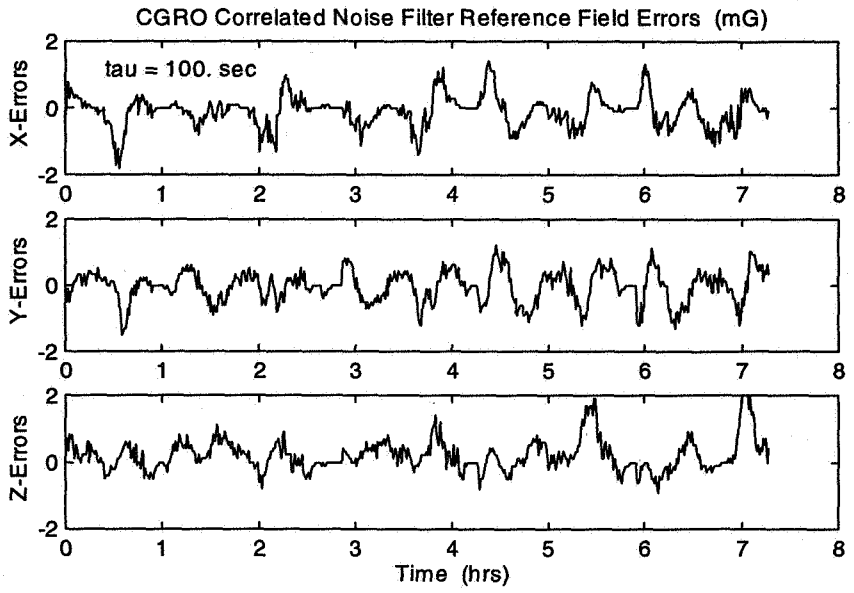

Figure 4. Reference field errors (mG) estimated by the Correlated Noise Filter for correlation time of 100 sec.

If the field errors shown in Figure 4 are an accurate estimate of systematic errors in the reference field, then the difference between them and the "true" residuals should equal the random sensor errors. The "true" residuals are obtained by rotating the reference field into the body frame using the OBC attitude and subtracting it from the measured magnetic field. This true residual has much lower attitude error (based on the star trackers) but still has systematic errors from the field model and random errors from the TAM. Subtracting the field errors (rotated into the body frame) should leave only the random TAM error. The result of this difference is shown in Figure 5. The systematics have been largely removed leaving a random component of a few tenths of a milliGauss. The TAM digitization in the CGRO telemetry is 0.3 mG.

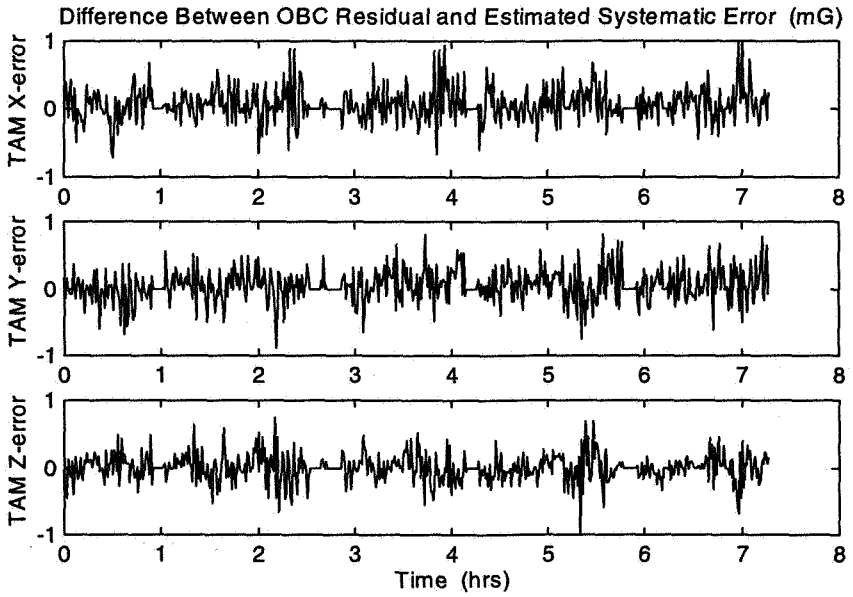

Figure 5. Difference between TAM residual based on OBC attitude and Correlated Noise Filter estimate of systematic error (mG); correlation time = 100 sec.

5. Conclusions

Problems with magnetometer/gyroscope based attitude and bias estimators were attributed to errors in the reference magnetic field. Tuning a Kalman filter to have a short memory time allowed the estimated IRU bias to follow these systematic errors. A modified filter was built and tested to account for the systematic error explicitly. Estimating these field errors improved the attitude and bias estimates significantly. The field error was modeled as an exponentially correlated random variable. This introduced two new parameters: the correlation time τ and the systematic noise σ_{corr}.

The correlated noise filter is not limited to the problem studied in this paper. This approach is useful in any situation where a sensor is subject to both random and systematic noise. The need for a nonzero value for the random noise should be emphasized. To avoid becoming ill-conditioned, the noise source ν in Eq. (20) cannot vanish. This term is the only effective sensor noise in the augmented filter. Without it, the augmented state error covariance goes to zero after a single filter update. On the next update, the Kalman gain avoids being singular only through the gyroscope process noise accumulated between measurements, which may be very small.

It is possible that even with nonzero random TAM noise, there may still be problems with this filter. Some peculiarities with the state error covariance have been seen. For many of the tests, it was found that the attitude and bias uncertainties are still increasing after 5 orbits. However, the covariance does appear to converge properly when the filter is initialized far from the known true state.

An alternative approach is given in Reference 9. This involves forming a linear combination of successive sensor residuals designed to cancel the correlated noise term, ε. The filter update then involves observations from two time steps. With this filter design, the update step actually is a smoother with a one-time-step look-ahead.

The results reported in this paper are still very preliminary. The next steps will involve a more thorough investigation of the tuning parameters. A wider range of values for τ, σ_{TAM}, and σ_{corr} should be tried along with various initial conditions. Then, stability questions must be addressed with studies using longer data sets. Finally, the one-time-step smoother approach of Reference 9 should be implemented and compared to the current results.

References

1. M. Challa, G. Natanson, and C. Wheeler, "Simultaneous Determination of Spacecraft Attitude and Rates Using Only a Magnetometer," *Proceedings of the AIAA/AAS Astrodynamics Specialists Conference*, July 1996
2. J. Hashmall, K. Liu, and M. Rokni, "Accurate Spacecraft Attitudes from Magnetometer Data," *Proceedings of the Spaceflight Dynamics Conference*, Toulouse, France, June 1996
3. J. Hashmall, "GRO TAM Calibration," informal presentation to NASA Goddard Space Flight Center, April 25, 1996
4. W. Davis, et al., "The Results of the In-Flight Attitude Sensor Calibration for the Arthur Holly Compton Gamma Ray Observatory," *Proceedings of the Flight Mechanics/Estimation Theory Symposium*, NASA Goddard Space Flight Center, May 1992

5. Goddard Space Flight Center, Flight Dynamics Division, 554-FDD-91/070R1UD0, *Multimission Three-Axis Stabilized Spacecraft (MTASS) Flight Dynamics Support System Functional Specifications, Revision 1*, J. Landis, September 1995

6. J. Sedlak and D. Chu, "Kalman Filter Estimation of Attitude and Gyro Bias with the QUEST Observation Model," *Proceedings of the AAS/GSFC International Symposium on Space Flight Dynamics*, April 1993

7. R. L. Farrenkopf, "Generalized Results for Precision Attitude Reference Systems Using Gyros," AIAA Paper 74-903, August 1974

8. J. Hashmall, H. Kang, and S. Underwood, "The On-Orbit Use of Spacecraft Attitude Magnetometers for Refining Near-Earth Magnetic Fields," presented at the *31st COSPAR Scientific Assembly*, Birmingham, UK, July 1996

9. A. E. Bryson Jr. and I. J. Henrikson, "Estimation Using Sampled Data Containing Sequentially Correlated Noise," *J. Spacecraft* and *Rockets*, Vol. 5, pp. 662-665, June 1968

10. E. J. Lefferts, F. L. Markley, and M. D. Shuster, "Kalman Filtering for Spacecraft Attitude Estimation," *J. Guidance, Control, and Dynamics*, Vol. 5, No. 5, Sept.-Oct. 1982, pp. 417-429

Page intentionally left blank

ESTIMATING ATTITUDE, TRAJECTORY, AND GYRO BIASES IN AN EXTENDED KALMAN FILTER USING EARTH MAGNETIC FIELD DATA FROM THE ROSSI X-RAY TIMING EXPLORER

Julie Deutschmann
National Aeronautics and Space Administration
Flight Dynamics Division/Code 552
Goddard Space Flight Center
Greenbelt, Maryland 20771
email: julie.deutschmann@gsfc.nasa.gov
fax: 301-344-8909

Itzhack Bar-Itzhack
Sophie and William Shamban Professor of Aerospace Engineering
Faculty of Aerospace Engineering
Technion-Israel Institute of Technology
Haifa 32000 Israel
email: ibaritz@techunix.technion.ac.il
fax: 972-4-823-1848

ABSTRACT

Traditionally satellite attitude and trajectory have been estimated with completely separate systems, using different measurement data. The estimation of both trajectory and attitude for low earth orbit satellites has been successfully demonstrated in ground software using magnetometer and gyroscope data. Since the earth's magnetic field is a function of time and position, and since time is known quite precisely, the differences between the computed and measured magnetic field components, as measured by the magnetometers throughout the entire spacecraft orbit, are a function of both the spacecraft trajectory and attitude errors. Therefore, these errors can be used to estimate both trajectory and attitude. This work further tests the single augmented Extended Kalman Filter (EKF) which simultaneously and autonomously estimates spacecraft trajectory and attitude with data from the Rossi X-Ray Timing Explorer (RXTE) magnetometer and gyro-measured body rates. In addition, gyro biases are added to the state and the filter's ability to estimate them is presented.

INTRODUCTION

In this work, we summarize the derivation of the EKF, highlighting the development of the measurement matrix, the crucial element in combining the dependence of the magnetic field residuals on both attitude and trajectory estimation errors. The dynamics of both the attitude and trajectory errors are also briefly presented. Results from two spans of RXTE magnetometer and gyro data (one span includes 12 hours of data, the other includes 24 hours of data) are processed by the EKF. Comparisons are made with very accurate operational estimates computed at the NASA Goddard Space Flight Center (GSFC) Flight Dynamics Division (FDD). These comparisons are presented in the paper. Finally, the state vector is expanded to include gyro biases. The ability of the EKF to estimate gyro biases along with the attitude and trajectory is presented.

Many future low-budget missions, such as the NASA Small and Mid-Size Explorer Series and university class explorers, are looking for low cost and autonomous approaches to orbit and attitude estimation. This work could prove valuable to these missions as a prime trajectory and attitude estimation system, with coarse accuracy requirements, or a backup to a prime system where more stringent accuracy is required.

The magnetometer, due to its reliability and low cost, has been the focus of many studies in the recent past. Emphasis has been placed on using the magnetometer alone, without any additional input, to estimate the spacecraft trajectory [1, 2, and 3] and attitude [4 and 5]. Studies have also been performed to determine the ultimate accuracy of the magnetometer in estimating attitude when accurate rate information is available [6].

Both attitude and trajectory have been successfully estimated using simulated magnetometer data and gyro data [7]. Large initial errors were applied with a resulting accuracy of 4 km root sum square (RSS) in position and less than 1 degree (RSS) in attitude. In this work, we continue the testing of [7], applying the EKF to real RXTE data. The ability of the filter to overcome large initial errors and estimate gyro bias in addition to the attitude and trajectory is presented, along with the final accuracy achieved once the filter has reached steady state.

EXTENDED KALMAN FILTER ALGORITHM

The EKF algorithm is based on the following assumed models:

System Model:

$$\dot{\underline{X}} = \underline{f}(\underline{X}(t),t) + \underline{w}(t) \tag{1}$$

Measurement Model:

$$\underline{Z}_k = \underline{h}_k(\underline{X}(t_k)) + \underline{v}_k \tag{2}$$

where $\underline{w}(t)$ is a zero mean white process noise, $\underline{v}_k$ is a zero mean white sequence measurement error, and $\underline{X}(t)$ is the state vector defined as

$$\underline{X}^T = [a, e, i, \Omega, \omega, \theta, C_d, \underline{q},]$$

The first six elements of $\underline{X}(t)$ are the classical Keplerian elements which determine the spacecraft position and velocity, namely, the semi-major axis (a), eccentricity (e), inclination (i), right ascension of the ascending node (Ω), argument of perigee (ω), and true anomaly (θ). C_d is the drag coefficient and $\underline{q}$ represents the attitude quaternion. When a considerable amount of gyro bias is present in the measured rates, the state $\underline{X}$ is expanded to include gyro bias, $\underline{b}$.

Measurement Update Stage:

The linearization of equation (2) results in

$$\underline{z}_k = H_k \underline{X'}_k + \underline{v}_k \tag{3}$$

where $H_k = [H_o \mid H_a]$

$\underline{X'}_k = [a, e, i, \Omega, \omega, \theta, C_d, \underline{\alpha}]$

H_o is the measurement matrix for the orbital states and is derived in [1]. H_a is the measurement matrix for the attitude states, $\underline{\alpha}$, a vector of three small angles, representing the error in the attitude estimate. The derivation of H_a is given in [7]. The effective measurement used by the filter is given as

$$\underline{z}_k = \underline{B}_{m,k} - \underline{B}(\hat{\underline{X}}_k, t_k) \tag{4}$$

where

$\underline{B}_{m,k}$ = the magnetic field vector measured by the magnetometer

$\underline{B}(\hat{\underline{X}}_k, t_k)$ = the estimated magnetic field vector as a function of the estimated state at time t_k

The estimated magnetic field vector is dependent on both the position and attitude, which is seen in the expansion of equation (3) in [7].

The state update equation is

$$\hat{\underline{X}}_k(+) = \hat{\underline{X}}_k(-) + K_k \underline{z}_k \tag{5}$$

where K_k is the Kalman gain computed according to

$$K_k = P_k(-)H_k^T[H_k P_k(-)H_k^T + R_k]^{-1} \tag{6}$$

R_k is the covariance matrix of the measurement error, $\underline{v}_k$. The covariance matrix of the estimation error is updated as usual with

$$P_k(+) = [I - K_k H_k]P_k(-)[I - K_k H_k]^T + K_k R_k K_k^T \tag{7}$$

Equation (5) is used to update the orbital states, but not the attitude states. The update of the attitude states is done as follows. As shown above, the state vector contains the attitude represented by a quaternion. The EKF estimates an error in the attitude, expressed as $\underline{\alpha}$. The estimated error is converted to a quaternion and is appropriately combined with the current estimate of the quaternion to give an updated estimate of the quaternion, which is then propagated to the next time point.

Propagation Stage:

The filter dynamics model is given as

$$\underline{X}'_{k+1} = A_k(\underline{X}'_k)\,\underline{X}'_k + [\underline{w}_o^T \; \underline{w}_a^T]^T \tag{8}$$

$A_k(\underline{X}'_k)$ is the transition matrix of the linearized dynamics equation. It is composed of A_o, the transition matrix for the linearized orbital dynamics and is a function of the estimated orbital states, and A_a, the transition matrix for the attitude error, $\underline{\alpha}$. A_a is based on the development from [8]. A_o is defined in [9]. The transition matrices A_o and A_a are first order approximations computed from the Jacobian $F_k(\underline{X}_k)$ derived from the linearization of equation (1). When there is a need, the added gyro bias is modeled as a constant, resulting in A_k being expanded to include an additional 3x3 identity matrix along the main diagonal and off-diagonal elements to tie the gyro bias to the propagation of the quaternion error, similar to the development given in [8].

The covariance matrix is propagated from time t_k to time t_{k+1} using:

$$P_{k+1}(-) = A_k(\hat{\underline{X}}'(+)_k)P_k(+)A_k(\hat{\underline{X}}'(+)_k)^T + Q_k \tag{9}$$

Q_k is the process noise covariance matrix for both the orbit and attitude states. The estimated orbit and attitude states are propagated by solving equation (1) numerically, without the noise component.

RESULTS

The EKF was tested with real magnetometer and gyro data from the RXTE satellite. The data selected was from January 19, 1996 (SPAN 1, covering 12 hours) and September 8, 1996 (SPAN 2, covering 24 hours), respectively. The tests performed with SPAN 1 did not include the estimation of gyro bias. However, for testing with SPAN 2, the state was expanded to include gyro bias. The test results for SPAN 1 are presented first. The results using SPAN 2 follow.

In SPAN 1 the spacecraft underwent a series of attitude maneuvers throughout the data span. Figure 1 shows the spacecraft attitude yaw, roll, and pitch angles, respectively. The attitude angles represent a 3-1-2 Euler rotation from inertial to spacecraft body coordinates.

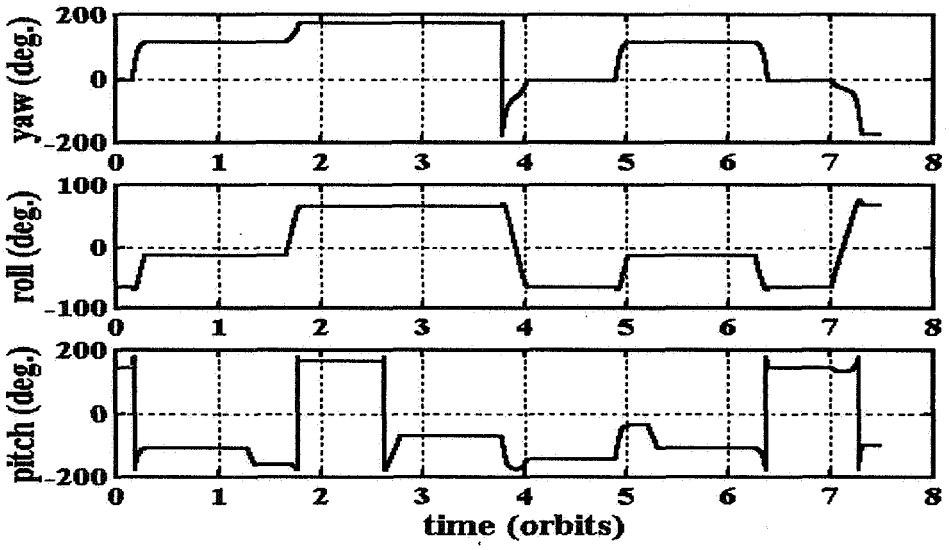

Figure 1: RXTE True Attitude

Using SPAN 1, the filter was initially started with large errors in position, velocity and attitude. The initial position error was 1425.4 km, the initial velocity error was 1.6 km/sec and the attitude error was 17.2 degrees (all RSS). The errors are determined by comparing the filter position, velocity, and attitude estimates to accurate position, velocity, and attitude estimates computed on the ground at the NASA GSFC FDD. Because of non-white components in the residuals ($\underline{z}_k$ from equation (4)), the filter state was expanded to include a first order Markov process and bias component as was done in [9], with the exception that the Markov and bias are uncoupled. The filter results are shown in Figures 2, 3, 4 (RSS position and velocity errors), and 5 (RSS attitude error). The final RSS position and velocity errors are reduced to averages of 25-30 km and less than 0.05 km/sec, respectively, and 1-3 degrees RSS for the attitude errors.

The steady state results of Figures 2, 3, 4 and 5 contain significant error. One possible cause of these errors may be the strong correlation of the position estimate to errors in the attitude estimate. When there is an increase in the attitude covariance (uncertainty), as shown in Figure 6, the position error increases. *The attitude covariance increases when the spacecraft undergoes an attitude maneuver, as would be expected. After a maneuver, the attitude estimate needs time to converge to the new attitude, this also*

affects the position estimate. The final filter estimates are also dependent on the choice of the initial state and initial covariance and also the values selected for the measurement noise matrix and the process noise covariance matrix. *Finally, the additional Markov parameters improve the final estimates but perhaps do not adequately model the disturbance in the measurement data.*

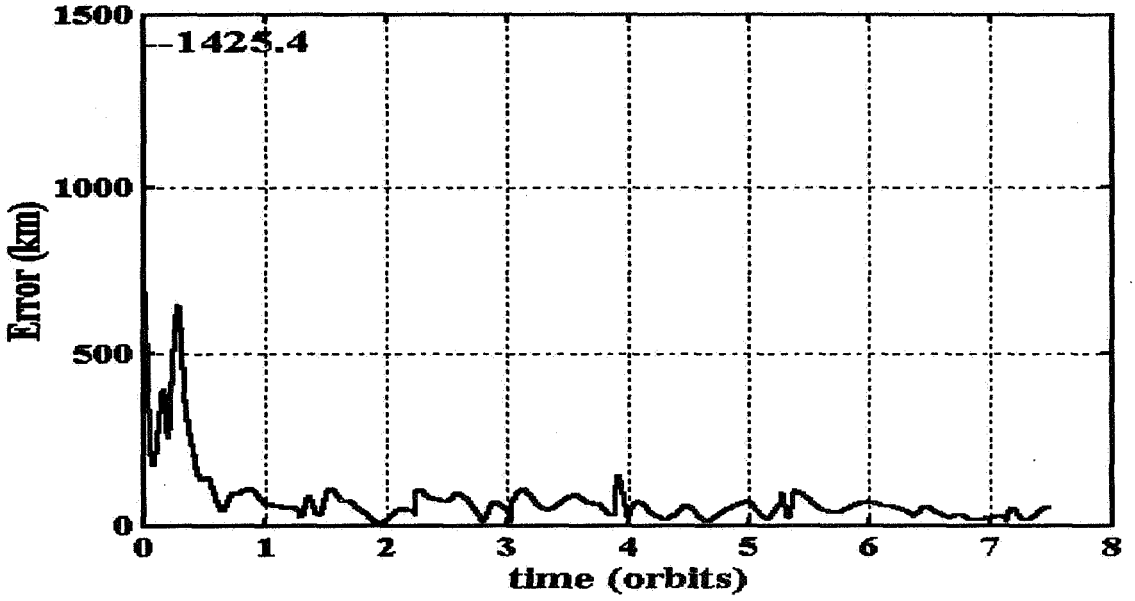

Figure 2. RSS Position Error (SPAN 1)

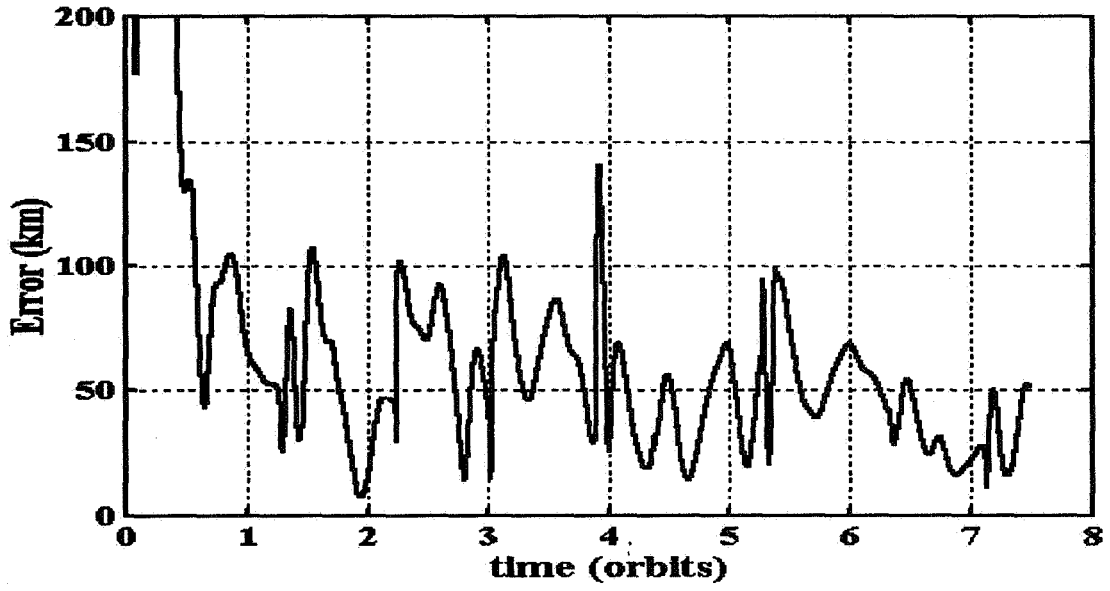

Figure 3. RSS Position Error with an Expanded Vertical Axis (SPAN 1)

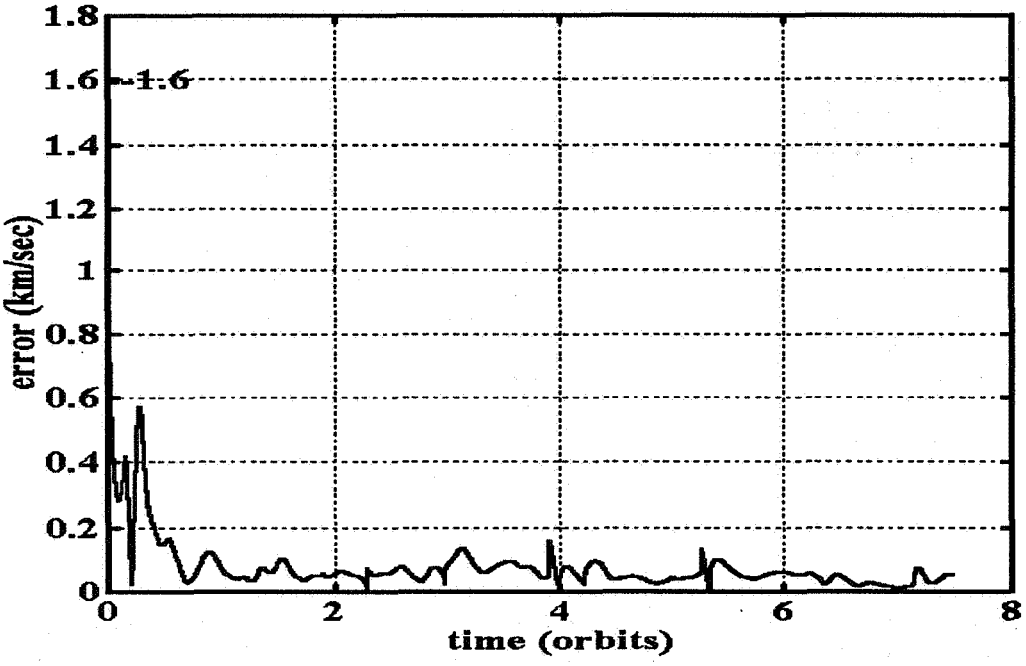

Figure 4. RSS Velocity Error (SPAN 1)

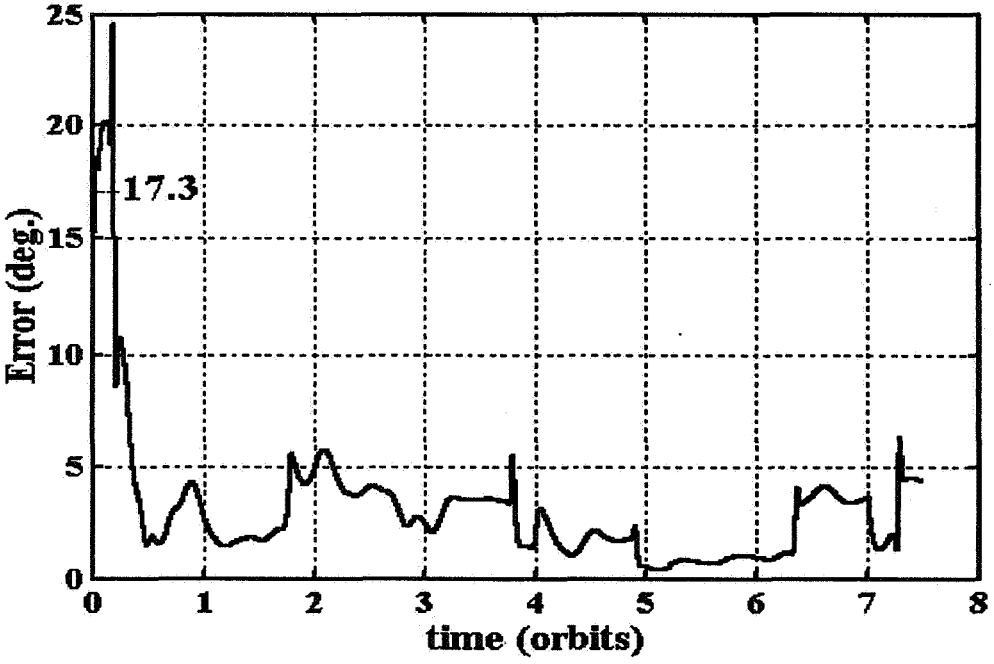

Figure 5. RSS Attitude Error (SPAN 1)

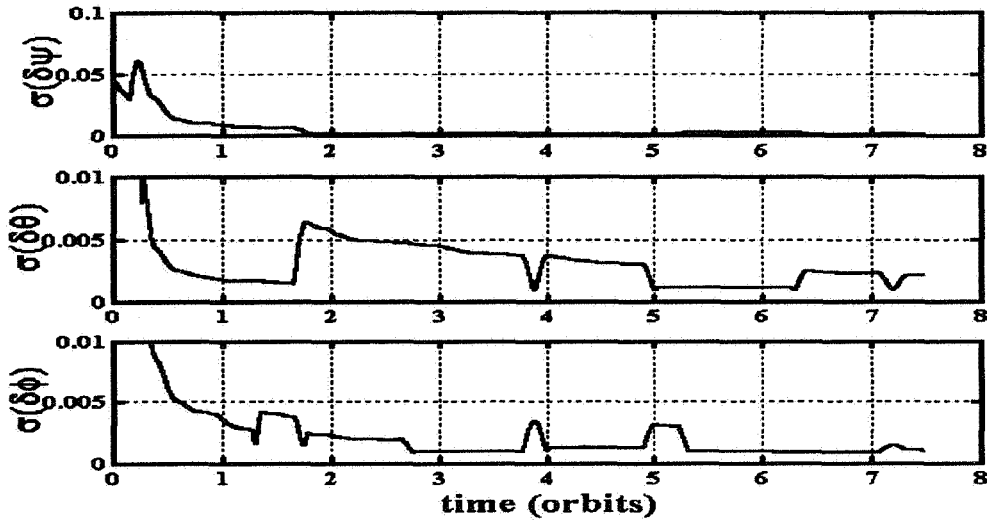

Figure 6. Uncertainty in Attitude Error

Tests were then conducted on the second set of RXTE data. In SPAN 2 RXTE underwent only 3 attitude maneuvers during the 24 hour span. The gyro data was not compensated for any bias and the filter state was expanded to include gyro bias. The state also includes the Markov and bias for the magnetometer.

Figures 7 through 12 show the RSS position, velocity, and attitude errors, full size and with an expanded vertical axis, respectively. The initial errors are shown on the figures. The initial position error is comparable to that used for SPAN 1, but the initial velocity and attitude errors are slightly smaller. Smaller errors were chosen in hopes of reducing the length of time for convergence. The final errors are lower than those for SPAN 1 for position, velocity, and attitude. The average steady state errors are approximately 20 km for position, 0.025 km/sec for velocity; and less than 1 degree for attitude (all RSS). Also, the filter has very large jumps initially in position, velocity, and attitude. They are considerably larger than the results using SPAN 1.

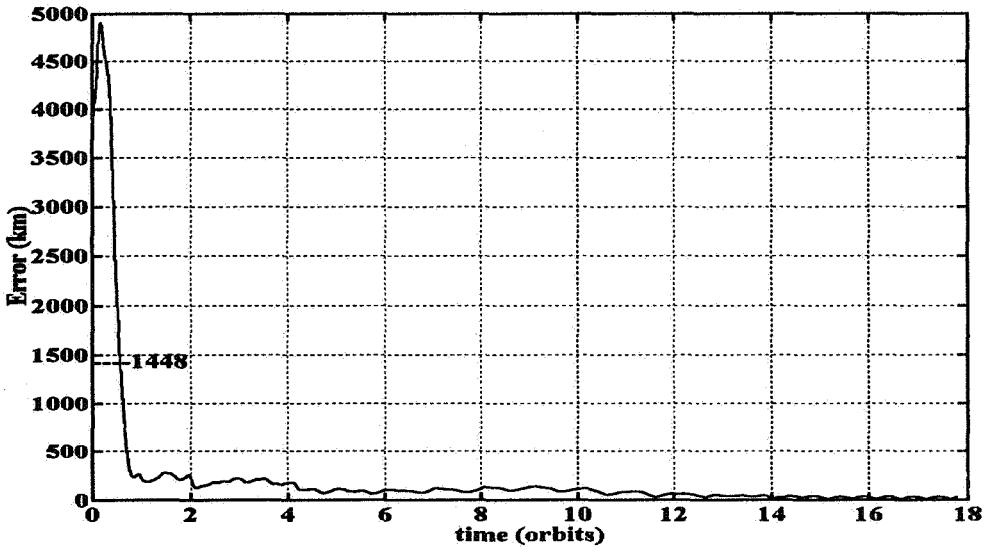

Figure 7. RSS Position Error Using SPAN2, Including Gyro Biases.

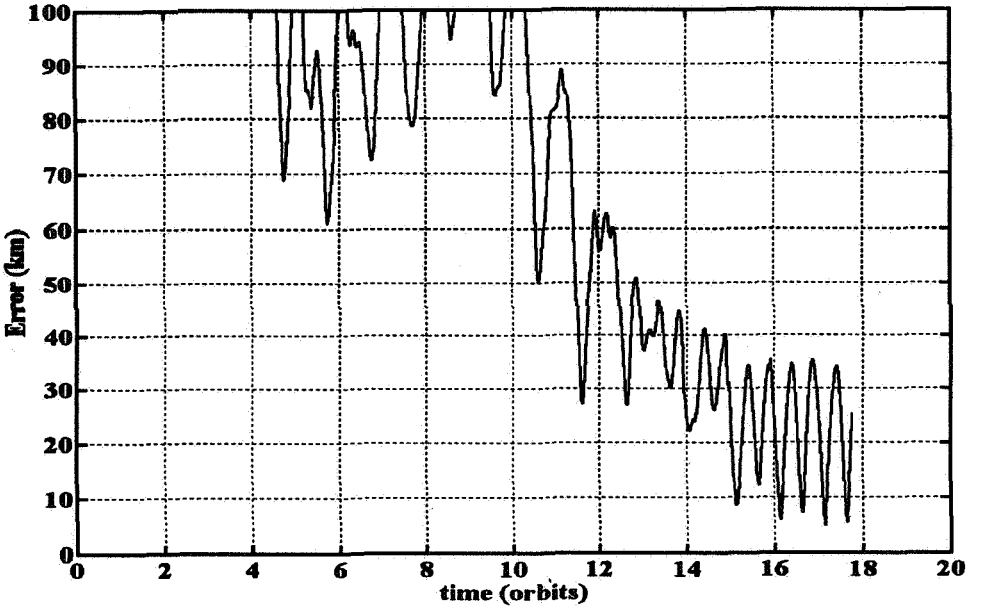

Figure 8. RSS Position Error Using, SPAN 2, Including Gyro Biases - Expanded Vertical Axis

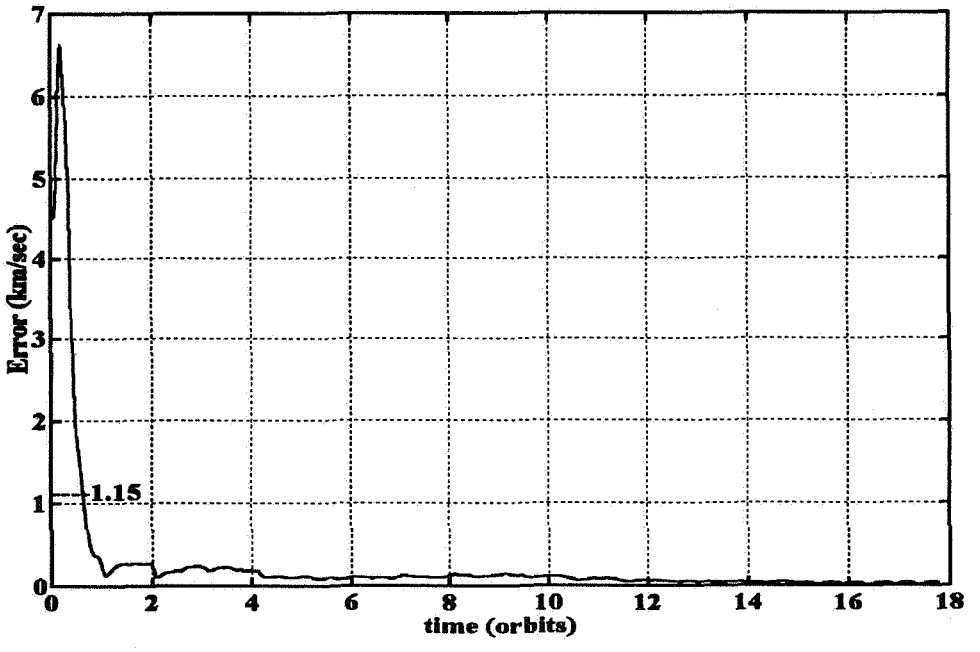

Figure 9. RSS Velocity Error Using SPAN 2, Including Gyro Biases

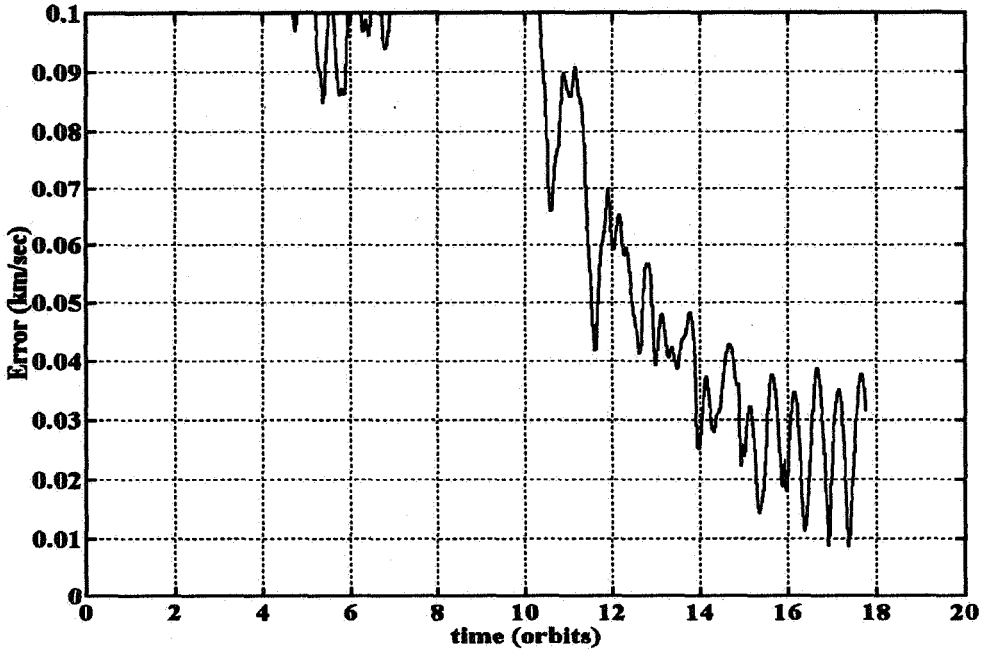

Figure 10. RSS Velocity Error Using SPAN 2, Including Gyro Biases, Expanded Vertical Axis

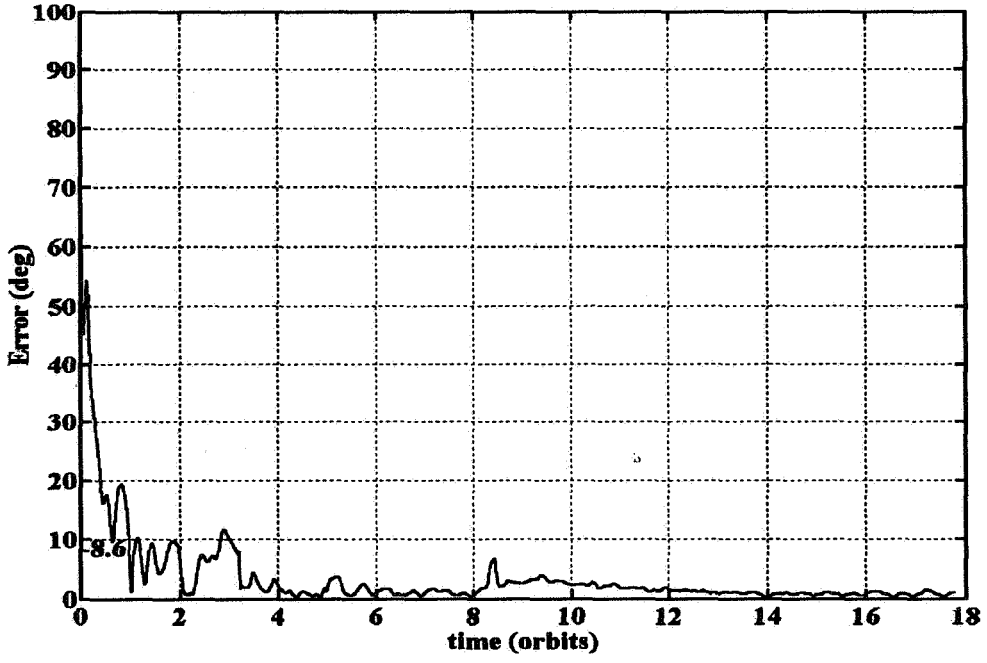

Figure 11. RSS Attitude Error Using SPAN 2, Including Gyro Biases

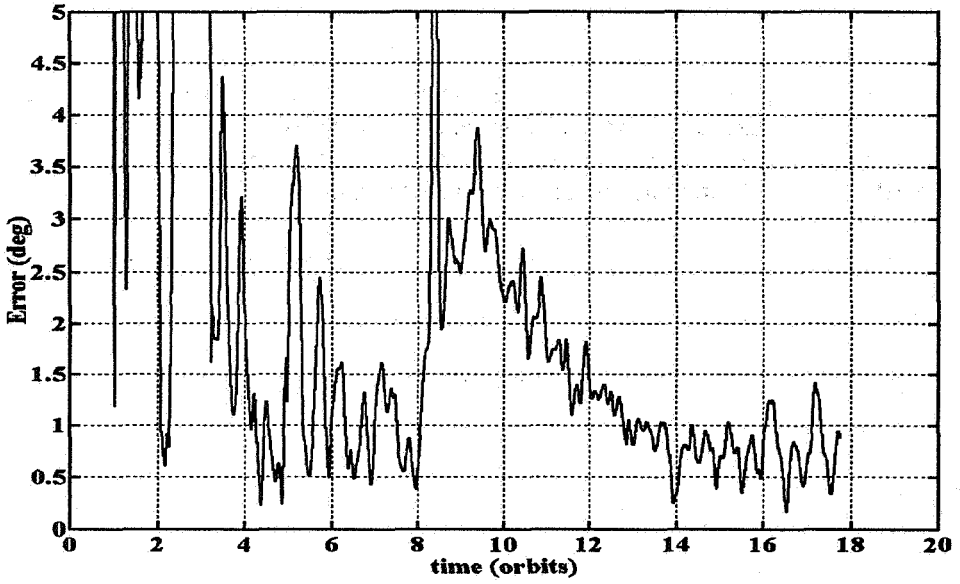

Figure 12. RSS Attitude Error Using SPAN 2, Including Gyro Biases, Expanded Vertical Axis

Finally, the estimates of gyro bias were compared to the bias computed operationally in the NASA GSFC FDD, considered as the 'true' gyro bias. The 'true' gyro bias available for comparison was a value computed on previous RXTE data. An operational gyro bias was not available for SPAN 2. The estimated gyro bias was considerably smaller than the 'true' gyro bias. An artificial gyro bias (0.2 deg/hr per axis) was then added to the gyro data of SPAN 2. The filter estimates of this artificial gyro bias are shown in Figures 13, 14, and 15, along with the 'truth' which is the 'true' bias plus the added bias. The estimates of the x and z gyro bias compare to the 'truth' to within 0.5 deg/hr (the x gyro bias begins to change at the end, though). This is a considerable difference for spacecraft gyros. The y

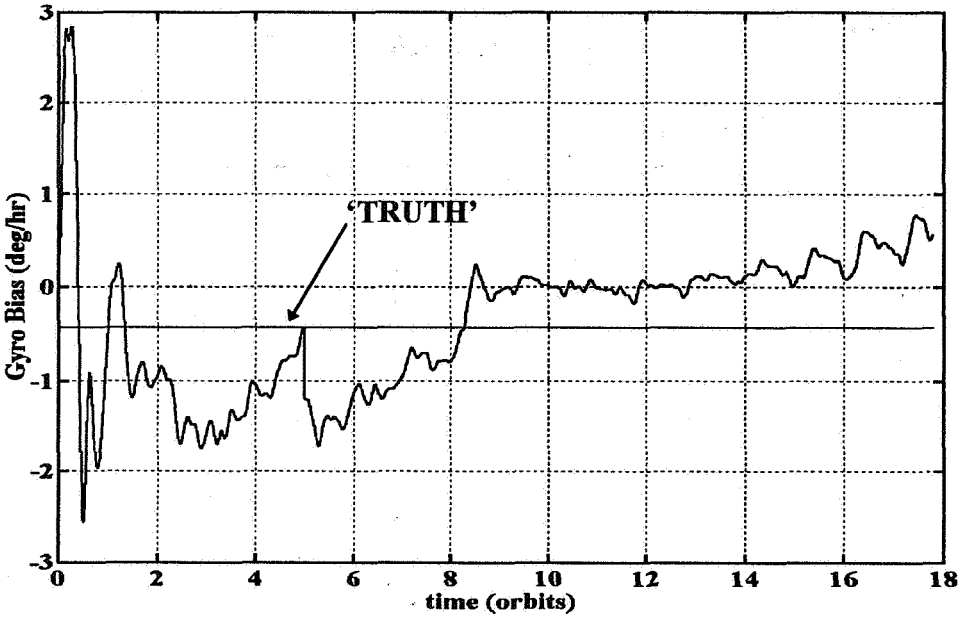

Figure 13. X Gyro Bias Estimate and 'Truth', Using SPAN 2

gyro bias appears to converge to the 'truth' at the end of the data, but could obviously continue beyond the 'truth'. Additional data would be necessary to determine if it has actually converged. Further tuning is necessary to determine if the accuracy of the gyro bias can be improved. Obtaining a true operational gyro bias for SPAN 2 would also be helpful in analyzing the accuracy.

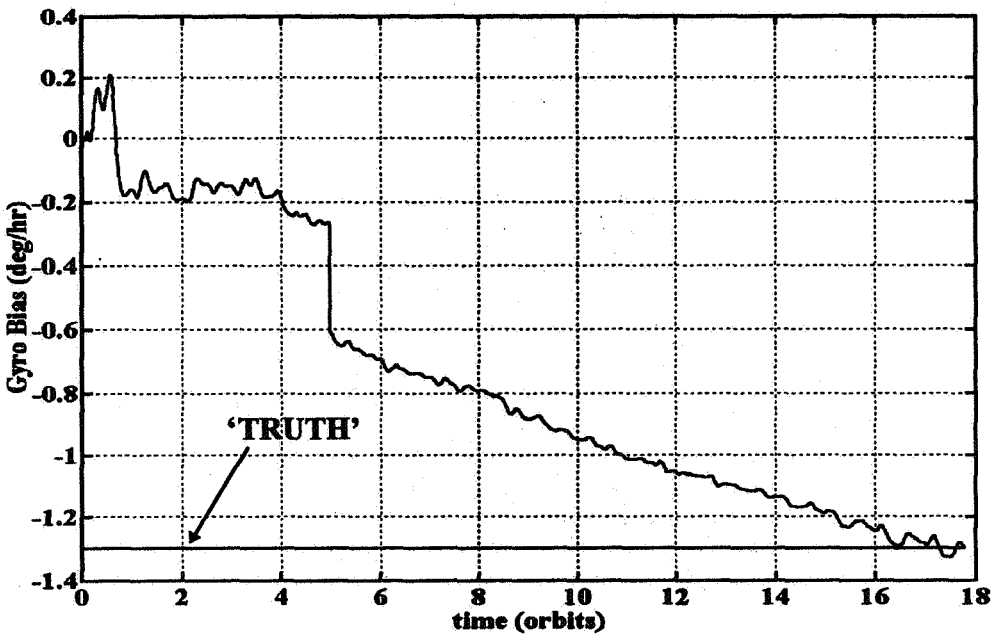

Figure 14. Y Gyro Bias Estimate and 'Truth', Using SPAN 2

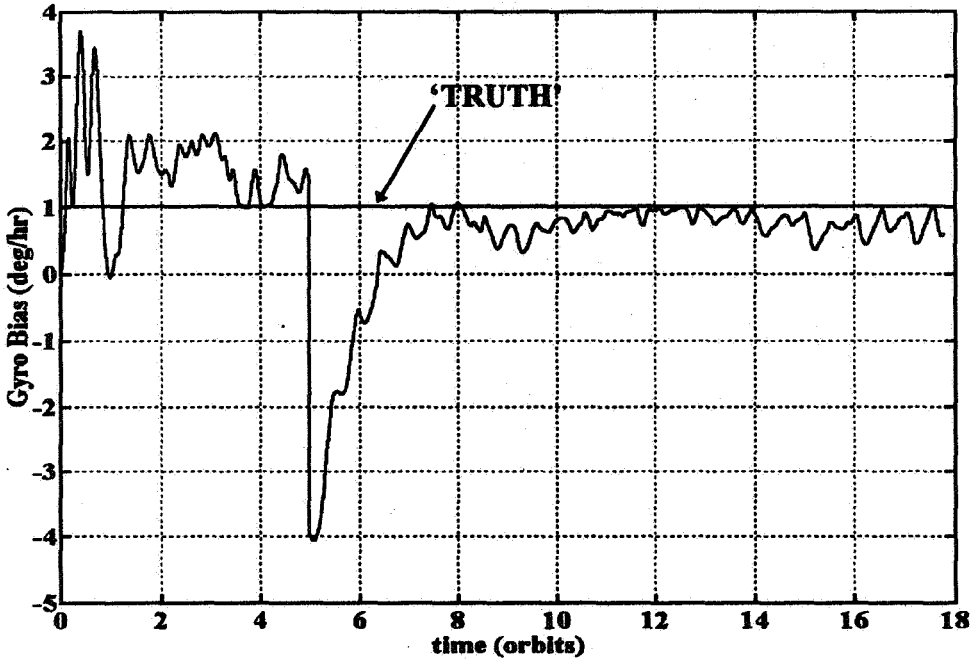

Figure 15. Z Gyro Bias Estimate and 'Truth', Using SPAN 2

The steady state results obtained from SPAN 2 show smaller errors in position, velocity, and attitude than those in the steady state of SPAN 1. SPAN 2 contains more data, with fewer attitude maneuvers. The estimate converges quicker with SPAN 1, but with a resulting steady state accuracy that is worse. Perhaps the multiple attitude maneuvers give increased observability, allowing for faster convergence, but result in larger steady state errors due to the correlation of the position with the attitude errors. When a significant gyro bias exists, estimating that bias may also improve the results slightly. Finally, conditions on the spacecraft may have changed from the time the data for SPAN 1 was recorded to the time of SPAN 2 and therefore the Markov model parameters may have changed. Further tuning studies are necessary to determine this.

CONCLUSIONS

The EKF presented was tested with 2 spans of real magnetometer and gyro data from the RXTE spacecraft. The filter was able to overcome very large initial errors, over 1400 km in position, 1.6 km/sec in velocity, and 17.2 degrees in attitude (all RSS), and converge to steady state averages less than 30 km in position, 0.05 km/sec in velocity, and 3 degrees in attitude (RSS) with the first span of data. With the second data span, the filter achieved steady state averages of approximately 20 km in position, 0.025 km/sec in velocity, and 0.75 degrees in attitude (all RSS), all lower than the steady state results of the first data span. In the first span, several attitude maneuvers and unknown disturbances in the measurement data, may be the reason for the larger final errors. In the second span, the data also contained unknown disturbances, but the length of the data span, lower initial errors in velocity and attitude, and the addition of the gyro bias may have improved the final results, even though the gyro bias was only estimated to within 0.5 deg/hr of the 'truth'. Additional analysis of the measurement data may help to identify the disturbances and further study and tuning may help to determine the extent of the correlation between the position and attitude error estimates, and improve the final results.

REFERENCES

1. Shorshi, G. , and Bar-Itzhack, I., "Satellite Autonomous Navigation Based on Magnetic Field Measurements", Journal of Guidance, Control, and Dynamics, Vol. 18, No. 4, July-August, 1995, pp. 843-850.

2. Ketchum, E., "Autonomous Spacecraft Orbit Determination Using the Magnetic Field and Attitude Information", Paper No. AAS 96-005, presented at the 19th Annual AAS Guidance and Control Conference, Breckenridge, Colorado, February 1996.

3. Psiaki, M., "Autonomous Orbit and Magnetic Field Determination Using Magnetometer and Star Sensor Data", Journal of Guidance, Control, and Dynamics, Vol. 18, No. 3, May-June 1995, pp. 584-592.

4. Challa, M., Natanson, G., Deutschmann, J., and Galal, K., "A PC-Based Magnetometer-Only Attitude and Rate Determination System for Gyroless Spacecraft", Paper No. 07, presented at the GSFC FDD Flight Mechanics/Estimation Theory Symposium 1995, NASA Goddard Space Flight Center, Greenbelt, Maryland, May 16-18, 1995.

5. Martel, F., Pal, P., and Psiaki, M., "Three-Axis Attitude Determination via Kalman Filtering of Magnetometer Data", presented at the GSFC FDD Flight Mechanics/Estimation Theory Symposium 1988, NASA Goddard Space Flight Center, Greenbelt, Maryland, May 10-11, 1988.

6. Hashmall, J., Liu, K., and Rokni, M., "Accurate Spacecraft Attitudes from Magnetometer Data", Paper No. MS95/007, presented at the CNES International Symposium on Space Dynamics, Toulouse, France, June 19-23, 1995.

7. Deutschmann, J. and Bar-Itzhack, I., "Attitude and Trajectory Estimation Using Earth Magnetic Field Data", Paper No. AIAA-96-3631, presented at the AIAA/AAS Astrodynamics Conference, San Diego, CA, July 29-31, 1996.

8. Deutschmann, J. Bar-Itzhack, I., and Rokni, M., "Comparison and Testing of Extended Kalman Filters for Attitude Estimation of the Earth Radiation Budget Satellite", presented at the GSFC FDD Flight Mechanics/Estimation Theory Symposium 1990, NASA Goddard Space Flight Center, Greenbelt, Maryland, May 22-24, 1990.

9. Shorshi, G. and Bar-Itzhack, I., "Satellite Autonomous Navigation Based on Magnetic Field Measurements", TAE No. 714, Technion-Israel Institute of Technology, Haifa, Israel, April 1994.

Page intentionally left blank

Attitude and Trajectory Determination Using Magnetometers and Estimated Rates†

J. D. Schierman
D. K. Schmidt
Flight Dynamics and Control Laboratory
University of Maryland
College Park, MD 20742-3200

J. Deutschmann
National Aeronautics and Space Administration
Goddard Space Flight Center
Greenbelt, MD 20771

Abstract

A simultaneous attitude and orbit determination algorithm which uses magnetometer measurements and *estimated* attitude rates is presented. This is an extension of an algorithm which uses magnetometer and rate gyro measurements. The new algorithm is intended for gyroless spacecraft, or in the case of gyro failures/saturation. Torque control input data is used in forming the rate estimates. Simulation tests of the algorithm are presented. First, tests were performed using the "true" rate values at each time step. This simulated using accurate gyro measurements. Then, tests were performed estimating the rates. Using estimated rates rather than "gyro measurements" did not significantly degrade the algorithm's performance if accurate estimates of the initial rates were available. An initial Root-Sum-Square (RSS) position error of 1,400 km was reduced to an average error of approximately 100 km within the first two minutes. The RSS attitude error converged to less than 1.5 degrees within three orbits.

1. Introduction

The motivation for the current study is based on the desire to autonomously estimate both attitude and orbit position using a reduced/low cost sensor complement. Because the Earth's magnetic field is both direction and position dependent, estimates of both attitude and orbit trajectory may be theoretically obtained using magnetometers. Using the magnetometer is advantageous because it is a historically reliable, inexpensive instrument. Some current and future spacecraft missions have only course accuracy requirements, and attitude/position estimates from magnetometers may be adequate for such missions. Magnetometers may also be useful as back-up systems in the event of other sensor failures.

A number of algorithms have been proposed that estimate spacecraft attitude and/or attitude rate utilizing Three Axis Magnetometer (TAM) measurements [1]-[6]. These include both deterministic and Extended Kalman Filtering (EKF) approaches. TAM measurements may also be used in estimating orbit position, and several algorithms have been proposed to accomplish this task [7]-[10]. These algorithms include deterministic, EKF and batch least-squares approaches. However, several of these algorithms assume accurate attitude information is available from other instruments, such as star sensors.

In Ref. [11], Deutschmann and Bar-Itzhack proposed a unique EKF algorithm that uses TAM measurements to *simultaneously* estimate both the spacecraft's attitude and orbit position. The algorithm requires attitude rate information, and it was assumed that accurate rate measurements were available from gyros.

Our research objective is to develop an attitude/orbit determination algorithm which uses TAM measurements, but does not require rate gyro measurements. Hence, the approach suggested herein is an extension of the approach of Ref. [11]. The new algorithm autonomously and simultaneously estimates attitude and position using TAM measurements and torque control input information. Control inputs may be from, for example, momentum wheels or magnetic torquers.

---

† Presented at the Flight Mechanics Symposium, NASA Goddard Space Flight Center, May, 1997

The paper is organized as follows. The development of the baseline algorithm is presented in Section 2, and test results with simulated data are presented in Section 3. Extensions to the algorithm are proposed in Section 4. Finally, conclusions and future directions are discussed in Section 5.

2. Baseline Algorithm Development

The estimation technique is based on an augmented EKF algorithm [12]-[14], which will be described after discussing the model of the system dynamics.

2.1 The "Truth" Model

The "truth" model consisted of the following nonlinear spacecraft dynamic model,

$$\dot{\vec{x}}(t) = \vec{f}(\vec{x}(t),\vec{u}(t),t) + \vec{w}(t) \equiv \begin{bmatrix} \dot{\vec{x}}_o(t) \\ \dot{\vec{q}}(t) \\ \dot{\vec{\omega}} \end{bmatrix} = \begin{bmatrix} \vec{f}_o(\vec{x}_o(t),t) \\ \vec{f}_q(\vec{q}(t),\vec{\omega}(t)) \\ \vec{f}_\omega(\vec{\omega}(t),\vec{u}(t)) \end{bmatrix} + \vec{w}(t) \tag{1}$$

The vector $\vec{w}(t)$ denotes zero mean white Gaussian process noise, and the torque control inputs are denoted by $\vec{u}(t)$. The state vector is defined as

$$\vec{x}(t) = [\vec{x}_o \quad \vec{q} \quad \vec{\omega}]^T \tag{2}$$

where $\vec{x}_o$ denotes the orbit states, $\vec{q}$ is the attitude quaternion, and $\vec{\omega}$ is the angular velocity. Specifically,

$$\begin{aligned} \vec{x}_o &= [a \quad e \quad i \quad \Omega \quad \omega \quad \theta \quad C_d]^T \\ \vec{q} &= [q_1 \quad q_2 \quad q_3 \quad q_4]^T \\ \vec{\omega} &= [\omega_x \quad \omega_y \quad \omega_z]^T \end{aligned} \tag{3}$$

The first six elements of $\vec{x}_o$ are the classical Keplarian orbital elements. Namely,

a = semi-major axis
e = eccentricity
i = inclination
Ω = right ascension of the ascending node
ω = argument of perigee
θ = true anomaly

Finally, C_d is the drag coefficient. Further details of the orbit dynamic model, (i.e. $\vec{f}_o(\vec{x}_o(t),t)$) can be found in Refs. [11] and [12].

The quaternion kinematics are governed by

$$\dot{\vec{q}}(t) = \frac{1}{2}\begin{bmatrix} 0 & \omega_z & -\omega_y & \omega_x \\ -\omega_z & 0 & \omega_x & \omega_y \\ \omega_y & -\omega_x & 0 & \omega_z \\ -\omega_x & -\omega_y & -\omega_z & 0 \end{bmatrix} \vec{q}(t) \equiv \vec{f}_q(\vec{q}(t),\vec{\omega}(t)) \tag{4}$$

where $\{\omega_x, \omega_y, \omega_z\}$ are the attitude rates expressed in body-fixed coordinates $\{\hat{x}, \hat{y}, \hat{z}\}$ [13].

The algorithm of Ref. [11] is extended here by estimating the attitude rates. The attitude dynamics are governed by the rotational equations of motion,

$$\vec{M}_c = \frac{d}{dt}(\vec{H}_c) + \vec{\omega} \times \vec{H}_c \tag{5}$$

where $\vec{H}_c$ denotes the spacecraft's total angular momentum about the center of mass. For the baseline "truth" model, it is assumed that the torque about the center of mass, $\vec{M}_c$, is dominated by applied torques, or that disturbance torques are negligible. Therefore, let

$$\vec{M}_c = \vec{T} = T_x \hat{x} + T_y \hat{y} + T_z \hat{z} \tag{6}$$

where T_x, T_y and T_z denote applied torques about each axis. Further, let the spacecraft be equipped with a momentum wheel with spin axis coincident to the spacecraft's $\hat{y}$-axis. The torque control vector is then defined as

$$\vec{u}(t) = [T_x \;\; T_y \;\; T_z \;\; \omega_w]^T \tag{7}$$

where ω_w denotes the wheel spin rate (assumed constant). Including the momentum wheel, the total angular momentum of the spacecraft is given by

$$\vec{H}_c = I_{sc}\vec{\omega} + \vec{I}_w \omega_w \tag{8}$$

where I_{sc} is the spacecraft's inertia tensor, and $\vec{I}_w = [0 \;\; I_w \;\; 0]^T$, with I_w the moment of inertia of the wheel. Substituting Eqs. (6) and (8) into Eq. (5) and solving for the angular acceleration results in

$$\dot{\vec{\omega}} = I_{sc}^{-1}\left\{\vec{T} - [\vec{\omega} \times] (I_{sc}\vec{\omega} + \vec{I}_w \omega_w)\right\} \equiv \vec{f}_\omega(\vec{\omega}(t),\vec{u}(t)) \tag{9}$$

where,

$$[\vec{\omega} \times] = \begin{bmatrix} 0 & -\omega_z & \omega_y \\ \omega_z & 0 & -\omega_x \\ -\omega_y & \omega_x & 0 \end{bmatrix} \tag{10}$$

Finally, the "truth" model also includes a measurement model. The measurements are considered to be taken at discrete intervals. The discrete measurement equation is

$$\vec{z}(k) = \tilde{B}_b(k) = \vec{h}(\vec{x}(k)) + \vec{v}(k) \tag{11}$$

where $\tilde{B}_b$ is the magnetic field vector measured in spacecraft-fixed coordinates. The measurement model, $\vec{h}(\vec{x}(k))$, is derived from the International Geomagnetic Reference Field (IGRF) model [12], [13]. The vector $\vec{v}(k)$ denotes zero mean white Gaussian measurement noise.

2.2 The EKF Algorithm

The EKF algorithm will be described in two stages, the propagation stage and the update stage.

Propagation Stage

The state estimate vector is denoted as $\hat{x}(t)$. State estimates are propagated over each time step from $\hat{x}_{k-1}(+)$ to $\hat{x}_k(-)$ according to the dynamic model of Eq. (1), without the noise component. Or,

$$\dot{\hat{x}}(t) = \vec{f}(\hat{x}(t),\vec{u}(t),t) \tag{12}$$

For the baseline algorithm, it is assumed that accurate torque control input information is available. Therefore, the same $\vec{u}(t)$ that drives the "truth" model in Eq. (1) is used in Eq. (12).

The quaternion is updated using estimates of three (assumed) small Euler angles [11], [15], calculated at the update stage to be discussed shortly. For the moment, assume the angles are available from the previous update, and denote them as

$$\vec{a} = [a_1 \quad a_2 \quad a_3]^T \tag{13}$$

Therefore, in the calculation of the error covariance and Kalman gains, the following "reduced" state vector is used,

$$\vec{x}_r(t) = [\vec{x}_o \quad \vec{a} \quad \vec{\omega}]^T \tag{14}$$

The error covariance matrix is propagated according to the equation

$$P_k(-) = \Phi(k,k-1)\, P_{k-1}(+)\, \Phi^T(k,k-1) + Q \tag{15}$$

Here, Q is the process noise spectral density matrix, and $\Phi(k,k-1)$ is an approximate state transition matrix, given by

$$\Phi(k,k-1) = I + F(k-1)\,\Delta T \tag{16}$$

Further, ΔT is the time step, and F(k-1) is the system Jacobian, evaluated at the current state estimate. That is,

$$F(k-1) = \left.\frac{\partial \vec{f}_r(\vec{x}_r(t),\vec{u}(t),t)}{\partial \vec{x}_r(t)}\right|_{\hat{x}_{r\,k-1}(+)} \tag{17}$$

Denoting,

$$F(k-1) = \begin{bmatrix} F_o & 0 & 0 \\ 0 & F_a & F_{a\omega} \\ 0 & 0 & F_\omega \end{bmatrix} \tag{18}$$

the Jacobian for the orbit dynamics, F_o (= 7x7), is developed in Ref. [12]. From Ref. [15],

$$F_a = \begin{bmatrix} 0 & \omega_z & -\omega_y \\ -\omega_z & 0 & \omega_x \\ \omega_y & -\omega_x & 0 \end{bmatrix} \tag{19}$$

Here, the estimates of the attitude rates are used in Eq. (19). In Refs. [11] and [15], rate gyro measurements are used instead. Further, $F_{a\omega}$ is

$$F_{a\omega} = \begin{bmatrix} 0 & -a_3 & a_2 \\ a_3 & 0 & -a_1 \\ -a_2 & a_1 & 0 \end{bmatrix} \tag{20}$$

Finally, the Jacobian of the attitude dynamics, F_ω (= 3x3), is obtained from

$$F_\omega = \frac{\partial \vec{f}_\omega(\vec{\omega}(t),\vec{u}(t))}{\partial \vec{\omega}(t)} \tag{21}$$

where $\vec{f}_\omega(\vec{\omega}(t),\vec{u}(t))$ is defined in Eq. (9).

Update Stage

The Kalman gain matrix is computed from

$$K(k) = P_k(-)\, H^T(k)\, [H(k)\, P_k(-)\, H^T(k) + R]^{-1} \tag{22}$$

where R is the measurement noise covariance matrix, and H(k) is the Jacobian of the measurement model, evaluated after state propagation. That is,

$$H(k) = \left.\frac{\partial \vec{h}(\vec{x}_r(t))}{\partial \vec{x}_r(t)}\right|_{\hat{x}_{r\,k}(-)} = [\; H_o \quad H_a \quad 0 \;] \tag{23}$$

The development of H_o (= 3x7) is detailed in Ref. [12], while H_a, as given in Ref. [11], is

$$H_a = \begin{bmatrix} 0 & -\tilde{B}_z & \tilde{B}_y \\ \tilde{B}_z & 0 & -\tilde{B}_x \\ -\tilde{B}_y & \tilde{B}_x & 0 \end{bmatrix} \tag{24}$$

where $\tilde{B}_b = [\tilde{B}_x \;\; \tilde{B}_y \;\; \tilde{B}_z]^T$ = measured magnetic field vector, (see Eq. (11)).

The update on the error covariance matrix is

$$P_k(+) = [I - K(k)H(k)]\, P_k(-)\, [I - K(k)H(k)]^T + K(k)\, R\, K^T(k) \tag{25}$$

Partitioning the Kalman gain matrix as follows,

$$K(k) = \begin{bmatrix} K_o(k) \;\; (7x3) \\ K_a(k) \;\; (3x3) \\ K_\omega(k) \;\; (3x3) \end{bmatrix} \tag{26}$$

the estimates of the orbit states and attitude rates are updated in the traditional manner as,

$$\begin{aligned} \hat{x}_{o\,k}(+) &= \hat{x}_{o\,k}(-) + K_o(k)[z(k) - \vec{h}(\hat{x}_k(-))] \\ \hat{\omega}_k(+) &= \hat{\omega}_k(-) + K_\omega(k)[z(k) - \vec{h}(\hat{x}_k(-))] \end{aligned} \tag{27}$$

where $[z(k) - \vec{h}(\hat{x}_k(-))]$ are the residuals.

However, a quaternion correction is used to update the quaternion. This correction is derived from the three small Euler angles, defined in Eq. (13). These angles, as given in Ref. [15], are found from

$$\vec{a} = K_a(k)[z(k) - \vec{h}(\hat{x}_k(-))] \tag{28}$$

and the quaternion correction is then

$$\delta\hat{q} = \left[\frac{1}{2} a_1 \quad \frac{1}{2} a_2 \quad \frac{1}{2} a_3 \quad 1 \right]^T \tag{29}$$

Finally, the quaternion estimate is updated, as in Ref. [15], or

$$\hat{q}_k(+) = \hat{q}_k(-) \otimes \delta\hat{q}^{-1} \tag{30}$$

where $\otimes$ denotes quaternion multiplication, and the inverse is a quaternion inverse [13]. As in Ref. [15], the updated quaternion is then normalized to satisfy the constraint: $q_1^2 + q_2^2 + q_3^2 + q_4^2 = 1$.

3. Simulation Results

A preliminary test of the algorithm has been performed with simulated data. A fixed-step, 4th-order Runge-Kutta routine was used to integrate both the "truth" model (Eq. (1)) and to propagate the state estimates (Eq. (12)). The step size was 5 seconds for both integrations. TAM measurements were generated from the "truth" model at each time step. Gaussian distributed noise with zero mean and a variance of 2 milliGauss was added to the measurements. In the EKF algorithm, measurements were taken and updates performed every 5 seconds as well.

The modeled spacecraft was similar to the Solar Anomalous and Magnetospheric Particle Explorer (SAMPEX), in an approximately polar low Earth orbit. Specifically, the orbit was 514 x 675 km, with an orbital period of 96.5 minutes. The algorithm was tested for 300 minutes (approximately 3 orbits). Table 1 presents the initial values for the "truth" model, as well as the initial a-priori estimates. The Euler angles in the table represent a 3-1-3 rotation from inertial geocentric coordinates to body-fixed coordinates. The initial values for the quaternion elements are determined from the Euler angles.

Table 1. Initial Parameter Values

Parameter	"Truth" Model	A-priori Estimate
a (km)	6967.3	8000
e	0.012	0.02
i (deg)	81.7	85
Ω (deg)	205.9	200
ω (deg)	45.9	50
θ (deg)	65.7	70
C_d	0.02	0.02
Euler $\angle$ 1 (deg)	20	19
Euler $\angle$ 2 (deg)	40	39
Euler $\angle$ 3 (deg)	60	61
ω_x (deg/min)	360/96.5	360/96.5
ω_y (deg/min)	0	0
ω_z (deg/min)	0	0

The numerical values for the spacecraft's inertia tensor and the moment of inertia of the momentum wheel are taken to be

$$I_{sc} = \begin{bmatrix} 15.516 & 0 & 0 \\ 0 & 21.621 & -0.194 \\ 0 & -0.194 & 15.234 \end{bmatrix} \text{kg-m}^2, \quad I_w = 0.0041488 \text{ kg-m}^2 \tag{31}$$

Since special attention is to be focused on attitude rate estimation, torques were applied to the spacecraft. The torque control inputs, defined below, cause the spacecraft to rotate about each axis with frequencies on the order of the orbital period. The time histories of the torque control inputs driving the "truth" model were defined as,

$$u_i(t) = \begin{cases} u_{i_{max}} \sin\left(\frac{\pi}{120} t\right), & 0 \le t < 120 \text{ sec} \\ \frac{u_{i_{max}}}{4} \sin\left(\frac{\pi}{120} t\right), & 120 \le t < 240 \text{ sec} \quad \text{for } i = 1,...4 \\ 0, & t \ge 240 \text{ sec} \end{cases} \tag{32}$$

where $u_1(t) = T_x(t)$, $u_2(t) = T_y(t)$, $u_3(t) = T_z(t)$, $u_4(t) = \omega_w(t)$ (see Eq. (7)). The maximum control values selected were

$$\begin{aligned} u_{1_{max}} &= \text{-6.2e-04 N-m} \\ u_{2_{max}} &= \text{1.8e-06 N-m} \\ u_{3_{max}} &= \text{1.6e-04 N-m} \\ u_{4_{max}} &= \text{31.4 rad/sec} \end{aligned} \tag{33}$$

Fig. 1 displays a generic control time history (i.e. Eq. (32) normalized to $u_{i\ max} = 1$).

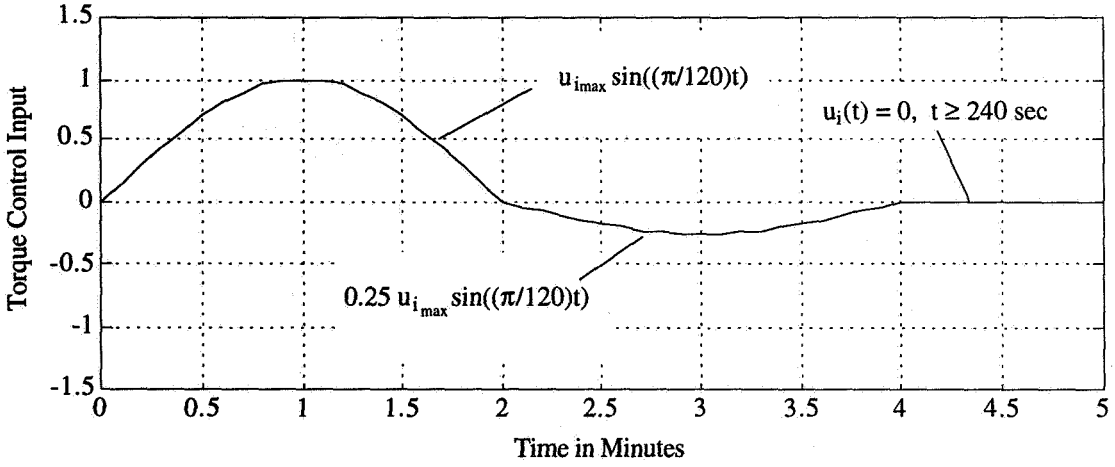

Figure 1. Generic Control Input History

Fig. 2 presents the attitude rate time histories. This figure shows that all rates lie within ±0.1 deg/sec, while the orbital period is 0.062 deg/sec. Fig. 3 presents the Euler angle time histories. The vehicle oscillates about the first rotation axis with a frequency nearly twice the orbital period. It oscillates about the second axis with a frequency approximately equal to the orbital period. Finally, it completely rotates about the third axis approximately 1.5 times per orbit.

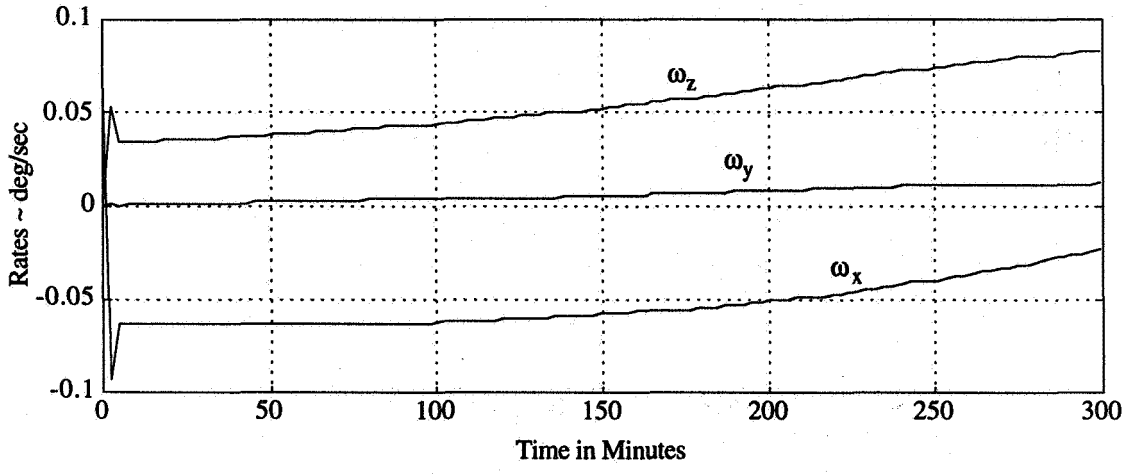

Figure 2. Attitude Rate Time Histories

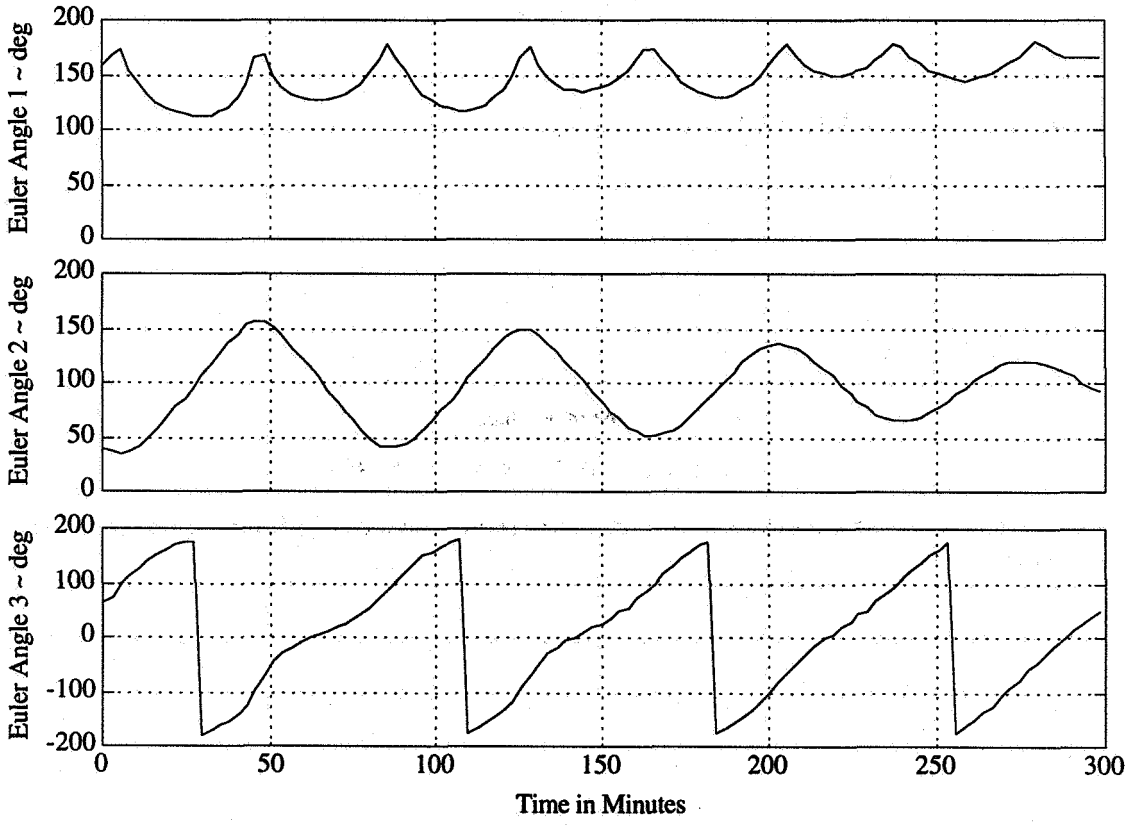

Figure 3. Euler Angle Time Histories

Fig. 4 presents the Root-Sum-Square (RSS) error in the inertial geocentric position estimates. The initial estimate errors (Table 1) resulted in an initial RSS position error of approximately 1,400 km. Fig. 4 shows that the error converges to a mean of approximately 100 km within the first two minutes. However, it should be noted that the error dynamics have not yet reached steady state. This can be clearly seen in, for example, the estimate for the argument of perigee, ω, shown in Fig. 5. This figure shows that the estimate has not yet converged to the "true" value after 300 minutes. Similar results were seen in the other state estimates. Again, 300 minutes is only approximately 3 orbits, while, for example, the simulation tests in Ref. [11] were performed for approximately 51 orbits.

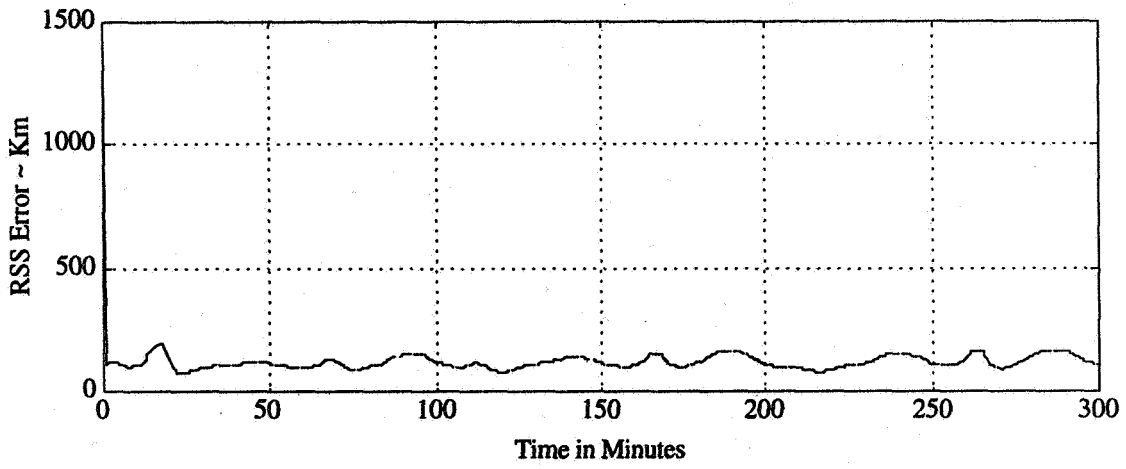

Figure 4. RSS Position Error

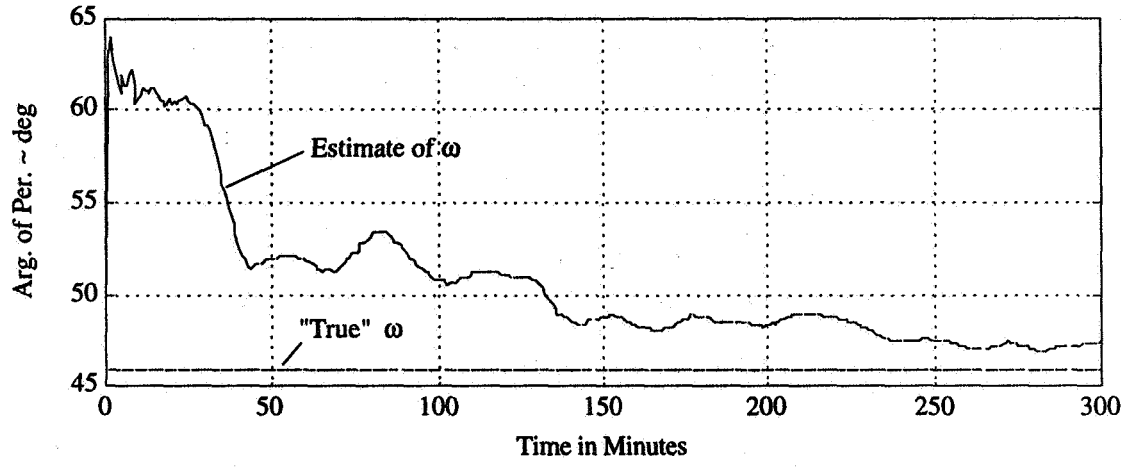

Figure 5. Argument of Perigee Time History

Fig. 6 presents the RSS error of the Euler angles. This figure shows that the attitude error converges to less than 1.5 degrees within three orbits.

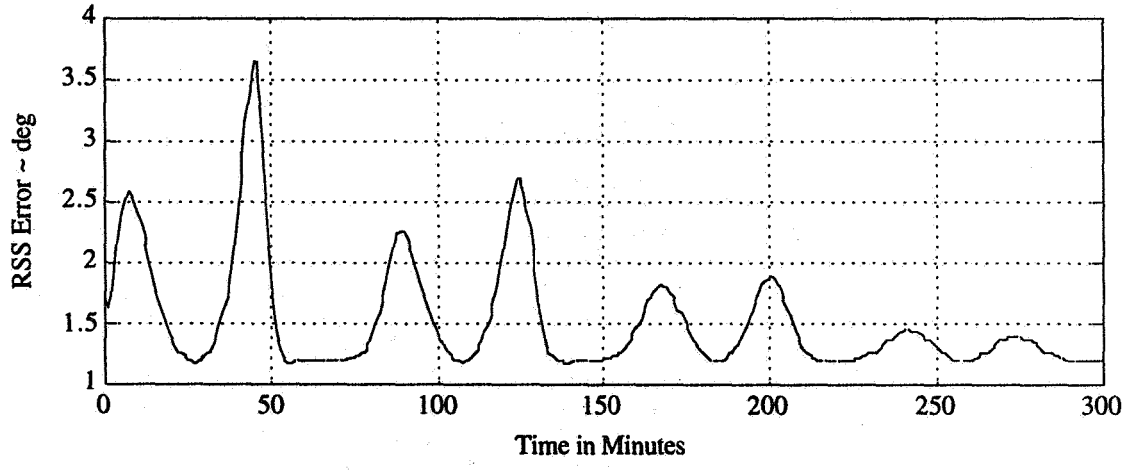

Figure 6. RSS Attitude Error

Finally, Fig. 7 presents the RSS measurement residuals. The results are similar to the RSS residuals shown in Ref. [11]. The residuals converged quickly from an initial RSS value of 164 milliGauss to an average value of approximately 4 milliGauss.

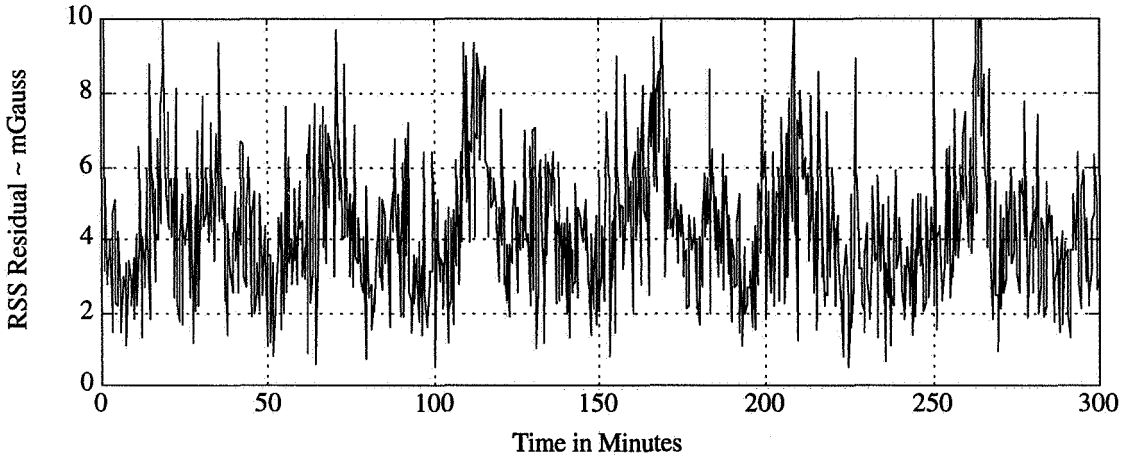

Figure 7. RSS Measurement Residuals

The algorithm was also tested substituting the "true" attitude rates for the estimated rates at each time step. This test simulated a case in which accurate rate gyro measurements are available. The RSS position and attitude error histories were nearly the same for either the estimated rates or the "true" rates. Therefore, in this case study, using estimated attitude rates, rather than using "rate gyro measurements," did not significantly degrade the filter's performance. This result holds for the initial conditions given in Table 1.

However, from Table 1, note that the initial attitude rate estimates were perfect. If attitude rates were known initially only to within 10% of their true values, then the position and attitude errors diverged after approximately one orbit. The error dynamics associated with the rates were not sufficiently fast. For example, at the beginning of the test run (time = 5 secs) the eigenvalues associated with the rate errors (for the continuous-time linearized error dynamics) were on the order of 10^{-3} rad/sec. It was also noted that the Kalman gains $K_{\omega}(k)$ were relatively small, and the updates of the attitude rates had little effect on their estimates (see Eq. (27)). Further tuning of the filter appears to be required.

4. Algorithm Extensions

In this section, some immediate extensions to the algorithm are discussed. These extensions involve the control inputs. First, in the baseline algorithm, the control vector involved a generic representation of the applied torque about each of the body-fixed axes (see Eq. (7)). However, more specific torque controls should be investigated. A magnetic torque assembly will first be considered [13]. Here, the applied moment is given by

$$\vec{T} = m_o\{u_x \hat{x} + u_y \hat{y} + u_z \hat{z}\} \times \tilde{B}_b(t) = T_x \hat{x} + T_y \hat{y} + T_z \hat{z} \tag{34}$$

where m_o is the maximum attainable magnetic moment, and u_x, u_y and u_z are commandable coil state parameters that are proportional to the current through the coil. Here, $-1 \le u_x, u_y, u_z \le 1$, and the sign depends on the direction of current flow. Therefore, the control inputs are u_x, u_y and u_z. Eq. (34) also indicates that these applied torques depend on the cross product of the control input vector and the instantaneous Earth magnetic field vector, $\tilde{B}_b(t)$. Hence, any errors in the model of the magnetic field vector will introduce errors in the model of the applied torques.

Other sources of errors are noisy control input data. The baseline algorithm assumed perfect control information was available. Instead, let the vector of torque control inputs, $\vec{u}$, be augmented to the state vector, and let *estimates* of the inputs be used in the estimation of the attitude rates. For example, let the actuator dynamics be given by

$$\dot{\vec{u}}(t) = \vec{f}_A(\vec{u}(t)) \tag{35}$$

Then, $\vec{f}_A(\vec{u}(t))$ must be incorporated into $\vec{f}(\vec{x}(t),\vec{u}(t),t)$ in Eqs. (1), and the Jacobian of the actuator dynamics included in the Jacobian in Eq. (18). Finally, the noisy torque inputs would be added to the measurement vector, or

$$\vec{z}(k) = [\tilde{\vec{B}}_b, \vec{u}]^T \tag{36}$$

The Jacobian of the measurement model in Eq. (23) is then

$$H(k) = \begin{bmatrix} H_o & H_a & 0 & 0 \\ 0 & 0 & 0 & I \end{bmatrix} \tag{37}$$

where the "reduced" state vector of Eq. (14) becomes

$$\vec{x}_r(t) = [\vec{x}_o \quad \vec{a} \quad \vec{\omega} \quad \vec{u}]^T \tag{38}$$

5. Conclusions and Directions

A simultaneous attitude and orbit determination algorithm which uses magnetometer measurements and torque control input data was developed for gyroless spacecraft. The new algorithm uses an Extended Kalman Filter to estimate not only the orbit position and attitude, but also the attitude rates.

The algorithm was tested with 300 minutes of simulated data, which corresponds to approximately three orbits. An initial Root-Sum-Square (RSS) position error of 1,400 km was reduced to an average error of approximately 100 km within the first two minutes, and the RSS attitude error converged to less than 1.5 degrees within three orbits.

It was noted that using rate estimates rather than "gyro measurements" did not significantly degrade the algorithm's performance if accurate estimates of initial rates were available. The attitude and position estimation errors diverged when there were small initial errors in the rate estimates.

Further testing of the algorithm with simulated data will be performed, followed by testing with real SAMPEX TAM data. The performance of the algorithm will then be evaluated by comparing the attitude and position estimates to orbit/attitude determination results from tracking data and additional sensors.

Acknowledgments

This work was sponsored by NASA Goddard Space Flight Center Grant NCC-585. The technical expertise of and inputs from Mr. Charles McConnell and Mr. Scott Reedy are greatly appreciated.

References

[1] Natanson, G.A., McLaughlin, S.F., Nicklas, R.C., "A Method of Determining Attitude From Magnetometer Data Only," *Proceedings of the Flight Mechanics/Estimation Theory Symposium*, NASA Goddard Space Flight Center, Greenbelt, Maryland, May, 1990, pp. 359-378.

[2] Natanson, G.A., Challa, M., Kotaru, S., Woodruff, C., "Attitude Dynamics Task: Attitude Determination Using Only Magnetometer Data for the Solar, Anomalous, and Magnetospheric Particle Explorer (SAMPEX)," Missions Operations and Data Systems Directorate, NASA Goddard Space Flight Center, Greenbelt, Maryland, August, 1993.

[3] Azor, Ruth, Bar-Itzhack, Itzhack, Harman, Richard R., "Satellite Angular Rate Estimation From Vector Measurements," *Proceedings of the Flight Mechanics/Estimation Theory Symposium*, NASA Goddard Space Flight Center, Greenbelt, Maryland, May, 1996, pp. 55-69.

[4] Natanson, G.A., Challa, M.S., Deutschmann, J., Baker, D.F., "Magnetometer-Only Attitude and Rate Determination for a Gyro-Less Spacecraft," *Proceedings of the 3rd International Symposium on Space Mission Operations and Ground Data Systems*, NASA Goddard Space Flight Center, Greenbelt, Maryland, November, 1994, pp. 791-798.

[5] Natanson, G.A., Challa, M.S., Deutschmann, J., Galal, K., "A PC-Based Magnetometer-Only Attitude and Rate Determination System for Gyroless Spacecraft," *Proceedings of the Flight Mechanics/Estimation Theory Symposium*, NASA Goddard Space Flight Center, Greenbelt, Maryland, May, 1995, pp. 83-96.

[6] Challa, M.S., Wheeler, C., "Accuracy Studies of a Magnetometer-Only Attitude-and-Rate-Determination System," *Proceedings of the Flight Mechanics/Estimation Theory Symposium*, NASA Goddard Space Flight Center, Greenbelt, Maryland, May, 1996, pp. 179-189.

[7] Psiaki, Mark L., "Autonomous Orbit and Magnetic Field Determination Using Magnetometer and Star Sensor Data," *Journal of Guidance, Control, and Dynamics*, Vol. 18, No. 3, May-June, 1995, pp. 584-592.

[8] Ketchum, E., "Autonomous Spacecraft Orbit Determination Using the Magnetic Field and Attitude Information" Paper No. AAS 96-005, *Proceedings of the 19th Annual AAS Guidance and Control Conference*, Breckenridge, Colorado, February, 1996, pp. 135-149.

[9] Psiaki, Mark L., Huang, Lejin, Fox, Stephen M., "Ground Tests of Magnetometer-Based Autonomous Navigation (MAGNAV) for Low-Earth-Orbiting Spacecraft," *Journal of Guidance, Control, and Dynamics*, Vol. 16, No. 1, January-February, 1993, pp. 206-214.

[10] Shorshi, Gil, Bar-Itzhack, Itzhack, "Satellite Autonomous Navigation Based on Magnetic Field Measurements," *Journal of Guidance, Control, and Dynamics*, Vol. 18, No. 4, July-August, 1995, pp. 843-850.

[11] Deutschmann, Julie, Bar-Itzhack, Itzhack, "Attitude and Trajectory Information Using Earth Magnetic Field Data," *Proceedings of the Flight Mechanics/Estimation Theory Symposium*, NASA Goddard Space Flight Center, Greenbelt, Maryland, May, 1996, pp. 135-149.

[12] Shorshi, Gil, Bar-Itzhack, Itzhack, "Satellite Autonomous Navigation Based on Magnetic Field Measurements," TAE No. 714, Technion-Israel Institute of Technology, Haifa, Israel, April, 1994.

[13] Wertz, J.R., ed., *Spacecraft Attitude Determination and Control*, D. Reidel Publishing Co., Boston, 1978.

[14] Gelb, A., ed., *Applied Optimal Estimation*, The M.I.T. Press, Cambridge Mass., 1974.

[15] Deutschmann, J., Bar-Itzhack, I., Rokni, M., "Comparison and Testing of Extended Kalman Filters for Attitude Estimation of the Earth Radiation Budget Satellite," presented at the Flight Mechanics/Estimation Theory Symposium, NASA Goddard Space Flight Center, Greenbelt, Maryland, May, 1990.

Efficient Sequential Attitude Estimation from Vector Observations

Yaakov Oshman* and F. Landis Markley†
National Aeronautics and Space Administration
Goddard Space Flight Center
Guidance, Navigation and Control Branch/Code 712
Greenbelt, MD 20771

Abstract

This paper presents a computationally efficient, sequential method for attitude matrix estimation using gyro and vector measurements. The method is based on a recently introduced, minimal-parameter third-order method for solving the orthogonal matrix differential equation in $\mathcal{R}^n$. In the three-dimensional case, these third-order attitude parameters can be interpreted as temporal-integrals of the body-frame angular velocity components. A nonlinear algorithm is developed, which uses this minimal set of three parameters to estimate the nine-parameter direction-cosine matrix. Having an extremely simple kinematic equation, these parameters render the resulting estimator highly computationally efficient. An orthogonalization procedure, incorporated into the measurement processing stage, enhances the accuracy and stability of the resulting algorithm, yet retains reasonable simplicity. The performance of the estimator is demonstrated via a Monte Carlo simulation study.

I Introduction

USING a sequence of vector measurements for attitude determination has been intensively investigated over the last three decades. First proposed in 1965 by Wahba [1], the problem is to estimate the attitude of a spacecraft based on a sequence of noisy vector observations, resolved in the body-fixed coordinate system and in a reference system. Body-fixed vector observations are typically obtained from on-board sensors, such as star trackers, Sun sensors, or magnetometers. Corresponding, reference observations, are obtained by using an ephemeris routine (for a Sun observation), or from orbit data and a magnetic field routine (for a magnetic field observation), or from a star catalog (for star observations). The use of attitude determination from vector observations was reported in [2].

Inertial reference systems typically utilize vector measurements in combination with strap-down gyros to estimate both the spacecraft attitude and the gyro drift rate biases. Several approaches have been proposed for the design of such systems, differing mainly in their choice of attitude representation method (a thorough survey of attitude representations appears in [3]).

The quaternion, a popular rotation specifier, was used in [4, 5], in the framework of extended Kalman filtering (EKF) algorithms. In [6], vector observations were used to estimate both the quaternion and the angular velocity of the spacecraft, in a gyroless attitude determination and control setting. The main advantage of using the quaternion representation is that it is not singular for any rotation. Moreover, its kinematic equation is linear and the computation of the associated attitude matrix involves only algebraic expressions. However, the quaternion representation is not minimal since it is four-dimensional. This leads to a normalization constraint that has to be addressed in filtering algorithms and increases the associated computation load.

Euler angles were used by only a few researchers [7, 8] to parameterize the attitude in the context of gyro-vector measurements attitude estimation. Although this parametrization is minimal, its use imposes a large computational burden due to the transcendental expressions involved in the computation of the attitude matrix. Moreover, Euler angles are singular, as are all three-dimensional (3-D) attitude representations.

*National Research Council Research Associate. On sabbatical leave from the Department of Aerospace Engineering, Technion—Israel Institute of Technology, Haifa 32000, Israel. Senior Member AIAA.
†Staff Engineer. Associate Fellow AIAA.

In a recent effort to alleviate the computational burden, an EKF attitude estimator was presented [9], that utilized the Rodrigues parameters (also known as the Gibbs vector). Being a minimal set of attitude parameters, the choice of this parametrization renders the resulting estimator computationally efficient, however, the Rodrigues parameters are singular for 180 degree rotations. The modified Rodrigues parameters (MRP), on the other hand, allow rotations up to 360 degrees. Using this observation, an MRP-based EKF has recently been presented [10].

The direction-cosine matrix (DCM), a natural attitude representation, was used in a gyro-star tracker setting by several researchers. Since it is inherently nonsingular, it requires no special singularity-handling procedures. Moreover, its kinematic equation is linear, as is its associated vector measurement equation, which greatly facilitate the filter implementation. A recursive, EKF-type DCM identification algorithm was introduced by Bar-Itzhack and Reiner in [11]. Although the advantages of directly parameterizing the attitude using the DCM are clear, the main disadvantage of this approach is computational, as it requires the estimation of a nine-dimensional parameter vector.

The work presented in this paper proposes to sequentially estimate the attitude matrix using a minimal-dimension filter, thus alleviating the computational burden normally associated with DCM identification. It is assumed, as usual, that the body-referenced angular velocity is measured by an orthogonal triad of rate gyros. The approach taken to this end is motivated by the idea of finding a minimal-parameter solution to the orthogonal matrix differential equation in $\mathcal{R}^n$, first introduced by Bar-Itzhack and Markley in [12]. In a recent work, they presented a minimal-parameter solution to the orthogonal matrix differential equation

$$\dot{V}(t) = W(t)V(t), \qquad V(t) \in \mathcal{R}^{n,n}, \quad W(t) = -W^T(t) \quad \forall t \geq t_0 \tag{1a}$$

$$V(t_0) = V_0, \qquad V_0 V_0^T = I \tag{1b}$$

where the raised dot indicates the temporal derivative. Exploiting the properties of V and W, Bar-Itzhack and Markley introduced a novel minimal parametrization of the orthogonal matrix V. Based on extended Rodrigues parameters (ERP), this parametrization enabled solving Eq. (1) using only $n(n-1)/2$ parameters, as opposed to n^2 integrations implied by a straightforward solution of Eq. (1).

Motivated by [12], Ronen and Oshman [13] have recently introduced a third-order method for the solution of the orthogonal matrix differential equation in $\mathcal{R}^n$. The method is based on a third-order, minimal parametrization of the orthogonal matrix V using the $n(n-1)/2$ off-diagonal terms of the skew-symmetric matrix $A(t,t_0) \triangleq \int_{t_0}^{t} W(\tau)\, d\tau$. For the 3-D case, these parameters, hereafter called integrated-rate parameters (IRP), are the angles resulting from time-integration of the body-frame components of the spacecraft angular velocity.

The idea underlying the work presented herein is to utilize the minimal, three-dimensional, IRP vector, to estimate the nine-parameter attitude matrix. Building upon this state vector, the resulting three-dimensional filter possesses an extremely simple time-propagation procedure, which is at the heart of its computational efficiency. The DCM orthogonality constraint is also addressed, contributing to the filter's accuracy and numerical stability, yet keeping its structure reasonably simple.

The following section briefly reviews the IRP minimal-parameter, third-order method for the solution of the attitude kinematic equation. In Sec. III we develop the filtering, orthogonalization and prediction stages of the attitude estimator. Special attention is given to the analysis of the potential effects of the orthogonalization step on the estimator's structure. Sec. VI presents a numerical study, consisting of Monte Carlo simulations of the new algorithm, which was carried out to demonstrate the performance of the method. Concluding remarks are offered in the last section.

II Third-Order, Minimal Attitude Parameters

As stated in the previous section, the attitude estimator developed in this paper is based on the IRP parameters [13]. For completeness, this section briefly reviews the minimal-parameter problem and the IRP method. Then, the method is adapted to the 3-D attitude kinematic equation.

The Minimal-Parameter Problem

First defined by Bar-Itzhack and Markley in [12], the minimal-parameter problem is the following.

Given the matrix differential equation Eq. (1), find: 1) a set of $m = n(n-1)/2$ parameters which unambiguously define $V(t)$, 2) the differential equation satisfied by these parameters, 3) the transformation which maps these parameters into the matrix V, and 4) a simple and efficient method to solve the parameters' differential equation and to compute $V(t)$.

Introducing a novel extension to the Rodrigues minimal set of parameters, Bar-Itzhack and Markley [12] were able to completely solve the minimal-parameter problem.

Motivated by [12], Ronen and Oshman [13] have recently introduced a new, third-order, minimal-parameter method for the solution of Eq. (1). The method is summarized in the following.

Let the skew-symmetric matrix $A(t,t_0)$ be defined as

$$A(t,t_0) \triangleq \int_{t_0}^{t} W(\tau)\,d\tau \tag{2}$$

Then, a third-order approximation of the solution $V(t)$ in terms of the entries of the matrix $A(t,t_0)$ is given by the matrix $\tilde{V}(t,t_0)$, defined as

$$\tilde{V}(t,t_0) \triangleq \left\{ I + A(t,t_0) + \frac{A^2(t,t_0)}{2!} + \frac{A^3(t,t_0)}{3!} + \frac{(t-t_0)}{3!}\Big[A(t,t_0)W_0 - W_0A(t,t_0)\Big] \right\} V_0 \tag{3}$$

where $W_0 = W(t_0)$. Moreover, $\tilde{V}$ is a third-order approximation of an orthogonal matrix, in the sense that

$$\tilde{V}(t,t_0)\tilde{V}^T(t,t_0) = I + \mathcal{O}\big((t-t_0)^4\big) \tag{4}$$

where $\mathcal{O}(x)$ denotes a function of x that has the property that $\mathcal{O}(x)/x$ is bounded as $x \to 0$.

Referring now to the minimal-parameter problem, the new parameters, which define the third-order solution of Eq. (1), are the $n(n-1)/2$ off-diagonal terms of $A(t,t_0)$. For the 3-D case, these parameters have a simple geometric interpretation: they are the angles resulting from a temporal-integration of the three components of the angular velocity vector

$$\omega(t) \triangleq \begin{bmatrix} \omega_1(t) & \omega_2(t) & \omega_3(t) \end{bmatrix}^T \tag{5}$$

where ω_i is the angular velocity component along the i-axis of the initial coordinate system, and $i = 1,2,3$ for x, y, z, respectively.

The differential equation satisfied by these parameters is

$$\dot{A}(t,t_0) = W(t), \qquad A(t_0,t_0) = 0 \tag{6}$$

which can be easily solved using any quadrature scheme. As demonstrated in [13], the new minimal-parameter method is both computationally efficient and accurate.

The Attitude Matrix Kinematic Equation

In the 3-D case, the orthogonal matrix referred to is the attitude matrix, or the direction cosine matrix (DCM), denoted by $D(t)$. The differential equation satisfied by this matrix is the well-known equation

$$\dot{D}(t) = \Omega(t)D(t), \qquad D(t_0) = D_0 \tag{7}$$

where

$$\Omega(t) = -\big[\omega(t)\times\big] \tag{8}$$

and $\big[\omega(t)\times\big]$ is the *cross product matrix* corresponding to $\omega(t)$, which is defined according to

$$\big[a\times\big] \triangleq \begin{bmatrix} 0 & -a_3 & a_2 \\ a_3 & 0 & -a_1 \\ -a_2 & a_1 & 0 \end{bmatrix} \qquad \forall a \in \mathcal{R}^3 \tag{9}$$

This notation reflects the fact that

$$\big[a\times\big]b = a \times b \qquad \forall a, b \in \mathcal{R}^3 \tag{10}$$

In this case, the matrix $A(t,t_0)$ takes the form

$$A(t,t_0) \triangleq -[\theta(t)\times] \tag{11}$$

where the parameter vector $\theta(t)$ is defined as

$$\theta(t) \triangleq \begin{bmatrix}\theta_1(t) & \theta_2(t) & \theta_3(t)\end{bmatrix}^T \tag{12}$$

and

$$\theta_i(t) \triangleq \int_{t_0}^{t} \omega(\tau)\,d\tau, \qquad i=1,2,3 \tag{13}$$

III The Attitude Estimator

In this section we develop the attitude estimation algorithm. The development of the algorithm relies on the choice of the parameter vector θ, defined in Eqs. (12) and (13), to be the estimator's state vector.

Let the sampling period be denoted by $T \triangleq t_{k+1} - t_k$. Using the notation $\theta(k) \triangleq \theta(t_k)$, the state vector at time t_k is

$$\theta(k) = \begin{bmatrix}\theta_1(k) & \theta_2(k) & \theta_3(k)\end{bmatrix}^T \tag{14}$$

and Eq. (13) implies

$$\theta_i(k) = \int_{t_0}^{t_k} \omega_i(\tau)\,d\tau, \qquad i=1,2,3 \tag{15}$$

where $\omega(t)$ is the spacecraft angular velocity vector, defined in Eq. (5). From Eq. (15) we have

$$\theta(k+1) = \theta(k) + \int_{t_k}^{t_{k+1}} \omega(\tau)\,d\tau \tag{16}$$

Defining $A(k+1,k)$ to be the discrete-time analog of $A(t,t_0)$, i.e.,

$$A(k+1,k) \triangleq -[(\theta(k+1)-\theta(k))\times] \tag{17}$$

Eq. (3) is rewritten as

$$D(k+1) = \left\{I + A(k+1,k) + \frac{1}{2}A^2(k+1,k) + \frac{1}{6}A^3(k+1,k) + \frac{1}{6}T\Big[A(k+1,k)\Omega(k) - \Omega(k)A(k+1,k)\Big]\right\}D(k) \tag{18}$$

In practice we only have access to the *measured* angular velocity, denoted by $\hat{\omega}(t)$, which satisfies

$$\hat{\omega}(t) = \omega(t) + \delta\omega(t) \tag{19}$$

Here $\delta\omega(t)$ is the rate-gyro (RG) measurement noise. For simplicity, this noise is assumed to be a zero-mean, white, Gaussian process, denoted as

$$\delta\omega(t) \sim \mathcal{WN}(0, Q(t)) \tag{20}$$

where its intensity, $Q(t)$ (the power spectral density matrix), is defined by

$$E\{\delta\omega(t)\delta\omega^T(s)\} = Q(t)\delta(t-s) \tag{21}$$

(The incorporation of more elaborate gyro noise models is straightforward [14]).

The estimation algorithm comprises three sub-algorithms. In the filtering stage, the state estimate and the estimation error covariance matrix are updated across the newly acquired measurement. Following the filtering stage, the estimated attitude matrix is orthogonalized, to enhance the algorithm stability by annihilating the numerical errors which have accumulated during the recent prediction and filtering stages. The prediction stage deals with the propagation in time of these variables between consecutive measurement updates. These three procedures are developed in the ensuing.

Filtering

Let the minimum mean-squared error (MMSE) estimate of $\theta(j)$ based on measurements up to and including t_k be denoted by $\hat{\theta}(j|k)$. Assume that at t_{k+1} we have on hand the predicted parameter vector $\hat{\theta}(k+1|k)$ and its corresponding prediction error covariance matrix, $P(k+1|k) \triangleq E\{\tilde{\theta}(k+1|k)\tilde{\theta}^T(k+1|k)\}$, where the estimation error is defined as

$$\tilde{\theta}(j|k) \triangleq \theta(j) - \hat{\theta}(j|k) \tag{22}$$

The purpose of the filtering scheme, to be developed in the sequel, is to compute the a posteriori estimate and the corresponding error covariance matrix by way of incorporating the new vector measurements acquired at t_{k+1}.

As the first step in developing the measurement update algorithm, we next derive the observation equation, relating the acquired vector measurements to the state.

The Observation Equation

Let $\mathcal{S}_u$ and $\mathcal{S}_v$ denote the reference Cartesian coordinate system and the body-fixed Cartesian coordinate system, respectively. The new pair of corresponding noisy vector measurements consists of the *unit* vectors $u(k+1)$ and $v(k+1)$, which represent the *measured* values of the same vector $r(k+1)$, resolved in $\mathcal{S}_u$ and in $\mathcal{S}_v$, respectively. The direction-cosine matrix $D(k+1)$, representing the true attitude of $\mathcal{S}_v$ relative to $\mathcal{S}_u$ at time t_{k+1}, transforms the *true* vector representation u_0 in $\mathcal{S}_u$ into its corresponding *true* representation v_0 in $\mathcal{S}_v$ according to

$$v_0(k+1) = D(k+1)u_0(k+1) \tag{23}$$

Assuming no constraint on the measurement noise direction, the body-frame measured unit vector, $v(k+1)$, is related to the true vector according to

$$v(k+1) = \frac{v_0(k+1) + n'_v(k+1)}{\|v_0(k+1) + n'_v(k+1)\|} \tag{24}$$

where the sensor measurement noise n'_v is a white, Gaussian noise sequence with

$$n'_v(k+1) \sim \mathcal{N}\big(0, R'_v(k+1)\big) \tag{25}$$

Since both $v_0(k+1)$ and $v(k+1)$ are unit vectors, it follows from Eq. (24) that

$$v(k+1) = v_0(k+1) + \mathcal{P}^{\perp}_{v_0}(k+1)n'_v(k+1) + \mathcal{O}\big(\|n'_v(k+1)\|^2\big) \tag{26}$$

where the idempotent matrix

$$\mathcal{P}^{\perp}_{v_0}(k+1) \triangleq I - v_0(k+1)v_0^T(k+1) \tag{27}$$

represents the orthogonal projector onto the orthogonal complement of $\text{span}\big\{v_0(k+1)\big\}$. Defining, therefore, the *effective* measurement noise associated with the measurement $v(k+1)$ as

$$n_v(k+1) \triangleq \mathcal{P}^{\perp}_{v_0}(k+1)n'_v(k+1) \tag{28}$$

yields the following measurement model

$$v(k+1) = v_0(k+1) + n_v(k+1) \tag{29}$$

where the effective measurement noise is, to a good approximation, a white, Gaussian sequence with

$$n_v(k+1) \sim \mathcal{N}\big(0, R_v(k+1)\big) \tag{30}$$

and the measurement noise covariance matrix is

$$R_v(k+1) \triangleq \mathcal{P}^{\perp}_{v_0}(k+1)R'_v(k+1)\mathcal{P}^{\perp}_{v_0}(k+1) \tag{31}$$

Remark 1. This measurement model is similar to that derived in [15] for *complete vector sensors.*

Remark 2. In practice, since $v_0(k+1)$ is not known, the projector matrix $\mathcal{P}_{v_0}^{\perp}(k+1)$ can be approximated using the *measured* value $v(k+1)$.

Remark 3. If, in the particular sensor used, n_v' is constrained to be orthogonal to v_0, then Eq. (31) reduces to

$$R_v(k+1) = R_v'(k+1) \tag{32}$$

The vector measurements relative to the reference coordinate system are commonly assumed to be accurately known. However, to account for non-ideal effects (e.g., star catalog errors), it is assumed in this work that the true unit vector and the measured unit vector are related according to

$$u(k+1) = u_0(k+1) + n_u(k+1) \tag{33}$$

where $n_u \perp u_0$ is a white, Gaussian measurement noise, that is uncorrelated with n_v and satisfies

$$n_u(k) \sim \mathcal{N}\big(0, R_u(k)\big) \tag{34}$$

with $R_u(k)$ being a known covariance matrix.

Since it is desired to relate the information contained in the measurements to the state vector at the corresponding time point, Eq. (23) is rewritten as

$$v_0(k+1) = D\big[\theta(k+1) - \theta(k), D(k)\big]u_0(k+1) \tag{35}$$

where the notation $D\big[\theta(k+1) - \theta(k), D(k)\big]$ reflects the fact that the attitude at time t_{k+1} is related to the attitude at time t_k via the IRP vector difference $\theta(k+1) - \theta(k)$ [see Eqs. (17) and (18)].

To exploit the information contained in the new vector measurements, the nonlinear measurement equation (35) is linearized about a *nominal* state, consisting of the most recent state estimate. Assuming that immediately after the previous measurement update (at t_k) linearization has been carried out about the *a posteriori* state estimate, the resulting nominal state at the current measurement update is the predicted estimate, $\hat{\theta}(k+1|k)$. Therefore, the predicted parameters are assumed to be related to the true ones according to

$$\theta(k+1) = \hat{\theta}(k+1|k) + \delta\theta(k+1) \tag{36}$$

where $\delta\theta(k+1)$ is the perturbation of the parameter vector about the nominal (i.e., predicted) state. Using now the most recent estimates for $D(k)$ and $\theta(k)$, namely $\hat{D}(k|k)$ and $\hat{\theta}(k|k)$, respectively, in Eq. (35), it follows from Eqs. (29), (33) and (36) that

$$v(k+1) - n_v(k+1) = D\big[\hat{\theta}(k+1|k) + \delta\theta(k+1) - \hat{\theta}(k|k), \hat{D}(k|k)\big]\big(u(k+1) - n_u(k+1)\big) \tag{37}$$

However, as shown in the sequel, the a posteriori state estimate is zeroed after each measurement update (due to full reset control of the state). Hence, we should use the reset value of the state estimate,

$$\hat{\theta}^c(k|k) = 0 \tag{38}$$

in Eq. (37). This allows us to rewrite Eq. (37) as

$$v(k+1) - n_v(k+1) = D\big[\hat{\theta}(k+1|k) + \delta\theta(k+1), \hat{D}(k|k)\big]\big(u(k+1) - n_u(k+1)\big) \tag{39}$$

where it is understood that Eq. (38) is used hereinafter in the computation of the third-order approximation for the attitude matrix. Now expand D about the nominal parameters using a first-order Taylor series expansion, i.e.,

$$D\big[\hat{\theta}(k+1|k) + \delta\theta(k+1), \hat{D}(k|k)\big] = D\big[\hat{\theta}(k+1|k), \hat{D}(k|k)\big] + \sum_{i=1}^{3} \frac{\partial}{\partial\theta_i} D\big[\theta(k+1), \hat{D}(k|k)\big]\big|_{\hat{\theta}(k+1|k)} \delta\theta_i(k+1) \tag{40}$$

where $(\bullet)\big|_{\hat{\theta}(k+1|k)}$ denotes 'evaluated at $\hat{\theta}(k+1|k)$'. Using Eq. (18), the sensitivity matrices appearing in Eq. (40) are computed as

$$\frac{\partial}{\partial\theta_i} D\big[\theta(k+1), \hat{D}(k|k)\big] = G_i(k+1)\hat{D}(k|k), \qquad i = 1,2,3 \tag{41}$$

where the matrices $\{G_i\}_{i=1}^3$ are

$$G_1 = \begin{bmatrix} 0 & \frac{1}{2}\theta_2 - \frac{1}{3}\theta_1\theta_3 - \frac{1}{6}T\omega_2 & \frac{1}{2}\theta_3 + \frac{1}{3}\theta_1\theta_2 - \frac{1}{6}T\omega_3 \\ \frac{1}{2}\theta_2 + \frac{1}{3}\theta_1\theta_3 + \frac{1}{6}T\omega_2 & -\theta_1 & 1 - \frac{1}{6}(\theta_2^2 + \theta_3^2) - \frac{1}{2}\theta_1^2 \\ \frac{1}{2}\theta_3 - \frac{1}{3}\theta_1\theta_2 + \frac{1}{6}T\omega_3 & -1 + \frac{1}{6}(\theta_2^2 + \theta_3^2) + \frac{1}{2}\theta_1^2 & -\theta_1 \end{bmatrix} \tag{42a}$$

$$G_2 = \begin{bmatrix} -\theta_2 & \frac{1}{2}\theta_1 - \frac{1}{3}\theta_2\theta_3 + \frac{1}{6}T\omega_1 & -1 + \frac{1}{6}(\theta_1^2 + \theta_3^2) + \frac{1}{2}\theta_2^2 \\ \frac{1}{2}\theta_1 + \frac{1}{3}\theta_2\theta_3 - \frac{1}{6}T\omega_1 & 0 & \frac{1}{2}\theta_3 - \frac{1}{3}\theta_1\theta_2 - \frac{1}{6}T\omega_3 \\ 1 - \frac{1}{6}(\theta_1^2 + \theta_3^2) - \frac{1}{2}\theta_2^2 & \frac{1}{2}\theta_3 + \frac{1}{3}\theta_1\theta_2 + \frac{1}{6}T\omega_3 & -\theta_2 \end{bmatrix} \tag{42b}$$

$$G_3 = \begin{bmatrix} -\theta_3 & 1 - \frac{1}{6}(\theta_1^2 + \theta_2^2) - \frac{1}{2}\theta_3^2 & \frac{1}{2}\theta_1 + \frac{1}{3}\theta_2\theta_3 + \frac{1}{6}T\omega_1 \\ -1 + \frac{1}{6}(\theta_1^2 + \theta_2^2) + \frac{1}{2}\theta_3^2 & -\theta_3 & \frac{1}{2}\theta_2 - \frac{1}{3}\theta_1\theta_3 + \frac{1}{6}T\omega_2 \\ \frac{1}{2}\theta_1 - \frac{1}{3}\theta_2\theta_3 - \frac{1}{6}T\omega_1 & \frac{1}{2}\theta_2 + \frac{1}{3}\theta_1\theta_3 - \frac{1}{6}T\omega_2 & 0 \end{bmatrix} \tag{42c}$$

In Eqs. (42) the components of θ are evaluated at t_{k+1}, and the components of ω are evaluated at t_k.

Remark 4. In a typical application, it can be assumed that the parameters $\{\theta_i\}_{i=1}^3$ are small, such that the second-order quantities $\{\theta_i\theta_j\}_{i,j=1}^3$ are negligible in Eqs. (42). Using this small-angle approximation results in much simpler forms for $G_i(k+1)$. The actual use of either Eqs. (42) or their small-angle approximation depends, in practice, on the dynamics of the specific application.

Using now Eq. (40) in Eq. (39) yields

$$\begin{aligned} v(k+1) &= D\big[\hat{\theta}(k+1|k), \hat{D}(k|k)\big]u(k+1) + \sum_{i=1}^{3} \frac{\partial}{\partial\theta_i} D\big[\theta(k+1), \hat{D}(k|k)\big]\big|_{\hat{\theta}(k+1|k)} \delta\theta_i(k+1)u(k+1) \\ &\quad - \sum_{i=1}^{3} \frac{\partial}{\partial\theta_i} D\big[\theta(k+1), \hat{D}(k|k)\big]\big|_{\hat{\theta}(k+1|k)} \delta\theta_i(k+1)n_u(k+1) - D\big[\hat{\theta}(k+1|k), \hat{D}(k|k)\big]n_u(k+1) + n_v(k+1) \end{aligned} \tag{43}$$

Rearranging and neglecting second-order terms yields

$$\begin{aligned} &v(k+1) - D\big[\hat{\theta}(k+1|k), \hat{D}(k|k)\big]u(k+1) \\ &\quad = \sum_{i=1}^{3} \frac{\partial}{\partial\theta_i} D\big[\theta(k+1), \hat{D}(k|k)\big]\big|_{\hat{\theta}(k+1|k)} \delta\theta_i(k+1)u(k+1) - D\big[\hat{\theta}(k+1|k), \hat{D}(k|k)\big]n_u(k+1) + n_v(k+1) \end{aligned} \tag{44}$$

Observe that the first member in the right-hand side (RHS) of Eq. (44) can be recast as

$$\sum_{i=1}^{3} \frac{\partial}{\partial\theta_i} D\big[\theta(k+1), \hat{D}(k|k)\big]\big|_{\hat{\theta}(k+1|k)} \delta\theta_i(k+1)u(k+1) = H(k+1)\delta\theta(k+1) \tag{45}$$

where the columns of the (observation) matrix

$$H(k+1) \equiv \begin{bmatrix} h_1(k+1) & h_2(k+1) & h_3(k+1) \end{bmatrix} \in \Re^{3,3} \tag{46}$$

are

$$h_i(k+1) = \frac{\partial}{\partial\theta_i} D\big[\theta(k+1), \hat{D}(k|k)\big]\big|_{\hat{\theta}(k+1|k)} u(k+1), \qquad i = 1, 2, 3 \tag{47}$$

Define now the *effective* measurement $y(k+1)$ to be

$$y(k+1) \triangleq v(k+1) - D\big[\hat{\theta}(k+1|k), \hat{D}(k|k)\big]u(k+1) \tag{48}$$

and the *effective* measurement noise to be

$$n(k+1) \triangleq n_v(k+1) - D\big[\hat{\theta}(k+1|k), \hat{D}(k|k)\big]n_u(k+1) \tag{49}$$

Then, using these definitions in Eq. (44) yields the following measurement equation:

$$y(k+1) = H(k+1)\delta\theta(k+1) + n(k+1) \tag{50}$$

The measurement noise is a white, Gaussian sequence with

$$n(k+1) \sim \mathcal{N}\big(0, R(k+1)\big) \tag{51}$$

where

$$R(k+1) \triangleq R_v(k+1) + D\big[\hat{\theta}(k+1|k), \hat{D}(k|k)\big] R_u(k+1) D^T\big[\hat{\theta}(k+1|k), \hat{D}(k|k)\big] \tag{52}$$

Having the linearized measurement equation (50) and the statistical characterization of the measurement noise (51) on hand, we can now derive the MMSE estimator for the parameter vector.

State and Covariance Update

Using Eqs. (22) and (36), we have

$$\delta\theta(k+1) = \theta(k+1) - \hat{\theta}(k+1|k) = \tilde{\theta}(k+1|k) \tag{53}$$

Since $\hat{\theta}(k+1|k)$ is an unbiased MMSE predictor, we have

$$E\big\{\delta\theta(k+1)\big\} = E\big\{\tilde{\theta}(k+1|k)\big\} = 0 \tag{54}$$

and

$$\operatorname{cov}\big\{\delta\theta(k+1)\big\} = \operatorname{cov}\big\{\tilde{\theta}(k+1|k)\big\} = P(k+1|k) \tag{55}$$

Hence

$$\delta\theta(k+1) \sim \mathcal{N}\big(0, P(k+1|k)\big) \tag{56}$$

Using the linearized measurement equation (50) and the statistical properties of the measurement and prediction errors, Eqs. (51) and (56), respectively, the MMSE estimator of $\delta\theta(k+1)$ is

$$\widehat{\delta\theta}(k+1|k+1) = K(k+1)y(k+1) \tag{57}$$

where $K(k+1)$, the estimator gain matrix, is computed as

$$K(k+1) = P(k+1|k)H^T(k+1)\big[H(k+1)P(k+1|k)H^T(k+1) + R(k+1)\big]^{-1} \tag{58}$$

Also, from Eq. (53) we have

$$\widehat{\delta\theta}(k+1|k+1) = \hat{\theta}(k+1|k+1) - \hat{\theta}(k+1|k) \tag{59}$$

Using Eq. (59) in Eq. (57) finally yields the state measurement update equation

$$\hat{\theta}(k+1|k+1) = \hat{\theta}(k+1|k) + K(k+1)y(k+1) \tag{60}$$

To derive the covariance update equation, we subtract $\theta(k+1)$ from both sides of Eq. (60) and use Eqs. (50) and (53) to obtain

$$\tilde{\theta}(k+1|k+1) = \big[I - K(k+1)H(k+1)\big]\tilde{\theta}(k+1|k) - K(k+1)n(k+1) \tag{61}$$

from which the familiar, Joseph-form, covariance update equation results

$$P(k+1|k+1) = \big[I - K(k+1)H(k+1)\big]P(k+1|k)\big[I - K(k+1)H(k+1)\big]^T + K(k+1)R(k+1)K^T(k+1) \tag{62}$$

where $P(k+1|k+1) \triangleq E\{\tilde{\theta}(k+1|k+1)\tilde{\theta}^T(k+1|k+1)\}$ is the filtering error covariance matrix.

Attitude Matrix Update

To compute the measurement-updated attitude matrix at time t_{k+1}, we use the most recent estimate of the parameter vector $\hat{\theta}(k+1|k+1)$, the estimated attitude matrix corresponding to time t_k, and the measured angular velocity matrix, defined as

$$\hat{\Omega}(k) \triangleq -[\hat{\omega}(k)\times] \tag{63}$$

in Eq. (18). This yields

$$\hat{D}(k+1|k+1) = \Big\{I + \hat{A}(k+1,k) + \frac{1}{2}\hat{A}^2(k+1,k) + \frac{1}{6}\hat{A}^3(k+1,k) + \frac{1}{6}T\Big[\hat{A}(k+1,k)\hat{\Omega}(k) - \hat{\Omega}(k)\hat{A}(k+1,k)\Big]\Big\}\hat{D}^*(k|k) \tag{64}$$

where the *a posteriori* estimate of $A(k+1,k)$ is defined as

$$\hat{A}(k+1,k) \triangleq -[\hat{\theta}(k+1|k+1)\times] \tag{65}$$

and $\hat{D}^*(k|k)$ is the a posteriori, *orthogonalized* estimate of the attitude matrix at time t_k, to be discussed in the sequel.

Remark 5. Eq. (64) is based on a third-order approximation of the attitude matrix using the updated estimates of the IRP vector. Obviously, the accuracy of this third-order approximation relies on the assumption that these parameters are small. In fact, it will be shown in the sequel that this is always the case, since the updated parameters are reset to zero after each measurement update. Moreover, the size of the parameter vector at each data point can be controlled by selecting a sufficiently small discretization interval.

Estimate Reset

As shown in Eq. (64), the a posteriori attitude matrix, $\hat{D}(k+1|k+1)$, is computed based on the a posteriori estimate, $\hat{\theta}(k+1|k+1)$. This estimate of the attitude matrix is then used in consecutive prediction and filtering steps, which, in turn, implies a full *reset control* of the parameter vector

$$\theta^c(k+1) = \theta(k+1) - \hat{\theta}(k+1|k+1) \tag{66}$$

where $\theta^c(k+1)$ is the *reset* state vector at t_{k+1}, and a corresponding reset of the state estimate

$$\hat{\theta}^c(k+1|k+1) = 0 \tag{67}$$

which is then used in the ensuing time propagation step.

Remark 6. Notice, that since the reset control is applied to *both* the state vector and its estimate, no changes are necessary in the estimation error covariance matrix.

Attitude Matrix Orthogonalization

Although the true attitude matrix is orthogonal, the filtered DCM will not be orthogonal, due to 1) numerical implementation errors, 2) the approximations involved in the development of the nonlinear filtering algorithm and 3) the third-order formula used to compute the attitude from the estimated parameters. To improve the algorithm's accuracy and to enhance its stability, an additional orthogonalization stage is introduced into the estimator, immediately following the measurement update stage. In the orthogonalization stage, the filtered attitude matrix is orthogonalized, that is, the orthogonal matrix closest to the filtered attitude matrix is found. This orthogonal matrix is then propagated to the next measurement update point.

In the sequel, the Euclidean norm (2-norm) will be used for vectors, and the Frobenius norm (F-norm) will be used for matrices.

Given the a posteriori attitude matrix $\hat{D}(k+1|k+1)$, the matrix orthogonalization problem is the following:

$$\min_{\hat{D}^*(k+1|k+1)} \quad \|\hat{D}(k+1|k+1) - \hat{D}^*(k+1|k+1)\| \tag{68a}$$

$$\text{subject to} \quad \hat{D}^{*T}(k+1|k+1)\hat{D}^*(k+1|k+1) = I \tag{68b}$$

Being a special case of the orthogonal Procrustes problem [16, p. 425], the matrix orthogonalization problem can be easily solved using the singular value decomposition (SVD). Thus, if

$$\hat{D}(k+1|k+1) = U(k+1)\Sigma(k+1)V^T(k+1) \tag{69}$$

is the SVD of the matrix $\hat{D}(k+1|k+1)$ where $U(k+1)$ and $V(k+1)$ are the left and right singular vector matrices, respectively, and $\Sigma(k+1)$ is the singular value matrix, then

$$\hat{D}^*(k+1|k+1) = U(k+1)V^T(k+1) \tag{70}$$

The excessive computational burden associated with the SVD might render its use prohibitive in certain applications, e.g., in *real-time* attitude determination and control. In such cases, an alternative orthogonalization scheme, introduced by Bar-Itzhack and Meyer in [17], can be used. According to this scheme, the orthogonalized matrix $\hat{D}^*(k+1|k+1)$ can be computed iteratively using the recursion:

$$X_{j+1} = \frac{3}{2}X_j - \frac{1}{2}X_jX_j^TX_j \tag{71a}$$

$$X_0 = \hat{D}(k+1|k+1) \tag{71b}$$

where $X_j \xrightarrow{j\to\infty} \hat{D}^*(k+1|k+1)$. This scheme was shown in [17] to be globally convergent, and to possess a quadratic convergence rate.

Noting the fast convergence rate of the recursive orthogonalization method shown above, this scheme is incorporated into our estimation algorithm using just a *single* step of the recursion (71). Thus, an improved (nearly orthogonal), a posteriori estimate for the attitude matrix, is computed as

$$\hat{D}^*(k+1|k+1) = N(k+1)\hat{D}(k+1|k+1) \tag{72}$$

where the linear transformation that maps the a posteriori attitude matrix into its orthogonal version is defined by

$$N(k+1) \triangleq \frac{3}{2}I - \frac{1}{2}\hat{D}(k+1|k+1)\hat{D}^T(k+1|k+1) \tag{73}$$

DCM Orthogonalization: Analysis

The introduction of the external orthogonalization step into the estimator may, conceivably, affect its performance and statistical characteristics, thus calling for appropriate adjustments in the algorithm in order to preserve its theoretical properties. In the remainder of this section, the possible effects of the orthogonalization procedure (72) on the a posteriori state estimate and error covariance matrix are analyzed. In fact, as the next theorem shows, to first-order accuracy the orthogonalization procedure does not affect the estimator.

Theorem 1. *Let* $\hat{D}^*(k+1|k+1)$ *denote the* orthogonalized *version of* $\hat{D}(k+1|k+1)$, *computed in Eq.* (72). *Then*

$$\hat{D}^*(k+1|k+1) = \Big[I + \eta[\hat{\theta}(k+1|k+1)]\Big]\hat{D}(k+1|k+1) \tag{74}$$

where $\eta[\hat{\theta}(k+1|k+1)]$ *is a matrix-valued function that satisfies*

$$\|\eta[\hat{\theta}(k+1|k+1)]\| \sim \mathcal{O}\big(\|\hat{\theta}(k+1|k+1)\|^2\big) \tag{75}$$

Proof. From Eq. (72), it is clear that in order to prove the theorem we need to show that

$$N(k+1) = I + \eta[\hat{\theta}(k+1|k+1)] \tag{76}$$

with $\eta[\hat{\theta}(k+1|k+1)]$ satisfying Eq. (75). To this end, rewrite Eq. (64) as

$$\hat{D}(k+1|k+1) = \Phi\big[\hat{A}(k+1,k)\big]\hat{D}^*(k|k) \tag{77}$$

which is an implied definition of the matrix-valued function $\Phi(\bullet)$. Using Eq. (77) in Eq. (73) and noting the orthogonality of $\hat{D}^*(k|k)$ yields

$$N(k+1) = \frac{3}{2}I - \frac{1}{2}\Phi\big[\hat{A}(k+1,k)\big]\Phi^T\big[\hat{A}(k+1,k)\big] \tag{78}$$

Using now the definition of $\hat{A}(k+1,k)$, Eq. (65), and the properties of the cross product matrix conveniently summarized in [3], we have

$$\hat{A}^2(k+1,k) = -\|\hat{\theta}(k+1|k+1)\|^2 I + \hat{\theta}(k+1|k+1)\hat{\theta}^T(k+1|k+1) \tag{79a}$$

$$\hat{A}^3(k+1,k) = \|\hat{\theta}(k+1|k+1)\|^2 [\hat{\theta}(k+1|k+1)\times] \tag{79b}$$

whence

$$\Phi[\hat{A}(k+1,k)] = I - [\hat{\theta}(k+1|k+1)\times] - \frac{1}{2}\|\hat{\theta}(k+1|k+1)\|^2 I + \frac{1}{2}\hat{\theta}(k+1|k+1)\hat{\theta}^T(k+1|k+1)$$
$$+ \frac{1}{6}\|\hat{\theta}(k+1|k+1)\|^2 [\hat{\theta}(k+1|k+1)\times] + \frac{1}{6}[(\hat{\theta}(k+1|k+1)\times\hat{\omega}(k)T)\times] \tag{80}$$

Now let $\{\mu_i[\hat{\theta}(k+1|k+1)]\}_{i=1}^3$ be the following matrix-valued functions

$$\mu_1[\hat{\theta}(k+1|k+1)] \triangleq \frac{1}{2}\left[-\|\hat{\theta}(k+1|k+1)\|^2 I + \hat{\theta}(k+1|k+1)\hat{\theta}^T(k+1|k+1)\right] \tag{81a}$$

$$\mu_2[\hat{\theta}(k+1|k+1)] \triangleq \frac{1}{6}\|\hat{\theta}(k+1|k+1)\|^2 [\hat{\theta}(k+1|k+1)\times] \tag{81b}$$

$$\mu_3[\hat{\theta}(k+1|k+1)] \triangleq \frac{1}{6}[(\hat{\theta}(k+1|k+1)\times\hat{\omega}(k)T)\times] \tag{81c}$$

It is easy to show that

$$\|\mu_1[\hat{\theta}(k+1|k+1)]\| \leq \sqrt{\frac{3}{2}}\|\hat{\theta}(k+1|k+1)\|^2 \tag{82}$$

Also, for any vector $a \in \mathcal{R}^3$,

$$\|[a\times]\| = \sqrt{2}\|a\| \tag{83}$$

whence

$$\|\mu_2[\hat{\theta}(k+1|k+1)]\| = \frac{1}{3\sqrt{2}}\|\hat{\theta}(k+1|k+1)\|^3 \tag{84}$$

Consider now the vector product $\hat{\theta}(k+1|k+1)\times\hat{\omega}(k)T$, appearing in Eq. (81c). As will be shown in the sequel [see the state prediction equation (93)], regarding $\hat{\omega}(t)$ as approximately constant over the small sampling interval $[t_k, t_{k+1}]$ yields

$$\hat{\omega}(k)T \approx \hat{\theta}(k+1|k) \tag{85}$$

Hence, using Eq. (59) we have

$$\|\hat{\theta}(k+1|k+1)\times\hat{\omega}(k)T\| = \|\hat{\theta}(k+1|k+1)\times\widehat{\delta\theta}(k+1|k+1)\|$$
$$\leq \|\hat{\theta}(k+1|k+1)\|\|\widehat{\delta\theta}(k+1|k+1)\| \leq \|\hat{\theta}(k+1|k+1)\|^2 \tag{86}$$

Using Eq. (86) in Eq. (81c) and noting Eq. (83) yields

$$\|\mu_3[\hat{\theta}(k+1|k+1)]\| \leq \frac{1}{3\sqrt{2}}\|\hat{\theta}(k+1|k+1)\|^2 \tag{87}$$

Letting now

$$\mu[\hat{\theta}(k+1|k+1)] \triangleq \mu_1[\hat{\theta}(k+1|k+1)] + \mu_2[\hat{\theta}(k+1|k+1)] + \mu_3[\hat{\theta}(k+1|k+1)] \tag{88}$$

and using this definition in Eq. (80) yields

$$\Phi[\hat{A}(k+1,k)] = I - [\hat{\theta}(k+1|k+1)\times] + \mu[\hat{\theta}(k+1|k+1)] \tag{89}$$

where, from Eqs. (82), (84) and (87),

$$\|\mu[\hat{\theta}(k+1|k+1)]\| \sim \mathcal{O}(\|\hat{\theta}(k+1|k+1)\|^2) \tag{90}$$

Using Eqs. (89) and (90) in Eq. (78) then yields Eq. (76), completing the proof. □

Now, from Eq. (74) we conclude that, after the initial transient period, the effects of the orthogonalization procedure on the filtered DCM are only of second-order in $\hat{\theta}(k+1|k+1)$. Hence, to first-order accuracy, no changes in $\hat{\theta}(k+1|k+1)$ are necessary as a result of the orthogonalization, and, consequently, no changes are required in the a posteriori covariance matrix.

Prediction

In the prediction step, the reset a posteriori state estimate at time t_k and its corresponding error covariance matrix, $\hat{\theta}^c(k|k)$ and $P(k|k)$, respectively, are propagated to time t_{k+1}.

Noting Eqs. (16) and (66) we have, after the state reset at time t_k,

$$\theta(k+1) = \theta^c(k) + \int_{t_k}^{t_{k+1}} \omega(\tau)\, d\tau = \tilde{\theta}(k|k) + \int_{t_k}^{t_{k+1}} \omega(\tau)\, d\tau \tag{91}$$

Hence, since the estimator is unbiased, the predicted state at t_{k+1} is

$$\hat{\theta}(k+1|k) = \int_{t_k}^{t_{k+1}} \omega(\tau)\, d\tau \tag{92}$$

In practice, however, we only have access to the measured value of the angular velocity. Thus, using the measured velocity in Eq. (92) yields the following state prediction equation

$$\hat{\theta}(k+1|k) = \int_{t_k}^{t_{k+1}} \hat{\omega}(\tau)\, d\tau \tag{93}$$

Any quadrature formula can be used in Eq. (93). Using Simpson's scheme yields

$$\hat{\theta}(k+1|k) = \frac{1}{6}T\Big[\hat{\omega}(k) + 4\hat{\omega}(k+\frac{1}{2}) + \hat{\omega}(k+1)\Big] \tag{94}$$

where $\hat{\omega}(k+\frac{1}{2}) \triangleq \hat{\omega}(t_k + \frac{T}{2})$.

Subtracting Eq. (93) from Eq. (91) and noting Eq. (19), the corresponding prediction error equation is

$$\tilde{\theta}(k+1|k) = \tilde{\theta}(k|k) - \int_{t_k}^{t_{k+1}} \delta\omega(\tau)\, d\tau \tag{95}$$

Noting that the two terms in the RHS of Eq. (95) are uncorrelated, the following, trivially simple covariance propagation equation results

$$P(k+1|k) = P(k|k) + \int_{t_k}^{t_{k+1}} Q(\tau)\, d\tau \tag{96}$$

Attitude Matrix Prediction

To predict the attitude matrix at t_{k+1} we use the most recent estimate of the parameter vector, $\hat{\theta}(k+1|k)$, the orthogonalized estimate of the attitude matrix corresponding to t_k, and the measured angular velocity matrix, in Eq. (18). This yields

$$\hat{D}(k+1|k) = \left\{ I + \bar{A}(k+1,k) + \frac{1}{2}\bar{A}^2(k+1,k) + \frac{1}{6}\bar{A}^3(k+1,k) + \frac{1}{6}T\Big[\bar{A}(k+1,k)\hat{\Omega}(k) - \hat{\Omega}(k)\bar{A}(k+1,k)\Big] \right\} \hat{D}^*(k|k) \tag{97}$$

where the *a priori* estimate of $A(k+1,k)$ is defined as

$$\bar{A}(k+1,k) \triangleq -\big[\hat{\theta}(k+1|k)\times\big] \tag{98}$$

IV Numerical Study

To demonstrate the performance of the new attitude estimation algorithm, a numerical simulation study was performed. The study consisted of Monte Carlo simulation runs in which simulated vector measurements and rate gyro data were processed using the estimator to obtain the estimated attitude matrix at each measurement processing point.

The angular velocity of $\mathcal{S}_v$ relative to $\mathcal{S}_u$ was $\omega(t) = \begin{bmatrix} 2 & 3 & 6 \end{bmatrix}^T \sin(0.2t)$ deg/s. The filter was run at a rate of 20 Hz, i.e., the sampling interval was $T = 0.05$ s, while the measurement processing rate was a slow 1 Hz.

The standard deviation of the gyro noise power spectral density was 0.01 deg/h$^{1/2}$. *Both* the body-frame and the reference frame vector measurements were contaminated by zero-mean, white, Gaussian noise sequences, orthogonal to the true directions, which were generated via the following algorithms

$$n_u(k+1) = x_u(k+1)\frac{w_u(k+1) \times u_0(k+1)}{\|w_u(k+1) \times u_0(k+1)\|} \tag{99}$$

$$n_v(k+1) = x_v(k+1)\frac{w_v(k+1) \times v_0(k+1)}{\|w_v(k+1) \times v_0(k+1)\|} \tag{100}$$

where $w_u(k+1)$ and $w_v(k+1)$ are randomly chosen vectors, and $x_u(k+1)$ and $x_v(k+1)$ are normal deviates satisfying

$$x_u(k+1) \sim \mathcal{N}(0, \sigma_u^2), \qquad x_v(k+1) \sim \mathcal{N}(0, \sigma_v^2) \tag{101}$$

implying

$$R_v = \sigma_v^2 I, \qquad R_u = \sigma_u^2 I \tag{102}$$

The noise equivalent angles were set to $\sigma_u = \sigma_v = 100$ arc-seconds. Notice that the values assumed for both the gyro white noise drift and the star tracker noise are very conservative, compared to the current technology state-of-the-art.

In all runs, the initial attitude estimate was set to the identity matrix (thus assuming that $\mathcal{S}_u$ and $\mathcal{S}_v$ coincide at t_0) while the true attitude corresponded to Euler angles of 30 deg, 20 deg and 10 deg in roll, pitch and yaw, respectively. Notice that, again, this constitutes a conservative assumption, as we can always use the first vector measurements to find a rough initial estimate of the attitude using some point-estimation scheme, e.g., QUEST [18], or the approximate initialization method suggested in [11]. However, in this work it was found that there was no need to use such an initialization scheme, as all simulation runs starting at the identity matrix successfully converged, thus demonstrating the robustness of the algorithm. To compare the estimated attitude matrix with the true matrix, the following metrics were defined. The convergence index, used to measure the convergence of the estimated attitude to the true attitude, was defined as the following ensemble average over M Monte Carlo runs

$$J_c(k+1) \triangleq \frac{1}{M}\sum_{n=1}^{M}\|\hat{D}_n^*(k+1|k+1) - D_n(k+1)\| \tag{103}$$

The orthogonality index, used to measure the degree of orthogonality of the estimated attitude, was defined as

$$J_o(k+1) \triangleq \frac{1}{M}\sum_{n=1}^{M}\|\hat{D}_n^{*T}(k+1|k+1)\hat{D}_n^*(k+1|k+1) - I\| \tag{104}$$

The performance indices, obtained from a 100-run Monte Carlo simulation, are presented in Fig. 1. As can be observed, the estimator performed satisfactorily, converging in all runs to an accurate and orthogonal DCM estimate after a relatively short transient period. In Fig. 2, the true roll angle and the corresponding roll estimation error (computed using the estimated attitude matrix) are shown for a typical run. The Euler angle sequence assumed was 3-2-1. Similar results were obtained for the pitch and yaw Euler angles. The steady-state estimation errors of the Euler angles computed from the estimated DCM in a typical run were smaller than 0.015 degrees (1-σ).

V Conclusions

A computationally efficient, nonlinear estimation algorithm has been presented, that uses vector measurements and gyro readings to estimate the direction-cosine matrix. The algorithm is based on a recently introduced, third-order

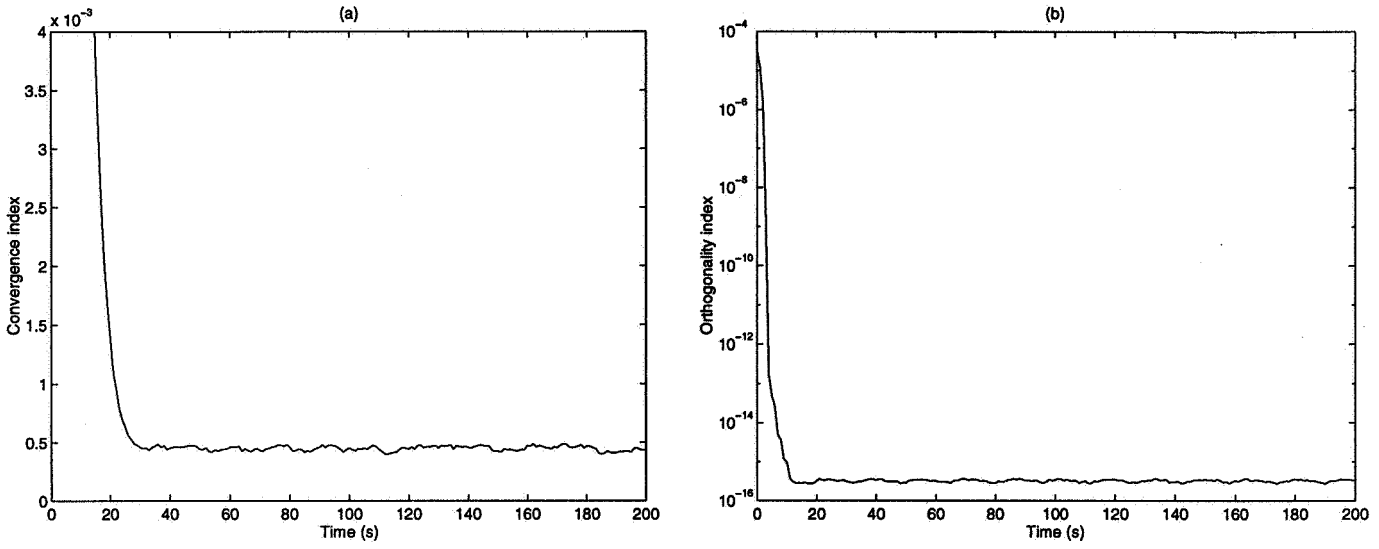

Fig. 1 Performance indices based on 100 Monte Carlo runs: (a) Convergence index; (b) Orthogonality index.

minimal parametrization of the attitude matrix. This facilitates the use of a three-dimensional filter to estimate the nine-parameter attitude matrix.

The extremely simple kinematics obeyed by the particular parameter vector chosen is inherited by the estimator's time propagation equations, which results in the filter's high numerical efficiency. The DCM orthogonality constraint is dealt with by incorporating an orthogonalization procedure following the measurement update stage. Based on a single-step implementation of an iterative orthogonalization technique, the incorporation of this procedure into the estimator was shown to not require any further modifications in the structure of the algorithm.

A numerical Monte Carlo simulation study has been presented, which demonstrates the performance of the proposed algorithm. Assuming very conservative gyro and vector measurements errors, the attitude estimated via the new algorithm has been shown to be both accurate and robust with respect to initialization errors.

Acknowledgement

This work was performed while the first author held a National Research Council — NASA Goddard Space Flight Center Research Associateship. This support is greatly appreciated.

References

[1] G. Wahba. A Least-Squares Estimate of Satellite Attitude. Problem 65-1. *SIAM Review*, 7(3):409, July 1965.

[2] L. Fallon III., I. H. Harrop, and C. R. Sturch. Ground Attitude Determination and Gyro Calibration Procedures for the HEAO Missions. In *Proceedings of the AIAA 17th Aerospace Sciences Meeting*, New Orleans, LA, January 1979. AIAA.

[3] M. D. Shuster. A Survey of Attitude Representations. *The Journal of the Astronautical Sciences*, 41(4):439–517, Oct.–Dec. 1993.

[4] E. J. Lefferts, F. L. Markley, and M. D. Shuster. Kalman Filtering for Spacecraft Attitude Estimation. *Journal of Guidance, Control, and Dynamics*, 5(5):417–429, Sept.–Oct. 1982.

[5] I. Y. Bar-Itzhack and Y. Oshman. Attitude Determination from Vector Observations: Quaternion Estimation. *IEEE Transactions on Aerospace and Electronic Systems*, AES-21(1):128–136, January 1985.

[6] E. Gai, K. Daly, J. Harrison, and L. Lemons. Star-Sensor-Based Satellite Attitude/Attitude Rate Estimator. *Journal of Guidance, Control, and Dynamics*, 8(5):560–565, Sept.-Oct. 1985.

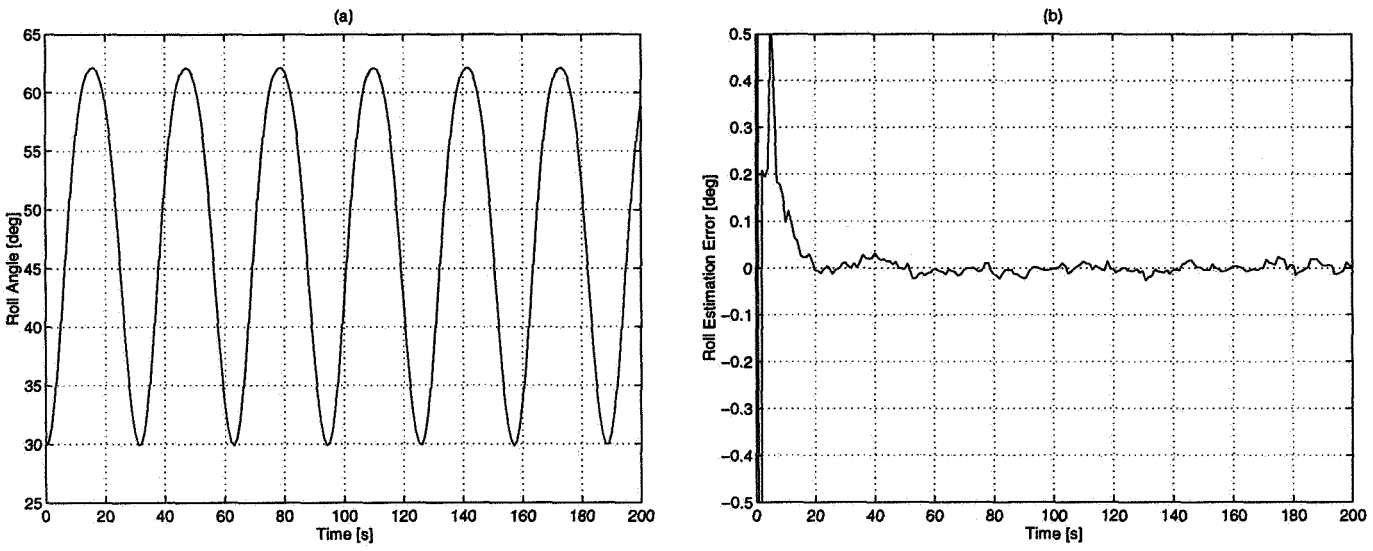

Fig. 2 (a) True roll angle; (b) Roll angle estimation error.

[7] J. L. Farrell. Attitude Determination by Kalman Filtering. *Automatica*, 6:419–430, 1970.

[8] I. Y. Bar-Itzhack and M. Idan. Recursive Attitude Determination from Vector Observations: Euler Angle Estimation. *Journal of Guidance, Control, and Dynamics*, 10(2):152–157, Mar.–Apr. 1987.

[9] M. Idan. Estimation of Rodrigues Parameters From Vector Observations. *IEEE Transactions on Aerospace and Electronic Systems*, AES-32(2):578–586, April 1996.

[10] J. L. Crassidis and F. L. Markley. Attitude Estimation Using Modified Rodrigues Parameters. In *Proceedings of Flight Mechanics/Estimation Theory Symposium*, pages 71–83, NASA Goddard Space Flight Center, May 14–16 1996. NASA.

[11] I. Y. Bar-Itzhack and J. Reiner. Recursive Attitude Determination from Vector Measurements: DCM Identification. *Journal of Guidance, Control, and Dynamics*, 7(1):51–56, Jan.–Feb. 1984.

[12] I. Y. Bar-Itzhack and F. L. Markley. Minimal Parameter Solution of the Orthogonal Matrix Differential Equation. *IEEE Transactions on Automatic Control*, AC-35(3):314–317, March 1990.

[13] M. Ronen and Y. Oshman. A Third-Order, Minimal-Parameter Solution of The Orthogonal Matrix Differential Equation. To appear, *Journal of Guidance, Control and Dynamics.*

[14] J. R. Wertz, editor. *Spacecraft Attitude Determination and Control.* D. Reidel, Dordrecht, Holland, 1978. Chapter 7.

[15] M.D. Shuster. Kalman Filtering of Spacecraft Attitude and the Quest Model. *The Journal of the Astronautical Sciences*, 38(3):377–393, Jul.-Sept. 1990.

[16] G. H. Golub and C. F. Van Loan. *Matrix Computations.* The Johns Hopkins University Press, Baltimore, MD, 1983.

[17] I. Y. Bar-Itzhack and J. Meyer. On the Convergence of Iterative Orthogonalization Processes. *IEEE Transactions on Aerospace and Electronic Systems*, AES-12:146–151, March 1976.

[18] M. D. Shuster and S. D. Oh. Three Axis Attitude Determination from Vector Obsevations. *Journal of Guidance, Control, and Dynamics*, 4:70–77, Jan.-Feb. 1981.

Page intentionally left blank

Quaternion Parameterization and Global Attitude Estimation

R. G. Reynolds
TRW Space & Electronics
Chantilly, Va.

abstract - Quaternions have become the attitude representation of choice for most spacecraft applications because of the ease with which they may be propagated, normalized, and employed in general computational schemes, not to mention the economy with which they may be stored. In this paper, we examine a decomposition of the quaternion attitude representation in observation space which allows for simpler computations, increased flexibility, and greater insight into the underlying quaternion group structure. Several applications of the decomposition are discussed. In particular, the decomposition is used to formulate a global attitude estimation algorithm which may be implemented recursively or in batch form. The batch estimation algorithm is then shown to be equivalent to the renowned QUEST algorithm of authors Shuster and Oh.

I. Introduction

Of the many representations which exist for attitude, quaternions are popular for several reasons:

1) The propagation differential equations have no singularities, in contrast to e.g., Euler's angles or Gibbs' vectors, which require special handling near these points.

2) Viewed as an element of three dimensional projective real space, $\mathbf{PR}^3$, the quaternion is a minimal three degree of freedom representation of attitude. This compares favorably with, e.g., direction cosine matrices, which are comprised of 9 elements, and whose rows and columns must be orthonormalized to provide an adequate representation of attitude.

3) There are a number of simple and direct methods available to implement controllers with quaternion feedback which are globally stable [1,2,4].

In this paper, we examine the decomposition of the quaternion attitude representation in observation space, and a number of direct applications of this result. In particular, we will consider the implementation of a global attitude estimation scheme in both recursive and batch form. The latter batch algorithm may be shown to be identical to the QUEST algorithm [3].

It is assumed that the reader has a passing acquaintance with quaternion algebra and quaternion attitude representations. An excellent source for information on these topics is Wertz [5]. In the following, we will make frequent use of the shorthand representation for a quaternion $q = (Q,q_4)$, in which the first variable in the parentheses is the vector part of the quaternion, and the second element is the scalar part.

II. Quaternion Parameterization in Observation Space

Suppose that a unit vector x_1 in a given reference frame 1 is to be transformed to a new unit vector x_2 in frame 2 by the operation of the quaternion q_{12}. The quaternion in question might take the form of

$$q_{12} \sim (x_2 \times x_1 , 1 + x_2 \bullet x_1) \tag{2.1}$$

where the ~ symbol has been used to indicate that q_{12} belongs to the equivalence class of four vectors in three dimensional projective real space, $\mathbf{PR}^3$, under which one vector is equivalent to another if they differ by a scaling parameter.

If we visualize the transformation process, it is the rotation about an axis orthogonal to both x_1 and x_2, as pictured below.

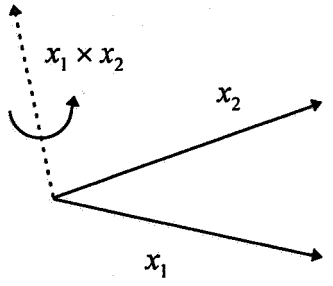

In fact, this quaternion represents the minimum rotation required to transform x_1 to x_2. (Note that the vector part of the quaternion here represents the negative axis of rotation. This is a fairly common convention.)

Another quaternion which would rotate x_1 into x_2 is given by

$$q_{12} \sim (x_2 + x_1 , 0) \tag{2.2}$$

which represents a 180° rotation as depicted below.

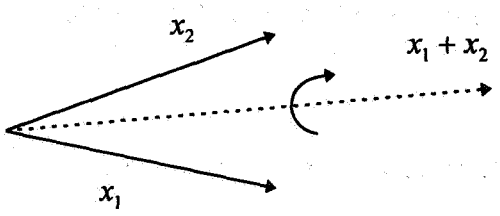

These two quaternions may be combined to create a parameterization of the set of quaternions which rotates x_1 into x_2

$$q_{12} \sim ((x_2 \times x_1)\cos\frac{\phi}{2} + (x_2 + x_1)\sin\frac{\phi}{2}, (1 + x_2 \bullet x_1)\cos\frac{\phi}{2}) \qquad (2.3)$$

so that the total rotation is as depicted below:

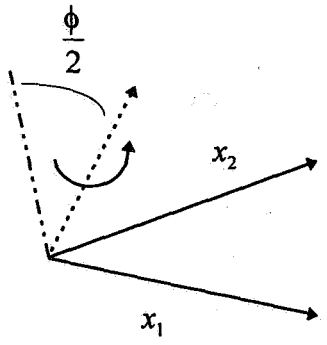

Another way to arrive at equation (2.3) is to combine the rotation of (2.1) with a twist about x_2:

$$q_{12} \sim (x_2 \times x_1, 1 + x_2 \bullet x_1) \circ (x_2 \sin\frac{\phi}{2}, \cos\frac{\phi}{2}) \qquad (2.4)$$

where $\circ$ denotes quaternion composition, i.e.,

$$q_1 \circ q_2 = (q_{14}Q_2 + q_{24}Q_1 + Q_1 \times Q_2, q_{14}q_{24} - Q_1 \bullet Q_2) \qquad (2.5)$$

Equation 3.3 completely parameterizes the set of quaternions which rotates unit vector x_1 into unit vector x_2 in terms of the angle ϕ. Similarly, we may parameterize the entire set of quaternions which rotate another unit vector y_1 into y_2 by

$$q_{12} \sim ((y_2 \times y_1)\cos\frac{\psi}{2} + (y_2 + y_1)\sin\frac{\psi}{2} , (1 + y_2 \bullet y_1)\cos\frac{\psi}{2}) \qquad (2.6)$$

in terms of the angle ψ.

Now suppose we wish to determine the unique quaterion (as a member of $\mathbf{PR}^3$) which transforms x_1 to x_2 *and* y_1 to y_2. One way to do this would be to equate equations (2.3) and (2.6), solve for ϕ or ψ, and plug the result back into the appropriate expression. However, a quicker way is to note that the vector part of the expression (2.3) lies in a plane orthogonal to x_2 - x_1. Similarly, the vector part of (2.6) lies in the plane orthogonal to y_2 - y_1. Thus, the vector part of the quaternion we seek must lie in the intersection of the planes, i.e., in the direction (x_2 - x_1) × (y_2 - y_1). The angle of rotation can be determined by projecting the vectors to be rotated and their destination vectors orthogonal to this rotation axis and performing a little trigonometry. The result is:

$$q_{12} \sim ((x_2 - x_1) \times (y_2 - y_1) , x_1 \bullet y_2 - x_2 \bullet y_1) \qquad (2.7)$$

If y_2 - y_1 is small, it is numerically better to calculate (2.7) as

$$q_{12} \sim ((x_2 - x_1) \times (y_2 - y_1) , (x_2 + x_1) \bullet (y_2 - y_1)) \qquad (2.8)$$

and vice versa, as this puts the vector part and the scalar part on a par in terms of magnitude.

This construction breaks down in two instances:

1) If the vectors x_2 - x_1 and y_2 - y_1 are parallel, we do not have enough information to construct a full quaternion.

2) If $x_1 = x_2$, or $y_1 = y_2$, then that set of vectors for which the equivalence holds *is* the axis of rotation, and the angle of rotation may be easily determined.

III. Applications of the Quaternion Decomposition

Direction Cosine Matrix to Quaternion

The first application of the quaternion decomposition which we will consider is initialization of the quaternion from a given direction cosine matrix[5]. Suppose this is given as $T_1^2 = [\alpha\ \beta\ \gamma]$, where α, β and γ are column 3-vectors which represent the transformation of $\hat{e}_1, \hat{e}_2$ and $\hat{e}_3$, the canonical basis vectors, from frame 1 to frame 2. The quaternion is given by any of the following three parameterizations:

$$\begin{aligned} q_{12} &\sim ((\alpha - \hat{e}_1) \times (\beta - \hat{e}_2), \beta_1 - \alpha_2) \\ q_{12} &\sim ((\alpha - \hat{e}_1) \times (\gamma - \hat{e}_3), \gamma_1 - \alpha_3) \\ q_{12} &\sim ((\beta - \hat{e}_2) \times (\gamma - \hat{e}_3), \gamma_2 - \beta_3) \end{aligned} \tag{3.1}$$

Target Quaternion Computation

Suppose we wish to find the quaternion which will rotate a spacecraft so that the *x* axis is pointing at a celestial object in the direction of a unit vector u_{targ} in inertial coordinates. Furthermore, suppose that, in order to shield sensitive components from the glare of the sun, we wish the unit vector u_{sun} to have minimal projection (maximally negative projection) on the *y* axis. Then, the desired quaternion may be found as:

$$q_{bi} = \left((u_{targ} - \hat{e}_1) \times \left(\left(\frac{u_{sun} \times u_{targ}}{|u_{sun} \times u_{targ}|} \right) - \hat{e}_3 \right) \ , \ \left(\frac{u_{sun} \times u_{targ}}{|u_{sun} \times u_{targ}|} \right) \bullet \hat{e}_1 - u_{targ} \bullet \hat{e}_3 \right) \tag{3.2}$$

The motivation behind this formula is to construct the spacecraft body coordinate triad in inertial space consisting of the *x* axis pointing in the direction of u_{targ}, the *z* axis pointing in the direction $u_{sun} \times u_{targ}$, and the *y* axis in the direction $(u_{sun} \times u_{targ}) \times u_{targ} = -(u_{sun} - (u_{sun} \bullet u_{targ}) u_{targ})$.

Global Attitude Estimation

Suppose that we have a set of N observation unit vectors v_i in a spacecraft body frame of reference, with corresponding unit vectors w_i in some

reference frame of reference. Let us assume that both frames are inertially fixed for the duration of observation.

Equations (2.1) and (2.2) show that the i^{th} set of vectors establishes a two dimensional orthonormal (in $\mathbf{R}^4$) basis for the quaternion from reference to body, q_{rb}, to wit

$$base_{1i} = \frac{\begin{bmatrix} v_i \times w_i \\ 1 + v_i \bullet w_i \end{bmatrix}}{\sqrt{2(1 + v_i \bullet w_i)}} \tag{3.3a}$$

$$base_{2i} = \frac{\begin{bmatrix} v_i + w_i \\ 0 \end{bmatrix}}{\sqrt{2(1 + v_i \bullet w_i)}} \tag{3.3b}$$

Similarly, there is a two dimensional orthonormal basis for the kernel or null space of the quaternion covector q_{rb}^T:

$$null_{1i} = \frac{\begin{bmatrix} w_i \times v_i \\ 1 - v_i \bullet w_i \end{bmatrix}}{\sqrt{2(1 - v_i \bullet w_i)}} \tag{3.3c}$$

$$null_{2i} = \frac{\begin{bmatrix} v_i - w_i \\ 0 \end{bmatrix}}{\sqrt{2(1 - v_i \bullet w_i)}} \tag{3.3d}$$

Clearly, errors in the observations will cause these basis and null vectors to be somewhat in error so that, in order to estimate attitude, we would want to put them in some sort of least squares estimation algorithm. One approach for this would be to seek to *minimize* the cost functional

$$J(q_{rb}) = \sum_{\substack{i=1,N \\ j=1,2}} a_i \left\langle null_{ji}, q_{rb} \right\rangle^2 \tag{3.4}$$

with weighting coefficients a_i, subject to the constraint that q_{rb} have unit length. Another approach would seek to *maximize* the cost

$$J(q_{rb}) = \sum_{\substack{i=1,N \\ j=1,2}} a_i \left\langle base_{ji}, q_{rb} \right\rangle^2 \tag{3.5}$$

subject to the same constraint.

Still a third approach would be to combine these two and seek to maximize

$$J(q_{rb}) = \sum_{\substack{i=1,N \\ j=1,2}} a_i \left[\left\langle base_{ji}, q_{rb} \right\rangle^2 - \left\langle null_{ji}, q_{rb} \right\rangle^2 \right] \tag{3.6}$$

or minimize the negative of this, whichever is preferred.

The addition of the constraint that q_{rb} be a unit quaternion results in an eigenvalue problem, with q_{rb} being the eigenvector associated with the maximum eigenvector of

$$K = \sum_{\substack{i=1,N \\ j=1,2}} a_i \left[base_{ji} base_{ji}^T - null_{ji} null_{ji}^T \right] \tag{3.7}$$

It is elementary to demonstrate that the matrix so derived is identical to that of Shuster and Oh [3], and the solution to this problem correspondingly identical to their QUEST algorithm.

Suppose we do not have the computing resources to implement this batch algorithm or, alternatively, suppose that our spacecraft frame of reference is really not inertial, and we wish to track the variation of the quaternion over time. A recursive algorithm is then called for.

The existence and knowledge of the two null vectors given above suggests an extremely simple algorithm based upon Gram-Schmidt orthogonalization, i.e., if the null vectors were known perfectly, we might take an initial estimate of the quaternion and orthogonalize it with respect to them:

$$q_{rb} \rightarrow q_{rb} - \left\langle null_1, q_{rb} \right\rangle null_1 - \left\langle null_2, q_{rb} \right\rangle null_2 \tag{3.8}$$

followed by normalization to maintain good numerical properties of the quaternion. The algorithm can be equipped with some small gain factor, and we have the following theorem.

Theorem

Given a unit quaternion q and an infinite sequence of quaternion null vectors $\{n_k\}$ in which any infinite subsequence spans $\aleph\{q^T\}$, the kernel of the quaternion covector q^T,and an initial quaternion estimate q_0 which does not lie entirely in $\aleph\{q^T\}$, the recursion

$$q_{k+1} = \frac{q_k - \alpha\langle q_k, n_k\rangle n_k}{\sqrt{1-\alpha(2-\alpha)\langle q_k, n_k\rangle^2}} \tag{3.9}$$

for some $\alpha \in (0,1]$ is globally convergent to the true quaternion q.

Proof:

Let M = M^2 = M^T be a non-negative definite symmetric projection matrix whose kernel spans the image of q. The function

$$V_k = q_k^T M q_k \tag{3.10}$$

is a radially unbounded Lyapunov function for which

$$\Delta V_k = V_{k+1} - V_k = \frac{\alpha(2-\alpha)\langle q_k, n_k\rangle^2}{1-\alpha(2-\alpha)\langle q_k, n_k\rangle^2}(V_k - 1) \tag{3.11}$$

demonstrating that V_k is monotonically decreasing except in two cases:

1) when $\langle q_k, n_k\rangle = 0$ which cannot persist unless $q_k = q$ as desired

2) when V_k = 1, which undermines our requirement that q_k have at least some component in Im{q}.

Thus, $V_k \to 0 \Rightarrow q_k \to q$.

To deal with imperfect data, we can specify α as small as we like. In general, an optimal gain factor will be the ratio of desired attitude variance, divided by the sum of attitude variance and measurement variance, however, the details will be left to the reader.

IV. Conclusions

The quaternion decomposition outlined herein reveals previously hidden structure and nuance in the quaternion attitude representation. In addition, it opens the way to some exceedingly simple and direct methods of accomplishing various attitude determination and control tasks.

In particular, the batch attitude determination algorithm was shown to be equivalent to the QUEST algorithm, while illuminating the actual mechanism by which the algorithm accomplishes its objective. The recursive algorithm given is simple, globally convergent, and may be optimized to some extent. Further obtimization of the algorithm could be accomplished by including a projection matrix or Kalman filter type covariance matrix to weight succeeding measurements based upon previous updates, however, the algorithm as given is adequate for a wide variety of applications.

References

[1] S.M. Joshi, A.G. Kelkar, and J.T.-Y. Wen, "Robust Attitude Stabilization of Spacecraft Using Nonlinear Quaternion Feedback," *IEEE Transactions on Automatic Control,* Vol. 40, No. 10, 1995

[2] F. Lizarralde and J.T. Wen, "Attitude Control without Angular Velocity Measurement: A Passivity Approach," *IEEE Transactions on Automatic Control,* Vol. 41, No. 3, 1996

[3] M.D. Shuster and S.D. Oh, "Three-Axis Attitude Determination from Vector Observations," *Journal of guidance and Control*, Vol.4, No. 1, 1981

[4] J.T.-Y. Wen and K. Kreutz-Delgado, "The Attitude Control Problem," *IEEE Transactions on Automatic Control,* Vol. 36, No. 10, 1991

[5] J.R. Wertz, ed., *Spacecraft Attitude Determination and Control*. Boston: Kluwer Academic Publishers, 1979

Page intentionally left blank

FLEXIBILITY OF MISSION PLANNING TO CHANGES IN OPERATING ENVIRONMENT AND MISSION REQUIREMENTS FOR THE MSTI-3 SPACECRAFT

Raymond Espiritu
Michelle Weldy

ANSER
Suite 800
1215 Jefferson Davis Highway
Arlington, VA 22202-3251

Abstract

The third Miniature Sensor Technology Integration Satellite (MSTI-3) is scheduled to collect over 1 million infrared background images of the earth and earthlimb. These images will improve and validate existing predictive infrared radiance models. In addition, the images will expand the statistical information for background scenes ranging from benign (little to no cloud cover) to stressing (multi-layer cloud cover) over a period of seasonal variations. Images used for model improvement and validation are given higher priority over images collected for statistical analysis and constitute the bulk of early spacecraft operations. Geographic regions affecting global climate changes, such as subtropical jet streams, and mountain ranges are of particular interest for images used in model assessment. In addition, mission requirements were expanded to encompass an independent validation of infrared images. The new plan includes collecting images over existing LIDAR sites in the United States as well as joint operations with aircraft-borne sensor measurements. Optimized planning ensures collection of model assessment and validation images over specific, and often irregularly shaped geographic regions, with statistical analysis images collected whenever camera operations and solar geometry allow.

The varying mission requirements for the spacecraft in the early phase of operations posed interesting challenges for Mission Planning. This paper focuses on these challenges and addresses the automated tools developed to make MSTI data collection a success. The interlocking nature of the computer programs is designed to calculate the solar geometry and configure sensor position for any combination of geometry requirements. The resulting MSTI-3 Mission Planning process is both flexible and responsive, accommodating schedule changes as well as any replanning efforts necessitated by spacecraft anomalies, post-operation data analysis, and the eclipse season.

1.0 Introduction

The Miniature Sensor Technology Integration 3 (MSTI-3) spacecraft was launched on May 16, 1996 into a low earth, sun synchronous orbit. An United States Air Force satellite, MSTI-3 is intended to demonstrate low-cost small satellite technology. Its mission is to characterize the Earth and earthlimb background, both for validation of predictive infrared radiance models and to expand existing statistical background data. The increased understanding of the Earth's atmospheric structure will improve sensor design for space-based satellites.

The MSTI-3 payload includes two radiometers, one in the short-wave (2.7 - 3.1 μm) and one in the mid-wave (3.5 - 4.5 μm) infrared band, each with a seven position filter wheel. The payload also houses a visible spectrometer, with a spectrum wedge filter covering about 80% of the field of view (FOV). Image collection is facilitated by a common two-axis gimballed pointing mirror and foreoptics assembly. The gimbals allow the mirror to roll and pitch 10°/sec about the spacecraft x-axis and y-axis respectively, allowing MSTI-3 to view a wide range of geometries during a camera operation.

Responsibility for commanding the spacecraft belongs to Detachment-2 of Onizuka Air Station in California, with round-the-clock support from the MSTI Payload Operation Center (MPOC) in Virginia. The Air Force Satellite Control Network (AFSCN) and a dedicated ground site in Fairbanks, Alaska are used to upload commands and to download spacecraft and payload data.

2.0 Mission Planning

The MSTI science working group (SWG) developed a set of requirements for gathering data, dividing image collection into seasons, geographical regions, filters, line-of-sight zenith angles, and solar scattering angles. Mission Planning's goal is to maximize the useful data collected for the SWG, while considering the operational capabilities of the spacecraft (see Figure 1).

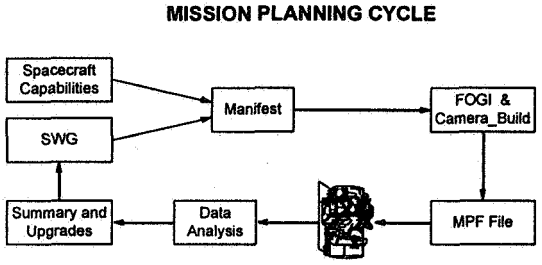

Figure 1: Mission Planning Flow Diagram. *Mission Planners plan operations based on science community requirements and spacecraft capabilities using a set of tools built to adapt quickly to new scenarios.*

During the initial phase of the mission, Mission Planning built the payload operations for both on-orbit spacecraft characterization and science collection. The characterization identifies any pointing errors or jitter due to spacecraft motion, vibration, or post-launch sensor alignment, and therefore received the highest priority. The SWG also had a set of special objectives during the beginning of the mission. This included image collection over certain geographic areas, as well as joint experiments with LIDAR facilities.

The challenges to Mission Planning to provide such a wide variety of experiments, some within specific windows of opportunity, were solved largely by software tools developed in-house. The modularity of these software tools enable Mission Planning to handle nominal, characterization, and LIDAR image collection requests in a timely manner, often with turnaround times of three days from identification of experiment changes to new experiment execution.

2.1 Experiment Plans

Experiment plans included on-orbit characterization, nominal operations, and the calibration of each operation. Each of these required different features in simulation software to build the necessary payload command scripts.

2.1.1 On-orbit Characterization

The on-orbit characterization phase required Mission Planning to plan 5 experiment types: two different benchmarks, point source response, jitter, and off-axis rejection. The benchmark tests characterized the payload performance by taking images of space and a warm blackbody mounted on the spacecraft and comparing the results to pre-launch measurements. The results of the benchmark test enabled the SWG to determine the payload performance and provide information about the quality of data received in nominal operations. The benchmark test will also be conducted at regular intervals throughout the mission to characterize payload sensor degradation, leading to possible changes in the SWG priorities. The point source response (PSR) tests characterized responsivity of the focal plane and relative alignment of the sensors by imaging IR stars in the center, and corners of the focal plane. Results from this test influence the way large mosaic scenes (described later) are performed, since the generation of these scenes requires large gimbal changes. The PSR test will also be used to predict the quality of images collected from event-driven observations, where targets of interest may not necessarily be at the center of the FOV. The jitter test determined the jitter contribution in the payload images due to the spacecraft, e.g. vibration due to the reaction wheels, thus characterizing the resolution that can be expected in the images collected. This test also assessed gimbal settling time by imaging the moon in the center of the field of view then repointing the mirror and imaging the moon at the corners of the sensor field of view. Gimbal settling time information has a significant influence on any experiment involving large gimbal changes. Finally the off-axis rejection test quantified the amount of off-axis contribution of the sun to radiance observed by the payload. This aids in image calibration by separating target image intensity from radiance scattered off the spacecraft. Since this was the first bus maneuver performed as part of a

payload observation, and due to the risk involved in decreasing the sun angle to the payload sensor, this test was performed within real-time contact of a ground station.

After a series of unpredicted changes of the pointing mirror, two characterization experiments were designed to more accurately assess the gimbal settling time and refine the pointing alignment of the sensors. These are known as the Diagnostic 10 and Star Alignment test. The Diagnostic 10 test is named after the diagnostic command which causes the payload software to downlink, in real-time, the roll and pitch gimbal angles of the mirror at a frequency of 500 Hz. Gimbal settling time data was then collected by executing several repoints of the mirror during real-time contact with a ground site. The Star Alignment test was a variation on the Jitter test, in that a star was substituted for the moon, with images taken of the star in the center, then the corners of the field-of-view (see Figure 2). Additionally, the spacecraft executed a bus maneuver such that during the star observation a large range of roll, pitch angles would be encountered. The Star Alignment test gave

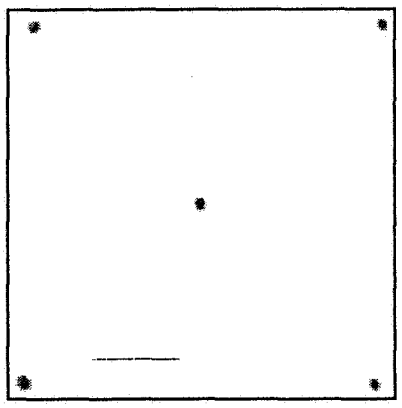

Figure 2: Star Alignment Test. *By positioning a star in each corner and the center of the focal plane, spacecraft jitter and pointing capabilities can be analyzed. This composite is the result of a July test.*

Mission Planners additional flexibility as stars can be imaged at any time, while the Jitter test required a particular lunar-solar-spacecraft geometry. The payload commands used to execute these characterization experiments were the same as those used in nominal operations, but since each experiment was assigned its own observation window, it was much easier to track and analyze the cause of characterization experiment failures. Most characterization experiments were scheduled to occur during access to a ground station for real-time observation. The real-time contact provided easy confirmation of test execution and helped to characterize the nature of any experiment failures.

Characterization experiments were scheduled for the second week of operations and were expected to be completed within 7 days, wherein the nominal operations phase of the mission would begin. This proved to be too short a timeframe, however, so a combination of science and operational goals were incorporated, with Mission Planning building background experiments with characterization operations inserted wherever possible.

2.1.2 Nominal Operations

Nominal experiments include not only the collection of Earth background data as determined by solar geometry and target location, but also event-driven observations such as aurora, forest fires, the jet stream, and stratospheric warming. The experiments are designed to provide information on the spatial and temporal background structure and the variation of the structure as a function of spectral bandpass, viewing geometry, solar, cloud and terrain type, geographical region, latitude, season, and tangent height. Figure 3 below shows the viewing and solar geometry, which comprise a part of the independent parameters and constraints inherent in each experiment. These experiments fall into four categories: model assessment collection, statistical scene measurements, large mosaic scenes, and event-driven observations. The number of experiment types within each category is too large to adequately describe in detail, however a description of the categories will give a general idea of the varied target and scheduling requirements expected to be fulfilled by Mission Planning. Unlike the characterization experiments, nominal operations attempt to maximize the number of experiments within a 20 minute camera observation window.

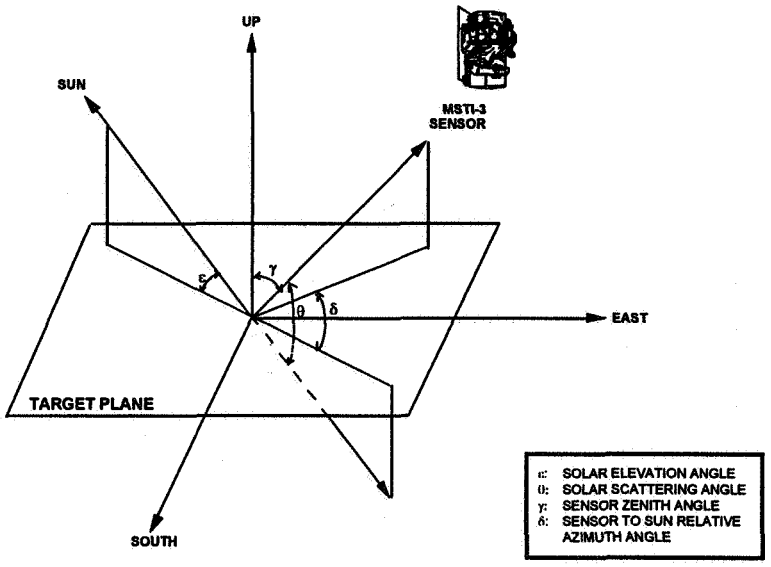

Figure 3: Target-Spacecraft Geometry. *Two parameters of interest to the SWG are the line-of-sight zenith angle and the solar scattering angle of each experiment. The solar scattering angle, in particular, requires careful planning, as availability is seasonal.*

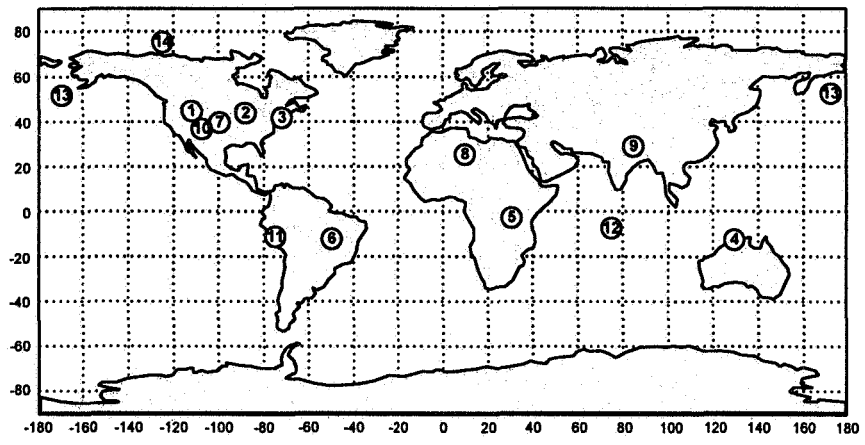

Figure 4: Model Assessment Regions. *The 14 model assessment regions and 6 experiment types make these high priority operations a challenge to plan.*

2.1.2.1 Model Assessment

Model assessment images were given the highest priority during the initial phase of operations and required image collection over specific geographic locations (see Figure 4). These regions define atmospheric truth, cloud truth, weather-driven sources, and orthographic regions. Joint experiments with LIDAR facilities and other programs provide the atmospheric and cloud truth collections (see Figure 5), while geographic regions known for large variation in cloud cover and weather provide the remaining data. Six experiment types are categorized as model assessment, three collecting images above the horizon, two below the horizon, and a third is a large mosaic scene collection either above or below the horizon. These experiments continue, but at a lower priority.

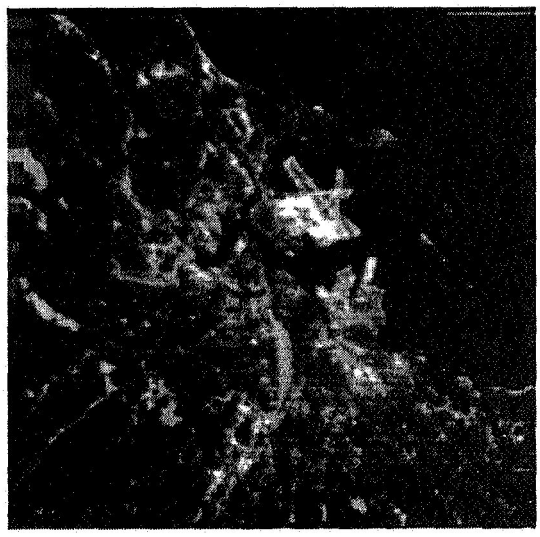

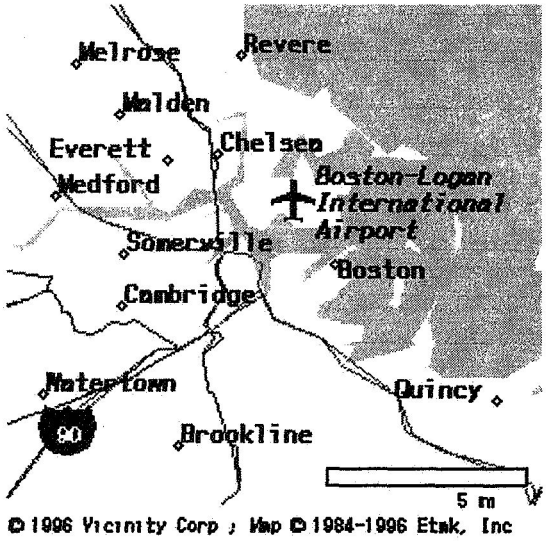

Figure 5: Truth Data. *MWIR image taken over the Boston, Massachusetts area adds to the truth data collected for the SWG.*

2.1.2.2 Statistical Scenes

While the Model Assessment images were initially given the highest priority, the images collected in statistical scene measurements composed the bulk of the MSTI-3 mission. These small mosaics (at most 3 x 3 FOVs) cover the entire globe, with 6 regions in the northern hemisphere, and 3 regions in the southern hemisphere. In each season, 6 solar scattering angles (SCA) and 4 line-of-sight zenith angles (LZA) constitute the range of geometric combinations requested by the science working group, and 13 of the 14 filters are used. This data will be used to relate seasonal, geometric, regional, and spectral interdependencies of background clutter. Three types of experiments: day, night, and temporal experiments, are included in this category.

2.1.2.3 Large Mosaics

This category contains a single experiment type to characterize spatial structure. Size of the mosaic is dependent on the LZA, and as shown in Table 1 below, ranges from a coverage of about 460 x 40 km to 990 x 80 km. As with the statistical scenes, large mosaic scene collection is broken down by season, region, geometry, and spectral band, with 9 SCA and 7 LZA comprising the range of viewing geometries requested. Regions of interest vary for each season, and are dependent on probability of cloud cover and the diversity of cloud conditions.

Table 1: Large Mosaic Scenes. *Large scenes range from 32 to 152 fields-of-view, depending on the LZA of interest. Mission Planners must build these scenes with LZA, SCA, gimbal roll, gimbal pitch, and FOV overlap in mind.*

LZA (deg)	FOV (wide)	FOV (long)	Est.Length (km)	Est. Width (km)
90	2	16	960	120
80	3	26	987.5	114
70	3	38	991	78
60	3	26	510	59
45	3	35	512	44
30	4	38	463	41

2.1.2.4 Event-driven Observations

The collection of images over auroral regions and other phenomenon is completed only upon notification by the MSTI chief scientist. Due to the time specific nature of such observations, a nominal experiment must be replaced by an event-driven observation if necessary to avoid scheduling conflicts. Mission planning is required to be able to plan and schedule such an observation given a minimum of 24 hours advance notice. The first such experiment was a forest fire blazing in Montana in early August (see Figure 6). Mission planning quickly replaced an existing nominal observation with an event-specific observation to collect a large mosaic of the target region. In fact, the observation required modification several times as the fire moved through the West. Only 24 hours prior to execution did the SWG agree on a final target.

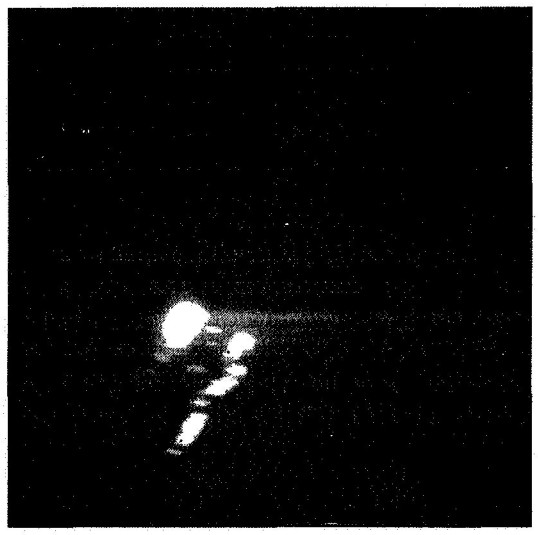

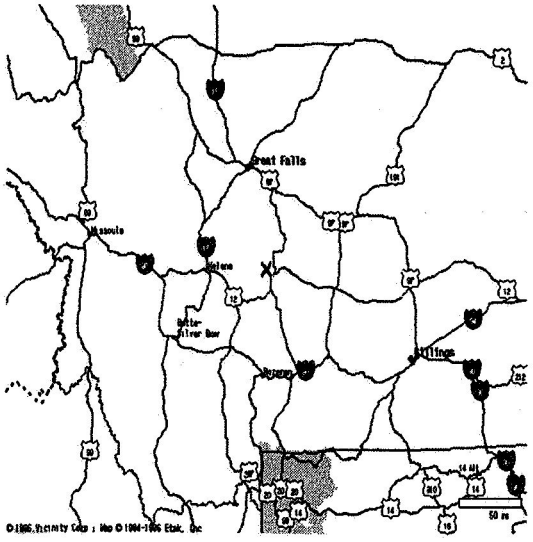

Figure 6: Event-Driven Observations. *Event-driven observations such as this fire in Montana require quick planning by Mission Planners. The "X" in the center of the map shows the exact geographical location of the image.*

2.1.2.5 Calibrations

Calibration of the IR sensors at the start and conclusion of each camera operation is required for every IR observation. The performance characteristics of the payload also require calibration to be performed every 5 minutes during the camera operation. Images are collected of deep space and a warm blackbody using the same camera settings as those used during the main IR observation. The data collected by these experiments provide the offset contributed by warm optics, filters, and other noise inherent in the observation.

2.1.3 Summer/Fall Results

Results are tracked primarily by experiment type and season. By the end of Fall, almost 600,000 images were collected, with approximately 60% experiment images and 40% calibration images. Table 2 shows the breakout of successfully completed experiments for Summer and Fall. Each season consists of three months, with June, July, and August comprising Summer and September, October, November rounding out Fall.

Table 2: Summer/Fall Results. *Over 12000 experiments of varying size and objective were successfully collected over the first two seasons. Special requests for Model Assessment include LIDAR and joint operations.*

	Summer	Fall
Model Assessment:		
normal	158	229
special request	22	17
Statistical Scenes	4768	6784
Large Mosaics	163	186
Event-Driven	1	9
Calibration/Characterization	16	11

Because of the sun synchronous nature of MSTI's orbit, MSTI was solar lit for Summer and most of Fall. During the last days of October, eclipse season started, with the Earth initially obstructing MSTI's view of the sun for 8 minutes per pass. This segment of darkness increased steadily until December 21, when darkness peaked at 24.75 minutes per 93 minute period. Due to these eclipses, Mission Planning restricted experiment planning to the southern hemisphere, where MSTI remained solar lit. However, during the weeks surrounding the peak period of eclipse season, power considerations and an unexpectedly weak battery temporarily halted payload operations. Partial operations resumed in January and full operations resumed in February.

2.2 Planning Software

Mission Planning developed a set of tools to handle the large and varied science requirements (see Figure 7). Visual Basic for Excel was used to build tools which generate a mission calendar of events (Manifest tool), and to sort through the results of the observation simulator (Camera_Build tool). Visual Basic was chosen due to its capability to display a user-friendly graphic interface and broad interconnectivity. The simulation tool FORTRAN Observation and Geometry Integrator program (FOGI), however, required more speed and memory capacity than was available on a personal computer. That tool was written in FORTRAN and is used on a Unix platform.

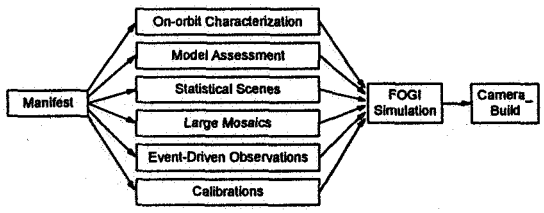

Figure 7: Software Tool Flowchart. *The mission Manifest provides a schedule of events and experiment types to plan. FOGI and Camera_Build then build the operations.*

2.2.1 Mission Manifest

The daily schedule of requested events is generated by a Manifest tool, written in Visual Basic for Excel to sort the SWG requirements, while incorporating the operational constraints of the spacecraft. This program keeps a series of easy-to-use priority lists and requirement worksheets which can be easily changed as requirements from the SWG change. The priority list controls which filters and experiment types receive the highest attention when distributing daily events, while the worksheets

contain the seasonal, regional, and geometrical breakdowns as well as the operational constraints of 4 twenty minute operations per day and a maximum of 10400 images per day. Key to this tool is the SCA matrices, which reflect which solar scattering angles are available at each of the 6 latitude bands during a season. This feature helps maximize the number of valid experiments for each operation by considering up front the seasonal solar illumination of the earth surface.

2.2.2 FORTRAN Observation and Geometry Integrator

The simulation tool, and the main component used to build an operation, is the FORTRAN Observation and Geometry Integrator program (FOGI). FOGI simulates the position of the earth, moon, sun, and a defined set of IR stars during any specific time period and compares them with MSTI-3's position (which is read from a NORAD propagated ephemeris). Using this information and specifying an attitude, FOGI determines the solar geometry of a particular target at any requested time. FOGI can also calculate aim points for a series of targets and can position a target in different locations on the field-of-view. The type of target information varies depending on target type, celestial or terrestrial, and mosaic size. Aim point descriptions can be in terms of pointing mirror gimbal angles; target latitude, longitude and altitude; right ascension and declination; or a relative repoint vector of pixel offsets in the focal plane coordinate system.

For nominal experiments, FOGI calculates target points based on desired solar geometries and geographic regions. This is largely a non-interactive process, requiring only the name of the user file. Large mosaic scenes require more user interaction to meet the specified length, width, and overlap specifications. In addition, FOGI monitors all gimbal roll and pitch angles necessary to complete an experiment. Invalid gimbal positions or those resulting in a line-of-sight blocked by the satellite are rejected and sent back through the FOGI process. This proves to be more of a problem with characterization experiments, since celestial targets are often at the extreme ranges of allowable gimbal angles. Other recycled experiments include those with unusable moon-satellite-Earth and sun-satellite-Earth angles.

Characterization experiments require a large amount of user interaction, since they are often constrained by real-time contacts to ground sites and FOGI is not yet capable of correlating ground contact information with experiment requests automatically. The short time window imposed by the real-time constraint also necessitates a dedicated camera operation, eliminating any joint nominal experiments. Fortunately the characterization experiments are infrequent and require only celestial targets, thereby allowing execution anywhere in the orbit.

2.2.3 Mission Planning Files

Once FOGI has calculated the target and spacecraft information for each experiment, the Camera_Build tool is used to sort through the results. This Visual Basic program uses the FOGI output files to create a chronological experiment timeline based on priority, adding calibration sequences at specified intervals. This resulting Mission Planning File (MPF) contains all the data necessary to build the payload command scripts, including bus maneuver quaternions (if required), time of execution, filter positions, gain settings, integration times, FOV size, experiment type, target latitude, target longitude, target altitude, gimbal roll angles, pitch angles, and calibration execution times and temperature settings for the warm calibration plate.

2.3 Information Dissemination

The final component to maximizing payload performance involves keeping the information loop among the SWG, Mission Planning, and Image Processing complete. To aid this effort, Mission Planning added some tools and additional procedures to collect, examine, and distribute data.

2.3.1 Time_Record and Summary

MPF files are distributed weekly to Command Generation to build payload commands, but the files can also provide a wealth of information to the entire MSTI team. Visual Basic was again used to automatically retrieve and tabulate the experiment specifications of interest to the MPOC and the SWG.

Built specifically to inform the MPOC, Time_record creates a one page report complete with operation names, day of year, time of execution, estimated number of data images, and estimated number of calibration images. It also identifies the operation objective: background (nominal), lidar, moon test, or a specific calibration or operational test, and whether a bus maneuver is necessary. From this, Image Processing has an easy means of identifying when each operation starts and ends, allowing them to more quickly classify the collection as successful, partially successful, or unsuccessful. Command Generation, on the other hand, uses the page to gauge the upcoming activities.

A more detailed description of the planned week is extracted by Summary. Summary creates an Excel workbook consisting of one sheet per operation and one overall accounting sheet. The individual operation sheets report the objective, target latitude, target longitude, start time, end time, filter usage, region coverage, LZA requested, SCA requested, LZA calculated, SCA calculated, and experiment type for each experiment in the operation. The overall page condenses the week in a table that identifies the objective, operation times, and the experiment types for each operation. Since these files are in Excel, they are easily transferable to the SWG members, who can then identify the strengths and shortcomings in meeting the science objectives.

2.3.2 Results Database

Mission Planning also helps Image Processing with the classification of downloaded data as successful, partially successful, or unsuccessful. By looking at parameters such as roll, pitch, target latitude, target longitude, and time of execution within the resulting image files, the validity of an operation can be determined. This information is kept in a "Results" database that the entire MPOC can access. Also, once this process is completed for an operation, the MPF files can be updated to reflect reality, and run through Summary once more to provide the SWG with their own "Results" file.

2.4 Data Analysis

In the context of Mission Planning, results pertain to how close actual observations corresponded with those planned. For the MSTI program this translates to a post operation analysis of downloaded data. Of primary interest are the location of the image (in either a geographical or celestial reference frame), the gimbal positions at the time of image collection, and the time the image was collected. This is then compared to the FOGI simulation as to target location, time requested for image collect, and gimbal positions expected, pinpointing any concerns.

Further, Mission Planning uses downloaded image files to analyze the large mosaics scenes, as they are considered the highest priority experiments in nominal operation. A Visual Basic tool, LMS_graph, imports image files, which also contain target information based on the actual spacecraft ephemeris and recorded gimbal angles, and graphs the FOV of the selected experiment (see Figure 8), and also shows how the LZA or SCA varied with time. This provides quick feedback on issues such as overlap and angle variation over a scan.

Data analysis was particularly critical during the second week of operations when both

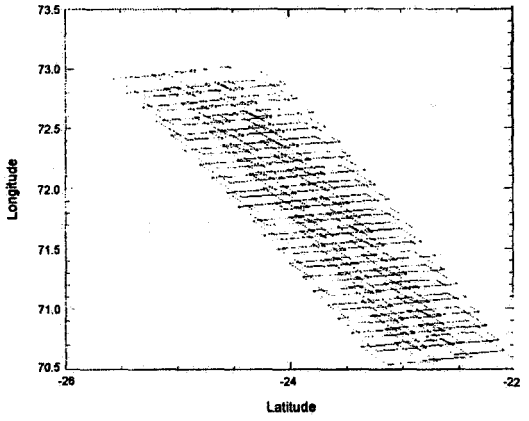

Figure 8: Graphing Image Data. *LMS_graph uses real image data to determine scan features. This can then be compared with the predicted values.*

successful and unsuccessful characterization experiments created further insight into how the spacecraft and payload would actually perform in its operational environment. The results of these initial tests forced Mission Planning to design additional experiments to characterize the spacecraft. Large safety margins were instituted

in operations so that nominal operations can be executed in concert with the new tests.

The flexibility of the planning process and tools enabled the team to rapidly adapt to these challenges with minimal impact. The first item of concern is spacecraft performance. Early assumptions considered mainly the solar geometry issues for terrestrial observations. As additional experiments and characterization tests were conducted, gimbal rolls and pitches were found to approach the software and physical constraints of the system. In addition the payload software did not stop the system from trying to point through the spacecraft structure. The flexibility of Mission Planning tools allowed the introduction of a large safety margin and some additional error flags until enough data was provided to define the system's field of regard.

The second issue was the timing required to change payload settings during an operation, especially filter wheel movement and calibration completion Again, until enough data was analyzed, large safety buffers in the timing were in place, significantly impacting the number of experiments planned for an operation. Once data analysis was complete, however, Mission Planning was able to adjust to the new parameters, increasing experiment numbers and success levels.

The flexibility of the programs and the ability to simulate payload activities enabled Mission Planning to double the number of experiments planned per operation. More importantly, the changes were implemented quickly. Data analysis continues to play a role in Mission Planning as the MSTI team attempts different experiments and continues to further maximize the experiments conducted in each operation.

3.0 Conclusion

Mission Planning has created a flexible and user-friendly architecture to build a myriad of experiment types and to disseminate information. The MSTI Mission Planning team has succeeded in building and replanning experiments in a short period, providing a responsivity critical to the success of the mission, as well as providing the SWG and MPOC with up-to-date objective sheets. Key to this effort has been the set of tools developed to build not only the nominal events, but the additional characterization tests as well. These tools have allowed a small team of planners to effectively plan each day's payload operation quickly and efficiently.

During on-orbit operations, Mission Planning identified key spacecraft parameters which have affected the quantity and quality of images collected. Rather than allowing spacecraft constraints to limit observations, it quickly devised and implemented new procedures in order to provide the SWG with as much data as possible. The ultimate success of the MSTI-3 mission lies in the dedication of the entire project team in overcoming such obstacles. For Mission Planning however, success lies in the modularity of its software tools, the clarity of the planning process, and the creativity of the team.

4.0 Acknowledgments

The authors would like to thank Steve Hearney and Todd Probert for their editing expertise, Anne Callahan for her formatting talents., and Howard Taylor for the image graphics.

5.0 References

Hood, J. 1995. "MSTI-3 Background Measurements Experiment Plan." *ANSER Corporation*, January.

Jeffrey, W. 1996. "MSTI-3 Experiment Plan." *Institute for Defense Analyses*, July 24.

Jeffrey, W., et al. 1996. "On-Orbit Characterization of MSTI-3." *Institute for Defense Analyses*, May 31.

Weldy, M. 1996. "Balancing Science Objectives and Operational Constraints: A Mission Planners Challenge." *ANSER Corporation*, May.

6.0 Biographies

Raymond Espiritu graduated from Yale University in May, 1993 with a Bachelors in Mechanical Engineering. In August 1993, he enrolled in the JIAFS program, a joint graduate school program between George Washington University and NASA Langley. His thesis work

was "Determining Venusian Upper Atmosphere Characteristics Using Magellan Attitude Control Data." He graduated from the JIAFS program in August, 1995 and shortly thereafter joined ANSER as part of the MSTI-3 Mission Planning Team.

Michelle Weldy received her BSE in Aerospace Engineering from the University of Michigan in 1993 and her MSE in Aerospace Engineering from the University of Texas at Austin in 1994. She currently works for the Space and Technology Division of Virginia-based ANSER corporation, where she is a member of the MSTI-3 Mission Planning team.

Page intentionally left blank

Orbital Stability Considerations for Millimeter Wave Communication

P. Christopher
Stanford Telecommunications, Inc.
Reston, VA 20190
pchristopher@sed.stel.com

Abstract

Millimeter wave satellite communication will require high ground elevation angle over large areas. Three orbital constellations which can supply this need are discussed. Elevation angle probability density functions are generated and shown for each of the three constellations. The first is a combination of two antipodal geostationary and three phased Molniya satellites. The 72 satellite Motorola M-Star LEO system is then shown, and orbital stability is compared to the TOPEX/Poseidon. Finally, a 48 satellite elliptic LEO system is described and its expected orbital lifetime is discussed. The Appendix shows orbital lifetime as a function of altitude of perigee and eccentricity.

I. Background

The ability of satellite constellations to supply continuous communication coverage over the entire Earth has been a matter of intense study since the '60s. Some of the studies in the mid sixties concentrated on geosynchronous satellites. J. Walker (1) introduced excellent orbital concepts and analysis to show that 5 phased geosynchronous satellites could supply continuous worldwide coverage. Figure 1-1 shows the spatial relations between the first two Walker satellites. The inclination is 43 degrees and the right ascensions differ by 72 degrees. Figure 1-2 indicates the subsatellite traces of all 5 Walker geosynchronous satellites. Walker also recognized that low earth orbits (LEO) systems had unique properties and advantages, and he proposed and analyzed a 48 satellite system concept which became the basis of the Loral Globalstar system in the '90s. Draim (2) later proposed a system of only 4 hypersynchronous satellites for worldwide coverage.

Motorola introduced another earth coverage constellation concept (Iridium) in 1990. All of these concepts assumed that ground antennas could achieve a good communication link performance at low elevation angles. This typically meant choosing frequencies which suffered little atmospheric attenuation. This assumption became less satisfactory in the early '90s as satellite communication frequencies increased rapidly above 14 GHz. The higher frequencies required shorter atmospheric path lengths and higher elevation angles for satisfactory communication.

This paper shows three constellation concepts which could be used for parts of the millimeter wave (30 - 300 GHz) band. The constellations are run for several hours to generate long term elevation statistics for each earth location. Elevation angle probability density functions (pdf) are discussed, and are shown to offer long term high elevation angles over large areas. The first system consists of two antipodal geostationary satellites and three Molniya satellites which offer key coverage in the Temperate and polar areas. This five satellite constellation has been known (3) to give consistently high elevation angles in the Northern Hemisphere. The elevation pdf for Molniya is seen to be remarkable. Motorola's new 50/40 GHz M-Star system concept is discussed next. The 72 satellite system is shown to clearly target the large number of communication users in the Temperate zones. An elliptic LEO system consisting of 48 critically inclined elliptic satellites (4) concludes the paper. It offers the high elevation angles and the convenience of constant ground track, but the low perigee introduces concerns about the useful lifetime. Perigee tradeoffs for useful lifetime are discussed.

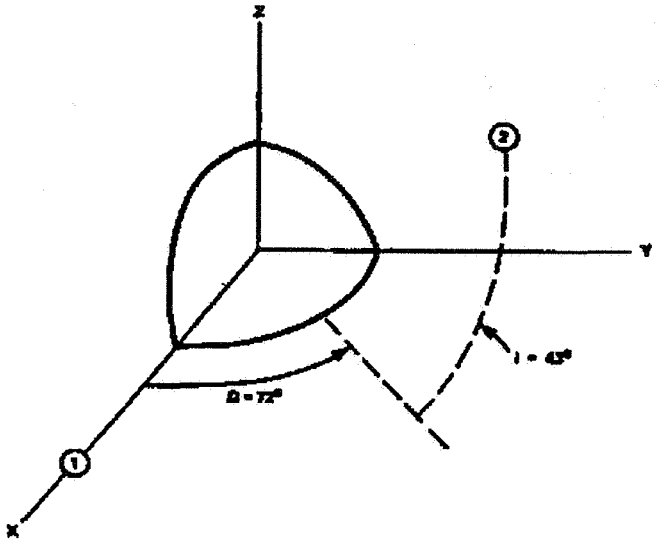

Figure 1-1. Two Walker Satellites in Inertial Space

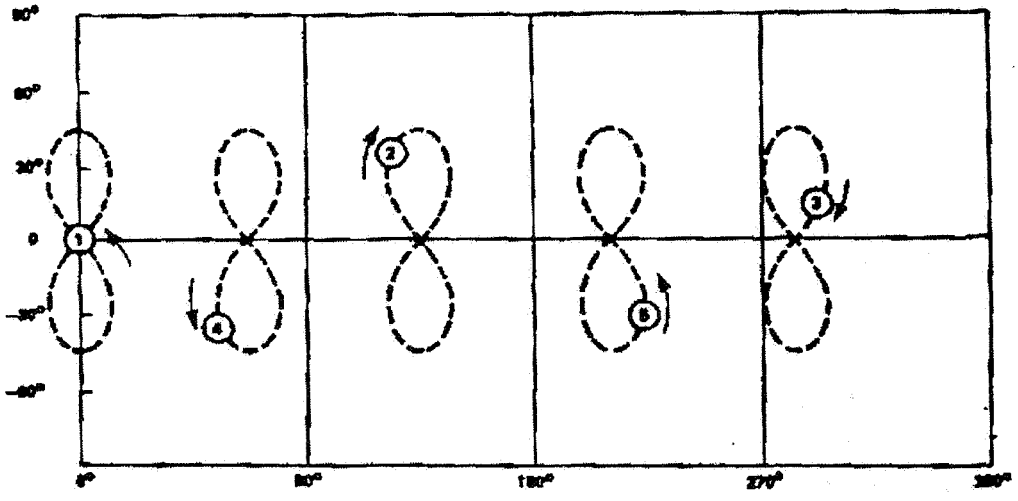

Figure 1-2. Subsatellite Traces for Five Geosynchronous Walker Satellites

2. Geostationary and Molniya Constellation

Geostationary satellites have been known to offer high elevation angles in the tropics, but their elevation is compromised in the Temperate zones. On the other hand, the productive Soviet Molniya series offers high elevation at high latitude. Figure 2-1 shows the positions of a Molniya satellite at one hour intervals of its 12 hour orbit. It offers both high elevation and convenient ground antenna pointing, as it appears to be nearly stationary for many hours near its apogee. The combination of two antipodal geostationary satellites and three phased Molniya satellites has been examined (3), and the constellation offers excellent elevation angle statistics throughout the Northern Hemisphere. Figure 2-2 was generated with the aid of the Stanford Graphics Analysis Tool (5) and indicates a snapshot of the 30 degree elevation coverage with the 5 satellite constellation. Note the excellent coverage offered by the two Molniya satellites near apogee, with one over Norway and the other over the Bering Straits. Figure 2-3 also shows that key parts of the U.S. also have the possibility of angle diversity to either of two Molniya or to a geosynchronous satellite. The third Molniya is waiting in the wings over Antarctica to relieve the Norway satellite as all of the Molniya advance eastward. The apogee positions are always filled, or nearly filled. This concern about the

long term adequacy of the satellite system can be relieved by checking all locations in the Northern Hemisphere for elevation angle at all times. Elevation angle statistics may then be represented as in Figure 2-4, where the density function is plotted vs. latitude and elevation angle. A cut at a given latitude will give a bell shaped curve which is suitable for that latitude for all time. The overall elevation statistics for the Northern Hemisphere have mean and standard deviation (52.45, 15.24) degrees, respectively. The constellation can be seen to give outstanding elevation angle to a large population of ground stations.

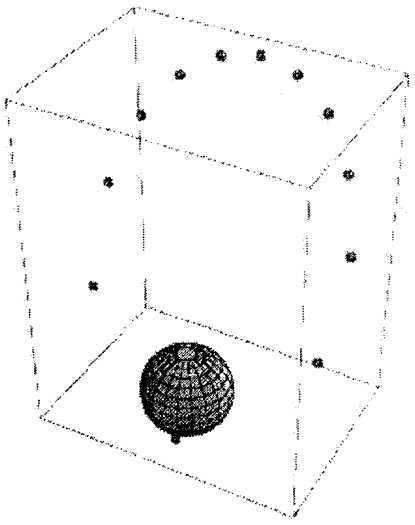

Figure 2-1. One Hour Snapshots of Molniya

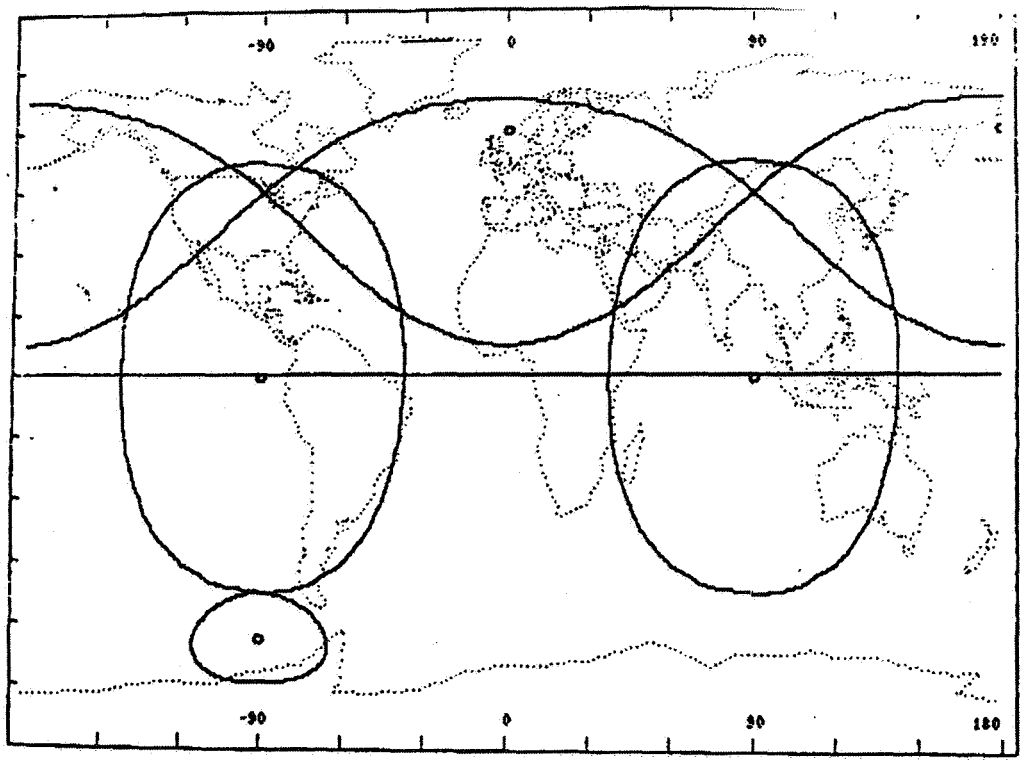

Figure 2-2. 30° Elevation Contours of Hybrid Satellite System at Epoch (3 Molniya + 2 Geosynchronous at 90E, 270E)

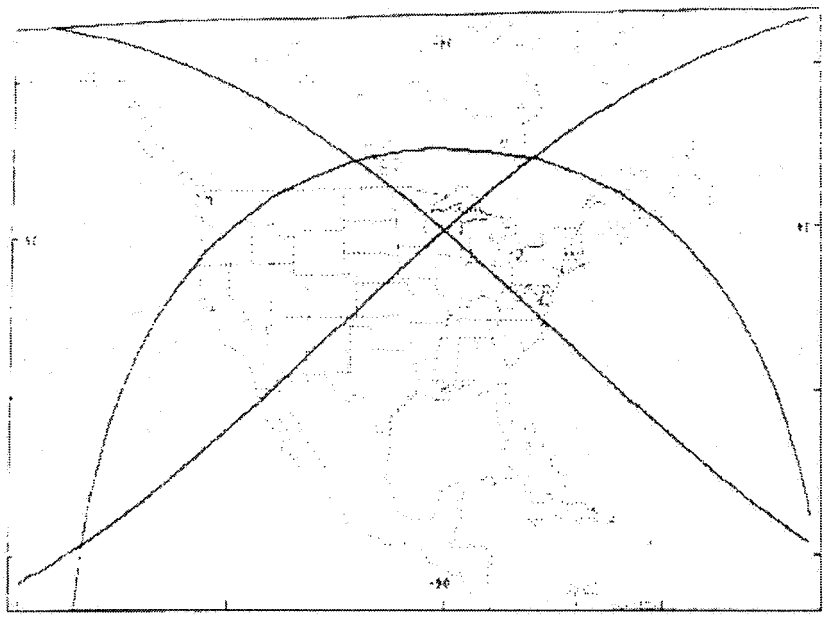

Figure 2-3. 30° Elevation Contours of Hybrid Satellite System at Epoch (CONUS)

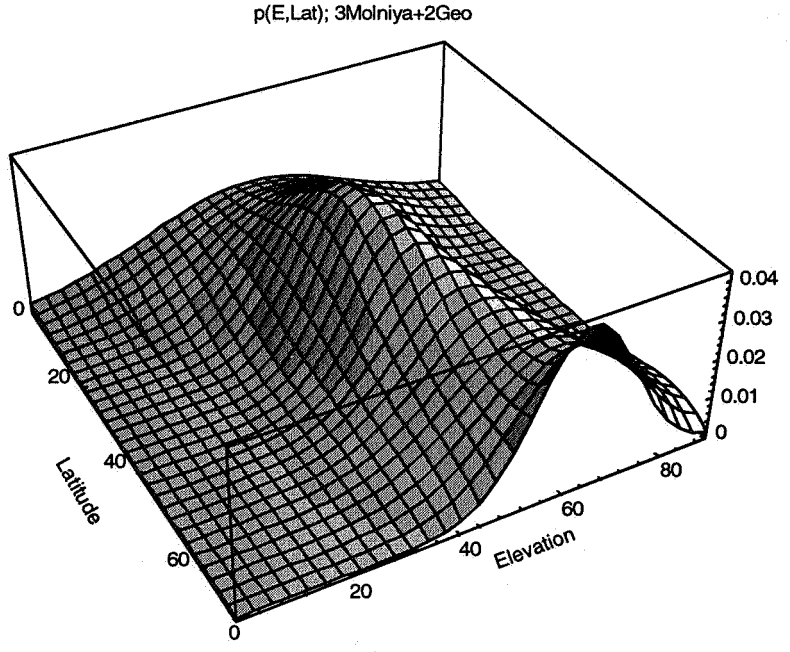

Figure 2-4. Probability Density Function for Elevation as a Function of Latitude 3 Molniya + 2 Geostationary

The constellation offers such convenient ground station antenna pointing angles that one may ask whether the system is stable. The geostationary satellites offer little reason for concern, with C.A. Wagner (6) addressing the unique stable points of the earth's gravitational field and, to a lesser extent, lunar perturbations and radiation pressure. However, the low perigee altitude of the critically inclined Molniya satellites raises immediate concerns about orbital decay and orbital lifetime. The lifetime (Appendix) may be approximated by

Lifetime =

$$2891.78 - 7545.15\,E^{e} + 6551.97\,E^{2\,e} - 1897.98\,E^{3\,e} - 16.5352\,E^{e\,*\,Hp/100} + 9.74402\,E^{2\,e\,+\,Hp/100} + 0.0005722\,E^{e\,+\,Hp/50} + 6.81128\,E^{Hp/100} - 0.000606174\,E^{Hp/50} \quad (2\text{-}1)$$

where Hp = perigee altitude, km (typically 463 km)
e = eccentricity (0.725 typically)

The orbital lifetime can be found to be well over 10 years, even under more severe conditions. Also, the intense inner Van Allen Belt can shorten the lifetime of the Molniya electronics. A method to avoid the inner Van Allen Belt is shown in the final section.

The nodal regression of the Molniya satellites, at a rate of 4.03 deg/month, must also be accounted for by the ground stations or with scheduled orbit corrections.

3. Motorola M-Star

As other telecommunication corporations moved vigorously into the 28 GHz region, Motorola recognized that frequencies greater than 40 GHz would be even more promising (7). They filed a plan for a 72 satellite system with the FCC in September, 1996. The 50 GHz uplink/40 GHz downlink system would have high ground antenna elevation angles and low atmospheric losses throughout the Temperate regions. The circular orbits are proposed a 12 planes of 6 satellites/plane at 1350 km altitude. Inclination is set at 47 degrees (This might be compared with the emphasis on the polar regions with the earlier Iridium polar orbits). Figure 3-1 shows the first plane of 6 satellites at epoch. Figure 3-2 allows the excellent coverage to be visualized at epoch. A probability density function for elevation angle as a function of latitude may be generated for all time, as Figure 3-3. Elevation angles can be seen to be high for all latitudes up to 60 degrees, and to deteriorate at 70 degrees N.

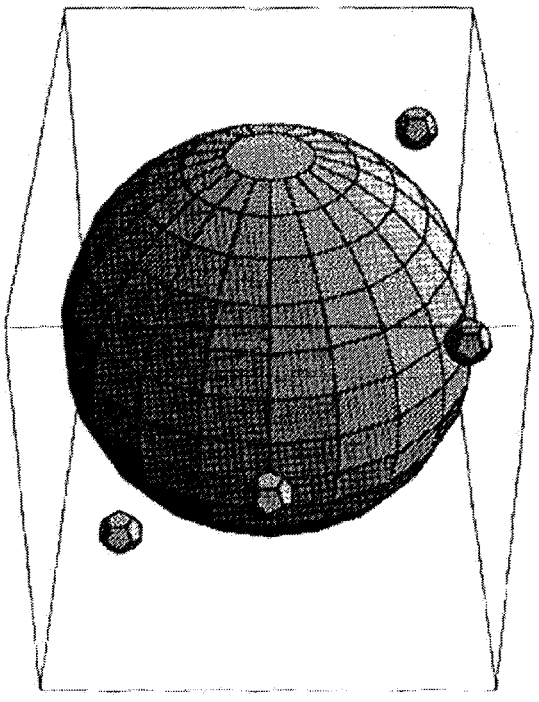

Figure 3-1. First Plane of Motorola M-Star

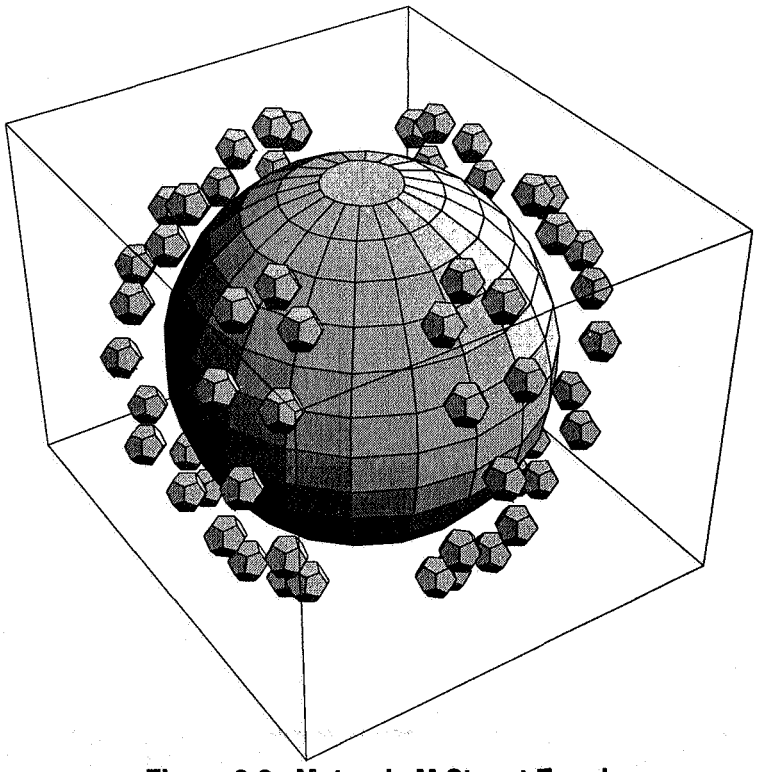

Figure 3-2. Motorola M-Star at Epoch

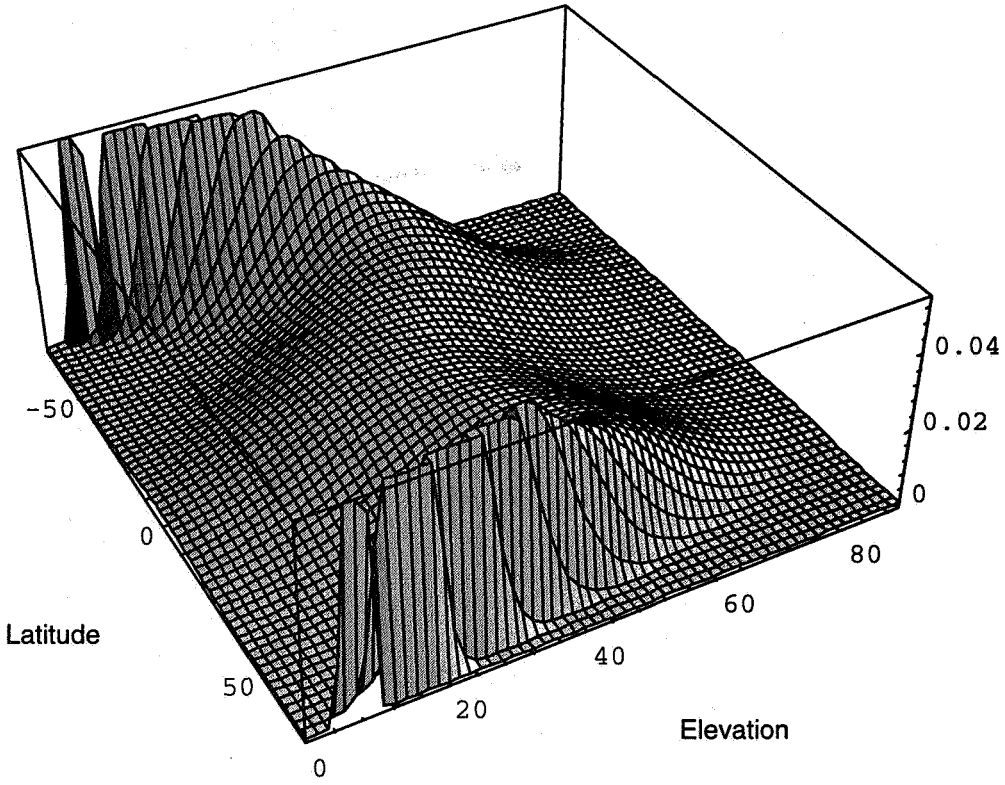

Figure 3-3. M-Star Elevation Probability Density Function

The elevation angle density function may be concisely approximated with the aid of Mathematica's Fortran form (8).

Out[20]//FortranForm=

```
      1/ (E** ((-37.67078605295647 -
     -            2.203517109853085e-12*LAT -
     -            0.01314712753576941*LAT**2 +
     -            5.575875699427762e-16*LAT**3 +
     -            3.955286161206665e-6*LAT**4 + x)**2/
     -         (2*(17.72772486955788 -
     -            0.0002899907822926401*LAT -
     -            0.001371693548972577*LAT**2 +
     -            7.185352764841304e-8*LAT**3 -
     -            4.170493335351661e-7*LAT**4)**2))*
     -       (17.72772486955788 -
     -         0.0002899907822926401*LAT -
     -         0.001371693548972577*LAT**2 +
     -         7.185352764841304e-8*LAT**3 -
     -         4.170493335351661e-7*LAT**4)*Sqrt(2*Pi))
```

where LAT = North Latitude (deg.)
x = elevation angle (deg.)

Figure 3-4 shows a contour plot of the density function can also help to visualize the worldwide coverage of the M-Star system. The emphasis is clearly on the large community of communication users in the Temperate regions.

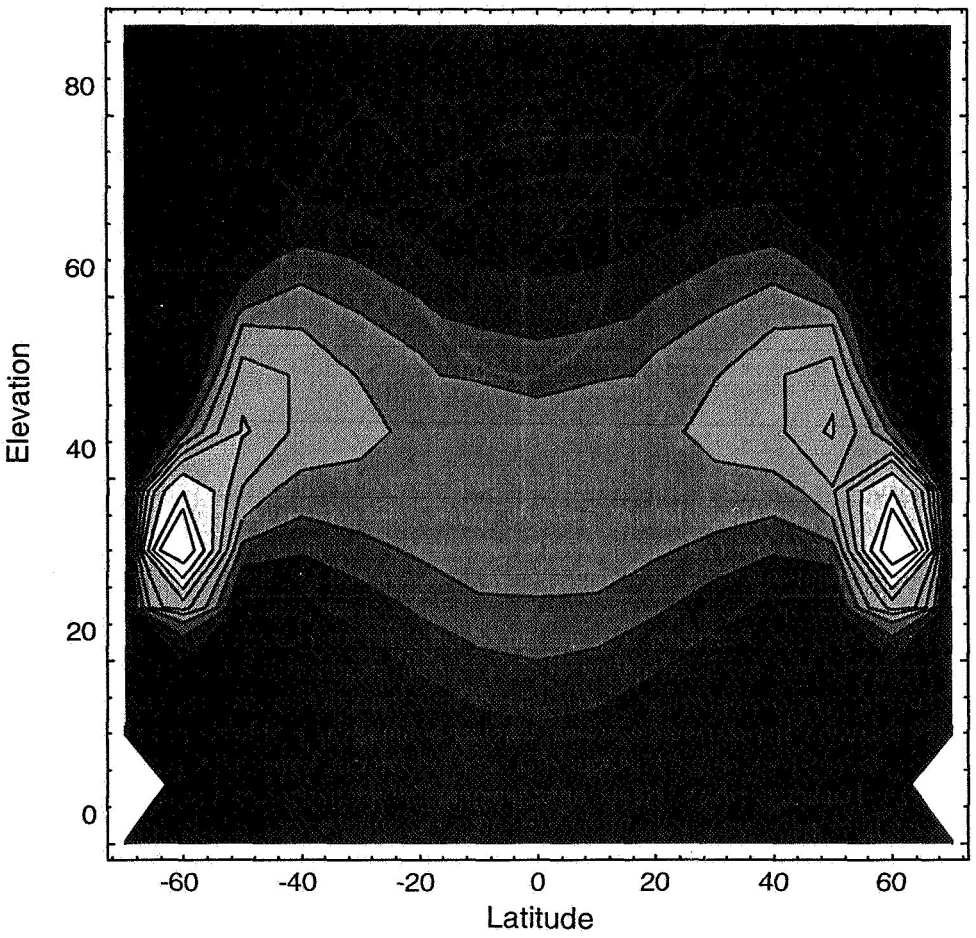

Figure 3-4. Contour Plot for M-Star PDF

The M-Star orbits also promising orbital stability. The semimajor axis, as 7728.14 km, may be compared favorably with the highly stable TOPEX orbit. Frauenholz (9) has listed the TOPEX mean orbital element computational accuracies as in Table 3-1.

Table 3-1. Orbital Element Computational Accuracies for TOPEX

Orbital Parameters	Reference Values	1 Sigma Computational Accuracy
Semimajor axis (km)	7714.42938	13 cm
Inclination (deg.)	66.0408	0.5 mdeg.
Eccentricity (ppm)	95	7 ppm

The rate of change of semimajor axis was expected (9) to be

$$\frac{da}{dt} = \rho C_D \frac{a}{M} \sqrt{\mu a} \left[1 - \frac{\omega e \cos(i)}{n} \right]^2$$

where ρ = atmospheric density (strongly a function of solar flux)

C_D = satellite drag coefficient

$\frac{a}{M}$ = satellite area-to-mass ratio

μ = earth gravitational constant

a orbit mean semimajor axis, km

Predicted decay rate for TOPEX depended strongly on the solar cycle. It ranged from -4 cm/day near solar minimum to -16 cm/day near solar maximum.

4. Minimal Constellation of Elliptic LEOs

A set of 48 phased elliptical satellites was examined (4) as an attempt to minimize the number of LEOs required for millimeter wave communication. The 2 hour orbits are critically inclined and intended to miss the most intense portion of the inner Van Allen Belt, as shown in the 10 minute snapshots of Figure 4-1. The 3010 km apogee offers a convenient communication altitude, but the 350 km perigee raises a question of orbital lifetime.

The satellites would be arranged as 3/plane and 8 planes for high elevation angles in the Northern Temperate zone. A snapshot of the first plane is shown as Figure 4-2. Figure 4-3 shows the first 24 satellites at epoch, as they give an indication of the high elevation angles they afford for the Northern Hemisphere. The small arrowheads indicate the velocity vector, and similar velocity vectors are seen for separations in right ascension of 90 deg. This implies that easy crosslinks should be possible between sister satellites at 90 deg. East and West. Figure 4-4 indicates the 30 deg. ground elevation contours at epoch. Figure 4-5 shows the results of exhaustive searches for elevation angle statistics for the Northern Hemisphere. For ground locations north of 40 deg., elevation is seen to be very promising. South Florida, however, at 20 deg. North, has sharply deteriorating elevation angle. A complementary set of 24 satellites is introduced in Figure 4-6 for a total of 48. The 30 deg. elevation contours are shown on Figure 4-7. The asymmetry between the northern and southern satellites can be seen at epoch. A full earth search for elevation angle statistics for all time, however, shows the long term symmetry for elevation statistics (Figure 4-8).

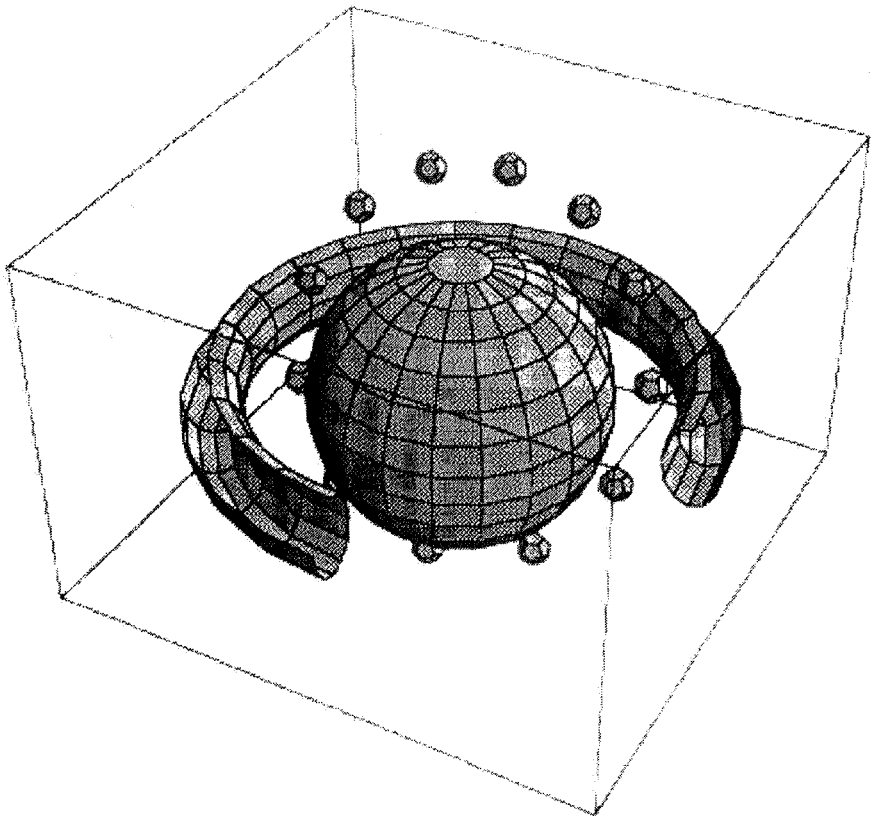

Figure 4-1. 10 Minute Snapshots of Elliptic LEO Inside Inner Van Allen Belt

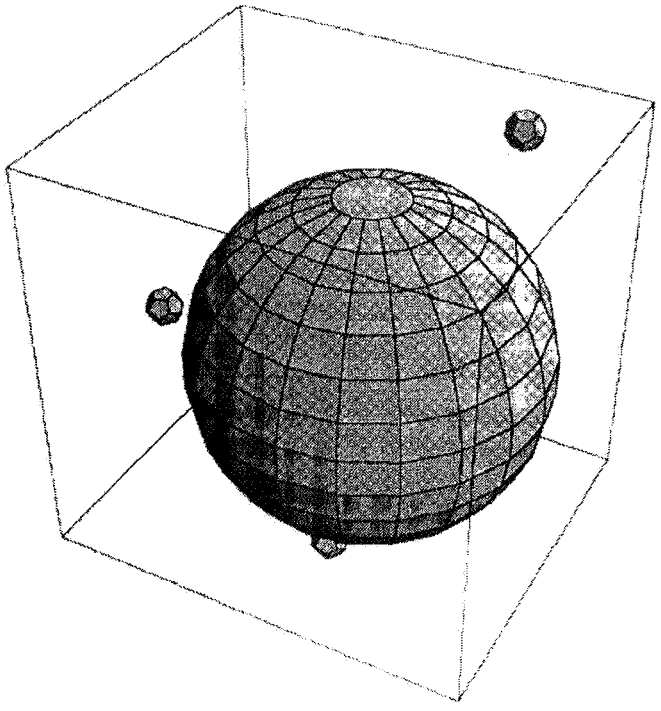

Figure 4-2. First Plane of Elliptic LEOs

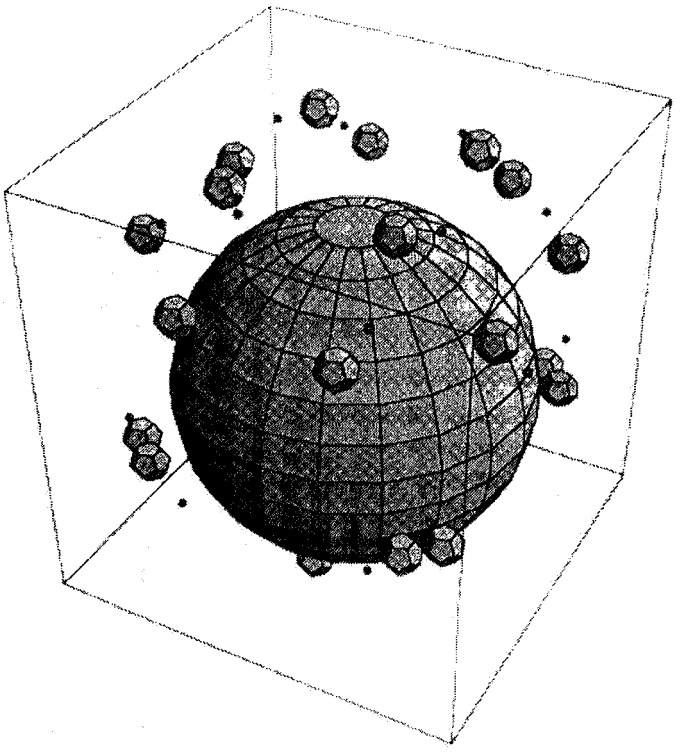

Figure 4-3. First 24 Elliptic LEOs for Northern Hemisphere Coverage

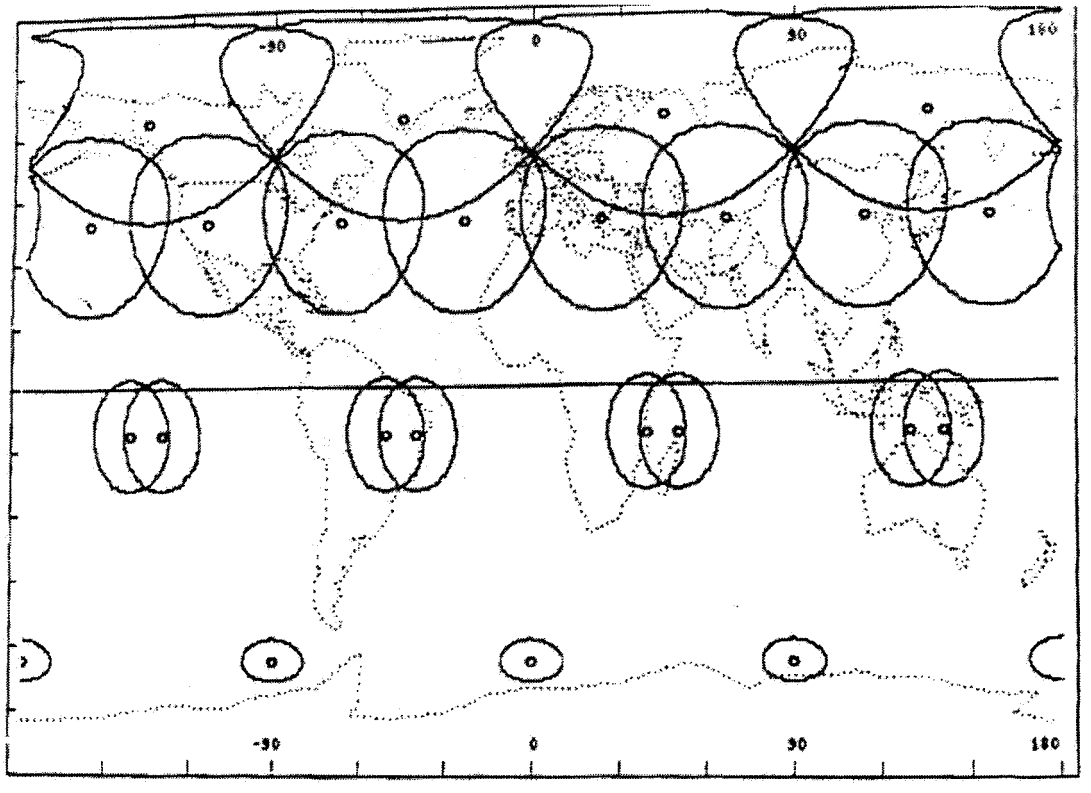

Figure 4-4. High Elevation Footprints for 24 LEOs at Epoch. Contours at 30° Elevation

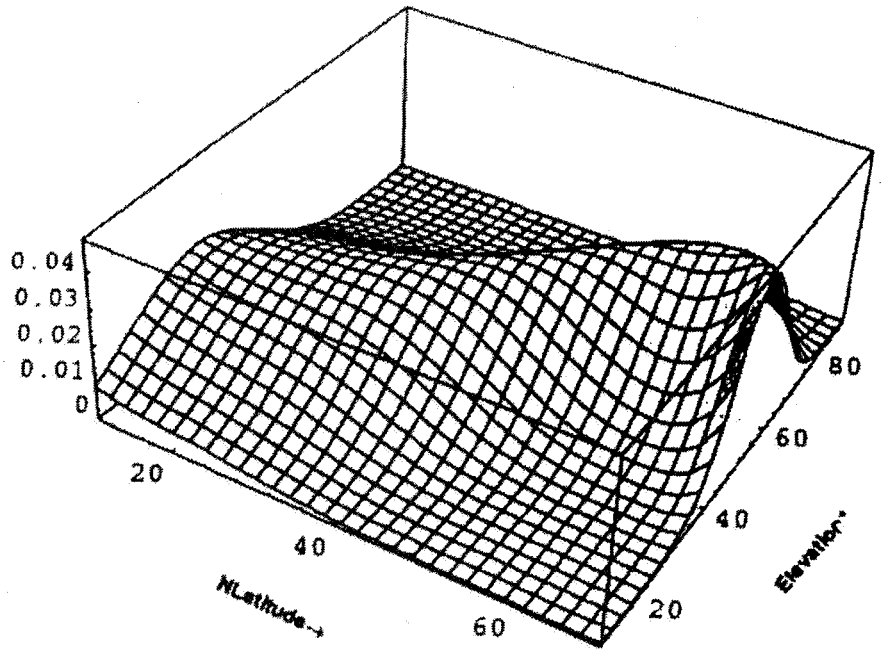

Figure 4-5. Elevation PDF vs NLatitude (24 sats.)

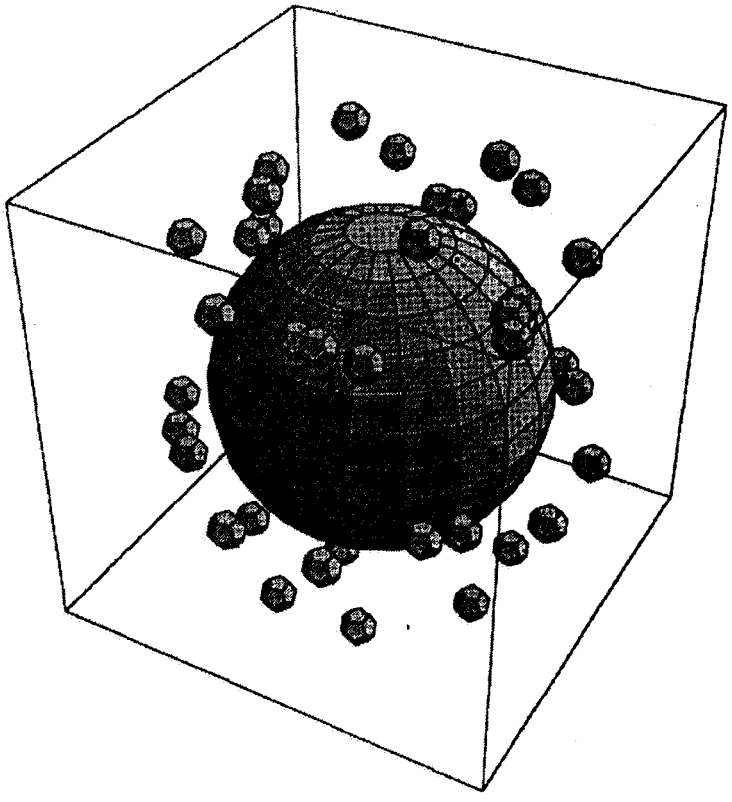

Figure 4-6. 48 Elliptic LEOs at Epoch

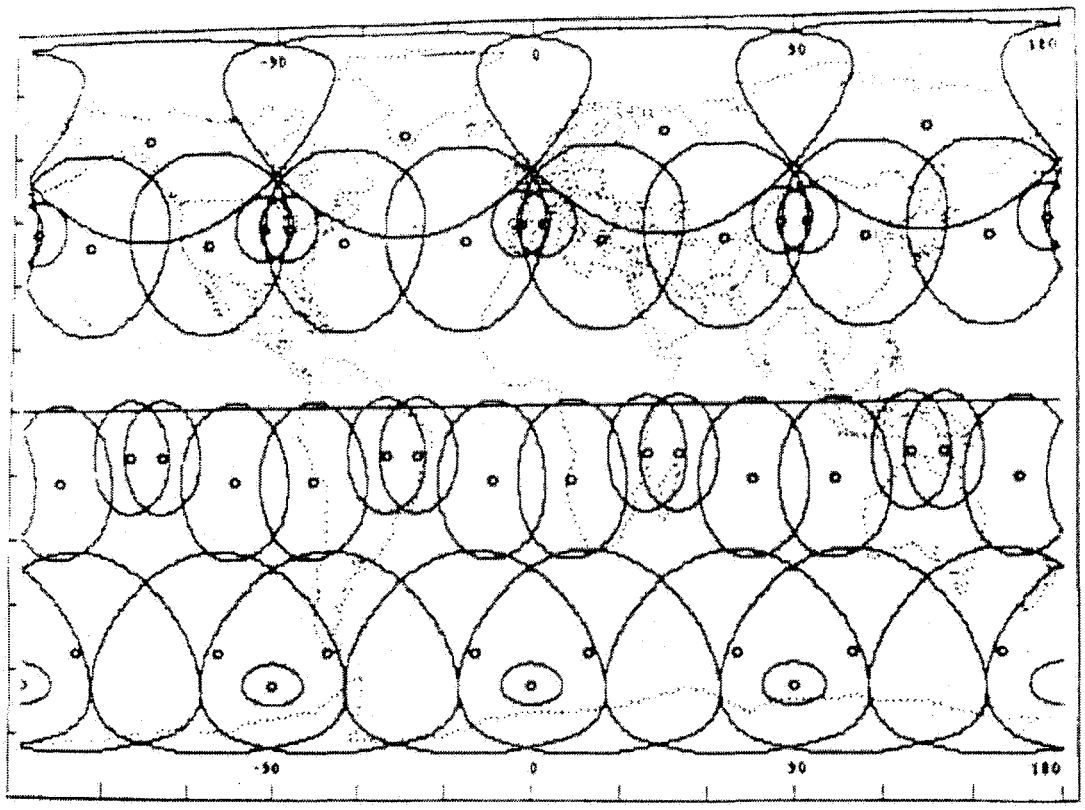

Figure 4-7. High Elevation Footprints for 48 LEOs at Epoch Contours at 30° Elevation

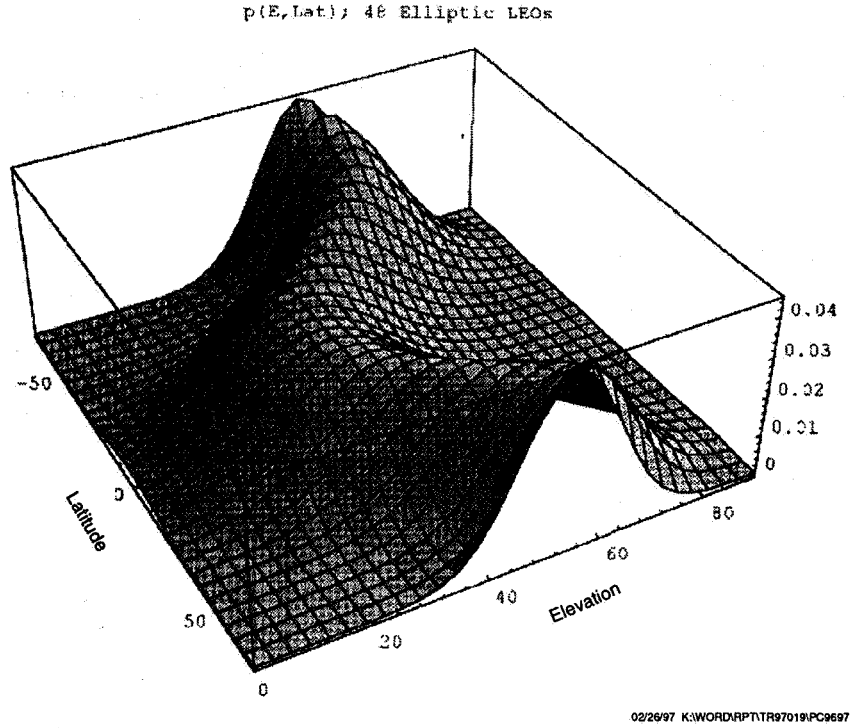

Figure 4-8. PDF (Elevation, Latitude) for 48 Elliptic Satellites

The density function may be found as:

```
Out[41]//FortranForm=
   1/(E**((-32.52082162419636 +
        -          5.039715796377119e-13*LAT -
        -          0.01522932047312205*LAT**2 -
        -          1.274872465286e-16*LAT**3 +
        -          2.237417639119951e-6*LAT**4 + x)**2/
        -       (2*(15.42016475784284 +
        -            1.583391651436639e-12*LAT -
        -            0.001422826592914807*LAT**2 -
        -            4.005909975141205e-16*LAT**3 +
        -            2.445116802724547e-8*LAT**4)**2))*
        -    (15.42016475784284 +
        -      1.583391651436639e-12*LAT -
        -      0.001422826592914807*LAT**2 -
        -      4.005909975141205e-16*LAT**3 +
        -      2.445116802724547e-8*LAT**4)*Sqrt(2*Pi))
```

The 2 hour orbit is intended to offer convenient repeat cycles at 3 hours for ground antenna pointing. Comparisons with the Explorer I satellite (10) indicate that continual orbital adjustments would be necessary for this convenience. To reduce the frequency of these adjustments by an order of magnitude, one may use the TOPEX/Poseidon equations to infer that perigee altitude should be changed from 350 km to 470 km. By analogy with the sunspot maximum of the 1959 Explorer I data, the decremention period would drop from -2.5 min/year to -0.25 min/year.

Conclusions

Three constellations which would be attractive for millimeter wave communication have been described. A hybrid constellation of Molniya and antipodal geostationary satellites would offer high elevation and convenient antenna pointing throughout the Northern Hemisphere, but continual adjustment for nodal regression may be required. The inner Van Allen belt also poses a threat to the Molniya electronics. The Motorola M-Star constellation would offer high elevation throughout the Temperate regions and have good stability. An elliptic LEO system would reduce the number of satellites required and offer better coverage for North Atlantic air traffic routes than M-Star. It would clearly have a shorter orbital lifetime than M-Star, but should be useful for more than a decade.

Acknowledgments

John Draim of Ellipsat has shown the advantages of many types of elliptical orbits. His recent patent (Feb. '97) for a constellation of three critically inclined retrograde orbits may also be promising for millimeter wave communication. Vickie Granberg skillfully handled the manuscript while also juggling a crushing workload.

References

1. J. G. Walker, "Circular Orbit Patterns Providing Continuous Whole Earth Coverage", Royal Aircraft Establishment, Technical Report 70211 (UDC 629.195:521.6), November, 1970.
2. J. E. Draim, "A Continuous Period Four-Satellite Continuous Global Coverage Constellation," Journal of Guidance, Control, and Dynamics, Vol. 10, No. 5, 1987.
3. Dorothy C. Rodgers, P. Christopher, "Satellite Orbits to Relieve Ionospheric Scintillation", Proc. of Ionospheric Effects Symposium, Alexandria, VA, April, 1981.
4. A. H. Jackson, P. Christopher, "Angle Diversity for Millimeter Wave Satellite Communications", Proc. IEEE Symposium on Mobile Satellite Communication, London, May, 1996.
5. Francesco Linsilata, Bruce Gribble, Barry Gribble, "SGAT User's Manual", Stanford Telecom Report, Reston, VA, 1988.

6. C. A. Wagner, "The Drift of a 24-Hour Equatorial Satellite Due to an Earth Gravity Field Through 4th Order", Proc. GSFC Space Technology, Vol. 2, 1964.
7. A. H. Jackson, P. Christopher, "A LEO Concept for Millimeter Wave Satellite Communication", Proc. of International Mobile Satellite Conference, Ottawa, June, 1995.
8. S. Wolfram, "Mathematica, A System for Doing Mathematics by Computer", Second Edition, Addison-Wesley, 1991.
9. Raymond B. Frauenholz, Ramachand S. Bhat, Bruce E. Shapiro, Robert K. Leavitt, "Analysis of the Orbit of the TOPEX/POSEIDON Satellite", JPL New Technology Report, NPO-19853, September, 1996.
10. Victor G. Szebehely, "Celestial Mechanics and Astrodynamics, Progress in Astronautics and Aeronautics", Vol. 14, AIAA Series, New York, 1964.

Appendix - Lifetime for Elliptic Orbits

The extensive simulations of Jensen may be fitted with a bivariate exponential function with the aid of Mathematica. The two key independent variables of Figure A-1 are perigee altitude (Hp, km) and eccentricity e. The lifetime estimate in years is shown on the vertical axis, and it is truncated at 10 years so that low altitudes may be examined closely. Figure A-2 is a contour plot of the same data. Contours are shown at 1, 2, 3, 4, 5, 6, 7, 8, 9, 10, 20, 30 -- 100 years. These estimates are useful for eccentricities up to 0.25 but they are in error for greater eccentricity. Satellites with higher eccentricities have longer lifetimes than shown here.

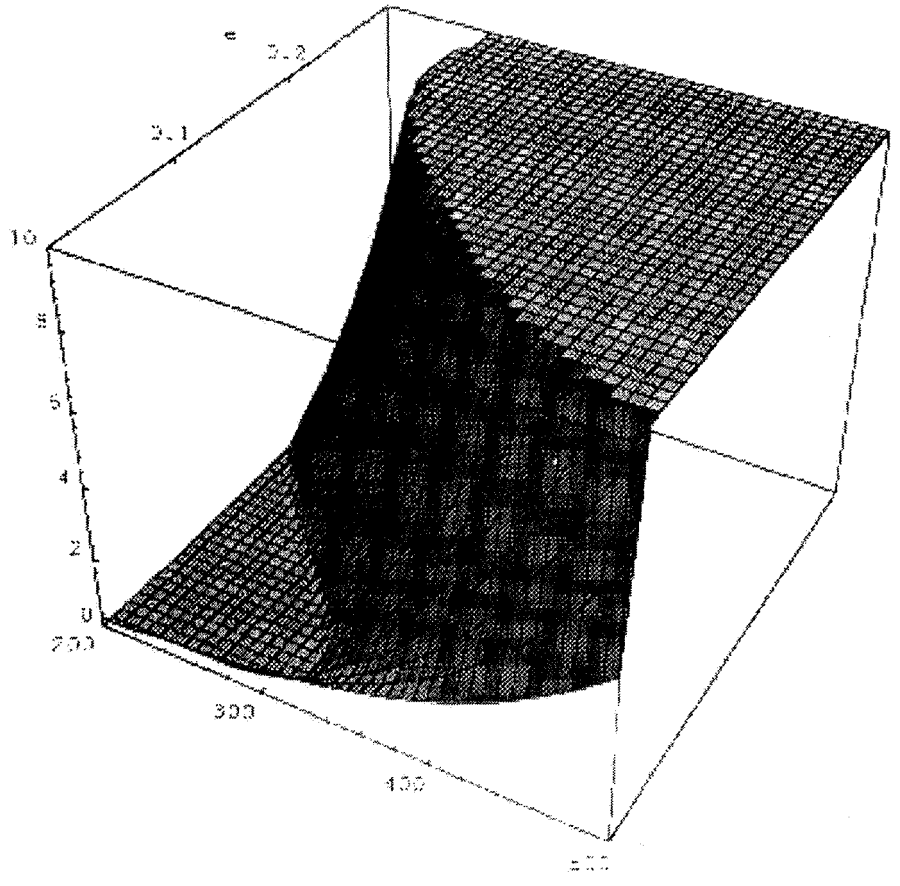

Figure A-1. Lifetime as a Function of Perigee Altitude and Eccentricity

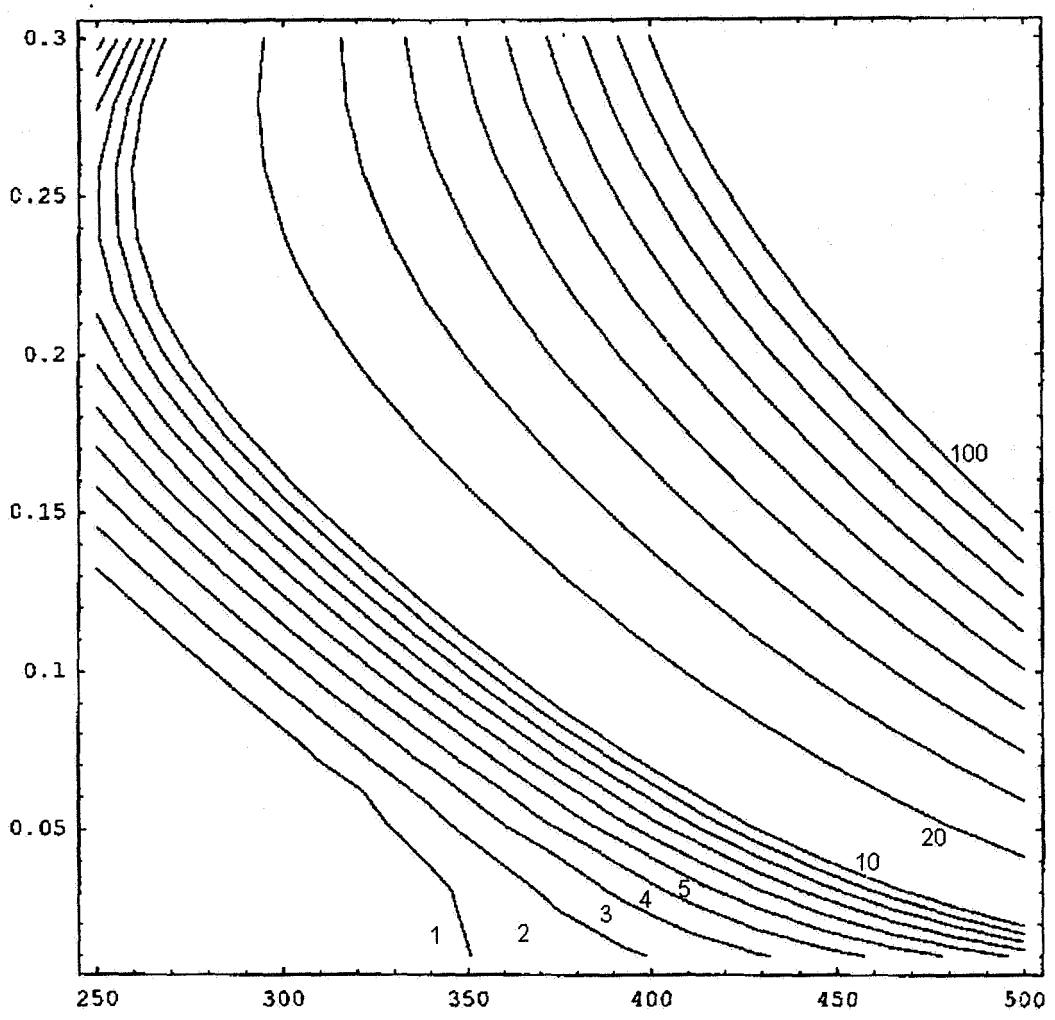

Figure A-2. Contour Plot of Lifetime

The functional fit is appropriate for satellites with mass/area = 1 slug/ft^2.

Lifetime =

$$2891.78 - 7545.15\,E^{e} + 6551.97\,E^{2\,e} - 1897.98\,E^{3\,e} -$$

$$16.5352\,E^{e\,+\,Hp/100} + 9.74402\,E^{2\,e\,+\,Hp/100} +$$

$$0.0005722\,E^{e\,+\,Hp/50} + 6.81128\,E^{\,Hp/100} - 0.000606174\,E^{\,Hp/50}$$

yrs

Page intentionally left blank

Venus 2000 Mission Design

David Folta, Greg Marr, Frank Vaughn
Flight Dynamics Division
and
Martin B. Houghton
Guidance, Navigation, and Control
Goddard Space Flight Center, NASA

Abstract

As part of the Discovery Program, National Aeronautics and Space Administration (NASA) has solicited proposals for interplanetary research to conduct solar system exploration science investigations. A mission, called Venus 2000 (V2k), has been proposed for exploration of the Venus Atmosphere. This is NASA's first voyage to Venus to investigate key science objectives since Magellan and will be launched in summer 2002. In keeping with discovery program requirements to reduce total mission cost and utilize new technology, V2k mission design and control will focus on the use of innovative and proven trajectory analysis programs and control systems provided by the Goddard Space Flight Center (GSFC).

1.0 INTRODUCTION

1.1 Venus 2000 Mission Description

The Flight Mechanics Branch, Code 552, and the Guidance, Navigation, and Control Branch, Code 712, were requested to support the formation of a Discovery proposal team for a mission to investigate the atmosphere of Venus. This support provided both the insight for a preliminary ACS, trajectory, and launch design and for the final analysis and creation of the proposal material.

First a preliminary study was conducted to determine the feasibility of the transfer trajectory to Venus, its insertion into a circular orbit, and the amount of fuel required to perform such a mission. As this study became the basis for the proposal effort, a more detailed study was undertaken for both mission design and the attitude control systems. Additionally, launch vehicle energy data was used to determine possible payload masses. The sections and tables below provide a brief explanation of these studies. Additionally, orbit determination error analysis was performed as input into the attitude control system specifications.

1.2 Trajectory Overview

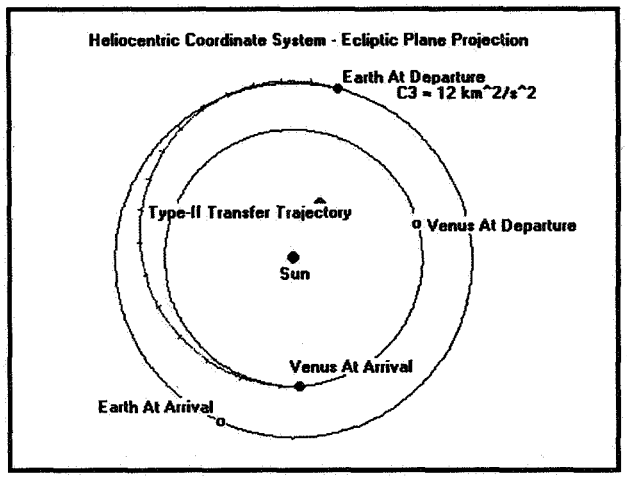

Figure 1- Venus Transfer Trajectory

The mission design of V2k is characterized by a Type-2 direct minimum energy transfer (figure 1) trajectory to Venus with an injection into an elliptical orbit which will be circularized into a 1000 km altitude polar mapping orbit via the use of aerobraking. The mission design will incorporate the optimization of the reference trajectory for a new launch vehicle. An attitude control system conceptual design was completed for the spacecraft based on the MARS Surveyor Program.

1.3 Requirements, Constraints and Assumptions

The performance requirements imposed are those related to the insertion ΔV and it's associate fuel and on the orbit determination requirements. The ΔV, and therefore the propellant budget, is constrained by the spacecraft design, ACS components, and bus mass. The original spacecraft bus design was based on the Mars mission. The orbit determination is constrained by the required attitude and ACS design, to less than 1km 3-sigma uncertainty. The orbital transfer times were limited to two cases, a Type-1 or Type-2 The optimum insertion ΔV in the Type-2 case as studied by Lockheed.

The trajectory design assumptions made for the preliminary study were derived from basic Astrodynamics, past Venus exploration experience and science, and orbit determination experience. Other assumptions regarding the fuel and payload mass are in the use of the rocket equation for fuel consumption and the data from the Orbital Launch Services (OLS) regarding launch Vehicle energy (C3) versus deliverable mass placed into orbit. The V2k study was therefore open ended without any major constraints and with common assumptions

For the detailed proposal study, the constraints used in the generation of the launch window analysis are:

- Launch energy (C3) < 17 km^2/sec^2
- Declination of Launch Azimuth (DLA) within the range of +/- 55 degrees
- Altitude at Venus Orbit Insertion (VOI) = 150 km
- Maximum period for spacecraft orbit ~ 12 hours
- Hyperbolic excess velocity (Vinf) at VOI (determined by insertion orbit period constraint and spacecraft ΔV capability)

C3 is defined here as the Earth departure energy (km2/sec2), the same as the square of the departure hyperbolic excess velocity. C3 is therefore the injection velocity squared minus two times the parking orbit velocity. The velocity Vinf is the venusian hyperbolic excess velocity, and is the square root of the vectorial subtraction of the heliocentric planetary orbital velocity from the spacecraft arrival heliocentric velocity at the planet.

1.4 Trajectory Analysis

Trajectories to Venus for several launch window opportunities were analyzed and data was generated with a focus on launch vehicle C3, ΔV insertion, and time of flight. The two types of transfer trajectories investigated were a Type-1, a trajectory with a time of flight such that the transfer is less than half the orbital period, and a Type-2 transfer, a trajectory with a transfer that is longer than half the orbital period. A sample Type-2 trajectory is shown in figure 1.

1.5 Venus Launch Windows for 2002

To determine a feasible launch window, a pork-chop plot of departure C3 plotted against the Earth departure and Venus arrival dates was generated to locate the optimum launch times based on minimum C3. Reference 1 was also used to determine the minimum C3 and Vinf for the 2002 launch. The figures below show these C3 contours for the years 2000 through 2004. The C3 contours in figure 1 range from 10 km^2/sec^2 to 100 km^2/sec^2. The contours in figure 2 range from 10 km^2/sec^2 to 25 km^2/sec^2. The available launch times will be restricted by the required launch declination which effectively reduce the total launch mass.

After the completion of a preliminary study using references 1, 2, and 3, it was decided that due to Discovery proposal schedule requirements, that it would be prudent to propose a launch in the year 2002 instead of 2000. This would minimize a schedule slip risk as the spacecraft manufacturer was still unselected and may be required need to complete the design and build the spacecraft in an unreasonable timeframe. Figure 2 presents the overall C3 contour for two launch opportunities, while figure 3 presents the data for the 2002 launch opportunity.

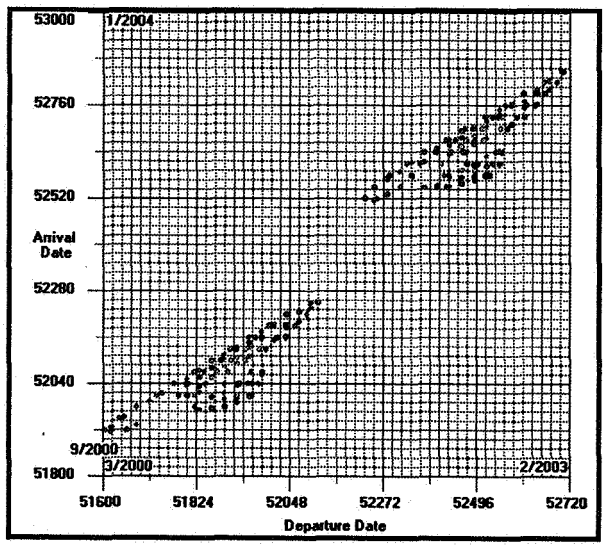

Figure 2-Launch Opportunities for 2000-2004

Figure 4 shows the minimum C3 and hyperbolic excess velocity (VHP) for each launch year from 1998 through 2002. The lines show the trending of these parameters for several years in which the spacecraft could be launched. The C3 is minimized for Type-I trajectories (trajectories of less

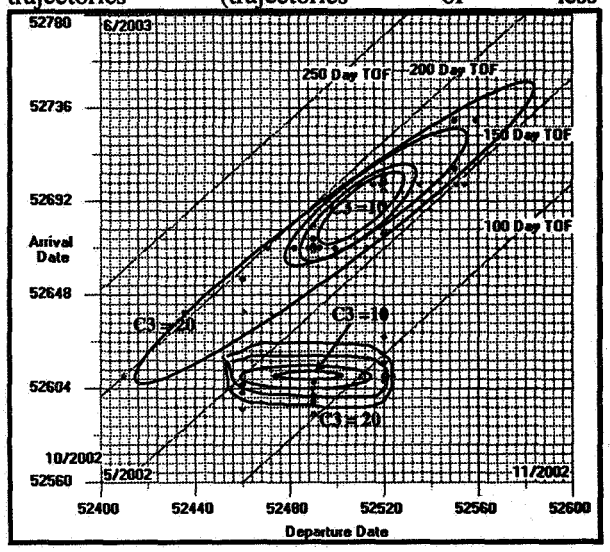

Figure 3 - Launch Opportunity for 2002

than 180 degrees in transfer anomaly). The C3 is important since it can be used to size the total spacecraft mass capable of being launched. The Vinf remains relatively constant at approximately 3.4 km/sec throughout.

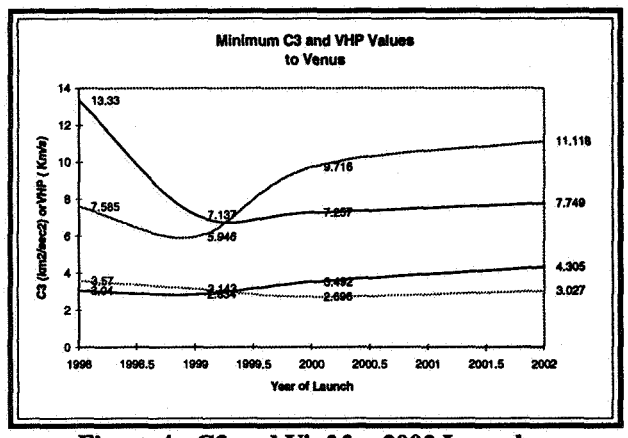

Figure 4 - C3 and Vinf for 2002 Launch

Table-1 was reproduced using data from reference 1 and shows the Earth to Venus Opportunity Energy Minima for 2002. The units of C3L are km^2/sec^2, and the units of Vinf are km/sec. Type 2 trajectories are available from 5/12/02 (C3 constraint) through 7/15/02 (Vinf constraint) for the 1.425 km/sec VOI maneuver. The window extends to 7/28/96 (Vinf constraint) for a 1.7 km/sec VOI

Table 1 - Minimum C3 and Vinf for 2002

Parameter	Value	Orbit Type	Departure Date	Arrival Date
C3	7.75	1	8/06/2002	12/15/2002
C3	11.12	2	9/08/2002	02/22/2003
Vinf	4.31	1	9/17/2002	12/21/2002
Vinf	3.03	2	6/11/2002	12/15/2002

maneuver. The optimum (minimum) Vinf can be achieved except for the period between 7/6/02 and 7/28/02 when a penalty of 0.01 to 0.17 km/sec is exacted to restrict the absolute value of DLA to no greater than 55 degrees. Optimum Vinf trajectories will require DLA angles up to -60 degrees during this period.

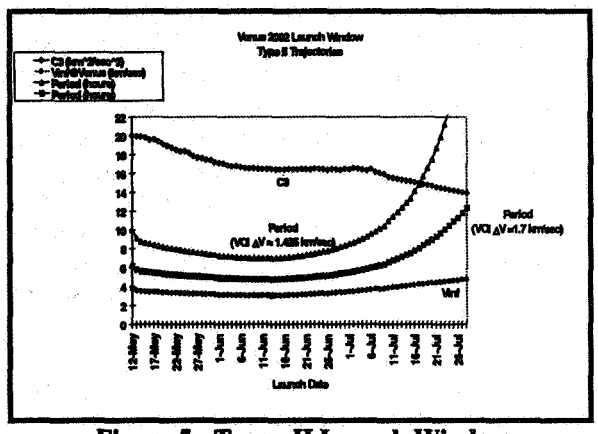

Figure 5 - Type - II Launch Window

Insertion orbit periods for the 1.425 km/sec VOI maneuver range from 9.5 hours at window open to a minimum of 6.7 hours for launch dates from 6/9/02 through 6/13/02 to a maximum of 12.6 hours at window close (7/15/02). Insertion orbit periods for the 1.7 km/sec VOI maneuver range from 6.1 hours at window open to a minimum of 4.8 hours for launch dates from 6/9/02 through 6/13/02 to a maximum of 12.3 hours at window close (7/28/02).

Type 1 trajectories are available for the 1.7 km/sec VOI maneuver from 8/21/02 (Vinf constraint) through 9/12/96 (C3 constraint). Insertion orbit periods range from a maximum of 12.1 hours at window open to a minimum of 8.7 hours at window close. Type I trajectories are also available for the 1.7 km/sec VOI maneuver from 6/8/02 (C3 constraint) through 6/13/02 (Vinf constraint) with insertion orbit periods ranging from a minimum of 8.7 hours at window open to a maximum of 12.6 hours at window close, but result in higher Vinf values than their Type II counterparts.

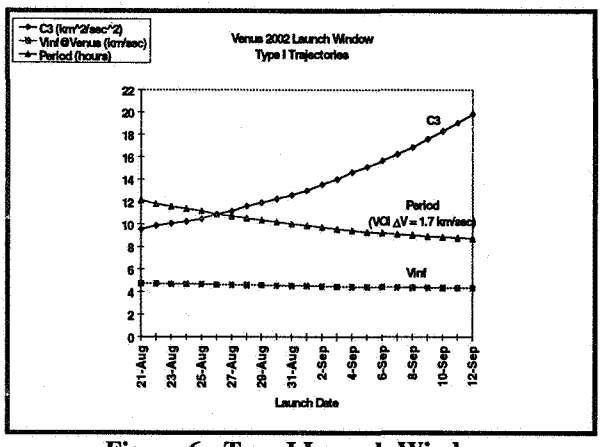

Figure 6 - Type I Launch Window

1.6 Launch Vehicle Performance

Figure 7 depicts the launch energy vs. maximum payload mass for the launch vehicle proposed for the Venus 2002 mission. The amount of mass available for a mission to Venus is directly dependent upon the trajectory's C3 requirements. Thus the importance of finding a trajectory which would minimize C3. A limiting C3 of 17.6 km^2/sec^2 was used for the proposal. This gave a maximum spacecraft wet mass of approximately 907 kg. With the dry mass of 413.6 kg this left a small margin for the total fuel for the insertion and the maintenance of the orbit. This propellant mass of approximately 494.4 kg gives a total useable ΔV of approximately 2.2 km/sec for the complete mission DV budget including launch corrections, midcourse correction, attitude maneuvers and possible aerobraking maneuvers. This would in turn limit the insertion DV allowable to less than 2.0 km/sec

1.7 Results of Preliminary and Proposal Analysis

Using the above guidelines, several trajectories were investigated to determine the required C3 and ΔV for insertion. This is shown in table 2. The table presents the departure and arrival dates, the required C3 for the departure date, the spacecraft mass as calculated from the following figure, the ΔV for orbit insertion and its associated fuel budget based on a simple rocket equation with Isp of 300 sec. The payload mass is computed simply by subtracting the fuel mass for the required insertion maneuver from the spacecraft mass column. The final two columns given the apoapsis radius and the number of days to achieve the mission orbit if the decay rate due to aerobraking were 100 km per day. This was done only for comparisons to the relative Vinf. The numbers are approximate since the curve is made from fitting a three coefficient polynomial to data points provided to Flight Dynamics by OLS.

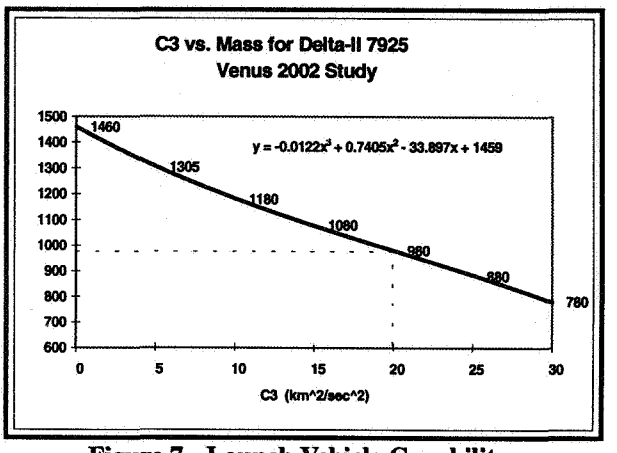

Figure 7 - Launch Vehicle Capability

1.8 Spacecraft Occultation Periods

A final piece of analysis was generated to provide the relative distances between Earth and Venus over a time span of 6 years. Figure 8 shows times when Venus, and therefore the spacecraft , would be occulted by the Sun in transit. This data was used for sizing the communications. The chart below depicts the occultation of the Venus orbiter by Venus from arrival on 12/15/02 through 01/03/05. The aerobraking phase

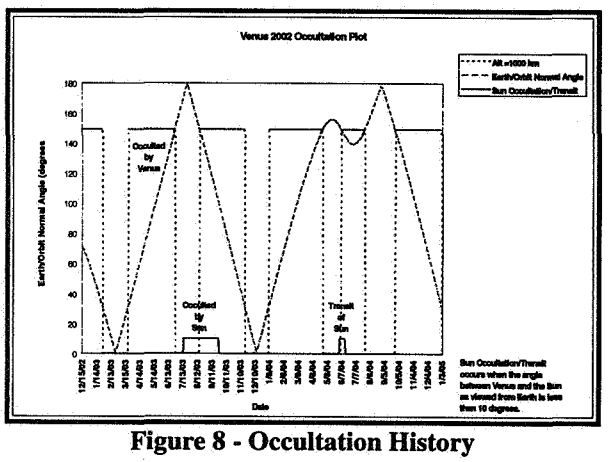

Figure 8 - Occultation History

has not yet been fully modeled, so it has been assumed that the spacecraft is inserted directly into a circular orbit at an altitude of 1000 km. Since the altitude will vary considerably during the aerobraking phase, the start and end times of the actual occultation periods will shift from those depicted.

Table 1- Preliminary Study Results

VENUS - 2000 Study												
					1000km Circular Orbit			Aerobrake				
Depart mm/dd/yy	Arrive mm/dd/yy	Orbit Type 1 or 2	C3 km^2/sec^2	S/C Mass Kg	Delta-V km/sec	Fuel kg (isp=300)	Payload Mass kg	Delta-V km/sec	Fuel kg	Payload Mass kg	Orbit periapsis =150 km Apoapsis	Days to Mssn Orbit at (100km/day)
1/3/01	5/12/01	1	7.257	1104	3.64	784	320	2	544	560	21000	150
12/9/00	5/23/01	2	12.068	998	3.183	660	338	2	492	506	15000	90
8/6/02	12/5/02	1	7.749	1093	4.09	820	273	2	539	554	35000	290
6/11/02	12/15/02	2	16.461	909	3.277	610	299	2	448	461	16000	100
3/31/04	9/18/04	2	8.718	1071	4.35	827	244	2	528	543	45000	390
12/18/03	7/13/04	2	28.121	716	3.332	484	232	2	353	363	16000	100
11/2/05	4/9/05	2	7.67	1095	3.86	800	295	2	540	555	27000	210
11/25/05	3/11/06	1	21.428	819	3.296	551	268	2	403	416	16000	100

1.9 Insertion and Aerobraking Analysis

The insertion of the V2k spacecraft into the required 1000 km circular polar orbit can be achieved in two ways. A direct insertion into the orbit, and a longer aerobraking strategy. To define an upper bound for fuel budget, the direct method was analyzed (ref 4). The ΔV to insert into the circular orbit can be computed to first order by subtracting the difference in the spacecraft V

Vinf from the circular orbit velocity. Therefore the insertion ΔV is a function of the approach Vinf. Back in table 1, the minimum Vinf was shown. It is obvious that the ΔV would required more than the available 2.0 km/sec from the launch mass budget. Figure 9 and 10 provide some insight to the challenge of the required ΔV for a direct insertion into a 1000 km circular polar orbit.

We analyzed an aerobraking test case. Earth departure occurred on May 27, 2002, and Venus orbit insertion occurred on December 2, 2002 (Type 2 trajectory). The periapsis and apoapsis radii at Venus orbit insertion were 6254.3 and 28451.8 km respectively. The objective was to reduce apoapsis radius to approximately 7052 km through the use of aerobraking. An impulsive maneuver was done at the first apoapsis to increase dynamic pressure at periapsis by decreasing periapsis radius. A plot of periapsis and apoapsis radii is shown in figure 11. The aerobraking duration was approximately 123 days in this scenario, and the average periapsis dynamic pressure was 0.45 N/m^2.

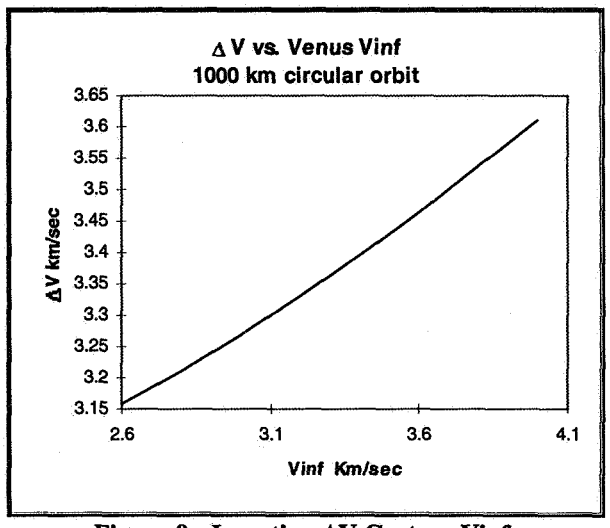

Figure 9 - Insertion ΔV Cost vs. Vinf

Figure 12 is an accelerated representation of an aerobraking scenario, the reduction in apoapsis altitude

(light blue) followed by circularization (purple). For V2k the final orbit would be a 1000 km altitude circular orbit. The venusian atmosphere has a different structure than that of he Earth since the density of the Venus atmosphere rapidly drops off after an altitude of 300km. The perisapsis of the aerobraking strategy is to maintain the periapsis to an altitude of 150 km. Below this would risk thermal heating problems and re-entry, above this altitude would not have an effective force to reduce the apoapsis altitude in the allotted time of 150 days.

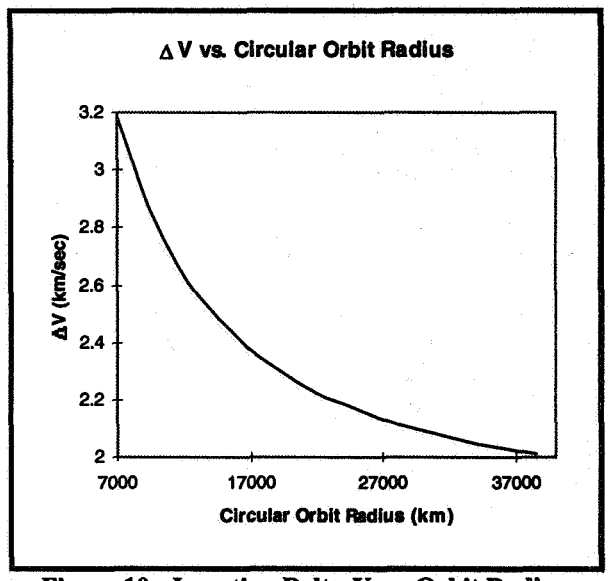

Figure 10 - Insertion Delta-V vs. Orbit Radius

Orbit maintenance is not required since the orbit is well above the definitive atmosphere and Venus does not have a potential to affect the orbit plane alignment.

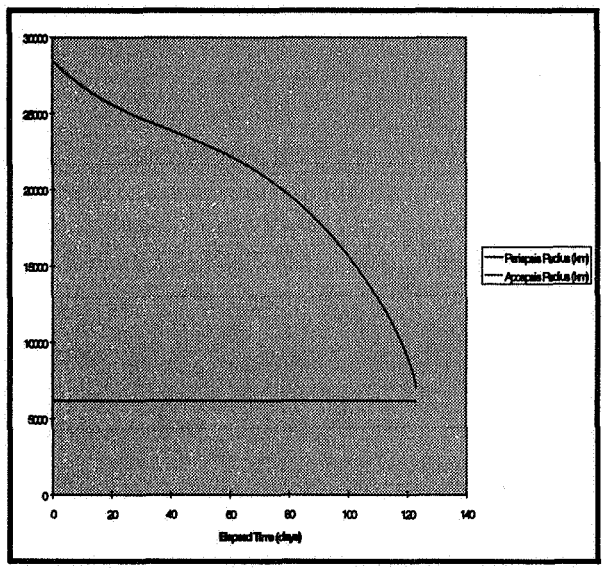

Figure 11 - Aerobrake Periapsis and Apoapsis Radius

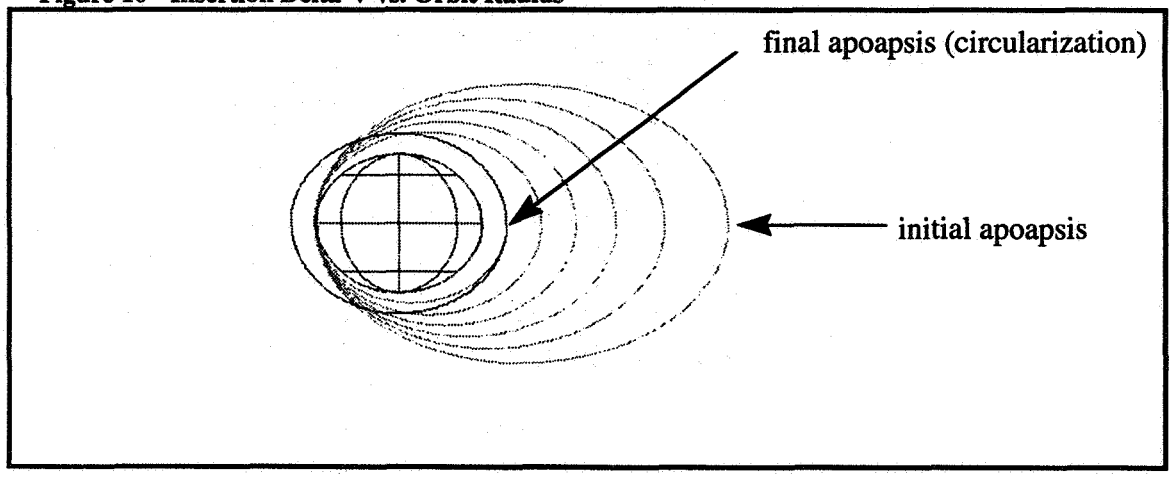

Figure 12 - Venus 2000 Aerobraking Scenario

2.0 Preliminary Orbit Determination Analysis

Preliminary analysis was been performed (ref 5) by the Flight Dynamics Division at Goddard Space Flight Center to assess the orbit determination accuracy achievable. Venus2000 is a Venusian polar orbiting spacecraft in a 1000 km circular orbit. The spacecraft will be tracked from the DSN approximately 4 hours per day.

Covariance analysis was performed to assess the orbital accuracy based upon known uncertainties in various dynamic and measurement models. The Venusian nonspherical potential was modeled using a 90x90 spherical harmonic expansion developed by Dr. Alex Konopliv at the Jet Propulsion Laboratory using Magellan tracking measurements.

Two different geometries will exist for this mission. The first is a face-on geometry where the spacecraft orbit plane is perpendicular to the Earth-Venus line. The spacecraft orbit will be fully visible from Earth in this geometry. The second is an edge-on geometry where the orbit plane is parallel to the Earth-Venus line. The line-of-sight of the spacecraft is occulted by Venus during periods of the orbit in this geometry.

The Venus2000 definitive orbital accuracy that can be expected is approximately 900 m. This is a 3-sigma number and also represents the maximum 3-sigma error over the entire definitive arc. Therefore, this is a worst case scenario. The leading error contributors to the orbital uncertainty are the Venusian GM, the solar GM, and tropospheric refraction from the Earth ground station.

The face-on geometry gives a much more accurate solution, approximately 370 m, 3-sigma. The visibility of the entire orbit contributes to the improved error estimate.

The errors seen in both the face-on and the edge-on geometries are almost all in the plane perpendicular to the radius vector. In other words, the error is mostly in the along-track and cross-track directions. The radial error component is an order of magnitude less. A more detailed analysis is not presented here because of the large numbers of variables in the tracking, models, and operations concepts.

Table 3 - Assumptions:

- 1000 km Circular Polar Venusian Orbit
- Tracking from One DSN (Goldstone) Site,
- Hours/Day Using a Three Day Arc of Data
- Range-Rate Measurements Only

Cases studied: -

Face-on: Full visibility from Earth,
Doppler Changes are small

Edge-on: Venus occults view
Doppler Changes are larger

Table 4 -Typical Magnitude of Errors Due to Each Source:

• Venus Potential:	30 meters
• Venus GM:	200-350 meters
• Solar GM:	15-850 meters
• Solar Position:	5 meters
• Solar Radiation:	Estimated
• Earth Tropospheric Refraction:	100 meters
• Earth Ionospheric Refraction:	75 meters
• DSN Measurement noise:	10 meters
• Venus Atmosphere:	Not Modeled

Table 5 - Results

Geometry	3σ Position Error	Leading Error Source
Face-on	**370 meters/Along-Track**	**Venus GM**
Edge-on	**900 meters/Cross-Track**	**Solar GM**

3.0 ATTITUDE CONTROL SYSTEM CONCEPTUAL DESIGN

Venus 2000 (V2k) carries two science instruments, the Submillimeter Limb Sounder (SLS) and the Deep Atmospheric Spectral Camera (DASC). The SLS will nominally be pointed to a particular altitude (tangent height) in Venus' limb, while the DASC will nominally be pointed nadir. The pointing requirements for the SLS are 30 arcsec accuracy and 20 arcsec / 30 sec stability. The pointing requirements on the DASC are much looser at 1° accuracy. The SLS requirements are clearly the drivers.

3.1 Hardware

The V2k attitude control system (ACS) hardware selection was driven by the Venusian environment and the spacecraft ACS requirements. First, Venus lacks a useable magnetic field. Therefore, magnetometers and magnetic torquer bars are useless, and momentum management needs to be done propulsively. Second, V2k's science pointing requirements cannot be met with either horizon sensors (Venus sensors) or star cameras. Star trackers are the only viable alternative.

The resultant V2k ACS hardware suite is given below. It consists of eight (8) coarse sun sensors, two (2) inertial measurement units, two (2) CCD star trackers, and a three (3) reaction wheel assembly. These components combine to form a system that is robust and capable of meeting all V2k ACS requirements.

3.2 Placement

Placement of the V2k ACS sensors (in particular, the two CCD star trackers) was driven by spacecraft accommodations and layout, along with the nominal orientation of the spacecraft (with respect to Venus) and the science instruments (with respect to the spacecraft).

The orientation of the SLS and DASC, relative to each other, is set by their respective science objectives. The DASC is nominally nadir pointing, while the SLS is to be pointed between the 60 and 120 km tangent heights of Venus' limb, which, for a 1000 km orbit around Venus, works out to be 60.575°±0.495° from nadir. The pointing requirements on the DASC instrument are loose enough to digest the ±0.495° variation in the SLS pointing. This allows for the two instruments to be fixed, relative to each other (and in the spacecraft), and used simultaneously.

The star trackers are being used to meet the tight requirements on the SLS pointing. They are least

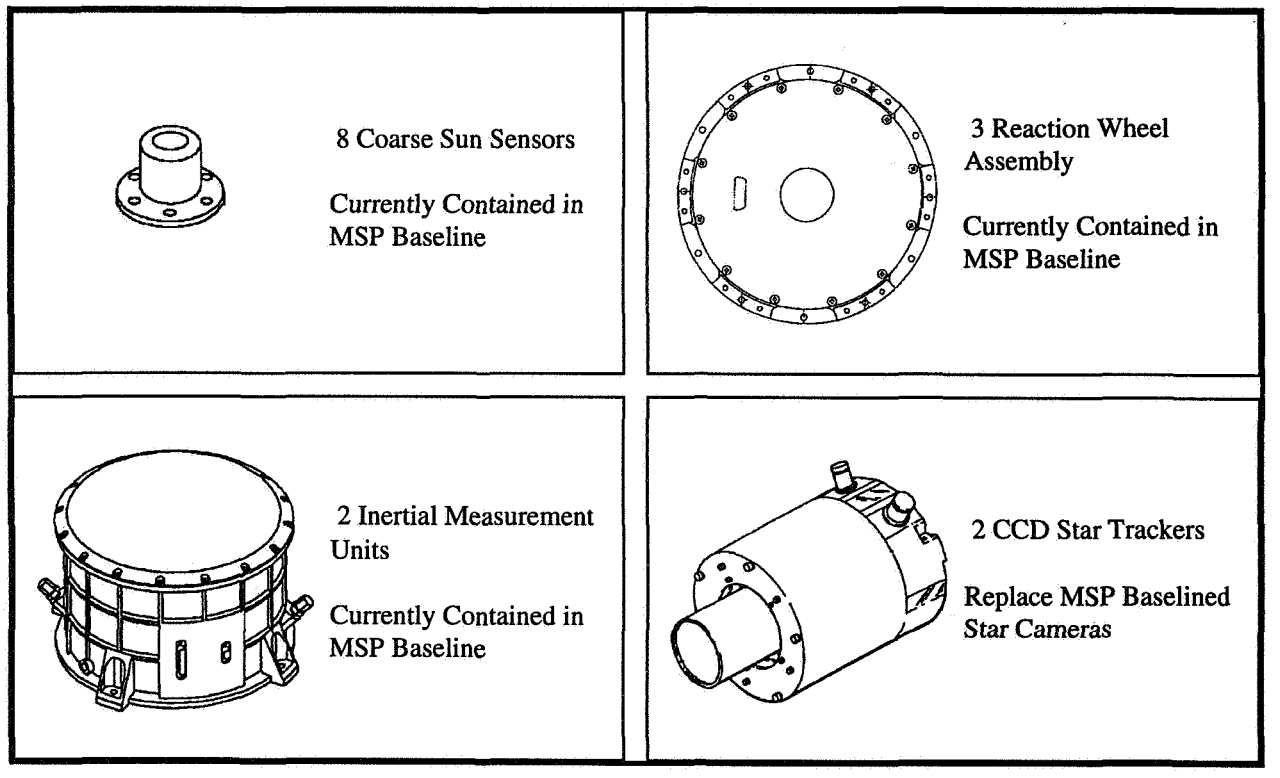

Figure 13 - V2K ACS Components

accurate about their boresight axes, and the SLS is insensitive to rotations about its boresight. Therefore, it would be ideal for the star trackers to be coaligned with the SLS. However, in the case of V2k, this is not possible. The SLS is pointed at Venus' limb. Coalligning the star trackers with the SLS in this case would render them useless. Venus would be in their fields of view. A possible (and equivalent) solution would be to align them opposite the SLS boresight. But, because of the way the V2k spacecraft is laid out, this, too, is impossible. There is no mounting surface that would allow the star trackers to point in that particular direction, and even if that obstacle could be overcome, the spacecraft's solar array lies in that direction. It would impinge upon the star trackers' fields of view. The best that can be done is to place the star tracker boresights as close to the SLS as possible, while avoiding any impingement (from Venus, or the solar array). The answer was to put them in the local horizontal (far enough away from Venus), in the plane of the DASC and SLS (as close to the SLS as possible). This arrangement is illustrated below with the spacecraft in its nominal orientation (DASC pointed nadir, and SLS pointed at the limb).

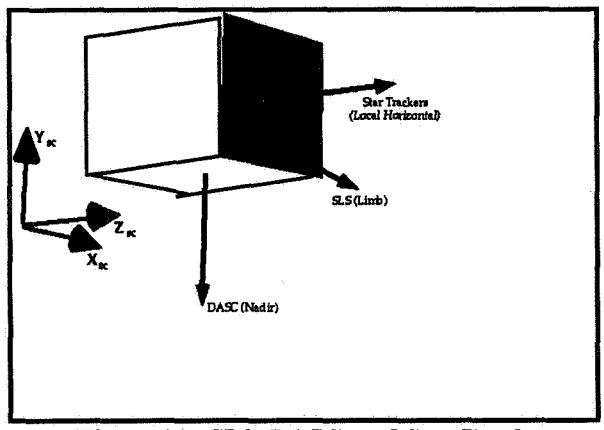

Figure 14 - SLS, DASC, and Star Tracker Orientations

3.3 Modes

As with any interplanetary mission, V2k is, by necessity, multiphased. The three (3) primary phases (after launch) are *Cruise*, *Aerobraking*, and *Science* . During the *Cruise* phase, V2k's solar array (SA) is deployed, where as its high gain antenna (HGA) remains stowed. Therefore, the spacecraft spends most of its time oriented in such a way that the HGA is pointed towards Earth (allowing for communications), while the SA is gimbaled towards the sun. The only deviations from this orientation are for mid-course corrections or momentum unloading maneuvers. Once at Venus, V2k enters the *Aerobraking* phase. The

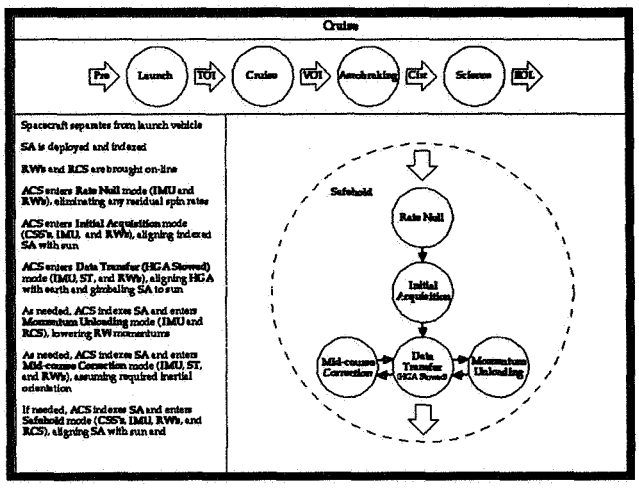

Figure 15 - Cruise Phase Summary

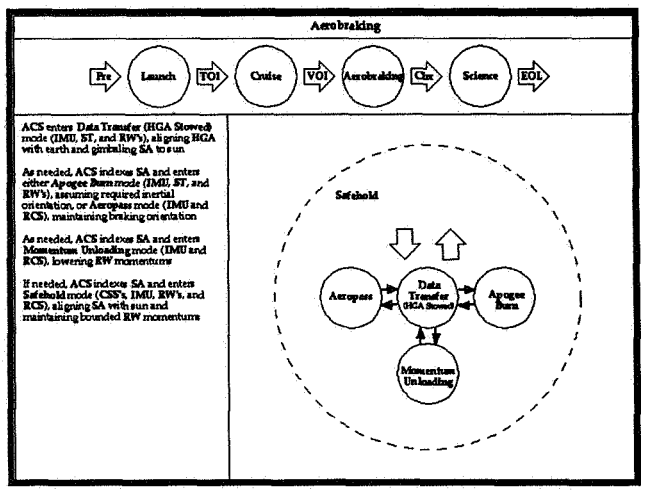

Figure 16 - Aerobraking Phase Summary

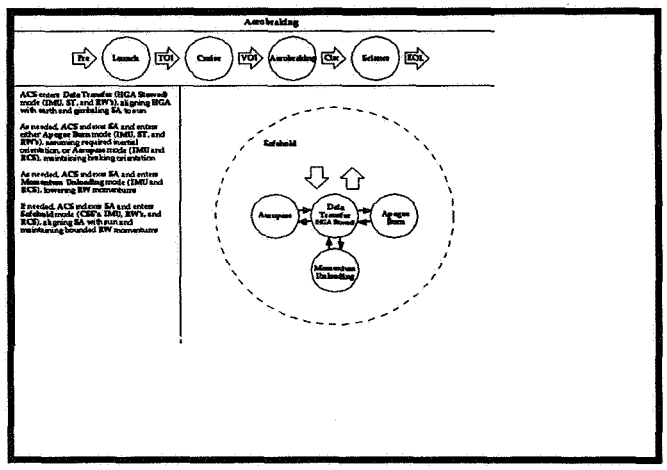

Figure 17 - Science Phase Summary

HGA remains stowed during this phase, and the spacecraft, subsequently, continues to use the same orientation that it used during *Cruise* for communications (HGA pointed towards Earth and SA gimbaled towards the sun). Here, however, the spacecraft repeatedly indexes the SA and adopts the appropriate orientations for apogee burns and aeropasses. Once the target orbit is obtained, V2k deploys its HGA and enters the *Science* phase. From here on out, the spacecraft maintains a nominal Venus pointing orientation, gimbaling the HGA towards Earth and the SA towards the sun. It spends most of its time in one of several science modes, which will be discussed in more detail in the next section. The following panels summarize the three primary V2k mission phases just described.

3.4 Pointing

V2k has two (2) primary science modes. They are left-right SLS pointing and front-back SLS pointing. Keeping in mind the nominal orientation given above (DASC pointed nadir and SLS pointed at the limb), left-right SLS pointing orients the SLS boresight normal to the velocity vector, out either the left, or right side of the spacecraft (as it moves through its orbit) below the local horizontal (i.e. at the limb). Front-back SLS pointing orients the SLS boresight ahead of, or behind the spacecraft (as it moves through its orbit) below the local horizontal (i.e. at the limb). Switching between modes is simply a rotation about nadir (i.e. the DASC boresight).
Because V2k's science pointing requirements are relative to Venus and V2k navigates via the stars (i.e. uses star trackers), extremely good orbit position knowledge is a necessity. V2k must look at the stars and deduce where that is relative to Venus. How well V2k's orbit position is known determines how well Venus' position is known relative to the stars.

V2k's orbital uncertainties are driven by the orientation of its orbit plane with respect to Earth, and will, therefore, vary over the course of the mission. The two extreme geometries are orbit plane face-on to Earth and orbit plane edge-on to Earth. Analysis performed by GSFC's Flight Dynamics Division indicates that for the face-on geometry, the orbital uncertainties will be on the order of 0.37 km and that they will be primarily in-track. The edge-on geometry yields uncertainties on the order of 0.90 km that were found to be primarily cross-track. The distinction

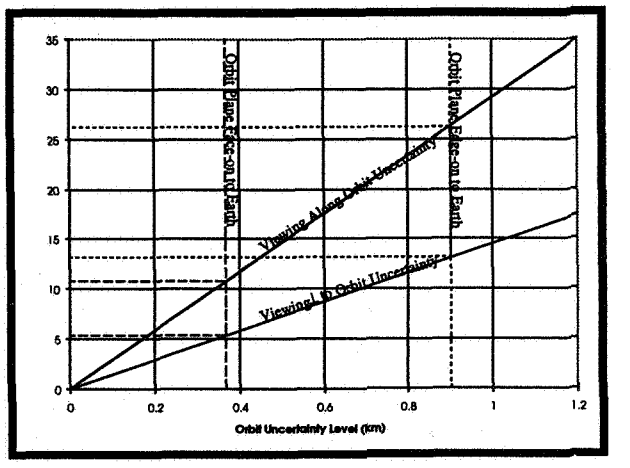

Figure 18 - Pointing Uncertainties from Orbit Uncertainties

between whether the uncertainties are in-track or cross-track is the relevant piece in light of V2k's various science modes. Left-right SLS pointing is most sensitive to cross-track errors and only half as sensitive to in-track errors. Front-back SLS pointing is most sensitive to in-track errors and only half as sensitive to cross-track errors. The result is that the effects of orbital uncertainties can be cut in half by intelligently planning the observation sequences over the coarse of the mission. The following figure illustrates the effects that orbital uncertainties have on pointing uncertainties.

As shown, the worst-case pointing uncertainties from orbit uncertainties will be less than 13 arcsec, as long as care is taken in planning the science mode usage. This provides sufficient margin (below the 30 arcsec requirement) for the other ACS error sources, such as alignment errors and spacecraft attitude knowledge and control errors. Larger orbit uncertainties could easily have rendered the V2k mission impossible. Advances in orbit determination techniques and the use of the most current Venus data available (e.g. Magellan data) have made this mission possible. Meeting V2k's science pointing requirements wasn't just an ACS problem. It required state of the art efforts from both the Flight Dynamics Division and the Guidance, Navigation, & Control Branch.

4.0 SUMMARY

V2k Mission requirements and constraints have been analyzed and factored into the design of both the spacecraft trajectory and attitude subsystems. For the launch window of 2002, a 45 day launch opportunity has been identified to meet mission goals. Operational experience from recent missions are being utilized to

guarantee a successful mission and to aid in the selection of the V2k proposal for a Discovery mission to Venus.

References

1. Interplanetary Mission Design Handbook (Volume-1, part 1, Earth to Venus Ballistic Mission Opportunities, 1991-2005, A. Sergeyevsky and N. Yin/JPL)

2. Mission Analysis and design Tool (Swingby) mathematical Principals, rev 1. September 1995, D. Folta, K Richon, GSFC

3. Mission Analysis Environment for Heliocentric High-Thrust Missions (MAnE), November 1995, J. Horsewood, AdaSoft Inc.

4. Spaceflight Dynamics, W. Wiesel, 1989

5. Venus 2000 Orbit Determination Error Analysis, M. Beckman, report to Venus 2000 Project, November 1996

Page intentionally left blank

AUTOMATIC MANEUVER PLANNING FOR MAINTENANCE OF SATELLITE CONSTELLATION GEOMETRY

Peter Brodsky,
Lockheed Martin Space Mission Systems & Services

Sam Ming-San Chen,
SkyStation International Inc.

Abstract

The recent advent of multi-satellite low earth orbiting (LEO) constellations being developed for global communications has necessitated some rethinking of traditional maneuver planning strategies. For many (if not all) of these constellations, specific "absolute" orbits which form repeating ground traces are not necessary. Therefore, maintenance of the constellation geometry in "relative" terms becomes the primary driving requirement. One would desire, therefore, a maneuver planning scheme which maintains relative geometry while optimizing use of available fuel as well as maintaining a manageable operations workload. We propose several methods for maneuver planning which exploit the intuitive sense that only satellites deviating "from the majority" (in some sense) need attention. We also provide associated methods to calculate corrective maneuver ΔV's. This paper is the result of analysis performed for the Globalstar satellite constellation, and the algorithms presented are being implemented in the Globalstar operations control center ground system.

I. Introduction

Globalstar is one of several satellite constellations planned for use in global communications. In its final operating form, Globalstar will consist of 48 satellites in a 48/8/1 Walker delta pattern, with nominally circular orbits inclined at 52°, at approximately 1400 km altitude. The operational cost of maintaining constellation geometry with this number of satellites (in terms of fuel usage and manpower) would be prohibitively high if traditional maneuvering strategies were used. Clearly some sort of "relative" maneuver planning strategy must be used to optimize fuel usage and manpower efficiency.

Most traditional maneuver planning involves either maintaining the satellite within an interval around a specific longitude (for geosynchronous imaging or communication satellites) or maintaining the satellite ground track within a narrow strip (for LEO imaging satellites). While these maneuver planning strategies serve their mission objectives very well and can also be used for maneuver planning of satellites in a constellation, they may well over-constrain the system into performing maneuvers unnecessary for mission objectives.

For the Globalstar satellite constellation the mission goal is to provide uninterrupted global communication coverage to users on the ground. Translated into a coverage requirement, it means that for every point on the earth surface between 60° south and 60° north there must be at least one Globalstar satellite in view with an elevation above 10° ready to provide service. In the temperate latitudes (25°-50°), continuous double-coverage is required. Therefore, there must be also enough overlap in coverage by neighboring satellites such that handover from satellite to satellite can be performed without interruption.

Extensive coverage analysis has determined that in order to achieve the required visibility, the following specifications must be met.

- Phase angle between neighboring satellites within a plane must be 60° +/- 2°. That is, two adjacent satellites in the same plane may be separated by anywhere between 58° and 62°.
- Phase angle between neighboring satellites in adjacent planes must be 7.5° +/- 2°.
- Difference in right ascension of ascending node (RAAN) between satellites in adjacent planes is to be 45°, +/- 2°.

The 60°, 7.5°, and 45° quantities are dictated by the Walker pattern.

Since it is not necessary for the satellites to maintain fixed orbits to achieve the goal of maintaining separation, the following relative formation-keeping strategies are proposed. We call them the "average" and "neighborhood" methods, and in both there are three primary steps:

- Constellation Evaluation
- Outlier Detection
- Maneuver Time and Magnitude (ΔV) Determination

II. "Average" Method

This method is based on the assumption, driven by extensive perturbation analysis, that all satellites in the constellation will generally behave similarly, and the only factor which might cause a significant change in separation angle is the deviation of some satellites from the "average" behavior of the constellation. Therefore, in order to maintain geometric separation one need only perform maneuvers on those satellites which deviate from "average", with the magnitude of the maneuver proportional to the deviation. The algorithm proceeds as follows:

Let X_{ij} be an orbital parameter X of satellite (i,j), where i is the plane index and j is the position-within-plane index. (X might be semi-major axis, or argument of latitude for example). For the 48/8/1 Globalstar Walker pattern, we use the convention that i runs through the letters A-H and j from 1-6. Because the parameters are changing with time and our concern is their relative values only, we arbitrarily select one satellite as the *reference*, say A1. We then consider the difference:

$$Y_{ij} = X_{ij} - X_{A1} \qquad (1)$$

Each difference has an associated nominal value, determined by the constellation requirements. Let N_{ij} be the nominal value of the parameter Y_{ij}. For the In-Plane positional parameters, we have for example: N_{A1} = 0, N_{A2}=60 and N_{B1}=7.5. These nominal constellation geometry constants are stored in the system database.

The first step in determining constellation status is to compute *the deviations from the average deviation*:

$$D_{ij} = \left(Y_{ij} - N_{ij}\right) - \frac{\Sigma W_{ij}(\mathrm{Y_{ij}} - \mathrm{N_{ij}})}{\Sigma W_{ij}} \qquad (2)$$

where W_{ij} are weights used to create a weighted average. When all weights are equal, as would normally be the case, the term on the right becomes the simple arithmetic mean of all deviations.

Introduction of weights into the average permits flexibility in maneuver planning decisions. An operator may not wish to maneuver certain satellites due to dwindling fuel supply or other concerns. Under such conditions, we don't want to treat all satellites equally and different weights will be assigned to handle the preference. Note that if A1 (the default reference satellite) is given a larger weight, then the operator may wish to change the reference satellite, since this will bias the weighted average. Under ordinary circumstances, all weights are equal.

For orbit geometry maintenance, we identify four parameters of interest:

- Mean Argument of Latitude, $\bar{L}$
- Mean Semi-Major Axis, $\bar{a}$
- Mean Right Ascension of Ascending Node, $\bar{\Omega}$
- Mean Inclination, $\bar{i}$

Note that rates of change of the first and third quantities are highly sensitive to change in the second and fourth respectively. This phenomena is exploited extensively in the process of calculating satellite orbital deviations.

Deviations in each of the four parameters are calculated for all satellites using equation (2) and denoted:

$$D_L, D_a, D_\Omega, D_i$$

The four resulting deviations are then combined into two quantities:

- In-Plane deviation, D_{IP}
- Out-of-Plane deviation, D_{OP}

by:

$$D_{IP} = C_1 D_L + C_2 D_a$$
$$D_{OP} = C_3 D_\Omega + C_4 D_i \qquad (3)$$

where the C_i are constants to be determined. D_{IP} and D_{OP} represent "total" deviations in argument of latitude and RAAN respectively, including both instantaneous deviations in these parameters plus the cumulative effects of deviations in SMA and inclination. For small errors in the latter parameters, we assume linear growth in the former with time.

We are essentially treating the maneuver planning process as a long-term PD feedback control. As such, the C_i become feedback coefficients, and are determined by the deadbands in maneuver planning cycle time and in angular separation tolerances. For example, we may initially set the system so that satellites are to maintain nominal In-Plane relative positions to +/- 1° for 60 days, and Out-of-Plane positions (RAAN) to +/- 1° for 400 days. The constant coefficients are set to 1. The growth coefficients are then computed by:

$$C_2 = \frac{dn}{da} x T_{IP}$$
$$C_4 = \frac{d\dot{\Omega}}{di} x T_{OP} \qquad (4)$$

where $\frac{dn}{da}$ is the dependence of mean motion on SMA, $\frac{d\dot{\Omega}}{di}$ is the dependence of the nodal regression rate on inclination, and T_{IP} , T_{OP} are the maneuver cycle deadband times. Differentiating well-known equations for mean motion and nodal regression, we have:

$$\frac{dn}{da} = \frac{-23328000}{\pi}\sqrt{\frac{\mu}{a^5}} \quad \text{(degrees/day)/km} \qquad (5)$$

$$\frac{d\dot{\Omega}}{di} = 129600 J_2 R_e^{\,2}\sqrt{\frac{\mu}{a^7}}\sin i \quad \text{(degrees/day)/degree} \qquad (6)$$

where μ is the earth's gravitational parameter, J_2 is the earth 2nd zonal harmonic, and R_e is the earth equatorial radius.

Inserting Globalstar specific parameters (a=7780 km , i=52°), we find:

$$\frac{dn}{da} \sim -0.876 \quad \text{(deg/day)/km}$$

$$\frac{d\dot{\Omega}}{di} \sim 0.068 \quad \text{(deg/day)/deg}$$

Then the growth coefficients become:

C_2=52.56 deg/km

C_1=27.2

These values account for the SMA and inclination contribution to drift in and out of plane respectively. The maneuver cycle deadbands, T_{IP} and T_{OP}, are stored in the system database and the initial values are set somewhat arbitrarily to "reasonable" drift correction cycle times.

Total In-Plane and Out-of-Plane deviations are computed this way for all satellites in the constellation. Each deviation is then compared to the angular deadband: currently 1° both In-Plane (phase angle) and Out-of-Plane (RAAN). If a satellite's deviation in either direction exceeds the threshold, the satellite is identified as a maneuver candidate.

The actual ΔV which will correct the detected deviation is computed by:

In-Plane Delta-V:

$$\Delta V_{IP} = K_1 D_{IP} \qquad (7)$$

Out-of-Plane Delta-V:

$$\Delta V_{OP} = K_2 D_{OP} \qquad (8)$$

where K_1 , K_2 are the *gain coefficients* determined as follows:

The expression for change in mean motion with velocity is inverted to yield the In-Plane ΔV dependence on n:

$$\frac{d\Delta V}{dn} = \frac{a\pi}{46656} \quad \text{(meters/second)/(degrees/day)} \qquad (9)$$

Then,

$$K_1 = \frac{d\Delta V}{\frac{dn}{T_{IP}}} \quad \text{(meters/second)/degree} \qquad (10)$$

Out-of-Plane deviations are handled with inclination-modifying maneuvers, to induce RAAN drift back toward the required location. The amount of inclination change required is given by:

$$\Delta i = \frac{\Delta\dot{\Omega}\sqrt{a^7}}{129600 J_2 R_e^{\,2}\sqrt{\mu}\sin i} \quad \text{(degrees)} \qquad (11)$$

where $\Delta\dot{\Omega}$ is the required change in nodal regression rate:

$$\Delta\dot{\Omega} = \frac{D_{OP}}{T_{OP}} \quad \text{(degrees/day)}$$

The precise formula for maneuver magnitude requires the necessary inclination change term inside the sin() function. However, we assume only small inclination changes are required and hence use a small angle approximation to yield:

$$K_2 = \frac{a^3\pi}{23328 J_2 R_e^{\,2}\sin i T_{OP}} \quad \text{(meters/second)/degree} \qquad (12)$$

Inserting Globalstar orbital quantities and assuming nominal In-Plane and Out-of-Plane deadband times of 60 and 400 days respectively, the coefficients become:

K_1=0.000873 (met/sec)/deg

K_2=4.57 (met/sec)/deg

Because the deviations are combinations of position and rate, they are subject to change immediately after a maneuver. This enables us to re-estimate constellation status with maneuver effects accounted for.

III. "Neighborhood" Method

Under certain conditions the average method may demand maneuvers even though the constellation is within specs as defined by allowed angular separations. As an independent check, we propose a second algorithm which also includes "local" information. To illustrate, we represent the Globalstar constellation as a 2-dimensional grid:

	A6	*B6*	*C6*	*D6*	*E6*	*F6*	*G6*	*H6*	
H6	A1	B1	C1	D1	E1	F1	G1	H1	*A2*
H1	A2	B2	C2	D2	E2	F2	G2	H2	*A3*
H2	A3	B3	C3	D3	E3	F3	G3	H3	*A4*
H3	A4	B4	C4	D4	E4	F4	G4	H4	*A5*
H4	A5	B5	C5	D5	E5	F5	G5	H5	*A6*
H5	A6	B6	C6	D6	E6	F6	G6	H6	*A1*

A "neighbor" of a satellite is any satellite immediately to its right or left or above or below on the grid. Each satellite has 4 neighbors. For example, the neighbors of D2 are: {D1, D3, C2, E2}. Neighbors combine to provide the necessary coverage. (Note that additional coverage is provided by non-neighbor satellites on opposite-direction paths. These are known as "key-partners" and are not considered in this analysis.) Under nominal conditions, each satellite is phased 60° from its neighbors above and below, and 7.5° from neighbors to the side.

The neighborhood algorithm begins by computing, for all satellites, the Total In-Plane and Out-of-Plane deviations for each satellite exactly as per equations 1-3 in section **II**. Now, however, rather than simply comparing each satellite's deviation to the angular threshold, we compare it to the deviations of its neighbors. For simplicity, consider only the In-Plane deviations. Denoting the differences *DN*, we have, for each satellite:

$$DN_{jk}=D_{IIPj}-D_{IIPk} \tag{13}$$

where *jk* indicates the differences in deviations between satellite *j* and its 4 neighbors (k=1,2,3,4). For each satellite *j* , therefore, we have a set of 4 differences:

$$\{DN_{j1}\,,\ DN_{j2}\,,\ DN_{j3}\,,\ DN_{j4}\}$$

We then compute, for each satellite:

$$DN_{jMax}=\text{Max}\{DN_{j1}\,,\ DN_{j2}\,,\ DN_{j3}\,,\ DN_{j4}\} \tag{14}$$

$$DN_{jMean}=\text{Mean}\{DN_{j1}\,,\ DN_{j2}\,,\ DN_{j3}\,,\ DN_{j4}\} \tag{15}$$

Any satellite for which DN_{Max} exceeds the angular threshold is called a *candidate*. We denote the set of candidates $\boldsymbol{C}$. Any satellite for which DN_{Mean} exceeds the threshold is called a *strong candidate*. The set of strong candidates is denoted $\boldsymbol{S}$. Obviously $\boldsymbol{S}$ is a subset of $\boldsymbol{C}$. Satellites selected for maneuvers are those which are boundary points of $\boldsymbol{S}$, i.e. points in $\boldsymbol{S}$ which have neighbors not in $\boldsymbol{S}$. The reason for selecting only boundary points of $\boldsymbol{S}$ is to allow for the case where a satellite itself is following the general trend of the constellation but all of its neighbors are not, i.e. a "good" satellite is completely surrounded by "bad" ones. This satellite would become an interior point of $\boldsymbol{S}$, and as such is excluded from maneuver selection in the above scheme.

The neighborhood algorithm is more involved because we are making global decisions based on local information. In addition, maneuvers are planned one at a time (unlike the average method, in which all maneuvers are planned at once). Once a single satellite is selected and a corrective ΔV determined, the entire evaluation process is repeated. Depending on implementation, the process can be adjusted so that all strong candidates are handled first, then all candidates, until no satellite violates the maximum deviation check.

The iterative nature of this scheme makes it more computationally intensive, especially when yaw-steering considerations (section **IV**) are included. As such, it will probably be used primarily in cases where maneuvers determined by the average method are inconvenient or which an analyst suspects may be unnecessary.

IV. Implementation Issues

There are complications in the implementation of the above described algorithms within the Globalstar ground system. Due to power considerations, Globalstar satellites must be yaw steered to maintain correct

solar array aspect. The result is that each satellite is in yaw motion about 6 weeks out of every 8. To avoid the interruption of service which would result from pulling a satellite out of yaw steering to point thrusters correctly, maneuver times are adjusted such that they only occur during non-yaw steering periods. Therefore, maneuvers are planned some 8 weeks in advance so that all maneuvers scheduled will execute before they are actually due.

The constellation status evaluation described in sections **II** and **III** are performed for the last day of the eighth week. The mean orbital elements at that time have been updated by numerical propagation from the most recent orbit determination solution. When a satellite is selected for maneuvering, we step backward in time until the last day of the latest non-yaw steering period and schedule the maneuver there. The actual ΔV is based on constellation status re-evaluated on that date.

Because of the heavy load on computer resources required, maneuver planning will be performed once per week. The long lead time also requires that ephemeris propagation and osculating-to-mean elements conversion be of extremely high accuracy. An internally developed orbit propagator is used in conjunction with the Jet Propulsion Lab's ***OSMEAN*** program to create the 8-week mean elements necessary for the calculation of deviations.

There is an additional complication which arises out of the non-negligible secular effect of inclination deviation on In-Plane position. The first order J_2 expression for period is:

$$T_P = 2\pi\sqrt{\frac{a^3}{\mu}}\left(1-\frac{3}{2}J_2\left(\frac{R_e}{a}\right)^2\left(4\cos^2 i-1\right)\right) \qquad (16)$$

When this equation is converted into mean motion dependence, we have:

$$\frac{dn}{di} = -518400 J_2 R_e^{\,2}\sqrt{\frac{\mu}{a^7}}\sin 2i \quad \text{(degrees/day)/degree} \qquad (17)$$

With Globalstar orbital parameters, this becomes about -0.34 °/day/°. Note that this is some 5 times greater than the sensitivity of RAAN regression to inclination error. For small inclination errors, the much larger Out-of-Plane deadband time (400 days vs. 60 days) will result in detection and correction by Out-of-Plane maneuvers before the In-Plane effect is detected. Larger inclination errors, however, may cause problems if the software attempts to correct the In-Plane deviation with SMA-adjusting maneuvers. This phenomena and possible corrective modifications are under investigation.

V. Test Results and Discussion

The algorithms described have been tested using scenarios simulating the constellation in various states of disorder. Much of the data was supplied by analysts at the satellite manufacturer's facility acting as an independent source of test cases. In all cases, the software detected all outliers. Even with a particularly poor initial constellation, planned maneuvers were such that subsequent propagation of orbits indicated that the constellation remained within nominal specifications for six weeks. With more realistic (i.e. better) initial conditions, we expect results to improve.

This constellation maintenance strategy is not yet completely mature. Use of a linear PD feedback control involves some compromise since we do not really know how satellite relative motion will evolve. However, because the coefficients can be easily changed through database functions, knowledge gained by evaluation of previous maneuvers can be used to make adjustments to improve accuracy of subsequent maneuvers. Neither the average nor the neighborhood method has been rigorously proven to provide

maximum efficiency in fuel consumption or minimization of maneuver number. Together, however, they provide a complementary pair of tools for handling the complex task of planning formation-keeping maneuvers for a large satellite constellation.

Acknowledgements

This work was performed under the Globalstar Satellite Operations Control Center contract. The authors wish to thank Globalstar and Lockheed Martin project management for support and encouragement during preparation of this work.

Several Lockheed Martin engineers contributed significantly, if indirectly to this paper. Antonino Pino, Geoff Pierce and Greg Walker performed analysis of orbit propagation and osculating/mean conversion accuracy, as well as studies of long-term predicted constellation behavior. Rob Gresdo and Milan Rami performed software coding and testing. Ideas, support, and important test data from Andy Turner of Space Systems Loral Space were invaluable.

OSMEAN is a product of JPL and was procured through NASA's COSMIC software clearinghouse.

References

1. Lamy, A. , Pascal, S., "Station Keeping Strategies for Constellations of Satellites", *Advances in the Astronautical Sciences,* 93-306
2. Glickman, R.E., "TIDE: The Timed-Destination Approach to Constellation Formationkeeping", AAS 94-122
3. Graziani, F. , Palmerini, G.B. , Teofilatto, P., "Design and Control Strategies for Global Coverage Constellations" , International Symposium on Spacecraft Control and Flight Dynamics, 1994
4. Pascal, S. , Lamy, A. , Foliard, J., "Design and Station Acquisition for Constellations of Satellites", AAS 94-xxx
5. Guinn, J.R., "Periodic Gravitational Perturbations for Conversion Between Osculating and Mean Orbit Elements", AAS/AIAA Astrodynamics Specialist Converence, 1991
6. Shapiro, B. , Pino, A., "Maintenance of an Exact Repeat Ground Track - The GEOSAT ERM"
7. Chobotov, V.A. (Editor), "Orbital Mechanics", AIAA Education Series

Numerous internal Lockheed Martin and Space Systems Loral communications.

Enhanced Formation Flying For The Earth Observing -1 (EO-1) New Millennium Mission

David Folta
Flight Dynamics Division
and
David Quinn
Navigation, Guidance, and Control
Goddard Space Flight Center, NASA

Abstract

With scientific objectives for Earth observation programs becoming more ambitious and spacecraft becoming more autonomous, the need for new technical approaches on the feasibility of achieving and maintaining formations of spacecraft has come to the forefront. The trend to develop small low cost spacecraft has led many scientists to recognize the advantage of flying several spacecraft in formation, an example of which is shown in the figure below, to achieve the correlated instrument measurements formerly possible only by flying many instruments on a single large platform. Yet, formation flying imposes additional complications on orbit maintenance, especially when each spacecraft has its own orbit requirements. However, advances in automation proposed by GSFC Codes 550 and 712 allow more of the burden in maneuver planning and execution to be placed onboard the spacecraft, mitigating some of the associated operational concerns. The purpose of this analysis is to develop the fundamentals of formation flying mechanics, concepts for understanding the relative motion of free flying spacecraft, and an operational control theory for formation maintenance of the Earth Observing -1(EO-1) spacecraft that is part of the New Millennium. Results of this development can be used to determine the appropriateness of formation flying for a particular case as well as the operational impacts. Applications to the Mission to Planet Earth (MTPE) Earth Observing System (EOS) and New Millennium (NM) were highly considered in analysis and applications.

This paper presents the proposed methods for the guidance and control of the EO-1 spacecraft to formation fly with the Landsat-7 spacecraft using an autonomous closed loop three axis navigation control, GPS, and Cross link navigation support. Simulation results using various fidelity levels of modeling, algorithms developed and implemented in MATLAB, and autonomous 'fuzzy

logic'control using AutoCon will be presented. The results of these analysis on the ability to meet mission and formation flying requirements will be presented.

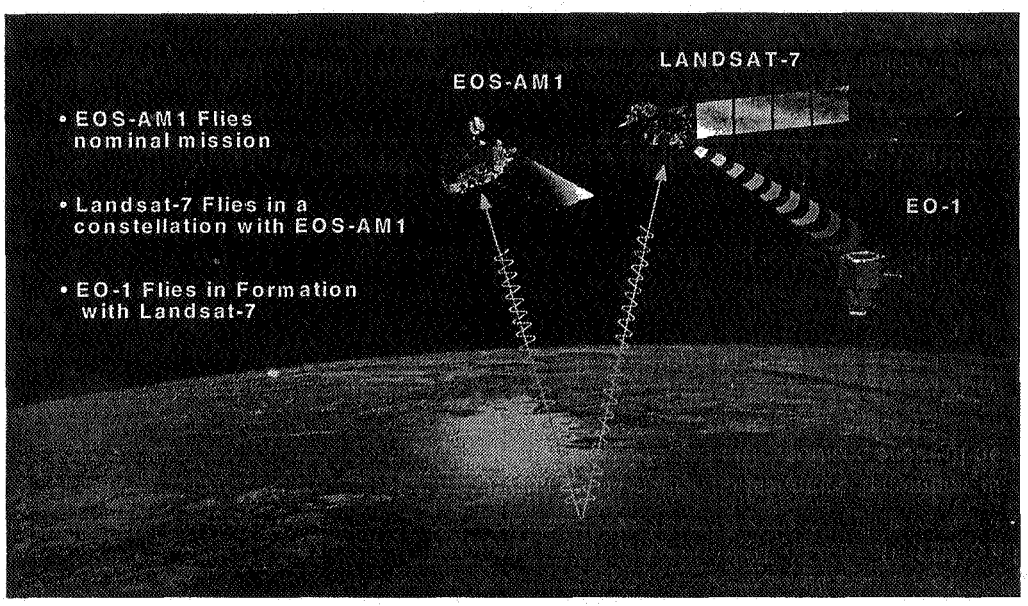

Figure 1 - Formation Flying Scenario for Landsat-7 and EO-1

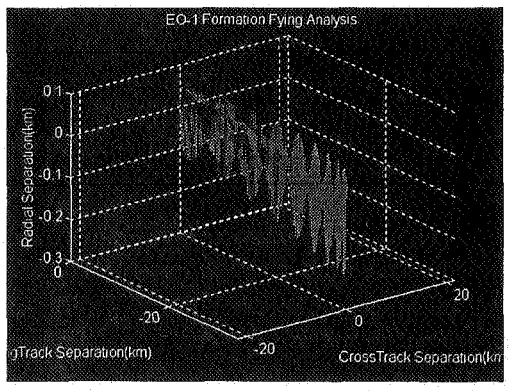

Figure 2- MATLAB Simulation 3-D Relative Motion

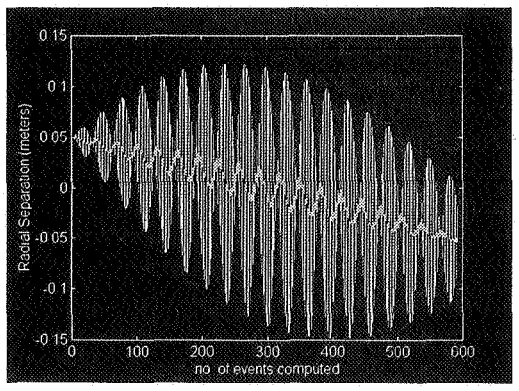

Figure 3 - MATLAB Simulation, Radial Component Vs Time

MATLAB RESULTS from SIMULATIONS

Lunar Prospector Mission Design

David Folta, Mark Beckman
Flight Dynamics Division
Goddard Space Flight Center, NASA

David Lozier, Ken Galal
Mission Operations / Pioneer Office
Ames Research Center, NASA

ABSTRACT

The National Aeronautics and Space Administration (NASA) has selected Lunar Prospector as one of the discovery missions to conduct solar system exploration science investigations. The mission is NASA's first lunar voyage to investigate key science objectives since Apollo and will be launched in September 1997. In keeping with discovery program requirements to reduce total mission cost and utilize new technology, Lunar Prospector's mission design and control will focus on the use of innovative and proven trajectory analysis programs. As part of this effort, the Ames Research Center and the Goddard Space Flight Center have become partners in the Lunar Prospector trajectory team to provide the trajectory analysis and orbit determination support.

The mission design of Lunar Prospector is characterized by a direct minimum energy transfer trajectory to the moon with an injection into a circular 100 km altitude polar mapping orbit. The mission design will incorporate the optimization of the reference trajectory for a new launch vehicle. An extended mission includes a periselene altitude approaching 10 km. As part of the navigation, a new lunar potential model will be used that incorporates data from the recent Clementine mission.

This paper provides understanding of the design of the Lunar Prospector mission and the optimization process of the nominal trajectory, orbit determination, launch windows, and lunar orbit targets, and discusses the feasibility of meeting the mission goals.

1.0 INTRODUCTION

1.1 Mission Description

The Lunar Prospector Mission is part of the NASA Discovery Program which is designed to foster more frequent launches of low-cost solar system exploration missions. The Lunar Prospector (LP) spacecraft is being built by the Lockheed-Martin Missile and Space Company and is designed to perform low altitude mapping of the moon for the purpose of studying lunar surface composition, magnetic fields, gravity fields and gas-release events. A total of six science experiments will help scientists improve our understanding of the origin, evolution and current state of the moon, and will build on data collected from previous missions (Apollo, Clementine and Galileo) to establish a more comprehensive map of lunar resources.

1.2 Spacecraft Description

LP is a 285 kg spacecraft with a cylindrical main body that is approximately 1.4 m tall with a diameter of 1.4 m (Fig. 1). Science instruments are mounted on three 2.5 m deployable masts. The spacecraft will be spin stabilized, spinning at a nominal rate of 12 revolutions per minute (rpm). Onboard attitude sensors will consist of a sun sensor and an Earth/moon limb sensor. Six 22 Newton (N) hydrazine thrusters (2 radial and 2 along both the positive and negative spin axis direction) will be used for spin axis precession maneuvers and orbit maneuvers.

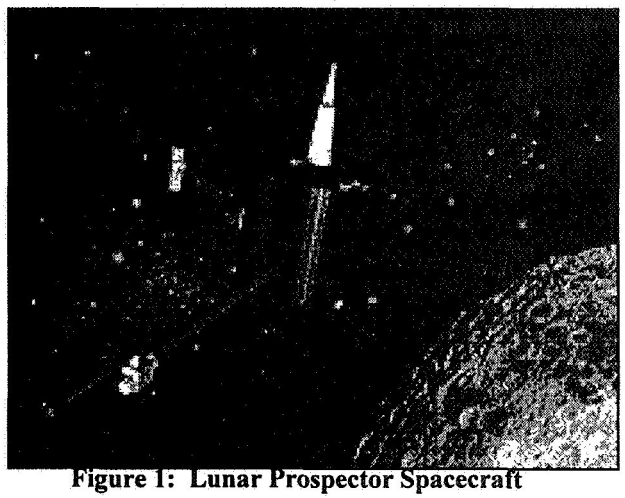

Figure 1: Lunar Prospector Spacecraft

Table 1: Lunar Prospector Mission Constraints

	Requirement	Angle Constraints
Power/Thermal	1. No shadowing during intermediate LOI orbits	$71^\circ < \lvert \emptyset_{N/s} - 90 \rvert$ @ 100km altitude
	2. No total eclipse during 1st year ops	$.7^\circ < \lvert \emptyset_{s\text{-}m} - 180 \rvert$
Communication	1. Coverage post-TLI for maneuver. to cruise att.	$\emptyset_E < 130^\circ$
	2. Station coverage during LOI maneuvers	$\emptyset_E < 130^\circ$
Attitude Determination/Control	1. Sun data post-TLI for maneuver. to cruise att.	$26^\circ < \emptyset_s < 154^\circ$
	2. Sun data in LOI attitude	$26^\circ < \emptyset_s < 154^\circ$
	3. Earth sensor roll observability post-TLI for maneuver to cruise attitude.	$30^\circ < \emptyset_{s/E} < 150^\circ$

Where: $\emptyset_{N/s}$ = Angle between orbit normal and s/c-to-sun vector
$\emptyset_{s\text{-}m}$ = Angle between sun vector and moon vector (relative to Earth)
$\emptyset_{s/E}$ = Angle between s/c-to-sun vector and s/c-to-Earth vector
$\emptyset_E$ = Angle between s/c spin axis and s/c-to-Earth vector
$\emptyset_s$ = Angle between s/c spin axis and s/c-to-Sun vector

1.3 Mission Profile

The LP spacecraft will be launched from the Eastern Test Range (ETR) on September 24, 1997 into a 100 nautical mile (nm) parking orbit using a Lockheed-Martin Launch Vehicle -2 (LMLV-2). After a short coast, a STAR 37 FM solid motor injection stage will boost the spacecraft into a direct trajectory to the moon with a nominal flight time of just over four days. Following separation from the STAR 37 stage, the spacecraft will be oriented normal to the ecliptic plane to satisfy power and communications constraints.

Upon approaching the moon, the spacecraft attitude will be re-oriented to permit an axial lunar orbit insertion (LOI) burn into a polar orbit with a 100 km altitude at periapsis and a 12 hour period. Successive orbit maneuvers over the next several days will then place the spacecraft into its 100 km circular mapping orbit about the moon. Occasional orbit altitude maintenance maneuvers will be performed during the nominal one year mission lifetime, with the possibility of an extended mission phase at lower periapsis altitudes of 10 km.

2.0 TRAJECTORY DESIGN

The trajectory design requirements for the LP mission consist of defining, a) launch and transfer orbit injection times, b) injection delta-V magnitude and direction, and c) lunar orbit insertion maneuvers necessary to place the spacecraft into a 100 km polar circular orbit about the moon. A minimum energy transfer orbit (launch C_3 = -2.1 km^2/sec^2 , insertion ΔV= 0.875 km/sec) is planned with a launch from the ETR. The resulting trajectory design is shaped by a number of constraints and the overriding goals of minimizing operational complexity and maximizing propellant remaining upon completion of LOI. A mid-course orbit correction maneuver is planned at approximately 4 hours after injection into the transfer orbit. This maneuver will use a vector burn capability (combined axial and radial thruster firing) to avoid re-orienting the spacecraft.

2.1 Mission Constraints

Mission constraints affecting LP trajectory design are driven by spacecraft communication, attitude control/determination, and power/thermal requirements. Table 1 summarizes those key requirements and associated geometric constraints.

Spacecraft power and thermal designs limit the duration of allowable lunar eclipses by the Earth during the mission. Such eclipse opportunities occur during lunar eclipse seasons every six months (as the moon crosses the ecliptic plane). When coupled with orbital shadowing by the moon, the worst case shadow duration can be nearly 5 hours long. Total eclipses during the first year of the mission can be avoided by proper selection of launch date. For an September 97 launch, only penumbral eclipses are expected in lunar orbit within the first year of the mission, with the first total lunar eclipse occurring not until July 28, 1999 [Ref. 1].

Spacecraft power/thermal designs also place constraints on shadow conditions at translunar injection (TLI) and LOI (Table 1). Transfer trajectories must be designed to preclude shadowing following TLI and during intermediate orbits of the LOI sequence.

The LP spacecraft uses an omni antenna for telemetry and command throughout the transfer orbit and early mission operations. The omni antenna is located along the positive spacecraft spin axis and has a nominal +/- 130 degree field of view about that axis. Communication requirements affecting trajectory design include the need to send real-time commands

to maneuver the spacecraft into the cruise attitude following TLI and the need to initiate LOI orbit maneuvers upon arriving at the moon.

Spacecraft attitude sensing is also required at key points in the mission to provide an attitude reference for planning and executing attitude and orbit maneuvers. Of particular concern are the post-TLI stage separation when the spacecraft will be maneuvered into its cruise attitude, the mid-course correction maneuvers when vector orbit burns will be performed, and the LOI approach when the spacecraft will be maneuvered into its burn attitude. During such maneuvers, valid sun sensor measurements are required to provide a roll reference in the spin plane from which to fire thrusters. For sun sensing to occur, the s/c spin axis pointing direction (which is established by delta-V requirements during TLI and LOI) is limited in terms of an acceptable range of sun aspect angles to between 26 and 154 degrees (Table 1).

Likewise, for maneuver planning purposes, valid data from both the sun sensor and the Earth/moon limb sensor are required to establish the spin axis attitude. The Earth/moon limb sensor requires a minimum Earth/moon subtended limb of 8 degrees, which places a limit on the distance from the Earth/moon at which measurements can be taken. Finally, the separation angle between the sun and Earth (for Earth limb sensing) and the sun and moon (for moon limb sensing) can affect attitude determination accuracy, with complete ambiguity occurring at angles of 0 or 180 degrees.

Figure 2 shows the Earth, sun and moon with a plot of the transfer trajectory for the nominal September 24 launch date.

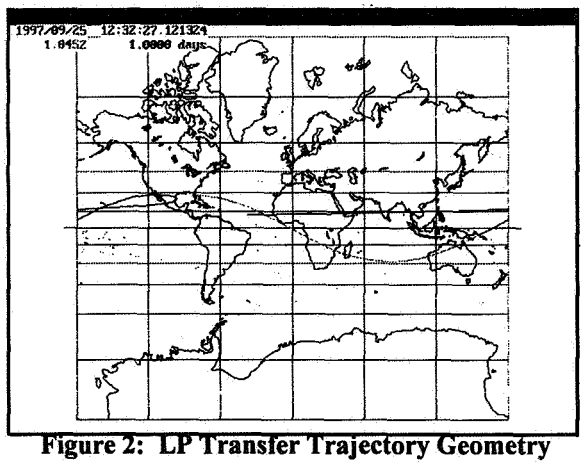

Figure 2: LP Transfer Trajectory Geometry

2.2 Launch Opportunity

A launch on a direct trajectory to the moon is theoretically possible during any day of the month. For a given launch day and a given launch site, two minimum energy trajectories to the moon are possible [Ref. 2]. These two trajectories are different only in terms of the launch time, the length of the coast time in the parking orbit prior to TLI, and the angle that each transfer orbit makes with the ecliptic plane.

For LP, the long coast trajectory is desirable because it minimizes the time between the TLI and first acquisition by the Goldstone DSN site and allows for a cruise attitude that is near-normal to both the sun (for power/thermal considerations) and the Earth (for

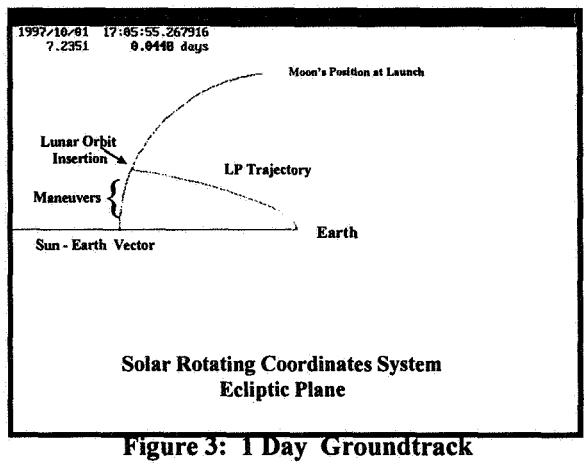

Figure 3: 1 Day Groundtrack

communication considerations). Figure 3 shows 1 day ground track for the nominal September 24, 1997 long coast trajectory with a 93 degree launch azimuth.

Considerations that factor into the selection of launch azimuth include range safety issues, launch vehicle performance and post-TLI station coverage profile. Initial station acquisition of the spacecraft downlink is provided by the 26 and 34 m antennas at Goldstone. Figure 4 provides a plot of station aspect angle for the first 8 hours following TLI separation for the September 24th trajectory.

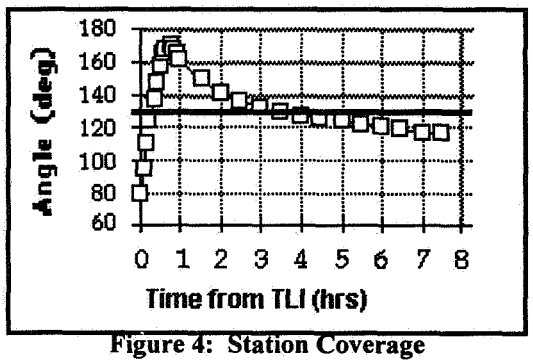

Figure 4: Station Coverage

As an additional risk mitigation and early orbit support effort, FDD will utilize the Space Network. This support will be accomplished with TDRS-West using a coherent link with the LP's transponder. This link will be used to provide a basis for early TLI error estimation using a coherent Doppler data. The

TLI error estimation is based on observed minus computed Doppler measurements. The significance of this support is to provide an early estimation of the LMLV-2 performance as real-time launch vehicle performance data will not be available to the project nor the Flight Dynamics Division. The duration of the TDRS coverage is approximately 10 minutes, from the TLI to the acquisition of signal by the Goldstone DSN site.

2.3 Mid-Course Correction Strategies

Every mission faces a number of possible launch and injection error sources, including those brought about by launch delays, launch vehicle dispersions, coast time errors, and injection stage dispersions. Station coverage closely following the TLI maneuver is necessary to obtain the tracking data needed to compute an orbit solution and prepare a mid-course correction maneuver. A nominal LP midcourse correction maneuver is planned for no later than 4 hours after TLI. A quick response in correcting launch and injection errors is crucial, as the required correction to a given delta-V error grows quickly as a function of time from TLI. With an error in the launch vehicle energy, the trajectory will need to be corrected. The effect of various error in the TLI are shown in Figure 5. Figure 6 shows the magnitude of required delta-V corrections for an under performance of the TLI stage as a function of maneuver start time from TLI.

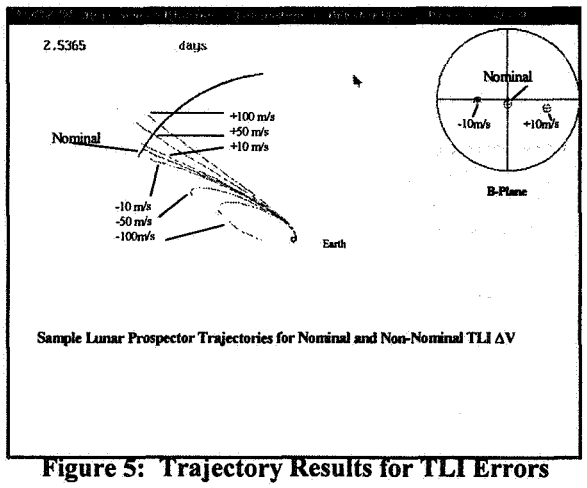

Figure 5: Trajectory Results for TLI Errors

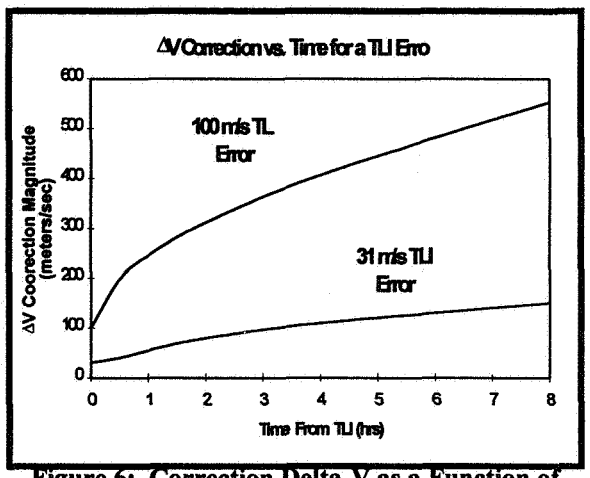

Figure 6: Correction Delta-V as a Function of Time From TLI

2.4 Launch Window

The LMLV-2 will place LP into a parking orbit with a 60.1 minute coast time. With the coast time fixed, launch delays of several minutes will result in an incorrect cislunar trajectory which will need to be corrected at approximately launch plus four hours. The desire to provide a useful launch window on any given launch date is constrained by the large correction delta-V penalties that would need to be absorbed (assuming a fixed launch azimuth capability over the window). Figures 7 and 8 show the magnitude of a required correction delta-V at 4 hours after TLI as a function of launch time error. The magnitude of the correction maneuver is dependent upon the lunar targets selected; B-plane and time of arrival. The use of a constrained time of arrival at the periselene rapidly increases the correction maneuvers, thereby limiting the duration of the launch window. As seen in figures 7 and 8, the usable duration of a constrained launch window is roughly one fourth that of an unconstrained time of arrival.

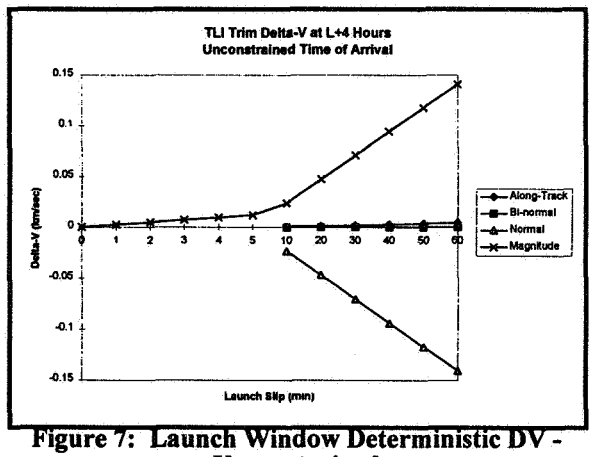

Figure 7: Launch Window Deterministic DV - Unconstrained

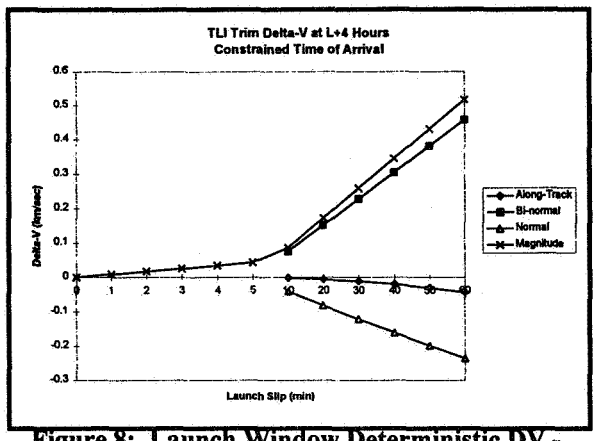

Figure 8: Launch Window Deterministic DV - Constrained

2.5 Lunar Orbit Insertion Strategy

For a given launch opportunity it is possible to select either a northerly or southerly approach trajectory to the moon [Ref. 3]. In the case of the LP mission, a northerly approach is currently favored since it minimizes the size of the re-orientation maneuver required to get from the cruise attitude to the LOI burn attitude. Figures 9 and 10 shows the lunar approach geometry for the northerly approach trajectory for an September 24th launch.

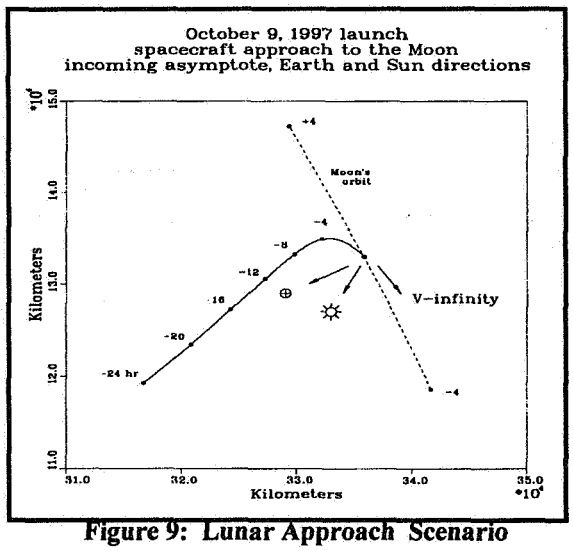

Figure 9: Lunar Approach Scenario

A key variable in defining a series of LOI maneuvers to achieve the 100 km nominal lunar mission orbit is the total number of burns in the sequence. Figure 10 shows an LOI maneuver sequence (as seen from the Earth) into a 12 hr orbit, a 3.5 hr orbit and finally the 100 km circular mapping orbit. The total nominal impulsive delta-V required to achieve the mission orbit is 836 m/s. Since LP burns will occur from an inertial attitude over a finite arc, a larger number of maneuvers (over shorter arcs) will result in more efficient burns and hence larger amounts of propellant remaining to conduct science operations.

Another consideration shaping the LOI strategy is the stability of intermediate orbits in the maneuver sequence. Intermediate orbits with a large apoapsis are more susceptible to Earth and solar perturbations. The impact of such perturbations depends on the orientation of the orbit plane with respect to the sun, which is a function of launch date. Figure 11 shows the effects of such perturbations on orbit inclination just 24 hours after insertion into a 100 km x 9750 km intermediate lunar orbit with an inclination of 90 degrees.

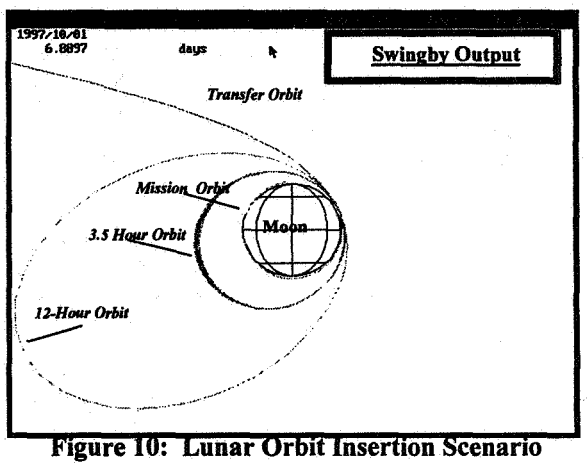

Figure 10: Lunar Orbit Insertion Scenario

For a given sequence of LOI maneuvers, it is possible to select a single inertial attitude from which all burns may be carried out. This attitude, which corresponds to the velocity direction at periselene, will maintain a fixed argument of periapsis throughout the LOI maneuver sequence. Depending on the sizes of the intermediate orbits that are chosen, it may be necessary to trim any inadvertent growth of periapsis altitude with a final burn by flipping the line of apsides and burning in a direction opposite to that used for initial burns in the sequence.

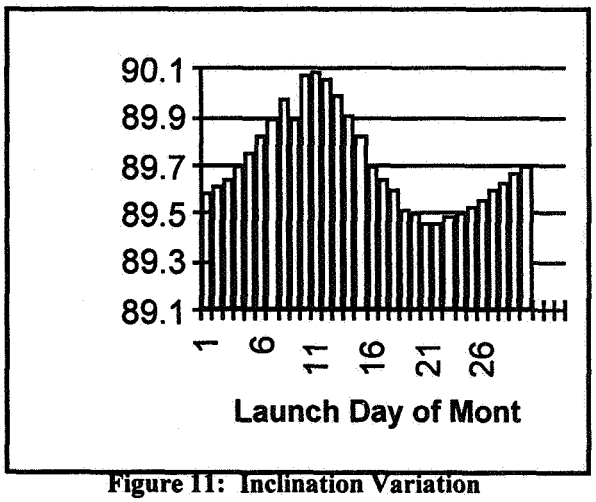

Figure 11: Inclination Variation

2.6 Lunar Orbit Maintenance Strategy

The effect of the Lunar potential on the apoapsis and periapsis of the 100 km circular orbit is to drive the periapsis lower and the apoapsis higher. This due to the non-uniform shape of the moon which explains why the moon displays the same side toward the earth. The requirement for the lunar orbit is to maintain the 100 km orbit to +/- 25 km over the mission life of one year. Early analysis indicated that maneuvers to reshape the orbit to its circular condition would be required approximately once per month. With the use of the newly generated lunar potential models, a truer representation of this 'decay' can be predicted. Figure 12 shows a long term prediction of the orbit and the effective change in the perisapsis and apoapsis for the lunar potential models used for Clementine (LUN75A) and the potential model generated at GSFC by Code 900 (GLGM-2) [Ref. 4]. The plot shows the perturbation as a result of the first 21 coefficients of the models. Higher order potential models are currently being implemented for further analysis. The results of these analyzes will allow the determination of the final orbit to maximize the time between maneuvers. As shown in the Figure 12, one can see that a half year can be reached before any maintenance maneuver are required. This is important since the amount of fuel conserved will be used in the extended mission when the periapsis is lower to only 10 km, about the height of commercial aircraft routes on Earth.

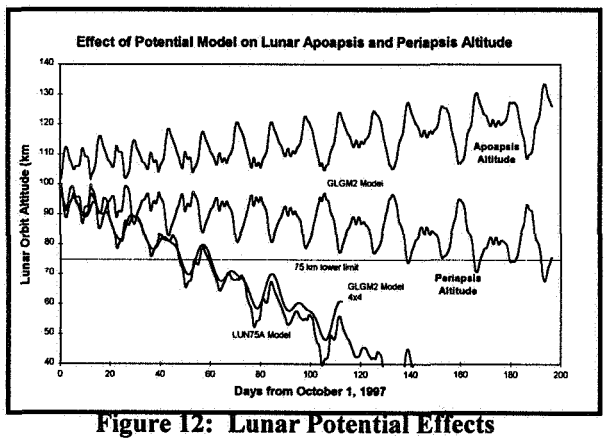

Figure 12: Lunar Potential Effects

3.0 ORBIT DETERMINATION

Orbit determination for the LP mission will be very similar to the support provided for the D.O.D. Clementine mission, also supported by Flight Dynamics at Goddard. There are two primary differences in the support. The first due to the direct insertion of LP. Clementine used 2 ½ phasing loops to reach lunar orbit in about 25 days. LP takes only 5 days leaving very little time to correct an off-nominal insertion. The second difference is due to the different mission orbits. Clementine flew in a 450 by 2900 km polar orbit while LP will fly in a 100 km circular polar orbit. The lower altitude of the LP mission will increase the orbital uncertainty due to the lunar potential model uncertainties.

The ground tracking coverage for LP will be from the three DSN ground sites: Canberra, Australia; Madrid, Spain; and Goldstone, California. Clementine tracking was very similar using Canberra, Madrid, and a Naval Research Laboratory tracking station in Pomonkey, Maryland. All of the tracking stations will provide Doppler tracking measurements accurate to 1 mm/sec for use in the orbit determination of LP. Range measurements will be used in the translunar phase and immediately after lunar insertion. Tracking measurements will be used to determine daily orbital estimates for spacecraft navigation, mission planning, and science processing. In addition, for the first few months after lunar insertion, the Doppler data will be used for gravity field experiments to be performed by the Jet Propulsion Laboratory (JPL). Tracking coverage is to be approximately 70% once in lunar orbit and near continuous from launch through lunar insertion.

To date, analysis has been completed in three areas. The first is analysis of post-TLI orbit estimation. The second is analysis of nominal lunar orbit estimation. The third is analysis of post-LOI orbit estimation.

3.1 Post-TLI

LP launches off of a LMLV-2 which provides no telemetry information as to actual spacecraft separation state. The LP project also believes there may be considerable uncertainty in the TLI burn magnitude due to nutation. Because of these, the LP project is interested in obtaining a rough estimate of TLI burn efficiency, as determined by the tracking measurements, as soon as possible.

The first ground station contact with LP after TLI is with the DSN station at Goldstone at 12 minutes after TLI burnout. Goldstone will provide two-way Doppler information for LP. Prior to Goldstone, TDRSS support has been obtained to provide two-way coherent Doppler immediately after TLI.
The LP project has indicated that the 3-sigma TLI magnitude uncertainty could be as high as 100 m/sec. With such large possible off-nominal TLI trajectories, immediate confirmation of TLI burn efficiency is needed to minimum fuel costs to correctly target the moon. Full state estimation would not be possible within the first few minutes after TLI. However, various off-nominal TLI trajectories were differenced with the nominal TLI trajectory to obtain expected range-rate residuals from TDRS-W when compared to the baseline trajectory. These estimated residuals are shown in Figure 13 [Ref. 5].

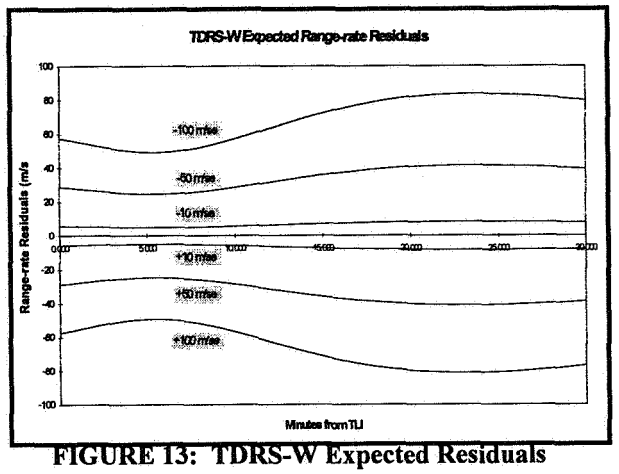

FIGURE 13: TDRS-W Expected Residuals

The uncertainty in each of the expected residual patterns shown in Figure 13, due to dynamic and measurement modeling, is less than 0.7 m/sec. The residuals expected from even a 10 m/s off-nominal TLI burn are on the order of 5 m/sec. Thus, a seriously off-nominal TLI burn can be identified from TDRS-W residuals just a few minutes after acquisition of signal.

After an initial determination of TLI efficiency, a full state estimation must be performed to plan for a MCC maneuver. The sooner this midcourse maneuver occurs, the less the fuel cost.

A number of different solutions were performed using batch estimation tracking arcs from 2 to 48 hr. The estimated LP state errors for each of these solutions were mapped back to TLI burnout. These position and velocity errors at TLI are shown in Figure 14 [Ref. 5].

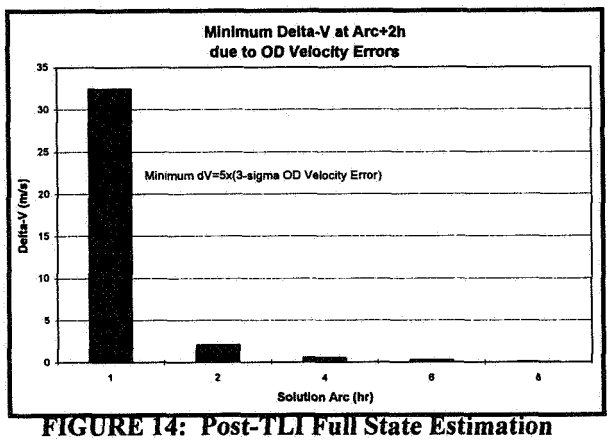

FIGURE 14: Post-TLI Full State Estimation

The results show a dramatic drop in orbit uncertainty when going from a 2 to a 4 hr solution. Another significant drop occurs between 4 and 6 hr. After 6 hr, the improvement in TLI state is smaller.

The position and velocity errors for the 6 hr. solution are shown in Figure 15 [Ref. 5]. The velocity error decreases as the solution state is propagated. This is due to the fact that the state is propagating away from perigee, where velocity is maximum. As the state moves farther from perigee, the velocity decreases. The percentage error, velocity error divided by total velocity, is actually increasing but Figure 15 shows a decrease because the actual velocity error decreases. This is due solely to the fact that total velocity decreases also. Position error effects are opposite in that the position error grows with propagation as the position magnitude also increases.

The determination of the placement of the first MCC maneuver will be from analysis of fuel costs and orbit determination uncertainties. While the 6-hr solution above appears to be the best choice from an orbit determination point of view, it may cost less fuel to perform the MCC earlier, in spite of the additional orbit determination uncertainties. The limiting factor to this approach is that any MCC maneuver's planned ΔV should be greater than five times the 3σ orbit determination velocity error at the time of the maneuver. Figure 16 shows the minimum ΔV for a number of different MCC maneuvers, placed two hours after the end of the tracking arc to provide time for determination, transmission, commanding, and upload.

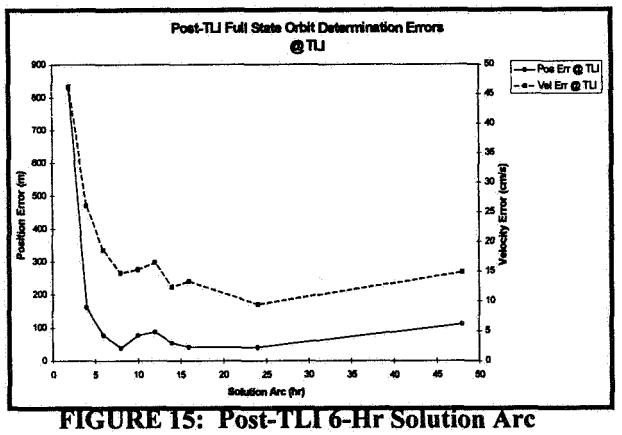

FIGURE 15: Post-TLI 6-Hr Solution Arc

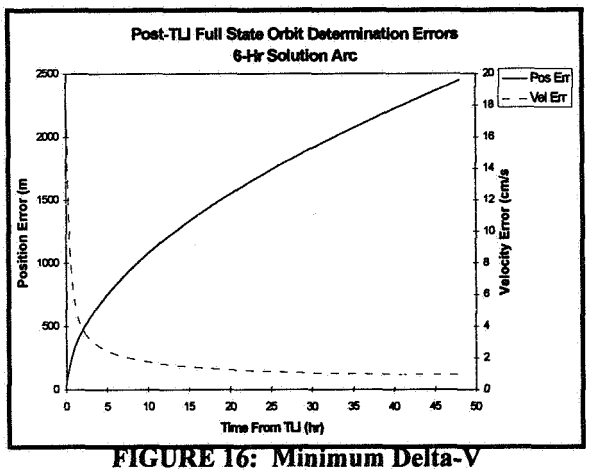

FIGURE 16: Minimum Delta-V

3.2 Nominal Lunar Orbit

The nominal mission orbit for LP is a 100 km polar circular orbit about the moon. The accuracy requirements are 1 km and 1 m/sec (1-σ) and apply to each of the three orbit components: radial, cross-track, and along-track.

The gravitational potential error is the leading source of error for the nominal lunar orbit phase because of the low altitude of the spacecraft. The GLGM-2 lunar potential model [Ref. 4] is the most recent and uses the most extensive tracking data set, including Clementine data. This model will be used for navigation for LP.

Assessing the expected errors introduced by using this model is somewhat difficult. The GLGM-2 force coefficients all have derived 1σ standard deviations but the correlation matrix between the error coefficients is not available. Thus, the error introduced to the state due to any single degree and order is easily obtainable, but the error introduced by the potential model as a whole is not. The errors due to each error coefficient are all correlated with each other and combining the errors due to each error coefficient into a single error is just an estimate without the full correlation matrix. For this reason, multiple error models have been used. Three different error models for the GLGM-2 potential model are shown in Table 2 [Ref. 6].

The LP orbit plane will rotate between two extreme geometries with respect to the Earth. In the edge-on geometry, the spacecraft orbit plane is parallel to the Earth-Moon line, thus causing regular lunar occultation. In the face-on geometry, the spacecraft orbit plane is perpendicular to the Earth-Moon line, allowing full visibility of the orbit. Four orbit geometries were investigated with angles of 0°, 30°, 60°, and 90° between the orbit plane and the Earth-Moon line.

The optimum batch arc length was determined to be between 200 and 250 minutes. Covariance analysis results using each of the three error models were broken down into orbit components. Table 3 shows the Root Mean Square of the 1σ position and velocity components: radial or height (H), cross-track (C), and along-track (L).

Results indicate that when the orbit plane is in the face-on geometry orbital requirements are easily met. When the orbit plane rotates to within 30° of edge-on however, the cross-track position (and velocity) requirement may be difficult to meet. [Note that the

TABLE 2: Gravitational Potential 1σ Error Models

Number	Derivation	Scale Factor	Size	Correlation Method
1	LUN50G minus Bills-Ferrari	1/3	50x50	algebraically added
2	GLGM-2 standard deviations	1	70x70	RSSed
3	GLGM-2 minus LUN60D	4/3	70x70	algebraically added

TABLE 3: Position and Velocity Components For Selected Cases

Error Model	Arc Length (min)	Position (km)*			Velocity (m/sec)*		
		H	C	L	H	C	L
Geometry A (Edge-on)							
1	250	**0.04**	**0.23**	**0.11**	**0.05**	**0.21**	**0.04**
2	200	**0.63**	1.92	**0.57**	**0.64**	1.46	**0.66**
3	200	**0.11**	23.18	3.83	3.45	19.45	**0.09**
% that met req		*100%*	*33%*	*67%*	*67%*	*33%*	*100%*
Geometry B							
1	250	**0.03**	**0.68**	**0.52**	**0.45**	**0.61**	**0.03**
2	250	**0.61**	1.75	**0.50**	**0.58**	1.42	**0.62**
3	250	**0.04**	**0.81**	**0.55**	**0.46**	**0.73**	**0.04**
% that met req		*100%*	*67%*	*100%*	*100%*	*67%*	*100%*
Geometry C							
1	200	**0.07**	**0.23**	**0.53**	**0.47**	**0.19**	**0.05**
2	200	**0.07**	**0.26**	**0.57**	**0.51**	**0.22**	**0.05**
3	250	**0.06**	**0.98**	2.21	1.98	**0.85**	**0.05**
% that met req		*100%*	*100%*	*67%*	*67%*	*100%*	*100%*
Geometry D (Face-on)							
1	200	**0.18**	**0.05**	**0.49**	**0.37**	**0.03**	**0.15**
2	200	**0.46**	**0.53**	**0.97**	**0.70**	**0.48**	**0.34**
3	200	**0.17**	**0.04**	**0.55**	**0.44**	**0.04**	**0.15**
% that met req		*100%*	*100%*	*100%*	*100%*	*100%*	*100%*

* Errors that meet 1 km or 1 m/sec requirement are shown in **bold**.

case A and C along-track position (and radial velocity) for error model 3 have been discarded because the other two error models gave more consistent results throughout the analysis.] But even for that specific case, requirements may very well be met since at least one of the error models indicated that.

Approximately three months into the lunar orbit phase, JPL will have developed an updated lunar potential model using two months of LP Doppler measurements. This model will then be used for the duration of the lunar orbit phase. This model will also be used to reestimate the first three months of definitive trajectory if statistics indicate that the accuracy requirements have not been fully met.

3.3 Post-LOI

The lunar orbit insertion sequence consists of three maneuvers. The first places the spacecraft into a 18.5 hr eccentric orbit about the moon. Quick orbit estimation is important to ensure capture into lunar orbit. Covariance analysis for a 3.5 hr tracking arc after LOI shows that an accurate solution can be obtained that gives a semi-major axis uncertainty of less than 200 m. The orbit geometry is near face-on, allowing continuous tracking coverage after LOI. The error sources are predominantly the lunar potential model and refraction errors through the Earth's atmosphere.

The second LOI maneuver places the spacecraft into a 3.5 hr eccentric orbit. Covariance analysis for a 5.5 hr tracking arc after LOI2 shows that a solution can be obtained that gives a semi-major axis uncertainty of less than 25 m. The only significant error source at this altitude is the lunar potential model.

The third and final LOI maneuver places the spacecraft into the nominal 118 minute circular orbit at 100 km altitude. Analysis of the nominal lunar orbit determination showed that the optimum arc length is between 200 and 250 minutes and would provide orbit estimates within the mission requirements.

4.0 SUMMARY

Lunar Prospector mission requirements and constraints have been analyzed and factored into the design of a nominal transfer trajectory and LOI sequence to place the spacecraft into its 100 km circular polar lunar orbit. For the month of September 1997, a ten day launch opportunity window (September 7-16) has been identified that will satisfy mission constraints. Operational experience and software capabilities from the most recent lunar orbit missions (Clementine and WIND) and previous planetary probes (Pioneer) are being utilized to address LP mission design needs quickly and cheaply. An improved lunar gravity potential model has been developed at GSFC and will be used to help meet the 1 km (1s) position component accuracy requirement for LP's 100 km lunar mapping orbit.

REFERENCES

1. The Astronomical Companion, G. Ottewell, 1979.

2. Design of Lunar and Interplanetary Ascent Trajectories, V. C. Clarke, Jr., AIAA Journal, Vol 1, No. 7, July 1963.

3. Trajectory Design for the Deep Space Program Science Experiment (DSPSE) Mission, D. Carrington et al., AAS /GSFC International Symposium on Space Flight Dynamics #93-260, March 1993.

4. GLGM-2: A 70th Degree and Order Lunar Gravity Model from Clementine and Historical Data, F. G. Lemoine (GSFC), et al., draft paper, July 5, 1995.

5. Lunar Prospector Post-TLI Orbit Determination Analysis, M. Beckman, report to Ames, January 1997.

6. Lunar Prospector Nominal Lunar Orbit Error Analysis, M. Beckman, report to Ames, August 1996.

Page intentionally left blank

A New Satellite Attitude Control System

Wendy I. Sullivan
Michael A. Paluszek
Princeton Satellite Systems, Inc.

Walter K. Daniel
CTA Space Systems, Inc.

Abstract

This paper describes a new satellite attitude control system architecture, called the SPACECRAFT CONTROL SYSTEM. A simplified version of this control system is scheduled to fly in 1997 onboard Indostar®, a commercial geosynchronous communications satellite. The control system includes transfer orbit, acquisition and mission orbit modes. The software architecture permits easy modification and upgrades making this system applicable to any satellite.

The control system described in this paper includes many innovative features. Several are designed to reduce operator workload, such as automatic momentum unloading, a simplified moding structure and automatic mode transitions. Others reduce the cost of accommodating changes to the spacecraft or porting the control system to other spacecraft, such as the use of the simplex algorithm onboard to distribute the three-axis torque commands among selected thrusters. The entire control system is constructed to be highly modular, and this characteristic is reflected in the C flight code. The modular nature of the control system makes modifications and additions easy to accomplish, and results in highly maintainable flight code.

This paper will describe the SPACECRAFT CONTROL SYSTEM architecture and algorithms in detail, with emphasis on the new features mentioned above. An overview of the control system design environment and high fidelity simulation will be provided. Finally, simulation results from the Indostar test program will be presented, along with results from the SPACECRAFT CONTROL SYSTEM simulation.

Background

Traditionally, satellite control has been ground operator intensive, requiring that most control operations be initiated from the ground. As the industry gains experience in satellite operations, it is possible to design more automation into satellite control systems.

Control System Architecture

There are three distinct phases during which the attitude control system (ACS) must operate: transfer orbit, which begins when the satellite separates from the launch vehicle and during which the satellite must attain its mission orbit; acquisition, which is the process of locating the sun and the earth and aligning the satellite properly on station so its mission can be carried out; and mission orbit, during which the satellite must maintain its correct attitude and station. A block diagram of the entire control system architecture is shown in Figure 1. The block diagram shows the interaction between the sensors, control modules and the actuators. The processors for all of the sensors are listed on the left-hand side of the diagram: horizon sensors (HSA), sun sensors (SSA), gyros, earth sensors (ESA), and the momentum wheel assembly (MWA) tachometer. The processed output from the sensors is used for error computation and input to the control systems (shown in the center of the diagram): transfer orbit control, earth acquisition control, and mission orbit control. Then, the outputs of the control systems are distributed to the actuators (on the right-hand side of the diagram): the rocket engine assembly (REA) thrusters, the momentum wheel motor, the magnetic torquers, and the electric hydrazine thrusters (EHTs). The modularity of the system is enhanced by separating error computation, the control laws, and the control distribution.

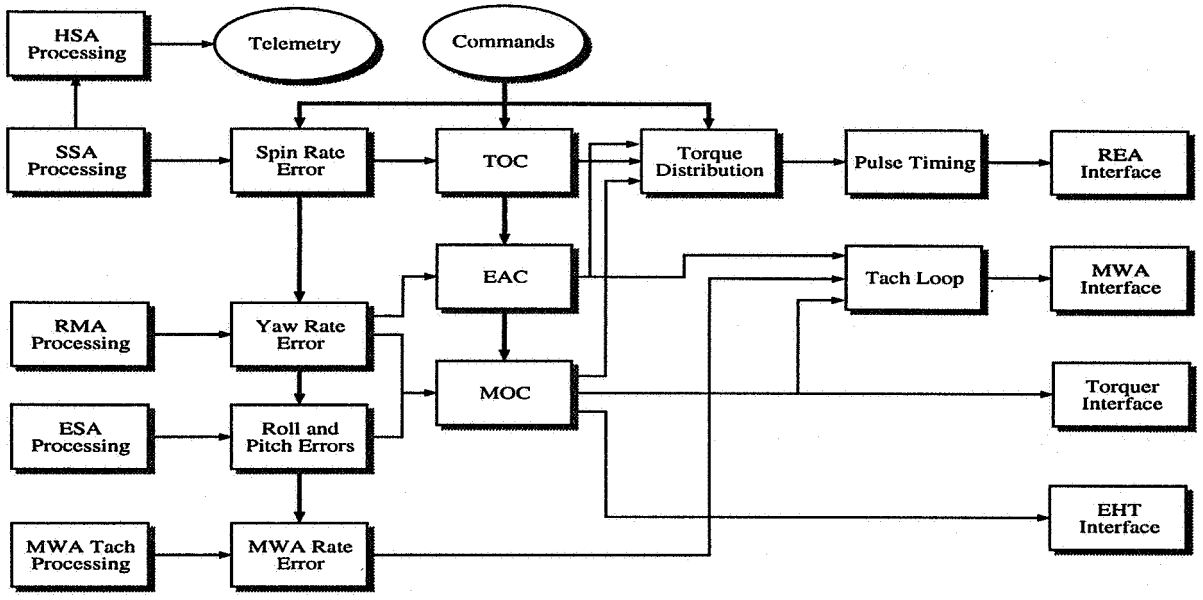

Figure 1. Control system architecture

The schematic shown in Figure 2 shows each of the ACS modes, and which mission phase they are used in, as well as

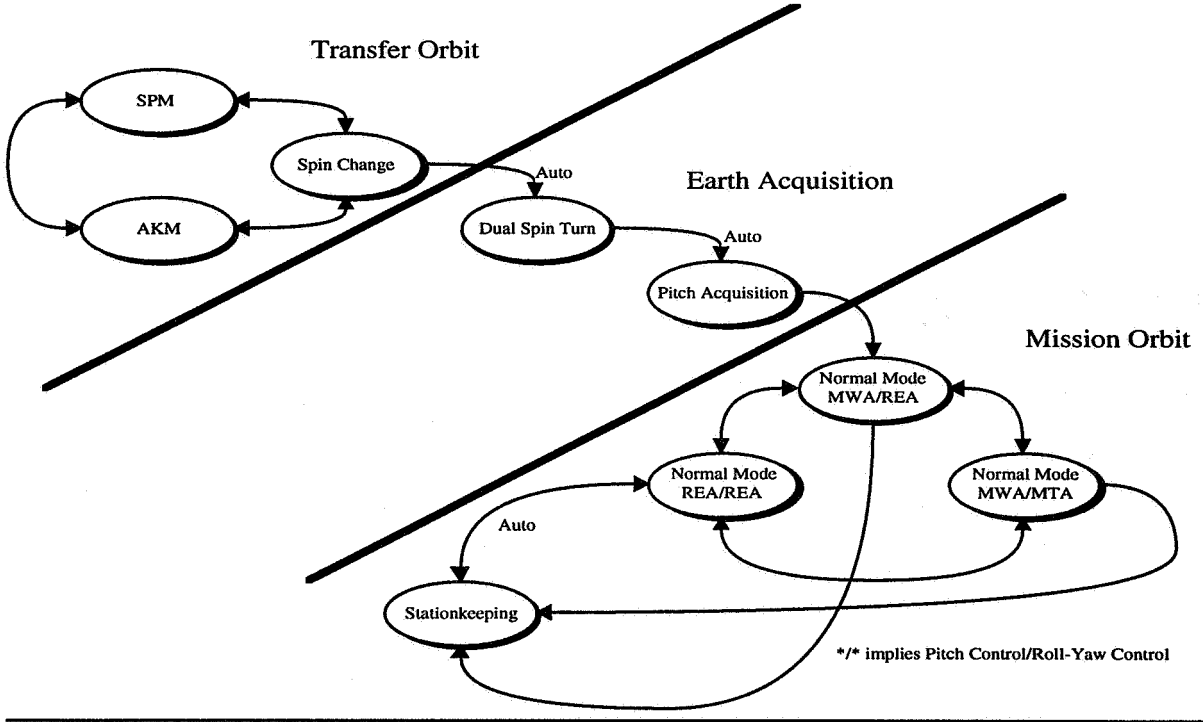

Figure 2. Moding diagram

the flow between modes. Notations indicate which mode transitions occur automatically; others must be initiated from the ground. This section will present the architecture in detail and describe each of the control loops in the system.

Transfer Orbit

During Transfer Orbit (TO) a solid rocket motor, called the apogee kick motor (AKM), is used for insertion into geo-synchronous orbit. The satellite is spin stabilized during the rocket firing. During this phase all control functions and mode transitions are initiated from the ground. After separation from the launch vehicle, the satellite operator commands the satellite to spin about the AKM firing axis. A proportional control law is used for the spin-up maneuver, based on a spin rate measurement from the SSA pulses and a spin rate estimator structure. The estimator accounts for spin rate changes due to firing thrusters. The estimator equations are:

$$\begin{aligned} \omega_E &= \omega + \alpha p \\ \omega_M &= \frac{2\pi}{T} + \frac{\alpha p^2}{2T} \\ \omega &= \omega_E + K(\omega_M - \omega_E) \end{aligned} \tag{1}$$

where α is the nominal acceleration per unit time, p is the thruster pulsewidth, and T is the measured spin period.

The operator also has the option of manually choosing and firing thrusters to change the spin rate. After the spin change maneuver, it is necessary to align the spin axis with the desired direction of the rocket firing. The reorientation is done using a spin precession maneuver (SPM) with pre-calculated thruster firings based on the sun pulse timing. If separation is not done at the AKM firing attitude a large spin precession maneuver will be required and the large spin precession maneuver will be done prior to spinning the spacecraft up to its AKM spin rate.

During the AKM firing, the spacecraft is spin stabilized, and no active control is needed. After the firing is completed, another spin change is needed to prepare for the acquisition sequence.

Earth Acquisition (EA)

During acquisition a dual-spin turn (DST) is used rotate the satellite into the correct attitude, and the resulting pitch rotation is damped to minus orbit rate. The control law during the DST is open loop, in that the maneuver is accomplished simply by commanding a MWA speed. The tachometer loop which controls the wheel speed is described in more detail in the mission orbit section.

After the DST, the spacecraft transitions to pitch acquisition mode.The pitch acquisition system is a simple proportional derivative controller using the thrusters. This pitch controller is also used during mission orbit and the gains are set prior to acquisition to emphasize rate damping as opposed to position control.

During acquisition, the spacecraft changes from spin stabilization to bias momentum three-axis control.

Mission Orbit (MO)

During the mission orbit phase the satellite uses a bias momentum design. Changing the speed of the momentum wheel controls pitch, and orthogonal magnetic torquers are used to control roll & yaw. The earth sensor measures roll and pitch; yaw is not directly sensed, but can be determined from the orbit rate coupling with roll. A yaw gyro is used to sense rate information during stationkeeping maneuvers. EHTs are used for north-south stationkeeping maneuvers, and REA thrusters are used for east-west stationkeeping control, for momentum wheel momentum unloading and for backup roll/yaw control. REAs can also be used as a backup to the EHTs for north/south stationkeeping. EHTs cannot be pulsed and are not used for attitude control.

The rest of this section will describe the attitude control loops in detail and provide insight into the thruster operations.

The control system has several modes. They are listed in Table 1.

There are five controllers that can be used during MO: two normal mode pitch controllers, a normal mode roll/yaw controller, and the stationkeeping controller. The normal mode pitch controllers both apply proportional derivative

Table 1: Modes

Mode (pitch/transverse)	Description	Controller Type (pitch/transverse)	Actuators
MWA	Pitch control using the MWA only	PI	MWA
MWAMTA	Normal 3-axis control	PI / Low bandwidth (phase stabilized)	MWA - pitch; MTA - roll/yaw
MWAREA	Pitch control using the MWA and roll/yaw control using thrusters	PI / Low bandwidth (phase stabilized)	MWA - pitch; REA - roll/yaw
REAREA	Three axis thruster control	PD/Low bandwidth (phase stabilized)	REA
Stationkeeping	Three axis thruster control	PID/PID (High bandwidth)	REA

(PD) control to the pitch axis; the MWA pitch loop is a proportional integral (PI) controller which controls the wheel speed demand and the REA pitch controller is a PD with control applied directly to the pitch axis. The normal mode roll/yaw controller is a low bandwidth controller which uses the roll/yaw coupling to control yaw. This controller structure is used for both the magnetic roll/yaw control system and thruster backup. During stationkeeping, all three axes are controlled by a high bandwidth proportional integral derivative (PID) controller.

Pitch Control. The basis for the pitch control using the MWA is a tachometer loop that maintains the speed of the momentum wheel. It is desirable to keep the wheel speed within a range of the nominal speed, normally ±10%, to keep the spacecraft gyroscopically stiff. A DC motor has the transfer function

$$\frac{\omega}{T} = \frac{1}{Js + \beta} \tag{2}$$

where β is due to the back emf and viscous friction in the motor. The simple control scheme used is to multiply the difference between the desired speed and the measured speed by a gain K and to filter the measured speed by a first order filter. The resulting closed loop system is

$$\Omega = \frac{(s + \omega_T)(K\Omega_C + T_C)}{Js^2 + (J\omega_T + \beta)s + \omega_T(K + \beta)} \tag{3}$$

where ω_T is the filter cutoff. ω_T was chosen to provide adequate damping and K is made sufficiently large to provide good disturbance rejection and command tracking.

The input to the tach loop is the wheel speed demand. The equation for the pitch loop is

$$I\ddot{\theta} + J\dot{\Omega} = T \tag{4}$$

so it follows that the wheel speed demand will be

$$\Omega = \frac{c\theta + k\int\theta}{J} \tag{5}$$

which is a proportional-integral controller. Since the term in the pitch body rate equation contains the derivative of Ω, this controller provides proportional derivative control action in pitch.

Normal mode pitch control may also be implemented using thrusters. In this case, a PD controller is used. The PD controller is of the form

$$T = K_P + K_R\frac{\omega_R s}{s + \omega_R} \tag{6}$$

The derivative term is multiplied by a first order filter to prevent differentiation at high frequencies. The gains are determined by selecting the closed loop pole locations. When selecting the pole locations, it is important to consider the phase lag introduced by the ESA noise filter.

During stationkeeping, pitch is controlled using the same high bandwidth controller as the roll and yaw axes.

Low Bandwidth Roll/Yaw Control. The roll yaw control system must accomplish two requirements. First, it must attenuate the external disturbances on the spacecraft. These are at harmonics of the orbit rate and generally have no significant components above twice orbit rate. The second requirement is nutation damping. Since there is no passive source of nutation damping, the control system must damp the nutation. Since the nutation frequency is much higher than orbit rate the controller is broken into two parts, one to attenuate low frequency disturbances and the second to damp nutation.

The first part of the controller takes the low frequency approximation to the open loop system and selects a pair of gains to meet the pointing requirements. This approach, a purely proportional control, is the simplest. The nominal plant of an earth pointing momentum bias spacecraft has poles at orbit rate and at the nutation frequency. Since the nutation poles are undamped adding the low frequency compensation will destabilize the nutation poles. Consequently, it is necessary to phase stabilize the nutation mode. A second order compensator is used to stabilize the nutation mode.

The low-frequency approximations of the roll yaw equations are

$$\begin{aligned} \frac{T_z}{h_w} &= \dot{\theta}_x - \omega_o \theta_z \\ \frac{T_x}{h_w} &= \dot{\theta}_z + \omega_o \theta_x \end{aligned} \tag{7}$$

and the torque command is

$$\begin{bmatrix} T_x \\ T_z \end{bmatrix} = h_w \begin{bmatrix} K_{xx} \\ K_{zx} \end{bmatrix} \theta_x \tag{8}$$

since only roll is measured. This control system is also used for the normal thruster control modes.

Nutation damping is accomplished by introducing a complex zero just before the nutation pole pair using the transfer function in (9) and a damped pole after the nutation mode.

$$\frac{s^2 + \omega_z^{\,2}}{s^2 + 2\zeta\omega_p + \omega_p^2} \tag{9}$$

As long as the zero is at a frequency less than that of the nutation pole pair the system will be stable. The compensator Bode plot is shown in Figure 3

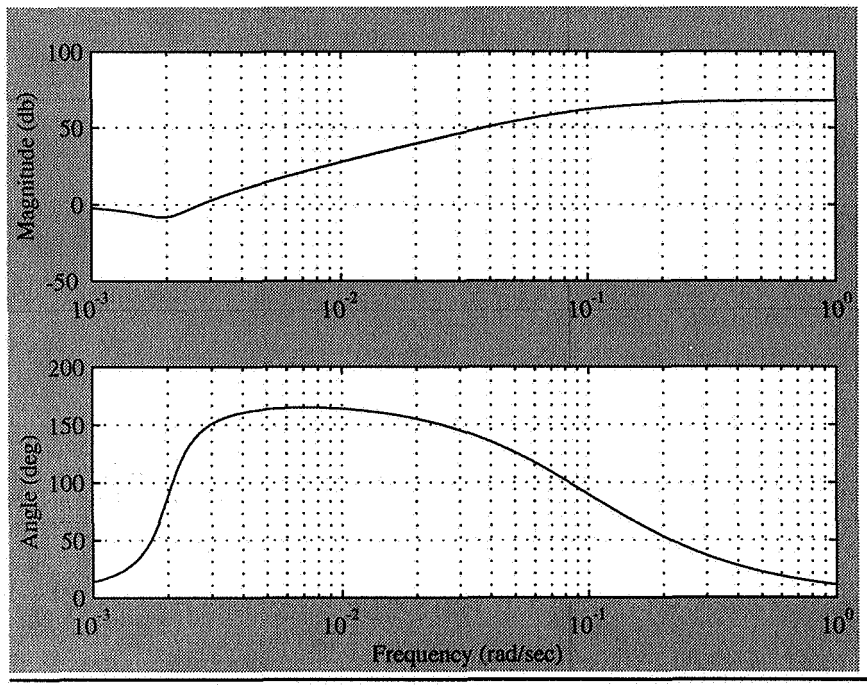

Figure 3. Nutation compensator Bode plot

The system with compensation is shown below.

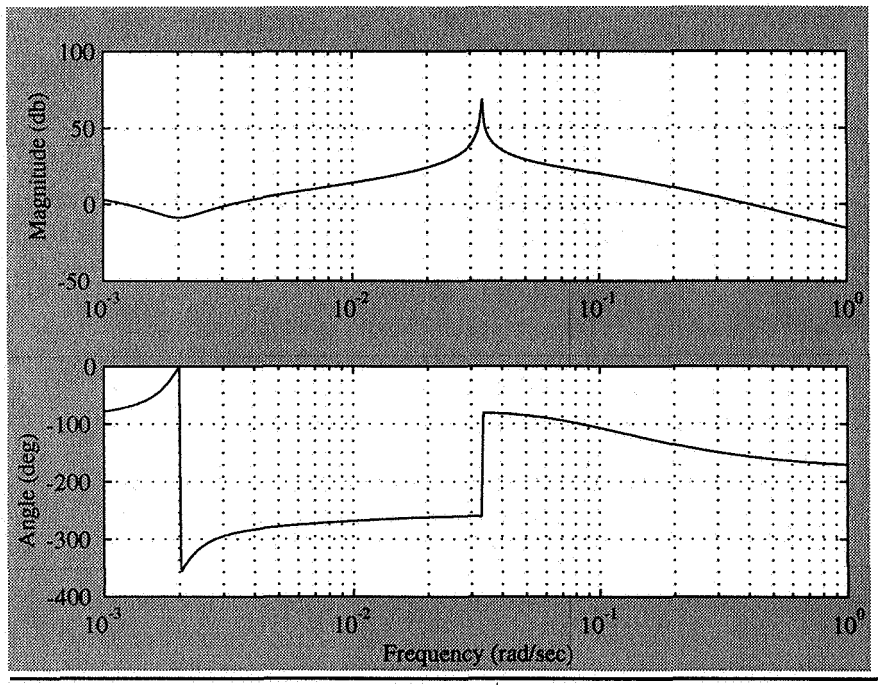

Figure 4. Compensated system

High Bandwidth Control. In high-bandwidth mode, each axis is controlled independently with a proportional-integral-differential controller. The yaw measurement is taken from the yaw gyro. The yaw gyro does not provide an absolute attitude reference and the control system assumes that the initial yaw attitude is zero. This does not pose a problem as long as the mode is not run for long periods of time.

It is assumed that the rates and attitude errors are small, and then the axes are decoupled and the control problem is reduced to

$$u = \ddot{\theta} \tag{10}$$

or three decoupled double integrators. These equations are valid if the flex modes are at much higher frequencies than the control bandwidth and, in our case, the bandwidth is much higher than the nutation mode. If this is the case then each axis can have an independent control loop.

The PID controller is of the form

$$T = K_P + K_R \frac{\omega_R s}{s + \omega_R} + \frac{K_I}{s} \tag{11}$$

The derivative term is multiplied by a first order filter to prevent differentiation at high frequencies.

In this system the plant is not a set of pure double integrators, instead it has the undamped nutation pole. Therefore, the bandwidth is set high enough so that the nutation pole is unobservable to the control system. This does not mean it has disappeared and the nutation mode will be excited by control activity and the disturbance torques. The normal mode thruster control is used to damp the nutation after the PID is turned off.

Thruster Operations. During thruster operations the 3-axis torque commands generated by the controllers are fed into the simplex algorithm, along with the positions and thrust vectors of the available thrusters. The simplex linear programming algorithm is used to determine the optimal set of pulsewidth commands. Optimal is defined as using the minimum amount of fuel necessary to produce the requested torque. The use of simplex allows the operator to account for thruster misalignments, plume disturbances and center-of-mass motion by changing ground loadable parameters without any reprogramming. The simplex implementation is customized for this application making it efficient enough for use with a relatively slow flight computer. The torque distribution law automatically limits the number of iterations in simplex and tests each pulsewidth command for validity.

All of the thruster control loops use thruster pulsewidth modulation. The minimum pulsewidth is relatively large which can lead to limit cycling if the disturbances are small (which is particularly true during non stationkeeping operation). The control system allows the operator to choose a pulsing period that is longer than the control period. For example, the stationkeeping loops run at 2 Hz but a typical pulsing period will be 8 seconds, meaning that thrusters will only fire once every 16 control cycles. This reduces limit cycling significantly.

Design Environment

The primary tool in the design process for this attitude control system was Princeton Satellite Systems' SPACECRAFT CONTROL TOOLBOX. The toolbox contains approximately 500 functions which support all phases of the design, from the underlying mathematics to preparation of pointing and fuel budgets.

Prior to any work being done, a MATLAB database was created for all the design parameters to ensure consistency and allow for easy updating of parameters. The next step was to design the control algorithms using MATLAB and the SPACECRAFT CONTROL TOOLBOX. Preliminary simulations were also done in MATLAB to verify the design.

Next, the control algorithms were ported to C, and the mode interfaces added. A high fidelity simulation was written in C including detailed models of the dynamics, hardware and interfaces. The simulation produces MATLAB plot files so the results can be more easily interpreted. Verification testing was performed using the C simulation.

The schematic in Figure 5 shows the design flow. The majority of the design work was done in MATLAB; only the performance verification and the simulation user interface design were done outside MATLAB.

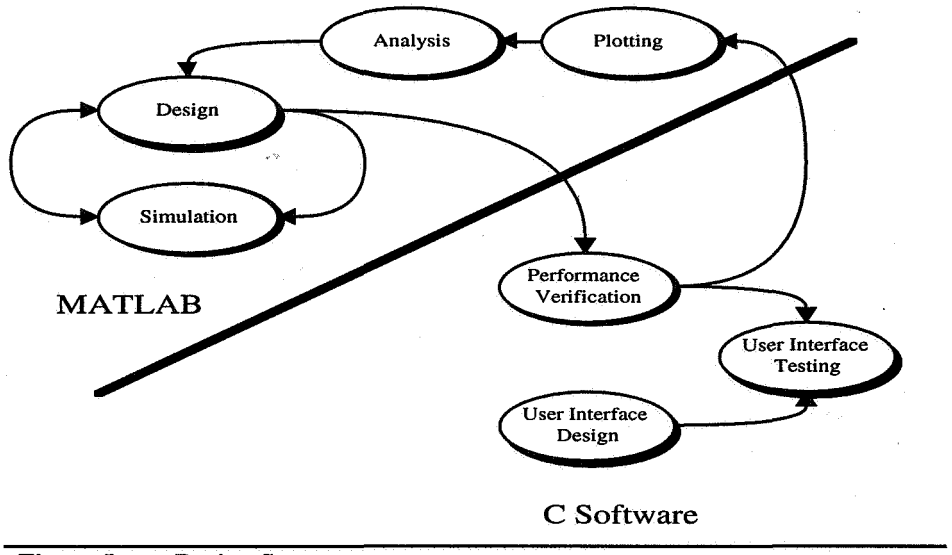

Figure 5. Design flow

Simulation

This section will discuss the simulation which was used to test the control system presented in this paper, including the models and user interface. The version of the SPACECRAFT CONTROL SYSTEM used and modified by CTA to test the Indostar flight software, INDOSIM, will be also be addressed.

Models

The spacecraft is represented by a non-linear multi-body model with the solar arrays and momentum wheels modeled as separate bodies each with a single axis of rotation. The kinematical equations of the core with respect to the inertial frame are represented with quaternions. The sensors modeled are a Barnes earth sensor, Adcole sun sensor, and Barnes horizon sensor. Environmental models include a solar pressure model, a constant magnetic field model, and a spherical gravitational model.

The earth sensor model models each of the twelve individual detectors and computes the amount of radiation impinging on each detector. The output of the model is in the exact binary format as the hardware.

User Interface

There are five parts to the SPACECRAFT CONTROL SYSTEM user interface: the command list, the telemetry file, the input file, the output file, and the output specification. The command list and telemetry file allow the simulation to be "flown," or operated, in the same way the actual satellite will be flown. The user is permitted to send one command list at the start of each simulation. Commands are tagged with a time for execution; the simulation will automatically send and execute the commands at the appropriate times. It is possible to run multiple simulations without further user interaction. The telemetry file collects all the telemetry from the spacecraft.

The commands and telemetry deal only with the flight software. The spacecraft model itself has all of its parameters embedded internally. However, many of them can be changed via the simulation input file. At the beginning of each simulation the file is read in and designated parameters are changed. The input file also allows the operator to start the simulation with any initial spacecraft state desired.

An output specification file tells the simulation how often to write to the output file, and which values to write. Outputs are allowed from both the flight software and the simulation. All output goes into a single ASCII text file, which can be imported into MATLAB or any other plotting package for plotting.

INDOSIM

The purpose of INDOSIM is to verify the performance of the flight software and to check interfaces to the 1750A flight computer used on Indostar. To meet this goal, two types of simulations were performed. First, pure software simulations were done, which included simulations of all of the flight software. Then, closed loop attitude determination and control system (ADACS) testing was done.

The ADACS closed-loop tests primarily involved two computers: the flight processor and the dynamics/environment simulator. The two machines communicated over a 1553 bus. The Indostar flight computer is a 1750 space-rated 16-bit processor. This device executes the ADACS flight software that is compiled using a pre-ANSI C 1750 compiler.

The attitude dynamics, orbital dynamics, and environment portions of the INDOSIM program are run on a 90 Mhz Pentium under MS-DOS version 6.2. The INDOSIM package was originally developed by Princeton Satellite Systems on a Macintosh computer and later modified by CTA Space Systems as the ADACS design evolved. The simulator receives actuator commands from the 1750, propagates dynamics, and returns simulated sensor data via the 1553 bus.

Results

Three categories of results are presented in this section. First, results from the SPACECRAFT CONTROL SYSTEM will be shown to demonstrate thruster pulsewidth modulation. Then, results from INDOSIM will be presented and compared with test results of the flight processor. These cases will show a stationkeeping maneuver, the transient response of the nutation control using MTAs, and the pitch acquisition performance.

In the following example, the SPACECRAFT CONTROL SYSTEM simulation was started with an initial roll rate with thruster control of all three axes. The normal mode (low bandwidth) controller is in use. The rate plots (on the left) in

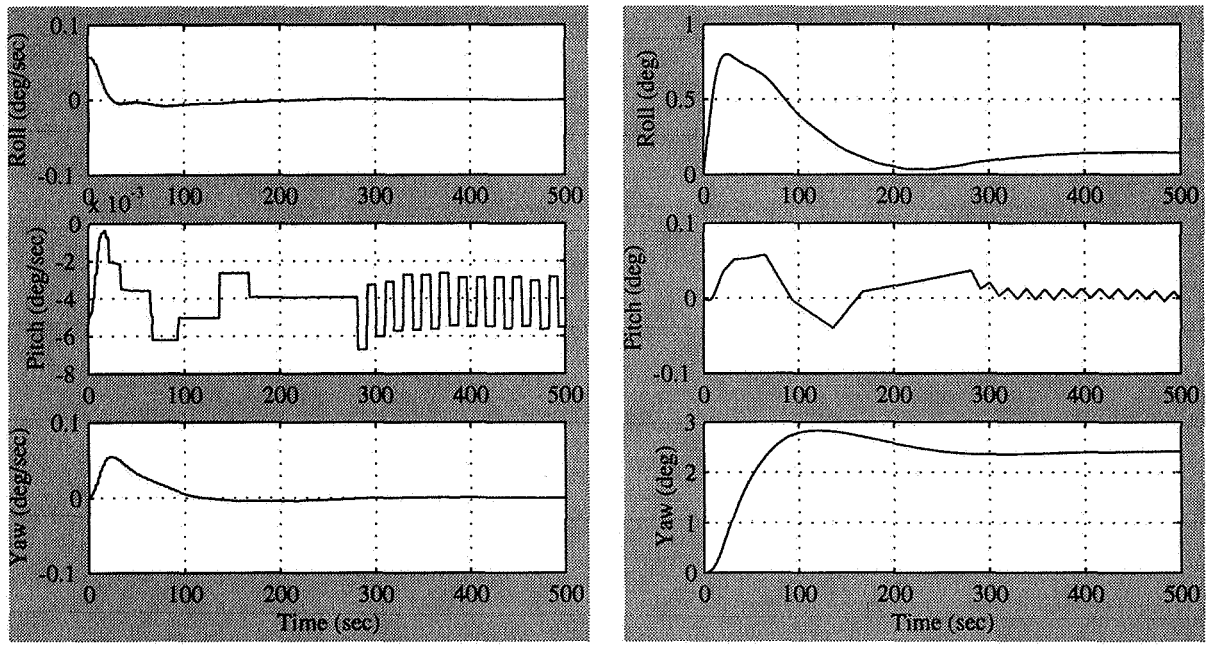

Figure 6. Thruster control

Figure 6 show nutation being damped; the attitude plots show the limit cycling in pitch. The thruster pulsing period was changed from 2 seconds to 8 seconds at 270 seconds. The trade-offs are demonstrated in the plot. Tighter control is achieved with the longer pulsing period, at the expense of more limit cycling and thruster firings. The plots of torque and torque demand shown in Figure 7 also show that with a shorter pulsing period it takes longer for the torque demand to reach the minimum pulsewidth, and therefore cause a thruster to fire. Notice that the torque is always delivered at the beginning of the control period. Care is required in choosing the pulsing period, because if it is too

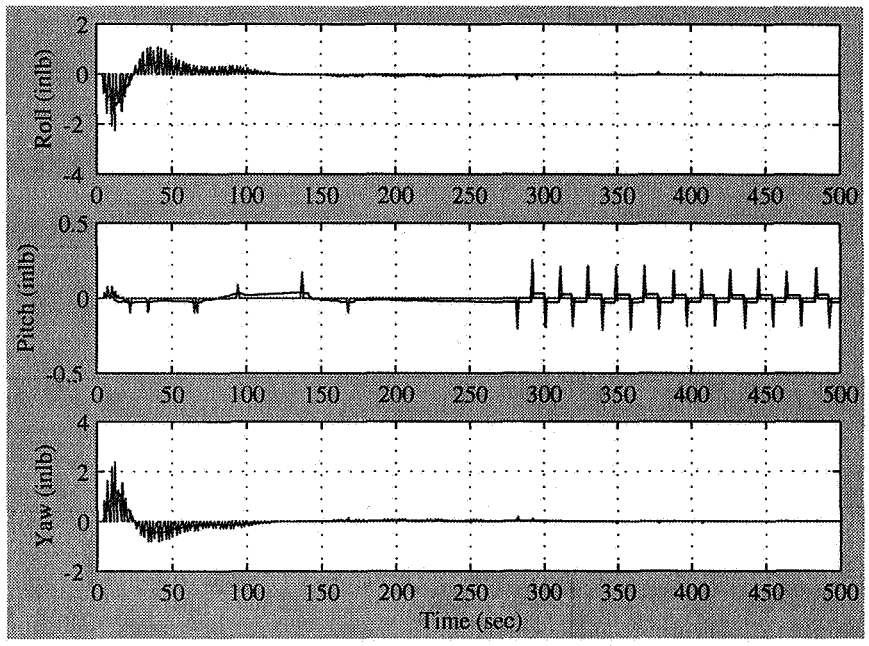

Figure 7. Torque and torque demand

long, and the delivered torque is not concentrated at the beginning of the period, then the control system will not work properly.

The next case shows a stationkeeping maneuver simulated completely within INDOSIM. The top plot in Figure 8

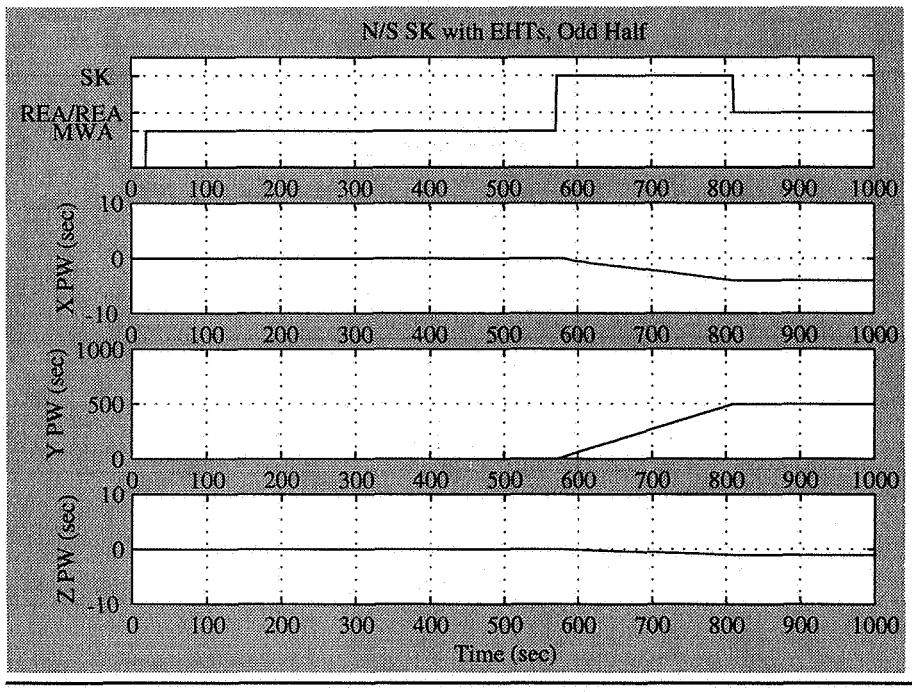

Figure 8. Stationkeeping modes and pulsewidths

shows the mode transitions, including the automatic transition from stationkeeping to REA/REA mode to enable nutation to be damped. Figure 9 shows the attitude during and after the maneuver, demonstrating that nutation was damped as soon as the maneuver ended. The limit cycling in pitch after the maneuver is due to the large minimum

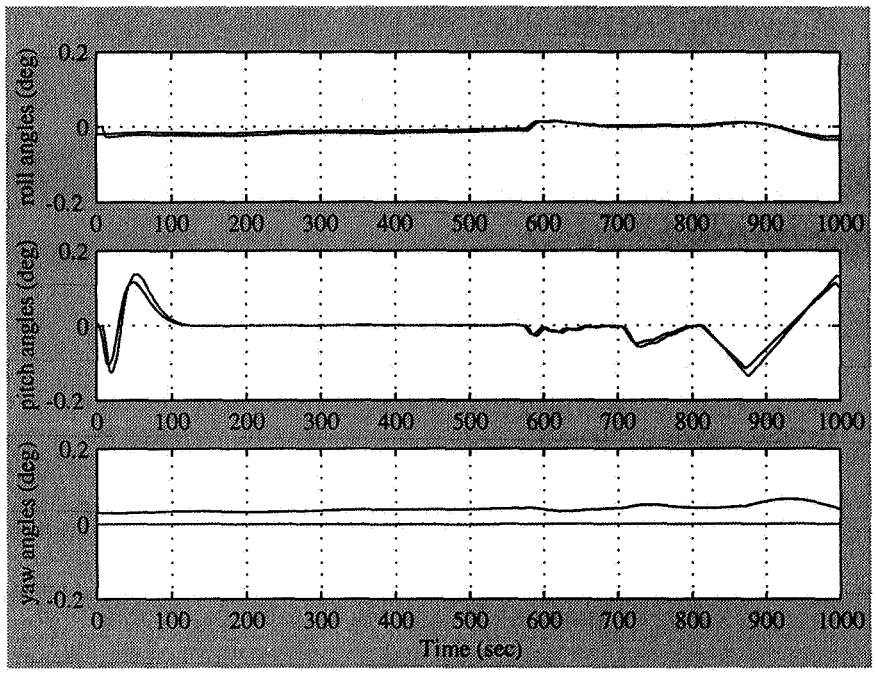

Figure 9. Attitude during stationkeeping maneuver

impulse of the thrusters relative to the pitch inertia of Indostar. A momentum dump was also executed during this stationkeeping maneuver, as shown in Figure 10.

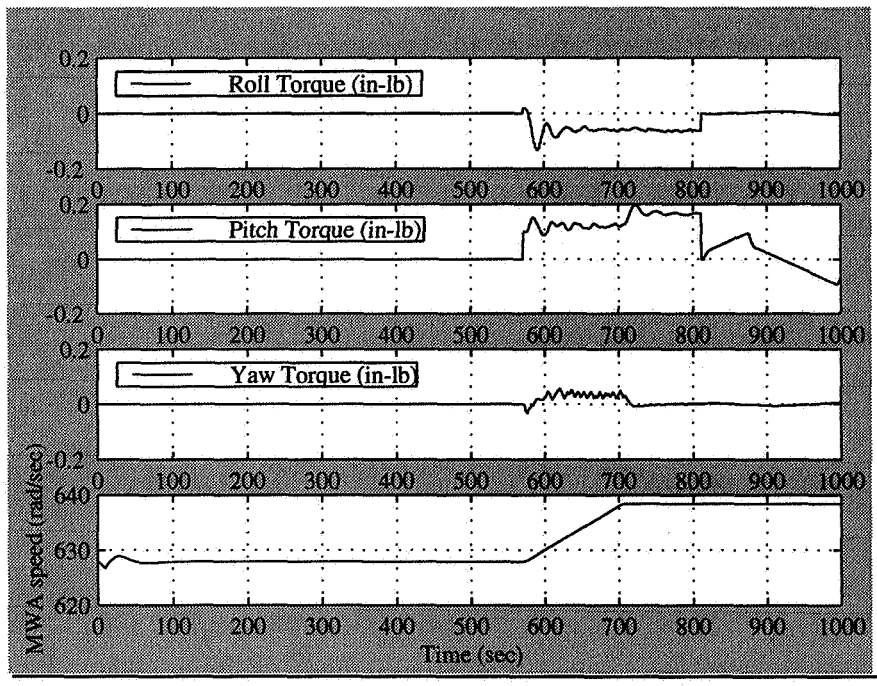

Figure 10. Momentum dump

The plots in Figure 11 show a pitch acquisition using thrusters simulated with INDOSIM. The spacecraft was given an initial rate of 0.2 RPM, and an initial angle of about 60°. The acquisition occurs as soon as the earth passes into the field of view of the ESA. The limit cycling that was examined in the first example is also seen at the end of this run.

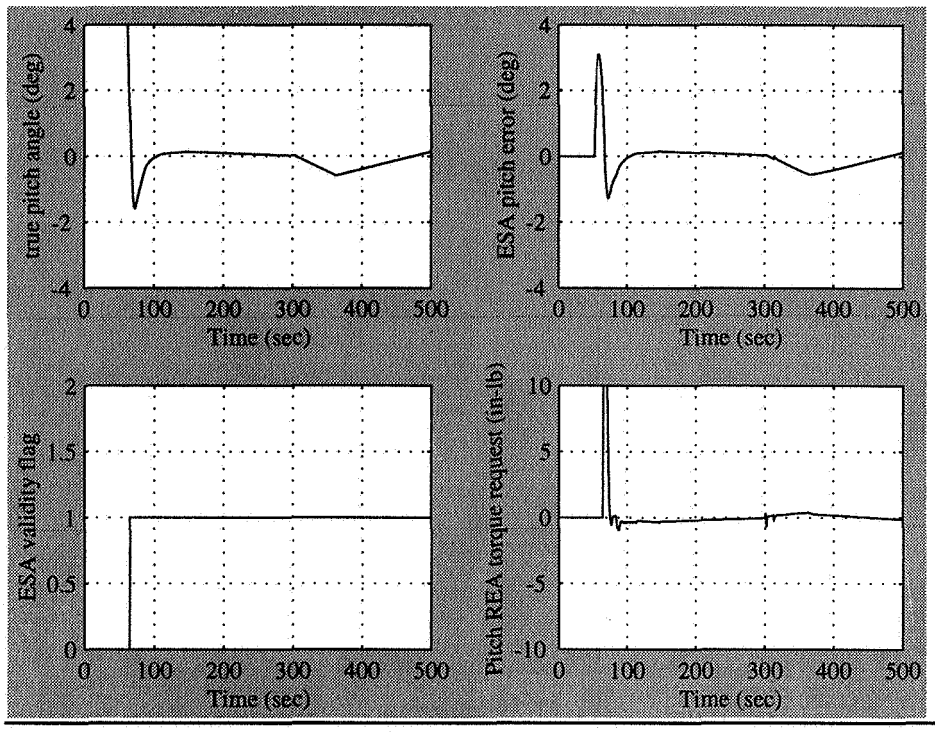

Figure 11. Indosim pitch acquisition

In the last case, the transient response is tested by manually firing a thruster to induce nutation, which is quickly damped by the MTAs. Figure 12 shows results from both the pure software version of INDOSIM and the version which used the 1750A to run the flight code. The results indicate that the control system is executing correctly on the flight processor.

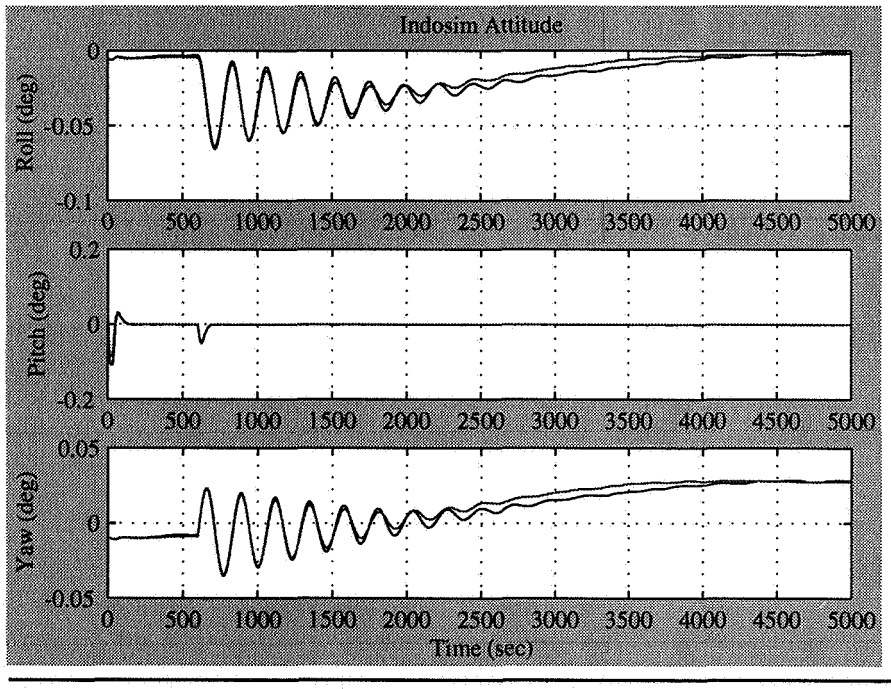

Figure 12. INDOSIM transient response- attitude

Conclusions and Suggestions for Future Work

In conclusion, a new satellite attitude control system has been designed which has several improvements over existing designs. These include the use of the simplex algorithm to distribute the torque commands and automatic damping of the nutation caused by stationkeeping maneuvers. Another advantage of this control system and the flight software which implements it is its modular design. The SPACECRAFT CONTROL SYSTEM allows for easy and realistic testing of the flight code.

Planned upgrades to the SPACECRAFT CONTROL SYSTEM include additional sensor models, an enhanced command language, and the creation of a simulation log file. The enhanced command language would allow loops and sublists of commands. The log file would record all major simulation events, such as commands, failures, and mode transitions. Another possible improvement to the simulation would be a graphical user interface (GUI) which allows the user to view the output data as the simulation is progressing. A GUI could also allow command lists to be sent at any time during the simulation, increasing the value of the simulation as an operator training tool.

Additional features of Version 2.0 of the attitude control system will include a complete gyro-based attitude determination system that can use earth sensor inputs, star sensor inputs or sun sensor inputs as measurements. A reaction wheel version will also be added with an advanced friction compensation system. An onboard spin-axis attitude determination system will also be ported from Princeton Satellite Systems' Spin Axis Attitude Determination Toolbox.

Page intentionally left blank

Environmental and Dynamic Models
Application to ATTDES - An Expert System for Satellite Attitude Determination and Control

Donald L. Mackison

University of Colorado
Aerospace Engineering Sciences
Campus Box 429
Boulder, CO 80309-0429

(303) 492-6417
(303) 492-7881 (FAX)
mackison@spot.colorado.edu (e-mail)

Abstract

A general Matlab model for design, analysis, and simulation of satellite attitude control and attitude determination systems is being developed. The goal is the inclusion of multibody attitude dynamic models, and environmental models including atmosphere and the geomagnetic field. The systems allows for simple linearization of the attitude dynamics for computing control and estimator gains, as well as the use of Simulink for nonlinear simulation.

Introduction

The design, analysis, and flight operations of satellite attitude control and determination (ACD) systems requires extensive mathematical formulation of the equations of motion, optimization studies, and computer simulations. This is best done by analysts with high levels of education and experience. The development of programs such as ATTDES permit the use of advanced techniques by analysts with lower levels of experience. Typical tasks include the mission analysis to select stabilization and damping schemes, to choose attitude determination sensors and algorithms, and to design control gains which provide a system performance which meets program requirements. ATTDES is a system that includes all of these activities, including high fidelity orbit and environmental models that can be used to perform preliminary analysis, parameter selection, stabilization schemes, the development of estimators, and to perform covariance analyses, and can support on-going orbit activities. The modification of existing simulations to model new configurations for these purposes an be an expensive, time consuming activity that becomes a pacing item in the development and operation of such new systems.

ATTDES has been written in Matlab, and is easily transportable among platforms. It has been our experience that developing such a software system in Matlab takes a small fraction of the time required for writing code in C or Fortran, and the extensive data base and graphics utilities of Matlab permit a simple overall structure for a large program, greatly simplifying the design of databases for the program. Further, the easy use of Matlab modules in signal processing, image processing, symbolic mathematics, wavelets, and neural networks provide a seamless interface of these analysis tools with the attitude dynamic model of ATTDES.

The current upgrades to ATTDES include generalized equations of motion for multi-body satellites (Roberson, 1966, Wittenburg, 1988), general perturbation orbit models (Long, 1976, Born, 1968, Cole, et al, 1968, Chao, 1978, Grf, 1974, Liu, 1981), and geomagnetic field models (Vokrouhicky, 1989, Schmitz, et al, 1989).

The user interface is being upgraded to the new version of Matlab GUI, which will enable the user to configure a satellite, specify the orbit, select a stabilization scheme, design control gains, and perform orbit mission analysis, attitude control and attitude determination studies. Driving the upgrade of the orbit, environment, and dynamic models is the goal of using this system for prediction and verification of the attitude motion of satellites for a wide variety of satellite configuration.

The full nonlinear attitude simulation has been constructed using Simulink, the graphically driven nonlinear simulation adjunct of Matlab. Existing, generalized attitude models can be easily modified with the graphical Simulink interface.

Current Matlab Implementation

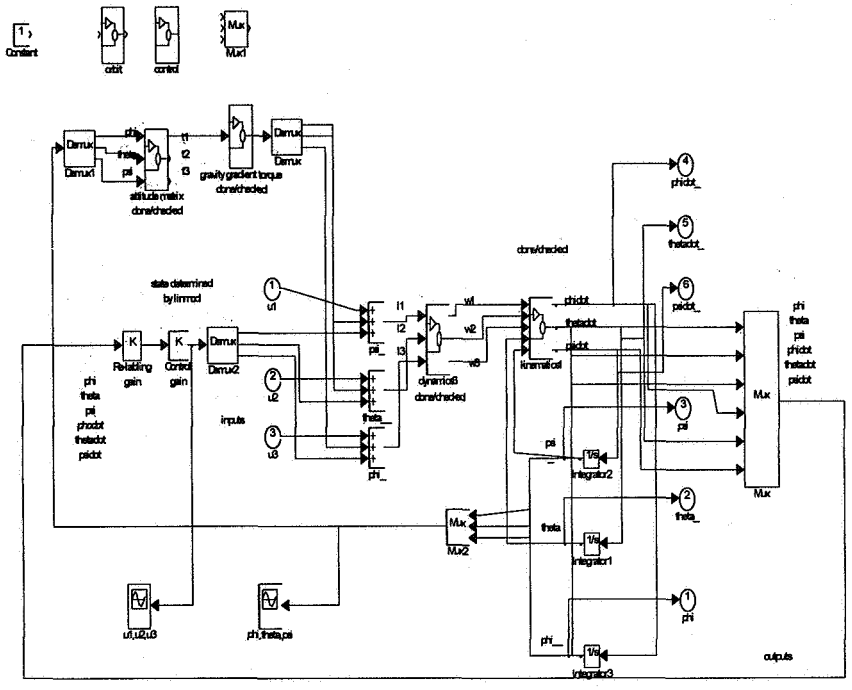

Rigid Body Model - Simulink Implimentation

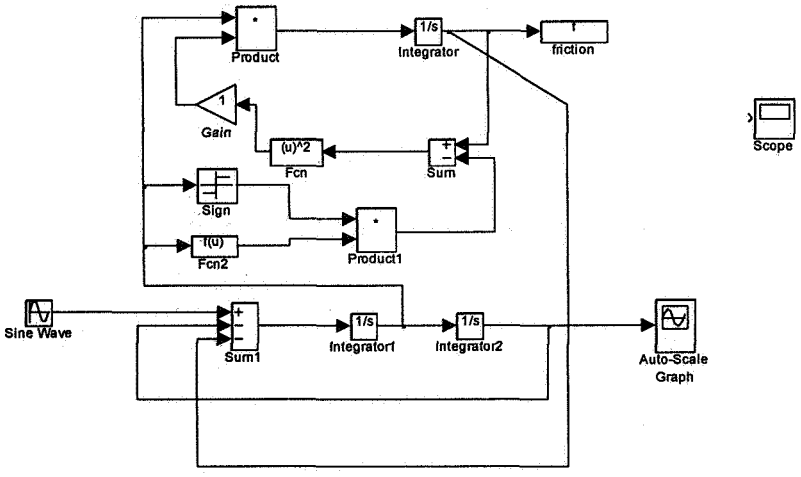

Dahl Friction - Simulink Model

Graphical User Interface

Matlab 5 has an extensive graphical user interface (GUI) capability, which permits the user simple access to the operation of the program, to the model database, and to the various dynamic, graphic, and control parameters throughout the model. In that ATTDES is intended as a general purpose work environment which permits simple integration of design, analysis, evaluation, and simulation capabilities, we wish the user to be free to add computing blocks where he may need them, but permit him to run many of the options of the program without adding more code, or modifying the existing code. In order do accomplish this, we will use the Matlab GUI system as much as possible. This permits viewing data, drop down windows, dynamically updated graphic windows, and the use of zoom features

Integrators

There are a number of integrators which can be chosen by the user at run time, via point and click menu. These include discrete, ode45 (Dormand-Prince), ode23 (Bogacki-Shampine), ode113 (Adams), ode153 (stiff/NDF), and oe23s (stiff, modified Rosenbrock). These may be selected in light of the nonlinearities included in the model, including magnetic hysteresis and Dahl friction models.

Atmospheric Models

Candidates for the atmosphere to be included in ATTDES include those considered by Dowd and Tapley (1979), Champion (1990), Liu (1987), and Ginzburg (1989). There are many other models available, but these are conveniently at hand.

The level of atmosphere required is a function of the amount of attitude perturbation to be considered for low altitude satellites. In particular, one of the goals of ATTDES is to model in detail the interaction of the attitude control of low altitude satellites with the orbit- this has been reported as being a noticeable error source in precision attitude determination.

In this we may consider the three dimensional time-dependent wind componenets of the global criculation (Ginzburg, 1989). Liu has considered the density evaluation of the atmosphere, to include the effects of known solar flux and geomagnetic activity (Ap) inputs. For highly eccentric orbits which span low to high altitude, the accuracy generated wihc has an altitude limitation of 1000 km remains

Dynamic Models

Typical dynamic models for multibody satellites have been developed by Kane (1983), Roberson (1966,1976), and Whittenburg (1988). Out goal here is to develop a "point and click" capability to rapidly generate models for inclusion in the Simulink attitude dynamics model.

Geomagnetic Field Models

Typical geomagnetic field models are reported in Schmitz (1989), Vokrouhlicky (1989). Although precision attitude determination using the geomagnetic field is not generally possible because of the diurnal and altitude dependence of the field, the residual magnetic dipole of the satellite will interact with the geomagnetic field to provide a steady state disturbance. We hope to choose an appropriate magnetic field model to include in ATTDES.

A Simple Example

As a simple example of the type of analysis that will be possible with ATTDES (such as dynamic response, covariance analysis, orbit mission analysis), we have chosen the simulation of a rigid body, spinning about and intermediate axis of inertia. Here we have chosen the following parameters

$$I_1 = 1$$
$$I_2 = 10$$
$$I_3 = 9$$
$$\omega_1 = 0$$
$$\omega_2 = .1$$
$$\omega_3 = 10$$

Here we chose the ode23 integrator (Bogacki-Shampine), with auto step size option. The results are the typical "spin a book" results, with the body axes tumbling in space.

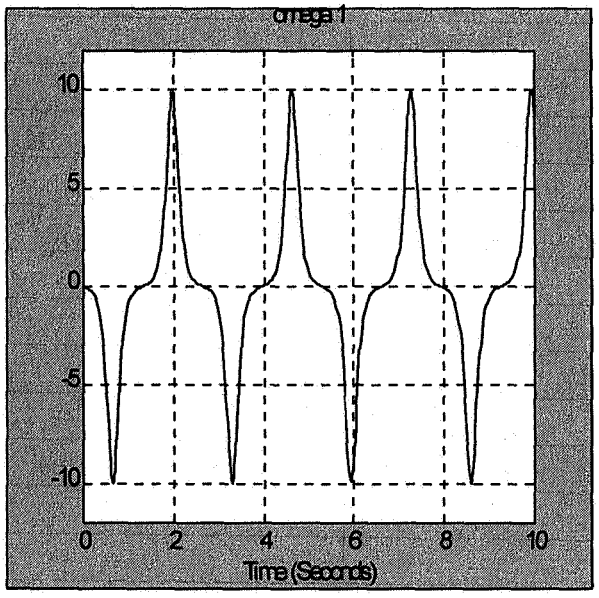

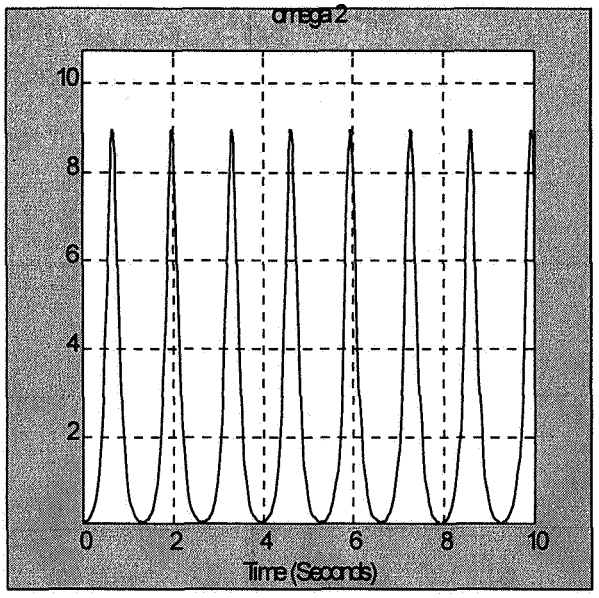

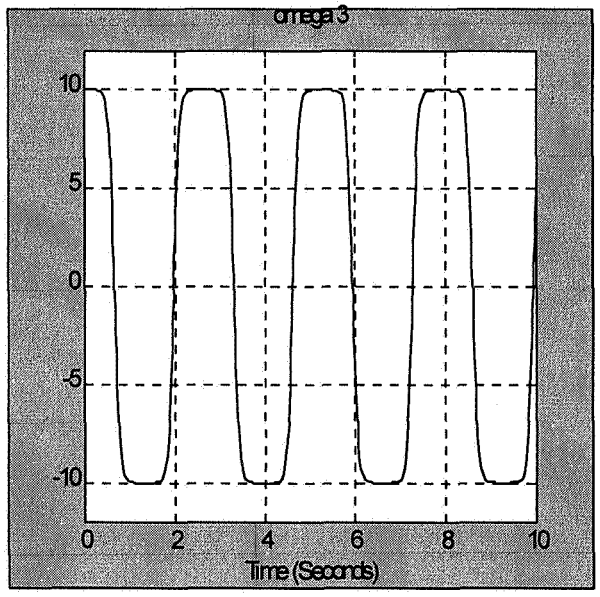

Next, we demonstrate a simple covariance analysis using the same rigid body satellite model. Here we have specified the measurements (angles, in this case, as from a star tracker), the measurement noise and process noise covariance, measurement sample rate, and have produced the attitude covariance vs. Time, the measurement history, attitude solution and attitude error vs. Time- all from selections from within attdes.

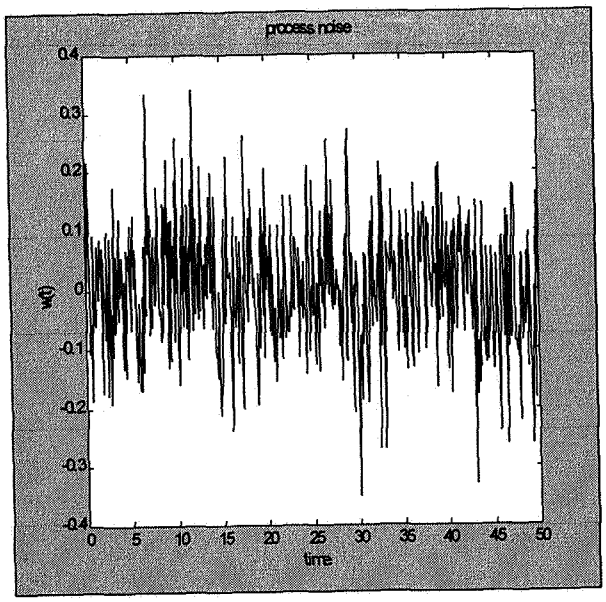
process noise
w(t)
time

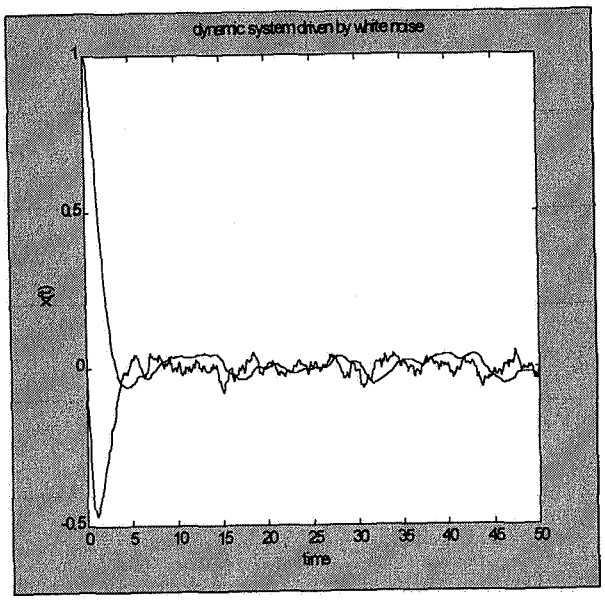
dynamic system driven by white noise
x(t)
time

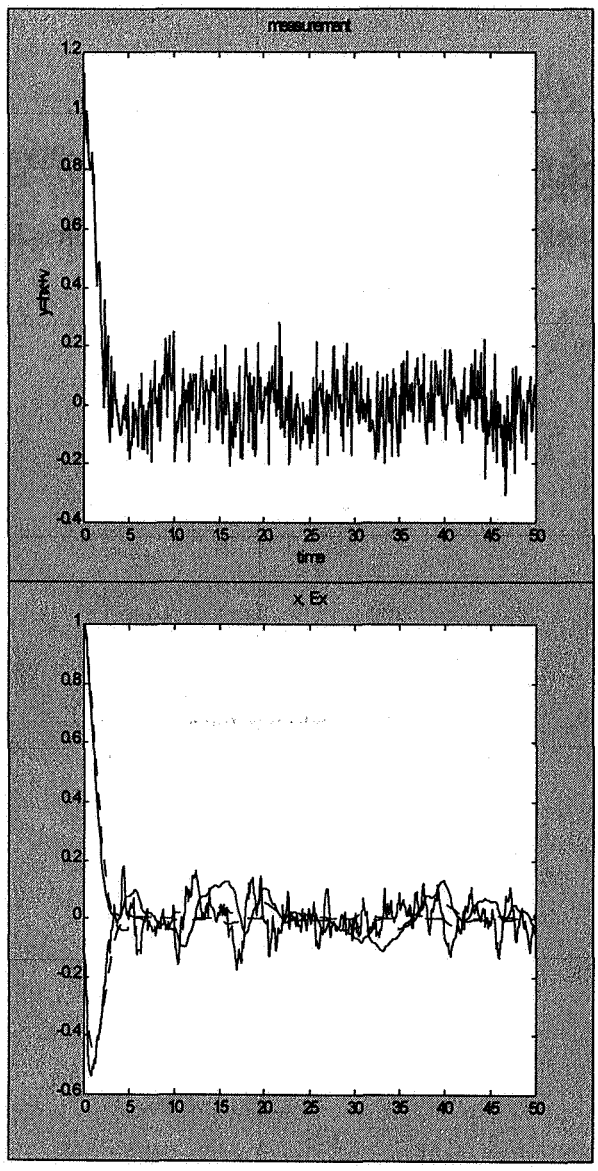
measurement
y(t)+v
time
X, Ex

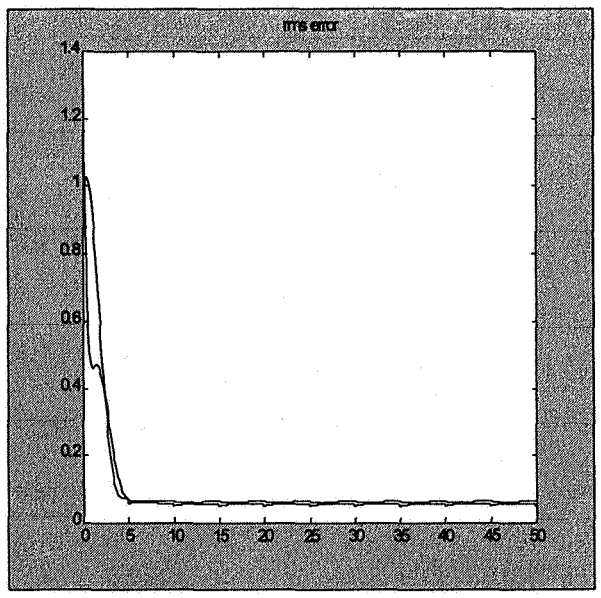

Conclusions

ATTDES is a model under continuing development. We plan to bring its development to the point where a multibody satellite in an arbitrary orbit can be developed, the environmental models examined, perturbations estimated, control laws chosen and control and estimator gains computed.

References

D.L. Mackison, et al, "ATTDES- An Expert System for Satellite Attitude Determination and Control", 6th AAS/AIAA Space Flight Mechanics Meeting, Austin, Texas, February 11-15, 1996.

D.L. Mackison, et al, "ATTDES, An Expert System for Satellite Attitude Determination and Control, II", NASA Goddard Space Flight Center, Flight Mechanics/Estimation Theory Symposium 1966, May 14-16, 1995,NASA Conference Publication 333

D.L. Mackison, et al, "Spacecraft Modeling with ATTDES", AIAA/AAS Astrodynamics Specialists Conference, San Diego, CA, July 1996

R.E. Roberson, et al, "Dynamics of a Gravitation-Oriented Satellite with Flywheels", (Kosmicheskie Issledovaniaa, vol. 13, Sept.-Oct. 1975, pp. 619-631), Cosmic Research, Vol. 13, No. 5, mar. 1976, pp. 555-566 (translation).

R.E. Roberson, et al, "A Dynamical Formalism for an Arbitrary Number of Interconnected Rigid Bodies, with Reference to the Problem of Satellite Attitude Control", International Federation of Automatic Control, 3rd Congress, London, England, June 20-25, 1966

J. Wittenburg, "Dynamics of Multibody Systems- A Brief Review", IAF Paper 88-316, Interbational Astronautical Congress, 39th, Bangalore, India, Oct. 8-15, 1988.

D.R. Schmitz, "Modeling the Earth's Geomagnetic Field to High Degree and Order", Geophysical Journal, Vol. 97, pp. 421-430, June 1, 1989.

D. Vokrouhlicky, "The Geomagnetic Effects on the Motion of an Electrically Charged Artificial Satellite", Celestial Mechanics and dynamical Astronomy, Vol. 46, No. 1, 1989, pp. 85-104.

L. Liu, et al, "The Third Order Solution of Orbital Perturbation of Artificial earth's Satellite", Scientia Sinica, June 1981, pp. 813-828.

Graf, "Multi-revolution methods for orbit integration", Conference on the Numerical Solution of Ordinary Differential Equations, Austin, Texas, October 19-20, 1972.

D.L. Dowd and B.D. Tapley, "Density Models for the Upper Atomosphere", Celestial Mechanics, Vol. 20, October 1, 1979, pp. 271-295.

K.S.W. Champion, "Middle atmosphere density data and comparison with models," Advances in Space Research, Vol. 10, Jan. 1, 1990.

Joseph. J.L. Liu, "NORAD/SPACECMD comments concerning the at5mospheric density models", NASA, Marshal Space Flight Center upper and middle atmospheric density modeling requirements for spacecraft design and operations, Feb. 1 , 1987, p. 95

Malcolm G. McCleod, "A predicted geomagnetic field model for epoch 1990.0", Naval Research Lab (Bay Saint Louis, MS), Report No. NRL/FR/7442-RS

D. Chu, Z. Wheeler, and J. Sedlak, "Motion Models in Attitude Estimation", NASA, Goddard Space Flight Center, Flight Mechanics/Estimation Theory Symposium, 1994, pp. 535-557.

Anon, Building GUIs with Matlab, Version 5, The Mathworks, Natick, Ma, December, 1996.

H-infinity/H2 Controller/Estimator Design for Precision Pointing Spacecraft

Dr. Mark Pittelkau

CTA Space and Telecommunications Systems, Inc.

ABSTRACT

This proposed paper discusses the design of an H-infinity/H2 controller for a high-performance attitude control system. In particular, the paper discusses the selection of weighting functions for disturbance and measurement noises (including wheel noise, environmental torques, pointing commands, star tracker noise, gyro bias, etc.), plant uncertainties (inertia changes and flexible-body modes), and weighting functions for robust performance. Model order reduction is applied to reduce the controller to a reasonable order. It is shown that the states of the controller are identifiable as the same states as in a Kalman filter designed for attitude determination in addition to the states of a dynamic compensator. Further, it is shown how to extract attitude, rate, and gyro bias estimates from the controller. Since the controller can run at a high cycle rate due to its low computational burden, these estimates can be more accurate than those of a computationally slow Kalman filter. Further, it is pointed out that putting an optimal Kalman filter in the feedback loop can result in poor stability margins. The H-infinity/H2 approach provides the best mean-square estimates of the states while maintaining robust stability and robust performance. Frequency domain and time domain simulation results are shown.

Page intentionally left blank

MSTI - 1, 2, 3 Attitude Determination & Control Hardware Architecture - A Historical Perspective

George A. Kyroudis, Christopher J. Clark
Spectrum Astro, Inc.

The series of MSTI (Miniature Sensor Technology Integration) small satellites were developed to flight demonstrate and test IR sensors designed for missile detection and tracking. The low-earth orbit, sun-synchronous missions were comprised of a unique combination of system requirements which included: active despin from 150 rpm after launch vehicle separation, autonomous sun / earth acquisition, transfer to mission orbit from lower injection orbit, off-nadir maneuvers to achieve latitude / longitude ground-track pointing, and on-board orbit determination. In addition, program requirements dictated a very short schedule (12 months from start to launch for MSTI-1). These requirements greatly influenced the attitude determination and control system (ADCS) architecture which placed high reliance on the functions provided by the ADCS hardware. The subject of this paper is the design of the ADCS architecture and the selection, usage and on-orbit performance of the ADCS equipment.

The MSTI Program used the "build-a-little, test-a-little" incremental approach for the development of each mission to facilitate the incorporation of the latest in state-of-the-art spacecraft components. Development of each small satellite was planned to occur over 12-18 months and each successive vehicle incorporated additional functional capabilities and evolutionary upgrades. Also, the selected launch vehicles imposed severe mass and power constraints on the overall bus design. Finally, delivery time became part of the hardware selection criteria given the short program schedule. Meeting these program objectives required taking calculated risks with the selection of new equipment designs that had not been flight qualified. Specifically, the ADCS architecture utilized functional redundancy to incorporate between 2-4 new hardware designs for each vehicle. No redundant units were used. The set of "first flight" equipment for MSTI-1, 2, 3 included a scanning horizon sensor, silicon photodiode array sun sensor, quartz rate sensor, dynamically-tuned gyro inertial reference unit, CCD star tracker, and C/A code GPS receiver. In addition, most of these sensing devices included an internal processor.

The ADCS architecture planned for anomalous behavior from sophisticated "first flight" components by augmenting simpler or flight-proven equipment for

functional redundancy and safing operations. Graceful degradation was achieved via autonomous control mode transitions based on sensor outputs. ADCS hardware anomalous or unexpected behavior was successfully adapted to without adversely affecting the mission. On-orbit data are discussed and design upgrades are recommended for some units. No on-orbit failures were experienced despite the rapid satellite development schedule and unproven designs. Indeed, most of these hardware designs have been flown on subsequent missions.

MAP Attitude Control System Design and Analysis

S. F. Andrews, C. E. Campbell, A. J. Ericsson-Jackson, F. L. Markley, J. R. O'Donnell, Jr.

Goddard Space Flight Center, Code 712, Greenbelt, MD, 20771

Abstract

The Microwave Anisotropy Probe (MAP) is a follow-on to the Differential Microwave Radiometer (DMR) instrument on the Cosmic Background Explorer (COBE) spacecraft. The MAP spacecraft will perform its mission in a Lissajous orbit around the Earth-Sun L_2 Lagrange point to suppress potential instrument disturbances. To make a full-sky map of cosmic microwave background fluctuations, a combination fast spin and slow precession motion will be used. MAP requires a propulsion system to reach L_2, to unload system momentum, and to perform stationkeeping maneuvers once at L_2. A minimum hardware, power and thermal safe control mode must also be provided. Sufficient attitude knowledge must be provided to yield instrument pointing to a standard deviation of 1.8 arc-minutes. The short development time and tight budgets require a new way of designing, simulating, and analyzing the Attitude Control System (ACS). This paper presents the design and analysis of the control system to meet these requirements.

Introduction

The Cosmic Background Explorer (COBE) satellite [1,2] was launched in 1989 with three instruments to measure the spectrum and spatial distribution of the Cosmic Microwave Background (CMB). The CMB is believed to be a remnant of the Big Bang, or Primordial Fireball, marking the birth of the universe [2]. In 1992, the Differential Microwave Radiometer (DMR) instrument on COBE made the first measurement of variations in the temperature of the CMB radiation, other than the dipole due to the observer's motion [3,4]. This anisotropy, at the level of one part in 10^5, is related to fluctuations in the density of matter in the early universe and thus carries information about the initial conditions for the formation of cosmic structures such as galaxies, clusters, and voids. The DMR had an angular resolution of 7° across the sky, 14 times larger than the Moon's apparent size. The Microwave Anisotropy Probe (MAP) has been designed with sensitivity 50 times that of DMR and angular resolution 20 times finer, specifically 0.3° or 18 arc-minutes [5]. These increases in sensitivity and resolution should enable MAP to determine the values of key cosmological parameters and to answer questions about the formation of structure in the early universe. A recent survey article discusses the physics involved [6].

MAP has been selected one of the first two Medium-Class Explorer (MIDEX) missions, and is scheduled to launch in the Fall of 2000 on a Delta launch vehicle. Since the major error sources in the DMR data arose from COBE's low Earth orbit, MAP will be placed in a Lissajous orbit around the Sun-Earth L_2 Lagrange point using a lunar assist with phasing loops. MAP will reach its final orbit about L_2 approximately 100 days after launch.

The MAP instrument includes radiometers at five frequencies, covering two fields of view (FOVs) 135° apart on the celestial sphere. To obtain a highly interconnected set of measurements over a large area of the celestial sphere, the MAP observatory will execute a fast spin (0.464 rpm) and a slower precession (0.1°/sec) of its spin axis about the Sun line (see figures 1 and 2). Figure 1 shows the scan pattern covered by one of the two FOVs in one complete spacecraft precession (1 hour), displayed in ecliptic coordinates in which the ecliptic equator runs horizontally across the map.

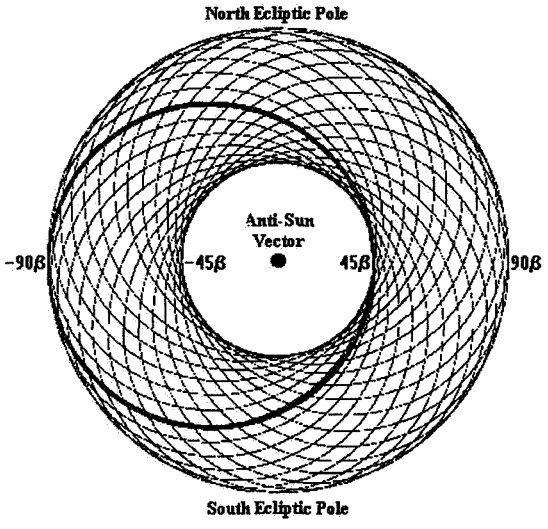

Figure 1: MAP Scan Pattern

The bold circle shows the path for a single spin (2.2 minutes). As the Earth revolves around the Sun, the annulus of coverage rotates about the ecliptic pole. Thus the entire celestial sphere will be observed once every six months, or four times in the planned on-station mission life of two years.

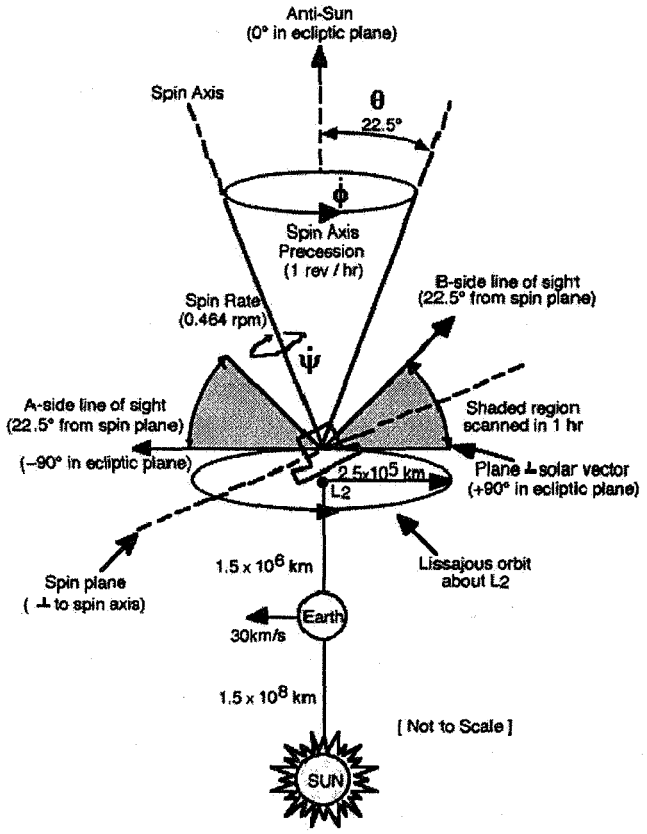

Figure 2: MAP Spin-Scan Concept

The remainder of the paper will give an overview of the Attitude Control System (ACS) and ACS components, as well as discussions of the individual control modes. This is followed by a description of the MatrixX tool set and its use in designing and simulating the MAP ACS, a departure from previous design practices of the Guidance, Navigation, and Control Branch.

ACS Overview

The MAP ACS must implement the observing mode spin-scan and provide for orbit maneuvers and safehold contingencies. It is also critical to the success of the mission to avoid locally-generated thermal or magnetic fluctuations, especially those synchronous with the spin period. The L_2 orbit was chosen to avoid contamination by the Earth's magnetic field, but this means that no appreciable magnetic field is available for sensing or momentum unloading. The propulsion system used to perform the orbit maneuvers to reach and maintain the L_2 orbit will also be used to unload excess system momentum. Solar radiation pressure torque is the only significant disturbance torque at L_2, and the uniform rotation of the spin axis reduces the average torque by more than two orders of magnitude compared to its instantaneous value. Gravity-gradient torques are significant in the phasing orbits prior to the lunar gravity assist to L_2, but analysis shows that the maximum accumulation of angular momentum is less than 1 Nms per orbit. Angular momentum due to these disturbances is stored in the reaction wheels and is only unloaded by the propulsion system at the conclusion of an orbit maneuver.

MAP uses three right-handed, orthonormal coordinate systems. The Geocentric Inertial frame (GCI) is an Earth-centered frame in which the x_I axis points to the vernal equinox, the z_I axis points to the North Celestial Pole (parallel to the Earth's spin axis), and $y_I = z_I \times x_I$. The Rotating Sun Referenced frame (RSR) is a spacecraft-centered frame in which z_R axis points to the Sun, $x_R = z_R \times z_I$, and $y_R = z_R \times x_R$. The RSR frame rotates at approximately 1°/day with respect to the GCI frame. The body frame is centered at the spacecraft center of mass with the z_B axis parallel to the spacecraft centerline, directed from the instrument to the solar arrays. The y_B axis is normal to the instrument radiator faces, and $x_B = y_B \times z_B$, as shown in figure 3.

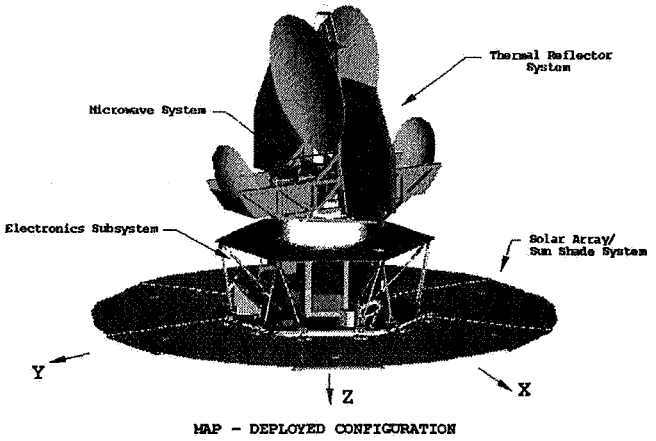

Figure 3: Spacecraft Layout and Body Coordinate Frame

ACS Hardware

The attitude sensors employed by MAP are an Inertial Rate Unit (IRU), an Autonomous Star Tracker (AST), a two-axis Digital Sun Sensor (DSS), and six Coarse Sun Sensors (CSSs). The spacecraft attitude will be controlled by three Reaction Wheel Assemblies (RWAs), and six Reaction

Engine Modules (REMs). The ACS control algorithms are implemented in software in the Mongoose V processor. Sensor data acquisition, actuator command generation, and an independent safehold algorithm are in the Attitude Control Electronics Remote Services Node (ACE RSN).

The IRU comprises two Kearfott Two-Axis Rate Assemblies (TARAs), one with input axes aligned with the z_B and x_B axes and the other with input axes aligned with the z_B and y_B axes. These are lower-cost, moderate-performance dynamically-tuned gyros, which have previously been employed on the NASA Total Ozone Mapping Spectrometer-Earth Probe (TOMS-EP) spacecraft.

The Lockheed-Martin AST tracks and identifies up to 50 stars simultaneously in its 8.8° square FOV, using an internal star catalog, and computes its attitude as a GCI-referenced quaternion. It points in the $-y_B$ direction, and has a measurement accuracy of 21 arc-seconds rotation around its boresight axis and 2.3 arc-seconds in the other two axes. (all accuracies are stated as standard deviations, or 1σ quantities)

The DSS is an Adcole two-axis digital sun sensor oriented to look out along the z_B axis, with a 64° square FOV and an accuracy of 1 arc-minute. This sensor has been employed on the NASA X-Ray Timing Explorer (XTE) spacecraft and several others.

The CSSs are cosine eyes located looking outward from the edges of the six solar array panels, pointing alternately 30° up and 30° down from the x_B-y_B plane.

The RWAs are Ithaco Type E wheels, each with a momentum storage capacity of at least 50 Nms. The available reaction torque is 0.3 Nm, but this will be limited to 0.175 Nm on MAP due to power considerations. The reaction wheels are oriented in a dispersed pyramid with their rotation axes tilted 45° from the spacecraft $-z_B$ axis, uniformly distributed (120° apart) in azimuth about this axis. These wheels have been employed on the NASA XTE and Tropical Rainfall Measuring Mission (TRMM) spacecraft.

ACS Operational Modes

There are six ACS operational modes: Inertial, Observing, Delta V, Delta H, Sun Acquisition, and Safehold. The first five modes are implemented in the Mongoose, while the Safehold mode resides in the ACE. Figure 4 shows the modes and the transitions among them. Anomalous behavior can result in autonomous transitions from any other mode to Safehold mode or Sun Acquisition mode, even though these transitions are not shown explicitly. (Note that this state transition diagram is the one used in the SystemBuild simulation, which will be discussed later in this paper.

SystemBuild is part of the MatrixX tool set supporting graphic block editing and system simulation. The two transitions labeled **INIT** are used to support single-mode software simulations, and are not present in the actual ACS design.)

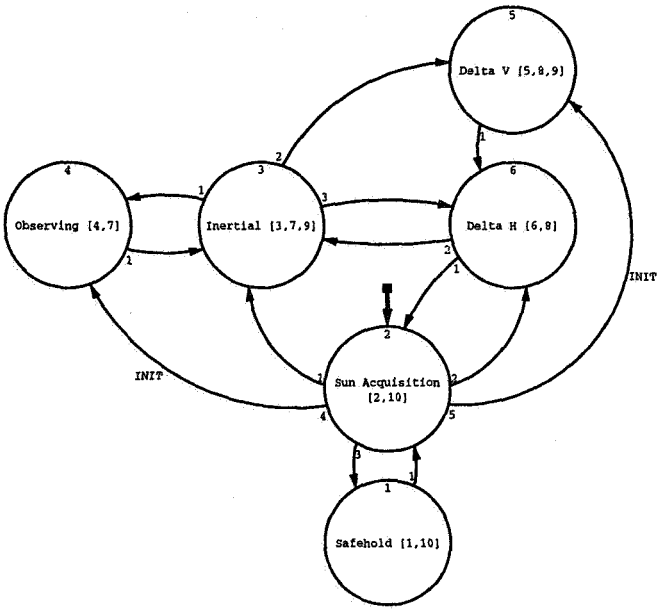

Figure 4: ACS Mode Transitions

As shown in the figure, Inertial mode acts as a staging mode between the other operations of the spacecraft; all Mongoose modes other than Delta V have the capability to enter this mode. Inertial mode can either hold the spacecraft in an inertially-fixed orientation or slew the spacecraft between two different orientations. This is an RWA- and IRU-based mode, with DSS and AST information used in a Kalman Filter to update the gyro bias and quaternion error estimates. Normal exits from Inertial mode are by ground command only.

Observing mode is used for science operations. The RWAs provide the angular momentum that maintains a near-zero system momentum and the torques that maintain both the 22.5° angle between the spin axis and anti-Sun line and the desired sky-scan rates. This is also an IRU-based mode, using the same Kalman Filter as Inertial mode. Normal transitions into or out of this mode are via Inertial mode.

Delta V mode uses the REMs to adjust the orbit. This mode is only entered by ground command from Inertial mode, and normal exit is autonomously to Delta H mode.

Delta H mode uses the REMs to unload excess angular momentum, and is normally entered autonomously from Delta V mode after completion of an orbit maneuver. Entry can also be ground-commanded from Inertial mode if it is necessary to unload excess momentum at some other time, although this is not expected. In either case, the ACS

autonomously transitions back to Inertial mode after the momentum has been reduced to an acceptable level. Delta H mode can also be entered from Sun Acquisition mode, as discussed below, in which case the autonomous exit upon completion of the momentum unloading is back to Sun Acquisition mode.

Sun Acquisition mode acquires and maintains a thermally-safe power-positive orientation for the spacecraft. Upon launch, the MAP ACS will be in Sun Acquisition mode, which will be used for initial acquisition. Normal exit from Sun Acquisition mode is to either Delta H or Inertial mode, depending on the residual spacecraft spin rate. If the rates exceed those that can be handled by the RWA-based Sun Acquisition mode, the REM-based Delta H mode is entered to reduce the rates to an acceptable level, after which the spacecraft returns to Sun Acquisition mode. Transition to Inertial mode can be commanded after the Sun has been acquired. Transition to the Mongoose control modes from the ACE Safehold mode is through Sun Acquisition mode.

The minimum-hardware Safehold mode, based on the International Ultraviolet Explorer (IUE) safemode, uses only the RWAs and CSSs to slew the spacecraft to a power-positive orientation and to maintain this attitude indefinitely. This mode is implemented in the ACE, so it can be entered in the event of a Mongoose anomaly. Exit from Safehold mode is by ground command only.

ACS Design and Performance

Each of the six operational modes of the MAP ACS will be discussed below. Each mode discussion will give the sensors and actuators used in that mode, discuss the control algorithm, and give an example of the performance of the mode. Note that further examples of mode performance will be shown in the multi-mode simulations shown later in this paper.

Inertial Mode

Inertial mode can either hold the spacecraft in an inertially-fixed orientation or slew the spacecraft to a different orientation. The desired orientation is ground-commanded as a desired GCI-to-body quaternion q_c [7,8]; a slew will be executed if this is not close to the current spacecraft orientation. The attitude control is by RWA torques, which are computed by a proportional-integral-derivative (PID) controller in terms of attitude and rate errors.

The attitude errors are expressed as the vector part $\vec{q}_e$ of an error quaternion, which is given as the quotient of the commanded quaternion and an estimated quaternion $\hat{q}$:

$$q_e = \pm q_c \otimes \hat{q}^{-1}$$

In this and the following we use the quaternion product convention of [8,9] rather than that of [7], so that the order of quaternion multiplication is the same as that of the corresponding direction cosine matrices. The sign in the equation above is chosen so that the scalar component of q_e, which should have magnitude close to unity for small pointing errors, is positive.

The estimated quaternion is computed by an onboard Extended Kalman Filter (EKF), with IRU, AST, and DSS measurements as input [9–11]. This is similar to EKFs employed on several previous missions, except that the AST produces an estimated attitude quaternion rather than merely observed star vectors. This simplifies the Mongoose computations by removing the burden of star identification and the necessity to carry an onboard star catalog.

Since the desired rates in Inertial mode are zero, the rate error vector $\vec{\omega}_e$ is the negative of the body rate vector $\vec{\omega}_{BI}$ measured by the IRU:

$$\vec{\omega}_e = -\vec{\omega}_{BI}$$

The commanded control torque in the body coordinate system is given by [12,13]:

$$\vec{T} = J\left[k_d\vec{\omega}_e + k_p\left(2\vec{q}_e\right) + k_i\int\left(2\vec{q}_e\right)\right]$$

where J is the MAP moment-of-inertia tensor, and k_d, k_p, and k_i are the derivative, proportional, and integral gains, respectively. The factors of two multiplying the error quaternion and its integral reflect the fact that the quaternion errors are half the angle errors when these are small. This torque is distributed to the RWAs using a torque distribution matrix defined by the orientation of the RWAs in the body coordinate system.

An example of the performance of the MAP ACS in Inertial and Observing modes will be shown in a multi-mode simulation shown in the Example Simulations section, later in this paper.

Observing mode

Observing mode is used for science operations to maintain the 22.5° angle between the spin axis and anti-Sun line and the desired sky-scan rates as shown in figure 2. Observing mode differs from Inertial mode in that the commanded quaternion is time-varying and the commanded rates are non-zero. There is also a commanded acceleration, which is used in a feedforward loop to eliminate an attitude hangoff.

The commanded inertial quaternion is computed as the product of an RSR-to-body and a GCI-to-RSR quaternion:

$$q_{BI} = q_{BR} \otimes q_{RI}$$

The GCI-to-RSR quaternion is computed onboard from ephemeris models. The desired RSR-to-body attitude is more conveniently expressed in terms of 3-1-3 Euler angles [7,8] than in terms of a quaternion. The commanded values of the three Euler rates are those that give the desired scan rates:

$$\dot{\phi}_c = 1 \text{ rev / hour} = 0.001745 \text{ rad / sec}$$
$$\dot{\theta}_c = 0$$
$$\dot{\psi}_c = 0.464 \text{ rpm} = 0.04859 \text{ rad / sec}$$

The commanded values of the three Euler angles are then given by:

$$\phi_c = \phi_0 + \int_{t_0}^{t} \dot{\phi}_c dt$$
$$\theta_c = 22.5° = 0.3927 \text{ rad}$$
$$\psi_c = \psi_0 + \int_{t_0}^{t} \dot{\psi}_c dt$$

where ϕ_0 and ψ_0 are set by the initial state and θ_c by the desired Sun angle. These 3-1-3 Euler angles are converted to the commanded RSR-to-body quaternion q_{BR} by the standard equations [7,8].

The rate error vector $\vec{\omega}_e$ is the difference between a commanded body rate vector $\vec{\omega}_c$ and the body rate vector $\vec{\omega}_{BI}$ measured by the IRU:

$$\vec{\omega}_e = \vec{\omega}_c - \vec{\omega}_{BI}$$

The commanded body rate vector $\vec{\omega}_c$ is computed from the commanded Euler angles and rates by the standard equations shown below [7,8].

$$\vec{\omega}_c = \begin{bmatrix} \sin\theta_c \sin\psi_c & \cos\psi_c & 0 \\ \sin\theta_c \cos\psi_c & -\sin\psi_c & 0 \\ \cos\theta_c & 0 & 1 \end{bmatrix} \begin{bmatrix} \dot{\phi}_c \\ \dot{\theta}_c \\ \dot{\psi}_c \end{bmatrix}$$

An additional acceleration feedforward term is added to the output of the controller in Observing mode to reduce the hangoff error. This is the acceleration the spacecraft needs to follow the commanded attitude and Euler rates, and is derived by differentiating the equation for $\vec{\omega}_c$ with respect to time. Since $\dot{\phi}_c$, $\dot{\psi}_c$, and θ_c are all constant, the commanded acceleration is:

$$\dot{\vec{\omega}}_c = \dot{\psi}_c \dot{\phi}_c \sin\theta_c \begin{bmatrix} \cos\psi_c \\ -\sin\psi_c \\ 0 \end{bmatrix}$$

This term is added to the commanded acceleration to give the control torque:

$$\vec{T} = J\left[k_d \vec{\omega}_e + k_p (2\vec{q}_e) + k_i \int (2\vec{q}_e) + \dot{\vec{\omega}}_c \right]$$

An example of the performance of the MAP ACS in Inertial and Observing modes will be shown in a multi-mode simulation shown in the Example Simulations section, later in this paper.

Delta V Mode

Delta V mode is designed for use in either the initial phasing or L_2 stationkeeping burns. The sensor used in this mode is the IRU, and the REM thrusters are used for actuation. MAP uses six thrusters, one pair each aligned to provide torque about each axis. Delta V mode can be configured to use any of these thruster sets as the primary set to impart the velocity change on the spacecraft, while the other two sets provide attitude and rate control.

Delta V mode uses a PD controller to hold the spacecraft to a commanded quaternion attitude while executing the Delta V burn. The output of the controller is transformed into thruster firing commands using a pulse width modulator with a minimum pulse width of 0.04 sec. The desired attitude is held during the burn by off-pulsing the primary set of thrusters and on-pulsing the other two sets.

The transition between Inertial and Delta V mode is ground commanded. To transition to Delta V mode, the spacecraft needs to receive the following commands and information: (1) desired attitude for Delta V burn, (2) burn start time, (3) burn duration, and (4) desired set of thrusters to be used for the Delta V. The spacecraft slews from the nominal inertially-fixed orientation to the desired Delta V orientation within Inertial mode. The spacecraft waits in Inertial mode until the desired burn time at which the transition to Delta V mode is enabled.

The x_B axis phase plane plot shown in figure 5 is for a 200 second Delta V burn along the z_B axis. It displays an attitude error drift of less than 0.4° in the x axis. Similar results were found for the y_B and z_B axes. Delta V simulations were done

for 5.4 and 53.4 minute burns as examples of stationkeeping burns and phasing loop maneuvers, respectively. All simulations show that the thruster logic will provide the required velocity changes for MAP's orbit maneuvers.

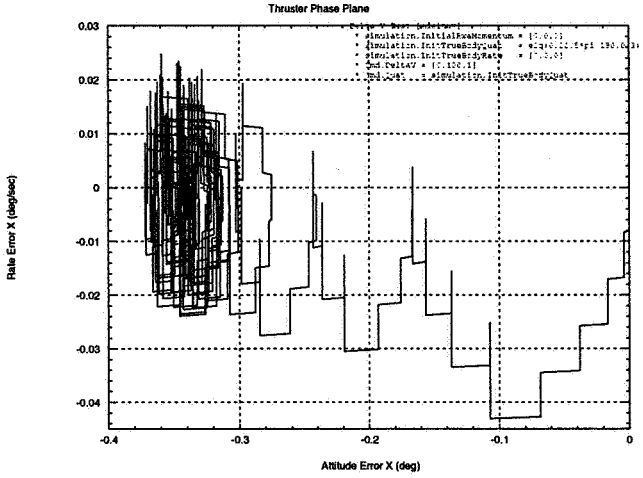

Figure 5: Delta V Mode Simulation

Delta H Mode

Delta H mode is designed to use the REM thrusters to reduce the spacecraft system momentum. It will be used primarily upon exit from Delta V mode to reduce the system momentum to less than 0.3 Nms. Delta H can also be entered from Inertial mode to reduce system momentum at a time other than after a spacecraft orbit maneuver, and can be entered from Sun Acquisition mode in the event that initial tip-off rates from the launch vehicle exceed the RWA capacity.

As in Delta V mode, Delta H uses the IRU as its primary sensor. In addition, RWA tachometers are used in calculation of total system momentum. The REMs are used as the actuators.

This mode uses a rate-only controller to command the thruster firings. The same pulse width modulator is used for Delta H as for Delta V, with the exception that all thruster pairs are operated in an on-pulsing manner for Delta H.

Simulations have been done for large initial tip-off rates of 3°/sec in the x_B and y_B axes and 12°/sec (2 rpm) in the z_B axis (see the results of this simulation later in this paper). Figure 6 shows the results of a simulation with initial tip-off rates of [5,5,5] Nms. For this case, the thrusters reduce the system momentum below 0.3 Nms within 35 seconds. Simulation runs with initial conditions typical of what would be seen prior to a Delta V were performed to ensure that spacecraft disturbances were not large enough to cause the pitch angle to exceed 25°.

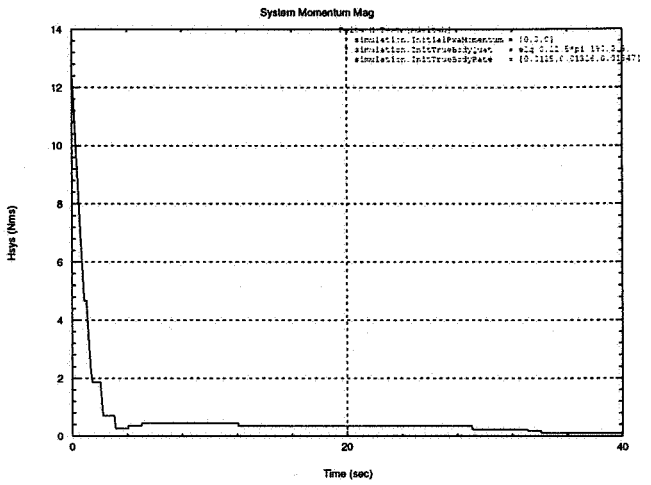

Figure 6: Delta H Mode Simulation

Sun Acquisition Mode

Sun Acquisition mode slews the spacecraft to a power-positive orientation within 25° of the sun. It uses the CSS outputs in its proportional control law and uses IRU information in its rate law. This mode is expected to operate after release from the launch vehicle, which can yield any initial angle and momentum up to worst-case initial body momentum of [30,30,70] Nms. After release from the launch vehicle, the ACS must slew the spacecraft to a power-positive orientation within 40 minutes. Because of the torque and momentum capabilities of the RWAs, the Sun Acquisition mode can achieve a power-positive orientation within this time limit only for initial body momentum up to approximately [30,30,50] Nms. Thus, the mode must also be able to transition to Delta H mode in the event of an initial body momentum exceeding its capabilities.

The Sun Acquisition controller has been shown to be asymptotically stable using a Lyapunov function similar to that analyzed in [13]. However, here the system momentum is constant and the control law's rate depends on $I\omega$ rather than ω, unlike the controllers analyzed there. The Lyapunov function is given by

$$V = \tfrac{1}{2} \Sigma I_i \omega_i^2 + K_p \Sigma (Q_j - Q_j)^2$$

where I_i are the diagonal elements of the inertia matrix and Q_j are the components of the quaternion.

Figure 7 gives the Sun Acquisition mode controller's response using for seven initial tip-off angles from 180° to 90° and an initial body momentum of [30,30,50] Nms.

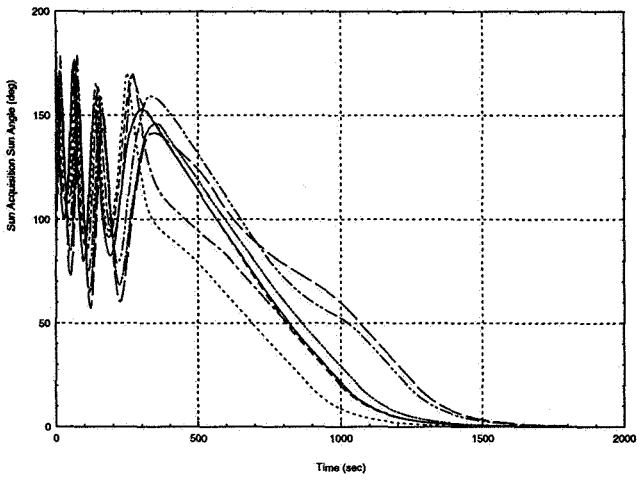

Figure 7: Sun Acquisition Mode Simulation

If a failure of some component other than CSS and IRU occurs, the Sun Acquisition controller will be used to slew the spacecraft from whatever state it is in towards the sun. Because it has body z rate information from the gyros, the Sun Acquisition algorithm can tolerate greater system momentum that will build up in the spacecraft due to environmental disturbances than can Safehold.

Safehold Mode

Based in the ACE, the Safehold mode slews the spacecraft to a power-positive orientation within 25° of the sun. Since the MAP science instruments are passively cooled, Safehold is required to keep the spacecraft to within 25° of the sun during its slew and hold. This mode uses CSSs and the RWA tachometers for sensors and the RWAs for actuators. The Safehold and Sun Acquisition modes are quite similar, and in fact share the same proportional law in their controllers. Safehold is a PD controller where the proportional law depends on the sun's angle with respect to the satellite's z axis, and the rate depends on numerically differentiating the sun angle. In addition, since the CSS are insensitive to rotations about the satellite's z axis, the tachometers are used to prevent uncontrolled spinning about the z axis.

There are three pairs of CSSs, with pair members pointing in opposite directions. Given that the RWAs are canted at β and the CSSs are canted at γ, the following formula converts the CSS readings from the six CSS eyes, designated with the letters a through f, into control torques for each reaction wheel.

$$2\,K_P / 9 \sin\beta \cos\gamma \begin{vmatrix} -1 & 2 & -1 \\ -1 & -1 & 2 \\ 2 & -1 & -1 \end{vmatrix} \begin{vmatrix} a-d \\ b-e \\ c-f \end{vmatrix}$$

The rates are formed by converting CSS readings into a Sun-line vector s, forming $s \times s_{desired}$, and using numerical differentiation. These rates are then multiplied by K_R to form rate-damping control torques if s is within 90° of the sun (otherwise the rate damping would have the wrong sign). The satellite is within 90° when $(a - d + b - e + c - f) \geq 0$.

Anti-runaway, used to prevent the wheels from uncontrolled spinning about the z axis, is accomplished by comparing the sum of the three wheel speeds to a preset value. When that value is exceeded, the wheel speeds are then equally damped, thereby suppressing z axis rotation.

A typical response with nonzero system momentum is shown in figure 8.

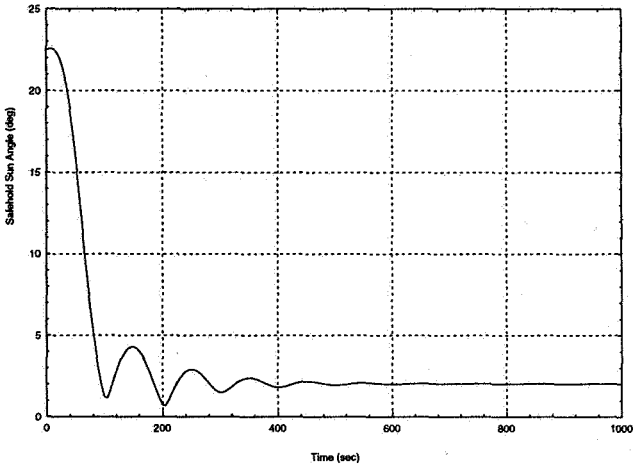

Figure 8: Safehold Mode Simulation

MAP ACS Development Using MatrixX

The MAP ACS development team, in an effort to design, analyze, and implement the ACS subsystem more efficiently than in previous spacecraft, has selected the MatrixX integrated tool set from Integrated Systems, Inc., as their primary design tool. The elements of the MatrixX tool set used for the MAP ACS design are:

XMath: mathematics analysis package used primarily for linear analysis and design, and simulation data processing and evaluation,

SystemBuild: graphical block diagram modeling and simulation software, used to develop and run low-fidelity (LoFi) and high-fidelity (HiFi) simulations,

AutoCode: real-time code generator used to reduce flight software development and testing time by generating portions of the ACS flight software directly from the SystemBuild HiFi, and

DocumentIt: automatic document generator, used to assist in the development of the ACS algorithm document.

In addition to the MatrixX tools described above, the ACS development will also include the development of a Hybrid Dynamic Simulator (HDS) to test the ACS algorithms. Also, note that only a portion of the ACS flight software to be flown on MAP will be automatically generated using AutoCode; the rest will be coded in the traditional manner.

ACS Development: MIDEX Strategy

Figure 9 illustrates the MIDEX concurrent engineering concept being employed for the MAP mission. The basic idea is to avoid duplication of effort by developing portions of the system in parallel, and to automate the generation of portions of the flight software and test code through the use of the real-time code generation capabilities built in to the simulation and analysis tool set.

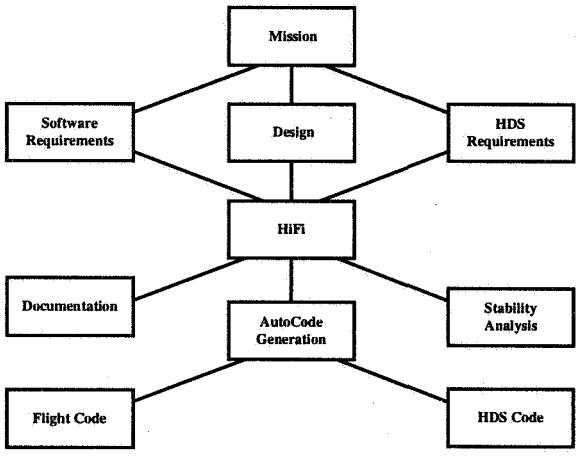

Figure 9: MIDEX Concurrent Engineering

By automatically generating portions of the flight software directly from the HiFi, there is a great savings of time and effort compared to hand coding the algorithm, as well as the elimination of a layer of work that can introduce errors into the implementation. For the portions of the flight software automatically coded, there is no need to develop an algorithm document *a priori*, and no need for the flight software developers to manually translate these algorithms. This results in the use of less staff hours, eliminates the possibility of translation errors, and allows a greater degree of configuration management on the ACS algorithms. Another benefit is that HiFi models can also be used to generate real-time software for the HDS, easing the testing effort.

By centralizing the development of the ACS subsystem in one place—within the HiFi simulation—it makes it possible for everyone to work from the same "plate". Flight software developers, analysis, simulation, and testing teams can all use the same system, meaning that there is no need for each to interpret the algorithms developed by the analysis team. Further, a single database of gains, inertias, and other system parameters can be maintained, making the configuration control process much easier.

A final benefit to this approach to ACS development will be seen in future missions. Because an object-oriented design approach is used—controllers, models, and other components are developed as separate blocks within the simulation environment—a high degree of reuse is possible. Once these blocks are developed and tested, they can be used for other missions with a minimum of redevelopment and retesting.

MAP HiFi Simulation

The heart of the MAP ACS development effort is the SystemBuild high-fidelity simulation. As shown in figure 9 above, it is from the HiFi that much of the design, analysis, testing, and implementation effort is based. Not only does the HiFi perform its traditional function of providing a test bed for the testing of the MAP ACS algorithms in as realistic a simulation of the space environment as possible, it also performs other functions. These include support for the linear and nonlinear stability analysis of the system, providing the basis for algorithm documentation, and automatic real-time code generation of flight software to implement portions of the ACS algorithms.

In order to perform these multiple functions, it has been important to involve members of the flight software and testing teams in the HiFi development from that start. The HiFi needed to be structured properly, and naming conventions for simulation and controller parameters developed, to be compatible with both the analysis and flight software needs.

Below, different aspects of the simulation development effort are discussed, including the flight software considerations that needed to be taken into account. The section ends with a presentation of several multi-mode simulations, demonstrating the capabilities of both the simulation environment and the MAP ACS.

Simulation Structure

SystemBuild uses a heirarchical block structure for the development of large simulations. Figure 10 shows the top-level block diagram of the MAP HiFi simulation. Each of the blocks shown, known as a *SuperBlock* in SystemBuild terminology, is a container that contains other blocks from which the HiFi is built.

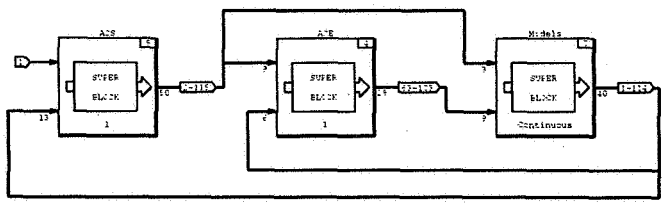

Figure 10: MAP ACS HiFi Overall Structure

As shown in figure 10, at the top level, the HiFi simulation is divided by function of spacecraft and system components. The ACS SuperBlock contains the algorithms that will be run in the Mongoose processor on MAP, while the ACE SuperBlock houses the functions that will take place within the MAP ACE. The Models SuperBlock contains the system and external simulation components, such as sensor and actuator models, spacecraft dynamics, and ephemeris processing.

Mode Transitions

SystemBuild includes the capability for using state transition diagrams (STDs) within a simulation. These diagrams provide a good way to run multi-mode simulations, and are used to provide this capability in the MAP HiFi. Figure 4, shown earlier in this paper, is the actual STD used in HiFi. It includes all of the allowed mode transitions, plus two transitions labeled **INIT** that are provided to support simulation testing.

The mode transition logic in the simulation is provided using a *BlockScript* code block to create the input for the MAP STD. (BlockScript is a programming language used by SystemBuild within its simulations.) The BlockScript code block implements the commanded and autonomous mode transitions by accepting a mode command input and simulation parameters such as system momentum, and generating the correct command to cause a mode transition in the STD. The STD outputs are the flags for each of the operational modes.

Flight Software Considerations

Because the MAP HiFi must support ACS design and analysis as well flight software development and testing, it was necessary to take this into account when the simulation was developed. Because only portions of the ACS will be used to automatically generate flight software using AutoCode, a natural division of the ACS was achieved, as shown in figure 11.

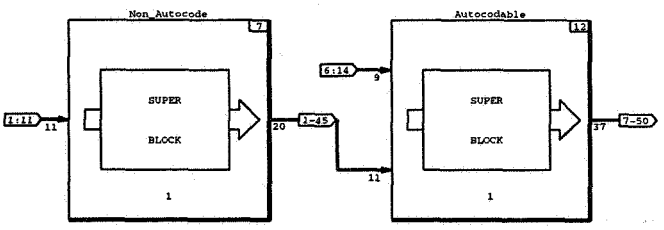

Figure 11: MAP ACS Partitioning

Within the Autocodable SuperBlock, shown in detail in figure 12, exist the controller command, error signal, and control signal algorithms for each mode, as well as the system momentum calculation. SystemBuild *Condition* SuperBlocks, allow the simulation to select from between multiple *Procedure* SuperBlocks based on an input signal. These Condition blocks, along with the mode flags generated by the STD, are used to select the correct controller algorithm given the current mode.

A final flight software requirement supported by the SystemBuild HiFi and XMath environment involves the nomenclature used for simulation and system parameters. XMath includes a partitioning mechanism, and SystemBuild allows XMath variables to be imported into the simulation at run time. The combination of these two abilities support the design and analysis effort by allowing different simulations to be set up and run very easily. At the same time, the flight software development effort is supported because the variables and partitions can very easily be mapped into the table structures used within the flight software.

Example Simulations

In this section, the results of several multi-mode HiFi simulations will be shown. These simulations will show some of the capabilities of both the MAP ACS as well as the SystemBuild simulation environment.

First, shown in figure 13, is an Inertial to Observing mode run. The plots show the Observing mode states of the spacecraft—the precession rate, Sun-line angle, and spin rate—as the spacecraft slews in Inertial mode from a Sun-line angle of 0° to 22.5° from 0 to 300 seconds, and then enters Observing mode for the rest of the simulation.

An example Delta V sequence is shown in figure 14. In this simulation, the spacecraft is slewed in Inertial mode from the Sun-line to 20° off the Sun-line from 0 to 250 seconds. A 100 second Delta V burn is then initiated. After the Delta V is terminated and after a short (< 10 seconds) Delta H burn to reduce system momentum to below 0.3 Nms, the spacecraft returns in Inertial mode and holds its pre-Delta V attitude.

The final example simulation, shown in figure 15, shows the performance of the system under worst-case tip-off

conditions: 180° initial angle from the Sun-line, and body momentum of [30,30,70] Nms. This initial momentum is high enough to trigger an immediate transition from Sun Acquisition to Delta H mode. The system stays in Delta H for approximately 70 seconds, during which time the system momentum is reduced to less than 0.3 Nms. (Note that the increase in momentum shown in the plots below beginning at approximately 20 seconds is a result of the Delta H controller being somewhat underdamped, resulting in body rates that pass through zero.) After the Delta H mode is completed, the system transitions back to Sun Acquisition mode, under which the attitude error is removed.

Conclusion

The attitude control system design presented in this paper satisfies the demanding requirements of the Microwave Anisotropy Probe. This design effort could not have been accomplished with the limited time and staff resources available without extensive use of the MatrixX tool set. One benefit of this new approach has been to promote closer cooperation between control system designers and software developers. The self-documenting features of the new analysis tools also eliminate the need for a manually-generated algorithm document, which saves time and eliminates a point in the development process where errors can be introduced. The automatic code generation capabilities of the new tools should lead to even greater savings in time and resources. Initial results obtained with the AutoCode tool appear very promising. This new way of developing attitude control systems is vitally important in the current climate of reduced development time and constrained resources.

References

[1] Bogges, N. W., *et al.*, *Astrophysical Journal*, vol. 397, p. 420 (1992).

[2] Gulkis, S., Lubin, P. M., Meyer, S. S., and Silverberg, R. F., *Scientific American*, vol. 262, no. 1, p. 132 (1990).

[3] Smoot, G. F., *et al.*, *Astrophysical Journal*, vol. 396, p. L1 (1992).

[4] Bennett, C.L., *et al.*, *Astrophysical Journal*, vol. 464, p. L1 (1996).

[5] MAP Home Page: http://map.gsfc.nasa.gov

[6] Hu, W., Sugiyama, N., and Silk, J., *Nature*, vol. 386, p. 37 (1997) (see also http://www.sns.ias.edu/~whu/physics/physics.html).

[7] Wertz, J. R., ed., *Spacecraft Attitude Determination and Control*, D. Reidel, (1978).

[8] Shuster, M. D., *Journal of the Astronautical Sciences*, vol. 41, p. 439 (1993).

[9] Lefferts, E. J., Markley, F. L., and Shuster, M. D., *Journal of Guidance, Control, and Dynamics*, vol. 5, p. 417 (1982).

[10] Murrell, J. W., AIAA Paper 78-1248, *AIAA Guidance, Navigation, and Control Conference*, Palo Alto, CA (1978).

[11] Bauer, F. H., Femiano, M. D., and Mosier, G. E., AIAA Paper 92-4334-CP, *AIAA Guidance, Navigation, and Control Conference*, Hilton Head, SC (1992).

[12] Mortensen, R. E., International Journal of Control, vol. 8, p. 297 (1968).

[13] Wie, B., and Barba, P. M., *Journal of Guidance, Control, and Dynamics*, vol. 8, p. 360 (1985).

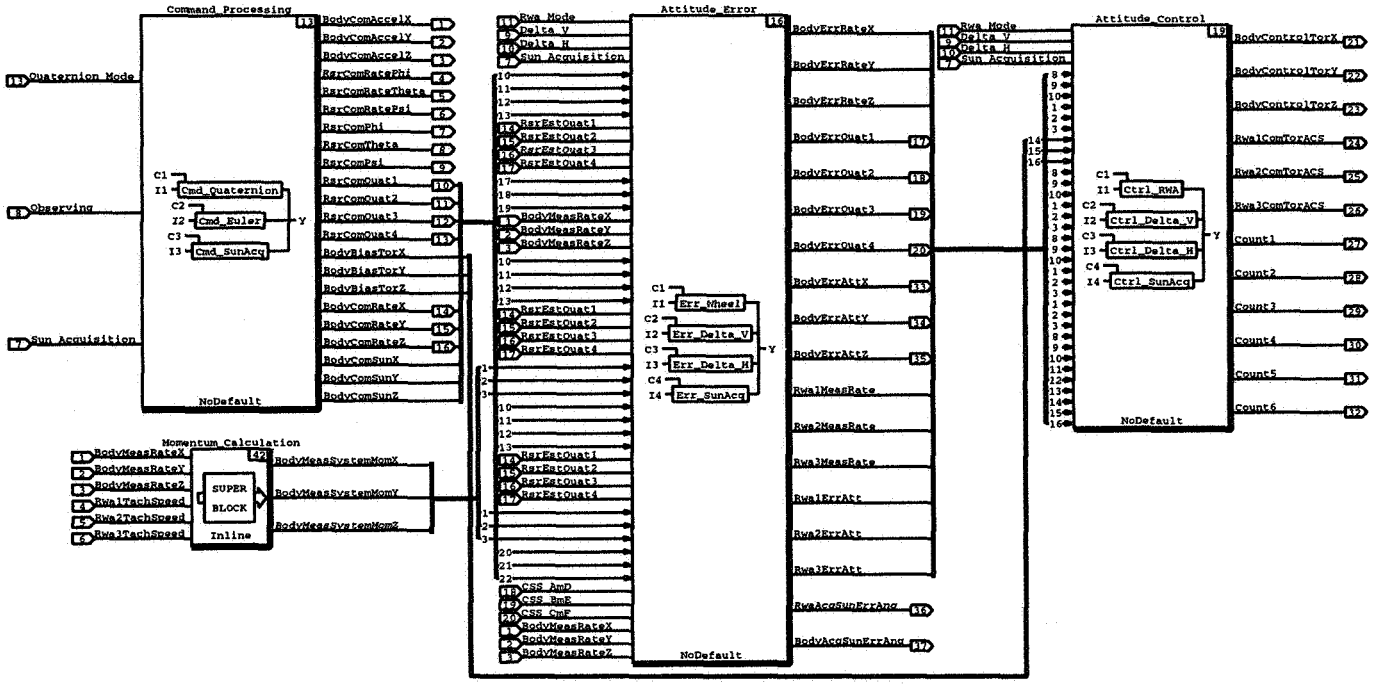

Figure 12: MAP ACS Algorithms to be Autocoded

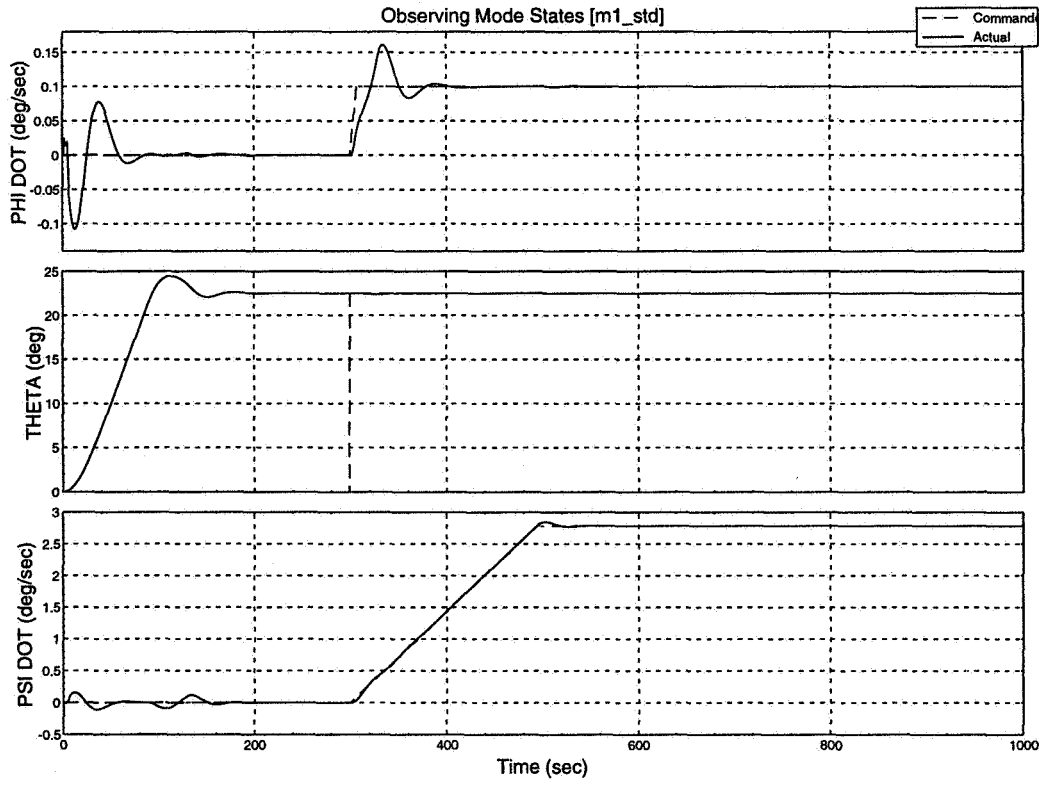

Figure 13: Inertial to Observing Mode Simulation

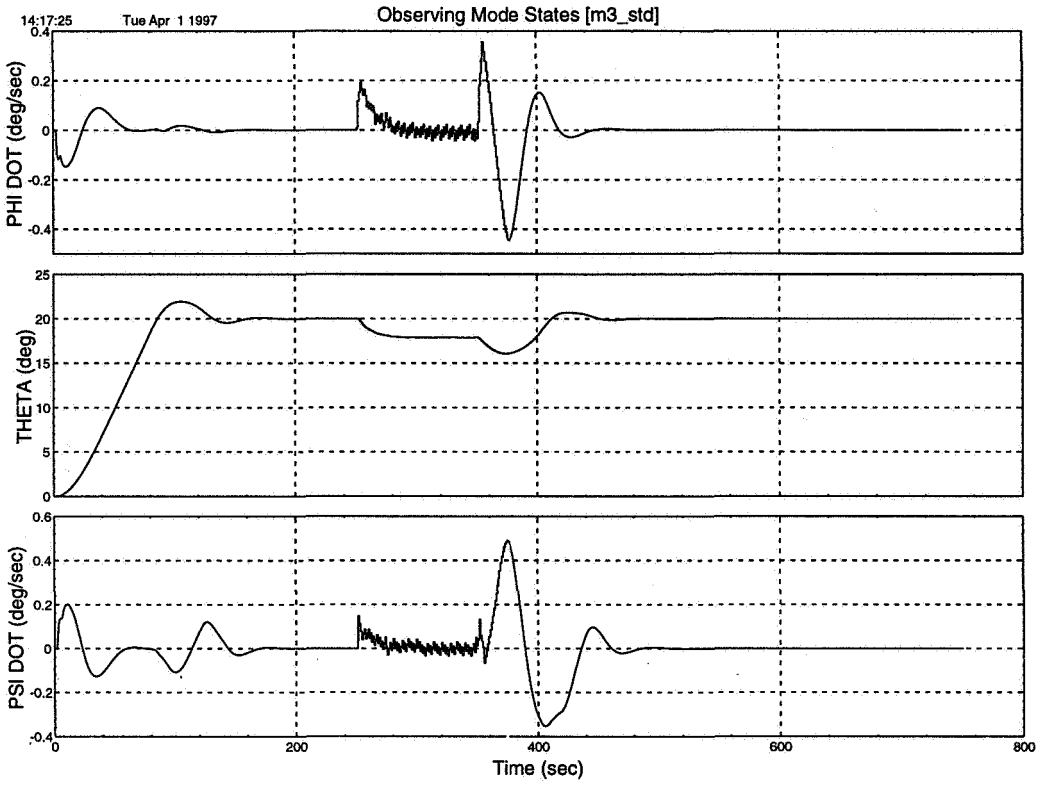

Figure 14: Delta V Sequence Simulation

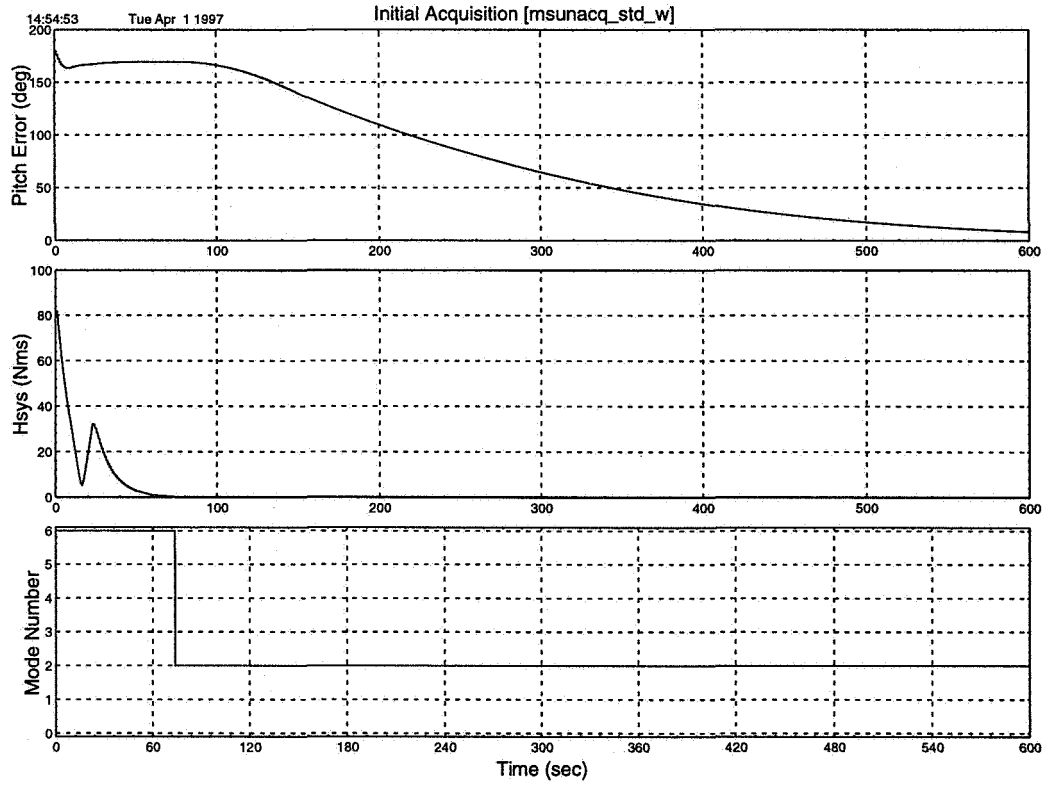

Figure 15: High-Rate Initial Acquisition Simulation

Development, Implementation, and Testing of the TRMM Kalman Filter

Stephen F. Andrews
Goddard Space Flight Center, Code 712
Greenbelt, MD, 20771

Jeff D'Agostino
the Hammers Co.
Greenbelt, MD, 20770

Abstract

The Tropical Rainfall Measuring Mission (TRMM) spacecraft is a nadir pointing spacecraft that was to control attitude based on the Earth Sensor Assembly (ESA) output. After a potential single point failure in the ESA was identified, the contingency attitude determination method chosen to replace the ESA-based system was a sixth-order extended Kalman filter that uses digital sun sensor and magnetometer measurements to update the attitude and the gyro biases. This algorithm was added to previously-tested flight code, and many software verification tests had to be run to ensure that both the new and the original software requirements were still met. The design, implementation, and testing of the TRMM Kalman filter will be discussed.

Introduction

The Tropical Rainfall Measuring Mission (TRMM) spacecraft is to be launched in November, 1997 from Tanegashima Space Center, Japan. The spacecraft is three-axis stabilized, in a near circular 350 km orbit at 35° inclination. The Mission Mode is nadir pointing, and due to Sun constraints, the spacecraft must be rotated 180° about nadir every few weeks. The sensors are a static Earth Sensor Assembly (ESA), two two-axis Digital Sun Sensors (DSS), a redundant three-axis Inertial Rate Unit (IRU), eight Coarse Sun Sensors (CSS), and two Three-Axis Magnetometers (TAM). The spacecraft will be controlled with four Reaction Wheels (RW), twelve thrusters (Reaction Engine Modules, REM), and three Magnetic Torquer Bars (MTB). Nominal attitude sensing is done with the ESA for roll and pitch, and integrated IRU rate for yaw. The yaw attitude is updated twice per orbit by the DSSs, and the IRUs are used for rate.

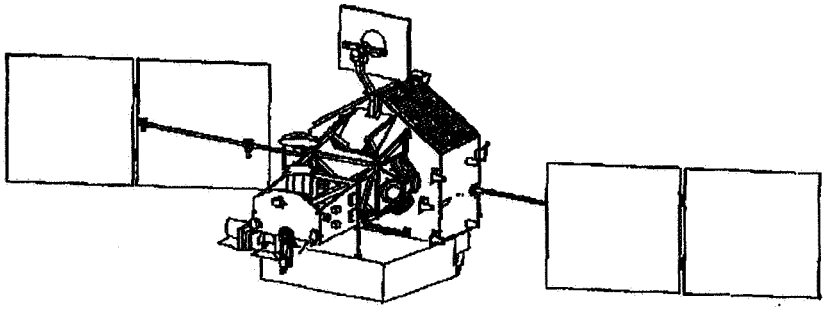

Figure 1 TRMM Spacecraft

The attitude knowledge requirement on the Attitude Control System (ACS) is 0.18° (3σ) per axis, and the baseline system meets this requirement A potential single point failure of the ESA was first described at Goddard in 1992, with the discovery of a "fogging" effect of the ESA lenses [1]. This effect could cause the ESA to fail the attitude determination requirement during Mission Mode. Several solutions were proposed, but it wasn't until 1994 that the decision was made to develop a backup attitude determination system using the existing TRMM sensors. The

only requirement the new attitude determination algorithm had to meet was 0.7° (3σ) per axis knowledge. The resulting trade study of contingency attitude determination algorithms was summarized at the 1995 FMET Symposium [2].

The result of the trade study was that a sixth-order extended Kalman filter was chosen as the contingency attitude determination algorithm. The filter provides updates to the IRU propagated attitude and the IRU drift rate biases with TAM and DSS measurements. The algorithm was adapted from the XTE Kalman filter; the star tracker processing was replaced with TAM processing, a second DSS was added, and new interfaces were coded to fit the algorithm into the existing, tested flight code.

Development

The main portion of the algorithm is the discrete Kalman filter [3]:

covariance propagation $$\mathbf{P}_k(-) = \Phi_{k-1}\mathbf{P}_{k-1}(+)\Phi_{k-1}^T + \mathbf{Q}_{k-1} \tag{1}$$

Kalman gain $$\mathbf{K}_k = \mathbf{P}_k(-)\mathbf{H}_k^T\left[\mathbf{H}_k\mathbf{P}_k(-)\mathbf{H}_k^T + \mathbf{R}\right]^{-1} \tag{2}$$

state estimate update $$\underline{\hat{x}}_k(+) = \underline{\hat{x}}_k(-) + \mathbf{K}_k[\underline{z}_k - \mathbf{H}_k\underline{\hat{x}}_k(-)] \tag{3}$$

covariance update $$\mathbf{P}_k(+) = [\mathbf{I} - \mathbf{K}_k\mathbf{H}_k]\mathbf{P}_k(-) \tag{4}$$

The ^ notation indicates an estimated quantity, and the subscript k or k-1 indicates the relevant computer cycle of interest. The system state vector is x, which will be defined later. The initial condition of the state covariance matrix **P** is a diagonal matrix whose elements are the expected values of the squares of the initial attitude and gyro drift bias estimation errors. The form of the state transition matrix Φ and the measurement matrix **H** are found from the dynamics and the geometry of the system. The state noise covariance matrix **Q** and the measurement noise covariance matrix **R** are determined from known errors in the system. The algorithm as implemented, however, does not use these vector/matrix equations. Instead, scalar processing of each measurement component is used to reduce the computational burden [4]. The scalar processing used in the TRMM algorithm is equivalent to the vector processing form of the equations, and this will be discussed later.

The system model includes the spacecraft dynamics and the sensor models. The spacecraft dynamics are modeled as:

$$\dot{q}_{I\hat{b}} = \frac{1}{2}\hat{\Omega}q_{I\hat{b}} \tag{5}$$

where $q_{I\hat{b}}$ is the inertial to estimated body quaternion, and $\hat{\Omega}$ is a skew-symmetric matrix of estimated body rates. The error quaternion is defined as:

$$\delta q_{\hat{b}b} = q_{I\hat{b}}^{-1} \otimes q_{Ib} \tag{6}$$

where q_{Ib} is the inertial to true body quaternion, and $\delta q_{\hat{b}b}$ is the estimated body to true body quaternion. The three vector components of $\delta q_{\hat{b}b}$ are related to the attitude determination errors by:

$$\delta q_{\hat{b}b}(i) = \frac{1}{2}\underline{\delta\theta}(i), \qquad i=1,2,3 \tag{7}$$

The gyro dynamics and noise model is [5]:

$$\begin{aligned} \underline{\omega}_g &= \underline{\omega} + \underline{b} + \underline{\eta}_v \\ \dot{\underline{b}} &= \underline{\eta}_u \end{aligned} \tag{8}$$

where $\underline{\omega}$ is the true spacecraft angular rate, $\underline{\omega}_g$ is the measured, uncompensated body rate, $\underline{b}$ is the gyro drift rate, and $\underline{\eta}_u$ and $\underline{\eta}_v$ are gaussian-distributed, white noise vectors with zero means and standard deviations $\sigma_u[1\ 1\ 1]^T$ and $\sigma_v[1\ 1\ 1]^T$, respectively. The random process $\underline{\eta}_u$ models the long-term drift rate variation as an integrated white noise process, and $\underline{\eta}_v$ models the instantaneous rate white noise.

To relate the attitude determination error dynamics to the gyro measurement errors, Equations 5, 6, 7, and 8 are combined. The resulting state vector $\underline{x} = [\underline{\delta\theta}\ \underline{\Delta b}]^T$ is composed of the three (small angle) attitude errors $\underline{\delta\theta} = \begin{bmatrix} \delta\theta_x & \delta\theta_y & \delta\theta_z \end{bmatrix}^T$, and three incremental gyro biases $\underline{\Delta b}$ [6]. The linear model of the system is:

$$\dot{\underline{x}} = \mathbf{F}\underline{x} + \underline{w} \tag{9}$$

The plant matrix F is, to first order:

$$\mathbf{F} = \begin{bmatrix} -[\underline{\hat{\omega}}\times] & -\mathbf{I} \\ \mathbf{0} & \mathbf{0} \end{bmatrix} = \begin{bmatrix} \mathbf{F}_1 & \mathbf{F}_2 \\ \mathbf{F}_3 & \mathbf{F}_4 \end{bmatrix} \tag{10}$$

where $[.\ \times]$ is the skew-symmetric cross product matrix, and $\underline{\hat{\omega}}$, the compensated gyro-measured body rates, is $\underline{\hat{\omega}} = \underline{\omega}_g - \underline{\hat{b}}$, where $\underline{\hat{b}}$ is the estimated gyro drift bias. The vector $\underline{w}$ is $\underline{w} = \begin{bmatrix} \underline{\eta}_v & \underline{\eta}_u \end{bmatrix}^T$ with covariance matrix [7]:

$$E\left\{\underline{w}(t)\underline{w}^T(\tau)\right\} = \begin{bmatrix} \sigma_v^2\mathbf{I}\delta(t-\tau) & 0 \\ 0 & \sigma_u^2\mathbf{I}\delta(t-\tau) \end{bmatrix} = \mathbf{U}\delta(t-\tau) \tag{11}$$

The three axis power spectral density matrix **U** is thus:

$$\mathbf{U} = \begin{bmatrix} \sigma_v^2\mathbf{I} & 0 \\ 0 & \sigma_u^2\mathbf{I} \end{bmatrix} \tag{12}$$

The solution to Equation 9, which has both a homogeneous and a particular part, has the form:

$$\underline{x}(t) = \Phi\underline{x}_0 + \int_0^t \Phi(t-\sigma)\underline{w}(\sigma)d\sigma \tag{13}$$

The discrete equivalent to this solution is:

$$\underline{x}_k = \Phi_{k-1}\underline{x}_{k-1} + \underline{d}_{k-1} \tag{14}$$

where $\underline{d}_{k-1}$ is a normally distributed random vector with zero mean, and covariance **Q**.

The state transition matrix Φ, by definition, must satisfy the same differential equation as the state $\underline{x}$. Also, $\Phi(t,t)=\mathbf{I}$ for any t; this becomes the initial condition $\Phi(0,0)=\mathbf{I}$ [8]. The homogeneous solution to Equation 9 has the form $\underline{x} = \Phi\underline{x}_0$, where $\Phi = e^{Ft}$. To find the explicit form of Φ, first partition Φ into submatrices, as shown in

Equation 15. Then, put Φ into the homogeneous differential equation, and apply the initial condition. Note that any part of the following derivation that involves an integral assumes constant inputs over the integration period. After some algebra, the state transition matrix of the homogeneous solution is:

$$\Phi = \begin{bmatrix} \Phi_1 & \Phi_2 \\ \Phi_3 & \Phi_4 \end{bmatrix} = \begin{bmatrix} e^{F_1 t} & -\int_0^t e^{-F_1(t-\tau)} d\tau \\ 0 & I \end{bmatrix} \tag{15}$$

where $\mathbf{F}_1$ is the upper left submatrix of $\mathbf{F}$. Using the series definition of $e^{\mathbf{F}t}$, and the series definitions of sine and cosine, the form of Φ as used in the algorithm is:

$$\Phi = \begin{bmatrix} \Phi_1 & \Phi_2 \\ 0 & I \end{bmatrix} \tag{16}$$

with

$$\Phi_1 = I + \hat{\omega}^{-1} F_1 \sin \hat{\omega} T + \hat{\omega}^{-2} F_1^2 (1 - \cos \hat{\omega} T) \tag{17a}$$

$$\Phi_2 = -[IT + \hat{\omega}^{-2} F_1 (1 - \cos \hat{\omega} T) + \hat{\omega}^{-3} F_1^2 (\hat{\omega} T - \sin \hat{\omega} T)] \tag{17b}$$

The propagation, or sampling, interval is T, and $\hat{\omega}$ is the magnitude of $\underline{\hat{\omega}}$, the compensated body rates.

The particular solution to Equation 9 is found by starting with the discrete equivalent to $\underline{w}(t)$:

$$\underline{d}_k \equiv \int_0^T \Phi(T - \sigma) \underline{w}(\sigma) d\sigma \tag{18}$$

The state noise covariance matrix tells how the random variable $\underline{d}_k$ behaves, and thus how the attitude and attitude knowledge (covariance matrix) propagate. Define the covariance of $\underline{d}_k$:

$$Q = E\left[\underline{d}_k \underline{d}_l^T\right] = E\left[\underline{d}_k(t_1) \underline{d}_l(t_2)^T\right] = 0 \qquad \text{for } k \neq l \tag{19}$$

Substitute in the equation for $\underline{d}_k$ and form:

$$Q = \int_0^T \Phi(T - \sigma) U(\sigma) \Phi^T(T - \sigma) d\sigma \tag{20}$$

Make the necessary substitutions for U, Φ_1, and Φ_2, use the series definitions of sine and cosine, and after some algebra and the elimination of higher order terms, the state noise covariance matrix can be written as shown in Equation 21.

$$Q = \begin{bmatrix} T\sigma_v^2 I + \frac{T^3}{3}\sigma_u^2 I & -\frac{T^2}{2}\sigma_u^2 I \\ -\frac{T^2}{2}\sigma_u^2 I & T\sigma_u^2 I \end{bmatrix} \tag{21}$$

The system matrices, the state transition matrix, and the state noise covariance matrix are available at this point. An explicit representation of the linearized measurement matrix **H** must be derived because this matrix is used in the measurement model and in the Kalman filter equations.

The measured vector is modeled as:

$$\underline{\tilde{s}}_k = \mathbf{A}_{Ib}(t_k)\underline{s}_I(t_k) + \underline{N}_k \tag{22}$$

and the estimated vector is:

$$\underline{\hat{s}}_k = \mathbf{A}_{I\hat{b}}(t_k)\underline{s}_I(t_k) \tag{23}$$

where ^ indicates estimate, ~ indicates measurement, and $\underline{N}_k$ is a white noise vector at the sample time t_k. The true inertial vector being measured or estimated at time t_k is shown as $\underline{s}_I(t_k)$.

In the sensor frame, the residual $\underline{z}$ is defined as follows:

$$\begin{aligned}\underline{z} &= \underline{\tilde{s}}_k - \underline{\hat{s}}_k \\ &= \mathbf{A}_{bs}\mathbf{A}_{Ib}(t_k)\underline{s}_I(t_k) + \underline{N}_k - \mathbf{A}_{bs}\mathbf{A}_{I\hat{b}}(t_k)\underline{s}_I(t_k) \\ &= \mathbf{A}_{bs}(\mathbf{A}_{Ib} - \mathbf{A}_{I\hat{b}})\underline{s}_I + \underline{N}\end{aligned} \tag{24}$$

The body to sensor alignment matrix is $\mathbf{A}_{bs}$. Note that some subscripts and time notation have been deleted for ease of presentation. If small angle differences $\underline{\delta\theta}$ are assumed between the inertial to true body orientation and the inertial to estimated body orientation, the inertial to estimated body matrix becomes:

$$\mathbf{A}_{I\hat{b}} = \mathbf{A}_{\delta\theta}\mathbf{A}_{Ib} \tag{25}$$

where the error matrix is:

$$\mathbf{A}_{\delta\theta} = \begin{bmatrix} 1 & -\delta\theta_z & \delta\theta_y \\ \delta\theta_z & 1 & -\delta\theta_x \\ -\delta\theta_y & \delta\theta_x & 1 \end{bmatrix} \tag{26}$$

When Equations 25 and 26 are substituted into Equation 24, and the attitude error cross product matrix is pulled out of $\mathbf{A}_{\delta\theta}$, the residual can be written:

$$\underline{z} = -\mathbf{A}_{bs}[\underline{\delta\theta}\times]\underline{s}_b + \underline{N} \tag{27}$$

The rows of the body to sensor transformation matrix $\mathbf{A}_{bs}$ are the sensor basis vectors in the body frame, that is:

$$\mathbf{A}_{bs} = \begin{bmatrix} \bar{u}_{sx} & \bar{u}_{sy} & \bar{u}_{sz} \end{bmatrix}^T \tag{28}$$

The overbar notation indicates a unit vector, and $\bar{u}_{si}$ is the i^{th} sensor coordinate frame axis defined in body coordinates. When the substitution is made into the residual equation, the measurement matrix vectors can be calculated. The entire equation is:

$$\underline{z} = -\begin{bmatrix} \bar{u}_{sx} & \bar{u}_{sy} & \bar{u}_{sz} \end{bmatrix}^T [\underline{\delta\theta}\times]\underline{s}_b + \underline{N} \tag{29}$$

Since all three axes are similar, only the x axis derivation will be shown. For the x axis:

$$z_x = -\bar{u}_{sx} \cdot [\underline{\delta\theta}\times]\underline{s}_b + N_x \tag{30}$$

The right hand side of Equation 30 includes a triple scalar product, so it can be rewritten as:

$$z_x = \left(\bar{u}_{sx} \times \underline{s}_b\right) \cdot \underline{\delta\theta} + N_x \equiv \underline{h}_x \cdot \underline{\delta\theta} + N_x \tag{31}$$

The full residual is thus of the form:

$$\underline{z} = \begin{bmatrix} \bar{u}_{sx} \times \underline{s}_b & \bar{u}_{sy} \times \underline{s}_b & \bar{u}_{sz} \times \underline{s}_b \end{bmatrix}^T \underline{\delta\theta} + \underline{N} \tag{32a}$$

or,

$$\underline{z} = \mathbf{H}_k \underline{x}_k + \underline{v}_k \tag{32b}$$

with

$$\mathbf{H}_k = \begin{bmatrix} \bar{u}_{sx} \times \underline{s}_b & \bar{u}_{sy} \times \underline{s}_b & \bar{u}_{sz} \times \underline{s}_b \\ 0_{3x1} & 0_{3x1} & 0_{3x1} \end{bmatrix}^T \tag{32c}$$

The linear form of the measurement matrix **H** is now available, and $\underline{v}_k$ is the measurement noise, a normally distributed random vector with zero mean and covariance **R**. The matrix **R** is calculated from the estimate of the noise from each update sensor.

The measurement matrix must be recalculated at each measurement because there is a different $\underline{s}_b$. At each timestep, the state transition matrix is also recalculated. Once the state transition matrix has been calculated, the covariance matrix can be propagated to the current timestep. The Kalman gain is then calculated, and the state estimate and the covariance matrix are updated. The first three filter states are used to update the inertial to body quaternion estimate as follows:

$$\delta q_{\hat{b}b}(i) = \frac{\hat{\underline{x}}_k(i)}{2} \qquad i=1,2,3$$

$$\delta q_{\hat{b}b}(4) = 1 \tag{33a}$$

$$\hat{q}_{Ib}(+) = q_{I\hat{b}}(-) \otimes \delta q_{\hat{b}b} \tag{33b}$$

$$\hat{q}_{Ib} = \frac{\hat{q}_{Ib}}{|\hat{q}_{Ib}|} \tag{33c}$$

The estimated gyro drift bias is updated with the last three elements of the filter state vector:

$$\hat{\underline{b}}_k(i) = \hat{\underline{b}}_{k-1}(i) + \hat{\underline{x}}_k(i+3) \qquad i=1,2,3 \tag{34}$$

The algorithm is not implemented using the vector/matrix equations as derived. Instead, scalar processing of each measurement component is used to avoid inverting 6x6 or 3x3 matrices. The scalar processing is equivalent to the vector processing form of the equations because the system equations have been linearized and the Kalman filter equations are linear; the principle of superposition applies to this linear system. Specifically, given a set of sensor measurements as input (a vector or a matrix), the output of the filter (updated states and covariance) is a combination of the outputs from each measurement component; each measurement, or each component of each measurement, can thus be processed individually, and the results can be added together to give the final state estimates.

Implementation

The ACS Flight Software (FSW) is required to provide onboard attitude determination, command processing to allow the users to modify internal data and to control ACS execution, and nominal three-axis control at 2 Hz. In addition, the FSW must acquire mission orientation from launch vehicle separation, do ephemeris propagation, and provide a yaw turn capability to keep one side of the spacecraft anti-sun. There is also a requirement for a CERES instrument inertial hold mode, and an 8 Hz thruster control mode to maintain the required orbit. The FSW is designed also to provide pointing for the High Gain Antenna and Solar Arrays. Finally, the ACS FSW provides some autonomous Failure Detection and Correction (FDC) capability, and performs assorted housekeeping tasks such as data and command processing, telemetry and command generation.

The ACS FSW is written in C, and is designed as an event-driven, independent task under the VRTX operating system. It resides on an 80386 ACS Processor, and communicates to the ACS sensors and actuators via software calls to an independently-developed Flight Data System (FDS). The FDS in turn communicates with the Attitude Control Electronics (ACE) processor, which provides the direct interface to the ACS hardware.

To meet the requirements stated above, the ACS FSW is divided into separate subsystems, or Computer Software Components (CSCs), as shown in Figure 2. Each CSC contains the functionality specified in the figure; e.g., CSC 6.0 is the Attitude Determination and Control subsystem, and CSC 3.0 is the Telemetry Generation subsystem. Each CSC provides data for the others through specific function calls or through globally-defined data structures, as needed.

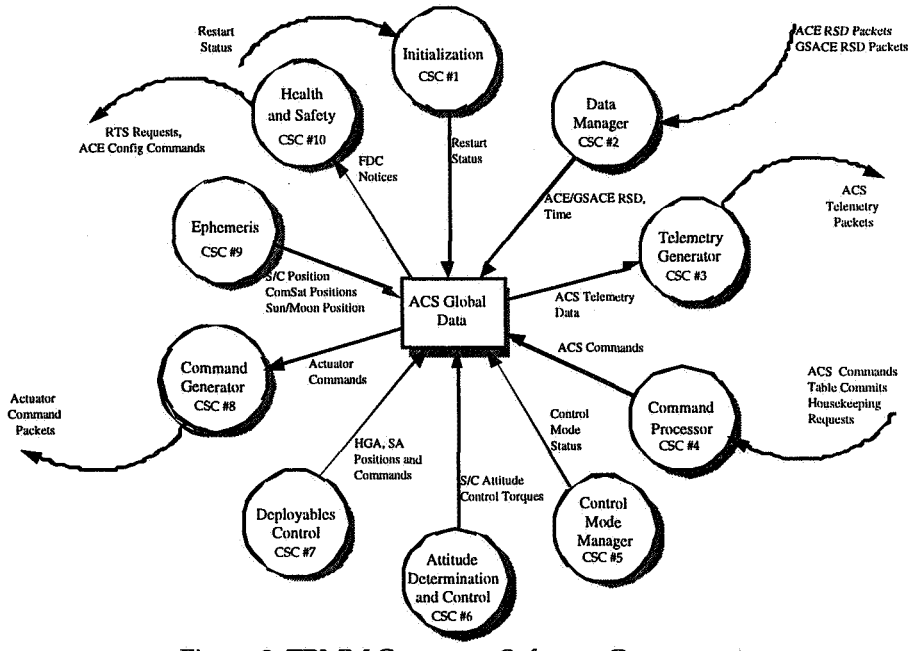

Figure 2 TRMM Computer Software Components

The intent of the TRMM ACS FSW design was to provide as much flexibility as possible to accommodate any unanticipated design changes. This flexibility was provided through the use of software tables – data structures that could be maintained and modified by ground operations after launch. The tables could be changed during the development process with minimum impact on the rest of the ACS code. Besides hardware parameter data such as scale factors, biases, and limits, the ACS FSW also uses tables to maintain function pointers and control configurations. By referencing tables to determine current configurations and to define the required code branching based on those configurations, the FSW accomplishes its decision logic without resorting to hard coding the criteria. This approach proved its value with the unplanned incorporation of the Kalman filter into the ACS FSW.

A key subsystem in the ACS FSW is the Control Mode Manager. An ACS FSW control mode can be thought of as a set of configurations required to perform specific spacecraft pointing tasks. The TRMM control modes that were designed to meet the requirements described above are shown in Figure 3.

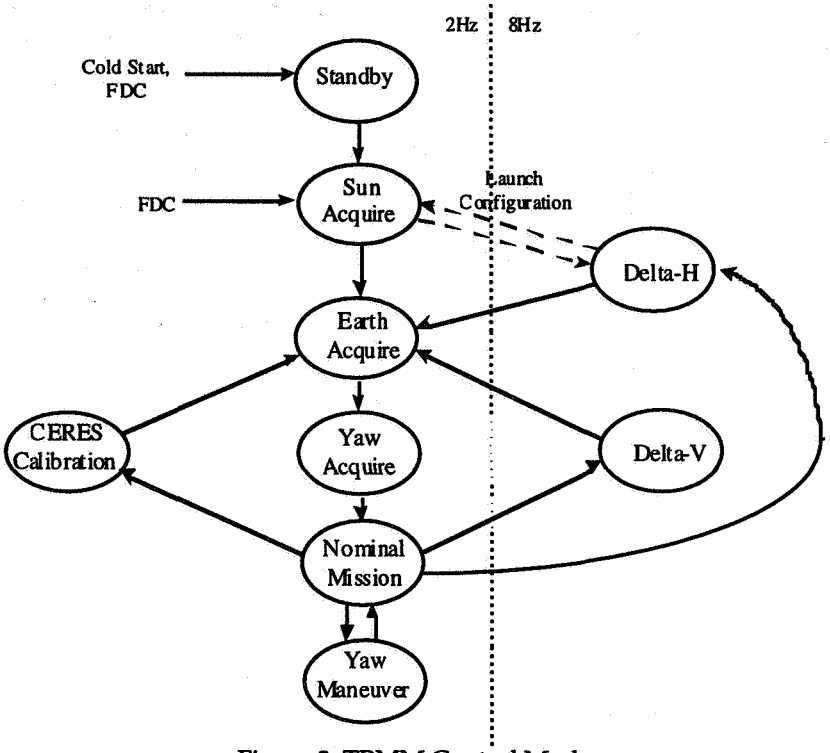

Figure 3 TRMM Control Modes

The main control modes operate at 2 Hz. The Sun Acquire mode is used to acquire a power and thermal safe attitude after separation from the launch vehicle. Earth Acquire is used to point the ESA at the Earth, and Yaw Acquire puts the spacecraft in the proper orientation about the nadir vector. Science is performed in Nominal Mission mode, and Yaw Maneuver mode keeps one side of TRMM anti-sun. The CERES Calibration mode is an inertial hold mode. The two thruster modes are implemented at 8 Hz; Delta-V mode is used for orbit maintenance and an end of life controlled deorbit, and Delta H mode unloads excess system momentum.

The control mode manager uses configuration tables to determine which data to process, which attitude determination methods to perform, and which control law to execute. The values read from the configuration tables provide indices into the function pointer tables to execute the proper functions for each task. For example, when the Kalman filter is executing, the acquisition to mission attitude is done with the mission mode controller. The changes are highlighted in Table 1. The Kalman filter capability was added to the TRMM ACS FSW by changing the configuration tables entries, creating the new function, and adding the function pointer to the appropriate table. This software design is flexible enough that only a small amount of existing code had to modified to accommodate the Kalman filter.

The Kalman Filter was added as a contingency method of attitude determination in the TRMM ACS FSW Build 5.0. The core Kalman Filter code was heritage from the X-Ray Timing Explorer (XTE) ACS FSW, but some associated subroutines and initialization functions were new code. Additionally, a Kalman Filter initialization command and DSS selection command were added to the ACS FSW, and a telemetry packet was created using a previously defined, but unused, telemetry packet. One new software table structure was created to allow in-flight modification of Kalman filter parameters.

Table 1 FSW Configuration Tables

Control Mode	A-Matrix Update	MTB Limiting	Next Mode	Attitude Determination			Att Ctl Law
				First	Second	Third	
Standby	Triad	Off	Sun Acquire	None	None	None	None
Sun Acquire	Triad	Off	Earth Acquire	ESA Att	Gyro Att	None	SunAcqCtl
Earth Acquire	Triad	Off	Yaw Acquire	ESA Att	Gyro Att	None	EarthAcqCtl
Yaw Acquire	Triad	Off	Nominal	ESA Att	Gyro Att	None	YawAcqCtl
Nominal	None	On	Nominal	ESA Att	Gyro Att	CondInert	NadirCtl
Yaw Maneuver	None	On	Nominal	ESA Att	Gyro Att	CondInert	NadirCtl
Delta-H	None	Off	Sun Acquire	Gyro Att	Inert Att	None	ThrusterCtl
Delta-V	None	Off	Earth Acquire	Gyro Att	Inert Att	None	ThrusterCtl
CERES Calibration	None	On	Earth Acquire	Gyro Att	CondInert	None	InertialCtl

Control Mode	A-Matrix Update	MTB Limiting	Next Mode	Attitude Determination			Att Ctl Law
				First	Second	Third	
Standby	Triad	Off	Sun Acquire	None	None	None	None
Sun Acquire	Kalman	Off	Earth Acquire	Gyro Att	Cntngcy	None	SunAcqCtl
Earth Acquire	Kalman	On	Yaw Acquire	Gyro Att	Cntgncy	CondInert	NadirCtl
Yaw Acquire	Kalman	On	Nominal	Gyro Att	Cntgncy	CondInert	NadirCtl
Nominal	Kalman	On	Nominal	Gyro Att	Cntgncy	CondInert	NadirCtl
Yaw Maneuver	Kalman	On	Nominal	Gyro Att	Cntgncy	CondInert	NadirCtl
Delta-H	None	Off	Sun Acquire	Gyro Att	Inert Att	None	ThrusterCtl
Delta-V	None	Off	Earth Acquire	Gyro Att	Inert Att	None	ThrusterCtl
CERES Calibration	Kalman	On	Earth Acquire	Gyro Att	Cntgncy	CondInert	InertialCtl

The attitude determination and control subsystem, CSC #6, required the most alterations to accommodate the Kalman filter. The nadir-pointing control law function module, the Tri-Axial Attitude Determination (TRIAD) module, the IRU sensor data processing module, the inertial attitude matrix module, the main subsystem module, the ADC commands module, and the ADC utilities module had to be modified.

The control mode management subsystem, CSC #5, required minor changes in the control setup module, the control mode initialization module, and the main subsystem module. The telemetry subsystem, CSC #3, needed changes to the main subsystem module and to the discrete telemetry generation module to incorporate the new telemetry requirements. The failure detection and correction (FDC) subsystem (CSC #10) required only three new test entries in existing tables. No additional code in the subsystem was necessary to support the Kalman filter.

The Kalman filter code, including functions, tables, telemetry, and pointers, is loaded in the default TRMM ACS FSW. To switch the TRMM ACS FSW from Normal operation to Contingency (Kalman Filter) operation, the flight operations team must load new control mode configuration tables and the new control law limits table. The ACS FSW will start executing the Kalman filter automatically once the new tables are loaded.

Table 2 shows the software metrics for TRMM ACS Builds 4.1 through 5.3. The Kalman Filter and supporting code account for less than 5% of the total ACS in RAM, and less than 4% of the total ACS in EEPROM. Additionally, no changes were required to the primary Kalman Filter functions after the first build.

A CPU utilization test was performed in April 1996 using the TRMM ACS Build 5.2 FSW. The results show that the average CPU utilization of the ACS FSW in Normal configuration (no Kalman filter, 2-Hz non-thruster mode) was 33% to 34% with all CSC modules executing. In the Contingency configuration (Kalman filter executing, 2-Hz non-thruster mode), the average CPU utilization increased to 37% to 38% with all CSC modules executing.

Table 2 Software Metrics

ACS Build	Build 4.1	Build 5.0	Build 5.1	Build 5.1a	Build 5.2	Build 5.2a	Build 5.3
Delivery Date	2/2/95	3/30/95	7/17/95	10/13/95			
Total ACS in RAM (bytes)	111527	123995	126627	126093	126987	127739	127775
Total ACS in EEPROM (bytes)	98558	106736	109075	108429	108901	109663	109727
Kalman Filter Code (bytes)*	0	3704	3704	3704	3704	3704	3704
Kalman Filter Data (bytes)*	0	2298	2298	2298	2298	2298	2298
Kalman Filter Total (bytes)	0	6002	6002	6002	6002	6002	6002
Percentage KF in RAM	0.00%	4.84%	4.74%	4.76%	4.73%	4.70%	4.70%
Percentage KF in EEPROM	0.00%	3.59%	3.51%	3.53%	3.52%	3.49%	3.49%
*Does not include code changes to supporting functions							

Testing

The Kalman filter was implemented in Build 5.0 of the TRMM ACS Flight Software. Testing was done on a Hybrid Dynamic Simulator (HDS), shown in Figure 4. The purpose of the HDS is to provide real-time, hardware-in-the-loop testing of the flight software. The HDS simulates the spacecraft's attitude and orbit dynamics, the sensors and actuators, and the internal and external disturbances. The HDS also allows the user either interactive control of the simulation test script file execution of a simulation. The data can be displayed or logged for off-line analysis.

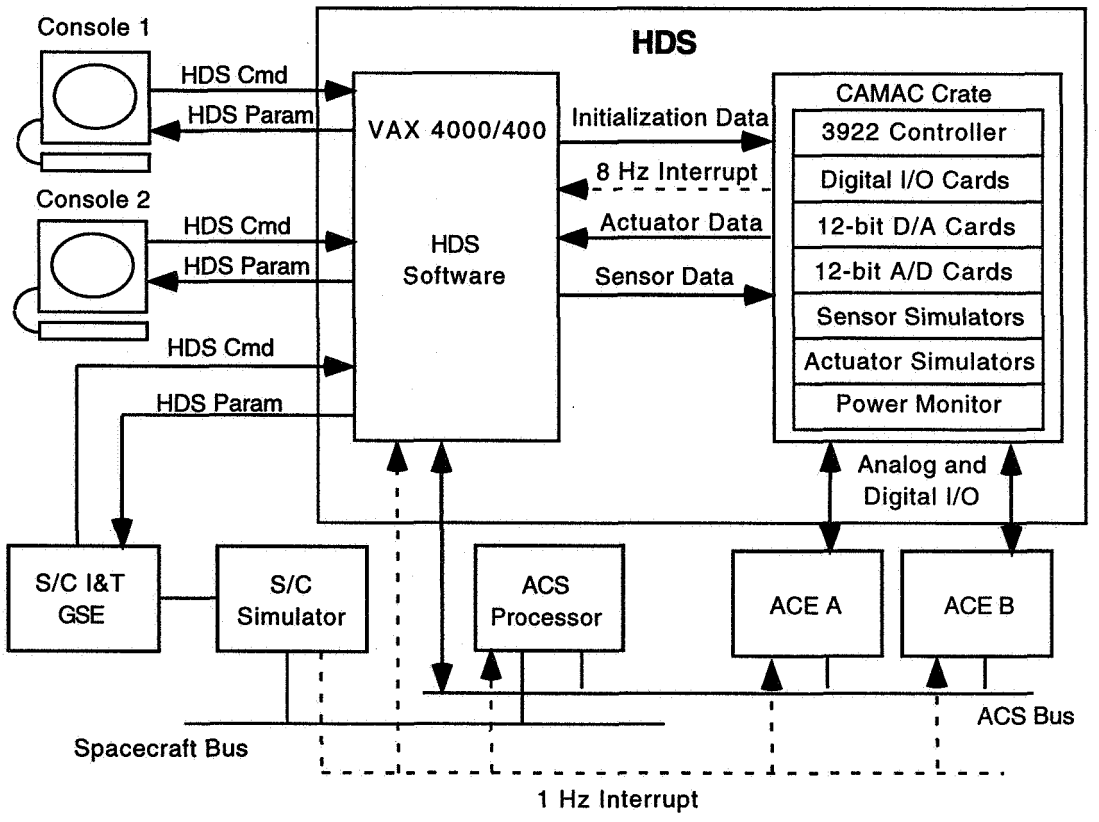

Figure 4 HDS Setup

Eight tests were run to verify that the Kalman filter algorithm and the interfaces to the original software met requirements. The top level requirement was to determine the spacecraft attitude to 0.7° per axis, 3σ. In addition, the top level TRMM ACS requirements still had to be met, including acquiring mission attitude and performing yaw maneuvers. Some of the tests were run to verify the new FDC, and other tests were run to determine system response to FSW restarts. In all cases, the FSW passed the tests.

Table 3 Software Requirements Tested

Test Name	Goals
cont1	overall system functionality start filter in sun acquisition acquire mission attitude
cont2	overall system functionality ESA to Kalman filter in mission mode,return to ESA control TAM-only filter performance
cont3	yaw maneuver performance
cont4	start filter in CERES cal mode transition to mission
cont5	covariance divergence FDC
contfdc	go to sun acq goto ACE B, then SA if mission acq times out
cont6	software response to warm restarts software response to cold restarts TDRS tracking no wheel saturation
cont7	PD control in yaw maneuvers

In addition to the HDS real-time, hardware in the loop simulations, a software-only high fidelity simulation (HIFI) written in FORTRAN was run to provide independent verification of the flight software. The same initial conditions were applied to in both simulation runs. An Enhanced TRIAD algorithm is used to determine inertial attitude in the Sun Acquire mode [2]. The HDS run started in Sun Acquire mode and stayed there until the Enhanced TRIAD quaternion was converged. Once this occurred, the Kalman filter was started with the initial Kalman filter quaternion set equal to the current Enhanced TRIAD quaternion. After about 2200 seconds, the Kalman filter was reinitialized, and TRMM was commanded to acquire mission attitude after the Kalman filter had converged (about 1500 seconds). In the HIFI simulation, the filter was commanded on only once, at the reinitialization time of the HDS run. After one orbit in mission mode, a 180° yaw maneuver was commanded. The filter maintained a good attitude and gyro bias estimate throughout the maneuver. The spacecraft was then allowed to settle out until the end of the run.

Results

The performance testing of the Kalman filter was done on the HDS simulator. Software verification, determining if the algorithm is executing as expected, was done by comparing the HIFI outputs to the HDS outputs. If the results are in agreement, then the algorithm is executing as expected. The HDS run and the HIFI run had noisy sensors, biased IRUs, and both low frequency and high frequency errors in the magnetic field model. There were no biases in either the DSS or the TAM measurements.

The Kalman filter algorithm can meet the contingency attitude determination requirement of 0.7° per axis, as shown in Figure 5. The magnitude of the quaternion estimation error is shown in Figure 6. The periods of large estimation errors occurs during acquisition slews (before 5000 seconds) or during the yaw maneuver (centered around 12,000 seconds), when the attitude control errors are large.

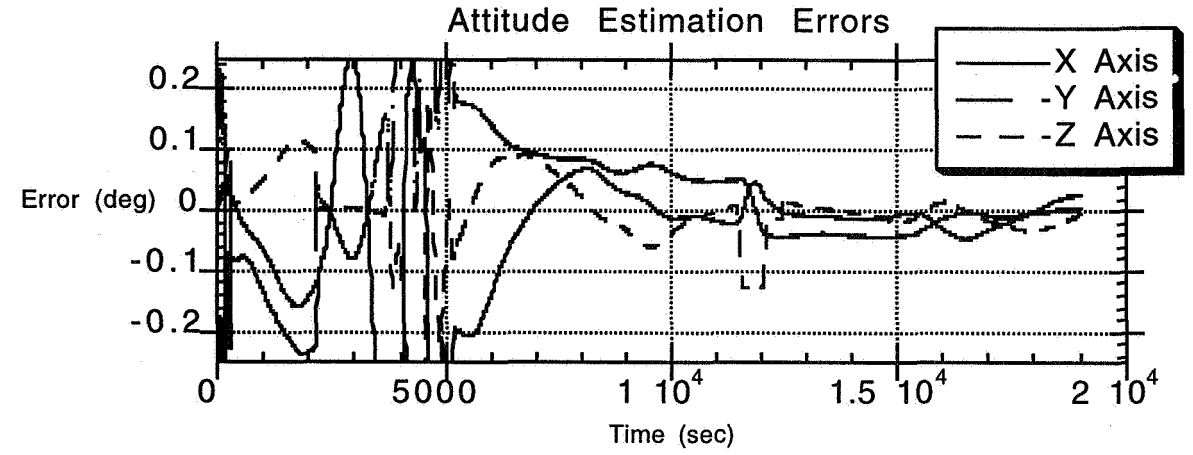

Figure 5

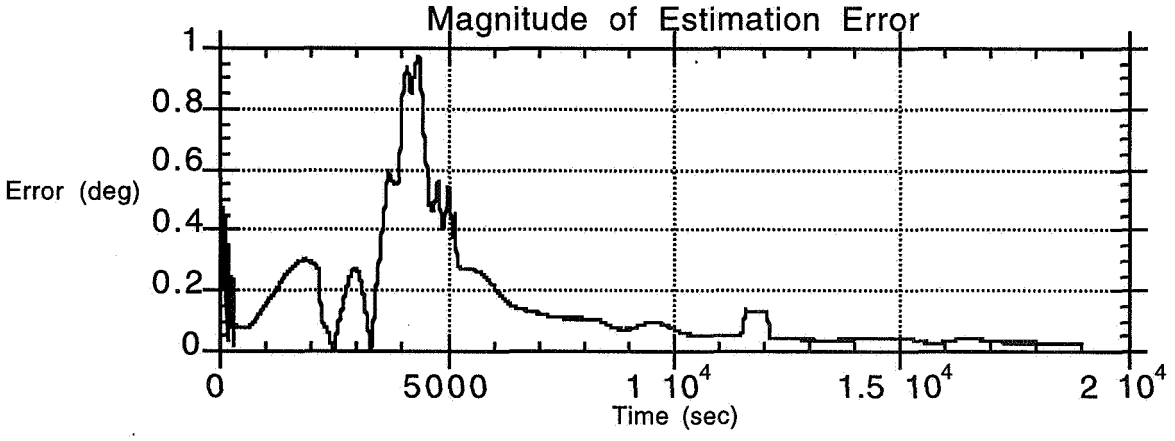

Figure 6

Figure 7 shows that the two simulations exhibit comparable control error. The HDS-only control error data is shown in Figure 8. The large control errors before 5000 seconds occur before the spacecraft has acquired mission attitude. The transients at 12,000 to 14,000 seconds are due to the start and end of the yaw maneuvers, when spacecraft rates are changing rapidly.

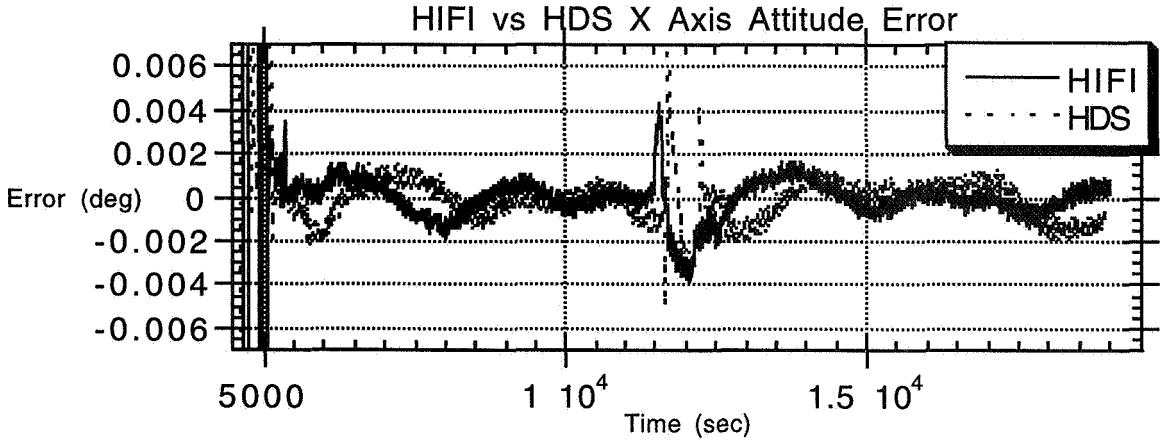

Figure 7

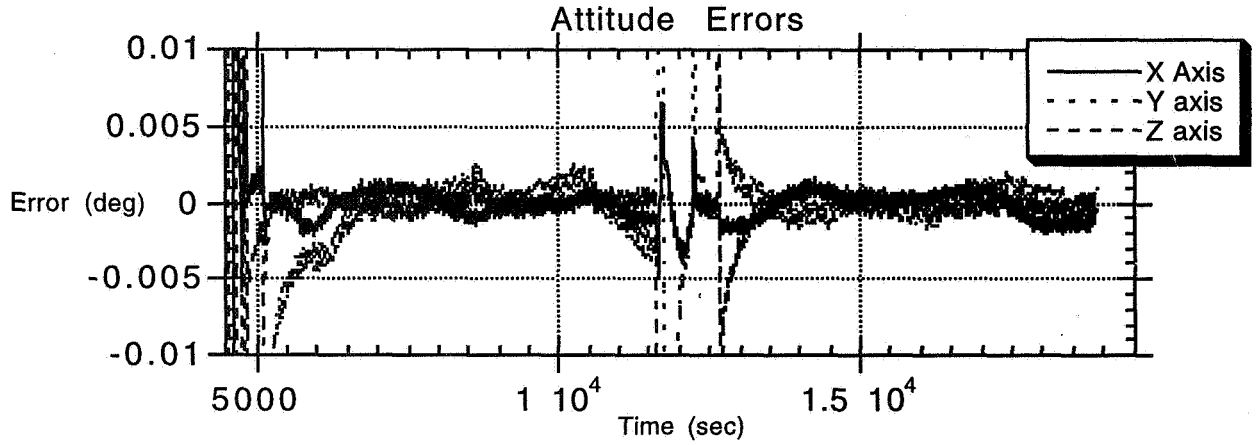

Figure 8

The HDS gyro bias estimation also compared favorably to the HIFI estimation, as shown in Figure 9. The inital transient differences are due to slightly different initial conditions, and the reinitialization of the HDS Kalman filter. Only the HDS bias estimation is shown in Figure 10.

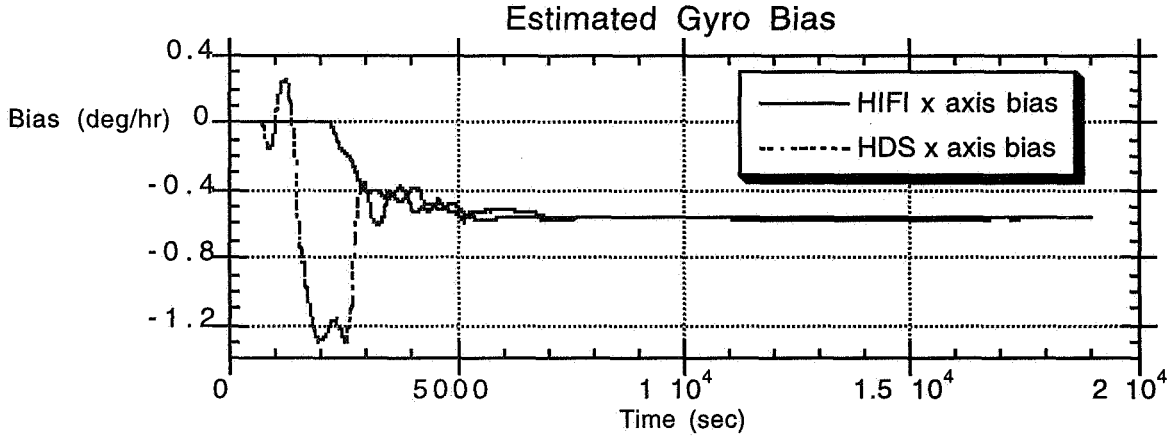

Figure 9

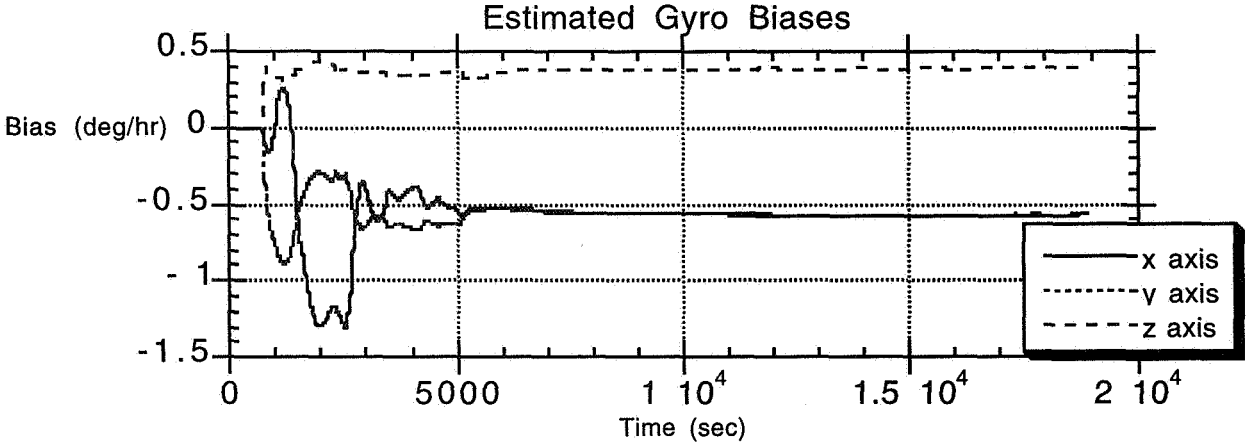

Figure 10

A measure of the Kalman filter's performance is the value of either the covariance or the standard deviation of the states. The attitude standard deviations start out large to cover initial estimation errors, but they converge to less than 0.015° about 2800 seconds after reinitialization, as seen in Figure 11. The sinusoidal motion of the deviation is due to the sun vector moving in the body as TRMM orbits. The y axis deviation is more constant because that spacecraft axis is generally perpendicular to the sunline at all times, but it increases during eclipse, when the TAM is the only update sensor, and it increases when the spacecraft is facing away from the sun. The gyro bias estimation converges much slower than the attitude estimate: about 5000 seconds is needed after reinitialization to converge to within 0.005 °/hr (see Figure 12).

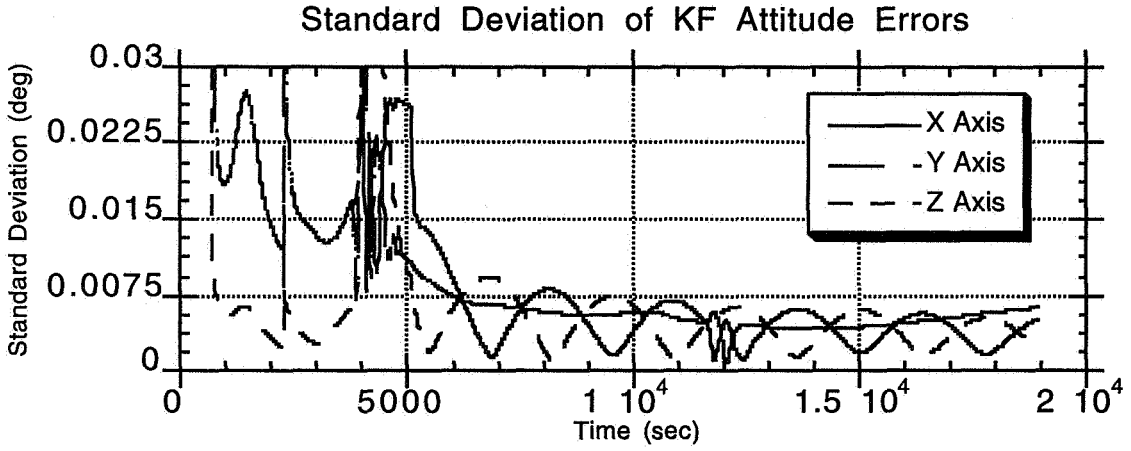

Figure 11

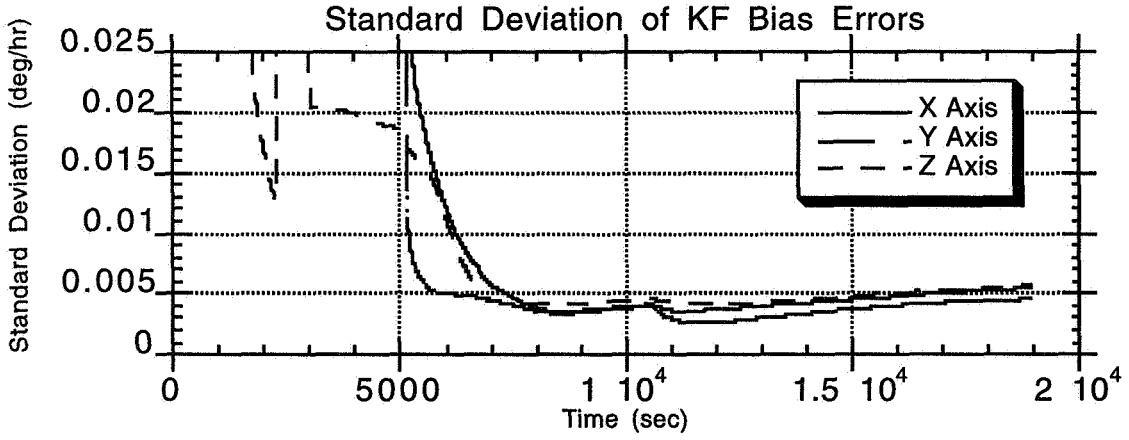

Conclusion

The design, implementation, and testing of the TRMM Kalman filter was presented in this paper. This contingency attitude determination algorithm meets the requirements established for accuracy, and does not affect the original performance of the flight software. The modular nature of the flight software allowed the Kalman filter to be implemented in a straightforward manner into previously tested code. The addition of this algorithm enables good science return in the event of an ESA failure on TRMM.

References

[1] D. Ward, memo, "TRMM ACS Peer Review Action Items Regarding Earth Sensor Assembly Concerns", August 18, 1992.

[2] J. L. Crassidis, S. F. Andrews, F. L. Markley, K. Ha, "Contingency Designs for Attitude Determination of TRMM", FMET Symposium - 1995.

[3] Gelb, A., ed., *Applied Optimal Estimation*, The MIT Press, Cambridge, 1974.

[4] Murrell, J. W., "Precision Attitude Determination for Multimission Spacecraft, "AIAA Paper 78-1248, Aug. 1978.

[5] Farrenkopf, R. L.,"Analytic Steady-State Accuracy Solutions for Two Common Spacecraft Attitude Estimators," *Journal of Guidance and Control*, Vol. 1, July-Aug. 1978, pp.282-284.

[6] Lefferts, E. J., Markley, F. L., and Shuster, M. D., "Kalman Filtering for Spacecraft Attitude Estimation," AIAA Paper 82-0070R, Sept. 1982.

[7] Papoulis, A., *Probability, Random Variables, and Stochastic Processes*, McGraw-Hill, New York, 1984.

[8] Friedland, B., *Control System Design*, McGraw-Hill, New York, 1986.

Page intentionally left blank

Innovative Educational Aerospace Research

at the

Northeast High School

Space Research Center

Audra Luyet

SPARC Student Representative

Northeast Aerospace Magnet School

Anthony Matarazzo

Director of SPARC

Northeast Aerospace Magnet School

David Folta

Flight Dynamics Division

Goddard Space Flight Center, NASA

Abstract

Northeast High Magnet School of Philadelphia, Pennsylvania is a proud sponsor of the Space Research Center (SPARC). SPARC, a model program of the Medical, Engineering, and Aerospace Magnet school, provides talented students the capability to successfully exericse full simulations of NASA manned missions. These simulations included low-Earth Shuttle missions and Apollo lunar missions in the past, and will focus on a planetary mission to Mars this year. At the end of each scholastic year, a simulated mission, lasting between one and eight days, is performed involving 75 students as specialists in seven teams. The groups are comprised of Flight Management, Spacecraft Communications (SatCom), Computer Networking, Spacecraft Design and Engineering, Electronics, Rocketry, Robotics, and Medical teams in either the mission operations center or onboard the spacecraft. Software development activities are also required in support of these simulations.

The objective of this paper is to present the accomplishments, technology innovations, interactions, and an overview of SPARC with an emphasis on how the program's educational activities parallel NASA mission support and how this education is preparing student for the space frontier.

Mission

The mission of Project SPARC is to promote(encourage) the development of leaders dedicated to the extention of mankind's grasp beyond that of planet Earth by educating students with interest in medical fields, computer programming, electronics, designing and engineering, flight management, rocketry, and robotics. Project SPARC provides practical, hands-on experience for students in their individual fields of interest. The teamwork and cooperation

intrinsic to the success of the program reflect the maturity and personal development acquired by involved students.

The History of Project SPARC

Project Space Research Center (SPARC) originated in late 1962 by Mr. Robert A. J. Montgomery and interested students. They called it Project Space Research Capsule. SPARC was recognized by the Federal Government as the first program of its kind ever attempted. The students were hand picked, and academics were of the utmost importance. There was one basic rule; the project mentors could answer questions and give advice, but all ideas had to be the students' originals.

The students united to test build a three-man capsule simulator to test the studied methods of handling space problems and space existence. At a time when NASA had barely begun their trek in space, these high school students were innovative and adventurous.

The project began with three steps:

1. the construction of a full scale mock-up and ground control system housed together in one unit called "Systems Evaluation Facility"
2. a continuous research and development program utilizing the Facility in order to perfect and integrate various functions
3. the actual building and testing of the fully equipped capsule which was in a gimbal and housed under a planetarium dome for circumlunar simulation.

Interest in Project SPARC was stimulated in industry and the School District Administration. With the help of a grant from the Southeastern Pennsylvania Heart Association, the program purchased electronic equipment and began a study in flight control instrumentation. Project SPARC was so highly recognized for its work that, during the summer of 1963, the National Aeronautics and Space Administration (NASA) invited 18 SPARC students to tour the Marshall Space Flight Center, Manned Spacecraft Ceter, Cape Canaveral, and the Goddard Space Flight Center.

By the end of 1963, the students had designed a simulated capsule and control area, and construction began on a wing of the stage at Northeast High School, Philadelphia, PA. The Home and School Association and the Alumni Association made many contributions to aid SPARC. In early May of 1964, the first capsule test took place. The chamber was constructed as a closed oxygen-replenishment system.

SPARC has attempted several simulations in a few different simulators to the moon, orbits around the earth, and now to Mars. The students of Project SPARC have always remained basically the same though, in that they are bright, young, motivated teenagers interested in making a difference. Project SPARC operates with approximately sixty-five students classified as full-time members. These students have regular responsibilities in the areas of their specialities and operate all research activities.

From the relatively large number of students in all of SPARC, approximetely nine students are chosen as astronaut candidates. After rigorous psychological, physical testing, examinations, and pre-flight tests, three students are then picked as astronauts for the main flight as the culminating product of the year. For the SPARC year of 1996-1997, the students have decided to have a 48-hour flight to Mars.

A Mission to Mars--

Our Plans for the 1997

In late May of 1997, SPARC will hold its annual culminating effort, a space craft simulated mission, though this year the effort will be considerably more innovative than the past few years. For the past several years, the project has paralleled its program to NASA's by simulating space shuttle missions, though with NASA's new contract with (?)Lockheed(?) and the recent suspection of life on Mars, it seems that this simulation is rather outdated. Therefore,

SPARC will design and carry out a simulated manned mission to Mars. The group chose Mars for several reasons:

-Mars is the nearest planet that astronauts can explore

-About 4 billion years ago, Mars seems to have had an Earth-like climate, with rivers, lakes, and perhaps even oceans. This would enable much study.

-Mars is a planet much like Earth and much thought and creativity is needed to travel there.

Experiments that are planned for the mission are:

-the psychological effects on the astronauts over a mission with such a long endurance. These include memory, maze tracing, and sentence completion tests.

-crystal growth in space

-the physical effects on the astronauts

-an yet undertermined physics experiment

SPARC/NASA

'The young technician listened intently to the voice in his headset as his eyes scanned the silver board jammed with buttons and flashing lights, then barked, "One, two, three, roll, Gary... keep going, that's it, that's it."

Behind him, a dozen young men and women were grouped around an impressive display of other flashing boards, television monitiors and computer terminals. On a well above the control center, panormic views of Earth could be seen as a rocket propelled itself toward the heavens.

The space shuttle had just separated from its rocket. Inside the shuttle, three astronauts were receiving detailed instructions from command central.

No, it wasn't Cape Kennedy or the Houston Space Center. It was all happening at Philadelphia's own Northeast High School, the culmination of a year's work by students in Project SPARC (Space Research Center).'

Philadelphia Daily News

May 13, 1983

Project Space Research Center is consistently on the cutting edge. In the 1960's, the students simulated missions to the moon before NASA's astronauts had ever touched the satellite's surface. They theorized many ideas of their own and recieved advice from mentors at NASA and other affiliated institutions. When space science was an uncharted world to the adult scientists of NASA, it was also an uncharted world to the student scientists of Project SPARC. Now, as rocket scientists are preparing ideas on how humans may get to Mars, high school students at Northeast High School are doing the same.

Students involved in the project truly become excited at the prospect of space exploration. Just like at NASA, each small group plays a huge part in the major goal. Without one group's expertise, an entire project could go to waste. Flight Management trains the astronauts by teaching proper radio transmission skills, functions of the craft, and among other things, mission control leadership. The Medical Group becomes liscensed in first aid and CPR, and learns what to do if an emergency should arise while carrying out a simulation. The Rocketry Group learns how to build rockets, while SatCom learns Ham Radio transmission and is attempting an effort to be able to communicate with the astronauts and cosmonauts on Mir. The Designing and Engineering Group makes intricate plans of what the craft will look like, and then builds it. The Robotics Group builds robots that enter several competitions. This year, one of their robots may be sent to Mars. Also there is Administrative Assistance which acts as a managerial team, keeping track of all paper work, and the Electronics Group takes care of the wiring system of the command control center and the simulator. The Computer Networking group pulls all of the work from each group together to make a simulated flight program. These

students are responsible for creating the intricate program that the astronauts will "fly" during the simulated mission. Without this program, there would be no mission. Just like NASA, there are leaders that run SPARC. These managers are responsible for ensuring that the members of SPARC learn and understand what they are taught, and for ensuring that a flight is carried out.

Project SPARC provides practical, hands-on experience for students in their individual fields of interest. Moreover, the teamwork and cooperation intrinsic to the success of the program reflect the maturity and personal development acquired by involved students. The students of Project SPARC, in addition to all of the basic knowlege that they accumulate, learn that working as a team is the most important thing to remember when working on any project, and this is a lesson that they will carry with them through life.

REPORT DOCUMENTATION PAGE

Form Approved
OMB No. 0704-0188

1. AGENCY USE ONLY *(Leave blank)*	2. REPORT DATE	3. REPORT TYPE AND DATES COVERED
	May 1997	Conference Publication/May 19-21, 1997

4. TITLE AND SUBTITLE

Flight Mechanics Symposium 1997

5. FUNDING NUMBERS

Code 550

6. AUTHOR(S)

Donna Walls, Editor

7. PERFORMING ORGANIZATION NAME(S) AND ADDRESS (ES)

Goddard Space Flight Center
Greenbelt, Maryland

8. PEFORMING ORGANIZATION REPORT NUMBER

97B00008

9. SPONSORING / MONITORING AGENCY NAME(S) AND ADDRESS (ES)

National Aeronautics and Space Administration
Washington, DC 20546-0001

10. SPONSORING / MONITORING AGENCY REPORT NUMBER

NASA CP-3345

11. SUPPLEMENTARY NOTES

Walls: Attitude Section, Flight Dynamics Support Branch, Goddard Space Flight Center, Greenbelt, Maryland

12a. DISTRIBUTION / AVAILABILITY STATEMENT

Unclassified - Unlimited
Subject Category 13

Availability: NASA CASI (301) 621-0390.

12b. DISTRIBUTION CODE

13. ABSTRACT *(Maximum 200 words)*

This conference publication includes papers and abstracts presented at the Flight Mechanics Symposium on May 19 - 21, 1997. Sponsored by the Flight Dynamics Division of Goddard Space Flight Center, this symposium featured technical papers on a wide range of issues related to orbit-attitude prediction, determination, and control; attitude sensor calibration; attitude determination error analysis; attitude dynamics; and orbit decay and maneuver strategy. Government, industry, and the academic community participated in the preparation and presentation of these papers.

14. SUBJECT TERMS

Flight Mechanics, Attitude Determination, Mission Analysis, Spacecraft Dynamics, Orbit Determination

15. NUMBER OF PAGES

492

16. PRICE CODE

17. SECURITY CLASSIFICATION OF REPORT	18. SECURITY CLASSIFICATION OF THIS PAGE	19. SECURITY CLASSIFICATION OF ABSTRACT	20. LIMITATION OF ABSTRACT
Unclassified	Unclassified	Unclassified	UL